

# Quantitative imaging (QI) and artificial intelligence (AI) in cardiovascular diseases

**Edited by**

Sebastian Kelle, Rene M. Botnar, Marcus R. Makowski, Daniel Rueckert and Alexander Meyer

**Published in**

Frontiers in Cardiovascular Medicine



## FRONTIERS EBOOK COPYRIGHT STATEMENT

The copyright in the text of individual articles in this ebook is the property of their respective authors or their respective institutions or funders. The copyright in graphics and images within each article may be subject to copyright of other parties. In both cases this is subject to a license granted to Frontiers.

The compilation of articles constituting this ebook is the property of Frontiers.

Each article within this ebook, and the ebook itself, are published under the most recent version of the Creative Commons CC-BY licence. The version current at the date of publication of this ebook is CC-BY 4.0. If the CC-BY licence is updated, the licence granted by Frontiers is automatically updated to the new version.

When exercising any right under the CC-BY licence, Frontiers must be attributed as the original publisher of the article or ebook, as applicable.

Authors have the responsibility of ensuring that any graphics or other materials which are the property of others may be included in the CC-BY licence, but this should be checked before relying on the CC-BY licence to reproduce those materials. Any copyright notices relating to those materials must be complied with.

Copyright and source acknowledgement notices may not be removed and must be displayed in any copy, derivative work or partial copy which includes the elements in question.

All copyright, and all rights therein, are protected by national and international copyright laws. The above represents a summary only. For further information please read Frontiers' Conditions for Website Use and Copyright Statement, and the applicable CC-BY licence.

ISSN 1664-8714  
ISBN 978-2-8325-2370-4  
DOI 10.3389/978-2-8325-2370-4

## About Frontiers

Frontiers is more than just an open access publisher of scholarly articles: it is a pioneering approach to the world of academia, radically improving the way scholarly research is managed. The grand vision of Frontiers is a world where all people have an equal opportunity to seek, share and generate knowledge. Frontiers provides immediate and permanent online open access to all its publications, but this alone is not enough to realize our grand goals.

## Frontiers journal series

The Frontiers journal series is a multi-tier and interdisciplinary set of open-access, online journals, promising a paradigm shift from the current review, selection and dissemination processes in academic publishing. All Frontiers journals are driven by researchers for researchers; therefore, they constitute a service to the scholarly community. At the same time, the *Frontiers journal series* operates on a revolutionary invention, the tiered publishing system, initially addressing specific communities of scholars, and gradually climbing up to broader public understanding, thus serving the interests of the lay society, too.

## Dedication to quality

Each Frontiers article is a landmark of the highest quality, thanks to genuinely collaborative interactions between authors and review editors, who include some of the world's best academicians. Research must be certified by peers before entering a stream of knowledge that may eventually reach the public - and shape society; therefore, Frontiers only applies the most rigorous and unbiased reviews. Frontiers revolutionizes research publishing by freely delivering the most outstanding research, evaluated with no bias from both the academic and social point of view. By applying the most advanced information technologies, Frontiers is catapulting scholarly publishing into a new generation.

## What are Frontiers Research Topics?

Frontiers Research Topics are very popular trademarks of the *Frontiers journals series*: they are collections of at least ten articles, all centered on a particular subject. With their unique mix of varied contributions from Original Research to Review Articles, Frontiers Research Topics unify the most influential researchers, the latest key findings and historical advances in a hot research area.

Find out more on how to host your own Frontiers Research Topic or contribute to one as an author by contacting the Frontiers editorial office: [frontiersin.org/about/contact](https://frontiersin.org/about/contact)

# Quantitative imaging (QI) and artificial intelligence (AI) in cardiovascular diseases

## Topic editors

Sebastian Kelle — German Heart Center Berlin, Germany

Rene M. Botnar — King's College London, United Kingdom

Marcus R. Makowski — Technical University of Munich, Germany

Daniel Rueckert — Technical University of Munich, Germany

Alexander Meyer — Department for Cardiovascular and Thoracic Surgery, German Heart Center Berlin, Germany

## Citation

Kelle, S., Botnar, R. M., Makowski, M. R., Rueckert, D., Meyer, A., eds. (2023).

*Quantitative imaging (QI) and artificial intelligence (AI) in cardiovascular diseases.*

Lausanne: Frontiers Media SA. doi: 10.3389/978-2-8325-2370-4

# Table of contents

- 05 **DeepStrain: A Deep Learning Workflow for the Automated Characterization of Cardiac Mechanics**  
Manuel A. Morales, Maaïke van den Boomen, Christopher Nguyen, Jayashree Kalpathy-Cramer, Bruce R. Rosen, Collin M. Stultz, David Izquierdo-Garcia and Ciprian Catana
- 21 **Respiratory Motion-Registered Isotropic Whole-Heart T<sub>2</sub> Mapping in Patients With Acute Non-ischemic Myocardial Injury**  
Karolina Dorniak, Lorenzo Di Sopra, Agnieszka Sabisz, Anna Glinska, Christopher W. Roy, Kamil Gorczewski, Davide Piccini, Jérôme Yerly, Hanna Jankowska, Jadwiga Fijałkowska, Edyta Szurowska, Matthias Stuber and Ruud B. van Heeswijk
- 33 **Randomized Trial of Anti-inflammatory Medications and Coronary Endothelial Dysfunction in Patients With Stable Coronary Disease**  
Allison G. Hays, Michael Schär, Gabriele Bonanno, Shenghan Lai, Joseph Meyer, Yohannes Afework, Angela Steinberg, Samuel Stradley, Gary Gerstenblith and Robert G. Weiss
- 43 **Myocardial Perfusion Imaging After Severe COVID-19 Infection Demonstrates Regional Ischemia Rather Than Global Blood Flow Reduction**  
George D. Thornton, Abhishek Shetye, Dan S. Knight, Kris Knott, Jessica Artico, Hibba Kurdi, Souhad Yousef, Dimitra Antonakaki, Yousuf Razvi, Liza Chacko, James Brown, Rishi Patel, Kavitha Vimalasvaran, Andreas Seraphim, Rhodri Davies, Hui Xue, Tushar Kotecha, Robert Bell, Charlotte Manisty, Graham D. Cole, James C. Moon, Peter Kellman, Marianna Fontana and Thomas A. Treibel
- 54 **Implementing Machine Learning in Interventional Cardiology: The Benefits Are Worth the Trouble**  
Walid Ben Ali, Ahmad Pesaraghader, Robert Avram, Pavel Overtchouk, Nils Perrin, Stéphane Laffite, Raymond Cartier, Reda Ibrahim, Thomas Modine and Julie G. Hussin
- 74 **Artificial Intelligence in Cardiac MRI: Is Clinical Adoption Forthcoming?**  
Anastasia Fotaki, Esther Puyol-Antón, Amedeo Chiribiri, René Botnar, Kuberan Pushparajah and Claudia Prieto
- 87 **SGLT2 Inhibition in HFpEF. Do We Need More Quantitative and Load Independent Metrics to Understand the Results of the EMPEROR-Preserved Trial?**  
Grigorios Korosoglou, Sorin Giusca and Sebastian Kelle
- 90 **Cardiac MR: From Theory to Practice**  
Tevfik F. Ismail, Wendy Strugnell, Chiara Coletti, Maša Božić-Iven, Sebastian Weingärtner, Kerstin Hammernik, Teresa Correia and Thomas Küstner

- 129 **Automatic Detection of Secundum Atrial Septal Defect in Children Based on Color Doppler Echocardiographic Images Using Convolutional Neural Networks**  
Wenjing Hong, Qiuyang Sheng, Bin Dong, Lanping Wu, Lijun Chen, Leisheng Zhao, Yiqing Liu, Junxue Zhu, Yiman Liu, Yixin Xie, Yizhou Yu, Hansong Wang, Jiajun Yuan, Tong Ge, Liebin Zhao, Xiaoqing Liu and Yuqi Zhang
- 142 **Imaging Assessment of Endothelial Function: An Index of Cardiovascular Health**  
Anum S. Minhas, Erin Goerlich, Mary C. Corretti, Armin Arbab-Zadeh, Sebastian Kelle, Thorsten Leucker, Amir Lerman and Allison G. Hays
- 155 **Regional Fat Distributions Are Associated With Subclinical Right Ventricular Dysfunction in Adults With Uncomplicated Obesity**  
Jing Liu, Jing Li, Jianqun Yu, Chunchao Xia, Huaxia Pu, Wenzhang He, Xue Li, Xiaoyue Zhou, Nanwei Tong and Liqing Peng
- 167 **Left Heart Chamber Volumetric Assessment by Automated Three-Dimensional Echocardiography in Heart Transplant Recipients**  
Yiwei Zhang, Chun Wu, Wei Sun, Shuangshuang Zhu, Yanting Zhang, Yuji Xie, Ye Zhu, Zisang Zhang, Yang Zhao, Yuman Li, Mingxing Xie and Li Zhang
- 181 **High-Resolution Free-Breathing Quantitative First-Pass Perfusion Cardiac MR Using Dual-Echo Dixon With Spatio-Temporal Acceleration**  
Joao Tourais, Cian M. Scannell, Torben Schneider, Ebrahim Alskaf, Richard Crawley, Filippo Bosio, Javier Sanchez-Gonzalez, Mariya Doneva, Christophe Schülke, Jakob Meineke, Jochen Keupp, Jouke Smink, Marcel Breeuwer, Amedeo Chiribiri, Markus Henningsson and Teresa Correia
- 191 **Radiomics and Machine Learning for Detecting Scar Tissue on CT Delayed Enhancement Imaging**  
Hugh O'Brien, Michelle C. Williams, Ronak Rajani and Steven Niederer
- 199 **Deep Learning for Detection of Exercise-Induced Pulmonary Hypertension Using Chest X-Ray Images**  
Kenya Kusunose, Yukina Hirata, Natsumi Yamaguchi, Yoshitaka Kosaka, Takumasa Tsuji, Jun'ichi Kotoku and Masataka Sata
- 208 **Deep learning-based end-to-end automated stenosis classification and localization on catheter coronary angiography**  
Chao Cong, Yoko Kato, Henrique Doria De Vasconcellos, Mohammad R. Ostovaneh, Joao A. C. Lima and Bharath Ambale-Venkatesh



# DeepStrain: A Deep Learning Workflow for the Automated Characterization of Cardiac Mechanics

Manuel A. Morales<sup>1,2</sup>, Maaïke van den Boomen<sup>1,3,4</sup>, Christopher Nguyen<sup>1,4</sup>, Jayashree Kalpathy-Cramer<sup>1</sup>, Bruce R. Rosen<sup>1,2</sup>, Collin M. Stultz<sup>2,5,6</sup>, David Izquierdo-Garcia<sup>1,2†</sup> and Ciprian Catana<sup>1\*†</sup>

## OPEN ACCESS

### Edited by:

Rene M. Botnar,  
King's College London,  
United Kingdom

### Reviewed by:

Anastasia Nasopoulou,  
King's College London,  
United Kingdom  
Fahmi Khalifa,  
Mansoura University, Egypt

### \*Correspondence:

Ciprian Catana  
ccatana@mgh.harvard.edu

<sup>†</sup>These authors share  
senior authorship

### Specialty section:

This article was submitted to  
Cardiovascular Imaging,  
a section of the journal  
Frontiers in Cardiovascular Medicine

**Received:** 24 June 2021

**Accepted:** 10 August 2021

**Published:** 03 September 2021

### Citation:

Morales MA, van den Boomen M,  
Nguyen C, Kalpathy-Cramer J,  
Rosen BR, Stultz CM,  
Izquierdo-Garcia D and Catana C  
(2021) DeepStrain: A Deep Learning  
Workflow for the Automated  
Characterization of Cardiac  
Mechanics.  
Front. Cardiovasc. Med. 8:730316.  
doi: 10.3389/fcvm.2021.730316

<sup>1</sup> Department of Radiology, Athinoula A. Martinos Center for Biomedical Imaging, Massachusetts General Hospital and Harvard Medical School, Boston, MA, United States, <sup>2</sup> Harvard-MIT Division of Health Sciences and Technology, Cambridge, MA, United States, <sup>3</sup> Department of Radiology, University Medical Center Groningen, University of Groningen, Groningen, Netherlands, <sup>4</sup> Cardiovascular Research Center, Massachusetts General Hospital and Harvard Medical School, Boston, MA, United States, <sup>5</sup> Department of Electrical Engineering and Computer Science, Massachusetts Institute of Technology, Cambridge, MA, United States, <sup>6</sup> Division of Cardiology, Massachusetts General Hospital, Boston, MA, United States

Myocardial strain analysis from cinematic magnetic resonance imaging (cine-MRI) data provides a more thorough characterization of cardiac mechanics than volumetric parameters such as left-ventricular ejection fraction, but sources of variation including segmentation and motion estimation have limited its wider clinical use. We designed and validated a fast, fully-automatic deep learning (DL) workflow to generate both volumetric parameters and strain measures from cine-MRI data consisting of segmentation and motion estimation convolutional neural networks. The final motion network design, loss function, and associated hyperparameters are the result of a thorough *ad hoc* implementation that we carefully planned specific for strain quantification, tested, and compared to other potential alternatives. The optimal configuration was trained using healthy and cardiovascular disease (CVD) subjects ( $n = 150$ ). DL-based volumetric parameters were correlated ( $>0.98$ ) and without significant bias relative to parameters derived from manual segmentations in 50 healthy and CVD test subjects. Compared to landmarks manually-tracked on tagging-MRI images from 15 healthy subjects, landmark deformation using DL-based motion estimates from paired cine-MRI data resulted in an end-point-error of  $2.9 \pm 1.5$  mm. Measures of end-systolic global strain from these cine-MRI data showed no significant biases relative to a tagging-MRI reference method. On 10 healthy subjects, intraclass correlation coefficient for intra-scanner repeatability was good to excellent ( $>0.75$ ) for all global measures and most polar map segments. In conclusion, we developed and evaluated the first end-to-end learning-based workflow for automated strain analysis from cine-MRI data to quantitatively characterize cardiac mechanics of healthy and CVD subjects.

**Keywords:** cine-MRI, deep learning, segmentation, motion estimation, myocardial strain

## INTRODUCTION

Cardiac mechanics reflects the precise interplay between myocardial architecture and loading conditions that is essential for sustaining the blood pumping function of the heart. The ejection fraction (EF) is often used as a left-ventricular (LV) functional index, but its value is limited when mechanical impairment occurs without an EF reduction (1). Alternatively, tissue tracking approaches for strain analysis provide a more thorough characterization through non-invasive evaluation of myocardial deformation from echocardiography or cinematic magnetic resonance imaging (cine-MRI) data (2), and could be used to identify dysfunction before EF is reduced (3). Unfortunately, various sources of discrepancies have limited the wider clinical applicability of these techniques, including factors related to imaging modality, algorithm, and operator (4). More accurate measures could be obtained from tagging-MRI data widely regarded as the reference standard for strain quantification (5, 6), but use of these data is less common partly due to lack of available analysis tools, whereas echocardiography and cine-MRI data are ubiquitously acquired and analyzed in clinical practice.

Irrespective of algorithm or modality, e.g., speckle tracking for echocardiography or feature tracking for cine-MRI, the main challenge is to estimate motion within regions along the myocardial wall (2). Operator-related discrepancies are introduced when the myocardial wall borders are delineated manually, a time-consuming process that requires considerable expertise and results in significant inter- and intra-observer variability (7, 8). Automatic delineation approaches have been implemented within computational pipelines (9), but other factors related to motion tracking algorithms also influence strain assessment, including the appropriate selection of tuneable parameters whose optimal values can differ between patient cohorts and acquisition protocols [e.g., the size of the search region in block-matching methods (10)]. Further, these algorithms often make assumptions about the properties of the myocardial tissue [e.g., incompressible and elastic (11, 12)], or use registration methods to drive the solution toward an expected geometry. However, recent evidence has shown the validity of these assumptions varies between healthy and diseased myocardium (13, 14), suggesting these approaches may not accurately reflect the underlying biomechanical motion. Modality-related image quality could also complicate interpretation of abnormal strain values since these could reflect either real dysfunction or artifact-related inaccuracies, leading to some degree of subjectivity or non-conclusive results (3).

**Abbreviations:** ACDC, automated cardiac diagnosis challenge; AHA, American heart association; ARV, abnormal right ventricle; CCN, categorical cross-entropy; CMAC, cardiac motion analysis challenge; CarMEN, cardiac motion estimation network; CarSON, cardiac segmentation network; CNN, convolutional neural network; DCM, dilated cardiomyopathy; DL, deep learning; ED, end-diastole; EF, ejection fraction; EPE, end-point error; ES, end-systole; ESS, end-systolic strain; HCM, hypertrophic cardiomyopathy; LV, left-ventricular; LVM, left-ventricular myocardium; MDC, multi-class Dice coefficient; MI, myocardial infarction; MRI, magnetic resonance imaging; MRXCAT, magnetic resonance-extended cardiac-torso; RC, relative change; RV, right-ventricular; SR, strain rate; SRe, early-diastolic strain rate; SRs, systolic strain rate; VCN, ventricular centering network.

Lastly, although automated segmentation and motion tracking commercial software is available for cardiac cine imaging, manual correction of delineated contours used for tracking is often required, resulting in significant variations in strain depending on segmentation procedure and type of commercial software (15).

Deep Learning (DL) methods have demonstrated the advantage of allowing real-world data guide learning of abstract representations that can be used to accomplish pre-specified tasks, and have been shown to be more robust to image artifacts than non-learning techniques for some applications (16, 17). DL segmentation methods have been proposed (18–21) and implemented within strain computational pipelines (22, 23), and recent studies have shown that cardiac motion estimation can also be recast as a learnable problem (24–28). These methods usually consist of an intensity-based loss function and a constrain term (24, 27), the latter using common machine learning techniques [e.g., L2 regularization of all learnable parameters (25)] or direct regularization of the motion estimates [e.g., smoothness penalty (24), anatomy-aware (28)]. However, none of these methods have considered the accuracy of myocardial strain as a design factor or have been applied to strain analysis.

We have recently developed a learning-based method for cardiac motion estimation that produces more accurate estimates than various techniques, including B-spline, diffeomorphic, and mass-preserving algorithms (29), and showed these estimates could potentially be used to detect regional dysfunction. Thus, incorporating our method within a strain analysis framework could potentially enable accurate, user-independent, and quantitative characterization of cardiac mechanics at a both global and regional level. While this framework could be based on echocardiography images (30), these data remain limited for strain mapping tasks by their low reproducibility of acquisition planes (4) and temporal stability of tracking patterns (31). In contrast, cine-MRI offers the most accurate and reproducible assessment of cardiac anatomy and function, thus providing a more thorough set of data for learning-based motion models.

We propose DeepStrain, a fast, automated workflow that derives global and regional strain measures from cine-MRI data by decoupling motion estimation and segmentation tasks. With decoupling, segmentations are not used for motion estimation during inference but rather to derive clinical parameters and to identify a cardiac coordinate system for strain analysis, further reducing the variability in strain directly related to segmentation. Although two-dimensional (2D) convolutional neural networks (CNN) for cardiac motion estimation from cine-MRI have been proposed (24, 26, 28, 32), DeepStrain is the first end-to-end learning based workflow for myocardial strain analysis from cine-MRI. In addition, motion predicted using 2D architectures could be influenced by out-of-plane motion during the cardiac cycle, resulting in overestimation of in-plane motion and reduced reproducibility (33). Instead, this paper describes a carefully designed strain quantification-specific 3D CNN that handles challenges associated with the anisotropic resolution of cine-MRI data. Our loss weighting strategy to find the optimal balance between motion regularization terms also differs from previous methods which have traditionally relied on registration

techniques as indirect measures of motion accuracy (24, 26, 28, 32). Instead, we simulated cine-MRI data with corresponding ground-truth cardiac motion to identify the hyperparameters yielding accurate motion and strain estimates. The optimal trained configuration is online at <https://github.com/moralesq/DeepStrain>. Finally, this paper also provides a comprehensive assessment of the accuracy and repeatability of DeepStrain measures, a task that has been mostly ignored in the deep learning literature but is critical to clinical adoption (4).

## METHODS

### Myocardial Strain Definitions

Strain represents percent change in myocardial length per unit length. The 3D analog for MRI is given by the Green-Lagrange strain tensor

$$\mathbf{E}(t) = \left( \nabla \mathbf{u}(t) + (\nabla \mathbf{u}(t))^T + (\nabla \mathbf{u}(t))^T \nabla \mathbf{u}(t) \right) / 2, \quad (1)$$

where  $\mathbf{u}(t)$  denotes myocardial displacement from a fully-relaxed end-diastolic (ED) phase at  $t = 0$ , to a contracted frame at  $t > 0$ . Radial and circumferential strain are the diagonal components of the tensor  $\mathbf{E}$  evaluated in cylindrical coordinates. *Strain rate* (SR) is the time derivative of (1). The time of acquisition of each frame was extracted from the DICOM and was used to interpolate  $\mathbf{E}(t)$ , such that  $\mathbf{E}(t)$  was defined at every millisecond. The time derivative was then evaluated using central differences and reported as change in strain per second with unit  $s^{-1}$ .

*Global strain* is defined as the average of  $\mathbf{E}$  over the whole LV myocardium (LVM) volume. *Regional strain* is defined as the average of  $\mathbf{E}$  over the volume of specific LVM segments defined by the American Heart Association (AHA) polar map (34), which requires labels of the right ventricle to construct. Specific parameters based on timing and magnitude are extracted from the measures evaluated over a whole cardiac cycle: *end-systolic strain* (ESS), defined as the global strain value at end-systole (ES); *systolic strain rate* (SRs), defined as the peak (i.e., maximum) absolute value of global SR during systole; *early-diastolic strain rate* (SRe), defined as the peak absolute value of global SR during diastole. Although only radial and circumferential strain were analyzed in this study, DeepStrain is also capable of generating shear (Supplementary Section 1). The code used to construct the AHA polar maps is available in the repo online.

### Centering, Segmentation, and Motion Estimation

DeepStrain (Figure 1) consists of a series of CNNs that perform three tasks: a ventricular centering network (VCN) for automated centering and cropping, a cardiac segmentation network (CarSON) to generate tissue labels, and a cardiac motion estimation network (CarMEN) to generate  $\mathbf{u}$ . Estimates of  $\mathbf{u}$  are used to calculate myocardial strain, and segmentations are used to derive volumetric parameters, identify a cardiac coordinate system for strain analysis, and generate tissue labels used for anatomical regularization of motion estimates at training time.

All networks have a common encoder-decoder architecture consisting primarily of convolution, batch normalization (35),

and PReLU (36) layers with residual connections (37). The specific architecture formulation and losses are discussed below and **Supplementary Section 2**.

#### VCN

Let  $V_t$  be a cine-MRI frame at time  $t$  defined over a  $n$ -D domain  $\Omega \subset \mathbb{R}^n$ , and let  $v \in \Omega$ . VCN uses a single-channel array  $V$  with size  $256 \times 256 \times 16$  to generate a single-channel array  $G_{pred}$  of equal size, where  $G_{pred}$  corresponds to a Gaussian distribution with mean defined as the LVM center of mass. This approach models the uncertainty associated with the center location, specially in pathological cases, and enables automated generation of ground-truth labels when manual segmentation of uncropped images is available. VCN was trained using the mean square error (MSE) loss function

$$\mathcal{L}_{MSE}(G_{gt}, G_{pred}) = \frac{1}{|\Omega|} \sum_{v \in \Omega} (G(v) - G_{pred}(v))^2, \quad (2)$$

where  $G_{gt}$  is the ground-truth Gaussian distribution. At inference, the input volume  $V$  is centered and cropped around the voxel with the highest value in  $G_{pred}$  to generate a new cropped array of size  $128 \times 128 \times 16$ , which is then the input to CarSON and CarMEN.

#### CarSON

CarSON is a 2D architecture that uses single-channel images  $V$  of size  $128 \times 128$  to generate a 4-channel segmentation  $M_{pred}$  of equal size, each channel corresponding to a label. We experimented with two different loss functions  $\mathcal{L}_{seg}$  to train CarSON using the manual segmentations  $M_{ms}$ : the pixel-wise categorical cross-entropy (CCE), and a multi-class Dice coefficient (MDC) loss function

$$\mathcal{L}_{MDC}(M_{ms}, M_{pred}) = -\frac{1}{K} \sum_{k=0}^3 2 \frac{|v_{ms}^k \cap v_{pred}^k|}{|v_{ms}^k| + |v_{pred}^k|}, \quad (3)$$

where  $k \in [0, 3]$  represents each of the tissue labels (i.e., background, RV, LVM, and LV), and  $v^k \in M$  denotes all the pixels with label  $k$ .

#### CarMEN

CarMEN estimates the motion  $\mathbf{u}_t$  of the heart from  $V_0$  to  $V_t$ , i.e., for each voxel  $v \in \Omega$ ,  $\mathbf{u}_t(v)$  is an approximation of the myocardial displacement during contraction such that  $V_0(v)$  and  $(\mathbf{u}_t \circ V_t)(v)$  correspond to similar cardiac regions. The operator  $\circ$  refers to application of a spatial transform to  $V_t$  using  $\mathbf{u}_t$  via trilinear interpolation (38). Thus, CarMEN uses a 2-channel input volume consisting of two concatenated arrays with size  $128 \times 128 \times 16$  to generate a 3-channel array  $\mathbf{u}$  of equal size, each channel representing the  $x$ ,  $y$ , and  $z$  components of motion.

Although the current formulation of CarMEN shares some similarities with our previous work, we have made several design modifications that were specific for accurate strain quantification. Here a combination of three loss functions was used for training: first, we used an unsupervised loss function  $\mathcal{L}_{intensity}$



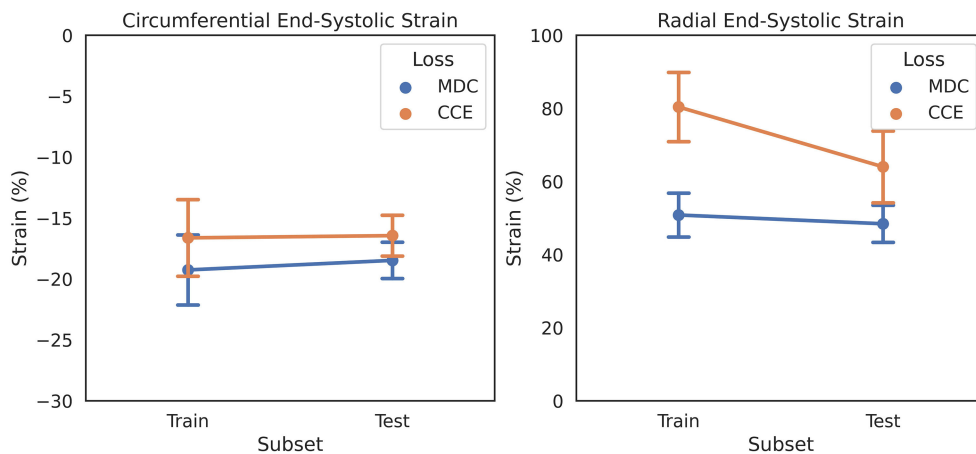


**FIGURE 2 |** Effect of anatomical regularization of motion estimates on strain on the ADCD dataset. Regularization with multiclass dice coefficient (MDC) and categorical crossentropy (CCE) functions result in different strain values in healthy subjects, shown as mean and standard deviation.

256 × 256 × 16 volume grid with 1.25 mm × 1.25 mm in-plane resolution and variable slice thickness (4–7 mm).

## DeepStrain Implementation

For optimization experiments and final model training, all networks were trained in TensorFlow ver. 2.0 with Adam optimizer parameters beta 1, 2 = 0.9, 0.999, random initialization, batchsize = 80 (5 for CarMEN), and learning rate = 1e-4.

### Design of a Strain Quantification-Specific CNN

Reported normal ranges of strain in healthy individuals using non-learning methods vary largely between the different deformation methodologies, limiting the clinical utility of strain measures (4). We used this concept as a heuristic in updating CarMEN, i.e., a useful design should minimize the variation in strain values in healthy individuals. To assess the impact of design choices on this heuristic, we separated the ACDC training set into two group-balanced train and test subsets, each with 50 subjects. We trained CarMEN for 300 epochs using two different layer operation sizes (i.e.,  $3 \times 3 \times k_z$  with  $k_z \in \{1, 3\}$ ), and two different implementations of (5) (i.e., MDC and CCE). With  $k_z = 3$ , comparison of losses showed that CCE leads to increased standard deviation in radial ESS in healthy train ( $n = 10$ ) and test ( $n = 10$ ) subjects, and large differences in the average radial ESS between training and testing sets (Figure 2). Multiple experiments with different regularization parameters showed similar results, and showed that setting  $k_z = 1$  reduces deviations in healthy strain (Supplementary Table 1). Thus, the new CarMEN design used  $3 \times 3 \times 1$  operations and was regularized using the MDC function.

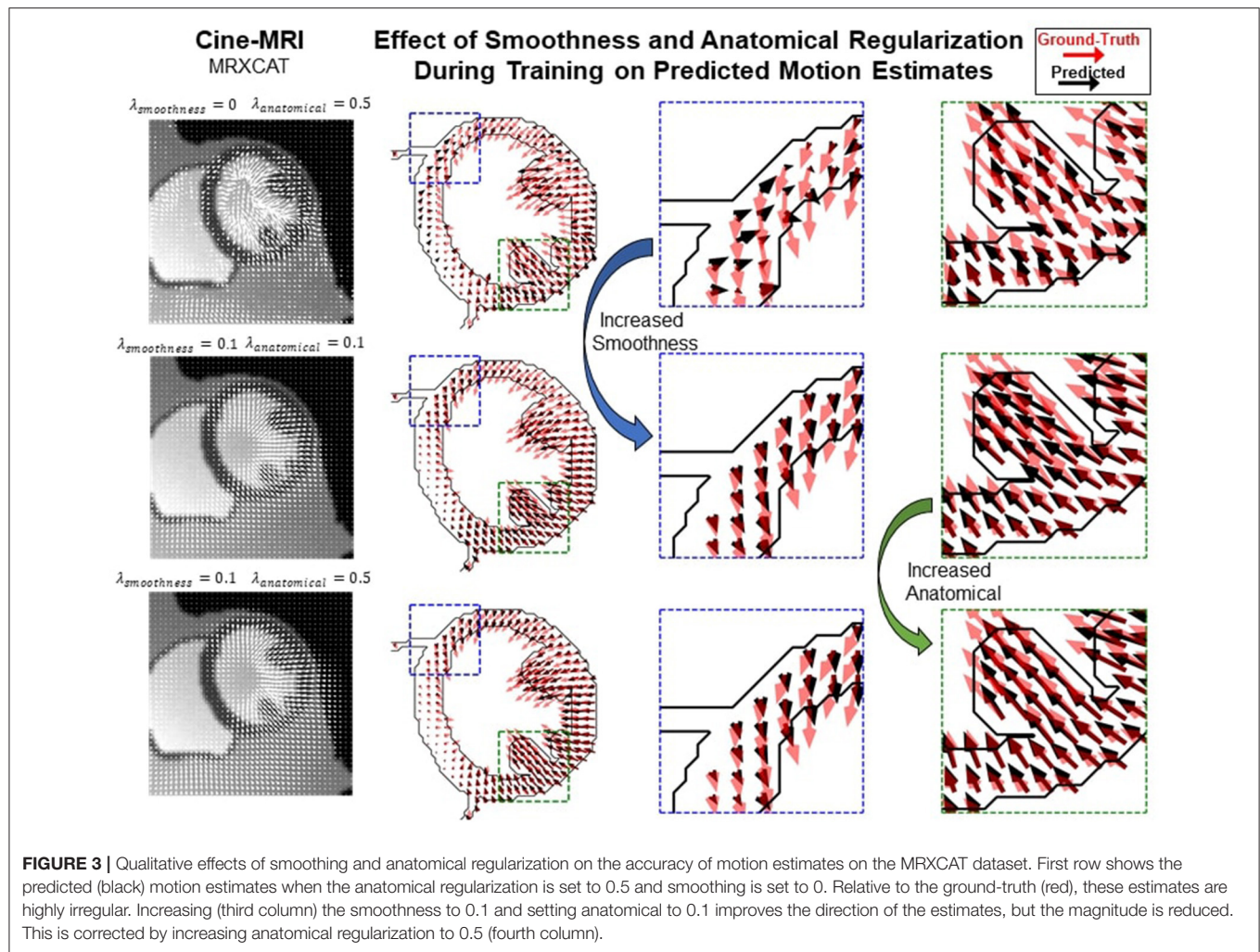
### Novel Loss Weighting Strategy for Accurate Motion and Strain Estimation

Most proposed networks to-date have used registration terms such as (4) and (5) to indirectly assess the accuracy of  $u_t$  on validation or test datasets. However, this approach is prone to

errors since inaccurate and even unrealistic  $u_t$  solutions can minimize these terms. To find an optimal balance between loss terms, we simulated 10 cardiac cine-MRI frames at ED and ES with known ground-truth motion using the MR-extended cardiac-torso (MRXCAT) (43, 44), a software phantom used extensively in imaging studies (45). The motion of the software phantom was modeled using gated patient 4D tagging data, producing highly realistic contracting and twisting motion of the normal heart that can be parameterized to generate population-wide characteristics, as previously described by us (29). We trained CarMEN with various regularization parameters for 300 epochs using 100 subjects from the ACDC training set, and tested the models on the MRXCAT data by evaluating the end-point error between ground-truth and predicted motion estimates within the LVM (Figure 3). Setting  $\lambda_s = 0$  leads to highly irregular motion vectors (e.g., off by more than 90 degrees) relative to ground-truth. Setting the smoothness and anatomical weights to  $\lambda_s = \lambda_a = 0.1$  leads to smoother and better aligned vectors, albeit with a slightly decreased magnitude. Increasing the anatomical weight to  $\lambda_a = 0.5$  further improves the estimates by generating vectors with similar magnitude and orientation to the ground-truth. Quantitative measures of motion accuracy showed similar results across various regularization values, and these changes in motion estimation accuracy were reflected as bias changes in strain values (Figure 4). We found the optimal parameters to be  $\lambda_i = 0.01$ ,  $\lambda_a = 0.5$ ,  $\lambda_s = 0.1$ , which in addition resulted in low strain deviation in healthy subjects as described in the previous section (Supplementary Table 1). Thus, the optimal architecture and hyperparameters were selected based on both the ACDC (i.e., to assess strain deviation in healthy subjects) and XCAT (i.e., to assess motion and strain accuracy).

### Final Model Training

Ground-truth distributions for VCN were created using the manual segmentations. VCN and CarSON were trained using the



ED and ES frames of the train set, as only these included ground-truth segmentations. This provided 200 training samples for VCN and 3200 for CarSON, the latter having more samples since it is a 2D architecture and all frames were resampled to a volume with 16 slices. VCN was tested by five-fold cross-validation, whereas the accuracy of CarSON was assessed by submitting the results to the challenge website. Once CarSON was trained, we generated segmentations of the test set to train CarMEN using the entire ACDC dataset, i.e., 100 subjects from the train set with manual segmentations and 50 from the test set with CarSON-predicted segmentations. Only the ED-ED and ED-ES pairs were used for training. The former pair is useful for the network to learn the identity transformation. Data augmentation included random rotations and translations, random mirroring along the x and y axes, and gamma contrast correction. All data augmentation was performed only in the x-y plane.

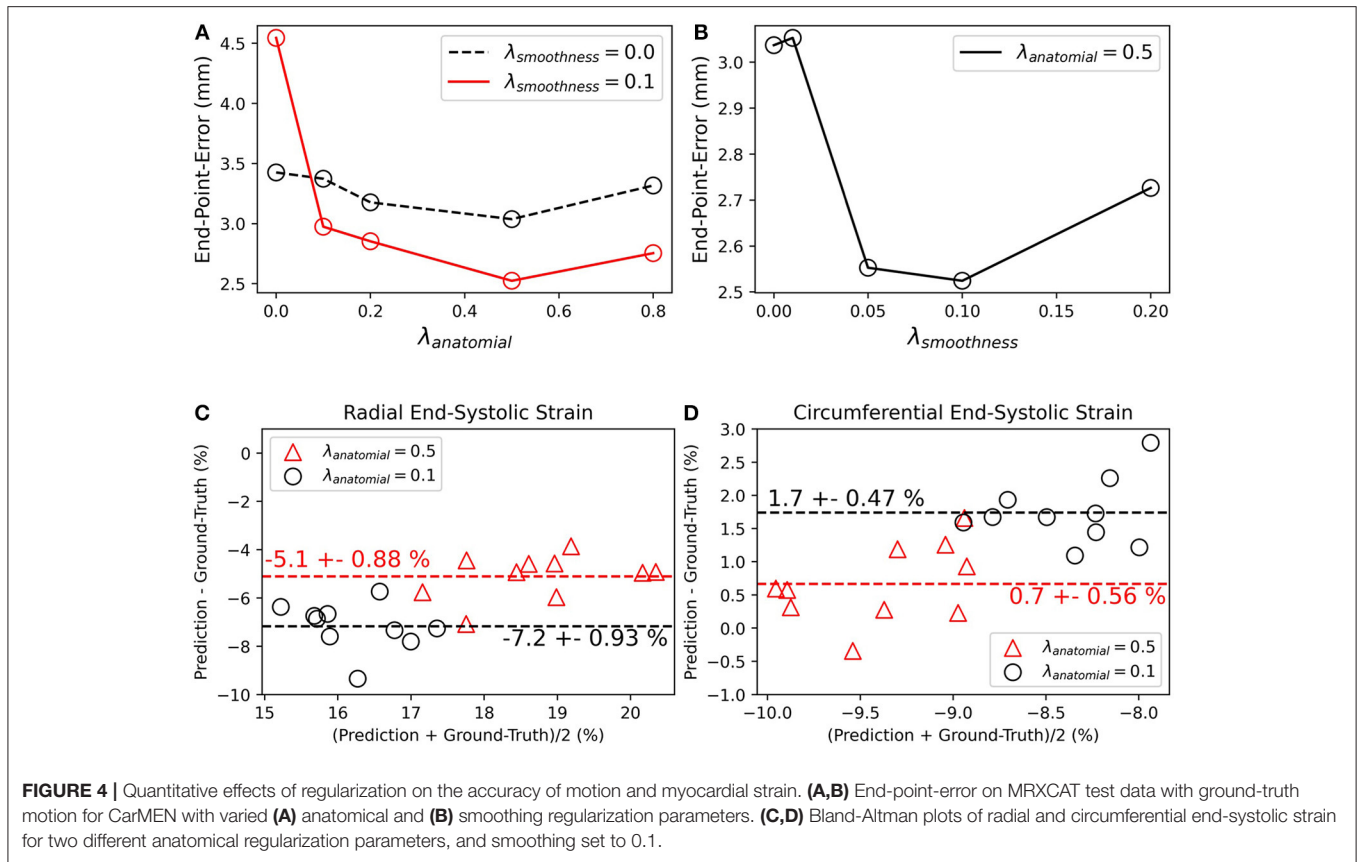
## Evaluation Metrics

### Segmentation and Motion Estimation

The CarSON-predicted and manual segmentations were compared using the Hausdorff distance (HD) and Dice Similarity

Coefficient (DSC) metrics at both ED and ES. Accuracy of LV volumetric measures derived from segmentations, including ED volume (EDV), EF, and LVM, was assessed using the correlation, bias, and standard deviation metrics. The mean absolute error (MAE) for the LV EDV and LVM were also computed for comparison against the intra- and inter-observer variability reported by (41). RV labels were not analyzed since they were not used to assess cardiac function but rather to define the direction of the septal wall, which is needed to construct the LV strain polar maps with a normalized orientation between subjects. We compared our results to top-3 ranked methods published for the ACDC test set as these appear in the leader-board of the challenge (18, 20, 21, 39).

CMAC organizers defined 12 landmarks at intersections of gridded lines on tagging images at ED, one landmark  $p_0$  per wall (septal, inferior, lateral, interior) per ventricular level (basal, mid, septal). These landmarks were manually-tracked on tagging images by two observers over the cardiac cycle, and each position was transformed from tagging to cine coordinates using DICOM header information. We used the CarMEN motion estimates  $u_t$  to automatically deform the landmarks at ED, and the accuracy



was assessed using the in-plane end-point error (EPE) between deformed  $p_t' = u_t \circ p_0$  and manually-tracked  $p_t$  landmarks, defined by

$$EPE(p, p') = \sqrt{(p_x - p_x')^2 + (p_y - p_y')^2}. \quad (7)$$

Due to temporal misalignment between the tagging and cine acquisitions, EPE was evaluated only at ES ( $t = t_{ES}$ ). Specifically, let  $p_{ij}(t)$  denote the manually-tracked landmarks of subject  $i$  at frame  $t$  by observer  $j$ . The accuracy of CarMEN was assessed using the average EPE

$$AEPE = \frac{1}{2n} \sum_{i=1}^n \sum_{j=1}^2 EPE(p_{ij}(t_{ES}), u_i(t_{ES}) \circ p_0). \quad (8)$$

Our results were compared to those reported by the four groups that responded to the challenge (42), MEVIS (46), IUCL (9), UPF (11), and INRIA (12, 47). All groups submitted tagging-based motion estimates, but only UPF and INRIA provided estimates based on cine-MRI.

### Strain Validation and Intra-Scanner Repeatability

The tagging-MRI method with the lowest AEPE at ES was used as the reference for strain analysis. The tagging-MRI-based motion estimates were registered and resampled to the cine-MRI space.

Global strain and SR values throughout the entire cardiac cycle were derived from the resampled estimates as described in (48). Global- and regional-based analyses were performed to assess the repeatability of measures from two acquisitions. Relative changes (RC) and absolute relative changes (aRC) were calculated, taking the first acquisition as the reference. ESS and SR were calculated for the global-based analysis, and for region-based analyses, ESS values were normalized using the AHA polar map, and both RC and aRC were evaluated for each of the segments in the polar map.

### Statistics

For validation, Bland-Altman analysis was used to quantify agreement between predicted and tagging strain measures. We used the term *bias* to denote the mean difference and the term *precision* to denote the standard deviation of the differences, the latter computed with 1-degree of freedom. Differences were also assessed using a paired *t*-test with Bonferroni correction for multiple comparisons. For global- and regional-based analyses of strain intra-scanner repeatability, ICC estimates and their 95% confidence intervals (CI) were calculated based on a single-rating, absolute agreement, 2-way mixed-effects model. Analyses were performed on Python v3.4 with the statistical pingouin module (49).

**TABLE 1** | State-of-the-art methods for left-ventricular segmentation shown at end-diastole (ED) and end-systole (ES) on the ACDC test set compared to proposed approach.

| Left-ventricle label |                              | Dice similarity coefficient |       | Hausdorff distance |       | Ejection fraction     |                |       | End-diastolic volume |                |       |
|----------------------|------------------------------|-----------------------------|-------|--------------------|-------|-----------------------|----------------|-------|----------------------|----------------|-------|
|                      |                              | ED                          | ES    | ED                 | ES    | Corr.                 | bias $\pm$ std |       | Corr.                | bias $\pm$ std |       |
|                      |                              | val.                        | val.  | mm                 | mm    | val.                  | %              | %     | val.                 | mL             | mL    |
| *                    | <b>CarSON</b>                | 0.967                       | 0.929 | 5.656              | 7.676 | 0.990                 | 0.252          | 3.183 | 0.996                | 0.762          | 6.672 |
| 1                    | Dong et al. (17)             | 0.967                       | 0.928 | 6.366              | 7.573 | 0.993                 | −0.360         | 2.689 | 0.998                | 2.032          | 4.611 |
| 2                    | Simantiris and Tziritas (18) | 0.967                       | 0.928 | 5.476              | 6.921 | 0.991                 | 0.490          | 2.965 | 0.997                | 1.530          | 5.736 |
| 3                    | Isensee et al. (19)          | 0.964                       | 0.912 | 6.180              | 8.386 | 0.990                 | −0.476         | 3.114 | 0.997                | 3.746          | 5.146 |
| Myocardium label     |                              | Dice similarity coefficient |       | Hausdorff distance |       | Left-ventricular mass |                |       | End-systolic volume  |                |       |
|                      |                              | ED                          | ES    | ED                 | ES    | Corr.                 | bias $\pm$ std |       | Corr.                | bias $\pm$ std |       |
|                      |                              | val.                        | val.  | mm                 | mm    | val.                  | g              | g     | val.                 | mL             | mL    |
| *                    | <b>CarSON</b>                | 0.898                       | 0.913 | 8.128              | 9.189 | 0.981                 | 1.405          | 10.32 | 0.985                | 1.152          | 9.391 |
| 1                    | Dong et al. (17)             | 0.904                       | 0.923 | 7.014              | 7.328 | 0.987                 | −2.547         | 8.28  | 0.988                | −1.984         | 8.335 |
| 2                    | Simantiris and Tziritas (18) | 0.891                       | 0.904 | 8.264              | 9.575 | 0.992                 | −2.904         | 6.46  | 0.983                | −2.134         | 10.11 |
| 3                    | Zotti et al. (20)            | 0.873                       | 0.895 | 8.197              | 8.318 | 0.989                 | −2.1           | 7.91  | 0.988                | −1.79          | 8.575 |

Red are the best results for each metric. \*Proposed segmentation method.

## RESULTS

### Segmentation and Motion Estimation

Centering, segmentation, and motion estimation for an entire cardiac cycle (~25 frames) was accomplished in <13 s on a 12GB GPU and <2.2 min on a 32 GB RAM CPU. VCN located the LV center of mass with a median error of 1.3 mm.

Training with a MDC loss function resulted in slightly more accurate segmentations compared to CCE (Supplementary Table 2), therefore the MDC-trained model was used for all remaining analyses. With this model, correlation of CarSON and manual LV volumetric measures was >0.98 across all measures (Table 1), and biases in EF ( $+0.25 \pm 3.2\%$ ), ED ( $+0.76 \pm 6.7$  mL), and ES ( $+0.19 \pm 5.8$  mL) volumes, and mass ( $+1.4 \pm 10.3$  g) were not significant. Further, these biases were smaller than those obtained with other methods, which were positive for LV EDV (1.5–3.7 mL), negative for LVM (−2.1 to −2.9 g), and close to zero ( $\pm 0.5\%$ ) for EF. Simantiris et al. (18) obtained the best precision for LV EF (2.7 vs. 3.2% variance with CarSON), EDV (4.6 vs. 6.7 mm), and LVM (6.5 vs. 10.3 g). Isensee et al. (39) obtained the best results on geometric metrics, i.e., lower HD for the LV (ED 5.5 vs. 5.7 mm; ES 6.9 vs. 7.7 mm) and LVM (7.0 vs. 8.1 mm; 7.3 vs. 9.2 mm), and higher DSC for the LVM (0.904 vs. 0.898; 0.923 vs. 0.913). The DSC for the LV was similar for all methods (~0.967, ~0.929). MAE for the LV EDV and LVM were  $5.3 \pm 4.1$  mL and  $6.8 \pm 6.5$  g.

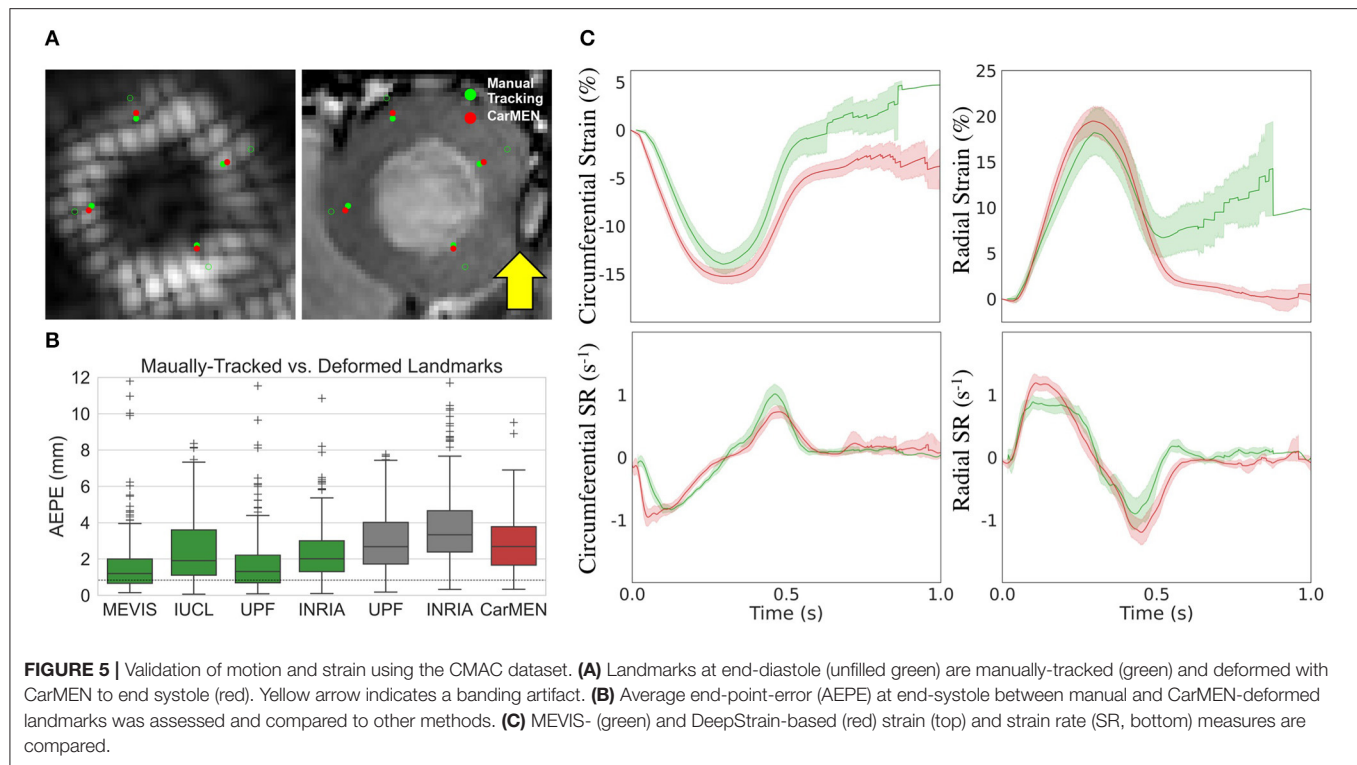
Figure 5A illustrates a representative example of the tagging and cine images from a CMAC subject. Landmarks defined at ED were deformed to ES using the CarMEN estimates and compared to manual tracking. Banding artifacts on cine images showed no clear effect on derived motion estimates or landmark deformation, as shown in ES (Figure 5A,

yellow arrow) or throughout the whole cardiac cycle (see Supplementary Video 1). The manual tracking inter-observer variability was 0.86 mm (Figure 5B, dotted line). Within cine-based techniques, CarMEN ( $2.89 \pm 1.52$  mm) and UPF ( $2.94 \pm 1.64$  mm) had lower ( $p < 0.001$ ) AEPE relative to INRIA ( $3.78 \pm 2.08$  mm), but there was no significant difference between CarMEN and UPF. All tagging-based methods had lower AEPE compared to cine approaches, particularly MEVIS ( $1.58 \pm 1.45$  mm). Finally, we evaluated the AEPE of the motion vectors in 10 synthetic datasets to compare our results against our previous CarMEN implementation. The AEPE was  $1.6 \pm 0.1$  mm ( $1.1 \pm 0.4$  pixels) at ED,  $2.1 \pm 0.1$  mm ( $1.33 \pm 0.03$  pixels) at ES, and  $1.8 \pm 0.2$  mm ( $1.20 \pm 0.2$  pixels) combined.

### Strain Analysis

Table 2 shows the normal ranges (mean [95% CI]) of strain derived from cine-MRI data for all healthy subjects, including subjects from the training, validation, and repeatability cohorts. Across datasets, DeepStrain generated values with narrow CI of ESS (circumferential: 1.1%, radial: 2.5%), SRs ( $0.13 \text{ s}^{-1}$ ,  $0.19 \text{ s}^{-1}$ ), and SRe ( $0.14 \text{ s}^{-1}$ ,  $0.26 \text{ s}^{-1}$ ). Specifically, circumferential and radial values across datasets were:  $-16.9\%$  [ $-17.4$   $-16.3$ ] and  $23.2\%$  [ $22$   $24.4$ ] for ESS,  $-1.1 \text{ s}^{-1}$  [ $-1.2$   $-1.1$ ] and  $1.4 \text{ s}^{-1}$  [ $1.3$   $1.5$ ] for SRs, and  $0.80 \text{ s}^{-1}$  [ $0.73$   $0.86$ ] and  $-1.5 \text{ s}^{-1}$  [ $-1.6$   $-1.3$ ] for SRe, accordingly. These values were similar to tagging-based ones, although circumferential SRe from cine-MRI data was lower, mostly in the train set ( $0.7 \pm 0.2 \text{ s}^{-1}$ ).

Comparison of tagging- and cine-based strain measures with matched subjects showed an overall agreement in timing and magnitude of strain and SR throughout the cardiac cycle,

**TABLE 2 |** Normal ranges of strain with DeepStrain in healthy subjects.

|  | ACDC (n = 20) | CMAC (n = 15)    |             | MARTINOS (n = 10)    |             | COMBINED (n = 45)   |
|--|---------------|------------------|-------------|----------------------|-------------|---------------------|
|  | Cine          | Tagging vs. Cine |             | Cine ACQ 1 vs. ACQ 2 |             | Cine                |
| End-systolic strain (%)                        |               |                  |             |                      |             |                     |
| Circumferential                                | −17.8 (1.6)   | −14.2 (2.2)      | −15.3 (1.5) | −17.3 (0.7)          | −17.5 (0.9) | −16.9 [−17.4 −16.3] |
| Radial   | 24.5 (2.9)    | 18.4 (5.1)       | 19.7 (3.4)  | 25.9 (3.4)           | 25.7 (4.1)  | 23.2 [22.0 24.4]    |
| Systolic strain rate (s <sup>−1</sup> )        |               |                  |             |                      |             |                     |
| Circumferential                                | −1.1 (0.2)    | −0.9 (0.1)       | −1.2 (0.2)  | −1.0 (0.2)           | −1.0 (0.2)  | −1.1 [−1.2 −1.1]    |
| Radial   | 1.3 (0.4)     | 1.0 (0.2)        | 1.3 (0.2)   | 1.7 (0.3)            | 1.6 (0.3)   | 1.4 [1.3 1.5]       |
| Early-diastolic strain rate (s <sup>−1</sup> ) |               |                  |             |                      |             |                     |
| Circumferential                                | 0.7 (0.2)     | 1.2 (0.2)        | 0.8 (0.1)   | 1.0 (0.2)            | 1.0 (0.2)   | 0.80 [0.73 0.86]    |
| Radial   | −1.4 (0.5)    | −1.2 (0.5)       | −1.4 (0.3)  | −1.8 (0.3)           | −1.7 (0.4)  | −1.5 [−1.6 −1.3]    |

Tagging-based measures are shown for the CMAC cohort. DeepStrain repeatability is shown for two acquisitions (ACQ). MEVIS was used to calculate tagging measures. Data are presented as mean (standard deviation), and as mean [95% confidence interval] for all three datasets combined.

although there were visual differences in peak SR parameters (Figure 5C). Visual inspection of image artifacts on cine data showed no evidence that these artifacts affected strain values derived with DeepStrain (Supplementary Figure 1). Quantitative comparisons of tagging- and cine-based measures showed biases in circumferential ESS ( $-14.2 \pm 2.2$  vs.  $-15.3 \pm 1.5\%$ ; bias  $-1.17 \pm 2.93\%$ ), radial ESS ( $18.4 \pm 5.1$  vs.  $19.7 \pm 3.4\%$ ;  $+1.26 \pm 5.37\%$ ), and SRe ( $-1.2 \pm 0.5$  vs.  $-1.4 \pm 0.3$ ;  $-0.21 \pm 0.52$  s<sup>-1</sup>) were not significantly different from zero (Supplementary Figure 2). However, there were larger differences ( $p < 0.01$ ) in radial SRs ( $1.0 \pm 0.2$  vs.  $1.3 \pm 0.2$  s<sup>-1</sup>;

$0.32 \pm 0.34$  s<sup>-1</sup>), and circumferential SRs ( $-0.9 \pm 0.1$  vs.  $-1.2 \pm 0.2$  s<sup>-1</sup>;  $0.30 \pm 0.22$  s<sup>-1</sup>) and SRe ( $1.2 \pm 0.2$  vs.  $0.8 \pm 0.1$  s<sup>-1</sup>;  $0.40 \pm 0.23$  s<sup>-1</sup>).

Global strain time series derived from repeated acquisitions are shown in Figure 6A. The overall bias in circumferential and radial ESS were 0.17 and  $-0.16\%$ , accordingly. Average RC between parameters was less than  $\pm 1\%$  for ESS and less than  $\pm 5\%$  for peak SR (Table 3). Average aRC was  $\sim 5\%$  for ESS (circumferential:  $3.0 \pm 2.0\%$ ; radial:  $5.1 \pm 5.8\%$ ),  $\sim 8\%$  for SRs ( $8.0 \pm 6.8\%$ ;  $7.7 \pm 4.0\%$ ), and  $\sim 10\%$  for SRe ( $10.2 \pm 7.8\%$ ;  $9.2 \pm 8.6\%$ ). Mean ICC values showed repeatability was

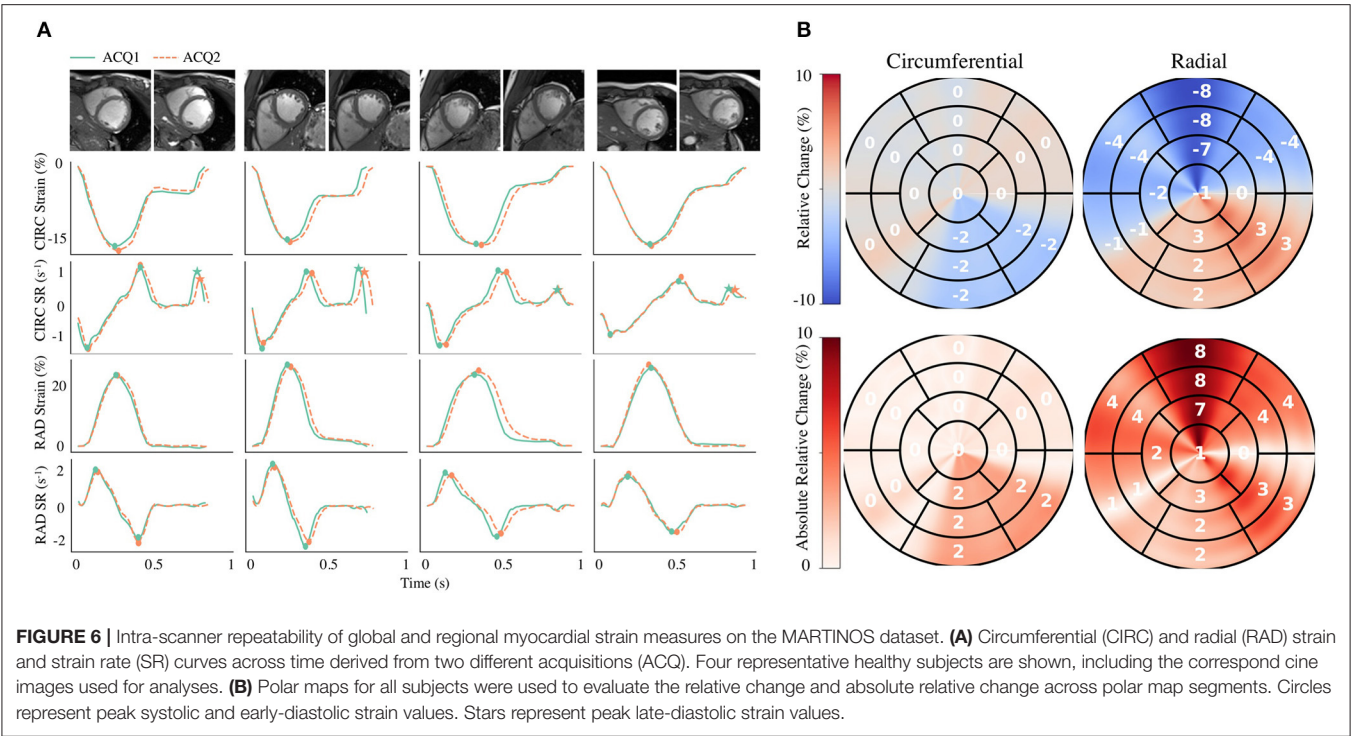


**TABLE 3 |** Intra-scanner repeatability of global circumferential and radial end-systolic strain (ESS) measures.

| Measure             | RC (%)      | aRC (%)    | ICC [95% CI]     | LoA                           |
|---------------------|-------------|------------|------------------|-------------------------------|
| Circumferential ESS | 1.0 (3.6)   | 3.0 (2.0)  | 0.75 [0.22–0.92] | [−1.36 1.02%]                 |
| Radial ESS          | −0.9 (7.9)  | 5.1 (5.8)  | 0.90 [0.64–0.97] | [−3.03 3.36%]                 |
| Circumferential SRs | 0.8 (10.8)  | 8.0 (6.8)  | 0.77 [0.31–0.94] | [−0.23 0.22 s <sup>−1</sup> ] |
| Radial SRs          | −4.9 (7.4)  | 7.7 (4.0)  | 0.91 [0.67–0.98] | [−0.15 0.34 s <sup>−1</sup> ] |
| Circumferential SRe | 2.5 (13.0)  | 10.2 (7.8) | 0.83 [0.47–0.96] | [−0.26 0.22 s <sup>−1</sup> ] |
| Radial SRe          | −2.5 (12.7) | 9.2 (8.6)  | 0.84 [0.50–0.96] | [−0.32 0.41 s <sup>−1</sup> ] |

good to excellent for ESS (0.75; 0.90), SRs (0.77, 0.91), and SRe (0.83, 0.84). The limits-of-agreement (LoA), which defines the interval where to find the expected differences in 95% of the cases assuming normally distributed data, were ~2 and ~6% for circumferential and radial ESS, and ~0.5 s<sup>−1</sup> for SR measures. Average RC and aRC across regional segments were within ±2% for circumferential and ±5% for radial ESS, except in anterior segments (±8%) radially (**Figure 6B**). Regional mean ICC values showed good to excellent repeatability across all segments, except circumferentially near inferoseptal, inferior, and inferolateral walls where repeatability was moderate (**Supplementary Table 3**). LoAs showed that 95% of differences occurred within ~5 and ~10% intervals for circumferential and radial ESS.

**Evaluation in Patients With Cardiovascular Disease**

Regional measures of ESS averaged over patient population (**Supplementary Figure 3**), as well as global values of strain and SR across the cardiac cycle (**Figure 7**) for all 100 subjects in the ACDC train set showed progressive decline in strain values

starting with HCM, followed by ARV, MI, and DCM. Specifically, relative to the healthy group, radial ESS was reduced in all patient populations. Radial systolic and early-diastolic SR were also reduced in all patient groups, except for systolic SR in HCM. **Figure 8** shows both the cine-MRI image and the circumferential ESS polar map of a healthy subject and two patients with MI. Strain values in the healthy polar map have a homogeneous distribution. In contrast, in one MI patient the map indicates a diffused reduction, and inspection of the myocardium on the cine-MRI image shows an anteroseptal infarct that coincides in location with segments with more prominent decreases in strain. In a different MI patient with an infarct located in a similar septal region, strain changes are focal and localized to the anteroseptal wall.

DISCUSSION

In this study we developed a fast DL framework for strain analysis based on cine-MRI data that does not make assumptions about the underlying physiology, and we benchmarked its segmentation, motion, and strain estimation components against the state-of-the-art. We compared our segmentations to other DL methods, motion estimates to other non-learning techniques, and strain measures to a reference tagging-MRI technique. We also presented the intra-scanner repeatability of DeepStrain-based global and regional strain measures, and showed that these measures were robust to image artifacts in some cases. Global and regional applications were also presented to demonstrate the potential clinical utilization of our approach. Our work is the first to report within a single study the characterization, validation, and repeatability of a learning-based method for strain analysis.

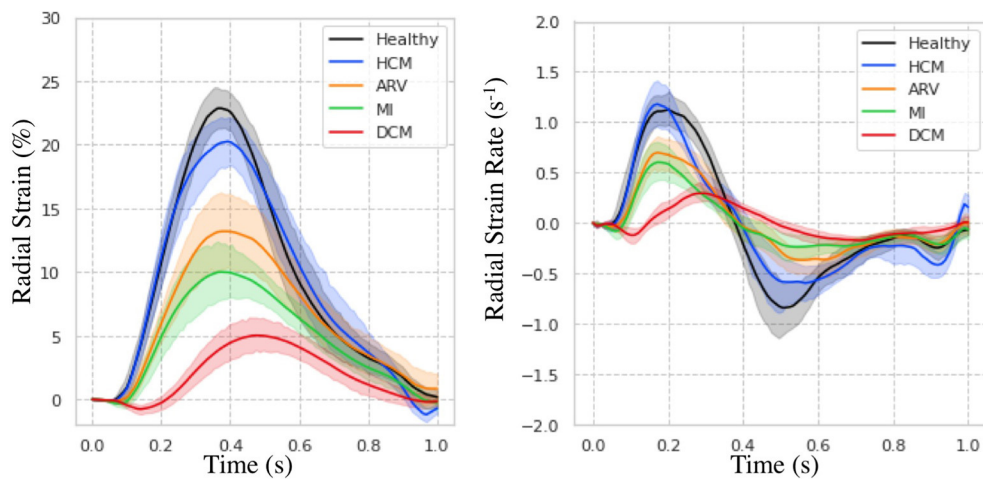


**FIGURE 7** | Strain measures on the ACDC train set. Radial strain (**Left**) and strain rate (**Right**) across time is shown for healthy subjects and patients with hypertrophic cardiomyopathy (HCM), abnormal right ventricle (ARV), myocardial infarction (MI), and dilated cardiomyopathy (DCM).

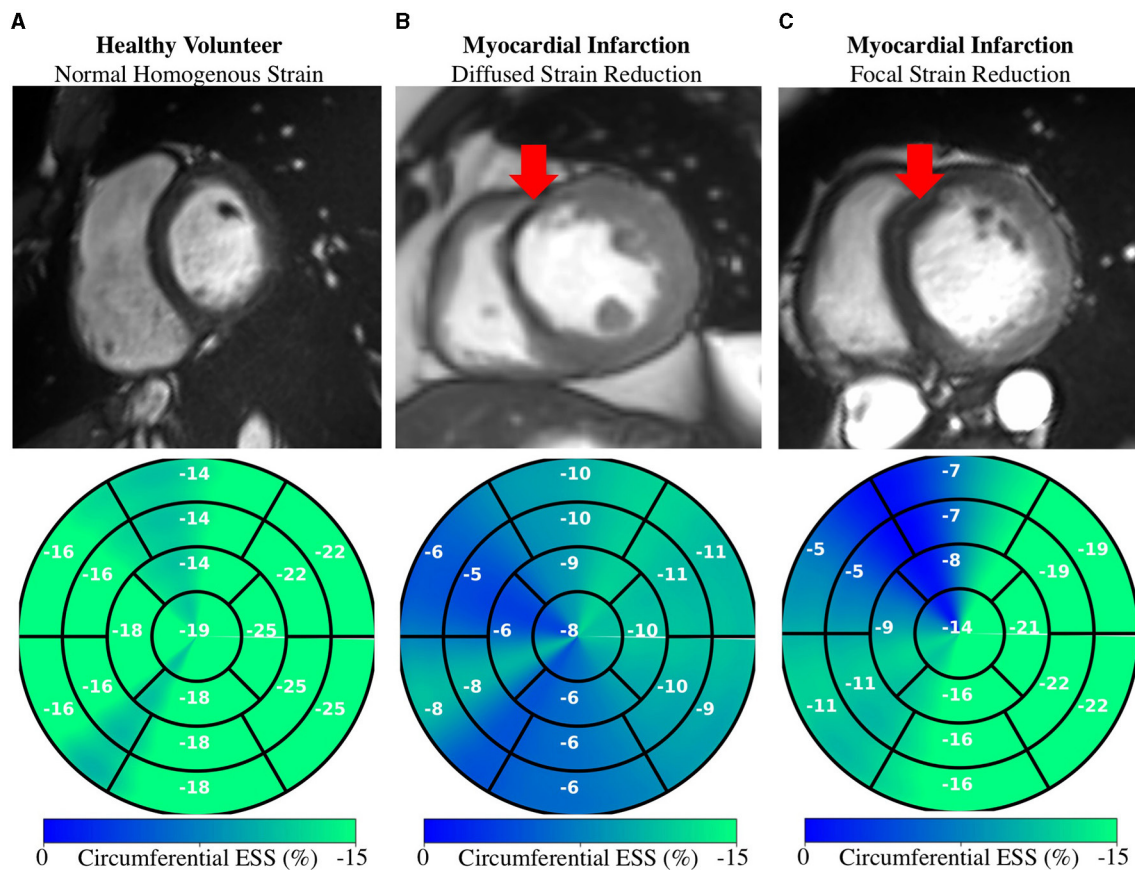


**FIGURE 8** | Regional Strain: Diffused vs. focal abnormalities. Anatomical (top) and regional (bottom) circumferential end-systolic strain (ESS) for healthy and MI subjects. **(A)** Healthy strain is homogeneously distributed. **(B)** MI subject shows diffused strain reduction with an MI in the anteroapical region. **(C)** Different MI subject shows a focal decrease in the anteroapical region co-localized with the infarcted region (red arrows). MI, myocardial infarction.

## Volumetric Measures

Segmentation from MRI data is a task particularly well-suited for CNNs given the excellent soft-tissue contrast, thus all top

performing methods on the ACDC test set were based on DL approaches. Isensee et al. (39) had remarkable success on geometric metrics, but this and other approaches result

in a systematic overestimation of the LV EDV and thus underestimation of LVM. In contrast, CarSON generated less biased measures of LV volumes and mass, which were not significant. Although Simantiris and Tziritas (18) obtained the most precise measures, possibly due to their extensive use of augmentation using image intensity transformations, across methods the precision of EF was within the  $\sim 3\text{--}5\%$  (50) needed when it is used as an index of LV function in clinical trials (51). Lastly, we showed that the error in our measures of LV EDV and LVM was almost half the inter-observer ( $\sim 10.6\text{ mL}$ ,  $12.0\text{ g}$ ), and comparable to the intra-observer ( $\sim 4.6\text{ mL}$ ,  $6.2\text{ g}$ ) MAE reported in (41), but further investigations are required to assess the performance on more heterogeneous populations. Lastly, CarSON tends to perform better on DSC metrics compared to HD. This is mainly due to inclusion or exclusion of myocardium labels in most basal slides as described by Bernard et al. (41). However, the smoothing penalty used to train CarMEN reduces the impact on strain estimates by promoting smooth motion values across the myocardial tissue.

## Strain Validation

The application of myocardial strain to quantify abnormal deformation in disease requires accurate definition of normal ranges. However, previously reported normal ranges vary largely between modalities and techniques, particularly for radial ESS (4). In this study we showed DeepStrain generated strain measures with narrow CI in healthy subjects from across three different datasets. Although direct comparison with the literature is difficult due to differences in the datasets, overall our strain measures agreed with several reported results. Specifically, circumferential strain is in agreement with studies in healthy participants based on tagging ( $-16.6\%$ ,  $n = 129$ ) and speckle tracking echocardiography ( $-18\%$ ,  $n = 265$ ) datasets (52, 53), as well a recently proposed ( $-16.7\%$  basal,  $n = 386$ ) tagging-based DL method (48). Our radial strain values are in agreement with some tagging-based studies ( $26.5\%$ ,  $n = 129$ ;  $23.8\%$  basal,  $n = 386$ ) (48, 52), but are lower than most reported values (4). This is a result of smoothing regularization used during training to prevent overfitting. However, lowering the regularization without increasing the size of the training set would lead to increased EPE and wider CI. SR measures derived with DeepStrain were also in good agreement with previous tagging-based studies (52).

The CMAC dataset enabled us to compare our results to non-learning methods using a common dataset. We found that AEPE at ES was lower with tagging-based techniques, reflecting the advantage of estimating cardiac motion from a grid of intrinsic tissue markers (i.e., grid tagging lines). Further, the tagging techniques also benefited from the fact that landmarks were placed near the center of the myocardial wall borders, whereas motion estimation from tagging data at the myocardial walls and in thin-walled regions of the LV is less accurate due to the spatial resolution of the tagging grid (4). In addition, some of the tagging-MRI images did not enclose the whole myocardium and some contained imaging artifacts, which resulted in strain artifacts toward the end of the cardiac cycle. Nevertheless, MEVIS-based motion estimates achieved the lowest AEPE at ES and thus represent a reliable reference for end-systolic strain

measures. This performance could be a result of their image term (4) that penalizes phase shifts in the Fourier domain instead of intensity values, an approach that is less affected by desaturation. The UPF approach also achieved a low AEPE using multimodal integration and 4D tracking to leverage the strengths of both modalities and improve temporal consistency (11). Specific differences in motion and strain measures between MEVIS and other techniques were thoroughly discussed by Tobon-Gomez et al. (42).

Using MEVIS as the tagging reference standard, we found no significant differences in measures of circumferential of radial and ESS. Validation studies have shown similar [ $\pm 1\%$ , (54–56)] or worse [ $\pm 11\%$  for radial, (55)] biases between cine feature tracking and tagging strain. However, these methods required manual contouring by an expert, whereas our method is fully-automatic. We found significant differences in SR measures between the two techniques that could be due to drift errors in the MEVIS implementation, i.e., errors that accumulate in sequential implementations in which motion is estimated frame-by-frame (42).

The AEPE on the synthetic dataset of 1.20 pixels was lower than our previously reported 1.7 pixels, which is expected as our previous implementation was not anatomically constrained. Although we did not observe considerable improvements in AEPE compared to tagging- and cine-based methods, an important advantage of our learning-based approach is the reduced computational complexity ( $\sim 13\text{ s}$  in GPU) relative to the proposed MEVIS (1–2 h), IUCL (3–6 h), UPF (6 h), and INRIA (5 h) approaches (42). Specifically, because once trained our network does not optimize for a specific test subject (i.e., it does not iterate on the cine-data to generate the desired output), centering, segmentation, and motion estimation for the entire cardiac cycle can be accomplished much faster ( $< 2\text{ min}$  in CPU). In addition, DeepStrain was trained on a relatively small dataset and was evaluated on data from different institutions and vendors, therefore its accuracy relative to non-learning methods could substantially improve through training with larger cohorts or application of data shift correction strategies. Furthermore, a joint optimization of segmentation and motion estimation CNNs could potentially improve the robustness of the workflow to undersampled data (24).

## Strain Repeatability

In this study we also evaluated the intra-scanner repeatability of strain measures in 10 healthy subjects, an important aspect to consider when assessing the potential clinical utility of DeepStrain. Confidence intervals in circumferential and radial ESS were  $0 \pm 1\%$  and  $0 \pm 3\%$ , better than the intra-observer variability reported using feature tracking in 10 healthy adults (57). A more recent study in 100 healthy individuals reported intra- and inter-observer repeatability for circumferential (ICC intra: 0.88, ICC inter: 0.88) and radial ESS (0.82, 0.79), which were comparable to our results for circumferential ESS (0.75) and radial ESS (0.90) using only 10 subjects. Finally, our repeatability of SR measures was good to excellent, similar to that reported for healthy ( $n = 20$ ) and patient ( $n = 60$ ) populations (58). Thus,

without requiring expert operators, DeepStrain achieved better or equal repeatability compared to feature tracking methods.

## Potential Clinical Applications

DeepStrain could be applied in a wide range of clinical applications, e.g., automated extraction of imaging phenotypes from large-scale databases (59). Such phenotypes include global and regional strain, which are important measures in the setting of existing dysfunction with preserved EF (3). DeepStrain generated measures of global strain and SR over the entire cardiac cycle from a cohort of 100 subjects in <2 min. These results showed that radial SRe was reduced in patients with HCM and ARV, despite having a normal or increased LV EF. Decreased SRe with normal EF is suggestive of subclinical LV diastolic dysfunction, which is in agreement with previous findings (60, 61). Our results also showed DeepStrain-based maps could be used to characterize regional differences between groups.

At an individual level, we showed that in MI patients, polar segments with decreased circumferential strain matched myocardial regions with infarcted tissue. Further, we showed that the changes in regional strain due to MI can be both diffuse and focal. These abnormalities could be used to discriminate dysfunctional from functional myocardium (62), or as inputs for downstream classification algorithms (63). More generally, DeepStrain could be used to extract interpretable features (e.g., strain and SR) for DL diagnostic algorithms (64), which would make understanding of the pathophysiological basis of classification more attainable (65).

## Study Limitations

A limitation of our study was the absence of important patient information (e.g., age), which would be needed for a more complete interpretation of our strain analysis results, for example to assess the differences in strain values found between the healthy subjects from the ACDC and CMAC datasets. Nevertheless, using publicly available data enables the scientific community to more easily reproduce our findings, and compare our results to other techniques. Another limitation was the absence of longitudinal analyses, i.e., longitudinal strain was not reported because it is normally derived from long-axis cine-MRI data not available in the training dataset. The size of the datasets is another potential limitation. The number of patients used for training is much smaller than the number of trainable parameters, potentially resulting in some degree of overfitting. To correct this, the training set for motion estimation could be expanded by validating the proposed segmentation network on more heterogeneous populations. The use of strain minimization deviation as a training heuristic also serves as a learning constrain but has not been validated, and could potentially prevent identification of subtle disease due to loss of sensitivity to abnormal strain. While our repeatability results were promising despite testing in only a small number of subjects, repeatability in patient populations was not shown. Further, reproducibility across sites and vendors was not assessed. In addition, the accuracy of the motion estimates on patient populations with regional dysfunction was not assessed, and we

did not quantify the effect of dataset shift errors that might occur when applying our method to new datasets.

## Conclusion

We developed an end-to-end learning-based workflow for strain analysis that is fast, operator-independent, and leverages real-world data instead of making explicit assumptions about myocardial tissue properties or geometry. This approach enabled us to derive strain measures from new data that were repeatable, and comparable to those derive from dedicated tagging data. These technical and practical attributes position DeepStrain as an excellent candidate for use in routine clinical studies or data-driven research.

## DATA AVAILABILITY STATEMENT

The datasets presented in this study can be found in online repositories. The names of the repository/repositories and accession number(s) can be found at: <https://github.com/moralesq>.

## ETHICS STATEMENT

The studies involving human participants were reviewed and approved by written consent was obtaining from all volunteers with approval of the institutional review board (2018P002912) and in agreement with the Health Insurance Portability and Accountability Act (HIPAA) at the Massachusetts General Hospital. The patients/participants provided their written informed consent to participate in this study.

## AUTHOR CONTRIBUTIONS

MM designed the workflow, performed data analysis, and drafted the manuscript. All other authors revised the drafted manuscript and contributed critical intellectual content. This manuscript has been revised and approved by all authors.

## FUNDING

This work was supported in part by the U.S. National Cancer Institute under Grant 1R01CA218187-01A1.

## ACKNOWLEDGMENTS

We acknowledge the support of NVIDIA Corporation with the donation of the Titan X Pascal GPU used for this research.

## SUPPLEMENTARY MATERIAL

The Supplementary Material for this article can be found online at: <https://www.frontiersin.org/articles/10.3389/fcvm.2021.730316/full#supplementary-material>

## REFERENCES

- Konstam MA, Abboud FM. Ejection fraction: misunderstood and over-rated (changing the paradigm in categorizing heart failure). *Circulation*. (2017) 135:717–9. doi: 10.1161/CIRCULATIONAHA.116.025795
- Claus P, Omar AMS, Pedrizzetti G, Sengupta PP, Nagel E. Tissue tracking technology for assessing cardiac mechanics. *JACC Cardiovasc Imaging*. (2015) 8:1444–60. doi: 10.1016/j.jcmg.2015.11.001
- Smiseth OA, Torp H, Opdahl A, Haugaa KH, Urheim S. Myocardial strain imaging: how useful is it in clinical decision making? *Eur Heart J*. (2016) 37:1196–207. doi: 10.1093/eurheartj/ehv529
- Amzulescu MS, De Craene M, Langet H, Pasquet A, Vancraeynest D, Pouleur AC, et al. Myocardial strain imaging: review of general principles, validation, and sources of discrepancies. *Eur Heart J Cardiovasc Imaging*. (2019) 20:605–19. doi: 10.1093/ehjci/jez041
- Osman NF, Sampath S, Atalar E, Prince JL. Imaging longitudinal cardiac strain on short-axis images using strain-encoded MRI. *Magn Reson Med*. (2001) 46:324–34. doi: 10.1002/mrm.1195
- Kim D, Gilson WD, Kramer CM, Epstein FH. Myocardial tissue tracking with two-dimensional cine displacement-encoded MR imaging: development and initial evaluation. *Radiology*. (2004) 230:862–71. doi: 10.1148/radiol.2303021213
- Risum N, Ali S, Olsen NT, Jons C, Khouri MG, Lauridsen TK, et al. Variability of global left ventricular deformation analysis using vendor dependent and independent two-dimensional speckle-tracking software in adults. *J Am Soc Echocardiogr*. (2012) 25:1195–203. doi: 10.1016/j.echo.2012.08.007
- Schuster A, Stahnke V-C, Unterberg-Buchwald C, Kowallick JT, Lamata P, Steinmetz M, et al. Cardiovascular magnetic resonance feature-tracking assessment of myocardial mechanics: intervendor agreement and considerations regarding reproducibility. *Clin Radiol*. (2015) 70:989–98. doi: 10.1016/j.crad.2015.05.006
- Wenzhe Shi, Xiahai Zhuang, Haiyan Wang, Duckett S, Luong DVN, Tobon-Gomez C, et al. A comprehensive cardiac motion estimation framework using both untaged and 3-D tagged MR images based on nonrigid registration. *IEEE Trans Med Imaging*. (2012) 31:1263–75. doi: 10.1109/TMI.2012.2188104
- Pedrizzetti G, Claus P, Kilner PJ, Nagel E. Principles of cardiovascular magnetic resonance feature tracking and echocardiographic speckle tracking for informed clinical use. *J Cardiovasc Magnet Res*. (2016) 18:51. doi: 10.1186/s12968-016-0269-7
- De Craene M, Piella G, Camara O, Duchateau N, Silva E, Doltra A, et al. Temporal diffeomorphic free-form deformation: application to motion and strain estimation from 3D echocardiography. *Med Image Anal*. (2012) 16:427–50. doi: 10.1016/j.media.2011.10.006
- Mansi T, Pennec X, Sermesant M, Delingette H, Ayache N. iLogDemos: a demons-based registration algorithm for tracking incompressible elastic biological tissues. *Int J Comput Vis*. (2011) 92:92–111. doi: 10.1007/s11263-010-0405-z
- Avazmohammadi R, Soares JS, Li DS, Eperjesi T, Pilla J, Gorman RC, et al. On the in vivo systolic compressibility of left ventricular free wall myocardium in the normal and infarcted heart. *J Biomech*. (2020) 107:109767. doi: 10.1016/j.jbiomech.2020.109767
- Kumar V, Ryu AJ, Manduca A, Rao C, Gibbons RJ, Gersh BJ, et al. Cardiac MRI demonstrates compressibility in healthy myocardium but not in myocardium with reduced ejection fraction. *Int J Cardiol*. (2021) 322:278–83. doi: 10.1016/j.ijcard.2020.08.087
- Lim C, Blaszczyk E, Riazzy L, Wiesemann S, Schüler J, von Knobelsdorff-Brenkenhoff F, et al. Quantification of myocardial strain assessed by cardiovascular magnetic resonance feature tracking in healthy subjects— influence of segmentation and analysis software. *Eur Radiol*. (2020) 31:3962–72. doi: 10.1007/s00330-020-07539-5
- Zhu B, Liu JZ, Cauley SF, Rosen BR, Rosen MS. Image reconstruction by domain-transform manifold learning. *Nature*. (2018) 555:487–92. doi: 10.1038/nature25988
- Dong P, Provencher B, Basim N, Piché N, Marsh M. Forget about cleaning up your micrographs: deep learning segmentation is robust to image artifacts. *Microsc Microanal*. (2020) 24(Suppl. 1):532–3. doi: 10.1017/S1431927620018231
- Simantiris G, Tziritis G. Cardiac MRI segmentation with a dilated CNN incorporating domain-specific constraints. *IEEE J Sel Top Signal Process*. (2020) 14:1235–43. doi: 10.1109/JSTSP.2020.3013351
- Isensee F, Jaeger PF, Full PM, Wolf I, Engelhardt S, Maier-Hein KH. Automatic cardiac disease assessment on cine-MRI via time-series segmentation domain specific features. In: Pop M, Sermesant M, Jodoin PM, Lalande A, Zhuang X, Yang G, Young A, Bernard O, editors. *Statistical Atlases Computational Models of the Heart. ACDC MMWH Challenges. Lecture Notes in Computer Science*. Vol. 10663. Cham: Springer International Publishing (2017). p. 120–9. doi: 10.1007/978-3-319-75541-0\_13
- Zotti C, Luo Z, Lalande A, Jodoin P-M. Convolutional neural network with shape prior applied to cardiac MRI segmentation. *IEEE J Biomed Health Inform*. (2019) 23:1119–28. doi: 10.1109/JBHI.2018.2865450
- Baldeon Calisto M, Lai-Yuen SK. AdaEn-Net: an ensemble of adaptive 2D–3D fully convolutional networks for medical image segmentation. *Neural Netw*. (2020) 126:76–94. doi: 10.1016/j.neunet.2020.03.007
- Hammouda K, Khalifa F, Abdeltawab H, Elnakib A, Giridharan GA, Zhu M, et al. A new framework for performing cardiac strain analysis from cine MRI imaging in mice. *Sci Rep*. (2020) 10:7725. doi: 10.1038/s41598-020-64206-x
- Puyol-Anton E, Ruijsink B, Bai W, Langet H, De Craene M, Schnabel JA, et al. Fully automated myocardial strain estimation from cine MRI using convolutional neural networks. In: *2018 IEEE 15th International Symposium on Biomedical Imaging (ISBI 2018)*. Washington, DC: IEEE (2018). p. 1139–43. doi: 10.1109/ISBI.2018.8363772
- Qin C, Bai W, Schlemper J, Petersen SE, Piechnik SK, Neubauer S, et al. Joint motion estimation segmentation from undersampled cardiac MR image. In: Knoll F, Maier A, Rueckert D, editors. *Machine Learning for Medical Image Reconstruction. Lecture Notes in Computer Science*. Cham: Springer International Publishing (2018). p. 55–63. doi: 10.1007/978-3-030-00129-2\_7
- Qiao M, Wang Y, Guo Y, Huang L, Xia L, Tao Q. Temporally coherent cardiac motion tracking from cine MRI: traditional registration method and modern CNN method. *Med Phys*. (2020) 47:4189–98. doi: 10.1002/mp.14341
- Yu H, Sun S, Yu H, Chen X, Shi H, Huang TS, et al. FOAL: fast online adaptive learning for cardiac motion estimation. In: *2020 IEEE/CVF Conference on Computer Vision and Pattern Recognition (CVPR)*. Seattle, WA: IEEE (2020). p. 4312–22. doi: 10.1109/CVPR42600.2020.00437
- de Vos BD, Berendsen FF, Viergever MA, Staring M, Išgum I. End-to-end unsupervised deformable image registration with a convolutional neural network. *arXiv:1704.06065*. (2017) 10553:204–12. doi: 10.1007/978-3-319-67558-9\_24
- Chen P, Chen X, Chen EZ, Yu H, Chen T, Sun S. Anatomy-aware cardiac motion estimation. *arXiv:2008.07579*. (2020). Available online at: <http://arxiv.org/abs/2008.07579> (accessed December 11, 2020).
- Morales MA, Izquierdo-Garcia D, Aganj I, Kalpathy-Cramer J, Rosen BR, Catana C. Implementation and validation of a three-dimensional cardiac motion estimation network. *Radiol Artif Intell*. (2019) 1:e180080. doi: 10.1148/ryai.2019180080
- Østvik A, Smistad E, Espeland T, Berg EAR, Lovstakken L. (2018) Automatic Myocardial Strain Imaging in Echocardiography Using Deep Learning. In: Stoyanov D, Taylor Z, Carneiro G, Syeda-Mahmood T, Martel A, Maier-Hein L, Tavares JMRS, Bradley A, Papa JP, Belagiannis V, Nascimento JC, Lu Z, Conjeti S, Moradi M, Greenspan H, Madabhushi A, editors. *Deep Learning in Medical Image Analysis and Multimodal Learning for Clinical Decision Support. DLMIA 2018, ML-CDS 2018. Lecture Notes in Computer Science, Vol 11045*. Cham: Springer. doi: 10.1007/978-3-030-00889-5\_35
- Voigt J-U, Pedrizzetti G, Lysyansky P, Marwick TH, Houle H, Baumann R, et al. Definitions for a common standard for 2D speckle tracking echocardiography: consensus document of the EACVI/ASE/Industry Task Force to standardize deformation imaging. *Eur Heart J Cardiovasc Imaging*. (2015) 16:1–11. doi: 10.1093/ehjci/jeu184

32. Qin C, Bai W, Schlemper J, Petersen SE, Piechnik SK, Neubauer S, et al. Joint learning of motion estimation and segmentation for cardiac MR image sequences. *arXiv:1806.04066 [cs]*. (2018). Available online at: <http://arxiv.org/abs/1806.04066> (accessed September 20, 2018).
33. Liu B, Dardeer AM, Moody WE, Hayer MK, Baig S, Price AM, et al. Reference ranges for three-dimensional feature tracking cardiac magnetic resonance: comparison with two-dimensional methodology and relevance of age and gender. *Int J Cardiovasc Imaging*. (2017) 34:761–75. doi: 10.1007/s10554-017-1277-x
34. American Heart Association Writing Group on Myocardial Segmentation Registration for Cardiac Imaging, Cerqueira MD, Weissman NJ, Dilsizian V, Jacobs AK, Kaul S, et al. Standardized myocardial segmentation and nomenclature for tomographic imaging of the heart: a statement for healthcare professionals from the cardiac imaging committee of the council on clinical cardiology of the American Heart Association. *Circulation*. (2002) 105:539–42. doi: 10.1161/hc0402.102975
35. Ioffe S, Szegedy C. Batch normalization: accelerating deep network training by reducing internal covariate shift. *arXiv:1502.03167 [cs]*. (2015). Available online at: <http://arxiv.org/abs/1502.03167> (accessed November 28, 2020).
36. Xu B, Wang N, Chen T, Li M. Empirical evaluation of rectified activations in convolutional network. *arXiv:1505.00853 [cs, stat]*. (2015). Available online at: <http://arxiv.org/abs/1505.00853> (accessed November 28, 2020).
37. He K, Zhang X, Ren S, Sun J. Deep residual learning for image recognition. *arXiv:1512.03385 [cs]*. (2015). Available online at: <http://arxiv.org/abs/1512.03385> (accessed November 28, 2020).
38. Jaderberg M, Simonyan K, Zisserman A, Kavukcuoglu K. Spatial transformer networks. *arXiv:1506.02025 [cs]*. (2015). Available online at: <http://arxiv.org/abs/1506.02025> (accessed July 5, 2018).
39. Isensee F, Jaeger P, Full PM, Wolf I, Engelhardt S, Maier-Hein KH. Automatic cardiac disease assessment on cine-MRI via time-series segmentation and domain specific features. *arXiv:1707.00587 [cs]*. (2018) 10663: doi: 10.1007/978-3-319-75541-0
40. Balakrishnan G, Zhao A, Sabuncu MR, Guttag J, Dalca AV. VoxelMorph: a learning framework for deformable medical image registration. *IEEE Trans Med Imaging*. (2019) 38:1788–800. doi: 10.1109/TMI.2019.2897538
41. Bernard O, Lalonde A, Zotti C, Cervensky F, Yang X, Heng P-A, et al. Deep learning techniques for automatic MRI cardiac multi-structures segmentation and diagnosis: is the problem solved? *IEEE Trans Med Imaging*. (2018) 37:2514–25. doi: 10.1109/TMI.2018.2837502
42. Tobon-Gomez C, De Craene M, McLeod K, Tautz L, Shi W, Hennemuth A, et al. Benchmarking framework for myocardial tracking and deformation algorithms: an open access database. *Med Image Anal*. (2013) 17:632–48. doi: 10.1016/j.media.2013.03.008
43. Segars WP, Sturgeon G, Mendonca S, Grimes J, Tsui BMW. 4D XCAT phantom for multimodality imaging research: 4D XCAT phantom for multimodality imaging research. *Med Phys*. (2010) 37:4902–15. doi: 10.1118/1.3480985
44. Wissmann L, Santelli C, Segars WP, Kozerke S. MRXCAT: realistic numerical phantoms for cardiovascular magnetic resonance. *J Cardiovasc Magnet Res*. (2014) 16:63. doi: 10.1186/s12968-014-0063-3
45. Segars WP, Tsui BMW. MCAT to XCAT: the evolution of 4-d computerized phantoms for imaging research. *Proc IEEE*. (2009) 97:1954–68. doi: 10.1109/JPROC.2009.2022417
46. Tautz L, Hennemuth A, Peitgen H-O. Motion analysis with quadrature filter based registration of tagged MRI sequences. In: Camara O, Konukoglu E, Pop M, Rhode K, Sermesant M, Young A, editors. *Statistical Atlases Computational Models of the Heart. Imaging Modelling Challenges. Lecture Notes in Computer Science*. Berlin, Heidelberg: Springer Berlin Heidelberg (2011). p. 78–87. doi: 10.1007/978-3-642-28326-0\_8
47. McLeod K, Prakosa A, Mansi T, Sermesant M, Pennec X. An incompressible log-domain demons algorithm for tracking heart tissue. In: Camara O, Konukoglu E, Pop M, Rhode K, Sermesant M, Young A, editors. *Statistical Atlases Computational Models of the Heart. Imaging Modelling Challenges. Lecture Notes in Computer Science*. Berlin, Heidelberg: Springer Berlin Heidelberg (2011). p. 55–67. doi: 10.1007/978-3-642-28326-0\_6
48. Ferdian E, Suinesiaputra A, Fung K, Aung N, Lukaschuk E, Barutcu A, et al. Fully automated myocardial strain estimation from cardiovascular MRI-tagged images using a deep learning framework in the UK biobank. *Radiol Cardiothor Imaging*. (2020) 2:e190032. doi: 10.1148/ryct.2020190032
49. Vallat R. Pingouin: statistics in Python. *JOSS*. (2018) 3:1026. doi: 10.21105/joss.01026
50. San Román JA, Candell-Riera J, Arnold R, Sánchez PL, Aguadé-Bruix S, Bermejo J, et al. Quantitative analysis of left ventricular function as a tool in clinical research. Theoretical basis and methodology. *Rev Esp Cardiol*. (2009) 62:535–51. doi: 10.1016/S1885-5857(09)71836-5
51. Kelly JP, Mentz RJ, Mebazaa A, Voors AA, Butler J, Roessig L, et al. Patient selection in heart failure with preserved ejection fraction clinical trials. *J Am Coll Cardiol*. (2015) 65:1668–82. doi: 10.1016/j.jacc.2015.03.043
52. Venkatesh BA, Donekal S, Yoneyama K, Wu C, Fernandes VRS, Rosen BD, et al. Regional myocardial functional patterns: quantitative tagged magnetic resonance imaging in an adult population free of cardiovascular risk factors: the multi-ethnic study of atherosclerosis (MESA): reference values of strain from tagged MRI. *J Magn Reson Imaging*. (2015) 42:153–9. doi: 10.1002/jmri.24749
53. Muraru D, Cucchini U, Mihăilă S, Miglioneza MH, Aruta P, Cavalli G, et al. Left ventricular myocardial strain by three-dimensional speckle-tracking echocardiography in healthy subjects: reference values and analysis of their physiologic and technical determinants. *J Am Soc Echocardiogr*. (2014) 27:858–71.e1. doi: 10.1016/j.echo.2014.05.010
54. Harrild DM, Han Y, Geva T, Zhou J, Marcus E, Powell AJ. Comparison of cardiac MRI tissue tracking and myocardial tagging for assessment of regional ventricular strain. *Int J Cardiovasc Imaging*. (2012) 28:2009–18. doi: 10.1007/s10554-012-0035-3
55. Augustine D, Lewandowski AJ, Lazdam M, Rai A, Francis J, Myerson S, et al. Global and regional left ventricular myocardial deformation measures by magnetic resonance feature tracking in healthy volunteers: comparison with tagging and relevance of gender. *J Cardiovasc Magn Reson*. (2013) 15:8. doi: 10.1186/1532-429X-15-8
56. Moody WE, Taylor RJ, Edwards NC, Chue CD, Umar F, Taylor TJ, et al. Comparison of magnetic resonance feature tracking for systolic and diastolic strain and strain rate calculation with spatial modulation of magnetization imaging analysis: CMR-feature tracking versus tagging. *J Magn Reson Imaging*. (2015) 41:1000–12. doi: 10.1002/jmri.24623
57. Lamy J, Soulat G, Redheuil A, Evim M, Mousseaux E, Kachenoura N. Inter-study repeatability of left ventricular strain measurement using feature tracking on MRI cine images. In: *2015 Computing in Cardiology Conference (CinC)*. Nice: IEEE (2015). p. 173–6. doi: 10.1109/CIC.2015.7408614
58. Maceira AM, Tuset-Sanchis L, López-Garrido M, San Andres M, López-Lereu MP, Monmeneu JV, et al. Feasibility and reproducibility of feature-tracking-based strain and strain rate measures of the left ventricle in different diseases and genders: MR-FT measures of myocardial strain. *J Magn Reson Imaging*. (2018) 47:1415–25. doi: 10.1002/jmri.25894
59. Meyer HV, Dawes TJW, Serrani M, Bai W, Tokarczuk P, Cai J, et al. Genetic and functional insights into the fractal structure of the heart. *Nature*. (2020) 584:589–94. doi: 10.1038/s41586-020-2635-8
60. Chen S, Yuan J, Qiao S, Duan F, Zhang J, Wang H. Evaluation of left ventricular diastolic function by global strain rate imaging in patients with obstructive hypertrophic cardiomyopathy: a simultaneous speckle tracking echocardiography and cardiac catheterization study. *Echocardiography*. (2014) 31:615–22. doi: 10.1111/echo.12424
61. Marian AJ, Braunwald E. Hypertrophic cardiomyopathy: genetics, pathogenesis, clinical manifestations, diagnosis, and therapy. *Circ Res*. (2017) 121:749–70. doi: 10.1161/CIRCRESAHA.117.311059
62. Götte MJW, van Rossum AC, Twisk JWR, Kuijter JPA, Marcus JT, Visser CA. Quantification of regional contractile function after infarction: strain analysis superior to wall thickening analysis in discriminating infarct from remote myocardium. *J Am Coll Cardiol*. (2001) 37:808–17. doi: 10.1016/S0735-1097(00)01186-4
63. Zhang N, Yang G, Gao Z, Xu C, Zhang Y, Shi R, et al. Deep learning for diagnosis of chronic myocardial infarction on nonenhanced cardiac cine MRI. *Radiology*. (2019) 291:606–17. doi: 10.1148/radiol.2019182304
64. Zheng Q, Delingette H, Ayache N. Explainable cardiac pathology classification on cine MRI with motion characterization by semi-supervised learning of

- apparent flow. *arXiv:181103433 [cs, stat]*. (2019). Available online at: <http://arxiv.org/abs/1811.03433> (accessed April 10, 2020).
65. Kampaktsis PN, Vavuranakis M. Diastolic function evaluation. *JACC Cardiovasc Imaging*. (2020) 13:336–7. doi: 10.1016/j.jcmg.2019.07.028

**Conflict of Interest:** The authors declare that the research was conducted in the absence of any commercial or financial relationships that could be construed as a potential conflict of interest.

**Publisher's Note:** All claims expressed in this article are solely those of the authors and do not necessarily represent those of their affiliated organizations, or those of

the publisher, the editors and the reviewers. Any product that may be evaluated in this article, or claim that may be made by its manufacturer, is not guaranteed or endorsed by the publisher.

Copyright © 2021 Morales, van den Boomen, Nguyen, Kalpathy-Cramer, Rosen, Stultz, Izquierdo-Garcia and Catana. This is an open-access article distributed under the terms of the Creative Commons Attribution License (CC BY). The use, distribution or reproduction in other forums is permitted, provided the original author(s) and the copyright owner(s) are credited and that the original publication in this journal is cited, in accordance with accepted academic practice. No use, distribution or reproduction is permitted which does not comply with these terms.



# Respiratory Motion-Registered Isotropic Whole-Heart T<sub>2</sub> Mapping in Patients With Acute Non-ischemic Myocardial Injury

Karolina Dorniak<sup>1</sup>, Lorenzo Di Sopra<sup>2</sup>, Agnieszka Sabisz<sup>3</sup>, Anna Glinska<sup>3</sup>, Christopher W. Roy<sup>2</sup>, Kamil Gorczewski<sup>4</sup>, Davide Piccini<sup>2,5</sup>, Jérôme Yerly<sup>2,6</sup>, Hanna Jankowska<sup>1</sup>, Jadwiga Fijałkowska<sup>3</sup>, Edyta Szurowska<sup>3</sup>, Matthias Stuber<sup>2,6</sup> and Ruud B. van Heeswijk<sup>2\*</sup>

<sup>1</sup> Department of Noninvasive Cardiac Diagnostics, Medical University of Gdansk, Gdansk, Poland, <sup>2</sup> Department of Radiology, Lausanne University Hospital (CHUV) and University of Lausanne (UNIL), Lausanne, Switzerland, <sup>3</sup> Second Department of Radiology, Medical University of Gdansk, Gdansk, Poland, <sup>4</sup> Siemens Healthineers, Erlangen, Germany, <sup>5</sup> Advanced Clinical Imaging Technology, Siemens Healthcare AG, Lausanne, Switzerland, <sup>6</sup> Center for Biomedical Imaging (CIBM), Lausanne, Switzerland

## OPEN ACCESS

### Edited by:

Rene M. Botnar,  
King's College London,  
United Kingdom

### Reviewed by:

Sebastian Weingärtner,  
Delft University of  
Technology, Netherlands  
PierGiorgio Masci,  
King's College London,  
United Kingdom  
Olivier Jaubert,  
University College London,  
United Kingdom

### \*Correspondence:

Ruud B. van Heeswijk  
ruud.mri@gmail.com

### Specialty section:

This article was submitted to  
Cardiovascular Imaging,  
a section of the journal  
Frontiers in Cardiovascular Medicine

**Received:** 20 May 2021

**Accepted:** 06 September 2021

**Published:** 29 September 2021

### Citation:

Dorniak K, Di Sopra L, Sabisz A, Glinska A, Roy CW, Gorczewski K, Piccini D, Yerly J, Jankowska H, Fijałkowska J, Szurowska E, Stuber M and van Heeswijk RB (2021) Respiratory Motion-Registered Isotropic Whole-Heart T<sub>2</sub> Mapping in Patients With Acute Non-ischemic Myocardial Injury. *Front. Cardiovasc. Med.* 8:712383. doi: 10.3389/fcvm.2021.712383

**Background:** T<sub>2</sub> mapping is a magnetic resonance imaging technique that can be used to detect myocardial edema and inflammation. However, the focal nature of myocardial inflammation may render conventional 2D approaches suboptimal and make whole-heart isotropic 3D mapping desirable. While self-navigated 3D radial T<sub>2</sub> mapping has been demonstrated to work well at a magnetic field strength of 3T, it results in too noisy maps at 1.5T. We therefore implemented a novel respiratory motion-resolved compressed-sensing reconstruction in order to improve the 3D T<sub>2</sub> mapping precision and accuracy at 1.5T, and tested this in a heterogeneous patient cohort.

**Materials and Methods:** Nine healthy volunteers and 25 consecutive patients with suspected acute non-ischemic myocardial injury (sarcoidosis,  $n = 19$ ; systemic sclerosis,  $n = 2$ ; acute graft rejection,  $n = 2$ , and myocarditis,  $n = 2$ ) were included. The free-breathing T<sub>2</sub> maps were acquired as three ECG-triggered T<sub>2</sub>-prepared 3D radial volumes. A respiratory motion-resolved reconstruction was followed by image registration of the respiratory states and pixel-wise T<sub>2</sub> mapping. The resulting 3D maps were compared to routine 2D T<sub>2</sub> maps. The T<sub>2</sub> values of segments with and without late gadolinium enhancement (LGE) were compared in patients.

**Results:** In the healthy volunteers, the myocardial T<sub>2</sub> values obtained with the 2D and 3D techniques were similar ( $45.8 \pm 1.8$  vs.  $46.8 \pm 2.9$  ms, respectively;  $P = 0.33$ ). Conversely, in patients, T<sub>2</sub> values did differ between 2D ( $46.7 \pm 3.6$  ms) and 3D techniques ( $50.1 \pm 4.2$  ms,  $P = 0.004$ ). Moreover, with the 2D technique, T<sub>2</sub> values of the LGE-positive segments were similar to those of the LGE-negative segments ( $T_{2LGE-} = 46.2 \pm 3.7$  vs.  $T_{2LGE+} = 47.6 \pm 4.1$  ms;  $P = 0.49$ ), whereas the 3D technique did show a significant difference ( $T_{2LGE-} = 49.3 \pm 6.7$  vs.  $T_{2LGE+} = 52.6 \pm 8.7$  ms,  $P = 0.006$ ).

**Conclusion:** Respiratory motion-registered 3D radial imaging at 1.5T led to accurate isotropic 3D whole-heart T<sub>2</sub> maps, both in the healthy volunteers and in a small patient

cohort with suspected non-ischemic myocardial injury. Significantly higher T<sub>2</sub> values were found in patients as compared to controls in 3D but not in 2D, suggestive of the technique's potential to increase the sensitivity of CMR at earlier stages of disease. Further study will be needed to demonstrate its accuracy.

**Keywords:** cardiac magnetic resonance(CMR), acute non-ischemic myocardial injury, isotropic 3D imaging, T<sub>2</sub> mapping, respiratory motion correction

## BACKGROUND

The T<sub>2</sub> relaxation time is one of the physiology-dependent properties of a tissue in a magnetic field that governs the image contrast in magnetic resonance imaging (MRI). In the myocardium, it increases in the presence of edema, which makes the T<sub>2</sub> relaxation time a useful indicator of acute myocardial injury irrespective of its etiology (e.g., inflammatory, toxic, or ischemic) (1). T<sub>2</sub> mapping, i.e., quantifying the T<sub>2</sub> relaxation time in every pixel, has therefore seen increased use for the diagnosis of acute myocardial injury in recent years (2). T<sub>2</sub> mapping has been shown as to be an effective complementary tool in inflammatory diseases such myocarditis (3), systemic sclerosis (4), and sarcoidosis (5).

Most current T<sub>2</sub> mapping techniques (6, 7) involve the acquisition of several thick 2D slices of the left-ventricular myocardium, which is largely adequate in the case of diseases that affect the entire myocardium or that have a well-defined pattern, such as acute ischemic myocardial injury. However, in a spectrum of inflammatory myocardial injuries such as viral myocarditis and sarcoidosis, the inflammation pattern is essentially irregular and unpredictable, despite typical patterns of segmental and transmural distribution. This may render the standard 2D T<sub>2</sub> mapping technique suboptimal, since the disease foci can be missed due to insufficient coverage. Moreover, the thick slices may mask the disease foci through partial volume effect by including healthy and injured tissue in the same voxels. On the other hand, scanning would need to be prolonged to a large series of breath holds to cover the entire myocardium. To address these challenges, free-breathing high-resolution 3D T<sub>2</sub> mapping techniques have been proposed in recent years (8–11), and have for example been applied in patients with graft rejection (12) and myocarditis (13).

Among these techniques, T<sub>2</sub> mapping based on a self-navigated 3D radial acquisition (14, 15) can make use of the intrinsic robustness of 3D radial imaging against undersampling and motion artifacts, but it faces a challenge in its low effective signal-to-noise ratio (SNR), which leads to a loss in precision of the T<sub>2</sub> maps. This 3D radial T<sub>2</sub> mapping has therefore mostly been applied at a magnetic field strength of 3T (8, 12), and not at 1.5T, which may be more commonly used for cardiac magnetic resonance (CMR). However, recently several new techniques have been developed that can be used to increase the precision of a 3D radial T<sub>2</sub> mapping, including resolving the motion instead of correcting it (16) in order to reduce motion streaking artifacts, and using compressed sensing (17) in order to reduce undersampling artifacts and to denoise the source images.

In this study, we therefore aimed to enable 3D radial T<sub>2</sub> mapping at 1.5T by improving the image reconstruction, and to demonstrate the efficacy of this reconstruction method in healthy volunteers as well as in a small cohort of patients with suspected acute non-ischemic myocardial injury. To this end, the T<sub>2</sub> maps were generated by first reconstructing respiratory motion-resolved source images, which were then registered to one another to decrease noise and motion artifacts, and thus to improve 3D T<sub>2</sub> mapping precision and accuracy at 1.5T. These 3D T<sub>2</sub> maps were then compared to routine 2D maps acquired in the same subjects.

## MATERIALS AND METHODS

### Study Participants

This study was approved by the Institutional Review Board of the Medical University of Gdansk (#NKBBN/72/2019). All participants provided written informed consent prior to the procedure and none of them had contraindications for MRI.

**TABLE 1 |** Subject characteristics.

|   | Healthy volunteers<br>(n = 9) | Patients<br>(n = 25) |
|---|-------------------------------|----------------------|
| Age, mean (SD) [years]  | 43(7)                         | 49(11)               |
| Gender, F n(%)  | 5 (56%)                       | 9 (36%)              |
| Heart rate, mean (SD) [bpm]                                   | 68 (11)                       | 67 (13)              |
| BMI, mean (SD) [kg/m <sup>2</sup> ]                           | 24.7 (1.0)                    | 27.2 (4.2)           |
| Hypertension, n(%)  | 0                             | 15(60)               |
| Diabetes, n(%)  | 0                             | 3(12)                |
| Hyperlipidemia, n(%)  | 0                             | 6(24)                |
| CAD, n(%)   | 0                             | 3(12)                |
| LV end-diastolic volume index, mean (SD) [ml/m <sup>2</sup> ] | 71(10)                        | 85(30)               |
| LV end-systolic volume index, mean (SD) [ml/m <sup>2</sup> ]  | 26(7)                         | 39(23)               |
| LV ejection fraction, mean (SD) [%]                           | 65(5)                         | 55(9)                |
| LV mass index, mean (SD) [g/m <sup>2</sup> ]                  | 59(6)                         | 72(18)               |
| Referral diagnosis, n(%)                                      |                               |                      |
| Sarcoidosis   | NA                            | 19(76)               |
| Systemic sclerosis  | NA                            | 2(8)                 |
| Acute graft rejection   | NA                            | 2(8)                 |
| Myocarditis   | NA                            | 2(8)                 |

BMI, body mass index; CAD, coronary artery disease; LV, left ventricular; SD, standard deviation.

To study the baseline relaxation times, healthy volunteers ( $n = 9$ , age =  $43 \pm 7$  y, 5(56%) women, **Table 1**) without any history or symptoms of cardiovascular disease were recruited.

Consecutive patients with suspected acute non-ischemic myocardial injury ( $n = 25$ , 19 cardiac sarcoidosis, 2 acute graft rejection, 2 systemic sclerosis, 2 myocarditis; 9 (36%) women, age  $49 \pm 10$  y; **Table 1**) were recruited.

## MR Acquisition

All MR scanning was performed on a 1.5T clinical scanner (MAGNETOM Aera, Siemens Healthcare, Erlangen, Germany). All participants underwent routine bSSFP cine imaging to assess cardiac function (18), routine breath-held 2D T<sub>2</sub> mapping (19), and the prototype free-breathing 3D T<sub>2</sub> mapping. In addition, the patients underwent routine late gadolinium enhancement (LGE)

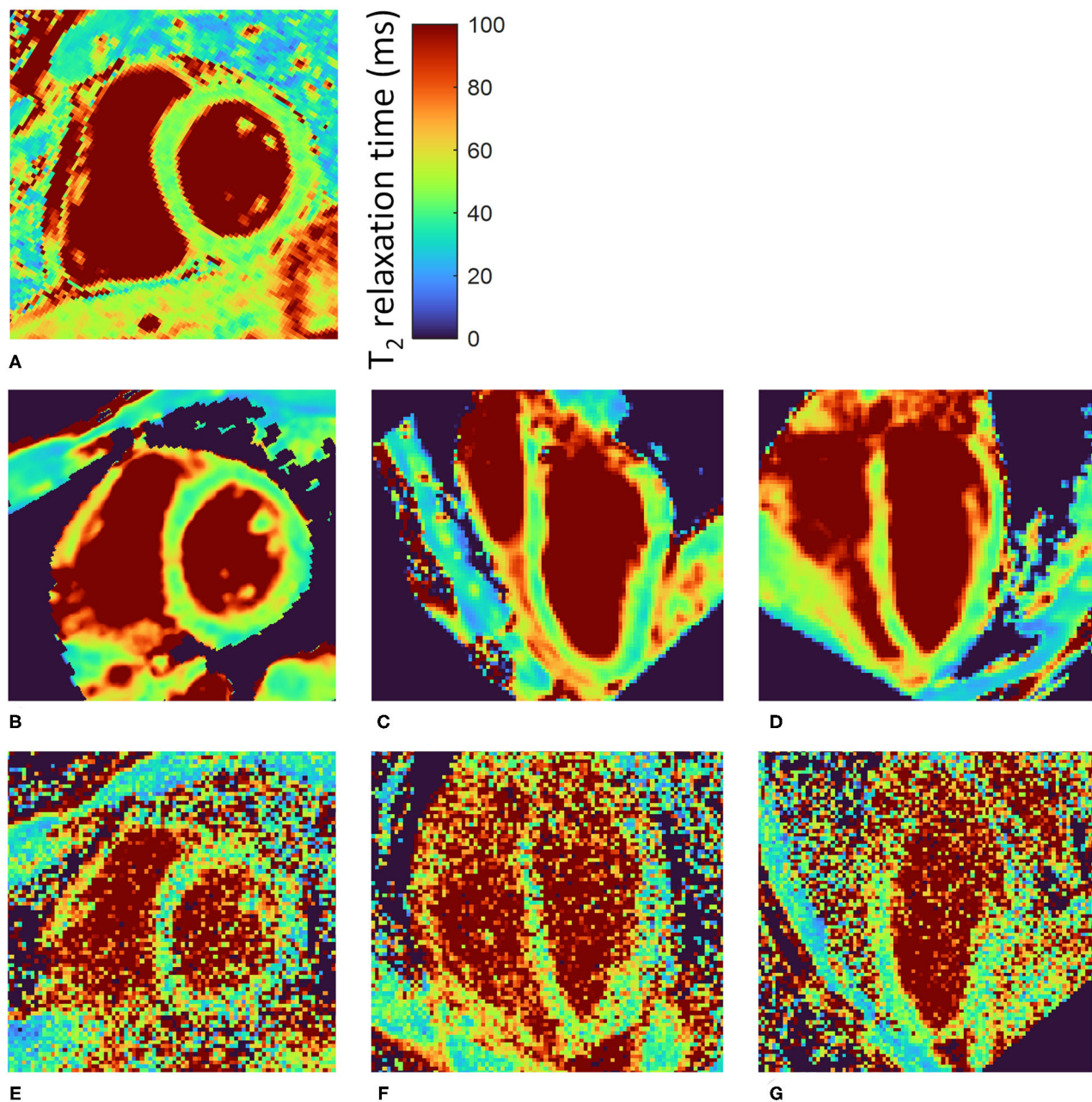


**FIGURE 1 |** Motion-registered 3D T<sub>2</sub> maps of the heart of a healthy volunteer. **(A)** Routine T<sub>2</sub>-prepared 2D bSSFP SAX T<sub>2</sub> map. **(B)** Matching single slice from the motion-registered 3D T<sub>2</sub> map; T<sub>2</sub> values closely match those of the routine map. **(C,D)** Perpendicular long-axis (LAX) maps from the same 3D datasets as in **(B)**. **(E–G)** Three orthogonal slices from a self-navigated reconstruction at approximately the same locations as **(B–D)**. There is a slight orientation mismatch due to manual rotation of the volumes. The color bar shows the T<sub>2</sub> relaxation time in ms.

imaging 7–15 min after injection of 0.1 mmol/kg of gadobutrol (Gadovist, Bayer AG, Leverkusen, Germany).

The routine T<sub>2</sub> maps were acquired as ECG-triggered Cartesian 2D T<sub>2</sub>-prepared bSSFP images (6) with repetition time TR = 2.5 ms, echo time TE = 1.1 ms, flip angle = 70°, pixel bandwidth = 1,184 Hz/px, field of view = 360 × 288 mm<sup>2</sup>, slice thickness = 8 mm, acquired pixel size 2.49 × 1.88 mm<sup>2</sup> interpolated to 1.88 × 1.88 mm<sup>2</sup>, T<sub>2</sub> prep duration = 0/25/55 ms, breath-hold duration nine heartbeats (data acquired every three heartbeats), and GRAPPA acceleration factor 2. Images were acquired in a short-axis (SAX) orientation at the basal and mid-ventricular level. Since the reconstructed 2D maps were immediately available on the scanner, visibly corrupted maps were re-acquired as per routine protocol.

The free-breathing T<sub>2</sub> maps were acquired as three ECG-triggered 3D radial bSSFP volumes with a phyllotaxis trajectory (14), TR = 2.6 ms, TE = 1.3 ms, flip angle = 35°, pixel bandwidth = 908 Hz/px, field of view = (220 mm)<sup>3</sup>, isotropic voxel size 1.6 mm<sup>3</sup>, T<sub>2</sub> prep duration = 0/30/60 ms, and interleaves of 49 k-space lines acquired every other heartbeat preceded by a superior-inferior line that could be used for self-navigation (15). This resulted in a total acquisition time of 112 interleaves × 3 T<sub>2</sub>preps × 2 heartbeats/interleave = 672 heartbeats, or 11.2 min at 60 bpm.

Bloch equation simulations of the abovementioned proposed pulse sequence were performed for a heart rate range from 40 to 90 bpm with an assumed myocardial T<sub>1</sub> relaxation of 1,050 ms and a true T<sub>2</sub> of 50 ms to assess the influence of the heart rate on the estimated T<sub>2</sub> relaxation time.

## T<sub>2</sub> Map Reconstruction

The routine 2D T<sub>2</sub> maps were reconstructed on the scanner (Siemens IDEA, Erlangen, Germany): the source images were non-rigidly registered (20) and a pixel-wise T<sub>2</sub> fit was performed with the standard two-parameter exponential decay without offset, which resulted in maps in the DICOM format.

The respiratory motion-resolved reconstruction of 3D radial volumes (**Supplementary Figure 1**) was performed in MATLAB (the Mathworks, Natick, USA) on a workstation equipped with two Intel Xeon CPUs, 512 GB of RAM, and an NVIDIA Tesla K40 GPU. Here, a principal component analysis (PCA) was performed on the superior-inferior profiles in order to partition the dataset into four different respiratory states. 4D (x-y-z-respiratory dimensions) images were then reconstructed with a parallel imaging and compressed sensing algorithm that exploits sparsity along the respiratory dimension (16, 21, 22), resulting in separate images for all T<sub>2</sub> preparation times and respiratory states. The compressed sensing optimization problem was solved with the conjugate gradient technique (17) using the finite difference operator as a sparsifying transform over the respiratory dimension with a weight  $\lambda$ . All respiratory bins were translationally and then non-rigidly registered to the end-expiration bin with Elastix (23), and were subsequently averaged in order to increase the SNR of each T<sub>2</sub>-prepared volume. After a second, similar, registration of the resulting three averaged T<sub>2</sub>-prepared volumes, voxel-wise T<sub>2</sub> mapping with an offset factor to account for T<sub>1</sub> recovery (24–26) was performed. Since

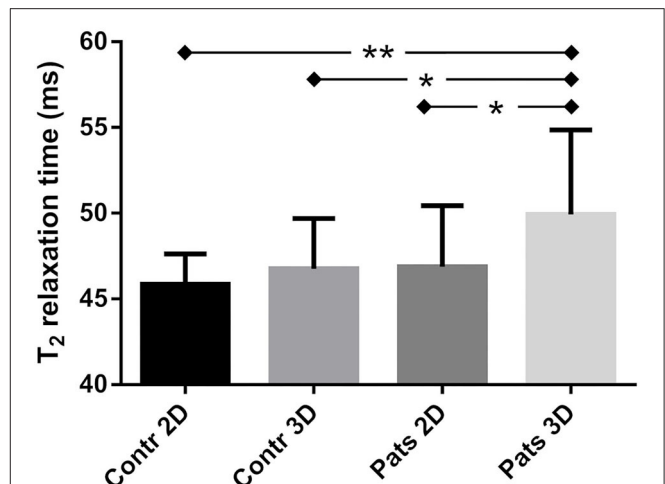


**FIGURE 2 |** Myocardial T<sub>2</sub> relaxation times obtained with the 2D and 3D T<sub>2</sub> mapping techniques in the left ventricle of healthy controls (Contr) and patients (Pats). There was a small but significant difference between the two groups as quantified with the 3D technique, but not with the 2D technique. Within the patient group, the 3D technique also resulted in a small difference compared to the 2D technique. \*indicates  $p < 0.05$ , \*\*indicates  $p < 0.01$ .

the motion is no longer resolved after these registrations, we named the resulting 3D maps “motion-registered” T<sub>2</sub> maps. The total reconstruction time from raw data to T<sub>2</sub> map was recorded.

The regularization weight was optimized by comparing T<sub>2</sub> map sharpness in maps reconstructed with  $\lambda = 0.01$ ,  $\lambda = 0.05$  (the commonly used value at this spatial resolution), and  $\lambda = 0.25$  in a subgroup of  $n = 6$  patients. T<sub>2</sub> map sharpness was assessed by fitting a line from the middle of the septal myocardium to the left-ventricular blood pool with a parametrized sigmoid function ( $T_2(x) = a/(1+e^{-k(b+x)})+c$ ), where  $a$ ,  $b$ , and  $c$  are scaling variables and  $k$  is the sharpness (in  $\text{px}^{-1}$  or  $\text{mm}^{-1}$ ; higher is better) (27). The sharpness assessment was repeated for a total of five adjacent lines and the average sharpness  $k$  was reported. To ascertain that there is no significant difference between the proposed map reconstruction and alternatively first mapping the T<sub>2</sub> relaxation time in each respiratory-resolved bin and then averaging these four bins, the T<sub>2</sub> map sharpness was also quantified in this alternative reconstruction in these  $n = 6$  patients.

In order to visually demonstrate that a self-navigated reconstruction (15) results in non-diagnostic maps at 1.5T due to too low SNR, a self-navigated reconstruction was performed in a single healthy volunteer, since the resulting maps were often too noisy for segmentation and quantitative analysis. This reconstruction was made with the same 3D radial data mentioned above. Here, the 1D displacement of the left-ventricular blood pool along the superior-inferior readouts acquired at the start of each interleave was used to correct each interleave for respiratory motion in k-space prior to image reconstruction (15, 28). The resulting three 3D images were translationally and then non-rigidly registered with Elastix, and voxel-wise T<sub>2</sub> mapping (8) was performed.

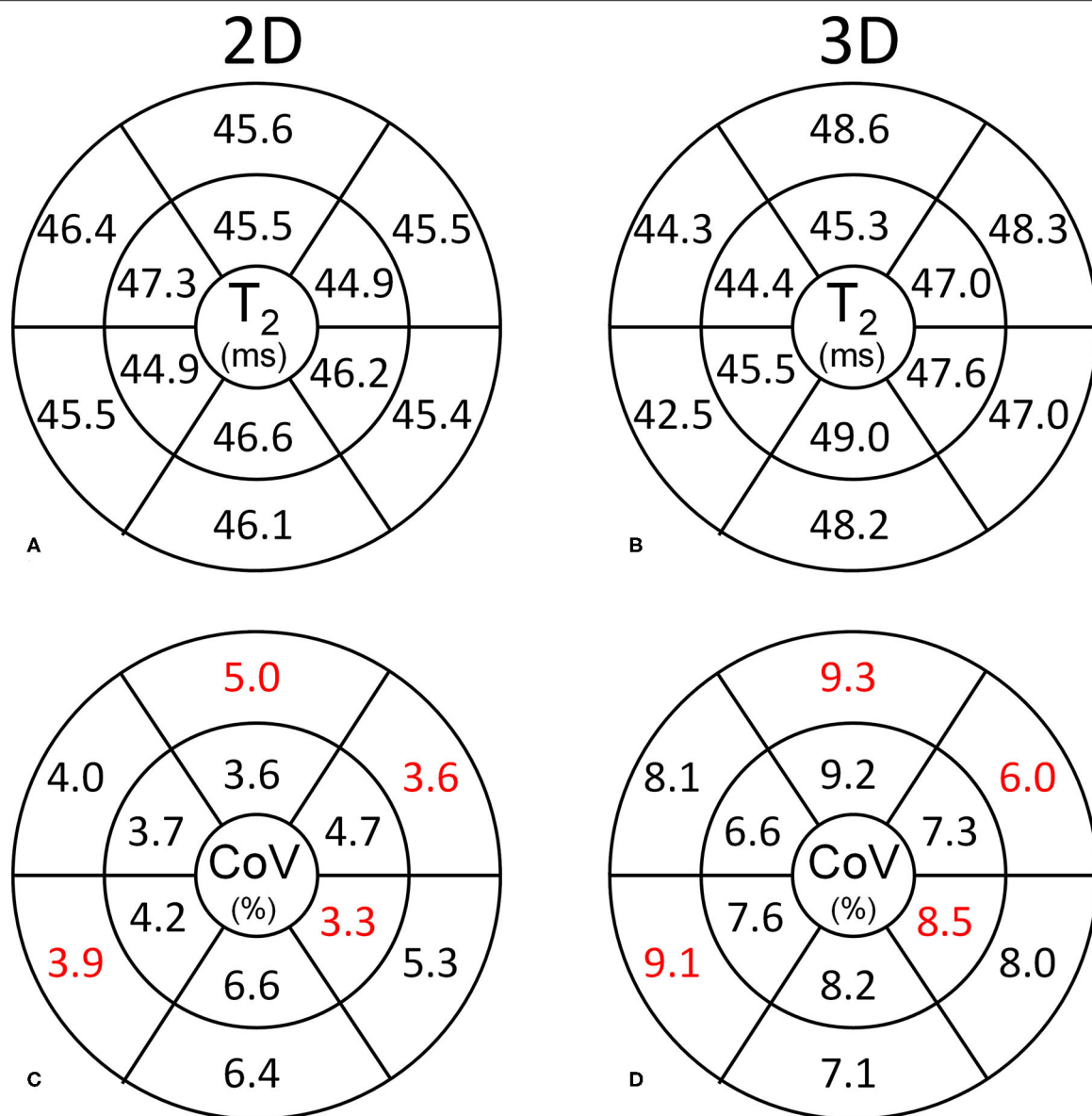
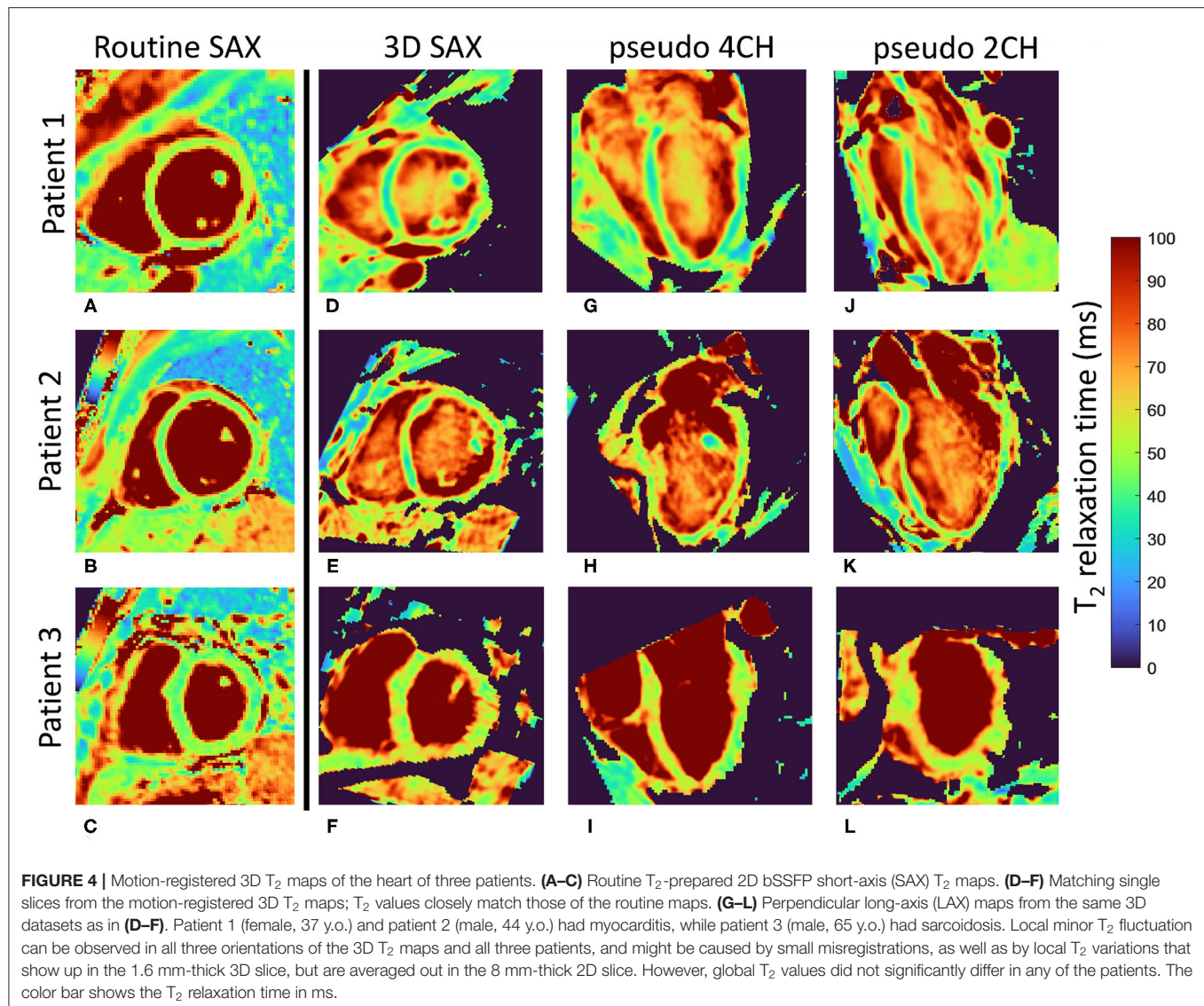


**FIGURE 3 |** Segmental analysis of the myocardial T<sub>2</sub> values in the healthy volunteers. Basal and mid-ventricular segmental T<sub>2</sub> values and CoVs are shown according to the standard AHA segmentation. **(A,B)** The segmental T<sub>2</sub> values obtained with the 2D and 3D techniques are highly similar. **(C,D)** The CoV is consistently lower for the 2D technique than for the 3D technique. Significantly different CoV values between the respective segments are marked in red.

## Map Analysis and Statistics

The visible myocardium in the routine 2D maps and their matching single slices in the 3D volumes were segmented in MATLAB. The T<sub>2</sub> values of the entire visible myocardium and the regional segments defined by the American Heart Association (AHA) (29) were then measured in all volunteers and patients by two independent observers (JF and AS, with 7 and 10 years of experience with cardiac MRI, respectively). For the whole myocardium and 12 out of 16 AHA segments of each subject (2D apical segments were not included as they are generally considered prone to partial volume effects that

may compromise the measurement accuracy) the T<sub>2</sub> values, coefficients of variation (CoV, the standard deviation divided by the average), and the inter-subject standard deviation obtained with the two techniques were calculated. Since segmental values can strongly vary both due to difference in local disease patterns and precision of the technique, segmental T<sub>2</sub> values were only directly compared in the healthy volunteers. In the patients, the segments that were LGE-positive were grouped for comparison with the LGE-negative segments. These values were then compared between the 2D and 3D techniques with paired Student's *t*-tests with a Bonferroni correction



when appropriate, with  $P < 0.05$  considered statistically significant when two quantities were compared. When multiple quantities were compared to one another a one-way ANOVA with a *post-hoc* Tukey correction for multiple comparisons was used.

The total number of segments that was not considered of diagnostic quality (i.e., not clearly defined or too thin for segmentation) by an experienced reader (KD) was counted for the 3D technique; this analysis could not be performed for the 2D technique, since visually corrupted maps were re-acquired, resulting in analyzable 2D T<sub>2</sub> maps in all study subjects. The visual quality of the maps was assessed by two experienced CMR specialists (KD, AG) on a continuous scale from 1 to 10 with a visual analogue (30).

Bland-Altman analyses were performed to assess the T<sub>2</sub> differences between the 2D and 3D techniques in the patients, as well as to assess the inter- and intra-observer agreement for the 3D technique. Trends in these

Bland-Altman plots were tested for significance with Spearman's rank correlation.

## RESULTS

The respiratory motion-resolved reconstruction resulted in visibly well-separated motion states in the source images (**Supplementary Animated Figure 1**), while motion-registered isotropic 3D T<sub>2</sub> maps of the heart were successfully obtained in all subjects (**Figure 1**). Several features in these 3D maps were visually more blurred than their equivalents in the 2D maps. The self-navigated reconstruction of the source images did not lead to diagnostic maps (**Figures 1E–G**). The total reconstruction time from raw data to T<sub>2</sub> map was  $1\text{ h }19 \pm 2\text{ min}$ .

The sharpness measurements in the patient subgroup resulted in  $k = 1.56 \pm 0.22\text{ mm}^{-1}$  for the proposed technique, i.e., respiratory-registered T<sub>2</sub> maps with  $\lambda =$

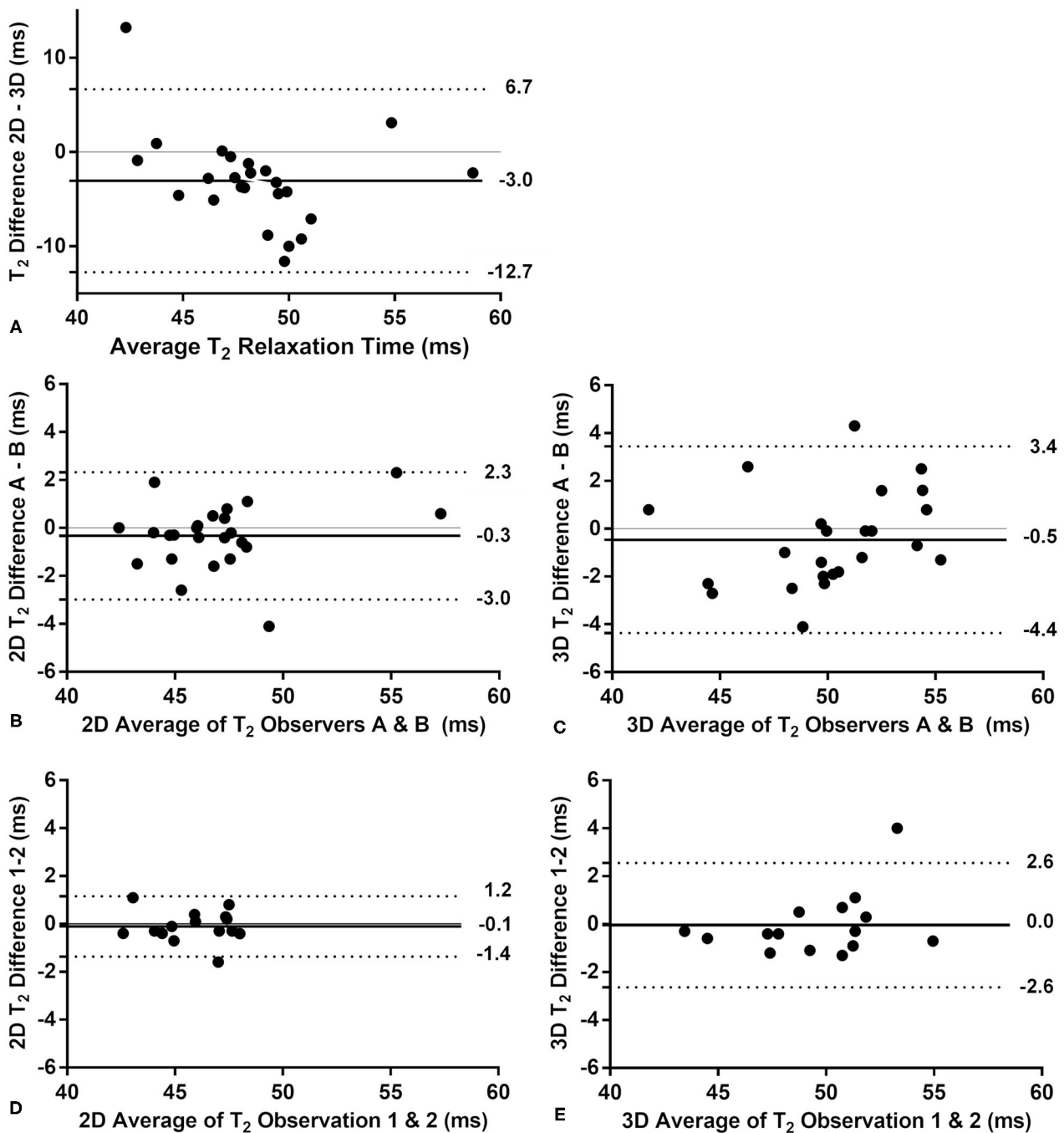


**FIGURE 5 |** Bland-Altman analyses of the 2D vs. the 3D T<sub>2</sub> mapping technique in the patients. The bias is indicated with a solid line, while the upper and lower limits of the 95% confidence interval are indicated with a dotted line. **(A)** The comparison of the 2D and 3D techniques shows a small bias, but no significant trend ( $P = 0.11$  for a linear correlation). **(B)** The interobserver comparison for the routine 2D technique indicates a very small bias and small confidence interval. **(C)** The interobserver comparison of the 3D technique has a similarly small bias and a slightly larger confidence interval than the 2D technique. Neither interobserver plot shows a significant trend ( $P > 0.21$ ). The intra-observer analysis performed in a subset of patients ( $n = 15$ ) showed no bias or trend for the 2D **(D)** and 3D **(E)** techniques, although the confidence interval for the 3D technique was twice as large as that of the 2D technique.

0.05 (Supplementary Figure 2). The motion-registered mapping with  $\lambda = 0.01$  and  $\lambda = 0.25$  resulted in  $k = 1.67 \pm 0.34 \text{ mm}^{-1}$  ( $P = 0.32$ ) and  $k = 1.49 \pm 0.29 \text{ mm}^{-1}$  ( $P = 0.34$ ), respectively.

Mapping each respiratory-resolved bin first and then averaging these maps as an alternative reconstruction resulted in  $k = 1.63 \pm 0.29 \text{ mm}^{-1}$  ( $P = 0.40$ ) for the motion-registered T<sub>2</sub> mapping.

Conversely, the entire patient group resulted in  $k = 1.71 \pm 0.29 \text{ mm}^{-1}$  and  $k = 1.89 \pm 0.40 \text{ mm}^{-1}$  ( $P = 0.038$ ) for the 3D and 2D techniques respectively, demonstrating the higher sharpness in the 2D technique despite the larger pixel size. This also held true in the healthy volunteers at  $k = 1.71 \pm 0.31$  vs.  $k = 1.98 \pm 0.38 \text{ mm}^{-1}$  ( $P = 0.037$ ).

In the healthy volunteers, the myocardial T<sub>2</sub> values obtained with the 2D and 3D techniques were highly similar at  $45.8 \pm 1.8$  and  $46.8 \pm 2.9 \text{ ms}$  ( $P = 0.33$ , **Figure 2**), respectively, while the CoV was lower in the 2D technique at  $4.5 \pm 0.8$  vs.  $8.2 \pm 1.5\%$  for the 3D technique ( $P \leq 0.001$ ). The segmental T<sub>2</sub> values did not significantly differ between the two techniques ( $P \geq 0.09$  for all, **Figures 3A,B**), while the CoV differed in 4 out of 12 segments (**Figures 3C,D**). Out of 108 analyzed segments in the 3D T<sub>2</sub> maps in healthy volunteers, 6 (5.6%, of which 4 [3.7%] in one subject) were deemed non-diagnostic due to inaccurately registered thin myocardium.

In the patients, the average myocardial T<sub>2</sub> relaxation times did differ between the 2D ( $46.7 \pm 3.6 \text{ ms}$ ) and 3D techniques ( $50.1 \pm 4.2 \text{ ms}$ ,  $P = 0.004$ , **Figures 2, 4**). The CoV was again lower in the 2D technique than in the 3D technique at  $6.8 \pm 1.5$  vs.  $10.4 \pm 1.8\%$  ( $P < 0.001$ ). When the myocardium was segmented according to the AHA guidelines, the two techniques resulted in significantly different T<sub>2</sub> values in the basal-anterior, basal-inferior, mid-inferoseptal and mid-inferior segments (segment numbers 1, 4, 9, and 10;  $P \leq 0.001$ ). Conversely, the segmental CoV in the patients was significantly lower for the 2D technique in all segments ( $P \leq 0.001$ ) except in the mid-antero-septal segment. Out of the 300 myocardial segments analyzed in the patients, 14 (4.6%, of which 8 (2.6%) in one patient) were deemed non-diagnostic. A Bland-Altman analysis of the 2D vs. the 3D technique demonstrated that there was a small bias of  $-3.0 \text{ ms}$  (**Figure 5A**). Although a slight trend can be observed for the difference to become more negative as the average increases, this trend was not significant ( $\rho = -0.33$ ,  $P = 0.11$ ). The patient T<sub>2</sub> values as measured with the 2D technique were not significantly different from those in healthy volunteers ( $P = 0.50$ ), while the difference was significant when measured with the 3D technique ( $P = 0.04$ ).

Inter-observer analyses of the 2D and 3D techniques showed very small biases between the observers, no visible or significant trends ( $\rho \leq 0.27$ ,  $P \geq 0.20$ ), and similar confidence intervals (**Figures 5B,C**). The intra-observer analyses of a subset of patients ( $n = 15$ ) showed a higher confidence interval for the 3D technique (**Figures 5D,E**) and no significant trend for either technique ( $\rho < 0.35$ ,  $P > 0.2$ ). The visual quality score was higher for the 2D maps than for the 3D maps at  $9.6 \pm 0.4$  vs.  $7.2 \pm 2.1$  ( $P < 0.001$ , **Supplementary Figure 3**).

The LGE-positive segments did not have a significantly higher T<sub>2</sub> relaxation when compared to their LGE-negative counterparts as quantified with the 2D technique ( $T_{2\text{LGE-}} = 46.2 \pm 3.7$  vs.  $T_{2\text{LGE+}} = 47.6 \pm 4.1 \text{ ms}$ ,  $P = 0.49$ , **Figures 6, 7**). Conversely, the 3D technique did result in a significant difference ( $T_{2\text{LGE-}} = 49.3 \pm 6.7$  vs.  $T_{2\text{LGE+}} = 52.6 \pm 8.7 \text{ ms}$ ,  $P = 0.006$ ) despite its larger spread in individual T<sub>2</sub> values. Both 2D segment groupings were also significantly different from their 3D equivalents ( $P < 0.001$ ). The Bloch equation simulations indicated that the

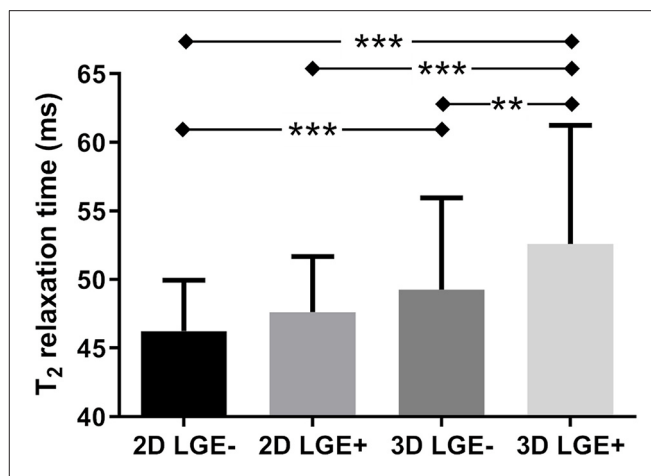


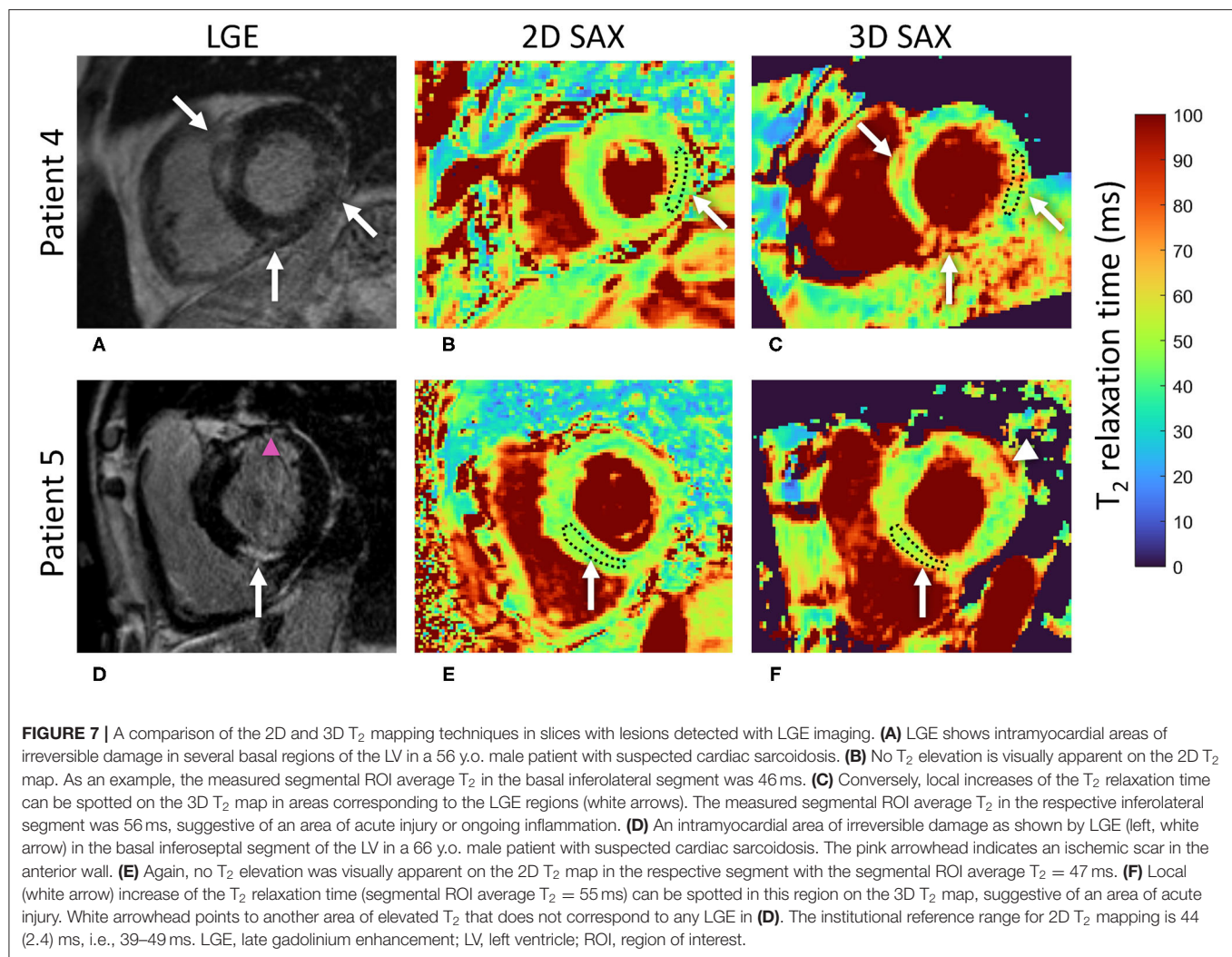
**FIGURE 6 |** T<sub>2</sub> relaxation times in myocardial segments with and without late gadolinium enhancement (LGE). The myocardium of the patients in the LGE images and T<sub>2</sub> maps was segmented according to the AHA guidelines, and all segments of all patients that were LGE-positive (LGE+) were grouped, as were all LGE-negative (LGE-) segments. While there was no difference between the LGE- and LGE+ segments as quantified with the routine 2D technique, a small but significant difference was detected with the proposed 3D T<sub>2</sub> mapping technique. \*\*indicates  $p < 0.01$ , \*\*\*indicates  $p < 0.001$ .

proposed 3D mapping technique will moderately underestimate (<5%) the T<sub>2</sub> relaxation times for high heart rates (80–90 bpm, **Supplementary Figure 4**).

## DISCUSSION

In this study, we proposed a novel method to obtain high-resolution respiratory motion-corrected 3D T<sub>2</sub> maps of the heart at 1.5T by extracting, resolving, and then registering the respiratory motion states, and tested this technique in patients and healthy volunteers. The respiratory motion was detected and visually resolved well in all subjects, and the resulting isotropic 3D T<sub>2</sub> values matched their routine 2D counterparts while also enabling the visualization of other views of the heart.

The T<sub>2</sub> CoV (i.e., the inverse of precision) agreed well with that obtained in previous 3D T<sub>2</sub> mapping studies (8, 12), but was higher than commonly reported for 2D T<sub>2</sub> mapping (31, 32). The main two causes of this are most likely the  $(1.9 \times 1.9 \times 8)/1.6^3 = 7$  times smaller voxel size and the radial acquisition itself, although this is partially compensated by the denoising effect of the compressed-sensing reconstruction and the 3D nature of the acquisition. The higher CoV values that are seen in some segments might result from these particular segments being more prone to small misregistrations due to the neighboring epicardial fat or small myocardial thickness. If a higher precision is desired, it can most likely be achieved by increasing the voxel size, the acquisition time, or the regularization parameters of the reconstruction. Similarly, the observed residual blurring in the short-axis plane could for example be caused by incorrect motion extraction or misregistration. The slightly (but not significantly) different T<sub>2</sub> averages in the healthy volunteers with the 2D and 3D techniques



most likely also have several origins, such as a different interplay with the  $T_1$  relaxation time during the acquisition (24), and a residual noise floor that promotes increased  $T_2$  relaxation time measurements (25). The observed map sharpness agrees well with previous map sharpness quantifications (33), while the minor (and non-significant) differences between the reconstructions with different regularization weights suggest a relatively broad optimum for the regularization parameter. The alternative reconstruction where  $T_2$  maps were obtained for the four respiratory motion bins, followed by averaging of these bins, also led to similar map sharpness, though at the cost of 4-fold longer map fitting time.

It is well-known that  $T_2$  reference values in healthy subjects may vary and that they are therefore not easily comparable between studies (34–36). In addition to magnetic field strength, pulse sequence type, and specific parameters (32), other factors play a role, including gender and cardiac physiology (34). Therefore, the assessment of institution-specific reference ranges with established scanner- and sequence-specific  $T_2$  values in healthy volunteers are strongly recommended (2). With scanner-

and sequence-specific reference values as a prerequisite, it was demonstrated that  $T_2$  values in studies of specific inflammatory conditions such as myocarditis (3), systemic sclerosis (37), and sarcoidosis (35) can unequivocally be used to identify myocardial injury. Therefore, the significant difference in  $T_2$  relaxation time that was found in patients using the 3D but not the 2D  $T_2$  mapping merits special attention, as this might suggest better sensitivity to detect tissue alterations with the proposed high-resolution motion-registered radial 3D  $T_2$  mapping technique at 1.5T. However, confounders such as the observed blurring, SNR, irregular breathing patterns of the patients, and the heart-rate dependence of the pulse sequence should also be taken into consideration. Of note, the patient population in our study was a fairly “healthy” patient population that included consecutive patients with suspected myocardial inflammation, where no large elevation of  $T_2$  was observed by conventional protocol. Therefore, the significantly higher  $T_2$  values in 3D maps in patients that were not seen in conventional 2D maps and were higher than 3D  $T_2$  values in controls suggest potential for the detection of more subtle changes or earlier stages of

disease. Further study will be required in a broader spectrum of disease severity to shed more light on these findings. The proposed 3D technique indicated a small but significant T<sub>2</sub> difference between the LGE+ and LGE- myocardial segments, while the routine 2D technique did not. This may again have a technical origin such as the smaller voxels in the 3D maps having less partial volume effect (especially through the much thinner slices) with healthy tissue that blunts the signal change and therefore reduces the sensitivity. Even though LGE presence by itself does not directly indicate edema or inflammation, it potentially colocalizes with patches of active disease in patients with an ongoing disease process. Thus, the slightly increased T<sub>2</sub> value in LGE+ segments suggests that smaller and isotropic voxels may be more appropriate in patients with potentially focal non-ischemic injury. Nevertheless, a higher sensitivity of 3D T<sub>2</sub> mapping would need to be confirmed with a clinical standard method such as positron emission tomography (38). While we did not evaluate short-axis apical segments in this study, it may be of interest to include these in future studies to take advantage of a reduced partial volume effect consistent with smaller voxel sizes.

The acquisition itself could be improved in several ways in future studies. By using a different radial k-space trajectory for each T<sub>2</sub>-prepared volume (39), the sparsity in the relaxation time dimension could also be exploited for a compressed sensing reconstruction (11), which should result in a higher precision. Calculating the T<sub>2</sub> in each pixel based on an individually patient-specific simulated dictionary (40, 41) could also be used to remove the constraint of acquiring every other heartbeat, which would significantly accelerate the acquisition, and would remove the heart-rate dependence of the T<sub>2</sub> relaxation time.

The higher variation in quality of the 3D maps as compared to the 2D maps is not surprising, as the 2D T<sub>2</sub> maps were immediately re-acquired during the scanning sessions if they were visually of unsatisfactory quality, which was not feasible for 3D T<sub>2</sub> maps because of time constraints. Of note, most of the segments that were termed non-diagnostic belonged to a single patient and a single volunteer, which suggests that there might have been a subject-specific challenge involved, such as particularly thin myocardium or a sub-optimal ECG triggering. Therefore, considering the inherent complexity of the isotropic 3D sequence and multiple reconstruction steps required in the proposed technique, the observed quality score scatter is an expected trade-off, especially with the improvement potential outlined above. Studies with a combination of pseudo-spiral Cartesian trajectory (instead of the 3D radial used here), a 2D respiratory motion correction (instead of the 1D correction), and the addition of patch-based denoising (which improves the apparent SNR) did result in consistent T<sub>2</sub> precision (11, 13). The patch-based denoising (42) in particular could improve the 3D T<sub>2</sub> mapping presented here, since it might improve the apparent SNR of the source images, resulting in better image registration as well as improved map precision.

In conclusion, respiratory motion-registered 3D radial imaging at 1.5T led to accurate isotropic 3D whole-heart T<sub>2</sub>

maps, both in the healthy volunteers and in a small patient cohort with suspected inflammatory myocardial injury. With the 3D technique, significantly higher T<sub>2</sub> values were found in patients as compared to controls, as well as in LGE-positive as compared to LGE-negative segments, both of which were not observed with the routine 2D technique. These findings are suggestive of the technique's potential to increase the sensitivity of CMR for localized inflammatory myocardial injury. Further study will be needed in a broader spectrum of disease severity to demonstrate its clinical utility.

## DATA AVAILABILITY STATEMENT

The raw data supporting the conclusions of this article will be made available by the authors, without undue reservation.

## ETHICS STATEMENT

The studies involving human participants were reviewed and approved by Institutional Review Board of the Medical University of Gdansk. The patients/participants provided their written informed consent to participate in this study.

## AUTHOR CONTRIBUTIONS

KD and RBvH designed the study. LD, CR, DP, MS, JY, and RBvH developed and implemented the pulse sequence and image reconstruction algorithm. KD, JF, and HJ recruited the volunteers and patients and performed their diagnoses. AS and AG performed the MR scanning. RBvH supervised the analysis of MRI results and the manuscript draft. KD, KG, AS, ES, and RBvH analyzed the results and performed the statistical analysis. All authors participated in manuscript drafting and editing, approved the final version of the submitted manuscript, and agreed to the submission of the manuscript to *Frontiers in Cardiovascular Medicine*.

## FUNDING

This study was funded by grants from the Swiss Heart Foundation and the Swiss National Science Foundation (grant number 32003B\_182615) to RH, as well as statutory grant (ST-98) of the Medical University of Gdansk, Poland to KD and HJ.

## ACKNOWLEDGMENTS

The authors wish to thank Beata Brzeska and Malgorzata Grzywinska for their help with the pulse sequence implementation and data handling, and technologists Bogumila Litka and Magdalena Tuzimek for their tireless engagement.

## SUPPLEMENTARY MATERIAL

The Supplementary Material for this article can be found online at: <https://www.frontiersin.org/articles/10.3389/fcvm.2021.712383/full#supplementary-material>

**Supplementary Figure 1 |** A flowchart of the proposed 3D T<sub>2</sub> mapping method. Data are indicated in colored boxes, while manipulations are mentioned as unboxed text.

**Supplementary Figure 2 |** Sharpness measurement and various reconstructions of a 3D T<sub>2</sub> map. **(A)** A T<sub>2</sub> map in grayscale with a display range from 0 to 300 ms to better visualize the blood pool, with red crosses indicating the start- and end-points of the assessed transition. Four horizontal pixel lines below it were also assessed. **(B)** Normalized T<sub>2</sub> values in the pixel (blue circles) and the parametrized sigmoid fit (red curve). The sharpness of the transition was characterized by  $k = 2.6 \text{ px}^{-1}$ , which at the 1.6 mm spatial resolution translated to  $k = 1.6 \text{ mm}^{-1}$ . This value was averaged with those obtained from the lines below it. **(C)** The proposed 3D T<sub>2</sub> mapping method in another patient. **(D)** An alternative reconstruction method in which the individual respiratory bins are all mapped first, and these bin

maps are then averaged. While the papillary muscle appears to resolve better, the sharpness of the blood-myocardium interface remains constant. **(E,F)** The proposed reconstruction method, but with  $\lambda = 0.01$  and 0.25. The blood-myocardium interfaces appear marginally sharper and more blurred, respectively, but this is balanced by respectively increased and decreased T<sub>2</sub> variation in the myocardium.

**Supplementary Figure 3 |** A paired comparison of the visual quality scores as agreed by two experienced readers. The 3D T<sub>2</sub> maps have a much higher variation in quality than the 2D T<sub>2</sub> maps ( $7.2 \pm 2.1$  vs.  $9.6 \pm 0.4$ ,  $P < 0.001$ ), although it should be noted that the 2D T<sub>2</sub> maps were immediately re-acquired during the scanning sessions if they were visually of unsatisfactory quality.

**Supplementary Figure 4 |** A Bloch equation simulation of the influence of the patient's heart rate on the estimated T<sub>2</sub> value. Since sampling occurs every other heartbeat, T<sub>1</sub> relaxation will cause a gradual underestimation of the T<sub>2</sub> value with the increase of the heart rate.

**Supplementary Animated Figure 1 |** An animation of the respiratory-resolved reconstruction of a source image with T<sub>2</sub>prep duration of 30 ms in a patient. The breathing motion is well-resolved, and results in a non-rigid translation of the heart.

## REFERENCES

- Friedrich MG. Myocardial edema—a new clinical entity? *Nat Rev Cardiol.* (2010) 7:292–6. doi: 10.1038/nrcardio.2010.28
- Messroghli DR, Moon JC, Ferreira VM, Grosse-Wortmann L, He T, Kellman P, et al. Clinical recommendations for cardiovascular magnetic resonance mapping of T<sub>1</sub>, T<sub>2</sub>, T<sub>2</sub>\* and extracellular volume: a consensus statement by the Society for Cardiovascular Magnetic Resonance (SCMR) endorsed by the European Association for Cardiovascular Imaging (EACVI). *J Cardiovasc Magn Reson.* (2017) 19:75. doi: 10.1186/s12968-017-0389-8
- Lurz P, Luecke C, Eitel I, Föhrenbach F, Frank C, Grothoff M, et al. Comprehensive cardiac magnetic resonance imaging in patients with suspected myocarditis. *J Am Coll Cardiol.* (2016) 67:1800–11. doi: 10.1016/j.jacc.2016.02.013
- Markousis-Mavrogenis G, Bournia V-K, Panopoulos S, Koutsogeorgopoulou L, Kanoupakis G, Apostolou D, et al. Cardiovascular magnetic resonance identifies high-risk systemic sclerosis patients with normal echocardiograms and provides incremental prognostic value. *Diagnostics.* (2019) 9:220. doi: 10.3390/diagnostics9040220
- Puntmann VO, Isted A, Hinojar R, Foote L, Carr-White G, Nagel E. T1 and T2 mapping in recognition of early cardiac involvement in systemic sarcoidosis. *Radiology.* (2017) 285:63–72. doi: 10.1148/radiol.2017162732
- Giri S, Chung YC, Merchant A, Mihai G, Rajagopalan S, Raman SV, et al. T2 quantification for improved detection of myocardial edema. *J Cardiovasc Magn Reson.* (2009) 11:56. doi: 10.1186/1532-429X-11-56
- Sprinkart AM, Luetkens JA, Träber F, Doerner J, Gieseke J, Schnackenburg B, et al. Gradient Spin Echo (GraSE) imaging for fast myocardial T2 mapping. *J Cardiovasc Magn Reson.* (2015) 17:12. doi: 10.1186/s12968-015-0127-z
- van Heeswijk RB, Piccini D, Feliciano H, Hullin R, Schwitter J, Stuber M. Self-navigated isotropic three-dimensional cardiac T2 mapping. *Magn Reson Med.* (2015) 73:1549–54. doi: 10.1002/mrm.25258
- Ding H, Fernandez-de-Manuel L, Schar M, Schuleri KH, Halperin H, He L, et al. Three-dimensional whole-heart T2 mapping at 3T. *Magn Reson Med.* (2015) 74:803–16. doi: 10.1002/mrm.25458
- Yang HJ, Sharif B, Pang J, Kali A, Bi X, Cokic I, et al. Free-breathing, motion-corrected, highly efficient whole heart T mapping at 3T with hybrid radial-cartesian trajectory. *Magn Reson Med.* (2015) 75:126–36. doi: 10.1002/mrm.25576
- Bustin A, Milotta G, Ismail TF, Neji R, Botnar RM, Prieto C. Accelerated free-breathing whole-heart 3D T<sub>2</sub> mapping with high isotropic resolution. *Magn Reson Med.* (2020) 83:988–1002. doi: 10.1002/mrm.27989
- van Heeswijk RB, Piccini D, Tozzi P, Rotman S, Meyer P, Schwitter J, et al. Three-dimensional self-navigated T2 mapping for the detection of acute cellular rejection after orthotopic heart transplantation. *Transplant Direct.* (2017) 3:e149. doi: 10.1097/TXD.0000000000000635
- Bustin A, Hua A, Milotta G, Jaubert O, Hajhosseiny R, Ismail TF, et al. High-spatial-resolution 3D whole-heart MRI T2 mapping for assessment of myocarditis. *Radiology.* (2021) 298:578–86. doi: 10.1148/radiol.202101630
- Piccini D, Littmann A, NIELLES-Vallespin S, Zenge MO. Spiral phyllotaxis: the natural way to construct a 3D radial trajectory in MRI. *Magn Reson Med.* (2011) 66:1049–56. doi: 10.1002/mrm.22898
- Piccini D, Littmann A, NIELLES-Vallespin S, Zenge MO. Respiratory self-navigation for whole-heart bright-blood coronary MRI: methods for robust isolation and automatic segmentation of the blood pool. *Magn Reson Med.* (2012) 68:571–9. doi: 10.1002/mrm.23247
- Di Sopra L, Piccini D, Coppo S, Stuber M, Yerly J. An automated approach to fully self-gated free-running cardiac and respiratory motion-resolved 5D whole-heart MRI. *Magn Reson Med.* (2019) 82:2118–32. doi: 10.1002/mrm.27898
- Lustig M, Donoho D, Pauly JM. Sparse MRI: the application of compressed sensing for rapid MR imaging. *Magn Reson Med.* (2007) 58:1182–95. doi: 10.1002/mrm.21391
- Kramer CM, Barkhausen J, Flamm SD, Kim RJ, Nagel E, Society for Cardiovascular Magnetic Resonance, Board of Trustees Task Force on Standardized Protocols. Standardized cardiovascular magnetic resonance (CMR) protocols 2013 update. *J Cardiovasc Magn Reson.* (2013) 15:91. doi: 10.1186/1532-429X-15-91
- Huang TY, Liu YJ, Stemmer A, Poncelet BP. T2 measurement of the human myocardium using a T2-prepared transient-state TrueFISP sequence. *Magn Reson Med.* (2007) 57:960–6. doi: 10.1002/mrm.21208
- Chefd'hotel C, Hermosillo G, Faugeras O. Flows of diffeomorphisms for multimodal image registration. In: *Proceedings IEEE International Symposium on Biomedical Imaging.* Washington, DC (2002). p. 753–6.
- Piccini D, Feng L, Bonanno G, Coppo S, Yerly J, Lim RP, et al. Four-dimensional respiratory motion-resolved whole heart coronary MR angiography. *Magn Reson Med.* (2017) 77:1473–84. doi: 10.1002/mrm.26221
- Feng L, Coppo S, Piccini D, Yerly J, Lim RP, Masci PG, et al. 5D whole-heart sparse MRI. *Magn Reson Med.* (2018) 79:826–38. doi: 10.1002/mrm.26745
- Klein S, Staring M, Murphy K, Viergever MA, Pluim JPW. elastix: a toolbox for intensity-based medical image registration. *IEEE Trans Med Imaging.* (2010) 29:196–205. doi: 10.1109/TMI.2009.2035616
- van Heeswijk RB, Feliciano H, Bongard C, Bonanno G, Coppo S, Lauriers N, et al. Free-breathing 3T magnetic resonance T2-mapping of the heart. *JACC Cardiovasc Imaging.* (2012) 5:1231–9. doi: 10.1016/j.jcmg.2012.06.010
- Bano W, Feliciano H, Coristine AJ, Stuber M, van Heeswijk RB. On the accuracy and precision of cardiac magnetic resonance T2 mapping: A high-resolution radial study using adiabatic T2 preparation at 3 T. *Magn Reson Med.* (2017) 77:159–69. doi: 10.1002/mrm.26107

26. Colotti R, Omoumi P, Bonanno G, Ledoux J-B, van Heeswijk RB. Isotropic three-dimensional T2 mapping of knee cartilage: Development and validation. *J Magn Reson Imaging*. (2018) 47:362–71. doi: 10.1002/jmri.25755
27. Ahmad R, Ding Y, Simonetti OP. Edge sharpness assessment by parametric modeling: Application to magnetic resonance imaging: EDGE SHARPNESS ASSESSMENT FOR MRI. *Concepts Magn Reson*. (2015) 44:138–49. doi: 10.1002/cmr.a.21339
28. Piccini D, Monney P, Sierro C, Coppo S, Bonanno G, van Heeswijk RB, et al. Respiratory self-navigated postcontrast whole-heart coronary MR angiography: initial experience in patients. *Radiology*. (2014) 270:378–86. doi: 10.1148/radiol.13132045
29. Cerqueira MD, Weissman NJ, Dilsizian V, Jacobs AK, Kaul S, Laskey WK, et al. Standardized myocardial segmentation and nomenclature for tomographic imaging of the heart. *Circulation*. (2002) 105:539–42. doi: 10.1161/hc0402.102975
30. Suther KR, Hopp E, Smevik B, Fiane AE, Lindberg HL, Larsen S, et al. Can visual analogue scale be used in radiologic subjective image quality assessment? *Pediatr Radiol*. (2018) 48:1567–75. doi: 10.1007/s00247-018-4187-8
31. Wassmuth R, Prothmann M, Utz W, Dieringer M, von Knobelsdorff-Brenkenhoff F, Greiser A, et al. Variability and homogeneity of cardiovascular magnetic resonance myocardial T2-mapping in volunteers compared to patients with edema. *J Cardiovasc Magn Reson*. (2013) 15:27. doi: 10.1186/1532-429X-15-27
32. Baessler B, Schaarschmidt F, Stehning C, Schnackenburg B, Maintz D, Bunck AC. A systematic evaluation of three different cardiac T2-mapping sequences at 1.5 and 3T in healthy volunteers. *Eur J Radiol*. (2015) 84:2161–70. doi: 10.1016/j.ejrad.2015.08.002
33. Wang X, Kohler F, Unterberg-Buchwald C, Lotz J, Frahm J, Uecker M. Model-based myocardial T1 mapping with sparsity constraints using single-shot inversion-recovery radial FLASH cardiovascular magnetic resonance. *J Cardiovasc Magn Reson*. (2019) 21:60. doi: 10.1186/s12968-019-0570-3
34. Granitz M, Motloch LJ, Granitz C, Meissnitzer M, Hitzl W, Hergan K, et al. Comparison of native myocardial T1 and T2 mapping at 1.5T and 3T in healthy volunteers: reference values and clinical implications. *Wien Klin Wochenschr*. (2019) 131:143–55. doi: 10.1007/s00508-018-1411-3
35. Snel GJH, van den Boomen M, Hernandez LM, Nguyen CT, Sosnovik DE, Velthuis BK, et al. Cardiovascular magnetic resonance native T2 and T2\* quantitative values for cardiomyopathies and heart transplantations: a systematic review and meta-analysis. *J Cardiovasc Magn Reson*. (2020) 22:34. doi: 10.1186/s12968-020-00646-8
36. Hamlin SA, Henry TS, Little BP, Lerakis S, Stillman AE. Mapping the future of cardiac MR imaging: case-based review of T1 and T2 mapping techniques. *RadioGraphics*. (2014) 34:1594–611. doi: 10.1148/rg.346140030
37. Galea N, Rosato E, Gigante A, Borrazzo C, Fiorelli A, Barchetti G, et al. Early myocardial damage and microvascular dysfunction in asymptomatic patients with systemic sclerosis: A cardiovascular magnetic resonance study with cold pressor test. *PLoS ONE*. (2020) 15:e0244282. doi: 10.1371/journal.pone.0244282
38. Chareonthaitawee P, Beanlands RS, Chen W, Dorbala S, Miller EJ, Murthy VL, et al. Joint SNMMI–ASNC expert consensus document on the role of 18F-FDG PET/CT in cardiac sarcoid detection and therapy monitoring. *J Nucl Cardiol*. (2017) 24:1741–58. doi: 10.1007/s12350-017-0978-9
39. Darçot E, Yerly J, Colotti R, Masci PG, Chaptin J, Feliciano H, et al. Accelerated and high-resolution cardiac T2 mapping through peripheral k-space sharing. *Magn Reson Med*. (2019) 81:220–33. doi: 10.1002/mrm.27374
40. Hamilton JL, Jiang Y, Chen Y, Ma D, Lo W-C, Griswold M, et al. MR fingerprinting for quantification of myocardial T1, T2, and M0. *Magn Reson Med*. (2017) 77:1446–58. doi: 10.1002/mrm.26216
41. Milotta G, Ginami G, Bustin A, Neji R, Prieto C, Botnar RM. 3D Whole-heart free-breathing qBOOST-T2 mapping. *Magn Reson Med*. (2020) 83:1673–87. doi: 10.1002/mrm.28039
42. Bustin A, Lima da Cruz G, Jaubert O, Lopez K, Botnar RM, Prieto C. High-dimensionality undersampled patch-based reconstruction (HD-PROST) for accelerated multi-contrast MRI. *Magn Reson Med*. (2019) 81:3705–19. doi: 10.1002/mrm.27694

**Conflict of Interest:** DP and KG are full-time employees of Siemens Healthcare.

The remaining authors declare that the research was conducted in the absence of any commercial or financial relationships that could be construed as a potential conflict of interest.

**Publisher's Note:** All claims expressed in this article are solely those of the authors and do not necessarily represent those of their affiliated organizations, or those of the publisher, the editors and the reviewers. Any product that may be evaluated in this article, or claim that may be made by its manufacturer, is not guaranteed or endorsed by the publisher.

Copyright © 2021 Dorniak, Di Sopra, Sabisz, Glinska, Roy, Gorczewski, Piccini, Yerly, Jankowska, Fijałkowska, Szurowska, Stuber and van Heeswijk. This is an open-access article distributed under the terms of the Creative Commons Attribution License (CC BY). The use, distribution or reproduction in other forums is permitted, provided the original author(s) and the copyright owner(s) are credited and that the original publication in this journal is cited, in accordance with accepted academic practice. No use, distribution or reproduction is permitted which does not comply with these terms.



# Randomized Trial of Anti-inflammatory Medications and Coronary Endothelial Dysfunction in Patients With Stable Coronary Disease

Allison G. Hays<sup>1</sup>, Michael Schär<sup>2</sup>, Gabriele Bonanno<sup>2</sup>, Shenghan Lai<sup>3,4</sup>, Joseph Meyer<sup>1</sup>, Yohannes Afework<sup>2</sup>, Angela Steinberg<sup>1</sup>, Samuel Stradley<sup>1</sup>, Gary Gerstenblith<sup>1</sup> and Robert G. Weiss<sup>1,2\*</sup>

<sup>1</sup> Division of Cardiology, Department of Medicine, Johns Hopkins University School of Medicine, Baltimore, MD, United States, <sup>2</sup> Division of Magnetic Resonance Research, Department of Radiology, Johns Hopkins University School of Medicine, Baltimore, MD, United States, <sup>3</sup> Department of Epidemiology, Johns Hopkins Bloomberg School of Public Health, Baltimore, MD, United States, <sup>4</sup> Institute of Human Virology, University of Maryland School of Medicine, Baltimore, MD, United States

## OPEN ACCESS

### Edited by:

Philipp von Hundelshausen,  
Ludwig Maximilian University of  
Munich, Germany

### Reviewed by:

Sebastian Kelle,  
Deutsches Herzzentrum  
Berlin, Germany  
Valery Bochkov,  
University of Graz, Austria

### \*Correspondence:

Robert G. Weiss  
rweiss@jhmi.edu

### Specialty section:

This article was submitted to  
Cardiovascular Imaging,  
a section of the journal  
Frontiers in Cardiovascular Medicine

**Received:** 23 June 2021

**Accepted:** 14 September 2021

**Published:** 15 October 2021

### Citation:

Hays AG, Schär M, Bonanno G, Lai S,  
Meyer J, Afework Y, Steinberg A,  
Stradley S, Gerstenblith G and  
Weiss RG (2021) Randomized Trial of  
Anti-inflammatory Medications and  
Coronary Endothelial Dysfunction in  
Patients With Stable Coronary  
Disease.  
Front. Cardiovasc. Med. 8:728654.  
doi: 10.3389/fcvm.2021.728654

**Aims:** Inflammation plays a critical role in the pathogenesis of coronary artery disease (CAD), however the impact of anti-inflammatory therapies to reduce those processes which promote atherosclerosis in CAD patients is unknown. We aimed to test the hypothesis that anti-inflammatory approaches improve impaired coronary endothelial function (CEF), a driver of coronary atherosclerosis, in stable CAD patients.

**Methods and Results:** We performed a single-center, randomized, placebo-controlled, double-blinded trial to assess whether low dose methotrexate (MTX), low dose colchicine (LDC), and/or their combination (MTX+LDC), improves CEF using non-invasive MRI measures in patients with stable CAD ( $N = 94$ ). The primary endpoint was the MRI-detected change in coronary cross-sectional area from rest to isometric handgrip exercise (IHE), a predominantly nitric oxide-dependent endothelial dependent stressor. Coronary and systemic endothelial endpoints, and serum inflammatory markers, were collected at baseline, 8 and 24 weeks. Anti-inflammatory study drugs were well-tolerated. There were no significant differences in any of the CEF parameters among the four groups (MTX, LDC, MTX+LDC, placebo) at 8 or 24 weeks. Serum markers of inflammation and systemic endothelial function measures were also not significantly different among the groups.

**Conclusion:** This is the first study to examine the effects of the anti-inflammatory approaches using MTX, LDC, and/or the combination in stable CAD patients on CEF, a marker of vascular health and the primary endpoint of the study. Although these anti-inflammatory approaches were relatively well-tolerated, they did not improve coronary endothelial function in patients with stable CAD.

**Clinical Trial Registration:** www.clinicaltrials.gov, identifier: NCT02366091.

**Keywords:** inflammation, coronary artery disease, coronary endothelial function, magnetic resonance imaging, flow mediated dilatation

## INTRODUCTION

Despite advances in contemporary preventive and treatment strategies, coronary atherosclerosis remains prevalent and its manifestations have a high personal and societal toll. Because coronary atherosclerosis is an inflammatory disease (1), there is renewed interest in inflammation as a treatment target (2–4). Endothelial cell injury occurs at the earliest stages of coronary atherosclerosis and inflammatory cells, cytokines, and mediators are involved in all stages of CAD (1, 5). Although coronary atherosclerosis is recognized as an inflammatory process, this important concept is still not applied in the management of patients with, or at risk for, the disease. One important reason is the lack of an established and easily obtained measure of the effect of inflammation on the processes which result in coronary atherosclerosis. Inflammation undoubtedly enhances the development and progression of coronary atherosclerosis via several mechanisms, but endothelial dysfunction is believed to be one common result of these mechanisms (6) and is thus a potential target for medical interventions (6, 7).

One of the principal manifestations of impaired coronary endothelial function is decreased elaboration of nitric oxide (NO) in response to interventions which stimulate endothelial-dependent NO release. NO-mediated changes in coronary cross sectional area and blood flow were historically measured by conventional coronary catheterization-based techniques which are not well-suited to clinical trials in stable patients. Fortunately, non-invasive CEF measures were developed that use 3T magnetic resonance imaging (MRI) to assess endothelial-dependent coronary vasomotor function and these MRI-CEF measures were shown to be reproducible, primarily NO-mediated, and to improve within weeks following LDL lowering with PCSK9 inhibition (8, 9).

Although statins have anti-inflammatory properties (10), cardiovascular event rates remain high in statin treated CAD patients (11), and statins alone do not fully suppress inflammation in many patients (4). Several very recent trials of anti-inflammatory strategies (canakinumab, methotrexate, colchicine) in CAD or myocardial infarction patients reported varied results from reduced events to no benefit (3, 4, 12). It is not clear whether the discrepancies are due to differences in the anti-inflammatory agents or to the populations studied. To date there are no head-to-head comparisons of anti-inflammatory agents in patients with CV disease in a single trial. Likewise, there are no studies of the direct effects of anti-inflammatory strategies on the endothelial processes that contribute directly to coronary atherosclerosis or its progression.

In this study, we performed a randomized double-blinded, placebo-controlled trial to test the hypothesis that anti-inflammatory approaches, namely low dose methotrexate (MTX), low dose colchicine (LDC), and/or their combination,

improve impaired local CEF compared to placebo in patients with stable CAD and either elevated markers of inflammation or diabetes/metabolic syndrome, both inflammatory states. We chose these agents because methotrexate and colchicine have been used in clinical practice for decades to treat inflammatory diseases, they are less expensive than canakinumab and, in observational studies are associated with reduced cardiovascular risk (13). The combination of MTX and LDC (MTX+LDC) is used to treat primary biliary sclerosis and its incorporation in one of the study arms is an additional novel aspect of this trial. In addition, to test whether anti-inflammatory strategies have a rapid, direct vascular effect akin to that previously demonstrated by statins (14), we assessed coronary artery endothelial function by MRI and systemic endothelial function by flow mediated dilation (FMD) in the brachial artery after 8 weeks and again after 24 weeks.

## METHODS

This was a single-center, randomized, double-blinded, placebo-controlled trial with a  $2 \times 2$  factorial design conducted at the Johns Hopkins Hospital and funded by the National Institutes of Health. The purpose was to test the hypothesis that anti-inflammatory strategies improve coronary and systemic arterial endothelial function. Stable CAD patients were recruited from the outpatient clinics at Johns Hopkins Medicine who were on conventional medical therapy (Table 1) and who had either (a) hsCRP  $> 2$  mg/L or (b) either the metabolic syndrome or diabetes. Potential participants underwent screening MRI to measure CEF and those with at least one coronary segment qualifying as “abnormal CEF” [defined as no change or a decrease in coronary cross-sectional area (CSA) during isometric handgrip exercise, i.e., a change of  $\leq 0\%$  of the resting value (8, 15, 16)] underwent additional screening procedures (Figure 1).

After completing all screening procedures, qualifying subjects were randomly assigned to one of the following groups by the Johns Hopkins Investigational Pharmacy:

- 1) MTX: methotrexate (15 mg weekly) + placebo for colchicine (daily) + folate (1 mg daily);
- 2) LDC: colchicine (0.6 mg daily) + placebo for methotrexate (weekly) + folate (1 mg daily);
- 3) MTX+LDC: methotrexate (15 mg weekly) + colchicine (0.6 mg daily) + folate (1 mg daily); or
- 4) Placebo: placebo for methotrexate (weekly) + placebo for colchicine (daily) + folate (1 mg daily).

Folate was administered to reduce potential side effects of MTX and was given to all groups to avoid confounding. The investigators and participants were blinded to the study drug assignment. The study protocol was approved by the Institutional Review Board at The Johns Hopkins Hospital and University School of Medicine and complies with the Declaration of Helsinki. All participants provided written informed consent. Enrollment began April 2015 and the trial ended December 2018. Additional details appear in the **Supplementary Material** and the trial was registered at [www.clinicaltrials.gov](http://www.clinicaltrials.gov) (NCT02366091).

**Abbreviations:** CAD, coronary artery disease; CEF, coronary endothelial function; CSA, cross-sectional area; CBV, coronary blood velocity; CBF, coronary blood flow; FMD, flow mediated dilatation; LDC, low dose colchicine; MRI, magnetic resonance imaging; MTX, methotrexate; NO, nitric oxide; PCSK9, proprotein convertase subtilisin/kexin type 9.

**TABLE 1 |** Demographic characteristics of trial population.

| Baseline characteristics of trial participants         | Both MTX and colchicine (n = 24) | Colchicine and placebo for MTX (n = 23) | MTX and placebo for colchicine (n = 24) | Placebo for both MTX and colchicine (n = 23) |
|--|----------------------------------|---|---|--|
| Median age (IQR)—year                                  | 63.4 (56.9–70.7)                 | 66.8 (56.2–67.9)                        | 61.6 (56.7–68.7)                        | 63.9 (55.9–69.5)                             |
| Male sex—no. (%)                                       | 21 (87.5)                        | 21 (91.3)                               | 18 (75.0)                               | 21 (91.3)                                    |
| Caucasian—no. (%)                                      | 21 (87.5)                        | 19 (82.6)                               | 20 (83.3)                               | 20 (87.0)                                    |
| Black—no. (%)  | 2 (8.3)                          | 3 (13.0)                                | 2 (8.3)                                 | 2 (8.7)                                      |
| Asian—no. (%)  | 0                                | 1 (4.3)                                 | 1 (4.2)                                 | 1 (4.3)                                      |
| Native American—no. (%)                                | 0                                | 0                                       | 0                                       | 1 (4.3)                                      |
| Other race—no. (%)                                     | 1 (4.2)                          | 0                                       | 1 (4.2)                                 | 0  |
| Not Hispanic ethnic group—no. /group number (%)        | 23 (95.8)                        | 22 (91.7)                               | 23 (95.8)                               | 22 (91.7)                                    |
| Current smoker—no. (%)                                 | 4 (16.7)                         | 2 (8.7)                                 | 2 (8.3)                                 | 2 (8.7)                                      |
| Ex-Smoker—no. (%)                                      | 16 (66.7)                        | 12 (52.2)                               | 10 (41.7)                               | 12 (52.2)                                    |
| Never smoked—no. (%)                                   | 4 (16.7)                         | 9 (39.1)                                | 12 (50.0)                               | 9 (39.1)                                     |
| Currently consumes alcohol—no. (%)                     | 20 (83.3)                        | 16 (69.6)                               | 18 (75.0)                               | 20 (87.0)                                    |
| Ex- Drinker of alcohol—no. (%)                         | 2 (8.3)                          | 5 (21.7)                                | 4 (16.7)                                | 3 (13.0)                                     |
| Never consumes alcohol—no. (%)                         | 2 (8.3)                          | 2 (8.7)                                 | 2 (8.3)                                 | 0  |
| Median body-mass index (IQR)                           | 29.6 (28.0–34.0)                 | 29.2 (26.4–32.6)                        | 30.0 (27.1–32.5)                        | 29.5 (27.7–32.9)                             |
| Hypertension—no. (%)                                   | 20 (83.3)                        | 21 (91.3)                               | 20 (83.3)                               | 19 (82.6)                                    |
| Myocardial infarction—no. (%)                          | 10 (41.7)                        | 12 (52.2)                               | 12 (50.0)                               | 14 (60.9)                                    |
| History of percutaneous coronary intervention—no. (%)  | 20 (83.3)                        | 15 (65.2)                               | 17 (70.8)                               | 19 (82.6)                                    |
| History of coronary-artery bypass grafting—no. (%)     | 0                                | 3 (13.0)                                | 3 (12.5)                                | 5 (21.7)                                     |
| History of hyperlipidemia—no. (%)                      | 22 (91.7)                        | 23 (100.0)                              | 21 (87.5)                               | 23 (100.0)                                   |
| History of congestive heart failure—no. (%)            | 1 (4.2)                          | 0                                       | 0                                       | 1 (4.3)                                      |
| Diabetes—no. (%)                                       | 8 (33.3)                         | 11 (47.8)                               | 12 (50.0)                               | 8 (34.8)                                     |
| Metabolic syndrome—no. (%)                             | 23 (95.8)                        | 22 (95.7)                               | 22 (91.7)                               | 22 (95.7)                                    |
| Diabetes and metabolic syndrome—no. (%)                | 8 (33.3)                         | 10 (43.5)                               | 10 (41.7)                               | 8 (34.8)                                     |
| Use of ACE inhibitor or ARB—no. (%)                    | 21 (87.5)                        | 18 (78.3)                               | 17 (70.8)                               | 15 (65.2)                                    |
| Use of statin—no. (%)                                  | 24 (100.0)                       | 23 (100.0)                              | 24 (100.0)                              | 23 (100.0)                                   |
| Use of beta-blocker—no. (%)                            | 11 (45.8)                        | 17 (73.9)                               | 17 (70.8)                               | 15 (65.2)                                    |
| Use of antiplatelet or antithrombotic agent—no. (%)    | 14 (58.3)                        | 9 (39.1)                                | 13 (54.2)                               | 9 (39.1)                                     |
| Median high-sensitivity C-reactive protein level (IQR) | 1.70 (0.80–3.03)                 | 1.00 (0.80–2.20)                        | 1.05 (0.60–2.48)                        | 0.70 (0.40–1.15)                             |

One participant in the placebo arm self-identified with more than one race.

## Study Procedures

Initial evaluation at baseline consisted of history, physical exam, and blood draw. Patients underwent MRI for CEF measures and brachial ultrasound for FMD at baseline, prior to study drug administration and after 8 and 24 weeks of study-drug administration. Study drug compliance was assessed by questionnaire and pill count at the 8, 16, and 24 week follow-up visits.

## MRI Methods for Coronary Endothelial Function (CEF)

Patients underwent MRI studies of CEF in the fasting state at baseline, 8- and 24-weeks using MRI methodology at rest and during continuous IHE as previously described (8, 15, 16). Detailed MRI parameters were previously published (15, 16), and further details are available in the **Supplementary Material**. Images were analyzed blinded to study-drug assignment and clinical information for CEF, as measured by change in cross-sectional area (CSA), coronary flow velocity (CFV), and coronary

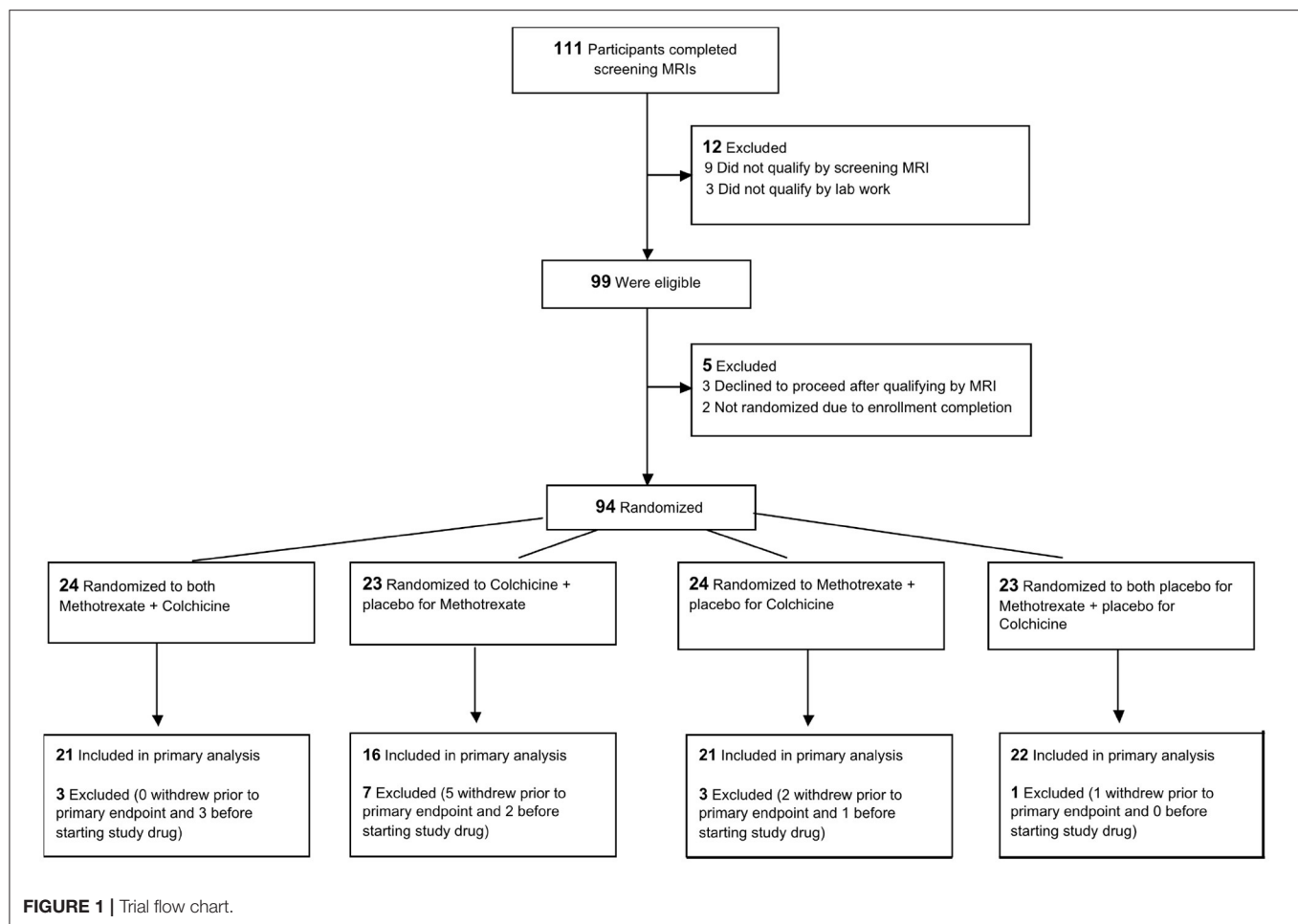
blood flow (CBF), as previously validated and described (15, 17). Our prior studies using this methodology demonstrated low intra- or inter-observer variability with good reproducibility over 8 weeks (8).

## Systemic Endothelial Function and Inflammatory Biomarkers

Brachial flow mediated dilatation (FMD) and velocity were measured in the fasting state using standard techniques and analyzed in blinded fashion. Inflammatory biomarkers were measured at the University of Vermont (**Supplementary Table 1**).

## Sample Size

To test whether any of the anti-inflammatory strategies (i.e., LDC, MTX, and/or their combination) improves CEF in stable CAD patients with increased inflammation and abnormal CEF as compared to that of patients receiving placebo, this  $2 \times 2$  factorial trial was designed with the primary endpoint of change



in coronary cross-sectional area (CSA) from rest to that during IHE at 8 weeks. We chose this parameter because it reflects NO-dependent CEF and was shown to be reproducible over 8 weeks (8). CSA increases during IHE in healthy subjects and is unchanged or declines in patients with CAD (15, 18) and so the sample size was powered on the assumption that an anti-inflammatory medication would improve the CSA change to values midway between those of CAD patients and healthy subjects, in line with methotrexate-induced changes in FMD in patients (19) and the improvement in coronary endothelial function observed with statins (20). With a sample of 88 (22 in each cell), the power was 0.83 ( $\alpha = 0.05$ , two-sided test) to detect a difference between the response in the placebo group and the response in each of the anti-inflammatory groups (8, 16). In November 2018, the CIRT trial was published showing no cardiovascular benefit of MTX (3). With guidance from the DSMB, this trial was stopped at a time when ~90% of the planned population had been enrolled (remaining power 0.8). Details of sample size calculations appear in the **Supplementary Material**.

## Statistical Approach

Demographic and baseline characteristics (e.g., age, race, sex, height, weight, etc.) were summarized using descriptive statistics

for all participants. The primary analysis used an intent-to-treat approach. The primary efficacy endpoint was the % change in CSA from rest to IHE at the end of 8 weeks of the anti-inflammatory or placebo administration periods. The secondary efficacy endpoints included stress-induced change in CBF after 8 weeks of treatment, and change in CSA and CBF with IHE after 24 weeks of treatment. Further statistical details and methods are in the **Supplementary Material**.

## RESULTS

There were no significant differences in baseline clinical and demographic characteristics among subjects randomized to the four study groups (**Table 1**). The median age was 63 years and 14% were women. Fifty-nine percent of the participants had metabolic syndrome with a median BMI of 29.5 kg/m<sup>2</sup>. Participants were clinically stable with a prior history of PCI in 75% and of prior myocardial infarction in 51%. Most patients were receiving guideline-recommended medical therapy for heart disease and all were on statin therapy. The median baseline hsCRP level for the entire cohort was 1.00 mg/L and the median low-density lipoprotein cholesterol level (LDL) was 74 mg/dL with no significant differences among the groups.

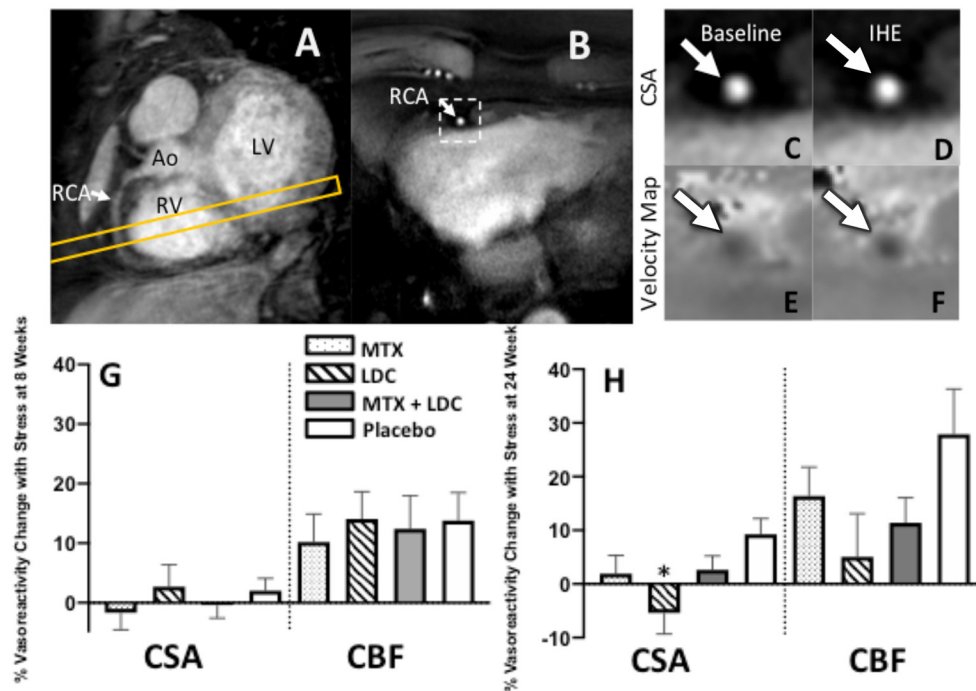


**FIGURE 2 |** Representative coronary artery MRI images for CEF. **(A)** A scout MRI obtained parallel to the right coronary artery (RCA) is shown with the location for subsequent cross-sectional imaging (yellow outline). **(B)** Image acquired along the yellow-outlined region in **(A)** with RCA in cross-section (white arrow). The dotted rectangle in **(B)** is magnified in subsequent panels and shows the region analyzed for cross-sectional area at rest **(C)** and during exercise **(D)**. Flow velocity images of the same segment at rest **(E)** and during IHE **(F)** using a phase contrast technique wherein signal darkness increases only slightly during IHE, indicating an impaired velocity response. **(G,H)** Relative changes (%) in coronary artery cross sectional area (CSA), and coronary blood-flow (CBF) detected by MRI during isometric handgrip exercise at 8 weeks **(G)** and 24 weeks **(H)** for those on methotrexate (MTX, black), colchicine (gray), MTX and colchicine (red), and placebo (blue). Error bars indicate standard error of the mean. There were no significant differences in coronary endothelial function parameters between the placebo and anti-inflammatory treatments at the 8 week (primary) end point. % CSA change was lower in colchicine than placebo ( $p = 0.02$ ) at 24 weeks. Ao, aorta; LV, left ventricle; RV, right ventricle.

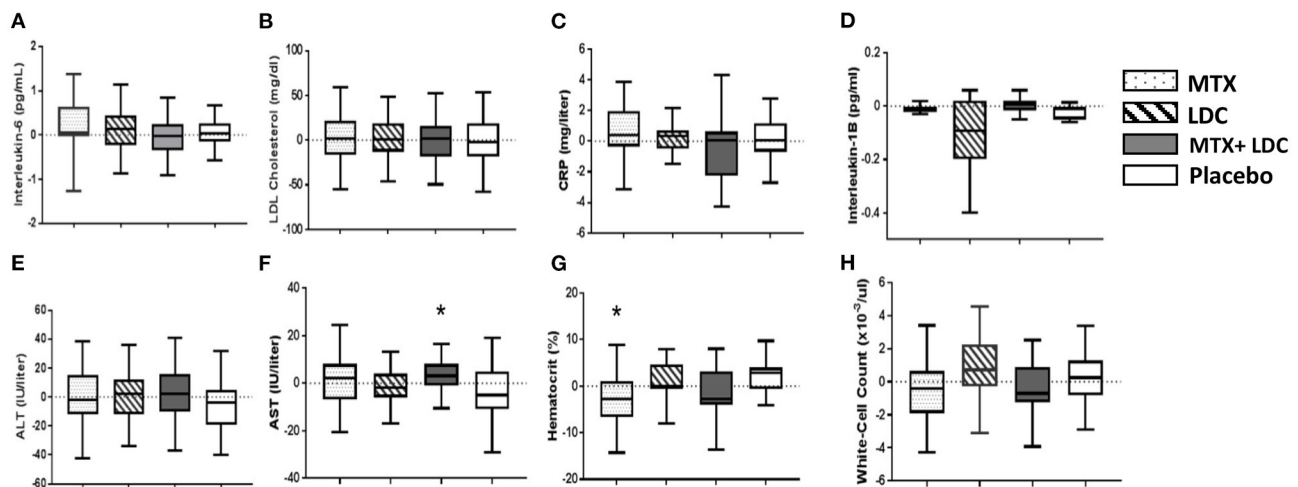


**FIGURE 3 |** Bar graphs showing the effects of low-dose methotrexate (MTX, dotted bar), colchicine (LDC, striped bar), the combination of MTX and LDC (gray bar), and placebo (white bar) on **(A)** interleukin-6, **(B)** low-density lipoprotein [LDL] cholesterol, **(C)** hsCRP, **(D)** interleukin-1 $\beta$ , hepatic enzyme levels **(E)** alanine aminotransferase [ALT] and **(F)** aspartate aminotransferase [AST], and hematologic measures **(G)** hematocrit level, **(H)** white-cell count. Data shown are the changes from study enrollment to 8 weeks after randomization. The horizontal line in each box represents the median, the top and bottom of the boxes represent the interquartile range, and the whiskers represent 1.5 times the interquartile range. \*Statistically significant difference ( $P \leq 0.05$ ) compared to placebo.

Nine subjects qualified by hsCRP >2 mg/L criteria alone, 67 by diabetes/metabolic syndrome criteria, and 18 participants by both hsCRP and diabetes/metabolic syndrome. The disposition of subjects during the trial is shown in **Figure 1**.

## Primary and Secondary End Points, Coronary Endothelial Function

Representative images are shown in **Figure 2**. At baseline, the mean percent change in coronary cross sectional area (CSA) change with IHE for qualifying coronary segments was  $-11.8\% \pm 1.1\%$  and for all coronary segments was  $+0.06\% \pm 1.1\%$ . The percent change at baseline in the endpoint coronary blood flow (CBF) with IHE for qualifying coronary segments was  $+1.6\% \pm 3.9\%$  and  $+14.3\% \pm 2.9\%$  for all coronary segments, consistent with previously published studies in patients with CAD with endothelial dysfunction (15, 16).

The primary endpoint for the study, the change in CSA with IHE following 8 weeks of the anti-inflammatory treatments (MTX, LDC, or MTX + LDC) vs. placebo, did not differ among the study groups (**Figure 2**). Following 8 weeks of MTX, the mean IHE-induced percentage change in CSA for all segments was  $-1.7\% \pm 2.9\%$ , following LDC:  $+2.7\% \pm 3.7\%$ , following MTX+LDC:  $-0.4\% \pm 2.2\%$ , and following 8 weeks of placebo was  $+2.0\% \pm 2.1\%$  ( $p = \text{NS}$ , **Figure 2G**). Similarly, there were no significant differences in % CBF change with IHE at 8 weeks between groups (**Figure 2G**). Similarly, there were no differences among the groups in CEF at 8 weeks if only qualifying coronary segments were included in the analysis. In terms of other secondary endpoints such as CEF at 24 weeks, the % CSA change in the placebo arm was higher than that with colchicine ( $p = 0.02$ ) but no significant differences in % CBF change among treatment

groups were observed at 24 weeks (**Figure 2H**). Detailed CEF results are presented in **Supplementary Tables 3, 4**.

## Secondary Endpoints, Systemic Endothelial Function, and Inflammatory Markers

At 8 weeks, administration of MTX, LDC, the combination or placebo did not result in significant changes in the inflammatory biomarkers of hsCRP, interleukin-6 (IL-6) or interleukin-1B from baseline values (**Figure 3**). At baseline, brachial FMD was  $3.7\% \pm 0.3\%$  (mean  $\pm$  standard error) for all study participants with no significant differences among groups (**Supplementary Table 3**). There were also no differences in brachial FMD among groups after either 8 or 24 weeks of study drug administration (**Supplementary Tables 3, 4**).

## Safety

Overall, study treatment was relatively well-tolerated (**Table 2**). The most common adverse events were gastrointestinal disorders, minor infections and joint and muscle aches. There were very few serious AEs during the course of the study and no difference among study groups (**Table 2**). The reasons for premature withdrawal due to an AE are presented in **Supplementary Table 2**, with the most common reason being gastrointestinal complaints (3 in LDC group and 3 in MTX group). There were no significant changes in AST, ALT, white blood cell count, or LDL cholesterol at 8 weeks as compared to baseline. At 8 weeks, there were small but significant differences in AST level (between the placebo and MTX + LDC groups) and hematocrit (placebo vs. MTX) (**Figure 3**), as well as in

**TABLE 2** | Adverse events are shown in each study group.

| Adverse event or laboratory value (No. of patients)  | Methotrexate<br>(n = 24) | Colchicine<br>(n = 23) | Methotrexate + Colchicine<br>(n = 24) | Placebo<br>(n = 23) |
|--|--------------------------|------------------------|---------------------------------------|---------------------|
| Adverse events                                       | 41                       | 38                     | 46                                    | 33                  |
| Infection (respiratory or other)                     | 8                        | 8                      | 9                                     | 6                   |
| Gastrointestinal disorder                            | 9                        | 9                      | 7                                     | 2                   |
| Joint/Muscle soreness/Stiffness                      | 5                        | 2                      | 7                                     | 7                   |
| Chest pain   | 1                        | 1                      | 1                                     | 1                   |
| Extremity swelling                                   | 1                        | 2                      | 0                                     | 1                   |
| Dental pain/Infection                                | 0                        | 1                      | 2                                     | 1                   |
| Rash   | 2                        | 2                      | 1                                     | 0                   |
| Palpitations   | 1                        | 1                      | 1                                     | 0                   |
| Physical injury                                      | 4                        | 2                      | 1                                     | 2                   |
| Anxiety/Depression                                   | 0                        | 1                      | 3                                     | 0                   |
| Increased aspartate amino trans >3X the normal range | 0                        | 0                      | 1                                     | 0                   |
| Increased alanine amino trans >3X the normal range   | 0                        | 0                      | 1                                     | 0                   |
| Decreased white blood cell count                     | 1                        | 2                      | 1                                     | 3                   |
| Decreased hematocrit                                 | 4                        | 6                      | 8                                     | 6                   |
| Decreased Est GFR                                    | 5                        | 1                      | 3                                     | 4                   |
| Serious adverse event                                | 3                        | 2                      | 0                                     | 1                   |

*There were no significant differences in each adverse event among groups by Cox analysis.*

thrombomodulin (placebo vs. colchicine) and sICAM3 (placebo vs. MTX + LDC) (**Supplementary Table 3**).

## DISCUSSION

We believe this to be the first trial comparing different anti-inflammatory strategies in patients with CAD. In this randomized, double-blinded, placebo-controlled clinical trial, an anti-inflammatory approach with MTX, LDC or the combination of the two did not improve coronary endothelial dysfunction in stable CAD patients on statin therapy. Treatment with MTX, LDC, and the combination did not result in significantly more adverse events or serious adverse events compared to placebo (**Table 2**). Moreover, we observed that treatment with these anti-inflammatory agents did not result in reductions of serum markers of inflammation or improvements in systemic brachial endothelial function in patients with stable CAD.

Endothelial-dependent coronary vasoreactivity is an important index of vascular health and predicts cardiovascular events (6, 21). CEF is impaired early in the atherosclerotic process and can now be measured using novel non-invasive MRI methods (15). Recent studies demonstrate that MRI measures of CEF performed during IHE quantify nitric oxide-mediated coronary endothelial vasoreactivity with excellent short- and longer-term reproducibility (8, 15). Primary and secondary prevention medications such as statins and ACE-inhibitors improve CEF (7, 22). We measured endothelial function at 8 and 24 weeks because prior studies showed that statins rapidly improve endothelial function in the short term (days to weeks) (20, 23, 24) and in the longer term (5–6 months) (7). More recently, we observed that the PCSK9 inhibitor evolocumab improves CEF measured with these MRI techniques in just 6 weeks in patients with dyslipidemia and people living with HIV (9), indicating that the MRI-handgrip technique is sensitive enough to detect relatively rapid improvements in CEF in response to treatment more rapidly and in smaller cohorts than studied here.

A growing body of evidence suggests that inflammation plays an important role in coronary atherosclerosis and endothelial dysfunction, and there is heightened interest in using therapies that target inflammatory pathways to treat atherosclerosis and its complications (25). Recently, several large randomized clinical trials reported varying results using different anti-inflammatory approaches in CAD patients. The CANTOS (Canakinumab Anti-inflammatory Thrombosis Outcome Study) trial showed that the monoclonal antibody canakinumab directed against IL-1B was effective in reducing recurrent cardiovascular events in patients with prior MI and elevated CRP (4). Canakinumab reduced systemic biomarkers of inflammation and vascular events, but was associated with an increased risk of fatal sepsis compared to placebo (4). The more recent CIRT (Cardiovascular Inflammation Reduction Trial) study evaluated the effect of low dose MTX vs. placebo in CAD patients with metabolic syndrome or diabetes and residual increased inflammation, and found that MTX did not reduce inflammatory markers or events compared to placebo and was stopped prematurely due

to futility (3). In the present study, we used a similar dose of MTX and many similar entry criteria and also observed that MTX did not lower markers of inflammation compared to placebo, and show here for the first time that MTX does not improve endothelial dysfunction at 8 and 24 weeks of administration.

Several recent trials evaluated the utility of colchicine to reduce cardiovascular events in patients with CAD (12, 26). While a higher dose of colchicine (0.5 mg twice daily) lowered CRP levels, a lower dose (0.5 mg daily) was used in subsequent endpoint trials (27). The LoDoCo-MI evaluated the acute effects of colchicine vs. placebo in patients following acute MI and with persistently elevated CRP (>2 mg/L), and found that colchicine did not reduce CRP levels 30 days after MI (28). The very recent and much larger COLCOT trial randomized acute MI patients to low dose colchicine vs. placebo and reported a reduction in a composite endpoint of cardiovascular events driven by a lower incidence of stroke and hospitalization for angina in the colchicine group (12). However the inflammatory states in the setting of acute MI as studied in COLCOT compared to stable CAD as studied in the present trial are likely different (12). Moreover, CRP levels declined after MI on both study drugs in COLCOT and there was no difference in CRP decline between colchicine and placebo. Importantly, there was no significant difference in cardiac events (acute infarct and ACS) and the composite event difference was driven by a stroke benefit with colchicine compared to placebo. The most recent LoDoCo2 trial in patients with chronic CAD showed that colchicine reduced a composite primary end-point of cardiovascular death, spontaneous myocardial infarction, ischemic stroke, or ischemia-driven coronary revascularization events but increased the risk of death from non-cardiovascular causes (29). Inflammatory biomarkers were not reported in LoDoCo2 so it is unclear if the effects of colchicine on clinical endpoints were due to suppressing inflammation, duration of treatment or patient specific factors. However, a proteomic sub-study of LoDoCo2 reported that hsCRP and other inflammatory biomarkers were significantly reduced in the colchicine group after 30 days of treatment (30). Other studies have reported that colchicine favorably improves coronary plaque morphology (31) and may play a role in reducing local cardiac inflammatory cytokine production (32). Our study is the first to compare multiple anti-inflammatory medications in the same trial (LDC, MTX, LDC + MTX) and we observe that colchicine alone or in combination with methotrexate does not improve coronary endothelial dysfunction over the short and intermediate term in stable CAD patients on statins. The finding that our anti-inflammatory approach with MTX, LDC or the combination did not reduce inflammatory markers such as CRP is also consistent with the findings in other randomized clinical trials (CIRT, LODOCO-MI, and COLCOT) that reported a neutral effect of similar anti-inflammatory strategies on CRP and other inflammatory markers.

## Adverse Events

There were no significant differences in serious adverse events experienced during treatment with anti-inflammatory agents compared to placebo. All reported AEs were only mild-moderate

in severity, and these findings confirm prior studies of the relative safety and tolerability of MTX and LDC. There are limited data using the combination of MTX and LDC which was not studied previously in CAD patients. A previous study in patients with primary biliary cirrhosis using the combination of LDC and MTX reported few side effects over a 3.4 year period (33). This is consistent with the results of our study, which provides important safety data for their combined use over a 24 week period in patients with stable CAD.

## Limitations

Our study was not powered for clinical outcomes but instead exploited powerful imaging approaches to directly evaluate coronary vascular health in response to the inflammatory interventions in a relatively modest sample size. The cohort size was justified with sample size estimates using prior published data of MRI measures of CE (8, 34). In addition, a prior study showed that this MRI-CEF approach can detect earlier improvements in CEF with PCSK9 inhibition in a smaller-sized cohort (9). The lack of trending differences for benefit among the study groups indicates that a considerably larger sample size is unlikely to have resulted in any significant group differences as well. It may be of interest in future trials to evaluate only subjects with biomarker evidence residual inflammatory risk, as done in the CANTOS trial (4). The MRI-CEF approach can safely detect coronary functional abnormalities in children and adolescents with type I diabetes (35) and thus can be applied to study vascular health and the impact of potential interventions across the lifespan.

## Conclusion

In summary, our study is the first to examine and compare the effects of anti-inflammatory approaches using MTX, LDC or the combination of the two on coronary endothelial dysfunction in patients with stable CAD and either elevated hsCRP or diabetes/metabolic syndrome on stable statin therapy. The anti-inflammatory agents MTX and LDC were generally well-tolerated; however, they did not improve coronary endothelial function, a well-established “barometer” of vascular health. Although MTX and LDC are commonly available, relatively inexpensive anti-inflammatory medications with well-known safety profiles, prior large trials suggest the benefits for cardiovascular disease are difficult to detect (MTX) or possibly limited to mostly cerebrovascular events in selected populations (colchicine). Although prior studies after CABG or post-MI suggested rapid effects of some of these agents to reduce inflammatory biomarkers (28), the current study demonstrates that these agents at these dosages do not reduce systemic markers of inflammation over 2 months in stable CAD patients.

These findings suggest that the short-term and intermediate-term use of these anti-inflammatory approaches in stable CAD patients do not significantly improve either coronary artery or systemic endothelial function, both well-established predictors of cardiovascular outcomes and measures of vascular health.

## DATA AVAILABILITY STATEMENT

The raw data supporting the conclusions of this article will be made available by the authors, without undue reservation.

## ETHICS STATEMENT

The studies involving human participants were reviewed and approved by Johns Hopkins Institutional Review Board. The patients/participants provided their written informed consent to participate in this study.

## AUTHOR CONTRIBUTIONS

This randomized trial was designed by RW, AH, GG, and SL. Patient visits, blood sample collection and preparation, and/or data entry and quality assurance were performed by AS and SS. The MRI and ultrasound data were collected and/or analyzed by AH, MS, GB, YA, and JM. Statistical analysis was performed by SL. This manuscript was drafted by AH. Critically edited by AH, GG, SL, and RW. Funding was obtained by RW. All authors contributed to the article and approved the submitted version.

## FUNDING

This work was supported by the National Institutes of Health (HL120905 to RW, HL147660 to AH), the American Heart Association (AHA 17GRNT33670943 to AH), and the Clarence Doodeman Endowment in Cardiology at Johns Hopkins University School of Medicine.

## ACKNOWLEDGMENTS

The authors thank the members of the Data Safety and Monitoring Board, the physicians who referred patients to this study and the patients who participated.

## SUPPLEMENTARY MATERIAL

The Supplementary Material for this article can be found online at: <https://www.frontiersin.org/articles/10.3389/fcvm.2021.728654/full#supplementary-material>

## REFERENCES

- Ross R. Atherosclerosis—an inflammatory disease. *N Engl J Med*. (1999) 340:115–26. doi: 10.1056/NEJM199901143400207
- Ridker PM. Clinician's guide to reducing inflammation to reduce atherothrombotic risk: JACC review topic of the week. *J Am Coll Cardiol*. (2018) 72:3320–31. doi: 10.1016/j.jacc.2018.06.082

3. Ridker PM, Everett BM, Pradhan A, MacFadyen JG, Solomon DH, Zaharris E, et al. Low-dose methotrexate for the prevention of atherosclerotic events. *N Engl J Med.* (2019) 380:752–62. doi: 10.1056/NEJMoa1809798
4. Ridker PM, Everett BM, Thuren T, MacFadyen JG, Chang WH, Ballantyne C, et al. Antiinflammatory therapy with canakinumab for atherosclerotic disease. *N Engl J Med.* (2017) 377:1119–31. doi: 10.1056/NEJMoa1707914
5. Libby P, Ridker PM, Maseri A. Inflammation and atherosclerosis. *Circulation.* (2002) 105:1135–43. doi: 10.1161/hc0902.104353
6. Deanfield JE, Halcox JP, Rabelink TJ. Endothelial function and dysfunction: testing and clinical relevance. *Circulation.* (2007) 115:1285. doi: 10.1161/CIRCULATIONAHA.106.652859
7. Treasure CB, Klein JL, Weintraub WS, Talley JD, Stillabower ME, Kosinski AS, et al. Beneficial effects of cholesterol-lowering therapy on the coronary endothelium in patients with coronary artery disease. *N Engl J Med.* (1995) 332:481–7. doi: 10.1056/NEJM199502233320801
8. Hays AG, Iantorno M, Soleimanifard S, Steinberg A, Schar M, Gerstenblith G, et al. Coronary vasomotor responses to isometric handgrip exercise are primarily mediated by nitric oxide: a noninvasive MRI test of coronary endothelial function. *Am J Physiol Heart Circ Physiol.* (2015) 308:H1343–50. doi: 10.1152/ajpheart.00023.2015
9. Leucker TM, Gerstenblith G, Schar M, Brown TT, Jones SR, Afework Y, et al. Evolocumab, a PCSK9-monoclonal antibody, rapidly reverses coronary artery endothelial dysfunction in people living with HIV and people with dyslipidemia. *J Am Heart Assoc.* (2020) 9:e016263. doi: 10.1161/JAHA.120.016263
10. Topol EJ. Intensive statin therapy—a sea change in cardiovascular prevention. *N Engl J Med.* (2004) 350:1562–4. doi: 10.1056/NEJMe048061
11. Cannon CP, Braunwald E, McCabe CH, Rader DJ, Rouleau JL, Belder R, et al. Intensive versus moderate lipid lowering with statins after acute coronary syndromes. *N Engl J Med.* (2004) 350:1495–504. doi: 10.1056/NEJMoa040583
12. Tardif JC, Kouz S, Waters DD, Bertrand OF, Diaz R, Maggioni AP, et al. Efficacy and safety of low-dose colchicine after myocardial infarction. *N Engl J Med.* (2019) 381:2497–505. doi: 10.1056/NEJMoa1912388
13. Crittenden DB, Lehmann RA, Schneck L, Keenan RT, Shah B, Greenberg JD, et al. Colchicine use is associated with decreased prevalence of myocardial infarction in patients with gout. *J Rheumatol.* (2012) 39:1458–64. doi: 10.3899/jrheum.111533
14. Antoniadis C, Bakogiannis C, Leeson P, Guzik TJ, Zhang MH, Tousoulis D, et al. Rapid, direct effects of statin treatment on arterial redox state and nitric oxide bioavailability in human atherosclerosis via tetrahydrobiopterin-mediated endothelial nitric oxide synthase coupling. *Circulation.* (2011) 124:335–45. doi: 10.1161/CIRCULATIONAHA.110.985150
15. Hays AG, Hirsch GA, Kelle S, Gerstenblith G, Weiss RG, Stuber M. Noninvasive visualization of coronary artery endothelial function in healthy subjects and in patients with coronary artery disease. *J Am Coll Cardiol.* (2010) 56:1657–65. doi: 10.1016/j.jacc.2010.06.036
16. Hays AG, Iantorno M, Schar M, Mukherjee M, Stuber M, Gerstenblith G, et al. Local coronary wall eccentricity and endothelial function are closely related in patients with atherosclerotic coronary artery disease. *J Cardiovasc Magn Reson.* (2017) 19:51. doi: 10.1186/s12968-017-0358-2
17. Iantorno M, Hays AG, Schar M, Krishnaswamy R, Soleimanifard S, Steinberg A, et al. Simultaneous noninvasive assessment of systemic and coronary endothelial function. *Circ Cardiovasc Imaging.* (2016) 9:e003954. doi: 10.1161/CIRCIMAGING.115.003954
18. Hays AG, Kelle S, Hirsch GA, Soleimanifard S, Yu J, Agarwal HK, et al. Regional coronary endothelial function is closely related to local early coronary atherosclerosis in patients with mild coronary artery disease: pilot study. *Circ Cardiovasc Imaging.* (2012) 5:341–8. doi: 10.1161/CIRCIMAGING.111.969691
19. Hjeltne G, Hollan I, Førre Ø, Wiik A, Lyberg T, Mikkelsen K, et al. Endothelial function improves within 6 weeks of treatment with methotrexate or methotrexate in combination with a TNF- $\alpha$  inhibitor in rheumatoid arthritis patients. *Scand J Rheumatol.* (2012) 41:240–2. doi: 10.3109/03009742.2012.656698
20. Wassmann S, Faul A, Hennen B, Scheller B, Böhm M, Nickenig G. Rapid effect of 3-hydroxy-3-methylglutaryl coenzyme a reductase inhibition on coronary endothelial function. *Circ Res.* (2003) 93:e98–103. doi: 10.1161/01.RES.0000099503.13312.7B
21. Schachinger V, Britten MB, Zeiher AM. Prognostic impact of coronary vasodilator dysfunction on adverse long-term outcome of coronary heart disease. *Circulation.* (2000) 101:1899–906. doi: 10.1161/01.CIR.101.16.1899
22. Anderson TJ, Meredith IT, Yeung AC, Frei B, Selwyn AP, Ganz P. The effect of cholesterol-lowering and antioxidant therapy on endothelium-dependent coronary vasomotion. *New Engl J Med.* (1995) 332:488. doi: 10.1056/NEJM199502233320802
23. John S, Schneider MP, Delles C, Jacobi J, Schmieder RE. Lipid-independent effects of statins on endothelial function and bioavailability of nitric oxide in hypercholesterolemic patients. *Am Heart J.* (2005) 149:473. doi: 10.1016/j.ahj.2004.06.027
24. Laufs U, Wassmann S, Hilgers S, Ribaudo N, Böhm M, Nickenig G. Rapid effects on vascular function after initiation and withdrawal of atorvastatin in healthy, normocholesterolemic men. *Am J Cardiol.* (2001) 88:1306. doi: 10.1016/S0002-9149(01)02095-1
25. Libby P. Inflammation in atherosclerosis. *Nature.* (2002) 420:868–74. doi: 10.1038/nature01323
26. Nidorf SM, Eikelboom JW, Budgeon CA, Thompson PL. Low-dose colchicine for secondary prevention of cardiovascular disease. *J Am Coll Cardiol.* (2013) 61:404–10. doi: 10.1016/j.jacc.2012.10.027
27. Nidorf M, Thompson PL. Effect of colchicine (0.5 mg twice daily) on high-sensitivity C-reactive protein independent of aspirin and atorvastatin in patients with stable coronary artery disease. *Am J Cardiol.* (2007) 99:805–7. doi: 10.1016/j.amjcard.2006.10.039
28. Hennessy T, Soh L, Bowman M, Kurup R, Schultz C, Patel S, et al. The Low Dose Colchicine after Myocardial Infarction (LoDoCo-MI) study: a pilot randomized placebo controlled trial of colchicine following acute myocardial infarction. *Am Heart J.* (2019) 215:62–9. doi: 10.1016/j.ahj.2019.06.003
29. Nidorf SM, Fiolet ATL, Mosterd A, Eikelboom JW, Schut A, Opstal TSJ, et al. Colchicine in patients with chronic coronary disease. *N Engl J Med.* (2020) 383:1838–47. doi: 10.1056/NEJMoa2021372
30. Opstal TSJ, Hoogeveen RM, Fiolet ATL, Silvis MJM, The SHK, Bax WA, et al. Colchicine attenuates inflammation beyond the inflammasome in chronic coronary artery disease: a LoDoCo2 proteomic substudy. *Circulation.* (2020) 142:1996–8. doi: 10.1161/CIRCULATIONAHA.120.050560
31. Vaidya K, Arnott C, Martinez GJ, Ng B, McCormack S, Sullivan DR, et al. Colchicine therapy and plaque stabilization in patients with acute coronary syndrome: a CT coronary angiography study. *JACC Cardiovasc Imaging.* (2018) 11(2 Pt 2):305–16. doi: 10.1016/j.jcmg.2017.08.013
32. Martinez GJ, Robertson S, Barraclough J, Xia Q, Mallat Z, Bursill C, et al. Colchicine acutely suppresses local cardiac production of inflammatory cytokines in patients with an acute coronary syndrome. *J Am Heart Assoc.* (2015) 4:e002128. doi: 10.1161/JAHA.115.002128
33. Kaplan MM, Bonder A, Ruthazer R, Bonis PA. Methotrexate in patients with primary biliary cirrhosis who respond incompletely to treatment with ursodeoxycholic acid. *Digest Dis Sci.* (2010) 55:3207–17. doi: 10.1007/s10620-010-1291-5

34. Schar M, Soleimanifard S, Bonanno G, Yerly J, Hays AG, Weiss RG. Precision and accuracy of cross-sectional area measurements used to measure coronary endothelial function with spiral MRI. *Magn Reson Med*. (2019) 81:291–302. doi: 10.1002/mrm.27384
35. Zwingli G, Yerly J, Mivelaz Y, Stoppa-Vaucher S, Dwyer AA, Pitteloud N, et al. Non-invasive assessment of coronary endothelial function in children and adolescents with type 1 diabetes mellitus using isometric handgrip exercise-MRI: a feasibility study. *PLoS ONE*. (2020) 15:e0228569. doi: 10.1371/journal.pone.0228569

**Conflict of Interest:** The authors declare that the research was conducted in the absence of any commercial or financial relationships that could be construed as a potential conflict of interest.

**Publisher's Note:** All claims expressed in this article are solely those of the authors and do not necessarily represent those of their affiliated organizations, or those of the publisher, the editors and the reviewers. Any product that may be evaluated in this article, or claim that may be made by its manufacturer, is not guaranteed or endorsed by the publisher.

Copyright © 2021 Hays, Schär, Bonanno, Lai, Meyer, Afework, Steinberg, Stradley, Gerstenblith and Weiss. This is an open-access article distributed under the terms of the Creative Commons Attribution License (CC BY). The use, distribution or reproduction in other forums is permitted, provided the original author(s) and the copyright owner(s) are credited and that the original publication in this journal is cited, in accordance with accepted academic practice. No use, distribution or reproduction is permitted which does not comply with these terms.



# Myocardial Perfusion Imaging After Severe COVID-19 Infection Demonstrates Regional Ischemia Rather Than Global Blood Flow Reduction

George D. Thornton<sup>1,2</sup>, Abhishek Shetye<sup>1,2</sup>, Dan S. Knight<sup>2,3</sup>, Kris Knott<sup>1</sup>, Jessica Artico<sup>1,2</sup>, Hibba Kurdi<sup>1</sup>, Souhad Yousef<sup>1</sup>, Dimitra Antonakaki<sup>1</sup>, Yousuf Razvi<sup>3,4</sup>, Liza Chacko<sup>3,4</sup>, James Brown<sup>3,4</sup>, Rishi Patel<sup>3,4</sup>, Kavitha Vimalasvaran<sup>5,6</sup>, Andreas Seraphim<sup>1,2</sup>, Rhodri Davies<sup>1,2</sup>, Hui Xue<sup>7</sup>, Tushar Kotecha<sup>2,3</sup>, Robert Bell<sup>8</sup>, Charlotte Manisty<sup>1,2</sup>, Graham D. Cole<sup>5,6</sup>, James C. Moon<sup>1,2</sup>, Peter Kellman<sup>7</sup>, Marianna Fontana<sup>3,4</sup> and Thomas A. Treibel<sup>1,2\*</sup>

## OPEN ACCESS

### Edited by:

Sebastian Kelle,  
Deutsches Herzzentrum  
Berlin, Germany

### Reviewed by:

Ali Yilmaz,  
University Hospital Münster, Germany  
Filippo Cademartiri,  
Gabriele Monasterio Tuscany  
Foundation (CNR), Italy

### \*Correspondence:

Thomas A. Treibel  
Thomas.Treibel@nhs.net

### Specialty section:

This article was submitted to  
Cardiovascular Imaging,  
a section of the journal  
Frontiers in Cardiovascular Medicine

**Received:** 25 August 2021

**Accepted:** 06 October 2021

**Published:** 07 December 2021

### Citation:

Thornton GD, Shetye A, Knight DS, Knott K, Artico J, Kurdi H, Yousef S, Antonakaki D, Razvi Y, Chacko L, Brown J, Patel R, Vimalasvaran K, Seraphim A, Davies R, Xue H, Kotecha T, Bell R, Manisty C, Cole GD, Moon JC, Kellman P, Fontana M and Treibel TA (2021) Myocardial Perfusion Imaging After Severe COVID-19 Infection Demonstrates Regional Ischemia Rather Than Global Blood Flow Reduction. *Front. Cardiovasc. Med.* 8:764599. doi: 10.3389/fcvm.2021.764599

<sup>1</sup> Barts Heart Center, Barts Health NHS Trust, London, United Kingdom, <sup>2</sup> Institute of Cardiovascular Science, University College, London, United Kingdom, <sup>3</sup> Royal Free London NHS Foundation Trust, London, United Kingdom, <sup>4</sup> Division of Medicine, National Amyloidosis Center, University College, London, United Kingdom, <sup>5</sup> Imperial College Healthcare NHS Trust, London, United Kingdom, <sup>6</sup> National Heart and Lung Institute, Imperial College London, London, United Kingdom, <sup>7</sup> National Heart, Lung, and Blood Institute, National Institute of Health, Bethesda, MD, United States, <sup>8</sup> Department of Cardiology, University College London Hospitals NHS Trust, London, United Kingdom

**Background:** Acute myocardial damage is common in severe COVID-19. Post-mortem studies have implicated microvascular thrombosis, with cardiovascular magnetic resonance (CMR) demonstrating a high prevalence of myocardial infarction and myocarditis-like scar. The microcirculatory sequelae are incompletely characterized. Perfusion CMR can quantify the stress myocardial blood flow (MBF) and identify its association with infarction and myocarditis.

**Objectives:** To determine the impact of the severe hospitalized COVID-19 on global and regional myocardial perfusion in recovered patients.

**Methods:** A case-control study of previously hospitalized, troponin-positive COVID-19 patients was undertaken. The results were compared with a propensity-matched, pre-COVID chest pain cohort (referred for clinical CMR; angiography subsequently demonstrating unobstructed coronary arteries) and 27 healthy volunteers (HV). The analysis used visual assessment for the regional perfusion defects and AI-based segmentation to derive the global and regional stress and rest MBF.

**Results:** Ninety recovered post-COVID patients {median age 64 [interquartile range (IQR) 54–71] years, 83% male, 44% requiring the intensive care unit (ICU)} underwent adenosine-stress perfusion CMR at a median of 61 (IQR 29–146) days post-discharge. The mean left ventricular ejection fraction (LVEF) was  $67 \pm 10\%$ ; 10 (11%) with impaired LVEF. Fifty patients (56%) had late gadolinium enhancement (LGE); 15 (17%) had infarct-pattern, 31 (34%) had non-ischemic, and 4 (4.4%) had mixed pattern LGE. Thirty-two patients (36%) had adenosine-induced regional perfusion defects, 26 out of

32 with at least one segment without prior infarction. The global stress MBF in post-COVID patients was similar to the age-, sex- and co-morbidities of the matched controls ( $2.53 \pm 0.77$  vs.  $2.52 \pm 0.79$  ml/g/min,  $p = 0.10$ ), though lower than HV ( $3.00 \pm 0.76$  ml/g/min,  $p < 0.01$ ).

**Conclusions:** After severe hospitalized COVID-19 infection, patients who attended clinical ischemia testing had little evidence of significant microvascular disease at 2 months post-discharge. The high prevalence of regional inducible ischemia and/or infarction (nearly 40%) may suggest that occult coronary disease is an important putative mechanism for troponin elevation in this cohort. This should be considered hypothesis-generating for future studies which combine ischemia and anatomical assessment.

**Keywords:** cardiac MRI, perfusion, COVID-19, microvascular dysfunction, myocardial blood flow

## INTRODUCTION

Coronavirus disease 2019 caused by severe acute respiratory syndrome coronavirus 2 (SARS-CoV-2), disproportionately affects patients with cardiovascular risk factors. Myocardial injury, particularly seen in severe and hospitalized COVID-19 and evidenced by raised cardiac troponin, heralds worse outcomes (1, 2). However, the mechanisms of injury remain only partially understood, and the potential coronary microcirculatory sequelae remain incompletely characterized (3). Several ischemic and non-ischemic mechanisms have been proposed, including supply-demand mismatch (type-2 myocardial infarction) and microangiopathic thrombosis (4). Accumulating evidence suggests that the vascular endothelium plays a critical role in the pathogenesis of severe COVID-19 as a nidus for both pro-coagulant and inflammatory dysregulation and may offer a unifying pathway through which all these sequelae may occur (5, 6). Autopsy results have shown microthrombi to be associated with myocyte necrosis (7). The implications for survivors and the potential long-term effects on coronary microcirculation remain unknown. Cardiovascular magnetic resonance can determine not only myocardial function, remodeling, and scar burden, but also quantify the stress myocardial blood flow (MBF), which has been validated invasively and against  $^{13}\text{N}$ -NH<sub>3</sub> PET (8–10). A recent pilot study of  $n = 22$  recovered COVID-19 patients used coronary sinus flow by cardiovascular magnetic resonance (CMR) to evaluate the myocardial perfusion found with significantly lower myocardial perfusion reserve (MPR) compared with an unmatched cohort of health controls and values similar to a cohort with hypertrophic cardiomyopathy (HCM) (11). We aimed to further evaluate the pattern of stress MBF in recovered COVID-19 patients.

**Abbreviations:** CMR, cardiovascular magnetic resonance; COVID-19, coronavirus disease 2019; ICU, intensive care unit; LGE, late gadolinium enhancement; sMBF, stress myocardial blood flow; LV, left ventricular; MI, myocardial infarction; MOLLI, modified look-locker inversion recovery; SARS-CoV-2, severe acute respiratory syndrome coronavirus 2.

## METHODS

### Patient Population COVID Cohort

Patients clinically referred for adenosine stress CMR following their admission for COVID-19 to three CMR centers (Royal Free London NHS Foundation Trust [RFH], Imperial College Healthcare NHS Trust [Imperial], and University College London Hospital [UCLH] NHS Foundation Trust) were recruited for the study at the time of their CMR. We included patients with stress perfusion imaging from our recently published multicenter study (12) to the overall cohort and performed dedicated quantitation of MBF. The patients had a diagnosis of COVID-19 made either by (i) a positive combined oro/nasopharyngeal throat swab or tracheal aspirate for SARS-CoV-2 by reverse-transcriptase-polymerase-chain-reaction (RT-PCR), or (ii) a negative swab for SARS-CoV-2 but with a triad of symptoms of viral illness (such as one or more of cough, fever, and myalgia), typical blood biomarkers (such as new lymphopenia, high d-dimer, high ferritin, and elevated liver transaminases), and reported findings of at least probable likelihood of COVID-19 infection on chest radiograph or CT (12). Indications for CMR included positive troponin during hospital admission ( $n = 85$ ; hsTnT  $> 14$  ng/L for RFH and UCLH; hsTnI  $> 14$  ng/L for females and  $> 34$  ng/L for males for Imperial) or persistent symptoms ( $n = 5$ ; chest pain or shortness of breath) in COVID-19 recovery. The exclusion criteria included patient refusal, severe renal impairment (estimated glomerular filtration rate (eGFR)  $< 30$  mL/min/m<sup>2</sup>, if local hospital policy excluded these patients), pregnancy, medical unsuitability assessed by the referring clinician (including severe co-morbid disease and/or frailty in which it was felt that the information acquired would be unlikely to alter clinical management), and standard CMR contraindications. Ethical approval was obtained from the West Midlands—Edgbaston Research Ethics Committee for the use of the clinical data of the patients for research purposes (RFH and Imperial sites; REC reference 20/WM/0208) and from the Joint University College London/University College London Hospitals Research Ethics Committee (UCLH site; REC reference 07/H0715/101).

## Control Cohort and Healthy Volunteers

### Control Cohort

Patients referred for clinical adenosine stress CMR with contemporaneous invasive or CT coronary angiography (CTCA) without obstructive coronary disease between May 2016 and December 2019 (Pre-COVID) were recruited at two centers: Barts Heart Center (BHC) and Royal Free Hospital (RFH). Patients with significant coronary artery disease (diameter stenosis on coronary angiography >30%), previous coronary revascularization, infarct pattern scar, non-ischemic scar, or cardiomyopathy (hypertrophic, arrhythmogenic, dilated, amyloid) were excluded. The control cohort was propensity-matched to the COVID-19 patient cohort. A control group of known unobstructed coronary arteries was selected as the cleanest possible control, as the coronary status of the majority of the COVID cohort was unknown and thus could not be adjusted for.

### Healthy Volunteers

Twenty-seven healthy volunteers {median age 33 [interquartile range (IQR) 30–42] years, 14[52%] male} were prospectively recruited and underwent adenosine stress CMR. These were individuals with no risk factors for coronary artery disease and were not taking any medication. The participants gave their written informed consent according to the local ethics applications. The control and healthy volunteer studies were approved by the National Health Service Research Ethics Committee (NHS REC) and Health Research Authority (HRA) and were conducted in accordance with the Declaration of Helsinki (Barts Bioresource - REC ID 14/EE/0007, Royal Free Hospital – REC ID 07/H0715/101).

### CMR Study Protocol

The CMR was performed in accordance with the local institutional and international infection control guidelines (13) on 1.5T scanners (Magnetom Aera, Siemens Healthcare, Erlangen, Germany). A standard CMR protocol including parametric mapping, adenosine stress perfusion, and post-contrast imaging was used (**Supplementary Figure 1**): standard long- (4-, 2-, 3-chamber) and short-axis cine images were performed with breath-hold or real-time imaging, as needed. Native T1 and T2 mapping were performed in at least one long axis and one mid-ventricular short-axis view. The T1 mapping used the modified Look-Locker inversion recovery (MOLLI) sequence after regional shimming with 5s(3s)3s sampling (14). The T2 mapping used single-shot T2-prepared images acquired at multiple echo times (TE) (15). Following the application of 0.1 mmol/kg gadoterate meglumine (Royal Free and UCLH) or gadobutrol (Imperial), bright-blood late gadolinium enhancement (LGE) images were acquired using respiratory motion-corrected sequences with magnitude and phase-sensitive inversion recovery reconstructions (16). The patients underwent adenosine stress perfusion after refraining from caffeine for at least 24 h. Three short-axis views were acquired during the adenosine hyperemia (140 mcg/kg/min adenosine for 4 min with two further minutes at 175 mcg/kg/min if needed). The acquisition was for 60 heartbeats using a 0.05 mmol/kg gadolinium bolus administered at 4 mL/s followed

by a 20-mL 0.9% saline flush. Perfusion maps (three short-axis slices per patient) were generated automatically and inline at the time of the scan as described by Kellman et al. (8). The perfusion is quantified for each pixel of the myocardium, each pixel encoding the MBF. The automated segmentation of the left ventricle (LV) using artificial intelligence (AI) techniques enables the calculation of global and segmental mean blood flow (in mL/g/min) as previously described (17).

### CMR Post-processing

The CMR studies were analyzed offline using CVI42 5.12.1 (Circle Cardiovascular Imaging, Calgary, Canada). All the cines, maps, first-pass perfusion images/maps, and early/late gadolinium enhancement images were analyzed by experienced observers blinded to the coronary data. When calculating the ventricular volumes and mass, the trabeculations and papillary muscles were included in the myocardial mass. For the patients with visual evidence of LGE, the endo and epicardial contours (10% offset) were drawn and automatically divided into six segments, a 3 SD approach was taken, and those without visual LGE were marked as zero. Limited right ventricular (RV) insertion point LGE was not included as an abnormal LGE finding. The native T1 and T2 relaxation times were measured within the myocardial septum in the basal inferoseptum on motion-corrected quantitative maps and away from any areas of LGE (remote myocardium). Where a non-infarct pattern LGE was seen, the native T1 and T2 in the same region were measured. Phantom quality assurance was performed to ensure the stability and inter-site comparability of T1 as reported previously (12). The perfusion defects were determined upon visual inspection of the first-pass perfusion images and corroborated with a visual inspection of the quantitative perfusion maps. The perfusion defects were compared against LGE imaging to match the perfusion defects to the areas of infarct-pattern LGE. The perfusion defects were defined as “unmatched” if it occurs in the absence of infarct-pattern LGE or if extending beyond the area of late enhancement. Quantitative myocardial perfusion maps were generated automatically, in-line without user input, however, all the studies were visually inspected for motion correction (MOCO) quality, artifact and graphically (review of the arterial input function), see **Supplementary Figure 2**. Where significant issues were identified, the maps were reviewed and reconstructed where possible.

### Statistical Analysis

Statistical analysis was performed using R Studio version 1.3 (R Studio, Boston, Massachusetts, United States). The data is presented as mean  $\pm$  SD and were normally distributed and median (25th–75th quartile) otherwise. The categorical variables are presented as absolute values and percentages. Comparison of data was performed using an unpaired *t*-test (two groups) or one-way ANOVA (three groups), and non-normally distributed the data using Mann–Whitney/Kruskal–Wallis tests as appropriate. The categorical data were compared using the Chi-Squared test or Fisher’s Exact test, where appropriate. Propensity score matching was used to adjust for the imbalance in the COVID and control cohorts as follows. Logistic regression was used to predict the propensity score for either the control or the COVID cohort.

The model was selected based on the characteristics of the patient that felt to be most clinically relevant to the study hypothesis, i.e. risk factors for cardiovascular/coronary artery disease. The balance of prognostic factors was inspected *via* standardized mean differences. Matching was performed without replacement using a “greedy” algorithm (nearest neighbor). Linear regression was performed to identify the multivariable predictors of global stress MBF in the COVID and control cohorts. Clinically relevant variables and those found to have a significant univariable association with global stress MBF were included. The model was then pruned using the backward stepwise selection by Akaike Information Criterion (AIC). All values with  $p < 0.05$  were considered statistically significant.

## RESULTS

### Clinical Characteristics

#### COVID Cohort

In this study, 90 patients were included (49 RFH, 37 UCLH, 4 Imperial)—see **Supplementary Figure 3**. Out of the 90 patients, 82 (91%) patients had a positive COVID-19 PCR test.

The median age was 64 (IQR 54–71) years, 75(83%) male. Comorbidities were diabetes mellitus 29 (32%), hypertension 43 (48%), dyslipidemia 34 (38%), smoking history 25 (28%), and previous coronary revascularization 5 (5.6%). The median stay was 12 days (IQR 7–28), of which 40 out of 90 (44%) had been admitted to the intensive care unit (ICU). The median time from the discharge to CMR was 61 days (IQR 29–146). The median peak troponin T concentration (excluding Imperial patients [ $n = 4$ ] who had troponin I assay) was 27 ng/ml (IQR 19–70), the peak NT-proBNP was 314 pg/ml (IQR 102–878), and the peak D-dimer was 3,444 ng/ml (IQR 1,217–10,092).

#### Controls

The control cohort was propensity-matched for age, sex, hypertension, type-2 diabetes, and smoking history ( $p$  for all  $>0.05$ ). The mean standardized differences before and after matching are presented in **Supplementary Table 1**.

### Cardiovascular Magnetic Resonance

The patient characteristics and CMR findings are summarized in **Table 1**, the case examples are shown in **Figure 1**.

**TABLE 1** | Baseline characteristics.

| Characteristic       | COVID<br>$n = 90^a$      | Controls<br>$n = 90^a$ | HV<br>$n = 27^a$ | $p$ -value (COVID<br>vs control) <sup>b</sup> | $p$ -value<br>(All groups) <sup>b</sup> |
|----------------------|--------------------------|------------------------|------------------|---|---|
| Age                  | 64 (54, 71)              | 60 (49, 68)            | 33 (30, 42)      | 0.074   | <b>&lt;0.001</b>                        |
| Sex                  |                          |                        |                  | 0.85  | <b>0.002</b>                            |
| Female               | 15 (17%)                 | 17 (19%)               | 13 (48%)         |   |   |
| Male                 | 75 (83%)                 | 73 (81%)               | 14 (52%)         |   |   |
| Type 2 diabetes      | 29 (32%)                 | 26 (29%)               | 0                | 0.75  | <b>0.003</b>                            |
| Hypertension         | 43 (48%)                 | 48 (53%)               | 0                | 0.55  | <b>&lt;0.001</b>                        |
| Dyslipidemia         | 34 (38%)                 | 45 (50%)               | 0                | 0.13  | <b>&lt;0.001</b>                        |
| Prior history of CAD | 23 (26%)                 | 0                      | 0                | <b>&lt;0.001</b>                              | <b>&lt;0.001</b>                        |
| PCI/CABG             | 5 (5.6%)                 | 0                      | 0                | $>0.99$                                       | $>0.99$                                 |
| Smoker               | 25 (28%)                 | 27 (30%)               | 0                | 0.87  | <b>0.005</b>                            |
| ICU Admission        | 40 (44%)                 | –                      | –                |   |   |
| Troponin (ng/L)*     | 27 (19, 70)              | –                      | –                |   |   |
| NT-proBNP (pg/ml)    | 314 (102, 878)           | –                      | –                |   |   |
| D-dimer (ng/ml)      | 3,444<br>(1,217, 10,092) | –                      | –                |   |   |
| CRP (mg/L)           | 223 (141, 344)           | –                      | –                |   |   |
| LV EDV (ml)          | 130 (112, 147)           | 142 (119, 164)         | 147 (127, 156)   | 0.075   | 0.063                                   |
| LV mass (g)          | 126 (109, 144)           | 110 (94, 132)          | 97 (86, 114)     | <b>&lt;0.001</b>                              | <b>&lt;0.001</b>                        |
| LVEF (%)             | 67 (10)                  | 67 (8)                 | 65 (4)           | 0.91  | 0.81                                    |
| RVEF (%)             | 59 (8)                   | –                      | –                |   |   |
| Native T1 (ms)       | 1,032<br>(1,008, 1,061)  | –                      | –                |   |   |
| T2 (ms)              | 46 (45, 47)              | –                      | –                |   |   |
| ECV (%)              | 26 (23, 29)              | –                      | –                |   |   |
| LGE Present          | 50 (56%)                 | 0                      | 0                | <b>&lt;0.001</b>                              | <b>&lt;0.001</b>                        |
| Infarct pattern LGE  | 15 (17%)                 | 0                      | 0                | <b>&lt;0.001</b>                              | <b>&lt;0.001</b>                        |
| Non-ischemic LGE     | 31 (34%)                 | 0                      | 0                | <b>&lt;0.001</b>                              | <b>&lt;0.001</b>                        |
| Mixed Pattern LGE    | 4 (4.4%)                 | 0                      | 0                | 0.12  | 0.11                                    |

<sup>a</sup>Mean (SD);  $n$  (%); Median (IQR), <sup>b</sup>One-way ANOVA; chi-square test of independence; Fisher's exact test; Kruskal-Wallis test.

\*Including patients with troponin T only (excluding four patients from Imperial College Healthcare NHS Trust (Imperial) who had troponin I assay).  $p$ -values reaching statistical significance ( $p < 0.05$ ) are highlighted in bold.

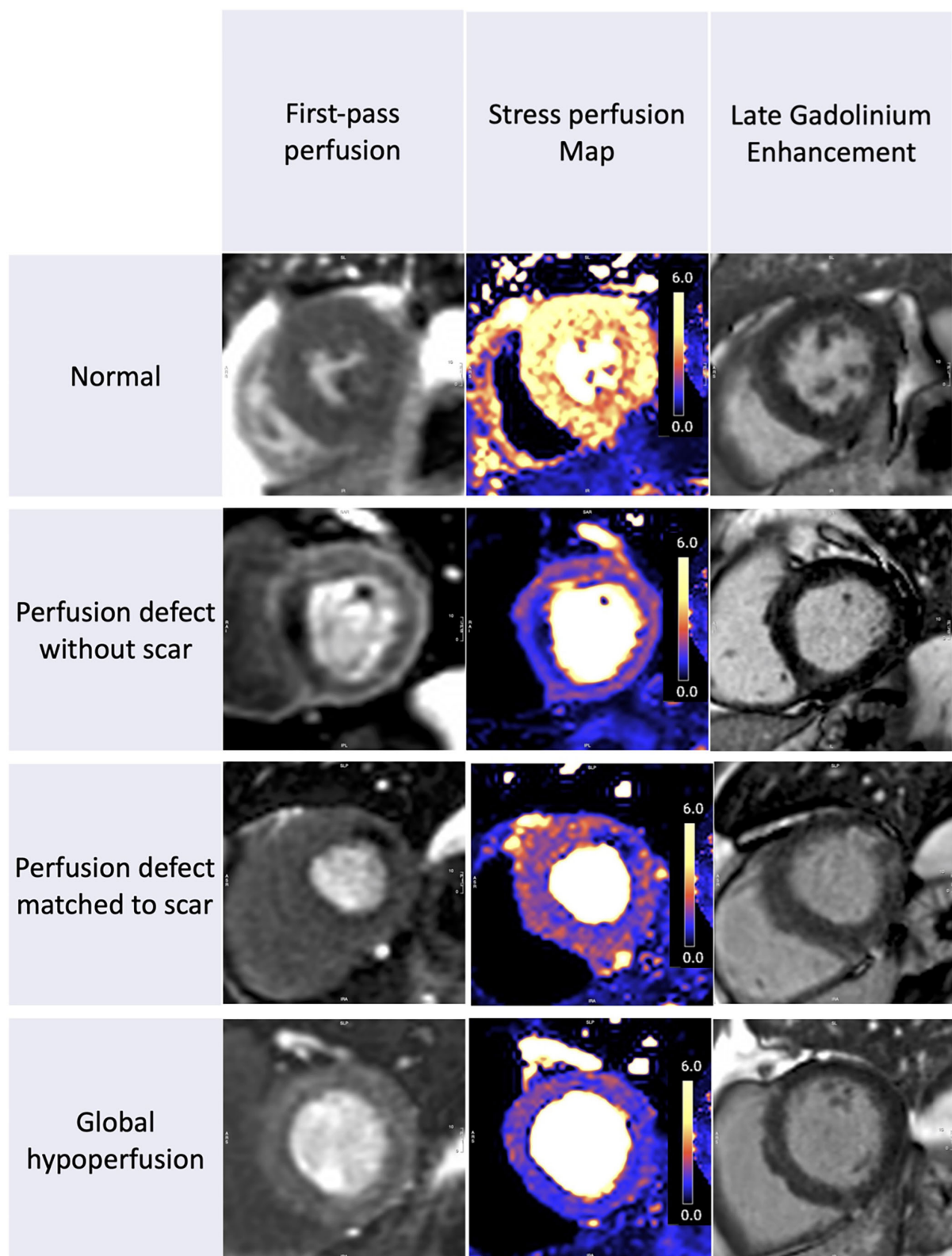
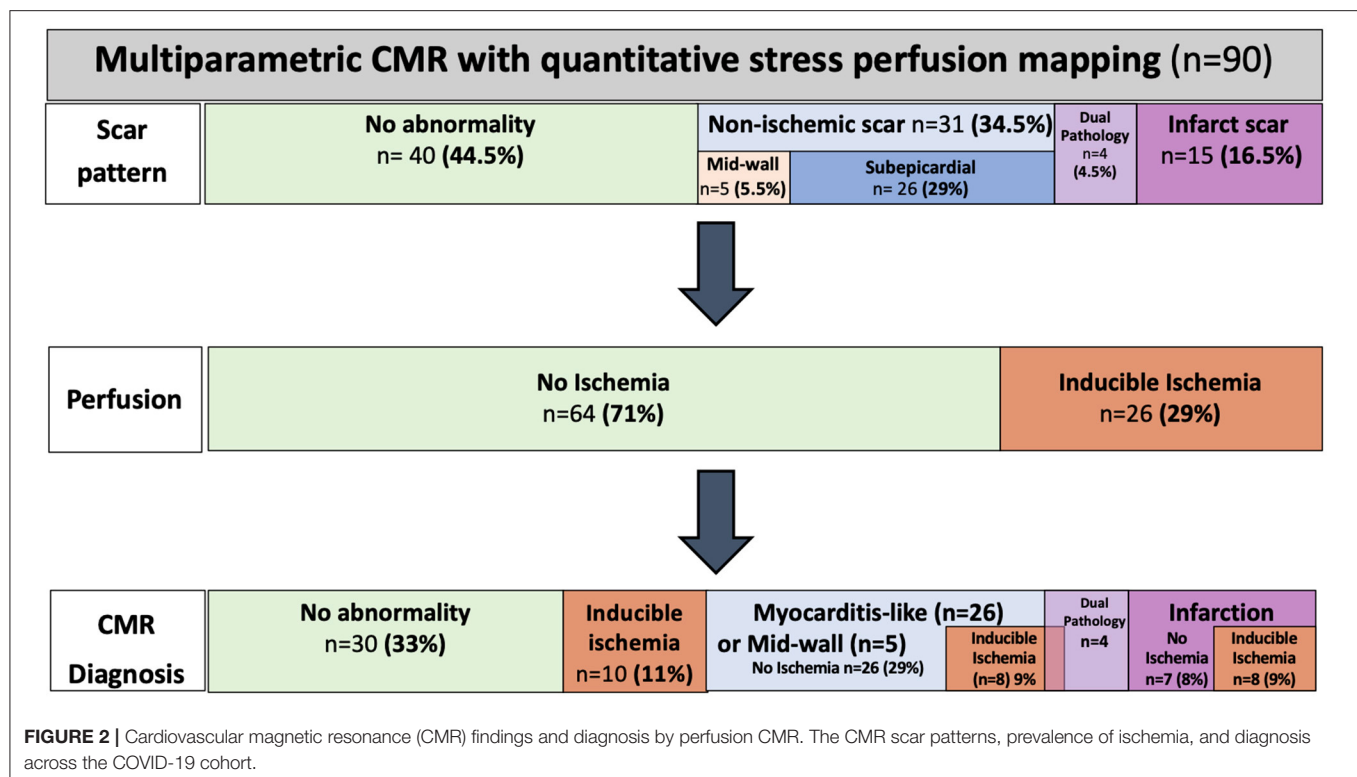


**FIGURE 1 |** Stress perfusion and scar in recovered COVID-19 patients. The spectrum of perfusion abnormalities. From left to right we show the first-pass perfusion images, quantitative stress perfusion maps, and free breathing-phase sensitive inversion recovery and motion corrected late gadolinium enhancement images (PSIR MOCO LGE). Patient 1: Normal. Patient 2: Regional ischemia without LGE. Patient 3: Regional ischemia with infarct late gadolinium enhancement (LGE). Patient 4: Global hypoperfusion without visual perfusion defects and no significant LGE.



### Cardiac Function and Myocardial Tissue Characterization

In the COVID cohort, the LV ejection fraction (EF) was  $67 \pm 10\%$  and the RV EF was  $59 \pm 8\%$  with 10 (11%) patients with LV systolic impairment and 6 (7%) patients with RV impairment. There was no difference in LVEF compared with the propensity-matched cohort or healthy volunteers ( $p = 0.81$ ).

In the post-COVID cohort, 50 (56%) patients had evidence of myocardial scar wherein 15 out of 90 (17%) patients had an infarct pattern, 31 out of 90 (34%) had a non-infarct pattern LGE, and four out of 90 (4.4%) patients had a dual/mixed pattern LGE. There was sub-epicardial myocarditis-like LGE in 26 out of the 90 (29%) patients, mid-wall LGE in 5, and four patients had both infarct and non-infarct pattern LGE. The control cohort was specifically selected for the absence of LGE; none of the healthy volunteers had LGE. For the breakdown of the scar patterns and CMR findings, see **Figure 2**.

The median T1 was 1,032ms (IQR 1,008–1,061ms) and the median T2 was 46 (IQR 45–47ms) in the basal inferoseptum, remote to the LGE. Thirteen patients had evidence of ongoing myocardial edema ( $T2 > 50\text{ms}$ ) in the regions coinciding with LGE. The normal ranges for T1 and T2 were from the data from the healthy volunteers from our recent phantom controlled work (native T1  $1008 \pm 35\text{ms}$ , T2  $48 \pm 2\text{ms}$ ) (12).

### Quantitative Stress MBF

#### Global Perfusion

There was no difference in global stress MBF ( $2.53 \pm 0.77$  vs.  $2.52 \pm 0.79$  ml/g/min,  $p = 0.10$ ) in the COVID patients vs.

propensity-matched controls. The healthy volunteers had higher stress MBF than either the COVID or control volunteers (sMBF  $3.0 \pm 0.76$  ml/g/min,  $p = 0.01$ ) (**Table 2**, **Figure 3**). The patients with infarct-pattern scar had a significantly lower global stress MBF than those with non-ischemic scar only or no scar (infarct vs. non-ischemic vs. no LGE;  $2.04 \pm 0.48$  vs.  $2.54 \pm 0.65$  vs.  $2.75 \pm 0.87$  ml/g/min,  $p = 0.003$ ; **Figure 4**). There was no difference in the global blood flow between patients with a non-ischemic scar and no scar ( $p = 0.26$ ). The MPR was lower in the COVID cohort than in the matched controls ( $2.67 \pm 0.87$  vs.  $2.95 \pm 1.03$  ml/g/min,  $p = 0.049$ ) driven by the higher resting MBF in the COVID cohort ( $0.99 \pm 0.34$  vs.  $0.89 \pm 0.24$  ml/g/min,  $p = 0.02$ ), but the values were in line with the normal values in the studies using the same quantitative perfusion methodology (9).

#### Predictors of Global Stress MBF

The multivariable predictors of low global stress MBF were age (OR 0.90, 95%CI 0.82–0.98,  $p = 0.02$ ), male sex (OR 0.60, 95%CI 0.46–0.78,  $p = <0.001$ ), and history of hypertension (OR 1.52, 95%CI 1.23–1.89,  $p = <0.001$ ). Prior COVID-19 illness was not associated with lower global stress MBF (OR 1.1, 95%CI 0.89–1.35,  $p = 0.4$ ) (**Table 3**).

#### Regional Stress Perfusion

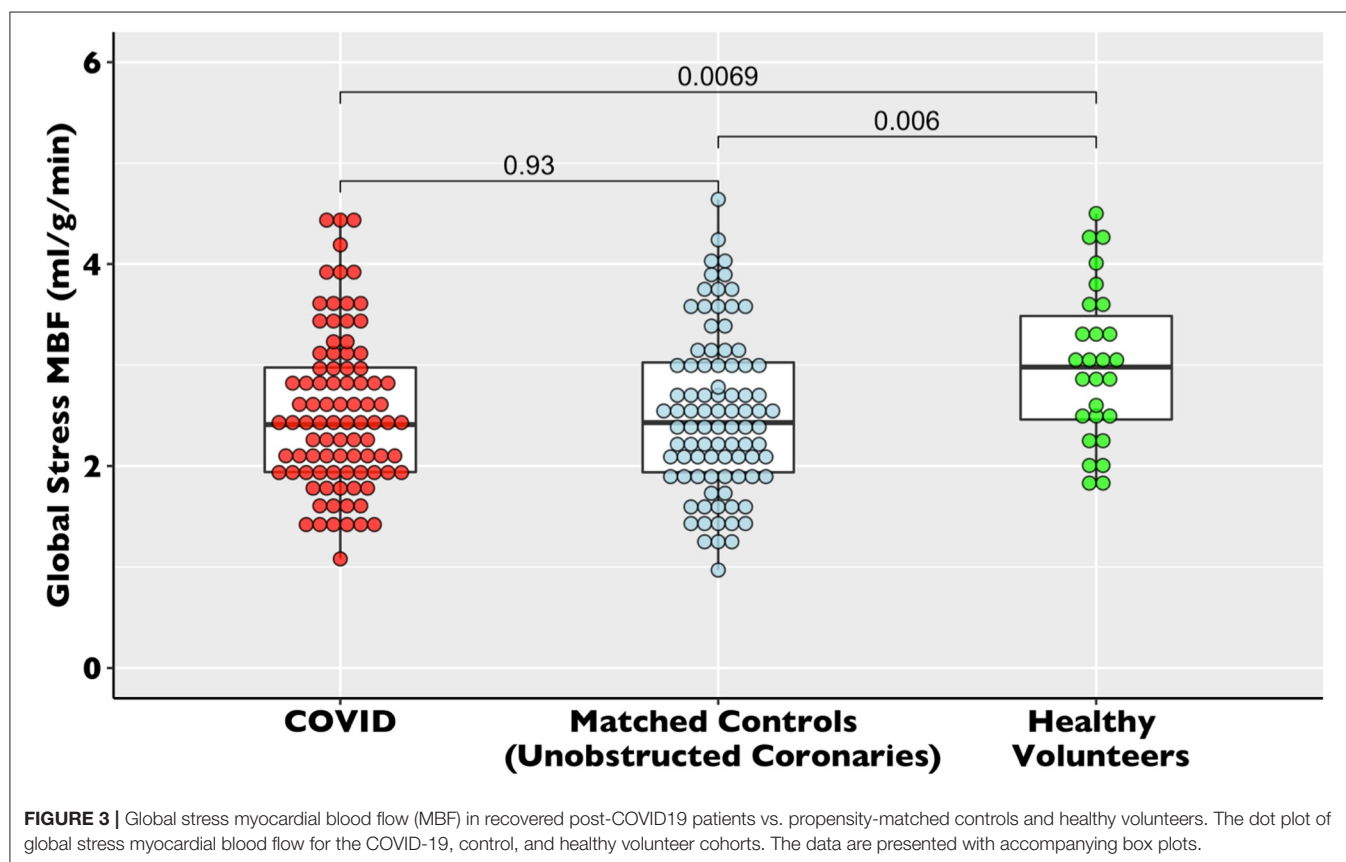
Thirty-two patients had localized segmental stress perfusion defects (median 3 [IQR 3–7] segments). Of those with perfusion defects, only six out of 32 had perfusion defects solely matched to a region of infarct-pattern LGE, whereas 26 out of 32 patients had unmatched perfusion defects (**Figures 2, 4**).

TABLE 2 | Results.

| Characteristic               | COVID<br><i>n</i> = 90 <sup>a</sup> | Control<br><i>n</i> = 90 <sup>a</sup> | HV<br><i>n</i> = 27 <sup>a</sup> | <i>p</i> -value <sup>b</sup> (COVID<br>vs. control) | <i>p</i> -value <sup>b</sup><br>(All groups) |
|------------------------------|-------------------------------------|---------------------------------------|----------------------------------|---|--|
| Global Stress MBF (ml/g/min) | 2.53 (0.77)                         | 2.52 (0.79)                           | 3.00 (0.76)                      | 0.93  | <b>0.012</b>                                 |
| Global Rest MBF (ml/g/min)   | 0.99 (0.34)                         | 0.89 (0.24)                           | 0.86 (0.26)                      | <b>0.018</b>  | <b>0.022</b>                                 |
| MPR                          | 2.67 (0.87)                         | 2.95 (1.03)                           | 3.63 (0.75)                      | <b>0.049</b>  | <b>&lt;0.001</b>                             |

<sup>a</sup>Statistics presented: Mean (SD); *n* (%).

<sup>b</sup>Statistical tests performed: One-way ANOVA; Fisher's exact test. *p*-values reaching statistical significance (*p* < 0.05) are highlighted in bold.



## DISCUSSION

In this multicenter study of COVID-19 survivors, we demonstrated that at 2 months after severe, hospitalized infection, the global stress MBF is comparable to the propensity-matched controls with proven unobstructed coronaries and no scar. However, over half of the COVID patients have evidence of either infarct or myocarditis-like scar, and almost a third had evidence of regional ischemia, suggestive of occult coronary artery disease, including a quarter of those with an otherwise normal CMR. While microvascular thrombosis may also play a role, there is little evidence here to suggest a significant impact on the global myocardial perfusion in surviving patients.

Myocardial damage during acute COVID-19 illness predicts the severity (18) and outcomes of acute infection, with

CMR scans demonstrating infarction and inflammation in convalescent patients (12). In accordance with previous publications, the prevalence of LGE in this cohort was high, but the overall burden and functional impact were relatively low (19). However, the effects of COVID-19 on myocardial perfusion have so far remained incompletely characterized. We demonstrated that stress myocardial blood flow after severe COVID-19 shows no difference to risk factor matched controls; importantly stress blood flow was not predicted by COVID status but by common risk factors for coronary artery disease.

While MPR was found to be slightly reduced in the COVID cohort compared with the controls, this was driven primarily by a higher resting MBF. In a recent study by Drakos et al., there was a significant reduction in MPR in *n* = 22 patients

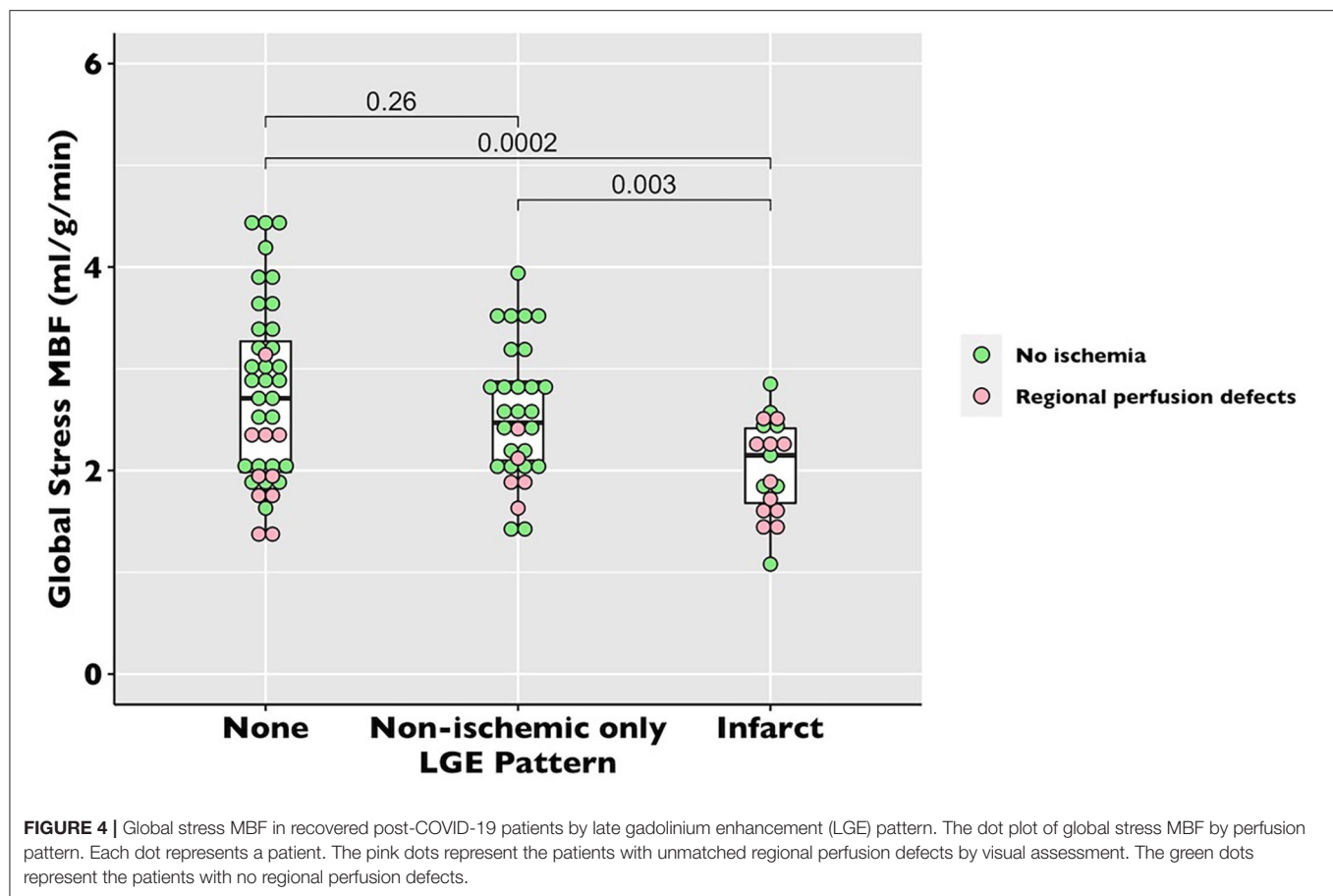


**TABLE 3 |** Multivariable analysis of global stress myocardial blood flow in the COVID and propensity-matched control cohorts.

| Characteristic       | Full model |                     |         | Final model |                     |                  |
|----------------------|------------|---------------------|---------|-------------|---------------------|------------------|
|                      | OR         | 95% CI <sup>a</sup> | p-value | OR          | 95% CI <sup>a</sup> | p-value          |
| COVID status         | 1.10       | 0.85, 1.41          | 0.5     | 1.10        | 0.89, 1.35          | 0.4              |
| Age*                 | 0.90       | 0.82, 0.99          | 0.027   | 0.90        | 0.82, 0.98          | <b>0.019</b>     |
| Male Sex             | 0.60       | 0.47, 0.79          | <0.001  | 0.60        | 0.46, 0.78          | <b>&lt;0.001</b> |
| Type 2 Diabetes      | 0.81       | 0.64, 1.02          | 0.071   | 0.80        | 0.64, 1.00          | 0.057            |
| Hypertension         | 1.50       | 1.20, 1.87          | <0.001  | 1.52        | 1.23, 1.89          | <b>&lt;0.001</b> |
| Hypercholesterolemia | 1.09       | 0.88, 1.35          | 0.4     |             |                     |                  |
| Infarct pattern LGE  | 0.70       | 0.47, 1.06          | 0.091   | 0.71        | 0.48, 1.03          | 0.074            |
| Non-ischemic LGE     | 0.97       | 0.71, 1.33          | 0.9     |             |                     |                  |

<sup>a</sup>CI, Confidence Interval.

\*Scaled by epochs of 10 years. p-values reaching statistical significance ( $p < 0.05$ ) are highlighted in bold.

with persistent symptoms post-COVID-19 when assessed by coronary sinus flow, driven by both a lower stress MBF and higher resting MBF (11). This study had several methodological and technological differences to this study (assessment of MBF by coronary sinus flow, unmatched cohorts, inclusion of patients with persistent symptoms only, and exclusion of severe COVID-19). There are alternative explanations for higher resting MBF in our cohort compared with the controls

(which may include differences in heart rate and medications between cohorts), thus we do not believe that these small borderline significant differences provide convincing evidence of microvascular dysfunction.

The finding of inducible ischemia in almost a third of the patients suggests that the putative mechanism of troponin elevation reflected a supply-demand-mismatch, whether epicardial or microvascular (20), representing “a COVID stress

test". It is important, however, to acknowledge the multiple mechanisms of troponin elevation in the context of severe illness (21). We hypothesize that the high burden of infarct-pattern LGE was pre-existing, and driven more by the demographics of included patients (older, high incidence of cardiovascular risk factors), than by the COVID-19 illness, especially given the relatively modest troponin rise seen. This is particularly relevant as our sample reflects a relatively sick group of patients (all admitted, 44% to ICU; 85 out of 90 with elevated troponin). The prevalence of the infarct pattern scar is similar to the previous studies which cited a rate of 17% of occult MI by CMR in a cohort with a similar cardiovascular risk profile. Our group has previously shown the rate of infarct pattern scar in a contemporary chest pain cohort referred for adenosine-stress CMR to be as high as 29.5% (22, 23). Cardiovascular magnetic resonance is the most suited non-invasive modality for the assessment of unexplained troponin rise, as it can confirm the presence, type, and extent of myocardial injury. Interestingly, nearly half of the troponin-positive patients (39/85) had no evidence of scar on CMR. This suggests that while troponin leak is associated with poor prognosis in acute illnesses, in many cases it is not followed by medium-term structural or functional effects, including sensitive LGE imaging or global MBF quantification.

Autopsy studies of COVID-19 patients have demonstrated microvascular thrombosis in the lungs and heart (7, 24, 25). In the cardiac studies, microthrombi were identified as the cause of myocyte necrosis in 64% of patients after COVID-19 related death. Other studies have also identified these in intra-myocardial small vessels (26, 27). Many of these thrombi were not associated with any significant myocardial injury. It is plausible that microthrombosis may lead to exceptionally localized myocyte injury. Although this study was designed specifically to take advantage of identical scanner platforms and access to state-of-the-art quantitative myocardial perfusion and myocardial tissue characterization CMR technology [supported by MRI phantom quality controlled analysis (22)], very localized myocyte injury may be undetectable by the current CMR technologies (LGE or T1/T2/ECV/MBF mapping) or may have resolved without detectable damage in convalescent patients. This entity is potentially somewhat distinct from what would conventionally be referred to as a "microvascular disease", which is commonly perceived as a global phenomenon in response to a systemic disease process (type 2 diabetes, for example), without demonstrable inducible perfusion defects or regional wall motion abnormalities (28).

Microvascular disease has also been shown to have regionality and may have a subendocardial distribution (29). The regional perfusion defects found in our study could be due to regional microvascular disease if the epicardial coronaries are found unobstructed. A normal global stress MBF in troponin-positive or persistently symptomatic individuals is reassuring to an extent but may not have the sensitivity to resolve regional microvascular complications.

Overall, multi-parametric stress perfusion CMR in convalescent post-COVID-19 patients identified previously unsuspected inducible ischemia, myocardial infarction, and

myocarditis-pattern non-ischemic scar. The addition of stress perfusion imaging offers incremental information by the detection of regional ischemia in the absence of a scar. There is little evidence of a reduction in global perfusion after severe COVID-19 compared to matched controls, which may reflect the limited impact of microvascular thrombosis on overall perfusion in surviving patients even if it causes persistent regional differences in myocardial blood flow.

## LIMITATIONS

This study reports findings in a group of patients who survived COVID-19 infection and is therefore affected by survivor bias. Patients with contraindications to CMR were excluded, though this is a small minority of the patients. We have characterized the spectrum of myocardial injury and perfusion abnormalities in recovered, predominantly severe, COVID-19 illness that persists to a median of 2 months after the infection (community and mild disease were not investigated). This study does not offer insights into myocardial blood flow, structure or function during the infection or in the immediate post-infective period, nor can it, without longitudinal data, determine if abnormalities detected evolve or regress over time. The wide time interval between the admission episode and CMR further compounds this. Data on persistent symptoms at the time of CMR was not available for the majority of patients, thus we cannot draw conclusions pertaining to the association of these with MBF. Furthermore, without anatomical data, we cannot confirm the presence and cause (epicardial vs. microvascular) of perfusion abnormalities. However, this study yields pertinent preliminary data which may have important clinical implications for patients. Further granularity will be determined with future ongoing United Kingdom and international studies, some of which will acquire or capture coronary anatomical data [COVID-HEART [ISRCTN58667920]; CISCO-19 (30)].

## CONCLUSION

This multicenter cohort of severe hospitalized COVID-19 infection identified no difference in the global stress MBF in COVID-19 survivors compared with the risk factor matched controls, but regional perfusion defects are common. Overall, the findings are reassuring that COVID-19 is unlikely to result in gross and persistent global microvascular phenomena. The high burden of regional ischemia may be due to regional microvascular disease but is more likely due to pre-existing coronary disease, but neither can be proven in the absence of anatomical imaging. This should therefore be considered hypothesis-generating for future studies.

## DATA AVAILABILITY STATEMENT

The raw data supporting the conclusions of this article will be made available by the authors, without undue reservation.

## ETHICS STATEMENT

The studies involving human participants were reviewed and approved by the West Midlands – Edgbaston Research Ethics Committee for the use of patient's clinical data for research purposes (RFH and Imperial sites; REC reference 20/WM/0208) and from the Joint University College London/University College London Hospitals Research Ethics Committee (UCLH site; REC reference 07/H0715/101). The patients/participants provided their written informed consent to participate in this study.

## AUTHOR CONTRIBUTIONS

GT: concept and design, writing for publication, revision of drafts, and submission of manuscript. TT: concept and design, data analysis, writing of manuscript, revision, and approval of final submission. MF, PK, GC, CM, RB, HX, RD, ASe, and DK: revision and approval of submission. JM, TK, KV, JB, LC, DA, SY, HK, JA, KK, ASe, and ASH: data analysis, revision of drafts, and approval of submission. List ASH with others who contributed data analysis, revision of drafts, and approval of submission. All authors listed have made a substantial, direct, and intellectual contribution to the work and approved it for publication.

## REFERENCES

- Chapman AR, Bularga A, Mills NL. High-sensitivity cardiac troponin can be an ally in the fight against COVID-19. *Circulation*. (2020) 141:1733–5. doi: 10.1161/CIRCULATIONAHA.120.047008
- Bonow RO, Fonarow GC, O'Gara PT, Yancy CW. Association of coronavirus disease 2019 (COVID-19) with myocardial injury and mortality. *JAMA Cardiology*. (2020) 5:751. doi: 10.1001/jamacardio.2020.1105
- Guo T, Fan Y, Chen M, Wu X, Zhang L, He T, et al. Cardiovascular implications of fatal outcomes of patients with coronavirus disease 2019 (COVID-19). *JAMA Cardiology*. (2020) 5:811. doi: 10.1001/jamacardio.2020.1017
- Montone RA, Iannaccone G, Meucci MC, Gurgoglione F, Niccoli G. Myocardial and microvascular injury due to coronavirus disease 2019. *European Cardiology Review*. (2020) 15:e52. doi: 10.15420/ecr.2020.22
- Lowenstein CJ, Solomon SD. Severe COVID-19 Is a microvascular disease. *Circulation*. (2020) 142:1609–11. doi: 10.1161/CIRCULATIONAHA.120.050354
- Ince C, Mayeux PR, Nguyen T, Gomez H, Kellum JA, Ospina-Tascón GA, et al. The endothelium in sepsis. *Shock*. (2016) 45:259–70. doi: 10.1097/SHK.0000000000000473
- Pellegrini D, Kawakami R, Guagliumi G, Sakamoto A, Kawai K, Gianatti A, et al. Microthrombi as a major cause of cardiac injury in COVID-19: a pathologic study. *Circulation*. (2021) 143:1031–42. doi: 10.1161/CIRCULATIONAHA.121.055585
- Kellman P, Hansen MS, Nilles-Vallespin S, Nickander J, Themudo R, Ugander M, et al. Myocardial perfusion cardiovascular magnetic resonance: optimized dual sequence and reconstruction for quantification. *Journal of Cardiovascular Magnetic Resonance*. (2017) 19:43. doi: 10.1186/s12968-017-0355-5
- Kotecha T, Martinez-Naharro A, Boldrini M, Knight D, Hawkins P, Kalra S, et al. Automated pixel-wise quantitative myocardial perfusion mapping by CMR to detect obstructive coronary artery disease and coronary microvascular dysfunction: validation against invasive coronary physiology. *JACC Cardiovascular Imaging*. (2019) 12:1958–69. doi: 10.1016/j.jcmg.2018.12.022
- Engblom H, Xue H, Akil S, Carlsson M, Hindorf C, Oddstig J, et al. Fully quantitative cardiovascular magnetic resonance myocardial perfusion ready for clinical use: a comparison between cardiovascular magnetic resonance imaging and positron emission tomography. *J Cardiovasc Magn Reson*. (2017) 19:78. doi: 10.1186/s12968-017-0388-9
- Drakos S, Chatzantonis G, Bietenbeck M, Evers G, Schulze AB, Mohr M, et al. A cardiovascular magnetic resonance imaging-based pilot study to assess coronary microvascular disease in COVID-19 patients. *Scientific Reports*. (2021) 11:15667. doi: 10.1038/s41598-021-95277-z
- T. Kotecha, D.S. Knight, Y. Razvi, K. Kumar, K. Vimalasvaran, G. Thornton, et al. Patterns of myocardial injury in recovered troponin-positive COVID-19 patients assessed by cardiovascular magnetic resonance. *European Heart Journal*. (2021) 1866–1878. doi: 10.34101/f.739571449.793583038
- Han Y, Chen T, Bryant J, Bucciarelli-Ducci C, Dyke C, Elliott MD, et al. Society for cardiovascular magnetic resonance (SCMR) guidance for the practice of cardiovascular magnetic resonance during the COVID-19 pandemic. *J Cardiovasc Magn Reson*. (2020) 22:26. doi: 10.1186/s12968-020-00628-w
- Kellman P, Hansen MS. T1-mapping in the heart: accuracy and precision. *Journal of Cardiovascular Magnetic Resonance*. (2014) 16:2. doi: 10.1186/1532-429X-16-2
- Giri S, Chung YC, Merchant A, Mihai G, Rajagopalan S, Raman SV, et al. T2 quantification for improved detection of myocardial edema. *J Cardiovasc Magn Reson*. (2009) 11:56. doi: 10.1186/1532-429X-11-56
- Kellman P, Arai AE. Cardiac imaging techniques for physicians: late enhancement. *J Magn Reson Imaging*. (2012) 36:529–42. doi: 10.1002/jmri.23605
- Xue H, Davies RH, Brown LAE, Knott KD, Kotecha T, Fontana M, et al. Automated inline analysis of myocardial perfusion MRI with deep learning. *Radiology: Artificial Intelligence*. (2020) 2:e200009. doi: 10.1148/ryai.2020200009
- Sabatino J, Rosa SDe, Salvo GD, Indolfi C. Impact of cardiovascular risk profile on COVID-19 outcome. A meta-analysis. *PLoS ONE*. (2020) 15:e0237131. doi: 10.1371/journal.pone.0237131

## FUNDING

GT was supported by a British Heart Foundation (BHF) Clinical Research Training Fellowship (FS/CRTF/21/24128). DK and RB were supported by the National Institute for Health Research (NIHR) University College London Hospitals (UCLH) Biomedical Research Center. JM was directly supported by the (UCLH) and Barts NIHR Biomedical Research Centers and through a BHF Accelerator Award. MF and TT (ICRF #34374) are funded by a British Heart Foundation (BHF) Intermediate Fellowship.

## SUPPLEMENTARY MATERIAL

The Supplementary Material for this article can be found online at: <https://www.frontiersin.org/articles/10.3389/fcvm.2021.764599/full#supplementary-material>

**Supplementary Table 1** | Table showing the covariate balance before and after propensity matching. The Data are presented as means and standardized mean differences.

**Supplementary Figure 1** | CMR imaging protocol for the study.

**Supplementary Figure 2** | Perfusion Mapping Quality Assurance and Outputs.

**Supplementary Figure 3** | CONSORT diagram describing the pathway from the clinical CMR post-COVID to the final number of patients who underwent stress CMR.

19. Kim JY, Han K, Suh YJ. Prevalence of abnormal cardiovascular magnetic resonance findings in recovered patients from COVID-19: a systematic review and meta-analysis. *Journal of Cardiovascular Magnetic Resonance*. (2021) 23:100. doi: 10.1186/s12968-021-00792-7
20. Chen T, Wu D, Chen H, Yan W, Yang D, Chen G, et al. Clinical characteristics of 113 deceased patients with coronavirus disease 2019: retrospective study. *BMJ*. (2020) 368:m1091. doi: 10.1136/bmj.m1091
21. Bansal M. Cardiovascular disease and COVID-19. *Diabetes & Metabolic Syndrome: Clinical Research & Reviews*. (2020) 14:247–50. doi: 10.1016/j.dsx.2020.03.013
22. Knott KD, Seraphim A, Augusto JB, Xue H, Chacko L, Aung N, et al. The prognostic significance of quantitative myocardial perfusion: an artificial intelligence based approach using perfusion mapping. *Circulation*. (2020) 141:1282–91. doi: 10.1161/CIRCULATIONAHA.119.044666
23. Schelbert EB, Cao JJ, Sigurdsson S, Aspelund T, Kellman P, Aletras AH, et al. Prevalence and prognosis of unrecognized myocardial infarction determined by cardiac magnetic resonance in older adults. *JAMA*. (2012) 308:890. doi: 10.1001/2012.jama.11089
24. Ackermann M, Verleden SE, Kuehnel M, Haverich A, Welte T, Laenger F, et al. Pulmonary vascular endothelialitis, thrombosis, and angiogenesis in Covid-19. *New England Journal of Medicine*. (2020) 383:120–8. doi: 10.1056/NEJMoa2015432
25. Magro C, Mulvey JJ, Berlin D, Nuovo G, Salvatore S, Harp J, et al. Complement associated microvascular injury and thrombosis in the pathogenesis of severe COVID-19 infection: A report of five cases. *Translational Research*. (2020) 220:1–13. doi: 10.1016/j.trsl.2020.04.007
26. Bois MC, Boire NA, Layman AJ, Aubry M-C, Alexander MP, Roden AC, et al. COVID-19-associated nonocclusive fibrin microthrombi in the heart. *Circulation*. (2021) 143:230–43. doi: 10.1161/CIRCULATIONAHA.120.050754
27. Elsoukary S, Mostyka SM, Dillard A, Berman R, Ma DX, Chadburn LA, et al. Steven, autopsy findings in 32 patients with COVID-19: a single-institution experience. *Pathobiology*. (2021) 88:56–68. doi: 10.1159/000511325
28. Panza JA, Laurienzo JM, Curiel RV, Unger EF, Quyyumi AA, Dilsizian V, et al. Investigation of the mechanism of chest pain in patients with angiographically normal coronary arteries using transesophageal dobutamine stress echocardiography. *Journal of the American College of Cardiology*. (1997) 29:293–301. doi: 10.1016/S0735-1097(96)00481-0
29. Rahman H, Scannell CM, Demir OM, Ryan M, Mcconkey H, Ellis H, et al. High-resolution cardiac magnetic resonance imaging techniques for the identification of coronary microvascular dysfunction. *JACC: Cardiovascular Imaging*. (2020) 14:987–98. doi: 10.1016/j.jcmg.2020.10.015
30. Mangion K, Morrow A, Bagot C, Bayes H, Blyth KG, Church C, et al. The chief scientist office cardiovascular and pulmonary imaging in SARS coronavirus disease-19 (CISCO-19) study. *Cardiovasc Res*. (2020) 116:2185–96. doi: 10.1093/cvr/cvaa209

**Conflict of Interest:** The authors declare that the research was conducted in the absence of any commercial or financial relationships that could be construed as a potential conflict of interest.

**Publisher's Note:** All claims expressed in this article are solely those of the authors and do not necessarily represent those of their affiliated organizations, or those of the publisher, the editors and the reviewers. Any product that may be evaluated in this article, or claim that may be made by its manufacturer, is not guaranteed or endorsed by the publisher.

Copyright © 2021 Thornton, Shetye, Knight, Knott, Artico, Kurdi, Yousef, Antonakaki, Razvi, Chacko, Brown, Patel, Vimalasvaran, Seraphim, Davies, Xue, Kotecha, Bell, Manisty, Cole, Moon, Kellman, Fontana and Treibel. This is an open-access article distributed under the terms of the Creative Commons Attribution License (CC BY). The use, distribution or reproduction in other forums is permitted, provided the original author(s) and the copyright owner(s) are credited and that the original publication in this journal is cited, in accordance with accepted academic practice. No use, distribution or reproduction is permitted which does not comply with these terms.



# Implementing Machine Learning in Interventional Cardiology: The Benefits Are Worth the Trouble

## OPEN ACCESS

### Edited by:

Alexander Meyer,  
German Heart Center Berlin, Germany

### Reviewed by:

Ernst Wellenhofer,  
Charité University Medicine  
Berlin, Germany  
Elmir Omerovic,  
Sahlgrenska University  
Hospital, Sweden

### \*Correspondence:

Walid Ben Ali  
dr.walidbenali@gmail.com

<sup>†</sup>These authors have contributed  
equally to this work and share first  
authorship

<sup>‡</sup>These authors share  
senior authorship

### Specialty section:

This article was submitted to  
Cardiovascular Imaging,  
a section of the journal  
Frontiers in Cardiovascular Medicine

**Received:** 18 May 2021

**Accepted:** 08 November 2021

**Published:** 08 December 2021

### Citation:

Ben Ali W, Pesaranghader A,  
Avram R, Overtchouk P, Perrin N,  
Laffite S, Cartier R, Ibrahim R,  
Modine T and Hussin JG (2021)  
Implementing Machine Learning in  
Interventional Cardiology: The Benefits  
Are Worth the Trouble.  
Front. Cardiovasc. Med. 8:711401.  
doi: 10.3389/fcvm.2021.711401

Walid Ben Ali<sup>1,2\*†</sup>, Ahmad Pesaranghader<sup>3,4†</sup>, Robert Avram<sup>3</sup>, Pavel Overtchouk<sup>5</sup>,  
Nils Perrin<sup>2</sup>, Stéphane Laffite<sup>1</sup>, Raymond Cartier<sup>2</sup>, Reda Ibrahim<sup>2</sup>, Thomas Modine<sup>1‡</sup> and  
Julie G. Hussin<sup>3‡</sup>

<sup>1</sup> Service Médico-Chirurgical, Valvulopathies-Chirurgie Cardiaque-Cardiologie Interventionnelle Structurale, Hôpital  
Cardiologique de Haut Lévêque, Bordeaux, France, <sup>2</sup> Structural Heart Program and Interventional Cardiology, Université de  
Montréal, Montreal Heart Institute, Montréal, QC, Canada, <sup>3</sup> Faculty of Medicine, Research Center, Montreal Heart Institute,  
Université de Montréal, Montréal, QC, Canada, <sup>4</sup> Computer Science and Operations Research Department, Mila (Quebec  
Artificial Intelligence Institute), Montreal, QC, Canada, <sup>5</sup> Interventional Cardiology and Cardiovascular Surgery Centre  
Hospitalier Régional Universitaire de Lille (CHRU de Lille), Lille, France

Driven by recent innovations and technological progress, the increasing quality and amount of biomedical data coupled with the advances in computing power allowed for much progress in artificial intelligence (AI) approaches for health and biomedical research. In interventional cardiology, the hope is for AI to provide automated analysis and deeper interpretation of data from electrocardiography, computed tomography, magnetic resonance imaging, and electronic health records, among others. Furthermore, high-performance predictive models supporting decision-making hold the potential to improve safety, diagnostic and prognostic prediction in patients undergoing interventional cardiology procedures. These applications include robotic-assisted percutaneous coronary intervention procedures and automatic assessment of coronary stenosis during diagnostic coronary angiograms. Machine learning (ML) has been used in these innovations that have improved the field of interventional cardiology, and more recently, deep Learning (DL) has emerged as one of the most successful branches of ML in many applications. It remains to be seen if DL approaches will have a major impact on current and future practice. DL-based predictive systems also have several limitations, including lack of interpretability and lack of generalizability due to cohort heterogeneity and low sample sizes. There are also challenges for the clinical implementation of these systems, such as ethical limits and data privacy. This review is intended to bring the attention of health practitioners and interventional cardiologists to the broad and helpful applications of ML and DL algorithms to date in the field. Their implementation challenges in daily practice and future applications in the field of interventional cardiology are also discussed.

**Keywords:** deep learning, interventional cardiology, cardiology, neural networks, prognosis

## INTRODUCTION

In recent years, the field of interventional cardiology has been characterized by innovation and technological progress as clinicians, in partnership with specialists in molecular biology, biomedical engineering, biophysics and imaging technology, have raised interventional cardiology to a vibrant and dynamic subspecialty in mainstream medical practice. As this field matures, the range of opportunities and applications continues to broaden, and there is an increasing need to focus not only on the effectiveness of treatments but also on safety issues. Novel advancements in the field of artificial intelligence (AI) can facilitate, accelerate, and improve this ongoing progress.

Fluoroscopy has been for long the pillar of interventional cardiology, and recent technological advances shake interventionists' habits by proposing multiple novel solutions to the setbacks of the X ray-based 2-dimensional fluoroscopy imaging. Human-controlled assistant robots and cardiovascular image processing are technological advancements applied to catheterization laboratories and hybrid rooms (1–4). Additionally, among a large number of percutaneous coronary intervention (PCI) operators worldwide, there exists an experiential learning curve for procedural success as it's been shown that the adjusted risk of in-hospital mortality has been higher for PCI procedures performed by low- and intermediate-volume operators compared with those performed by high-volume operators (5, 6). While an operator's success probability can be formulated as a statistical problem itself, deep learning assisted augmented reality could help with improving the learning curve associated with operator PCI success. Although autonomous and semi-autonomous robots used in interventional cardiology are probably still a few years of development and universal deployment away from routine clinical use, the vision of the operating room of the future, implementing decision-support algorithms for procedure planning and operator guidance, progressively takes shape (7). In structural heart procedures and interventional cardiology this is in particular of significant importance as, for example, studies have shown that robotic-assisted PCI (R-PCI) compared with manual PCI reduces radiation exposure to the cath lab staff, which could also improve precision (8, 9). The concept of “surgical data science” has recently been proposed, a data-driven surgical healthcare approach enhanced by decision support algorithms, context-aware automated assistants, and improvement of surgical training by digital assistance (10). As cardiac disease treatment tends to be transferred from operating theaters to hybrid rooms and catheterization laboratories, such concepts could be adapted to the cardiac interventional community.

The ability to effectively extract and store health data, powered by increasing computation power and the ability to efficiently process it yielded an explosion of AI applications aiming at improving care and reducing costs (11). More recently, deep learning (DL) has emerged as one of the most successful branches of machine learning (ML) and artificial intelligence and implements diverse architectures of deeper neural networks (DNN) (12). Additionally to electrocardiogram (ECG) data and

image/video processing, automated electronic health records (EHR), biological or genetic data mining to yield prognostic estimation of the probability of adverse outcomes, mortality included, have also been proposed for cardiology and general healthcare (13–17). And, there are signs that the implementation of AI into the catheterization laboratory has already started. For example, modeling in real-time the coronary fractional flow reserve (FFR) values from CT-angiography of the coronary vasculature using AI (instead of invasively using the dedicated wire) is feasible and if applied to coronary angiographies, it could accelerate the procedure, to reduce irradiation and to avoid possible complications associated with the wire (18, 19).

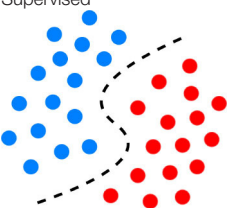
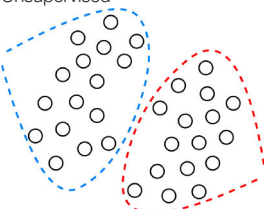
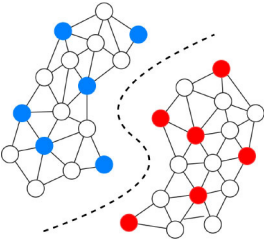
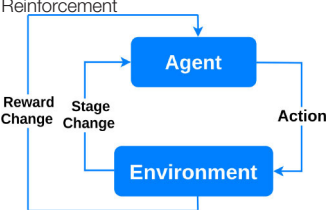
Despite the notable improvements in medical care that can be achieved using cutting edge analytical methods and algorithms in image and video processing, clinical decision support, robotic assistance, and advanced clinical database analysis, the current state of AI in interventional cardiology is in its very infancy. Yet, if practitioners and cardiologists in the field are aware and open to embracing these changes positively, it can foreseeably revolutionize interventional cardiology practice in the near future. Drawing the attention of researchers and practitioners in the field to this opportunity is the aim of this review. We first provide an overview of machine learning applications in interventional cardiology; subsequently, we discuss the demand for future improvements considering machine learning implementation challenges in daily practice and future applications in the field of interventional cardiology.

## MACHINE AND DEEP LEARNING OVERVIEW

In contrast to traditional static rule-based AI systems which are equipped with algorithms developed based on fact sheets and documented and approved clinical research subsequently validated to produce expected results, data-driven AI utilizes large datasets and complex statistical methodologies to discover new relationships between inputs, actions, and outcomes. These systems are not explicitly programmed to provide pre-determined outputs, but are heuristic, with the ability to learn and make judgements to yield improved decision making with minimal human intervention. Even though there is a large overlap between statistical modeling and ML techniques, a common understanding is that statistical models mainly refer to analysis and reporting over data, while ML is more concerned with prediction by being able to exploit and possibly improve data representation for the task of interest. In general, ML models developed for data-driven AI systems can be categorized into supervised, unsupervised, semi-supervised, or reinforcement learning (Table 1).

Supervised machine learning uses the independent features or variables to align and predict the known numerical or categorical validated outcome in the training dataset. Once properly trained, these models can then be used to predict outcomes when evaluating out-of-training samples (e.g., live patient cases). In the cardiovascular research, for example, supervised learning algorithms can identify and predict patterns in massive quantities

**TABLE 1** | Type of learning methods.

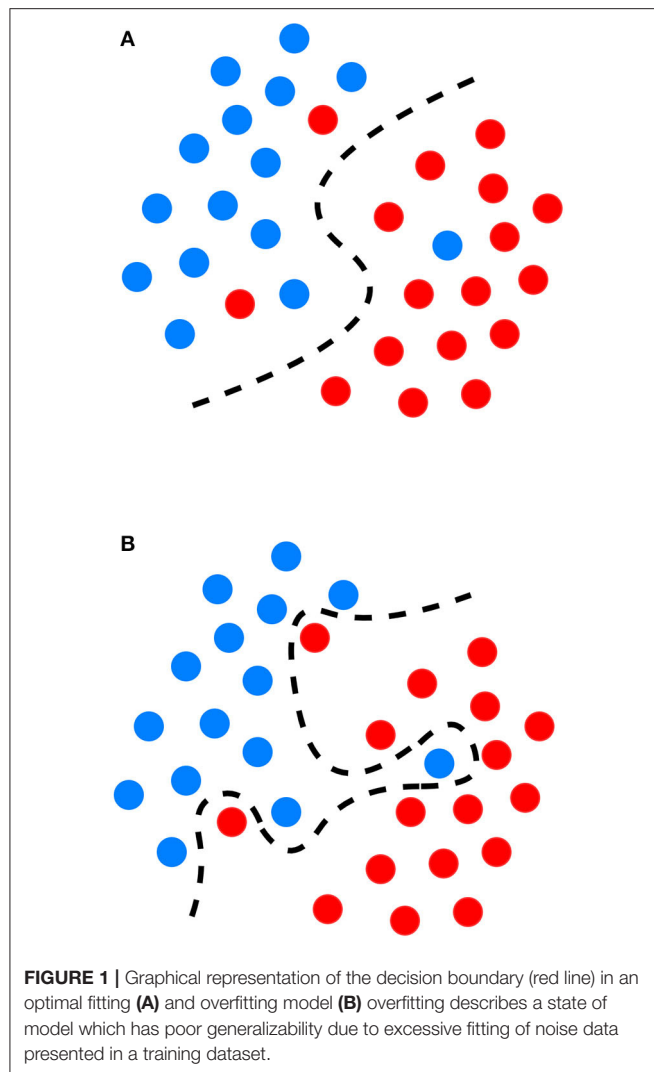
| Method   | Mechanism  | Implementation  |
|--|--|---|
| <b>Supervised</b><br>       | Uses labeled outcome data. The labels are typically assigned by experts in the field prior to model training (20, 21).   | Involves tasks such as regression, classification, predictive modeling, survival analysis (22, 23).   |
| <b>Unsupervised</b><br>     | No labeled outcome data. We observe similarities, relationships, and if possible causality among groups and variables (20, 21).  | Used for tasks such as dimensionality reduction, clustering, feature extraction (24).   |
| <b>Semi-supervised</b><br> | The input data contains both labeled and unlabeled outcome data (20, 21).  | Labeled data is used to identify specific groups in data and their parameters. These data are then inputted to the algorithm along unlabeled data to explore the boundaries of the parameters (22, 23). |
| <b>Reinforcement</b><br>  | Based on behavioral psychology. The learning agent interacts with the environment to maximize a reward, and updates its parameters based on the feedback it receives from the choices it makes. The learning stops when the “reward” criteria are met to handle a decision-making function (25). | Can be used in medical imaging analytics and personalized prescription selection. Popular in automated robotics (26).   |

of records, which are usually labeled by experts, and indicate the presence or absence of decreased systolic function on an echocardiogram or atrial fibrillation (AF) on an ECG (27). Regarding the model training, appropriate data preprocessing is typically done prior to separating data into distinct partitions of training, validation, and testing. This separation ensures fair and scientific evaluation and implementation of the model; while the validation partition would be employed for hyper-parameter selection of the model (e.g., numbers of layers in a DL network or how long model training should go on), test data must be used for final result reporting only.

Unsupervised learning, on the other hand, analyzes large amounts of typically unlabeled samples (e.g., EHR) to discover hidden patterns or innate structure which govern the existence of that data in order to substantially improve experts' understanding of that data including their involved representing features (28). In cardiology, for example, it has been shown that advanced

unsupervised models such as causal networks can evaluate causal relationships among variables beyond partial correlations and thus play a fundamental step in risk prediction of cardiovascular disease (CVD) (29).

Semi-supervised models work with datasets that are partially labeled. The labeling process of the unlabeled portion is done with the available training portion or with the help of unsupervised methods to do clustering first and then assign labels based on the characteristics of the recognized clusters (22). Generally, overfitting occurs when a supervised ML model approximates the system by available data correctly (**Figure 1**), but it is not able to produce proper results for verification or test data. It is especially a major problem in tasks for which enough labeled data is not available. Hence, semi-supervised learning can be a very useful technique for (semi-)automatically annotating lots of cases, e.g., to create a gold standard outcome label for all patients, without which it could be very expensive (22).



Closely related to semi-supervised learning, transfer learning is also another strategy to address overfitting. It is an ML technique where a model developed for one task is reused as the starting point for a model on a second task. For proper transfer learning, however, the studied tasks should be conceptually related [e.g., catheter segmentation in X-ray fluoroscopy using synthetic data (30)].

Finally, *reinforcement learning* algorithms aim at maximizing a “reward” function (26). Reinforcement learning algorithms consist of an agent at a particular time interacting with an environment. An action is selected for each time point according to some selection policy. Transitions to the next state are then performed, and a reward is received depending on the result of the transition. The restricted learning model aims to maximize the expectation of long-term rewards from each state visited. In interventional cardiology, reinforcement learning can provide tools to optimize sequences of decisions for long-term outcomes such as improving ST-segment elevation myocardial infarction outcomes or reducing errors in ECG diagnosis. Optimization of

treatment policies, real-time decisions and robot navigation are some other applications of reinforcement learning (31, 32).

Deep learning is applicable to any of the above-mentioned ML categories. It refers to the use of deep artificial neural networks to perform learning tasks. These networks are specific types of ML models where the learning happens in successive layers in such a way that each layer adds to the knowledge of the previous layer (33). DL models are capable of selecting and representing the right features on their own, thus eliminating the need for human intervention for manual definition of classification rules. For example, instead of defining that a ST elevation of  $\geq 1$  mm corresponds to a STEMI, DL models could automatically identify that the ST segment is the important feature, without any human input, and use that to predict the STEMI diagnosis. This revolutionary advancement in learning algorithms not only saves human time and labor but also minimizes the possibility of decision errors. For example, DL provided considerable advances in computer vision, a subfield in ML that matured first around 2012 and became highly popular in health and medicine, as they provide computers with the ability to learn visual features automatically from image or video content to produce diagnostic and prognostic information (34). It allowed automated analysis and interpretation of images such as computed tomography (CT), magnetic resonance imaging (MRI), electrocardiogram and echocardiography (35–38).

For instance, assessment of coronary stenosis during diagnostic coronary angiograms, one of the most commonly performed interventional cardiology procedures worldwide, is typically done using visual assessment. Thus, this method suffers from high inter-observer variability, operator bias and poor reproducibility (39–43). This variability in stenosis assessment has significant clinical implications, and likely contributes to inappropriate use of coronary artery bypass surgery in 17% of patients and of stents in 10% patients (40). While quantitative coronary angiography (QCA) using projection is able to validated quantitative measurements in coronary angiograms (44, 45), and is accepted as a gold standard for stenosis assessment, a study assessing 10 different QCA systems against a phantom stenosis gold-standard found absolute percentage differences of  $-26\%$  to  $+29\%$  in coronary stenosis assessments between systems and are semi-automatic, as they allow vessel contour modification by the human expert, which can bias the results. Deep learning algorithms can currently perform all tasks required for automatic interpretation of coronary angiograms, such as identification of left/right coronary arteries, anatomy description, vessel segmentation, stenosis localization and stenosis severity prediction leading to reduced variability and higher standardization of diagnostic angiograms (46, 47).

## MACHINE AND DEEP LEARNING FOR CARDIOVASCULAR APPLICATIONS

Rather than a comprehensive review of all studies at the intersection of interventional cardiology and AI, this section aims at giving practitioners and researchers in interventional cardiology an overview of the past and recent state-of-the-art

of ML algorithms and DL architectures, as well as examples of their cardiovascular applications (Table 2). For an all-embracing review of ML and DL approaches applied to cardiology, an avid reader may refer to more exhaustive review papers by Krittanawong et al. (38), Sardar et al. (7), Savakula et al. (82), Bizopoulos and Koutsouris (83), Cuocolo et al. (64), Siegersma et al. (84), Ribeiro et al. (85), and Quer et al. (86).

Decision Trees (DT) are interpretable supervised learning techniques that can be used for classification or regression (87). They are tree-structured models, where internal nodes represent the features of a dataset, branches represent the learned decision rules, and each leaf node represents the outcome. *Random Forests* (RF) are an ensemble learning method that operates by constructing a multitude of decision trees at training time to correct for overfitting. Other ensembles of trees such as gradient boosted trees, including LogitBoost (88) and XGBoost (89), address the same drawback.

Ambale-Venkatesh et al. tested the ability of RF, to predict several cardiovascular outcomes, including coronary heart and atherosclerotic cardiovascular diseases, in comparison to standard cardiovascular risk scores from clinical, ECG, imaging, and biomarker data (15). They showed the RF technique performed better than established risk scores with high prediction accuracy. Mortazavi et al. and Frizzell et al. worked with clinical data from the index admission, and showed RF methods improved the prediction of readmission after hospitalization for heart failure when compared with logistic regression (LR) and provided the greatest predictive range in observed readmission rates (49, 50). In another application, Motwani et al. investigated the feasibility and accuracy of iterative LogitBoost to predict 5-year all-cause mortality (ACM) in patients undergoing coronary computed tomographic angiography (CCTA) and compared the performance to existing clinical or CCTA metrics (48). They showed combining clinical and CCTA data was found to predict 5-year ACM significantly better than existing clinical or CCTA metrics alone.

Risk stratification and prognosis prediction are critical in identifying high-risk patients and decision making for the treatment of patients with acute myocardial infarction (AMI). Long-existing MI risk scoring systems including TIMI (90), GRACE (91), and ACTION (92) are based on conventional statistical methods, so there is a possibility of a loss of important information. Hence, Khara et al. with the help of the XGBoost model showed an accurate prediction of risk of death following AMI can guide the triage of care services and shared decision-making (51). They studied patients in the Cardiology Chest Pain-MI Registry hospitalized with AMI and discussed contemporary ML may improve risk prediction by identifying complex relationships between predictors and outcomes. The employed registry data included patient demographics, presentation information, pre-hospital vital signs, selected laboratory data from the hospital course, procedures, timing of procedures, and select in-hospital outcomes. Using the XGBoost model also, Rosendael et al. demonstrated an ML-based risk score that utilized standard 16 coronary segment stenosis and composition information derived from detailed CCTA reading had greater prognostic accuracy than current CCTA integrated risk scores

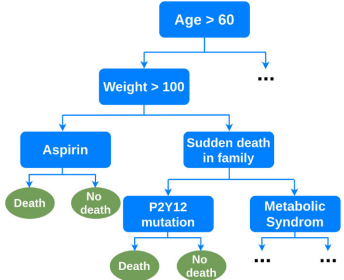
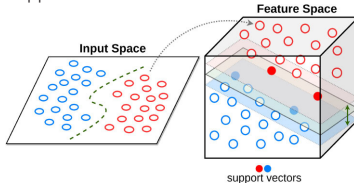
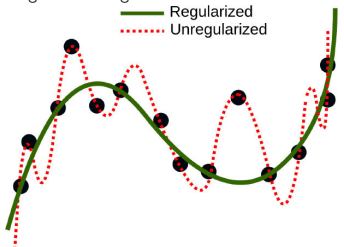
(52). They suggested ML-based algorithms can improve the integration of CCTA derived plaque information to improve risk stratification. Similarly, machine learning has been used in small datasets to improve in-stent restenosis over conventional risk scores such as PRESTO-1, PRESTO-2, EVENT and GRACIA-3 (93, 94).

Support Vector Machines (SVM) are popular supervised learning algorithms, which are used for classification and regression problems (95). The goal of the SVM algorithm is to create the best line or decision boundary (or hyperplane) that can segregate high-dimensional space into classes so that we can easily put the new data point in the correct category in the future. SVM chooses the extreme points, i.e., support vectors, that help in creating the hyperplane. Moghaddasi and Nourian have used SVM in the context of Mitral Regurgitation (MR), a common heart disease that does not cause symptoms until its end-stage (53). Early diagnosis of MR is however of crucial importance in the treatment process, and their SVM model with the radial basis function (RBF) kernel function can differentiate between the four groups of Normal, Mild MR, Moderate MR and Severe MR subjects among echocardiography videos. Transcatheter aortic valve implantation (TAVI) has become a commonly applied procedure for high-risk aortic valve stenosis patients. However, for some patients, this procedure does not result in the expected benefits. Lopes et al. demonstrated the accuracy of various traditional ML algorithms, including SVM, RF and XGBoost, in the prediction of TAVI outcomes (54).

Regularized Regression is a type of linear regression where the high-magnitude coefficient estimates are penalized (or regularized) to be small. The regularization methods provide a mean to control the regression coefficients (or weights) in datasets containing a large number of features; this can reduce the variance and decrease the out-of-sample error. Therefore, by appropriate choice of penalizing weights the model prevents overfitting to the training data. Two commonly used types of regularized regression methods are ridge regression (96) and lasso regression (97). Burcheri et al. developed a lasso-penalized Cox-proportional hazard regression model to identify independent predictors of 1-year all-cause mortality, in patients who undergo MitraClip implantation (55). In another study, Wang et al. proposed new variable selection methods for Poisson and naive Bayes regression and used plasma and urine biomarkers to help with early identification and prediction of adverse clinical outcomes after pediatric cardiac surgery (56). They discovered that early postoperative urine biomarkers independently predict prolonged hospital length of stay (LOS).

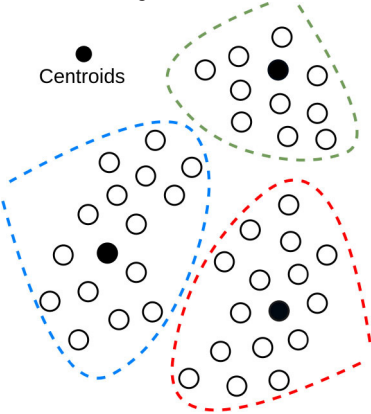
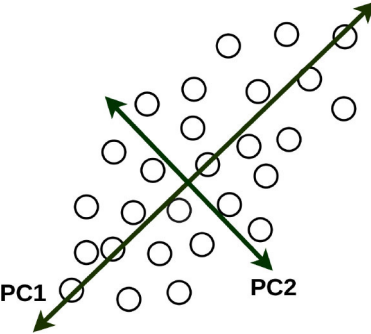
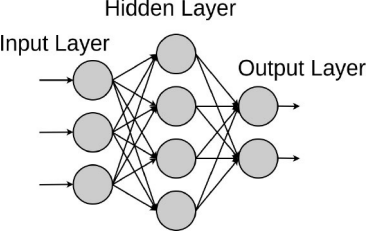
K-Means Clustering is an unsupervised learning algorithm that groups the unlabeled dataset into different clusters (98). A point is considered to be in a particular cluster if it is closer to that cluster's centroid than any other centroid. K-Means finds the best centroids by alternating between assigning data points to clusters based on the current centroids and choosing centroids based on the current assignment of data points to clusters. Mehta et al. proposed clustering algorithms could be used for the detection of QRS-complexes, the prominent feature of the ECG (57). In their study, the K-Means algorithm was used to separate QRS and non-QRS-region in the ECG signal. The onsets and

**TABLE 2 |** Algorithmic overview with prominent examples of implementation in cardiology.

| Type of algorithm  | Functioning   | Advantages   | Drawbacks  | Implementation   |
|--|---|--|--|--|
| <b>SUPERVISED LEARNING</b>   |   |  |  |  |
| Decision trees, random forest, boosting<br> | Decision trees are flowchart-type algorithms. Each variable is a condition on which the tree splits into branches, until the outcome “leaf.” Random forest and boosting are it’s derivatives. | Interpretability. Integrated feature selection. No preprocessing. Handles non-linear relationships. Requires less data than neural networks. | Computationally expensive. Can overfit or create biased trees in case of unbalanced outcome classes. | Long-term cardiovascular outcomes prediction from clinical, ECG, imaging, biomarker data (15)<br>5-year mortality prediction from clinical and coronary CT data (48)<br>30-day readmission after heart failure hospitalization (49, 50)<br>In-hospital mortality prediction after acute myocardial infarction (51)<br>Long-term death or myocardial infarction prediction from coronary CT data (52) |
| Support vector machine<br>                  | Builds a hyperplane in a high-dimensional space to separate the data into 2 outcome categories with the maximum margin.   | Can integrate many sparse features, limits overfitting and is computationally effective  | Needs preprocessing. Limited interpretability  | Automated echocardiographic assessment of mitral regurgitation (53)<br>Mortality prediction of TAVI outcomes (54)  |
| Regularized regression<br>                | Type of regression where coefficient estimates are constrained by penalty terms (ex: LASSO, ridge)  | Familiar interpretations for association of variables to outcomes applied to high-dimensional data   | Variable pre-selection is often advisable. Performance stalls for very high-dimensional data         | 1-year mortality predictors after MitraClip implantation (55)<br>Identification and prediction of adverse clinical outcomes after pediatric cardiac surgery (56)   |

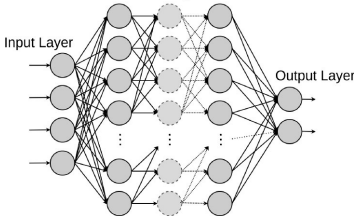
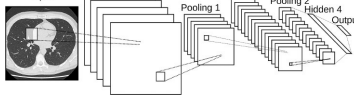
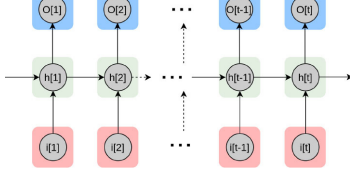
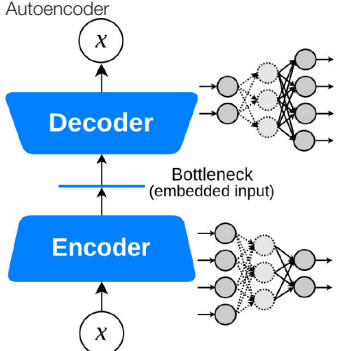
(Continued)

TABLE 2 | Continued

| Type of algorithm  | Functioning  | Advantages  | Drawbacks   | Implementation  |
|--|--|---|---|---|
| <b>UNSUPERVISED LEARNING</b>   |  |   |   |   |
| K-mean clustering<br>             | Assigns each data point to a cluster (group; with k the number of groups) based on its distance from the other points  | Easy to implement. Computationally fast.  | Number of groups must be known or assigned.                               | Separate QRS and non-QRS-region in the ECG signal (57)  |
| Principal component analysis<br> | Uses orthogonal transformation to convert possibly correlated variables into a set of linearly uncorrelated principal components.  | Can be used for dimensionality reduction.   | Only captures linear relationships. Limited interpretability              | MACE prediction from clinical and biomarker data representing metabolic syndrome (58)<br>Evaluating 3D aortic shape and hemodynamics (59) |
| <b>SHALLOW NEURAL NETWORKS AND DEEP LEARNING (MAINLY USED FOR SUPERVISED LEARNING)</b>                             |  |   |   |   |
| Shallow neural networks<br>     | A set of nodes ("neurons") is arranged in layers connected by edges (weights). The network connects input data to the outcome to predict through a paralleled set of parameterized non-linear transformations. | Can explore non-linear relationships (often encountered in real-life datasets) as well as linear ones. NN can handle heteroskedasticity, have been praised for the generalizability of the trained models, and are computationally effective. Flexible. | Variable pre-selection is often advisable. Needs variable pre-processing. | Diagnosis of coronary artery disease from myocardial perfusion scintigraphy (60)  |

(Continued)

TABLE 2 | Continued

| Type of algorithm  | Functioning  | Advantages   | Drawbacks  | Implementation   |
|--|--|--|--|--|
| <p>Deep fully connected neural network</p>  | <p>An extension of the shallow NN architecture, but that uses many hidden layers (layers between input and output). Weights and biases of the NN are trained via back-propagation.</p> | <p>Performance increases with the quantity of data. Surpass other machine learning methods for very high-dimensional data. Flexible architecture and basis of CNN, RNN</p> | <p>Requires a high quantity of data. Can easily overfit. Low interpretability Sensible to changes in input data.</p> | <p>Mortality, readmission, LOS and diagnosis prediction from EHR (13)<br/>Mid-term mortality prediction from EHR (14)<br/>Computation of Fractional Flow Reserve (FFR) from Coronary Computed Tomography (18, 19)<br/>Risk stratification for mortality of AMI patients (61)</p> |
| <p>Convolutional neural network</p>         | <p>Type of NN which learns multiple levels of feature sets at different levels of abstraction.</p>   | <p>One of the most popular deep learning architectures. Flexible. Optimal for image classification.</p>  | <p>Requires a high quantity of data. Can easily overfit. Low interpretability</p>                                    | <p>3D aortic valve annulus planimetry in TAVI (62)<br/>TTE view identification from images (63)<br/>Popular for automated heart chamber segmentation and measurement (64)<br/>Early Detection of STEMI (65)</p>  |
| <p>Recurrent neural network</p>             | <p>Type of NN which encodes sequential data by capturing context into memory.</p>  | <p>Adapted for natural language processing, text or video, genetic sequences or any other temporal data (66–69).</p>   | <p>Computationally expensive. Limited quantity of encodable data.</p>  | <p>EHR text data extraction for mortality prediction in congenital heart disease (70)<br/>Diabetes, high cholesterol, high BP, and sleep apnoea prediction using sensor data (71)<br/>Automated selection of myocardial inversion time (72)</p>                                  |
| <b>UNSUPERVISED DEEP LEARNING</b>  |  |  |  |  |
| <p>Autoencoder</p>                         | <p>Encodes the most valuable unlabeled inputs into short codes, then uses those to reconstruct the original input as output.</p>   | <p>Dimensionality reduction. Optimal for denoising filtering, image segmentation (73).</p>   | <p>Low interpretability</p>  | <p>MRI-extracted cardiac motion model denoising for survival prediction (74)<br/>U-Net for the segmentation of major vessels in X-ray coronary angiography (75)</p>  |

(Continued)

TABLE 2 | Continued

| Type of algorithm                               | Functioning   | Advantages  | Drawbacks  | Implementation   |
|---|---|---|--|--|
| <p>Deep generative models</p> <p><b>GAN</b></p> | <p>Model a distribution that is as similar as possible to the true data distribution with the help of GANs or VAEs</p>  | <p>Data augmentation and preserving data privacy with the help of synthetic data samples. Domain translation and domain adaptation. Content and style matching using adversarial inference (76, 77).</p>  | <p>Could be computationally expensive. The models are still in the stage of getting mature for high-fidelity data sample generation. Lack of stability at training time.</p> | <p>Noise reduction in low-dose CT (78)<br/>GANs for multiphase coronary CT angiography (25)<br/>Synthetic electrocardiogram generation (79)</p>    |
| <b>REINFORCEMENT LEARNING</b>                   |   |   |  |  |
| <p>Deep reinforcement learning</p>              | <p>RL learns how to maximize a reward function by exploring the actions available from certain states. A deep RL agent tests an action to see what reward will be returned by the environment in which it acts.</p> | <p>Besides robotic assistance, potential applications include: microrobots that can travel through blood vessels to deliver medications; interventional training simulator and tele-intervention (7).</p> | <p>Still in the state of infancy. Complexity and cost. Not preferable to use for solving simple problems. Huge training data demand.</p>                                     | <p>The control of an electrophysiology catheter by robots (32)<br/>Robotic-PCI reducing contact with COVID-19 patients undergoing PCI (80, 81)</p> |

AMI, acute myocardial infarction; EHR, electronic healthcare records; LASSO, least absolute shrinkage and selection operator; MACE, major adverse cardiovascular event; NN, neural network; CV, cardiovascular; MRI, magnetic resonance imaging; ECG, electrocardiogram; BP, blood pressure; CT, computed tomography; TAVI, transcatheter aortic valve implantation; PCI, percutaneous coronary intervention; VAE, variational autoencoders; GAN, generative adversarial networks; RL, reinforcement learning; STEMI, ST-segment elevation myocardial infarction.

offsets of the detected QRS-complexes were found well within the tolerance limits.

Principal Component Analysis (PCA) is another popular unsupervised learning algorithm that is used for dimensionality reduction, exploratory data analysis and predictive modeling (99). Agarwal et al. used PCA to derive a continuous measure of metabolic syndrome-based on the multiple interrelated risk factors (58). This metabolic syndrome score was a better predictor of CVD events in multiethnic cohorts than the National Cholesterol Education Program (NCEP) definition, derived predominantly from populations of European ancestry. Quail et al. in their studies evaluated 3D aortic shape and hemodynamics using principal PCA, proposed as an important determinant of adverse hemodynamics following coarctation repair (59). They concluded that shape is not the major determinant of vascular load following coarctation repair, and that caliber is more important than curvature.

Artificial neural networks are ML models that consist of an architecture of intertwined nodes (“neurons”) and edges regrouped in hidden layers connecting the input data and the outputted prediction. Whenever several hidden layers of neurons are used, the model can be described as a deep neural network (DNN), in which millions of connections can be trained in parallel. These algorithms can learn complex non-linear functions to minimize the classification error. We will detail the different DNN model architectures below.

*Shallow Neural Networks* are predecessors of DL. In contrast to deep neural networks, shallow neural networks generally use predefined features, a characteristic that they share with traditional ML algorithms. A study by Guner et al. developed and analyzed an open-source artificial intelligence program built on shallow artificial neural networks that can participate in and support the decision making of nuclear medicine physicians in detecting coronary artery disease (CAD) from myocardial perfusion SPECT (MPS) (60).

Deep Fully Connected Neural Networks (FNN) are networks that consist of multiple perceptrons (i.e., linear binary classifiers) stacked in width and depth. In FNN, every unit in each layer is connected to every unit in the layers immediately before and after. Rajkomar et al. proposed a representation of patients’ entire raw EHR records based on the Fast Healthcare Interoperability Resources (FHIR) format (13). They demonstrated that FNN models using this EHR representation were capable of accurately predicting multiple medical events from multiple centers without site-specific data harmonization. Their models achieved high accuracy for tasks such as predicting in-hospital mortality, 30-day unplanned readmission, LOS, and all of a patient’s final discharge diagnoses. In the context of palliative care services, Avati et al. proposed an interpretable FNN model trained on the EHR data from previous years, to predict all-cause 3–12 month mortality of patients, as a proxy for patients that could benefit from palliative care (14). Their predictions enabled a palliative care team to take a proactive approach in reaching out to such patients, rather than relying on referrals from treating physicians or conducting time-consuming chart reviews of all patients.

Recently, physics-based models such as computational fluid dynamics (CFD) have shown great promise in being able to

non-invasively estimate FFR from patient-specific anatomical information, e.g., obtained from computed tomography scans of the heart and the coronary arteries (100, 101). However, these models have high computational demand, limiting their clinical adoption. Itu et al. developed a FNN for predicting FFR, speeding up physics-based approaches (18). The model is trained on a large database of synthetically generated coronary anatomies, using the physics-based model. They showed that the correlation between ML and physics-based predictions was significant and without systematic bias. Coronary computed tomographic angiography is another reliable modality to detect coronary artery disease. In their study, Coenen et al. showed that on-site CT-fractional flow reserve (CT-FFR) improves the performance of CCTA by correctly reclassifying hemodynamically nonsignificant stenosis (19). Their DNN model performs equally well as computational fluid dynamics-based CT-FFR. Kwon et al. developed an FNN risk stratification model that predicted the in-hospital mortality and 12-month mortality of AMI patients more accurately than the existing risk scores and other ML methods including RF (61). In their model, they used the demographic information and laboratory data of AMI patients as the predictor variables. Such models could be improved by adding more modalities to the input data (e.g., text in EHR and images of CT) as discussed in a study by Myers et al. (102).

Convolutional Neural Networks (CNN), widely used in computer vision, consist of a convolutional and pooling part, where hierarchical feature extraction takes place, and a fully connected part for classification or regression. The models can recognize low-level features, such as edges and corners, and high-level features such as parts of objects thanks to convolutional layers that are much better feature optimizers, while fully connected layers are good classifiers. In TAVI procedures, the sizing of devices is done from ECG-gated CT angiographic image volumes. The most crucial step of the analysis is the determination of the aortic valve annular plane. Theriault-Lauzier et al. developed an expert-level CNN to infer the location and orientation of the aortic valve annular plane (62). Madani et al. investigated the application of CNNs to echocardiography view classification that classified 15 major transthoracic echocardiograms (TTE) views with expert-level quality (63). They used a training set that reflected a wide range of clinical and physiological variations, demonstrating applicability to real-world data. They found that the model used some of the same features in echocardiograms that human experts use to make their decisions. CNNs were also used to fully interpret echocardiograms and diagnose certain diseases with a high level of accuracies such as hypertrophic cardiomyopathy or pulmonary hypertension. These models usually use a single frame to predict the corresponding view or measurement. Recently, video-based AI was used for analyzing a whole echocardiogram video to better predict cardiac function (103). CNNs were also employed for the segmentation of the heart chamber in a work by Cuocolo et al. (64). Segmentation of heart regions in advance can help the subsequent problems in hand. For example, as discussed in their study, segmentation of the epicardium and endocardium from the left ventricle can be important for the assessment of the cardiovascular system function (e.g., hypertrophy vs. normal

cases). Most importantly, CNNs can also be used to predict new diseases that were previously not possible. Recently, a CNN was used to derive a digital biomarker that can detect diabetes using a photoplethysmography signal, which is traditionally used for pulse oximetry or for heart rate measurements (104). Such novel digital biomarkers could be derived using data readily available in interventional cardiology, such as coronary angiograms, to predict device failures or certain conditions such as spontaneous coronary artery dissection.

Recurrent Neural Networks (RNN) are ideal for time-series or sequential data. These networks consist of feedback loops, so they can use their internal state to process the input. To estimate prognosis in a large cohort of patients with adult congenital heart disease (ACHD) or pulmonary hypertension, Diller et al. designed an RNNs model that categorized diagnosis and disease stages with high accuracies (70). Ballinger et al., proposed a semi-supervised sequence learning for cardiovascular risk prediction, the DeepHeart model (71). They demonstrated their multi-task RNN model outperforms hand-engineered biomarkers from the medical literature. Working with off-the-shelf wearable heart rate sensors, they suggested that methods such as theirs could help with patient risk stratification based on cardiovascular risk scores derived from popular wearables such as Fitbit, Apple Watch, or Android Wear.

Delayed myocardial enhancement imaging is an essential component of cardiac MRI, which is used widely for the evaluation of myocardial scar and viability (105). The selection of optimal inversion time or null point to suppress the background myocardial signal is required. In their study, Bahrami et al. showed that merging the spatial and temporal characteristics of CNN and LSTM was capable of automated prediction of myocardial inversion time from an inversion-recovery experiment (72). In clinical practice, early ST-segment elevation myocardial infarction (STEMI) detection is of great clinical significance because the very early stages of STEMI are the most vulnerable periods during which most sudden cardiac deaths occur (106); hence, an accurate and efficient warning system based on an ECG can help with patient delay. Zhao et al. proposed a CNN trained on 12-lead ECG that outperforms clinicians in early detection of STEMI (65). They also argue ML-based algorithms have the potential to empower a wide range of physicians to more accurately diagnose STEMI on ECG and reduce the inappropriate activation of catheter labs.

Autoencoders (AE) are neural networks that are trained with the objective to reconstruct the output from the input by encoding useful properties of the data. It usually consists of an encoding part that downsamples the input down to a linear feature and a decoding part that up-samples this representation back to the original dimensions. In a human survival prediction study, Bello et al. used image sequences of the heart acquired using cardiac MRI, to create time-resolved three-dimensional segmentation using a network trained on anatomical shape priors (74). This dense motion model formed the input to a supervised denoising autoencoder, a special AE that randomly turns some input values to zero to prevent overfitting.

U-Net is a modification of the convolutional autoencoders, i.e., encoder-decoder, architecture, first introduced by

Ronneberger et al. for medical image segmentation (107). U-Net incorporates additional links between the encoder layers and the decoder layers of the network, resulting in a U-shape structure (107). Although quantitative coronary angiography (QCA) provides morphological information of coronary arteries with objective quantitative measures, considerable training is required to identify the target vessels and understand the tree structure of coronary arteries. Yang et al. proposed a robust method for major vessel segmentation using an adjusted U-Net network (75). Even though the model is evaluated intrinsically with the help of segmentation labels, the same model could be extrinsically used and evaluated by replacing traditional segmentation methods in coronary catheterization for prediction of FFR in intermediate coronary artery lesions (108).

Deep Reinforcement Learning (DRL) uses deep learning and reinforcement learning principles to create efficient algorithms applied to areas such as robotics, natural language processing, computer vision and healthcare. Implementing deep learning architectures with reinforcement learning algorithms is capable of scaling to previously unsolvable problems (25). In a recent work by You et al., a robot was developed to reduce the radiation exposure of personnel during an interventional procedure for arrhythmia (32). Experiments on the control of an electrophysiology catheter by robots were conducted. Using the DRL, they showed that such a robot learned to manipulate a catheter to reach a target in a simulated environment and subsequently control a catheter in an actual environment. Additionally, several studies evaluated the feasibility and technical success of reinforcement learning-based R-PCI for the treatment of CAD in clinical practice when compared with manual PCI (8, 109). As a vivid recent example, to minimize the risk of exposure to severe acute respiratory syndrome coronavirus 2 (SARS-CoV-2) and reduce personal protective equipment needed by the procedural team during the COVID-19 pandemic, studies by Tabaza et al. and Virk et al. showed R-PCI could help to reduce contact with COVID-19 patients undergoing PCI (80, 81).

Deep Generative Models (DGM) are powerful ways of learning any kind of data distribution using unsupervised learning. Since it is not always possible to learn the exact distribution of the data, DGMs try to model a distribution that is as similar as possible to the true data distribution. Two of the most commonly used and relatively efficient approaches are Variational Autoencoders (110) (VAE) and Generative Adversarial Networks (111) (GAN). Considering that advanced image reconstruction from low-dose CT data is needed to improve the diagnostic performance, which is a challenging problem due to its ill-posed nature, Wolterink et al. used a GAN to transform low-dose cardiac CT images into routine-dose CT images (78). In another study, Kang et al. trained a GAN to reduce noise in CCTA images (112). Their proposed unsupervised network learns the image distributions from the routine-dose cardiac phases by eliminating the need to exactly matched low- and routine- dose CT images. A hybrid DL architecture developed by Zhu et al. showed that an LSTM-CNN GAN could generate ECG data with high morphological similarity to real ECG recordings (79). This is of interest, as

such an approach could be used to generate a large dataset of ST segment elevation ECGs for training an algorithm that would identify STEMI due to obstructive CAD vs. non-obstructive disease (pericarditis, for example).

## IMPLEMENTATION OF MACHINE LEARNING AND ITS CHALLENGES

### AI in the Real World

Since data-driven AI is different from traditional rule-based systems and medical devices it demands adequate control to ensure its safety and effectiveness. Also, because these differences will not be the same for the full range of systems, it is important to identify what aspects of AI are of concern (113). The safety and effectiveness of medical devices entering the market today are governed by regulations and private-sector consensus standards. Whereas, in most cases, they were developed alongside current technologies and are based on an extensive, shared understanding of how and how well they work. With an emergent technology like AI, real-world experience is limited, which can hinder regulators and practitioners' ability to fully assess its effectiveness. Similarly, a lack of real-world experience with AI limits the understanding of its associated risks. AI-related risks are harder to quantify and mitigate as there may be unforeseeable and unpredictable hazards arising from the unique nature or function of AI. This is particularly important in raw health data that generally lack maintenance and validation and raise important interoperability problems (113, 114). AI may become untrustworthy also because data was not representative or not fit for the task to which it was applied. The availability of data is essential as a source of information for training AI systems, but it is also a source of noise, especially when data quality is poor, labeling is inconsistent, or sampling is biased. Iterative preprocessing of data must be done before it is considered to be of adequate quality for downstream ML tasks, such that quality management of data is understood as an important issue by AI practitioners. Recently, there is a push toward a more data-centric approach to ML to increase accuracy based on improving the datasets (115), in contrast to the widespread model-centric approach that focuses on changing the model to improve performance. Improving the quality of a dataset does not necessarily mean increasing dataset size, it can be achieved by fixing incorrect labels, adding examples that represent edge cases, or apply data augmentation.

Furthermore, the nature of the application either rule-based, data-driven locked (i.e., non-adaptive through time), or data-driven while continuously learning (i.e., life-long learning), as well as the context of application which can be informative or provide decision support with or without a human in the loop play major roles (113). Given that AI or data has the ability to change over time, the processes of verification and validation cannot be a onetime premarket activity, but instead must continue over the life cycle of an AI system from the initial design and clinical substantiation, across its post market use, until decommissioning. Such life cycle consists of data quality assurance, pre-market risk management and assurance

of effectiveness, pre-specification and algorithm change, and real-world performance monitoring. Continual assurance of the AI-based device's safety and performance across its life cycle will help regulators, clinicians, and patients gain trust in data-driven AI. To this end, a recent initiative by a group of medical device regulators from several countries, including Food and Drug Administration (FDA) from USA, has established International Medical Device Regulators Forum (IMDRF) to harmonize the regulatory requirements for medical products under a notion named Software as a Medical Device (SaMD) (116). The FDA's Center for Devices and Radiological Health (CDRH) is also considering a total product life-cycle-based regulatory framework for these technologies that would allow for modifications to be made from real-world learning and adaptation, while ensuring that the safety and effectiveness of the software as a medical device are maintained (117). As further advancements are made in AI technology, regulators will need to consider additional approaches for addressing the safety and effectiveness of AI in healthcare, including how international standards and other best practices are currently used to support the regulation of medical software, along with differences and gaps that will need to be addressed for AI solutions. One key aspect will be the need to generate real-world clinical evidence for AI systems throughout their life cycles, and the potential for additional clinical evidence to support adaptive systems. Next to AI systems themselves, regulators must also consider that there are ethical, social and political challenges comprising issues regarding trust, liability, privacy and risk (118). These complexities of applications of AI require further reflection, proof of their medical utility, economic valuing, and development of interdisciplinary strategies for their wider application (119).

Last but not least, the capacity of complex decision-making in interventional cardiology or in performing a procedure independently would be very challenging for current AI and ML algorithms. Understandably, by considering the speed of progress and development, AI technologies could not completely replace human interventional cardiologists in the foreseeable future. It can be easily anticipated, however, that AI will widely assist rather than replace the human operator in the catheterization laboratory. Hence, the reception and integration of AI in a specialty which needs quick decision-making by the operator should be discussed and practiced prior to the actual deployment of innovations brought by ML and DL models.

### Domain Expertise

Beyond AI algorithm development, several additional issues should be tackled before implementing AI into clinical practice (86). First, domain-experts, such as cardiologists should collaborate with data scientists and AI engineers in order to jointly develop AI algorithms that is as bias free as possible, respects the regulatory framework for development and addresses a clinically relevant need (86, 120). By addressing accurate and reliable implementation of ML and DL algorithms in cardiology, the Proposed Requirements for Cardiovascular Imaging-Related Machine Learning Evaluation (PRIME) checklist provided by Sengupta et al. lays down seven items to be reported for reducing

algorithmic errors and biases aiming to standardize reporting on model design, data, selection, assessment, evaluation, replicability, and limitations (121). Next, clinical trials need to be conducted to demonstrate that such algorithms are positively influencing morbidity, mortality or healthcare delivery. The SPIRIT-AI and CONSORT-AI working groups have put forward guidelines for clinical trials for interventions involving AI and represent a framework by which to conduct and report such trials (122, 123). It is crucial to perform extensive external validation on multiple datasets to demonstrate the algorithm's robustness. Finally, once the algorithm is found to positively influence healthcare, further real-world quality control must be conducted to assure that the algorithm is providing accurate predictions and that its performance does not deteriorate over time. This could be done by routinely collecting feedback on the predictions from the domain-experts. Further, continuous learning of AI Algorithms, post-commercialization, to improve predictions on reported errors and to adapt to new data, remains an area of active research.

Large electronic healthcare databases (LEHD) are being built from electronic health records and already used by several countries to implement AI in healthcare (124, 125). Some prominent examples of such databases are the UK Biobank (UK), Million Veterans Initiative (USA), NIH precision medicine initiative (USA), large Scandinavian national registries in Denmark, Sweden, and Norway. If dispersed big data are to disrupt current research models then there is a need for searchable catalogs of data, metadata, feasibility counts (and ideally sample data) and access arrangements. The creation of public, standards-driven metadata and data portals can assist researchers in locating the right dataset for their research question and obtaining up to date details on data availability and accessibility. Moreover, contemporary LEHD often contain multi-omics data (transcriptomics, genomics, proteomics, metabolomics, microbiomics, radiomics) intended for deep phenotyping of patients (126, 127). However, the size does not always ensure the precision of the model built, nor that the intent of improving care for all people is met. What is more, further progress in automation of data harvesting and inter-database harmonization (e.g., EHR and national statistical organisms which record vital status) would facilitate the construction of high-quality high-dimensional databases (128).

## Underspecification

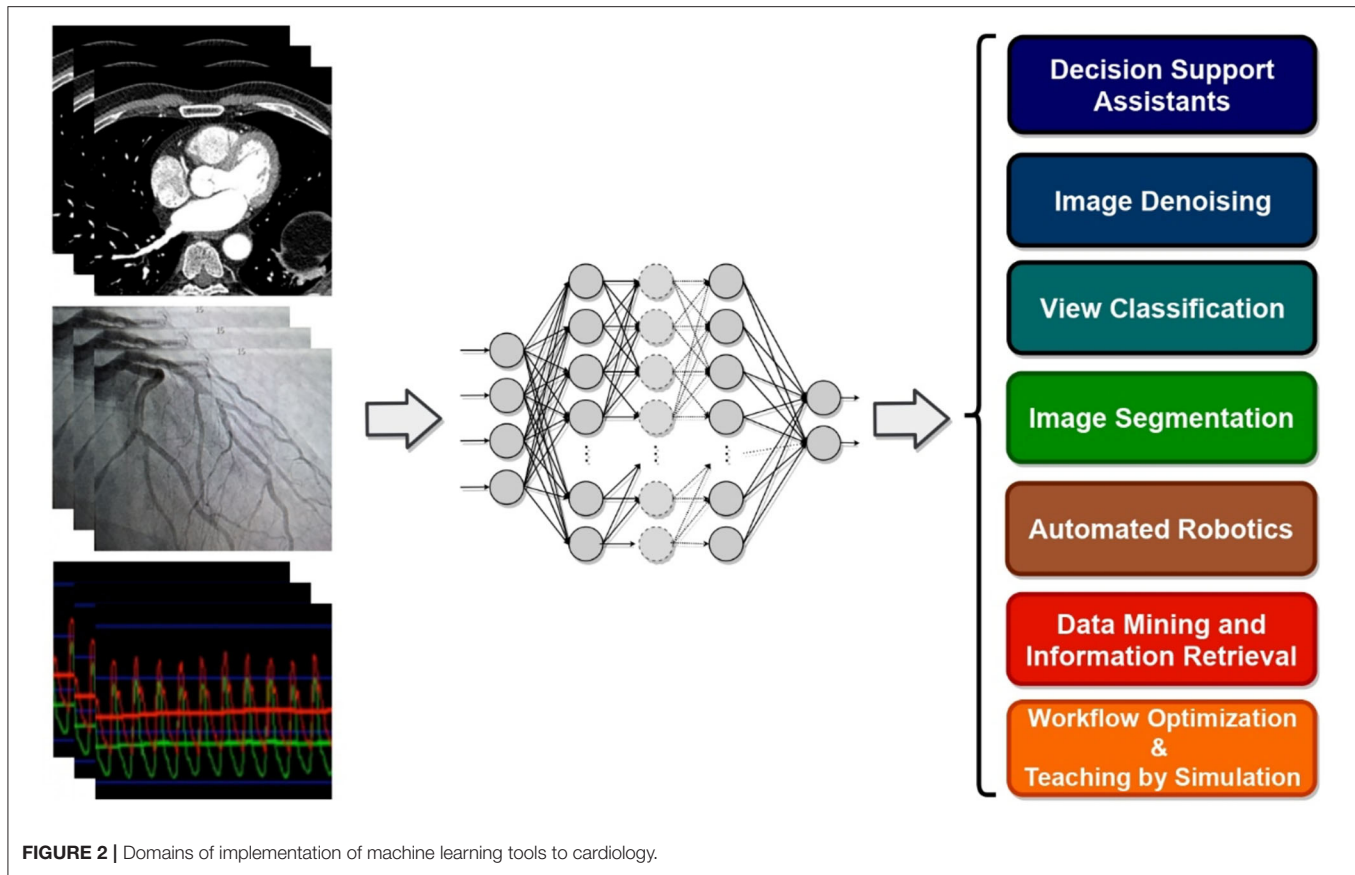
As stated above, the quality of the training samples provided to an ML algorithm is of central importance in data-driven AI. This is because ML models often exhibit unexpectedly poor behavior when they are deployed in real-world domains due to underspecification (129). An ML or DL pipeline could be underspecified when it returns many predictors (e.g., several predictive models with distinct and dissimilar weights) with equivalently strong held-out performance in the training domain yet these models perform significantly different when generalized, therefore questioning the credibility of the predictors in practice. For many medical applications, a key challenge is the robustness of the ML model under the distribution shift of data in the deployment domain, and as a result,

several studies confirm the need for explicitly testing and monitoring ML models in settings that accurately represent the deployment domain (122, 123, 130). In addition, heterogeneity in the representation of different ethnicities, gender inequalities, socioeconomic status, geography in datasets could generate biased estimations and automate inequalities (131). Therefore, to address underspecification, next to improving the training and testing process, and also considering multiple ML models as alternatives at deployment time, limiting model complexity as well as designing stress tests to probe stratified performance evaluations, shifted evaluations, and contrastive evaluations should be considered (129).

Despite their performance, expecting to achieve perfect prediction with DL models is probably vain. The chaos theory states that even with a deterministic (non-random) process, even simple non-linear systems cannot be precisely predicted into the distant future (11, 132). Conventional statistical approaches often use a standardized stepwise approach. After univariate feature analysis, a model is selected and uses cohorts with manually entered structured databases. This differs from the machine learning approach which tends to avoid model selection and uses “fuzzier” emerging sources of data that are more prone to contain some quantity of bias (11, 70). Without appropriate oversight, ML models can easily overfit in noisy datasets, impairing their capacity to generalize to new data due to over-interpretation of noise (**Figure 1**). This is particularly true when the number of examples (patients) are limited compared to the number of variables measured for each patient or when the outcome of interest is of rare occurrence, which is often the case in some present-day medical applications. Besides, building predictive models is inherently based on past events, and the future will not necessarily resemble the past, nor will they necessarily perform well on a population different from the one represented in the training cohort (11). Numerous teams have successfully applied DL algorithms to yield high-performance predictive models through the mining of EHR with the idea of assisting doctors through decision-support algorithms by combining all the available information, irrespective of their time of occurrence (11, 13, 14, 35). However, for decision-support algorithms to be implemented in clinical practice, we would expect them to be accurate and pertinent at the time the decision is taken, without assuming to know everything in advance (**Figure 2**) as developed by Diller et al. to guide therapy in adult congenital heart disease (70).

## Overfitting and Interpretability

Despite ML models being theoretically superior to usual statistical models in terms of predictive power (15, 133), their practical use must also be rigorous along with its reporting and reviewing (134). Furthermore, the computationally demanding DL algorithms also require efficient programming libraries (such as PyTorch and TensorFlow), and specific hardware (such as Graphics or Tensor Processing Unit instead of the usual Central Processing Unit). Additionally, all ML and DL models may suffer from overfitting if data is limited and/or algorithms are complex. Indeed, in clinical studies, DL provided similar results to statistical models (e.g., logistic regression) (38). Transfer



learning, data augmentation with the help of deep generative models, as well as integration of different data sources can be solutions to overfitting problems, but in some cases the curse of dimensionality will prevent some types of analyses on small datasets. Future studies may integrate DL with statistical classification. Furthermore, doctors and patients would also need to understand the exact reasons that led to a medical decision. However, evaluating ML model decisions can be a very difficult task. Once a model is trained, it requires additional approaches to understand the reason behind a particular prediction to a set of data inputs (135). In particular, the numerous intertwined relationships captured by the layers of a DNN are only partially understood, leading to being frequently labeled as “black boxes,” and the observed trade-off between accuracy and interpretability of machine learning models (136). Explaining single predictions or the entire model behavior of DNNs is important to correct their malfunctions, bias, and susceptibility to slight modifications of analyzed data (137). Interpretability may be enabled by capsule based networks or strategies that systematically censor inputs to define those that most affect classification. Meta-analyses of several DL algorithms applied to the same data may increase confidence in results. A number of techniques may enable “model-agnostic” metrics for interpretability of complex models (138). Marblestone et al. (139) hypothesized analogies between DL and human cognitive functioning, proposing that integrating heterogeneous “cost functions” over time may

simplify learning. Thus, speculatively, insights into human cognition may ultimately provide insights to interpret DL models. Encouragingly, much research is ongoing aiming at improving our understanding of ML and DL models (140).

## Missing Data

Similar to statistical tasks, the performance of DL can be highly sensitive to missing data as well. Missing data is a common problem in routine medical records, hence, measures of data management and pre-processing should be addressed in line with the extra complexity they impose on the robustness ML (141, 142). Decisions on how to treat missing data can be made by evaluating if the presence or absence of specific elements correlates with desired outcomes or predictors. Those data that are correlated are “non-ignorable,” those that are not correlated may be “ignorable” (i.e., no relationship to any variables) (143). Additionally, instead of omitting patients with missing data, it is ideal to impute missing data points to obtain more patients for training process and ML analysis. Using k-nearest neighbor (k-NN) to fill in missing values of a data point with the closest known ones, or simply relying on mean or most frequent values of variables to fill in missing positions are standard approaches. Another popular method for imputing missing values is called “multiple imputation using chained equations” (MICE) (144). MICE statistically measures the uncertainty of

the missing values and is able to impute different variable types (i.e., continuous, unordered and ordered categorical, etc.) that may reside in the medical records while each variable is imputed by its own model. Another frequently used imputation technique in mixed data is the “factor analysis of mixed data” (FAMD) algorithm (145). FAMD is a principal component method which balances the influence of all the variables that are continuous and categorical in the construction phase of the dimensions. MICE and FAMD, however, are computationally intensive making them suboptimal for pre-processing steps in DL models. Hence, designing strategies, developing imputation algorithms, and their suitable evaluation for realistic settings of medical domain are of great importance. While still an active area of research, many studies have already shown desirable imputation results obtained by autoencoders models such as denoising autoencoders (146, 147).

## ETHICAL ISSUES: PATIENT DATA MISUSE MUST BE AVOIDED

A current worrying tendency to exploit patient data for financial purposes must be acknowledged, discussed, and acted upon. A Dutch startup CathSuite aims to automatically extract patient information from various catheterization laboratory report sources and hospitals, and store it in a standardized form, notably on mobile phones. Among their intended purposes of data use is research, but also monetization through contracts with insurance companies (148). It is appropriate that patient data is extracted with their consent for research purposes that will aim at improving healthcare. However, it is hardly conceivable that patient data could be exploited for private company financial gains, at the detriment of the patient, by sharing their data with insurance companies or other private actors that could use it against patients.

Data privacy has been the subject of the European General Data Protection Regulation (149). A legislative context is lacking for the specific context of patient data protection, although protecting patient data could be even more important than the data of healthy individuals. De-identification should not be seen as inviolable protection since the power of ML algorithms could allow the data extraction and storing of the path to be reversed and traced back to the patient. Reports of EHR data breaches are not infrequent (150). The Hippocratic Oath states “Whatever I see or hear in the lives of my patients, whether in connection with my professional practice or not, which ought not to be spoken of outside, I will keep secret, as considering all such things to be private.” Information and Technology (IT) professionals, private companies wishing to exploit patient data, let alone insurance companies, do not abide by the medical secret, the main guardian of the patient-physician relationship of care. More than ever, physicians must protect their patients’ data, verify that its use is intended at improving care, and guard against monetization at the detriment of patients. Regulators and international medical

associations must address the gap in the guidelines of patient data exploitation and provide limitations of possible applications to research. Companies and researchers must be held responsible for the data they are entrusted with, their use of it and the tools they create to exploit it, including data misuse.

Furthermore, letting private industry companies shaping the future of AI is not the only path toward progress in medicine through technology. An industrial profit-maximizing approach is likely to diverge from public interest (23). Independent quality research is important. Hospitals should employ data scientists and IT professionals under hospital authority to ensure patient data protection and appropriate exploitation directed at improving healthcare. An upgrade of cyber protection of hospital informatics systems storing EHRs should be considered.

## Final Comments

Once the hype of AI is passed, a backlash against this very promising field of research remains possible. Reticence from patients toward the use of their data, and physicians’ reluctance to the use of technology as an intermediate between them and patients could fuel discontent. Patient misuse must not be tolerated. Recent progress in the field of AI interpretability suggests that this setback can be overcome (136) and the focus should be on developing approaches that are human-interpretable, to allow reliable strategies to be deployed to assist clinicians in their medical practice. Several trials are ongoing to develop algorithms predicting procedural success, in-hospital mortality, and 1-year mortality after transcatheter aortic valve replacement. This is of big interest, especially in the era of expanding indications to lower risk and younger population, to help heart teams in the decision-making process and in the selection of optimal candidates and devices.

## AUTHOR CONTRIBUTIONS

WB, AP, and JH: substantial conception, drafting of the article for important intellectual content, and revising the article for final approval of the submitted paper. RA: drafting of the article for important intellectual content and revising the article for final approval of the submitted paper. PO and NP: drafting of the article for important intellectual content. SL, RC, RI, and TM: revising the article for final approval of the submitted paper. All authors contributed to the article and approved the submitted version.

## FUNDING

RA received support from the Fonds de la recherche en santé du Québec (FRSQ) (grant 274831). JH is a FRSQ Junior 1 Research Scholar (252997) and is funded by IVADO (PRF-2019-3378524797) and Montreal Heart Institute Foundation (FICM-1132).

## REFERENCES

- Pourdjabbar A, Ang L, Behnamfar O, Patel MP, Reeves RR, Campbell PT, et al. Robotics in percutaneous cardiovascular interventions. *Expert Rev Cardiovasc Ther.* (2017) 15:825–33. doi: 10.1080/14779072.2017.1377071
- Gillinov AM, Suri R, Mick S, Mihaljevic T. Robotic mitral valve surgery: current limitations and future directions. *Ann Cardiothorac Surg.* (2016) 5:573–6. doi: 10.21037/acs.2016.03.13
- Thériault-Lauzier P, Andalib A, Martucci G, Mylotte D, Cecere R, Lange R, et al. Fluoroscopic anatomy of left-sided heart structures for transcatheter interventions: insight from multislice computed tomography. *JACC Cardiovasc Interv.* (2014) 7:47–57. doi: 10.1016/j.jcin.2014.06.002
- Overtchouk P, Sudre A, Delhay C, Juthier F, Van Belle E, Coisne A, et al. Advanced image processing with fusion and calcification enhancement in transcatheter aortic valve implantation: impact on radiation exposure. *Interact CardioVasc Thor Surg.* (2018) 27:512–9. doi: 10.1093/icvts/ivy136
- Fanaroff AC, Zakrofsky P, Dai D, Wojdyla D, Sherwood MW, Roe MT, et al. Outcomes of PCI in relation to procedural characteristics and operator volumes in the United States. *J Am Coll Cardiol.* (2017) 69:2913–24. doi: 10.1016/j.jacc.2017.04.032
- Young MN, Secemsky EA, Kaltenbach LA, Jaffer FA, Grantham JA, Rao SV, et al. Examining the operator learning curve for percutaneous coronary intervention of chronic total occlusions: a report from the National Cardiovascular Data Registry. *Circ Cardiovasc Interv.* (2019) 12:e007877. doi: 10.1161/CIRCINTERVENTIONS.119.007877
- Sardar P, Abbott JD, Kundu A, Aronow HD, Granada JF, Giri J. Impact of artificial intelligence on interventional cardiology: from decision-making aid to advanced interventional procedure assistance. *JACC Cardiovasc Interv.* (2019) 12:1293–303. doi: 10.1016/j.jcin.2019.04.048
- Walters D, Omran J, Patel M, Reeves R, Ang L, Mahmud E. Robotic-assisted percutaneous coronary intervention. *Intervent Cardiol Clin.* (2019) 8:149–59. doi: 10.1016/j.iccl.2018.11.005
- Bergman P, Blacker SJ, Kottenstette N, Saber O, Sokhanvar S. Robotic-assisted percutaneous coronary intervention. In: Abedin-Nasab M, editor. *Handbook of Robotic and Image-Guided Surgery.* Amsterdam: Elsevier (2020), p. 341–62.
- Hung AJ, Chen J, Gill IS. Automated performance metrics and machine learning algorithms to measure surgeon performance and anticipate clinical outcomes in robotic surgery. *JAMA Surg.* (2018) 153:770–1. doi: 10.1001/jamasurg.2018.1512
- Chen JH, Asch SM. Machine learning and prediction in medicine—beyond the peak of inflated expectations. *N Engl J Med.* (2017) 376:2507. doi: 10.1056/NEJMp1702071
- LeCun Y, Bengio Y, Hinton G. Deep learning. *Nature.* (2015) 521:436–44. doi: 10.1038/nature14539
- Rajkomar A, Oren E, Chen K, Dai AM, Hajaj N, Hardt M, et al. Scalable and accurate deep learning with electronic health records. *NPJ Digit Med.* (2018) 1:18. doi: 10.1038/s41746-018-0029-1
- Avati A, Jung K, Harman S, Downing L, Ng A, Shah NH. Improving palliative care with deep learning. *BMC Med Inform Decis Mak.* (2018) 18:122. doi: 10.1186/s12911-018-0677-8
- Ambale-Venkatesh B, Yang X, Wu CO, Liu K, Hundley WG, McClelland R, et al. Cardiovascular event prediction by machine learning: the multi-ethnic study of atherosclerosis. *Circ Res.* (2017) 121:1092–101. doi: 10.1161/CIRCRESAHA.117.311312
- Christophersen IE, Rienstra M, Roselli C, Yin X, Geelhoed B, Barnard J, et al. Large-scale analyses of common and rare variants identify 12 new loci associated with atrial fibrillation. *Nat Genet.* (2017) 49:946–52. doi: 10.1038/ng.3843
- Chua W, Purmah Y, Cardoso VR, Gkoutos GV, Tull SP, Neculau G, et al. Data-driven discovery and validation of circulating blood-based biomarkers associated with prevalent atrial fibrillation. *Eur Heart J.* (2019) 40:1268–76. doi: 10.1093/eurheartj/ehy815
- Itu L, Rapaka S, Passerini T, Georgescu B, Schwemmer C, Schoebinger M, et al. A machine-learning approach for computation of fractional flow reserve from coronary computed tomography. *J Appl Physiol.* (2016) 121:42–52. doi: 10.1152/japplphysiol.00752.2015
- Coenen A, Kim Y-H, Kruk M, Tesche C, De Geer J, Kurata A, et al. Diagnostic accuracy of a machine-learning approach to coronary computed tomographic angiography-based fractional flow reserve: result from the MACHINE consortium. *Circ Cardiovasc Imaging.* (2018) 11:e007217. doi: 10.1161/CIRCIMAGING.117.007217
- James G, Witten D, Hastie T, Tibshirani R. *An Introduction to Statistical Learning.* Berlin: Springer (2013).
- Bishop CM. *Pattern Recognition and Machine Learning.* Berlin: Springer (2006).
- Madani A, Ong JR, Tibrewal A, Mofrad MRK. Deep echocardiography: data-efficient supervised and semi-supervised deep learning towards automated diagnosis of cardiac disease. *NPJ Digit Med.* (2018) 1:1–11. doi: 10.1038/s41746-018-0065-x
- Benkler Y. Don't let industry write the rules for AI. *Nature.* (2019) 569:161–2. doi: 10.1038/d41586-019-01413-1
- Segar MW, Patel KV, Ayers C, Basit M, Tang WHW, Willett D, et al. Phenomapping of patients with heart failure with preserved ejection fraction using machine learning-based unsupervised cluster analysis. *Eur J Heart Fail.* (2020) 22:148–58. doi: 10.1002/ehf.1621
- Sutton RS, Barto AG. *Reinforcement Learning: An Introduction.* Cambridge, MA: MIT Press (2018).
- Gottesman O, Johansson F, Komorowski M, Faisal A, Sontag D, Doshi-Velez F, et al. Guidelines for reinforcement learning in healthcare. *Nat Med.* (2019) 25:16–8. doi: 10.1038/s41591-018-0310-5
- Hagiwara Y, Fujita H, Oh SL, Tan JH, San Tan R, Ciaccio EJ, et al. Computer-aided diagnosis of atrial fibrillation based on ECG signals: a review. *Inf Sci.* (2018) 467:99–114. doi: 10.1016/j.ins.2018.07.063
- Xiao C, Choi E, Sun J. Opportunities and challenges in developing deep learning models using electronic health records data: a systematic review. *J Am Med Inform Assoc.* (2018) 25:1419–28. doi: 10.1093/jamia/ocy068
- Shakibaei N, Hassannejad R, Mohammadifard N, Marateb HR, Mansourian M, Mañanas MA, et al. Pathways leading to prevention of fatal and non-fatal cardiovascular disease: An interaction model on 15 years population-based cohort study. *Lipids Health Dis.* (2020) 19:1–12. doi: 10.1186/s12944-020-01375-8
- Gherardini M, Mazomenos E, Mencias A, Stoyanov D. Catheter segmentation in X-ray fluoroscopy using synthetic data and transfer learning with light U-nets. *Comput Methods Prog Biomed.* (2020) 192:105420. doi: 10.1016/j.cmpb.2020.105420
- Shortreed SM, Laber E, Lizotte DJ, Stroup TS, Pineau J, Murphy SA. Informing sequential clinical decision-making through reinforcement learning: an empirical study. *Mach Learn.* (2011) 84:109–36. doi: 10.1007/s10994-010-5229-0
- You H, Bae E, Moon Y, Kweon J, Choi J. Automatic control of cardiac ablation catheter with deep reinforcement learning method. *J Mech Sci Technol.* (2019) 33:5415–23. doi: 10.1007/s12206-019-1036-0
- Goodfellow I, Bengio Y, Courville A, Bengio Y. *Deep Learning.* Cambridge, MA: MIT Press (2016).
- Martin-Isla C, Campello VM, Izquierdo C, Raisi-Estabragh Z, Baesler B, Petersen SE, et al. Image-based cardiac diagnosis with machine learning: a review. *Front Cardiovasc Med.* (2020) 7:1. doi: 10.3389/fcvm.2020.00001
- Topol EJ. High-performance medicine: the convergence of human and artificial intelligence. *Nat Med.* (2019) 25:44–56. doi: 10.1038/s41591-018-0300-7
- Narula S, Shameer K, Omar AMS, Dudley JT, Sengupta PP. Machine-learning algorithms to automate morphological and functional assessments in 2D echocardiography. *J Am Coll Cardiol.* (2016) 68:2287–95. doi: 10.1016/j.jacc.2016.08.062
- Chilamkurthy S, Ghosh R, Tanamala S, Biviji M, Campeau NG, Venugopal VK, et al. Deep learning algorithms for detection of critical findings in head CT scans: a retrospective study. *Lancet.* (2018) 392:2388–96. doi: 10.1016/S0140-6736(18)31645-3
- Krittanawong C, Johnson KW, Rosenson RS, Wang Z, Aydar M, Baber U, et al. Deep learning for cardiovascular medicine: a practical primer. *Eur Heart J.* (2019) 40:2058–73. doi: 10.1093/eurheartj/ehz056

39. Zir LM, Miller SW, Dinsmore RE, Gilbert JP, Harthorne JW. Interobserver variability in coronary angiography. *Circulation*. (1976) 53:627–32. doi: 10.1161/01.CIR.53.4.627
40. Leape LL, Park RE, Bashore TM, Harrison JK, Davidson CJ, Brook RH. Effect of variability in the interpretation of coronary angiograms on the appropriateness of use of coronary revascularization procedures. *Am Heart J*. (2000) 139:106–13. doi: 10.1016/S0002-8703(00)90316-8
41. Sirnes PA, Myreng Y, Mølstaad P, Golf S. Reproducibility of quantitative coronary analysis. *Int J Cardiac Imaging*. (1996) 12:197–203. doi: 10.1007/BF01806223
42. Zhang H, Mu L, Hu S, Nallamothu BK, Lansky AJ, Xu B, et al. Comparison of physician visual assessment with quantitative coronary angiography in assessment of stenosis severity in China. *JAMA Intern Med*. (2018) 178:239–47. doi: 10.1001/jamainternmed.2017.7821
43. Nallamothu BK, Spertus JA, Lansky AJ, Cohen DJ, Jones PG, Kureshi F, et al. Comparison of clinical interpretation with visual assessment and quantitative coronary angiography in patients undergoing percutaneous coronary intervention in contemporary practice: the Assessing Angiography (A2) project. *Circulation*. (2013) 127:1793–800. doi: 10.1161/CIRCULATIONAHA.113.001952
44. Hermiller JB, Cusma JT, Spero LA, Fortin DF, Harding MB, Bashore TM. Quantitative and qualitative coronary angiographic analysis: review of methods, utility, and limitations. *Catheter Cardiovasc Diagn*. (1992) 25:110–31. doi: 10.1002/ccd.1810250207
45. Keane D, Haase J, Slager CJ, Van Swijndregt EM, Lehmann KG, Ozaki Y, et al. Comparative validation of quantitative coronary angiography systems: results and implications from a multicenter study using a standardized approach. *Circulation*. (1995) 91:2174–83. doi: 10.1161/01.CIR.91.8.2174
46. Avram R, Olgin JE, Wan A, Ahmed Z, Verreault-Julien L, Abreau S, et al. CathAI: fully automated interpretation of coronary angiograms using neural networks. *arXiv preprint arXiv:2106.07708* (2021).
47. Du T, Xie L, Zhang H, Liu X, Wang X, Chen D, et al. Training and validation of a deep learning architecture for the automatic analysis of coronary angiography. *EuroIntervention*. (2021) 17:32–40. doi: 10.4244/EIJ-D-20-00570
48. Motwani M, Dey D, Berman DS, Germano G, Achenbach S, Al-Mallah MH, et al. Machine learning for prediction of all-cause mortality in patients with suspected coronary artery disease: a 5-year multicentre prospective registry analysis. *Eur Heart J*. (2017) 38:500–7. doi: 10.1093/eurheartj/ehw188
49. Mortazavi BJ, Downing NS, Bucholz EM, Dharmarajan K, Manhapra A, Li S-X, et al. Analysis of machine learning techniques for heart failure readmissions. *Circ Cardiovasc Qual Outcomes*. (2016) 9:629–40. doi: 10.1161/CIRCOUTCOMES.116.003039
50. Frizzell JD, Liang L, Schulte PJ, Yancy CW, Heidenreich PA, Hernandez AF, et al. Prediction of 30-day all-cause readmissions in patients hospitalized for heart failure: comparison of machine learning and other statistical approaches. *JAMA Cardiol*. (2017) 2:204–9. doi: 10.1001/jamacardio.2016.3956
51. Khera R, Haimovich J, Hurley N, McNamara R, Spertus JA, Desai N, et al. Machine-learning to improve prediction of mortality following acute myocardial infarction: an assessment in the NCDR-chest pain-myocardial infarction registry. *bioRxiv*. (2019) 540369. doi: 10.1101/540369
52. van Rosendaal AR, Maliakal G, Kolli KK, Beecy A, Al'Aref SJ, Dwivedi A, et al. Maximization of the usage of coronary CTA derived plaque information using a machine learning based algorithm to improve risk stratification; insights from the CONFIRM registry. *J Cardiovasc Comput Tomogr*. (2018) 12:204–9. doi: 10.1016/j.jcct.2018.04.011
53. Moghaddasi H, Nourian S. Automatic assessment of mitral regurgitation severity based on extensive textural features on 2D echocardiography videos. *Comput Biol Med*. (2016) 73:47–55. doi: 10.1016/j.compbiomed.2016.03.026
54. Lopes RR, van Mourik MS, Schaft EV, Ramos LA, Baan Jr J, Vendrik J, et al. Value of machine learning in predicting TAVI outcomes. *Netherlands Heart J*. (2019) 27:443–50. doi: 10.1007/s12471-019-1285-7
55. Buccheri S, Capodanno D, Barbanti M, Rubbio AP, Di Salvo ME, Scandura S, et al. A risk model for prediction of 1-year mortality in patients undergoing MitraClip implantation. *Am J Cardiol*. (2017) 119:1443–9. doi: 10.1016/j.amjcard.2017.01.024
56. Wang Z, Ma S, Zappitelli M, Parikh C, Wang C-Y, Devarajan P. Penalized count data regression with application to hospital stay after pediatric cardiac surgery. *Stat Methods Med Res*. (2016) 25:2685–703. doi: 10.1177/0962280214530608
57. Mehta SS, Shete DA, Lingayat NS, Chouhan VS. K-means algorithm for the detection and delineation of QRS-complexes in Electrocardiogram. *Irbm*. (2010) 31:48–54. doi: 10.1016/j.irbm.2009.10.001
58. Agarwal S, Jacobs DR, Vaidya D, Sibley CT, Jorgensen NW, Rotter JJ, et al. Metabolic syndrome derived from principal component analysis and incident cardiovascular events: the multi ethnic study of atherosclerosis (MESA) and health, aging, and body composition (Health ABC). *Cardiol Res Pract*. (2012) 2012:919425. doi: 10.1155/2012/919425
59. Quail MA, Segers P, Steeden JA, Muthurangu V. The aorta after coarctation repair—effects of calibre and curvature on arterial haemodynamics. *J Cardiovasc Magn Reson*. (2019) 21:1–9. doi: 10.1186/s12968-019-0534-7
60. Guner LA, Karabacak NI, Akdemir OU, Karagoz PS, Kocaman SA, Cengel A, et al. An open-source framework of neural networks for diagnosis of coronary artery disease from myocardial perfusion SPECT. *J Nucl Cardiol*. (2010) 17:405–13. doi: 10.1007/s12350-010-9207-5
61. Kwon J-m, Jeon K-H, Kim HM, Kim MJ, Lim S, Kim K-H, et al. Deep-learning-based risk stratification for mortality of patients with acute myocardial infarction. *PLoS ONE*. (2019) 14:e0224502. doi: 10.1371/journal.pone.0224502
62. Theriault-Lauzier P, Alsosaimi H, Mousavi N, Buithieu J, Spaziano M, Martucci G, et al. Recursive multiresolution convolutional neural networks for 3D aortic valve annulus planimetry. *Int J Comput Assist Radiol Surg*. (2020) 15:577–88. doi: 10.1007/s11548-020-02131-0
63. Madani A, Arnaout R, Mofrad N, Arnaout R. Fast and accurate view classification of echocardiograms using deep learning. *NPJ Digit Med*. (2018) 1:1–8. doi: 10.1038/s41746-017-0013-1
64. Cuocolo R, Perillo T, De Rosa E, Ugga L, Petretta M. Current applications of big data and machine learning in cardiology. *J Geriatr Cardiol*. (2019) 16:601. doi: 10.11909/j.issn.1671-5411.2019.08.002
65. Zhao Y, Xiong J, Hou Y, Zhu M, Lu Y, Xu Y, et al. Early detection of ST-segment elevated myocardial infarction by artificial intelligence with 12-lead electrocardiogram. *Int J Cardiol*. (2020) 317:223–30. doi: 10.1016/j.ijcard.2020.04.089
66. Pesaranhader A, Matwin S, Sokolova M, Pesaranhader A. DeepBioWSD: effective deep neural word sense disambiguation of biomedical text data. *J Am Med Informat Assoc*. (2019) 26:438–46. doi: 10.1093/jamia/ocy189
67. Pesaranhader A, Pesaranhader A, Matwin S, Sokolova M. *One Single Deep Bidirectional LSTM Network for Word Sense Disambiguation of Text Data*. Berlin: Springer (2018), 96–107.
68. Jiang X, de Souza EN, Pesaranhader A, Hu B, Silver DL, Matwin S. *TrajectoryNet: an embedded GPS trajectory representation for point-based classification using recurrent neural networks*. Armonk, NY: IBM Corp (2017). p. 192–200.
69. Pesaranhader A. *Concept Embedding for Deep Neural Functional Analysis of Genes and Deep Neural Word Sense Disambiguation of Biomedical Text*. Halifax, NS: Dalhousie University (2019).
70. Diller G-P, Kempny A, Babu-Narayan SV, Henrichs M, Brida M, Uebing A, et al. Machine learning algorithms estimating prognosis and guiding therapy in adult congenital heart disease: data from a single tertiary centre including 10 019 patients. *Eur Heart J*. (2019) 40:1069–77. doi: 10.1093/eurheartj/ehy915
71. Ballinger B, Hsieh J, Singh A, Sohoni N, Wang J, Tison GH, et al. DeepHeart: semi-supervised sequence learning for cardiovascular risk prediction. *arXiv preprint arXiv:1802.02511*. (2018).
72. Bahrami N, Retson T, Blansit K, Wang K, Hsiao A. Automated selection of myocardial inversion time with a convolutional neural network: spatial temporal ensemble myocardium inversion network (STEMI-NET). *Magn Reson Med*. (2019) 81:3283–91. doi: 10.1002/mrm.27680
73. Pesaranhader A, Pelletier J, Grenier J-C, Poujol R, Hussin J. Imputecovnet: 2d resnet autoencoder for imputation of sars-cov-2 sequences. *bioRxiv*. (2021). doi: 10.1101/2021.08.13.456305

74. Bello GA, Dawes TJW, Duan J, Biffi C, de Marvao A, Howard LSGE, et al. Deep-learning cardiac motion analysis for human survival prediction. *Nat Mach Intell.* (2019) 1:95–104. doi: 10.1038/s42256-019-0019-2
75. Yang S, Kweon J, Roh J-H, Lee J-H, Kang H, Park L-J, et al. Deep learning segmentation of major vessels in X-ray coronary angiography. *Sci Rep.* (2019) 9:16897. doi: 10.1038/s41598-019-53254-7
76. Lao Q, Havaei M, Pesaranghader A, Dutil F, Jorio LD, Fevens T. Dual Adversarial Inference for Text-to-Image Synthesis. In: *Proceedings of the IEEE/CVF International Conference on Computer Vision.* Seoul (2019). p. 7567–76.
77. Pesaranghader A, Wang Y, Havaei M. CT-SGAN: Computed tomography synthesis GAN. In: *Deep Generative Models, and Data Augmentation, Labelling, and Imperfections.* Strasbourg: Springer (2021). p. 67–9.
78. Wolterink JM, Leiner T, Viergever MA, Išgum I. Generative adversarial networks for noise reduction in low-dose CT. *IEEE Trans Med Imaging.* (2017) 36:2536–45. doi: 10.1109/TMI.2017.2708987
79. Zhu F, Ye F, Fu Y, Liu Q, Shen B. Electrocardiogram generation with a bidirectional LSTM-CNN generative adversarial network. *Sci Rep.* (2019) 9:6734. doi: 10.1038/s41598-019-42516-z
80. Tabaza L, Virk H.U.H, Janzer S, George JC. Robotic-assisted percutaneous coronary intervention in a COVID-19 patient. *Cathet Cardiovasc Intervent.* (2021) 97:E343–5. doi: 10.1002/ccd.28982
81. Virk HUH, Lakhter V, Tabaza L, George JC. Do we need robotics for coronary intervention more than ever in the COVID-19 era? *Catheter Cardiovasc Intervent.* 96:E563–4. doi: 10.1002/ccd.28949
82. Sevakula RK, Au-Yeung W-TM, Singh JP, Heist EK, Isselbacher EM, Armoundas AA. State-of-the-art machine learning techniques aiming to improve patient outcomes pertaining to the cardiovascular system. *J Am Heart Assoc.* (2020) 9:e013924. doi: 10.1161/JAHA.119.013924
83. Bizopoulos P, Koutsouris D. Deep learning in cardiology. *IEEE Rev Biomed Eng.* (2018) 12:168–93. doi: 10.1109/RBME.2018.2885714
84. Siegersma K, Leiner T, Chew D, Appelman Y, Hofstra L, Verjans J. Artificial intelligence in cardiovascular imaging: state of the art and implications for the imaging cardiologist. *Netherlands Heart J.* (2019) 27:403–13. doi: 10.1007/s12471-019-01311-1
85. Ribeiro JM, Astudillo P, de Backer O, Budde R, Nuis RJ, Goudzwaard J, et al. Artificial intelligence and transcatheter interventions for structural heart disease: a glance at the (near) future. *Trends Cardiovasc Med.* (2021) S1050-1738 (21) 00017-7. doi: 10.1016/j.tcm.2021.02.002
86. Quer G, Arnaout R, Henne M, Arnaout R. Machine learning and the future of cardiovascular care: JACC state-of-the-art review. *J Am Coll Cardiol.* (2021) 77:300–13. doi: 10.1016/j.jacc.2020.11.030
87. Quinlan JR. Induction of decision trees. *Mach Learn.* (1986) 1:81–106. doi: 10.1007/BF00116251
88. Friedman J, Hastie T, Tibshirani R. Additive logistic regression: a statistical view of boosting (with discussion and a rejoinder by the authors). *Ann Stat.* (2000) 28:337–407. doi: 10.1214/aos/1016218223
89. Chen T, Guestrin C. Xgboost: A Scalable Tree Boosting System. *Proceedings of the 22nd ACM SIGKDD International Conference on Knowledge Discovery and Data Mining.* (2016). p. 785–94. doi: 10.1145/2939672.2939785
90. Antman EM, Cohen M, Bernink PJLM, McCabe CH, Horacek T, Papuchis G, et al. The TIMI risk score for unstable angina/non-ST elevation MI: a method for prognostication and therapeutic decision making. *JAMA.* (2000) 284:835–42. doi: 10.1001/jama.284.7.835
91. Tang EW, Wong C-K, Herbison P. Global Registry of Acute Coronary Events (GRACE) hospital discharge risk score accurately predicts long-term mortality post acute coronary syndrome. *Am Heart J.* (2007) 153:29–35. doi: 10.1016/j.ahj.2006.10.004
92. Eagle KA, Lim MJ, Dabbous OH, Pieper KS, Goldberg RJ, Van de Werf F, et al. A validated prediction model for all forms of acute coronary syndrome: estimating the risk of 6-month postdischarge death in an international registry. *JAMA.* (2004) 291:2727–33. doi: 10.1001/jama.291.22.2727
93. Avram R, Olgin JE, Tison GH. The rise of open-sourced machine learning in small and imbalanced datasets: predicting in-stent restenosis. *Can J Cardiol.* (2020) 36:1574–6. doi: 10.1016/j.cjca.2020.02.002
94. Sampedro-Gómez J, Dorado-Díaz PI, Víctor Vicente-Palacios E, Antonio Sánchez-Puente P, Jiménez-Navarro M, San Roman JA, et al. Machine learning to predict stent restenosis based on daily demographic, clinical and angiographic characteristics. *Can J Cardiol.* (2020) 36:1624–32. doi: 10.1016/j.cjca.2020.01.027
95. Cortes C, Vapnik V. Support-vector networks. *Mach Learn.* (1995) 20:273–97. doi: 10.1007/BF00994018
96. Hoerl AE, Kennard RW. Ridge regression: biased estimation for nonorthogonal problems. *Technometrics.* (1970) 12:55–67. doi: 10.1080/00401706.1970.10488634
97. Tibshirani R. Regression shrinkage and selection via the lasso. *J R Stat Soc Ser B (Methodological).* (1996) 58:267–88. doi: 10.1111/j.2517-6161.1996.tb02080.x
98. Kanungo T, Mount DM, Netanyahu NS, Piatko CD, Silverman R, Wu AY. An efficient k-means clustering algorithm: analysis and implementation. *IEEE Trans Pattern Anal Mach Intell.* (2002) 24:881–92. doi: 10.1109/TPAMI.2002.1017616
99. Wold S, Esbensen K, Geladi P. Principal component analysis. *Chemometr Intell Lab Syst.* (1987) 2:37–52. doi: 10.1016/0169-7439(87)80084-9
100. Coenen A, Lubbers MM, Kurata A, Kono A, Dedic A, Chelu RG, et al. Fractional flow reserve computed from noninvasive CT angiography data: diagnostic performance of an on-site clinician-operated computational fluid dynamics algorithm. *Radiology.* (2015) 274:674–83. doi: 10.1148/radiol.14140992
101. Koo B-K, Erglis A, Doh J-H, Daniels DV, Jegere S, Kim H-S, et al. Diagnosis of ischemia-causing coronary stenoses by noninvasive fractional flow reserve computed from coronary computed tomographic angiograms: results from the prospective multicenter DISCOVER-FLOW (Diagnosis of Ischemia-Causing Stenoses Obtained Via Noninvasive Fractional Flow Reserve) study. *J Am Coll Cardiol.* (2011) 58:1989–97. doi: 10.1016/j.jacc.2011.06.066
102. Myers PD, Scirica BM, Stultz CM. Machine learning improves risk stratification after acute coronary syndrome. *Sci Rep.* (2017) 7:1–12. doi: 10.1038/s41598-017-12951-x
103. Zhang J, Gajjala S, Agrawal P, Tison GH, Hallock LA, Beussink-Nelson L, et al. Fully automated echocardiogram interpretation in clinical practice: feasibility and diagnostic accuracy. *Circulation.* (2018) 138:1623–35. doi: 10.1161/CIRCULATIONAHA.118.034338
104. Avram R, Olgin JE, Kuhar P, Hughes JW, Marcus GM, Pletcher MJ, et al. A digital biomarker of diabetes from smartphone-based vascular signals. *Nat Med.* (2020) 26:1576–82. doi: 10.1038/s41591-020-1010-5
105. Franco A, Javidi S, Ruehm SG. Delayed myocardial enhancement in cardiac magnetic resonance imaging. *J Radiol Case Rep.* (2015) 9:6. doi: 10.3941/jrcr.v9i6.2328
106. Ibanez B, James S, Agewall S, Antunes MJ, Bucciarelli-Ducci C, Bueno H, et al. 2017 ESC Guidelines for the management of acute myocardial infarction in patients presenting with ST-segment elevation: the task force for the management of acute myocardial infarction in patients presenting with ST-segment elevation of the European Society of Cardiology (ESC). *Eur Heart J.* (2018) 39:119–77. doi: 10.1093/eurheartj/ehx393
107. Ronneberger O, Fischer P, Brox T. U-net: Convolutional Networks for Biomedical Image Segmentation. Berlin: Springer (2015). p. 234–41.
108. Cho H, Lee JG, Kang SJ, Kim WJ, Choi SY, Ko J, et al. Angiography-based machine learning for predicting fractional flow reserve in intermediate coronary artery lesions. *J Am Heart Assoc.* (2019) 8:e011685. doi: 10.1161/JAHA.118.011685
109. Mahmud E, Naghi J, Ang L, Harrison J, Behnamfar O, Pourdjabbar A, et al. Demonstration of the safety and feasibility of robotically assisted percutaneous coronary intervention in complex coronary lesions: results of the CORA-PCI study (Complex Robotically Assisted Percutaneous Coronary Intervention). *JACC Cardiovasc Interv.* (2017) 10:1320–7. doi: 10.1016/j.jcin.2017.03.050

110. Kingma DP, Welling M. Auto-encoding variational bayes. *arXiv:1312.6114 [cs, stat]*. (2014).
111. Goodfellow I, Pouget-Abadie J, Mirza M, Xu B, Warde-Farley D, Ozair S, et al. Generative Adversarial Nets. In: Ghahramani Z, Welling M, Cortes C, Lawrence ND, Weinberger KQ, editors. *Advances in Neural Information Processing Systems*. Red Hook, NY: Curran Associates, Inc. (2014). p. 2672–80.
112. Kang E, Koo HJ, Yang DH, Seo JB, Ye JC. Cycle-consistent adversarial denoising network for multiphase coronary CT angiography. *Med Phys*. (2019) 46:550–62. doi: 10.1002/mp.13284
113. Turpin R, Hoefer E, Lewelling J, Baird P. *AAMI and BSI Machine Learning AI in Medical Devices (PDF)*. Arlington, VA: AAMI and BSI (2020).
114. Gebru T, Morgenstern J, Vecchione B, Vaughan JW, Wallach H, Daumé III H, et al. Datasheets for datasets. *arXiv preprint arXiv:1803.09010*. (2018).
115. Motamedi M, Sakharlykh N, Kaldewey T. A data-centric approach for training deep neural networks with less data. *arXiv*. (2021).
116. Proposed Regulatory Framework for Modifications to Artificial Intelligence/Machine Learning (AI/ML)-Based Software as a Medical Device (SaMD)—Discussion Paper and Request for Feedback. (2019). Available online at: <https://www.regulations.gov/document/FDA-2019-N-1185-0001>
117. Artificial Intelligence and Machine Learning in Software as a Medical Device. (2021). Available online at: <https://www.fda.gov/medical-devices/software-medical-device-samd/artificial-intelligence-and-machine-learning-software-medical-device> (accessed November 19, 2021).
118. Fenech ME, Bustin O. AI in cardiac imaging: A UK-based perspective on addressing the ethical, social, and political challenges. *Front Cardiovasc Med*. (2020) 7:54. doi: 10.3389/fcvm.2020.00054
119. Hamet P, Tremblay J. Artificial intelligence in medicine. *Metabolism*. (2017) 69:S36–40. doi: 10.1016/j.metabol.2017.01.011
120. Larson DB, Harvey H, Rubin DL, Irani N, Justin RT, Langlotz CP. Regulatory frameworks for development and evaluation of artificial intelligence-based diagnostic imaging algorithms: summary and recommendations. *J Am Coll Radiol*. (2021) 18:413–24. doi: 10.1016/j.jacr.2020.09.060
121. Sengupta PP, Shrestha S, Berthon B, Messas E, Donal E, Tison GH, et al. Proposed requirements for cardiovascular imaging-related machine learning evaluation (PRIME): a checklist: reviewed by the American College of Cardiology Healthcare Innovation Council. *Cardiovasc Imaging*. (2020) 13:2017–35. doi: 10.1016/j.jcmg.2020.07.015
122. Rivera SC, Liu X, Chan A-W, Denniston AK, Calvert MJ. Guidelines for clinical trial protocols for interventions involving artificial intelligence: the SPIRIT-AI extension. *BMJ*. (2020) 370:m3210. doi: 10.1136/bmj.m3210
123. Liu X, Rivera SC, Moher D, Calvert MJ, Denniston AK. Reporting guidelines for clinical trial reports for interventions involving artificial intelligence: the CONSORT-AI extension. *BMJ*. (2020) 370:m3164. doi: 10.1136/bmj.m3164
124. Hemingway H, Asselbergs FW, Danesh J, Dobson R, Maniadas N, Maggioni A, et al. FBO Big data from electronic health records for early and late translational cardiovascular research: challenges and potential. *Eur Heart J*. (2018) 39:1481–95. doi: 10.1093/eurheartj/ehx487
125. Sun J, McNaughton CD, Zhang P, Perer A, Gkoulalas-Divanis A, Denny JC, et al. Predicting changes in hypertension control using electronic health records from a chronic disease management program. *J Am Med Inform Assoc*. (2014) 21:337–44. doi: 10.1136/amiajnl-2013-002033
126. Gillies RJ, Kinahan PE, Hricak H. Radiomics: images are more than pictures, they are data. *Radiology*. (2016) 278:563–77. doi: 10.1148/radiol.2015151169
127. Pesaraghader A, Matwin S, Sokolova M, Beiko RG. simDEF: definition-based semantic similarity measure of gene ontology terms for functional similarity analysis of genes. *Bioinformatics*. (2016) 32:1380–7. doi: 10.1093/bioinformatics/btv755
128. Heitner JF, Kim RJ, Kim HW, Klem I, Shah DJ, Debs D, et al. Prognostic value of vasodilator stress cardiac magnetic resonance imaging: a multicenter study with 48 000 patient-years of follow-up. *JAMA Cardiol*. (2019) 4:256. doi: 10.1001/jamacardio.2019.0035
129. D'Amour A, Heller K, Moldovan D, Adlam B, Alipanahi B, Beutel A, et al. Underspecification presents challenges for credibility in modern machine learning. *arXiv preprint arXiv:2011.03395*. (2020).
130. Collins GS, Reitsma JB, Altman DG, Moons KG. Transparent reporting of a multivariable prediction model for individual prognosis or diagnosis (TRIPOD): the TRIPOD statement. *J Br Surg*. (2015) 102:148–58. doi: 10.1002/bjs.9736
131. Israni ST, Verghese A. Humanizing artificial intelligence. *JAMA*. (2019) 321:29. doi: 10.1001/jama.2018.19398
132. Lorenz EN. Deterministic nonperiodic flow. *J Atmos Sci*. (1963) 20:130–41.
133. Goldstein BA, Navar AM, Carter RE. Moving beyond regression techniques in cardiovascular risk prediction: applying machine learning to address analytic challenges. *Eur Heart J*. (2017) 38:1805–14. doi: 10.1093/eurheartj/ehw302
134. Luo W, Phung D, Tran T, Gupta S, Rana S, Karmakar C, et al. Guidelines for developing and reporting machine learning predictive models in biomedical research: a multidisciplinary view. *J Med Internet Res*. (2016) 18:e323. doi: 10.2196/jmir.5870
135. Petsiuk V, Das A, Saenko K. Rise: randomized input sampling for explanation of black-box models. *arXiv preprint arXiv:1806.07421*. (2018).
136. Gilpin LH, Bau D, Yuan BZ, Bajwa A, Specter M, Kagal L. Explaining explanations: an overview of interpretability of machine learning. In: IEEE. Turin (2018), p. 80–9.
137. Levin O, Meng Z, Singh V, Zhu X. Fooling computer vision into inferring the wrong body mass index. *arXiv preprint arXiv:1905.06916*. (2019).
138. Ribeiro MT, Singh S, Guestrin C. Model-agnostic interpretability of machine learning. *arXiv preprint arXiv:1606.05386*. (2016).
139. Marblestone AH, Wayne G, Kording KP. Toward an integration of deep learning and neuroscience. *Front Comput Neurosci*. (2016) 10:94. doi: 10.3389/fncom.2016.00094
140. Mueller ST, Hoffman RR, Clancey WJ, Emery AK, Klein G. *Explanation in Human-AI Systems: A Literature Meta-Review Synopsis of Key Ideas and Publications and Bibliography for Explainable AI*. Pensacola, FL: Florida Institute for Human and Machine Cognition Pensacola United States (2019).
141. Wells BJ, Chagin KM, Nowacki AS, Kattan MW. Strategies for handling missing data in electronic health record derived data. *Egms*. (2013) 1:1035. doi: 10.13063/2327-9214.1035
142. Jakobsen JC, Gluud C, Wetterslev J, Winkel P. When and how should multiple imputation be used for handling missing data in randomised clinical trials—a practical guide with flowcharts. *BMC Med Res Methodol*. (2017) 17:1–10. doi: 10.1186/s12874-017-0442-1
143. Dong Y, Peng C-YJ. Principled missing data methods for researchers. *Springerplus*. (2013) 2:222. doi: 10.1186/2193-1801-2-222
144. White IR, Royston P, Wood AM. Multiple imputation using chained equations: issues and guidance for practice. *Stat Med*. (2011) 30:377–99. doi: 10.1002/sim.4067
145. Audigier V, Husson F, Josse J. A principal component method to impute missing values for mixed data. *Adv Data Anal Classif*. (2016) 10:5–26. doi: 10.1007/s11634-014-0195-1
146. Beaulieu-Jones BK, Moore JH, CONSORTIUM PRO-AACT. Missing data imputation in the electronic health record using deeply learned autoencoders. In: *Pacific Symposium on Biocomputing*. Puako, HI: World Scientific (2017). p. 207–18.
147. Gondara L, Wang K. Mida: multiple imputation using denoising autoencoders. In: *Pacific-Asia Conference on Knowledge Discovery and Data Mining*. Melbourne, VIC: Springer (2018). p. 260–72.
148. Daemen J, Kretov E, O'Hair D, Parma R, Salvatore DR and Taramasso M. *Machine Learning, Artificial Intelligence, E-health: Application for Percutaneous Intervention*. European Association of Percutaneous Cardiovascular Interventions. (2019). Available online at: <https://www.pcronline.com/Cases-resources-images/Resources/Course-videos-slides/2019/Machine-learning-artificial-intelligence-e-health-application-for-percutaneous-intervention> (accessed November 19, 2021).
149. Voigt P, Von dem Bussche A. *The eu General Data Protection Regulation (gdpr) A Practical Guide*. 1st ed. Cham: Springer International Publishing (2017).

150. NHS data breach affects 150,000 patients in England. *BBC News* (2018).

**Conflict of Interest:** RA owns NVIDIA, a company making graphic cards for artificial intelligence analyses, stocks. RA received speaker fees from Novartis Inc. and has a patent pending (R31-07141: METHOD AND SYSTEM FOR ASSESSMENT OF VENTRICULAR EJECTION FRACTION). JH received speaker honoraria from District 3 Innovation Centre and DalCor Pharmaceuticals.

The remaining authors declare that the research was conducted in the absence of any commercial or financial relationships that could be construed as a potential conflict of interest.

**Publisher's Note:** All claims expressed in this article are solely those of the authors and do not necessarily represent those of their affiliated organizations, or those of the publisher, the editors and the reviewers. Any product that may be evaluated in this article, or claim that may be made by its manufacturer, is not guaranteed or endorsed by the publisher.

*Copyright © 2021 Ben Ali, Pesaranghader, Avram, Overtchouk, Perrin, Laffite, Cartier, Ibrahim, Modine and Hussin. This is an open-access article distributed under the terms of the Creative Commons Attribution License (CC BY). The use, distribution or reproduction in other forums is permitted, provided the original author(s) and the copyright owner(s) are credited and that the original publication in this journal is cited, in accordance with accepted academic practice. No use, distribution or reproduction is permitted which does not comply with these terms.*



# Artificial Intelligence in Cardiac MRI: Is Clinical Adoption Forthcoming?

Anastasia Fotaki<sup>1,2\*</sup>, Esther Puyol-Antón<sup>1</sup>, Amedeo Chiribiri<sup>1,2</sup>, René Botnar<sup>1,3</sup>,  
Kuberan Pushparajah<sup>1,2†</sup> and Claudia Prieto<sup>1,3†</sup>

<sup>1</sup> Department of Biomedical Engineering, School of Biomedical Engineering and Imaging Sciences, King's College London, London, United Kingdom, <sup>2</sup> Guy's and St. Thomas' NHS Foundation Trust, London, United Kingdom, <sup>3</sup> Escuela de Ingeniería, Pontificia Universidad Católica de Chile, Santiago, Chile

## OPEN ACCESS

### Edited by:

Sebastian Kelle,  
Deutsches Herzzentrum  
Berlin, Germany

### Reviewed by:

Mona Bhatia,  
Fortis Escorts Heart Institute, India  
Ali Yilmaz,  
University Hospital Münster, Germany

### \*Correspondence:

Anastasia Fotaki  
anastasia.fotaki@kcl.ac.uk

<sup>†</sup>These authors have contributed  
equally to this work and share senior  
authorship

### Specialty section:

This article was submitted to  
Cardiovascular Imaging,  
a section of the journal  
Frontiers in Cardiovascular Medicine

**Received:** 19 November 2021

**Accepted:** 15 December 2021

**Published:** 10 January 2022

### Citation:

Fotaki A, Puyol-Antón E, Chiribiri A,  
Botnar R, Pushparajah K and Prieto C  
(2022) Artificial Intelligence in Cardiac  
MRI: Is Clinical Adoption  
Forthcoming?  
Front. Cardiovasc. Med. 8:818765.  
doi: 10.3389/fcvm.2021.818765

Artificial intelligence (AI) refers to the area of knowledge that develops computerised models to perform tasks that typically require human intelligence. These algorithms are programmed to learn and identify patterns from “training data,” that can be subsequently applied to new datasets, without being explicitly programmed to do so. AI is revolutionising the field of medical imaging and in particular of Cardiovascular Magnetic Resonance (CMR) by providing deep learning solutions for image acquisition, reconstruction and analysis, ultimately supporting the clinical decision making. Numerous methods have been developed over recent years to enhance and expedite CMR data acquisition, image reconstruction, post-processing and analysis; along with the development of promising AI-based biomarkers for a wide spectrum of cardiac conditions. The exponential rise in the availability and complexity of CMR data has fostered the development of different AI models. Integration in clinical routine in a meaningful way remains a challenge. Currently, innovations in this field are still mostly presented in proof-of-concept studies with emphasis on the engineering solutions; often recruiting small patient cohorts or relying on standardised databases such as Multi-ethnic Study on atherosclerosis (MESA), UK Biobank and others. The wider incorporation of clinically valid endpoints such as symptoms, survival, need and response to treatment remains to be seen. This review briefly summarises the current principles of AI employed in CMR and explores the relevant prospective observational studies in cardiology patient cohorts. It provides an overview of clinical studies employing undersampled reconstruction techniques to speed up the scan encompassing cine imaging, whole-heart imaging, multi-parametric mapping and magnetic resonance fingerprinting along with the clinical utility of AI applications in image post-processing, and analysis. Specific focus is given to studies that have incorporated CMR-derived prediction models for prognostication in cardiac disease. It also discusses current limitations and proposes potential developments to enable multi-disciplinary collaboration for improved evidence-based medicine. AI is an extremely promising field and the timely integration of clinician's input in the ingenious technical investigator's paradigm holds promise for a bright future in the medical field.

**Keywords:** cardiac MRI, artificial intelligence, clinical integration, neural network, machine learning

## INTRODUCTION

### Artificial Intelligence

(AI) is an academic discipline founded in the early 1950's and is considered as any method that allows computers to accomplish functions, that require human intelligence. AI introduces speed in performing tedious and time-consuming tasks, precision in tasks requiring analysis and can draw sophisticated interconnections/ deep interpretation of digital data. It is already widely adopted in various scientific fields including space craftsmanship, navigation, meteorology and every-day tasks including social media, banking, digital voice assistants (1–3). The clinical uptake of the advances made by computer scientists and engineers has been progressive but slow.

Cardiovascular Magnetic Resonance imaging (CMR) is already an established tool for routine clinical decision-making including diagnosis, follow-up, pre-procedural planning and real-time procedures. It is ideally suited for various AI techniques due to the digitalisation of the MRI signal and the diversity in the contrast and parametric information that can be obtained from the images.

This review article explores the basic AI concepts that are currently adopted in CMR along with relevant clinical applications. We have only included studies that are prospectively designed and applied. The aim is to familiarise clinicians with the basics in AI, demonstrate the feasibility of relevant applications and discuss current shortcomings that could be addressed in future work.

### AI Basics

Machine learning (ML) is a subcategory of AI that teaches computers to do what humans and animals naturally do: learn from experience. ML uses algorithms to find patterns and make extrapolations from large amounts of data. The algorithms adaptively enhance their performance as the amount of datasets for learning expands. In the workflow of ML, feature extraction is the first step, and this is followed by the development of the model. The accuracy of the ML model is highly dependent on the features extracted.

ML is further divided into supervised learning, unsupervised learning and reinforcement learning. The differentiation lies on the extent and type of supervision that is provided to the algorithms during training. Supervised learning uses datasets, annotated by a knowledgeable supervisor, to create models that predict or categorise future events or identify the most appropriate patterns to the outcome (4). The progress of the predictive model is dependent on the diversity of the data used in training along with the underlying algorithm. In unsupervised learning the computer programme is able

to identify hidden structures in collections of databases, without previous labelling. The software can potentially determine novel relationships and clusters inside the data. Reinforcement learning constitutes a computational path to learn through interactions with the environment. It is a reward-based learning model, where positive and negative feedback contribute to the creation of effective predictive models (see **Figure 1** for a schematic approach to the different types of ML categories).

Deep learning (DL) is a subset of ML that applies neural networks with hidden layers to correlate between the given input and the correct output, so that feature extraction and model development are performed simultaneously. DL algorithms are inspired from the network and the connections of the biological neurons in the brain that enable cognitive tasks. The nodes in a neural network mimic the neuronal function, i.e., they receive input signals, that can be excitatory or inhibitory, causing them to fire or withhold an output respectively. In mathematical terms, a neuron in the AI field is a placeholder for a numerical expression, which creates an output by applying the function on the given inputs. The data are progressively processed and fine-tuned through this hierarchy to extract high level features from simplified data. The predictive properties of the algorithm are learnt through a sequence of iterations.

Convolutional neural network (CNN) is a popular subgroup of DL networks, widely applied in CMR, as it is designed to work with imaging data (**Figure 2**). Several characteristics have made this technique more adaptive compared to conventional ML methods. While in ML methods the learned weights are manually engineered, after sufficient training, CNN can extract features automatically (i.e., learn filters), enabling the enhanced feature extraction to be a section of the classification learning process. CNN learns multiple features in parallel for a given input. Therefore, the data-mining needed in a CNN is lower, in contrast to other algorithms and it requires minimal human intervention (5). The architecture of CNN consists of three layers: (1) convolutional (feature extraction), (2) pooling (reduction in the number of input variables), and (3) fully-connected layer (connects neurons between layers). The convolutional layer, being the first layer, applies the mathematical operation of convolution, that is several filters to the input variable in order to recognise a large number of relevant features. The pooling layer minimises the size of the convolved feature map, thereby reducing the overall computational demands and costs of the network. The fully-connected layer connects the neurons between different layers. Based on the type of the data and the required accuracy, the network is optimised by iterating the convolution-pooling series numerous times. In any DL method, evaluating the loss function is a significant process, in order to warrant that the algorithm will model the data in the expected way. From a simplified viewpoint, the loss function can be formulated as a function which determines the relation between two variables, namely the deviation of the predicted output from the ground truth output. The training of the convolutional neural networks comprises multiple iterations (known as epochs), which compare the performance of the training set against the

**Abbreviations:** AI, Artificial Intelligence; CHD, Congenital Heart Disease; CMR, Cardiovascular Magnetic Resonance; CNN, Convolutional Neural Network; DL, Deep-learning; HCM, Hypertrophic Cardiomyopathy; LGE, Late-gadolinium enhancement; LV, Left ventricle; ML, Machine-learning; MRI, Magnetic Resonance Imaging; RV, Right ventricle; TA, Texture analysis; TRIPOD, Transparent Reporting of a multivariable prediction model for Individual Prognosis Or Diagnosis; 3D, Three-dimensional; 4D, Four-dimensional.

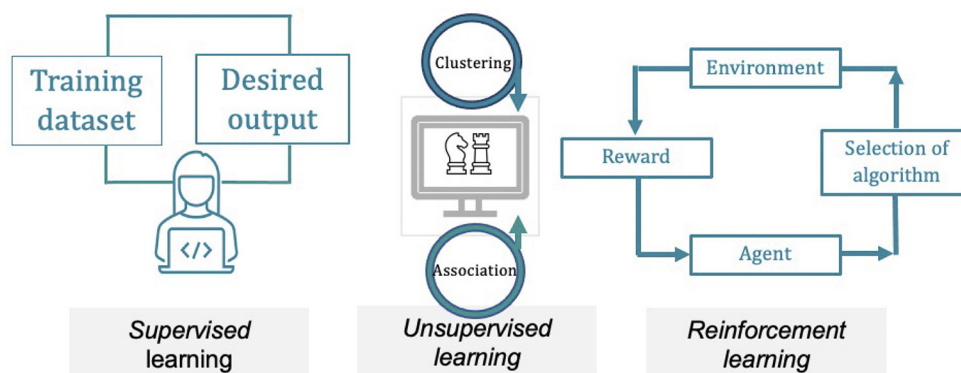


**FIGURE 1 |** Simplified graph describing the three principal machine-learning methods. Supervised learning utilises hand-labelled datasets to design algorithms that predict future events, classify data into defined categories or distinguish the most relevant variables to the output. The predictive model learns through data training and improves over time. In unsupervised learning the software accomplishes the processing of raw data, finding hidden structures in datasets, without prior annotation, identifying meaningful relationships and clusters within the data. Reinforcement learning is a reward-based learning. Its foundation lies in the interactions with an environment, in which positive and negative feedback (reinforcements) contribute to the optimisation of the model.

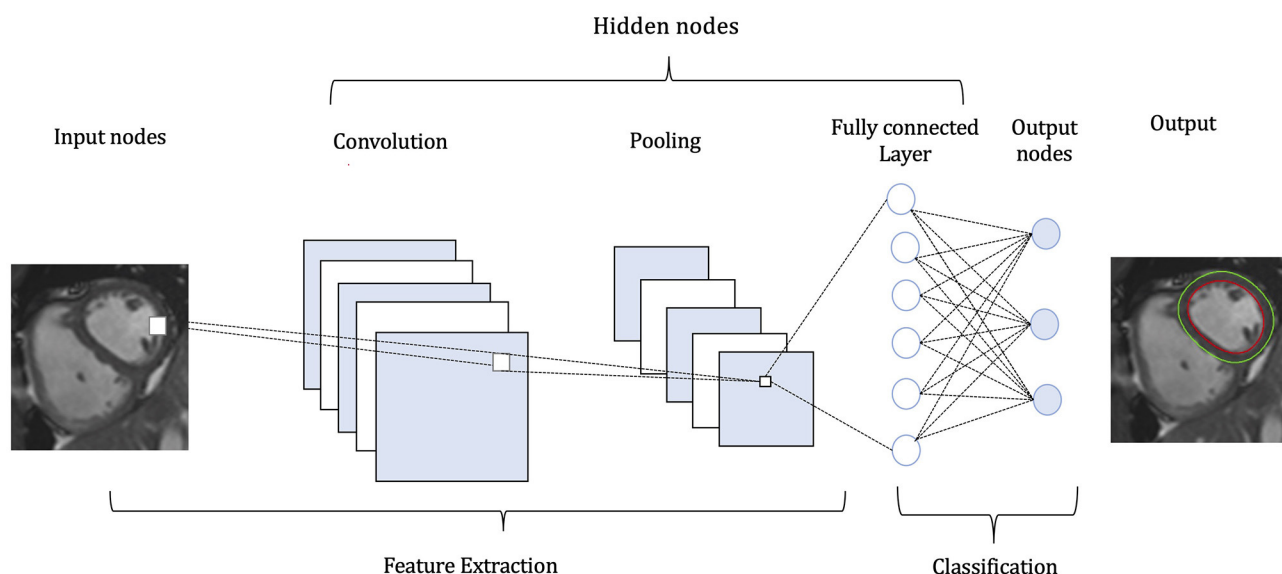


**FIGURE 2 |** Pipeline of a convolutional neural network (CNN). A CMR image functions as input to the CNN. The CNN identifies and classifies the various attributes (features) of the image for analysis in a procedure named Feature Extraction, including a stack of convolutions and pooling operations. In the convolution operation different-level features, such as edges, colour, gradient orientation are extracted from the input image. The pooling layer reduces the dimensionality of the convolved features, in order to decrease the computational requirements. The nodes in the fully-connected layer are connected directly to all nodes in the previous layer. This layer compiles the data extracted by previous layers and applies various filters to form the final output.

validation one, diminishing the loss function. One epoch means that a new input sample from the training dataset will be assigned to the network, thus the weights of each convolutional layer will be optimised (6). Learning curves, which depict loss vs. epochs and accuracy vs. epochs, are utilised to optimally train the network.

## Present Clinical Motivation

CMR offers comprehensive assessment of cardiovascular disease and is a rapidly expanding imaging modality. A recent study showed a 10-year increase of 573% in the number of scans

performed in UK (7). This rise comes with an exponential increase in the resources required to support this, including availability and time of experts for image acquisition, post-processing and reporting, along with scan-time cost. Novel developments in CMR, including high resolution, contrast-free coronary artery and congenital heart disease (CHD) imaging, quantitative multi-parametric and perfusion MRI and MRI-derived biomarkers necessitate a cost-effective and time-efficient strategy for their successful integration in clinical routine (8). AI can have a significant role in this, in view of its potential to accelerate MRI scanning, image post-processing and

reporting, introduce novel biomarkers and incorporate those in decision-making and prognostication models. Acceleration in image acquisition can have additional benefits for patients with claustrophobia, anxiety and inability to follow breath-holding commands.

Furthermore, recent data illustrate disparities with regards to the access to CMR services around the globe. Scan and post-processing acceleration along with automated analysis through AI can facilitate wider availability of sustainable, faster and cheaper CMR, resulting in improvement in patient care in less privileged areas (9).

## Clinical Applications

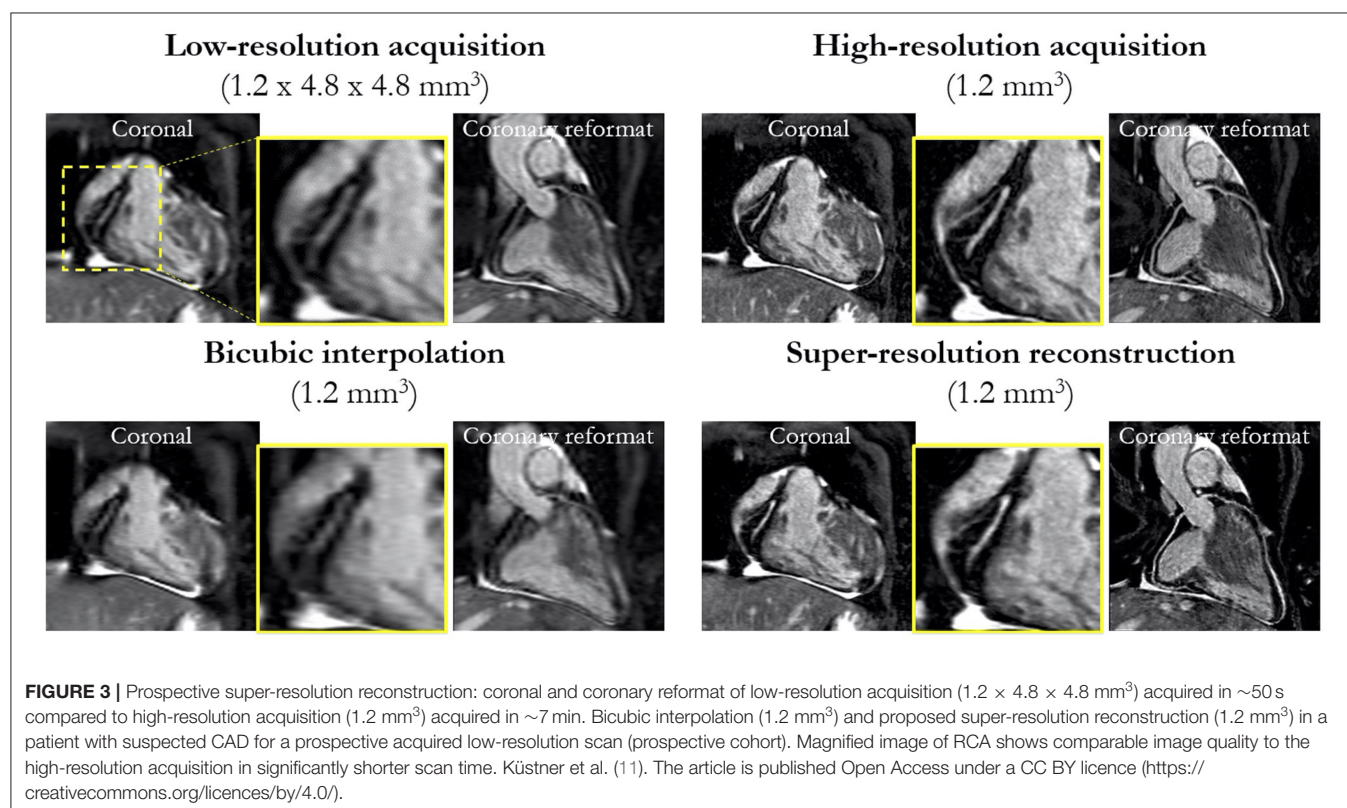
ML algorithms have been optimised and introduced in all aspects of the imaging workflow and implemented prospectively in diverse patient cohorts (10). Extensive applications have been investigated in undersampled image-acquisition, automated analysis and post-processing and development of predictive models.

## Time-Efficiency

### Acquisition and Reconstruction

AI applications in CMR have contributed significantly to the acceleration of image acquisition and analysis. Neural networks have been applied to reconstruct data from rapidly acquired undersampled MRI images across different sequences. A deep-learning based, super-resolution CMR Angiography framework has enabled reconstruction of low resolution  $1.2 \times 4.8$

$\times 4.8 \text{ mm}^3$  data acquired in 50 s scan time (11). The proposed method showed similar quantitative and perceivable image quality of the high resolution  $1.2 \text{ mm}^3$  images, achieving 16 x acceleration in acquisition time (**Figure 3**). Similar results have been attained with a Multi-Scale Variational Neural Network undersampled reconstruction (12), achieving 9x acceleration, in CMR Angiography  $1.2 \text{ mm}^3$  acquisition outperforming compressed sensing (CS) reconstruction. Steeden et al. (13) has successfully employed a subset of convolutional neural network, specifically the 3D residual U-net to perform super-resolution reconstruction on low-resolution three-dimensional whole heart balanced Steady State Free Precession (bSSFP) datasets, achieving similar diagnostic confidence and accuracy with high-resolution whole heart bSSFP in patients with CHD, **Figure 4**. Besides acquisition speed, AI has the potential to reduce breath-holds. Kuestner et al. (14) has introduced 9–15x acceleration in 3D cine images in a single 10–15 s breath hold utilising a DL-based approach. For a more detailed technical review of these methods, we refer the reader to a recent review by Alzubaidi et al. (15). Zhang et al. (16) developed an AI-based virtual native enhancement (VNE) imaging technology, using streams of CNN to employ and optimise the acquired signal from native T1 mapping and cine imaging sequences, depicting them as LGE-analogous images. This technology allows for contrast-free and efficient tissue characterisation, achieving high agreement in the quantification of tissue burden and superior image quality compared to the late gadolinium enhancement (LGE) images (see **Figure 5**) (16).



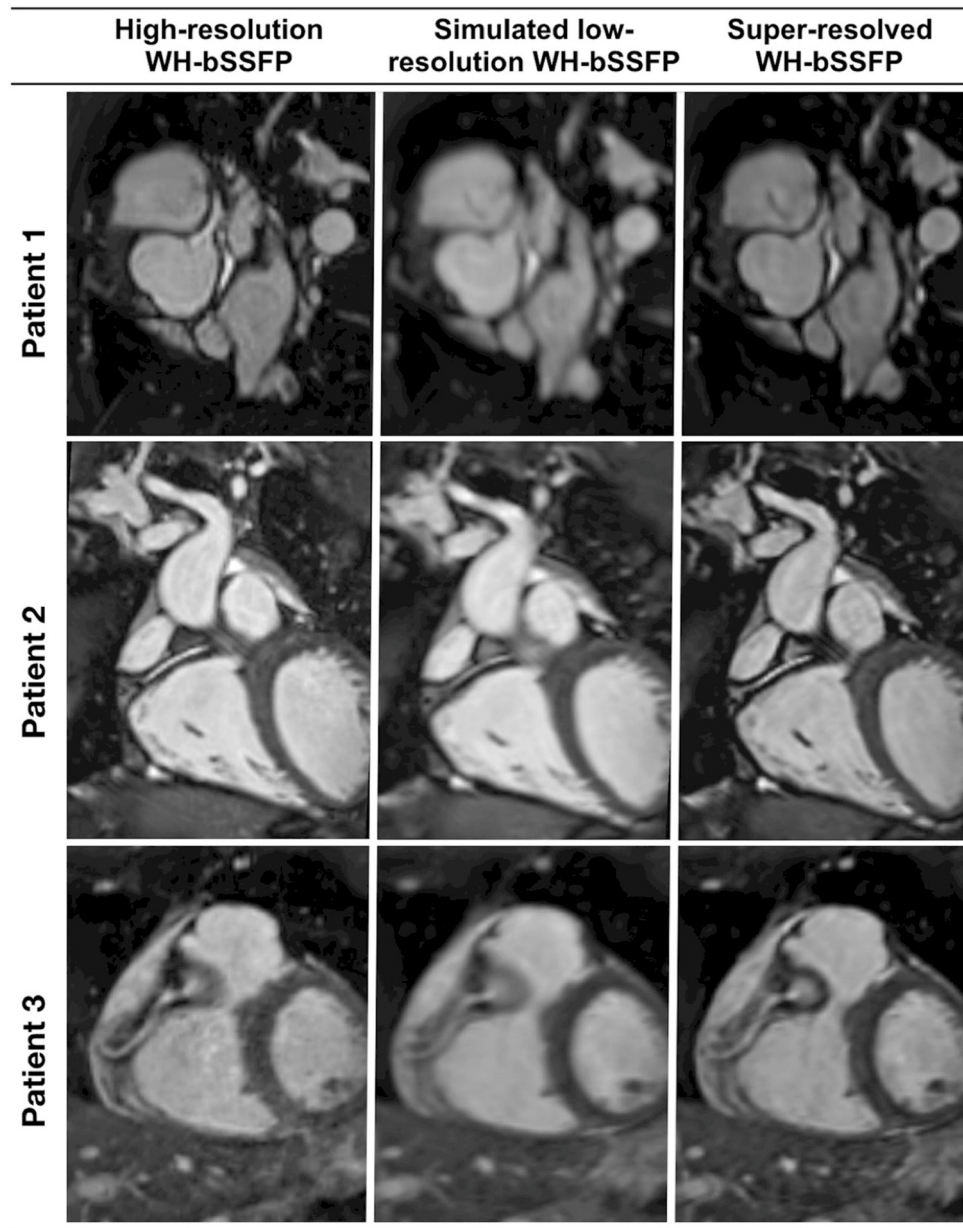
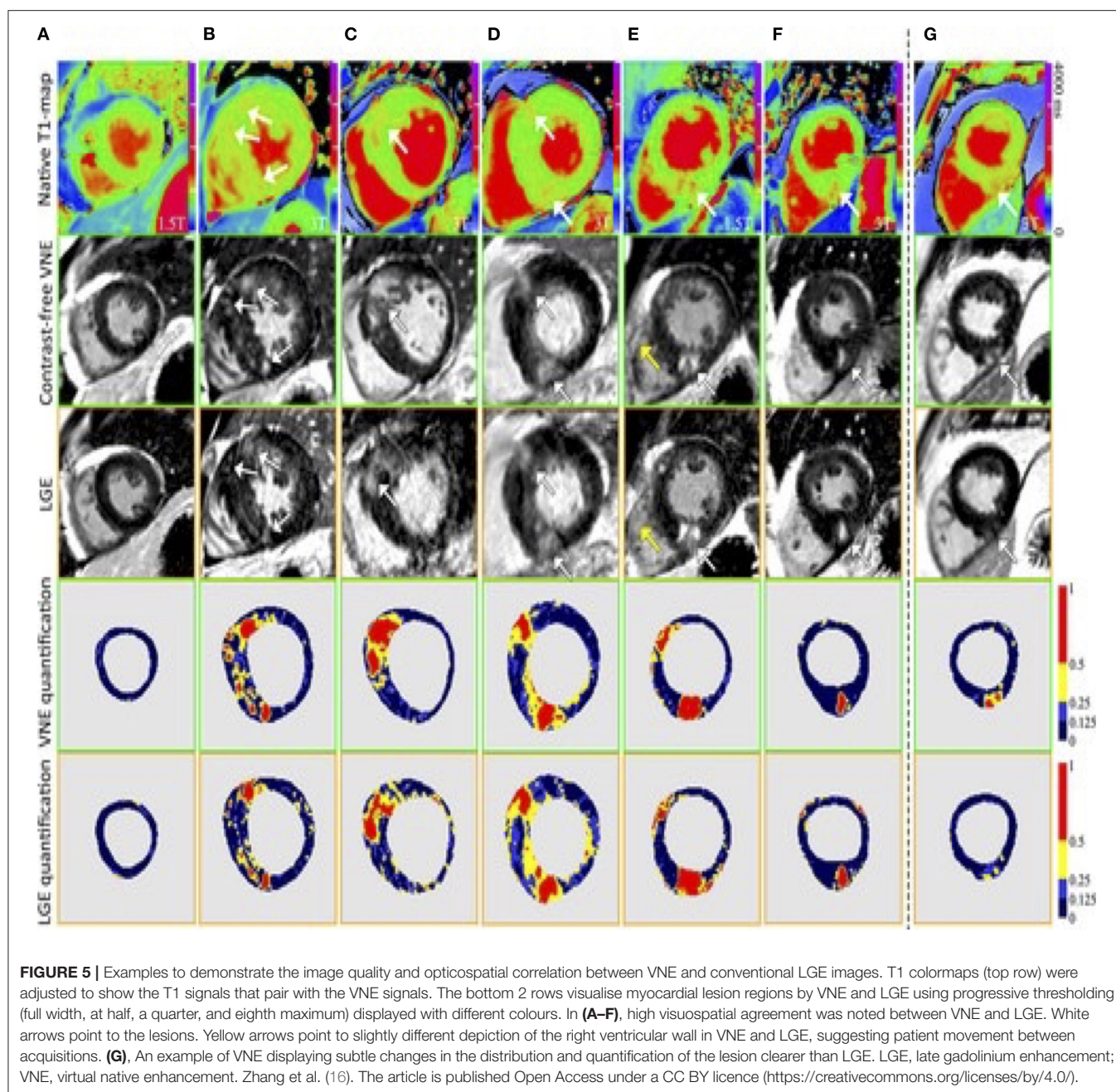


**FIGURE 4 |** Representative image quality of the coronaries from a prospective, clinically integrated study, that utilised a residual U-Net network to facilitate super-resolution reconstruction of rapidly acquired low-resolution three-dimensional whole-heart balanced Steady State Free Precession datasets. Multi-planar reformats of the coronary artery from the respective conventional high-resolution acquisition, low-resolution acquisition, and the corresponding super-resolution reconstruction dataset. Sharpness of vascular borders is enhanced and image distortion is attenuated in the super-resolution reconstruction dataset vs. the low-resolution volume. This is particularly beneficial in the delineation of small vessels, such as the coronary arteries. Qualitative image quality analysis demonstrated no statistically significant differences between the super-resolution and the high-resolution data. Steeden et al. (13). The article is published Open Access under a CC BY licence (<https://creativecommons.org/licenses/by/4.0/>).

## Segmentation

Manual delineation of image contours by experts is currently the standard clinical practise in CMR. However, this is laborious and prone to intra- and inter-observer variability. Various AI models have been proposed and clinically validated to accelerate the segmentation of right and left ventricles in

adult populations (17–19). Limitations include the training in homogenous datasets like the UK Biobank (20) or cardiac atlas project, that include adult patients, the majority being with structurally normal hearts. Winther et al. (21) performed experiments utilising datasets from four independent sources for training and for validation of the network. The network



proved to be capable of reliably producing high quality segmentations, independent of aspects such as different image acquisition techniques, and diverse MRI protocols and vendors. The neuronal network performed equally or outperformed the human cardiac expert in all parts of left ventricle (LV) and right ventricle (RV) volumetry and mass measurements. Bidhendi et al. (22) expanded the approach and created a fully convolutional network that was applied successfully in paediatric patients with CHD and proved to be superior to the algorithms clinically used in a commercially

available platform. An extensive review on these techniques is presented in Chen et al. (23). In a recent study, employing deep fully convolutional neural network, an automated segmentation for the quantification of tissue characterisation for native T1 mapping in patients diagnosed with hypertrophic cardiomyopathy (HCM) has been developed; showing robustness in inter-observer variability and minimising analysis time to under a second (24). A similar approach was employed for automatic quantification of LV mass and scar volume on LGE images and has been successfully applied in patients

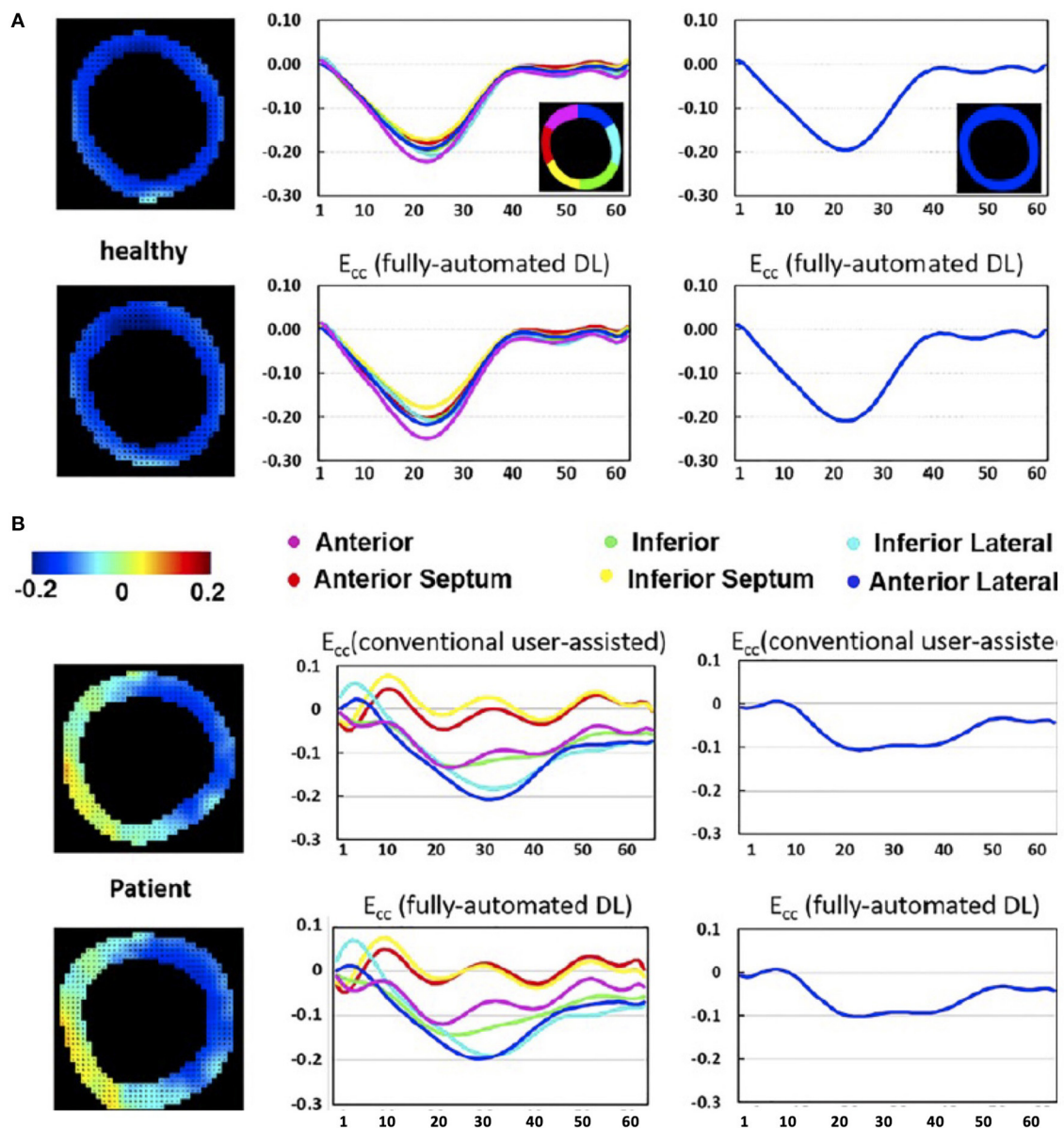


**FIGURE 6** | DL-based computation of global and segmental circumferential strain is compared to the clinician-assisted DENSE analysis. The AI-based end-systolic circumferential strain ( $E_{cc}$ ) maps (left column), segmental (middle column) and global (right column) circumferential strain–time curves for a healthy subject (**A**) and a heart failure patient (**B**) demonstrate very close agreement with the conventional segmentation in the depicted mid-ventricular slices. Ghadimi et al. (26). The article is published Open Access under a CC BY licence (<https://creativecommons.org/licenses/by/4.0/>).

post myocardial infarction (25). Additional applications of convolutional neural networks include automated phase velocity estimation and four-dimensional flow dataset segmentation along with the estimation of global and segmental myocardial strain in Displacement Encoding with stimulated echoes (DENSE) images, **Figure 6** (26, 27). Significant benefits include efficient CMR reporting and high levels of reproducibility in the measurements.

## Novel Imaging Biomarkers Texture Analysis/Radiomics

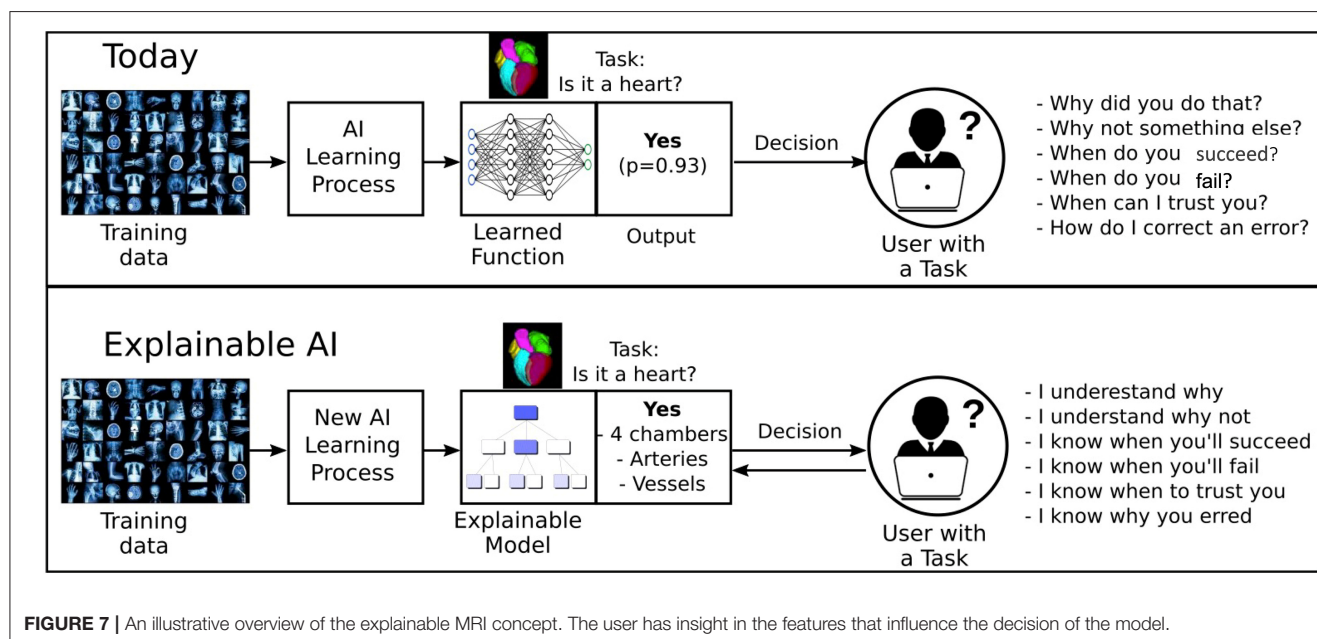
A recently applied technique, called texture analysis (TA), employs various ML algorithms, to quantify the spatial heterogeneity and relationship of adjacent pixels, in order to compute sophisticated imaging metrics. Texture features derived from CMR, have demonstrated potential for further research and clinical integration. It is assumed that the distribution

of pixel grey-level values constitutes significant information beyond the measured mean signal. For instance, although global T1 and extra-cellular volume can differentiate HCM and Hypertensive Heart Disease from normal hearts but not between the two, as values overlap; TA features, generated though supervised ML models, have been shown to distinguish and quantitatively evaluate the subtle discrepancies between the two entities (28). A study, by Wang et al. (29) utilising similar supervised technique, is going one step further and found that TA could differentiate between patients with MYH7(b-myosin heavy chain) gene mutation from those with MYBPC3 (B-myosin binding protein C). A different approach has been investigated by other groups, who introduced motion features as a biomarker. Mancio et al. (30) exploited routine cine images from high dimensional data to objectively characterise and quantify subtle tissue alterations of the ventricular myocardium beyond the typical CMR indices in a cohort of HCM patients. The proposed method, that exploits a supervised-learning algorithm, can potentially serve as screening tool identifying HCM patients with low probability of scar, who constitute around one third of the total cohort, for whom LGE imaging would not be necessary (30). Hence, texture feature analysis could contribute to reducing patient exposure to contrast-agents and the associated service costs.

### New Insights in Predictive Models

Various predictive models, incorporating different clinical and imaging parameters, have been introduced in cardiovascular medicine over the last decades to estimate the personalised risk for an individual patient to develop a certain outcome. A major challenge for CMR is to incorporate imaging biomarkers in clinically relevant predictive models. For the effective characterisation of cardiac disease phenotype, the use of

conventional parameters of cardiac output like ejection fraction might be insufficient (31). Refined ventricular shape and motion analysis could potentially accomplish profound evaluation of cardiac motion and the extraction of its spatiotemporal patterns, which are attributed to specific diseases. Dawes et al. (32) performed computational analysis of RV 3D longitudinal, circumferential and radial motion, relative to its long-axis (defined from the tricuspid orifice and RV apex) between end-diastole and end-systole. The derived data, which represented the systolic displacement of the right ventricle and septum, were then analysed by a supervised ML algorithm, with the aim, to identify those 3D cardiac motion patterns in this high-dimensional dataset, which were more closely linked to survival. The ML survival model showed that altered contraction pattern in distinct segments of the RV free wall and septum is associated with poor prognosis and has incremental predictive performance when added to conventional biomarkers (32). In a similar direction, a fully convolutional neural network was trained to perform cardiac segmentation from hand-labelled CMR images, computing smooth time-resolved 3D renderings of the cardiac motion. Those 3D representations were employed as input data to a supervised denoising autoencoder prediction network, designed to capture robust discriminative features for survival prediction in patients with pulmonary hypertension (33). The predictive accuracy for the deep-learning based survival model outperformed benchmark models of volumetric manually-derived CMR parameters. In a different patient group, a U-net algorithm, based on CNN architecture, was designed to automatically trace the endocardial border and calculate right atrial area and feature-tracking based strain measurements from CMR cine images in the four-chamber view and short-axis view at the papillary muscles level. Those indices, computed directly from raw medical images, correlated significantly with prognosis



in a cohort of patients with repaired Tetralogy of Fallot (34). Knott et al. (35) applied a convolutional- neural network for automated quantitative myocardial perfusion analysis, in the first prospective two-centre outcome study, evaluating global mean stress myocardial blood flow and myocardial perfusion reserve with AI-based techniques. Cox hazard regression analysis demonstrated that stress myocardial blood flow and myocardial perfusion reserve were associated with events after adjusting for potential confounders and concluded that those parameters are predictive of adverse outcomes surpassing the performance of conventional cardiovascular risk factors (35). A differentiated approach was adopted by MacGregor et al. (36) who in addition to incorporating ML-derived measurements in predictive models, proposed a deep-learning based predictive clinical algorithm, advancing previously applied statistical predictive models. This preliminary investigation showed that the regional distribution patterns of machine-detected, CMR-derived, regional contractile injury could have predictive value with regards to clinical endpoints in Idiopathic Dilated Cardiomyopathy Heart Failure patients. The regional strain measurements were the input variables in a deep neural network algorithm, that could differentiate patients who responded to medical therapy from those with no response, with an area under the curve of 0.94 and 85% accuracy (36). Kotu et al. (37) incorporated CMR image-based texture features from post myocardial infarction patients, which delineate the extent, distribution, and heterogeneity of the myocardial scar in a combination of supervised ML-based algorithms and other classification methods, to distinguish between high and low arrhythmic risk group of patients.

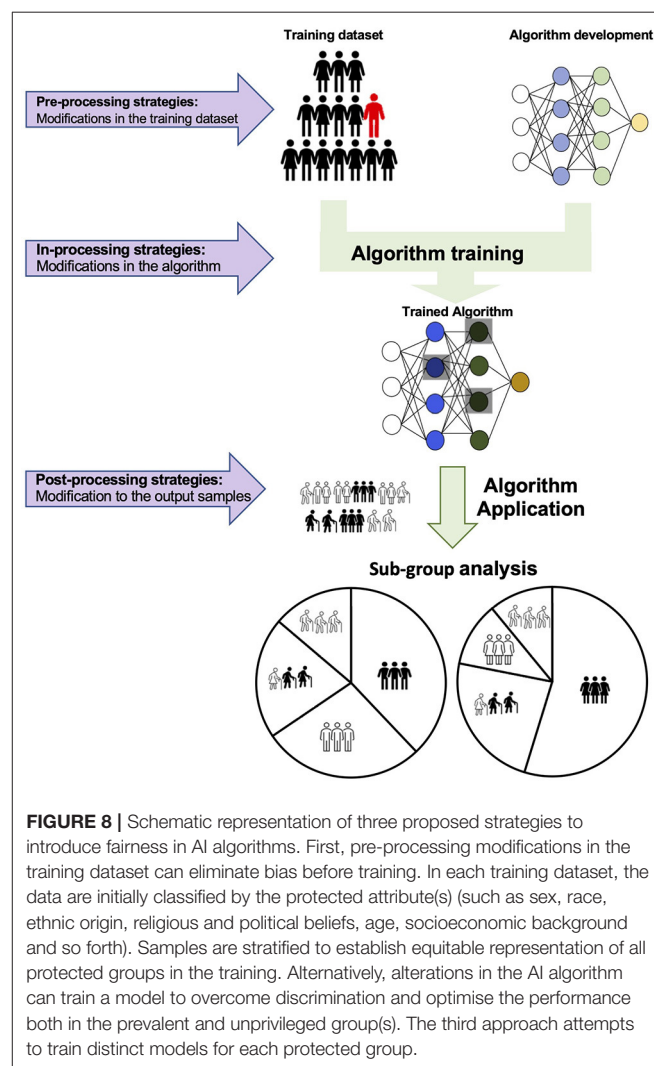
## Current Challenges

Despite the large volume research that has been performed in CMR, real world clinical deployment of AI in clinical practise is still rare.

While AI can extract novel insights from existing data, it is often difficult to justify why the network reached a certain output; the so-called “black-box problem” (38). Furthermore, regulations such as the European General Data Protection Regulation (GDPR) is enforcing the retraceability of the decision outcomes, calling into question the use of black-box models in healthcare. This calls for an approach that supports the interpretability of the machine decision-making process and the reproduction and comprehension of both the learning and knowledge extraction process. Ongoing efforts to face this challenge have resulted in the design of explainable AI models, that constitute a selection of procedures and techniques that enable human subjects to perceive and trust the outcome and the prediction derived by ML methods. In explainable AI, the expected impact and potential biases of the AI model are described. Holzinger et al. (39) presents a very helpful overview of current research topics in explainable AI. Neural network models with incorporated quality control layers are proposed. A schematic representation of the network is shown in **Figure 7**. Puyol-Antón et al. (40) demonstrated a novel framework to predict response to cardiac resynchronisation therapy of patients with cardiomyopathy from cine cardiac imaging. The proposed model allows the extraction of visual

features in the image domain of the secondary categorisation task so that the reviewer can appraise whether the learned features correlate with the clinical domain knowledge. In this method, a weakly supervised network was taught the concept of septal flash, which corresponds to a favourable response to cardiac resynchronisation therapy and was able to illustrate this, by disentangling the latent space. An additional study, utilising CNNs in cardiac cine image segmentation, incorporated robust Quality Control in two distinct phases; an initial pre-analysis assessment of image quality, employing two additional CNNs, was followed by the image segmentation and computation of cardiac functional parameters. The final step was a post analysis qualitative evaluation of the output, thus allowing automated processing of considerable numbers of CMR studies, obviating the requirement for clinician's input (19).

A different approach to this problem employs the use of predictive uncertainty estimates of the segmentation model (41). The key idea is that the model generates confidence intervals of the predictions, giving insight into why the network has



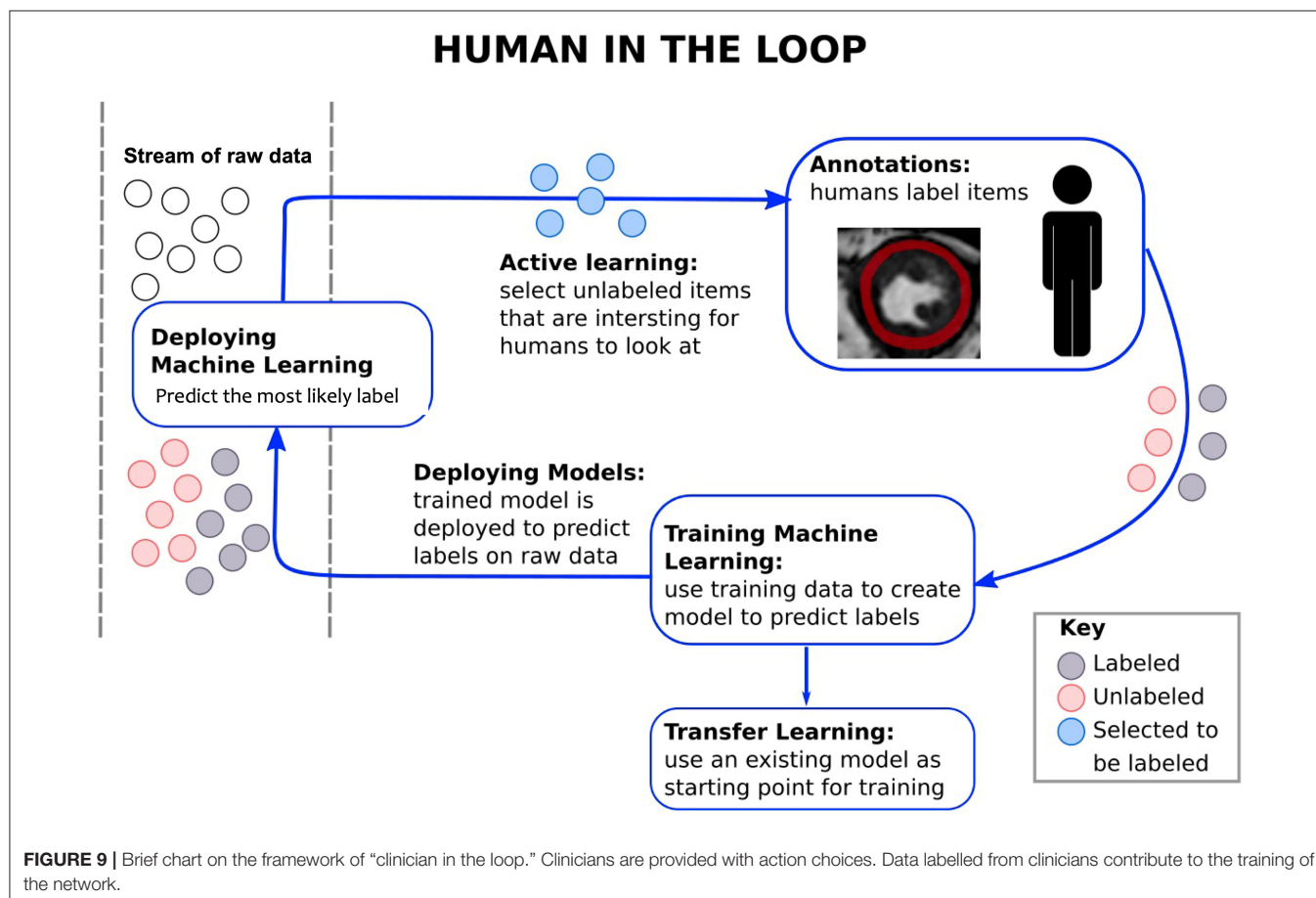
decided the output. Segmentation outputs with low uncertainty are likely correct while outputs with high uncertainty are likely problematic. This may improve workflow efficiency and accuracy by guiding the reviewer to focus mainly on problematic segmentations.

### Limitations Paving the Steps Forward

The greater part of AI research has utilised retrospectively acquired data. The term “AI chasm” has been introduced to express the case that the predictive accuracy of an AI model does not epitomise clinical effectiveness (42). This is because, despite the favourable results, outlining excellent network performance in preliminary, single institutional, proof-of-concept studies, the adoption in clinical practise is limited and the generalisability has not been proven. Few multi-centre, multi-vendor studies have been attempted with good results that were retrospective in nature showing the feasibility of the design and encouraging the execution of similar prospective studies (43). To enhance the validity and clinical acceptance of AI applications, multi-institutional prospective studies across different clinical teams and vendors should be designed, ultimately followed by randomised controlled trials. To the best of our knowledge, in clinical CMR there is currently no prospective randomised control trial published demonstrating the clinical benefit that AI applications could potentially accomplish. Challenges that

need to be faced include the lack of standardisation in image acquisition, reconstruction and analysis along with optimisation, transparency and adherence to reporting standards on trial design and methodology. Few randomised controlled trials have been conducted for different clinical applications, showing that incorporation of AI systems did not have superior outcomes when compared to the current clinical practise or decisions made the by senior clinicians (44). Lin et al. (45) showed that AI achieved high patient satisfaction due to shorter examination times, however further research is warranted as to investigate whether AI solutions can be an alternative triage tool, when a senior consultant is not available. The critical appraisal of the current studies has raised additional confounding factors influencing the methodological approaches in AI randomised control trials that could be considered for improvement in future work (46). Future directions to minimise bias would include methods to warrant effective blinding for the clinicians, inclusion of adequate number of clinicians with different levels of experience and expertise and the design of long-running studies to allow for clinicians to comprehend, adapt and utilise the AI systems effectively.

Recent studies have introduced the significance of “fairness” in DL models (47), demonstrating that training data imbalance, can lead to statistically significant differences in the performance of the proposed models between different racial groups, potentially



exacerbating disparities in healthcare (47). DL algorithms can be optimised to address this issue. Potential strategies to minimise bias include the modification of the training dataset to mitigate discrimination (pre-processing strategies), modifications of the learning algorithm to diminish bias (in-processing strategies) or lastly correcting the output of the applied algorithm to meet the fairness prerequisites (post-processing strategies). **Figure 8** shows an example of the different bias mitigation strategies.

Meticulous clinical reporting of studies, that adopt AI methods, is critical to adequately evaluate image quality, interpret the results and assess the potential usefulness of prediction models, in order for them to be embraced in clinical routine. Forthcoming studies should include patients from diverse backgrounds and report performance per gender and race to minimise bias. It has been often stressed that the area under the curve of a receiver operating characteristic curve is not the optimal metric to assess clinical performance and is not readily comprehensible by many clinicians, although it is widely used in AI studies (48). Sensitivity and specificity should be determined at the defined model operating point (required to transform the continuous model outcome variables into discrete decision groups) and positive and negative predictive values should be reported. Published papers should include information on several measures, summarising the performance of a model, as no single measure captures all the necessary and clinically relevant properties. In addition to the extensive analysis of the results, significant attention should be paid to the practical implementation of the model and whether this achieves a favourable shift in the current patient care pathway. Hence, this is ultimately reflective of the clinical relevance of the study. For instance, various ML-based algorithms have been developed to predict hospital readmissions, showing superior predictive accuracy to conventional parameters, including initial diagnosis and demographic factors. Nevertheless, their clinical uptake is currently limited, because they fail to incorporate and measure competing parameters like clinician's time, staff availability, socio-economic background and so on (49). To progress the comprehension and clinical integration of ML research studies, researchers are asked to adhere to best practise guidance, such as the Transparent Reporting of a multivariable prediction model for Individual Prognosis Or Diagnosis (TRIPOD), developed to support the thorough and transparent reporting of studies that design, validate or update a prediction model (50). An additional version of the TRIPOD statement that is tailored to ML prediction algorithms (TRIPOD-ML) is in progress. This will be intended for the development of a robust framework to provide methodological and reporting guidance for ML studies in healthcare (51).

A recently introduced concept, that is promising and, as far as we know, has not yet been adopted in cardiac MRI is the so-called clinician in-the-loop (52). This is a type of reinforcement learning, where the model keeps learning based on the input of the clinician (**Figure 9**). Further studies are required to investigate whether this method can improve the quality of AI applications in different tasks, including segmentation

and development of predictive models along with gaining clinicians' trust.

## Clinician Engagement

At present, clinician's input is mandatory not only in labelling the data and appraising the developed frameworks, but more importantly in the decision-making process. Most clinicians are currently far away from entrusting computers to match the comprehensive skills of a radiologist. While it is important to encourage the adoption of an AI curriculum for medical students and practising clinicians to allow them to critically review, evaluate and apply AI tools safely in clinical routine, excessive confidence in AI technology is not yet topical. Clinical skills, starting from elaborate history taking, to physical examination along with the enriching and therapeutic patient-physician relationship have been the mainstay of medicine for centuries and should constantly be fostered and harnessed in the parallel development and application of AI tools.

In the years to come, a dedicated collaboration between computer scientists, medical imaging physicists and clinicians in CMR is promising exciting strides in this field. Explainable AI techniques are expected to enable faster integration of AI models into the clinical practise, and will aid in fostering the necessary integrity and trust with their users.

## CONCLUSION

AI is envisaged as a useful tool to accelerate CMR imaging acquisition, analysis and reporting, while introducing new diagnostic and prognostic biomarkers. Careful design and assessment of future studies alongside improved interpretability of the algorithms and enhanced clinician's input will accelerate potential clinical adoption.

## AUTHOR CONTRIBUTIONS

AF, EP-A, KP, and CP devised and wrote the manuscript. AC and RB reviewed the manuscript. All authors contributed to the article and approved the submitted version.

## FUNDING

The authors acknowledge financial support from the BHF PG/18/59/33955, EPSRC EP/P001009, EP/P032311/1, EP/P007619, Wellcome EPSRC Centre for Medical Engineering (NS/A000049/1), and the Department of health via the National Institute for Health Research (NIHR) comprehensive Biomedical Research Centre award to Guy's and St. Thomas' NHS Foundation Trust. The views expressed are those of the authors and not necessarily those of the NHS, the NIHR, or the Department of Health. This research was funded in part, by the Wellcome Trust (NS/A000049/1). For the purpose of open access, the author has applied a CC BY public copyright licence to any Author Accepted Manuscript version arising from this submission.

## REFERENCES

- Hao Z, Shyam RBA, Rathinam A, Gao Y. Intelligent spacecraft visual GNC architecture with the state-of-the-art AI components for on-orbit manipulation. *Front Robot AI*. (2021) 8:639327. doi: 10.3389/frobt.2021.639327
- Huang B, Ji Z, Zhai R, Xiao C, Yang F, Yang B, et al. Clock bias prediction algorithm for navigation satellites based on a supervised learning long short-term memory neural network. *GPS Solutions*. (2021) 25:80. doi: 10.1007/s10291-021-01115-0
- Ding M. A second generation of the neural network model for predicting weighted mean temperature. *GPS Solutions*. (2020) 24:1–6. doi: 10.1007/s10291-020-0975-3
- Erickson BJ, Korfiatis P, Akkus Z, Kline TL. Machine learning for medical imaging. *Radiographics*. (2017) 37:505–15. doi: 10.1148/rg.2017160130
- Sony S, Dunphy K, Sadhu A, Capretz M. A systematic review of convolutional neural network-based structural condition assessment techniques. *Engineering Structures*. (2021) 226:11137. doi: 10.1016/j.engstruct.2020.111347
- Ravi D, Wong C, Deligianni F, Berthelot M, Andreu-Perez J, Lo B, et al. Deep Learning for Health Informatics. *IEEE J Biomed Health Inform*. (2017) 21:4–21. doi: 10.1109/JBHI.2016.2636665
- Keenan NG, Captur G, McCann GP, Berry C, Myerson SG, Fairbairn T, et al. Regional variation in cardiovascular magnetic resonance service delivery across the UK. *Heart*. (2021). doi: 10.1136/heartjnl-2020-318667
- Scannell CM, Veta M, Villa ADM, Sammut EC, Lee J, Breeuwer M, et al. Deep-learning-based preprocessing for quantitative myocardial perfusion MRI. *J Magn Reson Imaging*. (2020) 51:1689–96. doi: 10.1002/jmri.26983
- Menacho K, Ramirez S, Segura P, Nordin S, Abdel-Gadir A, Illatopa V, et al. INCA (Peru) study: impact of non-invasive cardiac magnetic resonance assessment in the developing world. *J Am Heart Assoc*. (2018) 7:e008981. doi: 10.1161/JAHA.118.008981
- Leiner T, Rueckert D, Suinesiaputra A, Baessler B, Nezafat R, Isgum I, et al. Machine learning in cardiovascular magnetic resonance: basic concepts and applications. *J Cardiovasc Magn Reson*. (2019) 21:61. doi: 10.1186/s12968-019-0575-y
- Kustner T, Munoz C, Pseniczny A, Bustin A, Fuin N, Qi H, et al. Deep-learning based super-resolution for 3D isotropic coronary MR angiography in less than a minute. *Magn Reson Med*. (2021) 86:2837–52. doi: 10.1002/mrm.28911
- Fuin N, Bustin A, Kustner T, Oksuz I, Clough J, King AP, et al. A multi-scale variational neural network for accelerating motion-compensated whole-heart 3D coronary MR angiography. *Magn Reson Imaging*. (2020) 70:155–67. doi: 10.1016/j.mri.2020.04.007
- Steeden JA, Quail M, Gotschy A, Mortensen KH, Hauptmann A, Arridge S, et al. Rapid whole-heart CMR with single volume super-resolution. *J Cardiovasc Magn Reson*. (2020) 22:56. doi: 10.1186/s12968-020-00651-x
- Kustner T, Fuin N, Hammernik K, Bustin A, Qi H, Hajhosseiny R, et al. CINENet: deep learning-based 3D cardiac CINE MRI reconstruction with multi-coil complex-valued 4D spatio-temporal convolutions. *Sci Rep*. (2020) 10:13710. doi: 10.1038/s41598-020-70551-8
- Alzubaidi L, Zhang J, Humaidi AJ, Al-Dujaili A, Duan Y, Al-Shamma O, et al. Review of deep learning: concepts, CNN architectures, challenges, applications, future directions. *J Big Data*. (2021) 8:53. doi: 10.1186/s40537-021-00444-8
- Zhang Q, Burrage MK, Lukaschuk E, Shanmuganathan M, Popescu IA, Nikolaidou C, et al. Toward replacing late gadolinium enhancement with artificial intelligence virtual native enhancement for gadolinium-free cardiovascular magnetic resonance tissue characterization in hypertrophic cardiomyopathy. *Circulation*. (2021) 144:589–99. doi: 10.1161/circulationaha.121.054432
- Duan J, Bello G, Schlemper J, Bai W, Dawes TJW, Biffi C, et al. Automatic 3D Bi-ventricular segmentation of cardiac images by a shape-refined multi-task deep learning approach. *IEEE Trans Med Imaging*. (2019) 38:2151–64. doi: 10.1109/TMI.2019.2894322
- Avendi MR, Kheradvar A, Jafarkhani H. A combined deep-learning and deformable-model approach to fully automatic segmentation of the left ventricle in cardiac MRI. *Med Image Anal*. (2016) 30:108–19. doi: 10.1016/j.media.2016.01.005
- Ruijsink B, Puyol-Anton E, Oksuz I, Sinclair M, Bai W, Schnabel JA, et al. Fully automated, quality-controlled cardiac analysis from CMR: validation and large-scale application to characterize cardiac function. *JACC Cardiovasc Imaging*. (2020) 13:684–95. doi: 10.1016/j.jcmg.2019.05.030
- Sudlow C, Gallacher J, Allen N, Beral V, Burton P, Danesh J, et al. UK Biobank: an open access resource for identifying the causes of a wide range of complex diseases of middle and old age. *PLoS Med*. (2015) 12:e1001779. doi: 10.1371/journal.pmed.1001779
- Winther HB, Hundt C, Schmidt B, Czerner C, Bauersachs J, Wacker F, et al. v-net: deep learning for generalized biventricular mass and function parameters using multicenter cardiac MRI data. *JACC Cardiovasc Imaging*. (2018) 11:1036–8. doi: 10.1016/j.jcmg.2017.11.013
- Karimi-Bidhendi S, Arafati A, Cheng AL, Wu Y, Kheradvar A, Jafarkhani H. Fullyautomated deeplearning segmentation of pediatric cardiovascular magnetic resonance of patients with complex congenital heart diseases. *J Cardiovasc Magn Reson*. (2020) 22:80. doi: 10.1186/s12968-020-00678-0
- Chen C, Qin C, Qiu H, Tarroni G, Duan J, Bai W, et al. Deep learning for cardiac image segmentation: a review. *Front Cardiovasc Med*. (2020) 7:25. doi: 10.3389/fcvm.2020.00025
- Fahmy AS, El-Rewaify H, Nezafat M, Nakamori S, Nezafat R. Automated analysis of cardiovascular magnetic resonance myocardial native T1 mapping images using fully convolutional neural networks. *J Cardiovasc Magn Reson*. (2019) 21:7. doi: 10.1186/s12968-018-0516-1
- Fahmy AS, Rausch J, Neisius U, Chan RH, Maron MS, Appelbaum E, et al. Automated cardiac MR scar quantification in hypertrophic cardiomyopathy using deep convolutional neural networks. *JACC Cardiovasc Imaging*. (2018) 11:1917–8. doi: 10.1016/j.jcmg.2018.04.030
- Ghadimi S, Auger DA, Feng X, Sun C, Meyer CH, Bilchick KC, et al. Fully-automated global and segmental strain analysis of DENSE cardiovascular magnetic resonance using deep learning for segmentation and phase unwrapping. *J Cardiovasc Magn Reson*. (2021) 23:20. doi: 10.1186/s12968-021-00712-9
- Bratt A, Kim J, Pollie M, Beecy AN, Tehrani NH, Codella N, et al. Machine learning derived segmentation of phase velocity encoded cardiovascular magnetic resonance for fully automated aortic flow quantification. *J Cardiovasc Magn Reson*. (2019) 21:1. doi: 10.1186/s12968-018-0509-0
- Neisius U, El-Rewaify H, Nakamori S, Rodriguez J, Manning WJ, Nezafat R. Radiomic analysis of myocardial native T1 imaging discriminates between hypertensive heart disease and hypertrophic cardiomyopathy. *JACC Cardiovasc Imaging*. (2019) 12:1946–54. doi: 10.1016/j.jcmg.2018.11.024
- Wang J, Yang F, Liu W, Sun J, Han Y, Li D, et al. Radiomic analysis of native T1 mapping images discriminates between MYH7 and MYBPC3-related hypertrophic cardiomyopathy. *J Magn Reson Imaging*. (2020) 52:1714–21. doi: 10.1002/jmri.27209
- Mancio J, Pashakhanloo F, El-Rewaify H, Jang J, Joshi G, Csecs I, et al. Machine learning phenotyping of scarred myocardium from cine in hypertrophic cardiomyopathy. *Eur Heart J Cardiovasc Imaging*. (2021) jeab056. doi: 10.1093/ehjci/jeab056. [Online ahead of print].
- Sinclair M, Peressutti D, Puyol-Anton E, Bai W, Rivolo S, Webb J, et al. Myocardial strain computed at multiple spatial scales from tagged magnetic resonance imaging: Estimating cardiac biomarkers for CRT patients. *Med Image Anal*. (2018) 43:169–85. doi: 10.1016/j.media.2017.10.004
- Dawes TJW, de Marvao A, Shi W, Fletcher T, Watson GMJ, Wharton J, et al. Machine learning of three-dimensional right ventricular motion enables outcome prediction in pulmonary hypertension: a cardiac MR imaging study. *Radiology*. (2017) 283:381–90. doi: 10.1148/radiol.2016161315
- Bello GA, Dawes TJW, Duan J, Biffi C, de Marvao A, Howard LSGE, et al. Deep-learning cardiac motion analysis for human survival prediction. *Nat Mach Intell*. (2019) 1:95–104. doi: 10.1038/s42256-019-0019-2
- Diller GP, Orwat S, Vahle J, Bauer UMM, Urban A, Sarikouch S, et al. Prediction of prognosis in patients with tetralogy of Fallot based on deep learning imaging analysis. *Heart*. (2020) 106:1007–14. doi: 10.1136/heartjnl-2019-315962
- Knott KD, Seraphim A, Augusto JB, Xue H, Chacko L, Aung N, et al. The prognostic significance of quantitative myocardial perfusion: an artificial intelligence-based approach using perfusion mapping. *Circulation*. (2020) 141:1282–91. doi: 10.1161/CIRCULATIONAHA.119.044666

36. MacGregor RM, Guo A, Masood ME, Cupps BP, Ewald GA, Pasque MK, et al. Machine learning outcome prediction in dilated cardiomyopathy using regional left ventricular multiparametric strain. *Ann Biomed Eng.* (2021) 49:922–32. doi: 10.1007/s10439-020-02639-1
37. Kotu LP, Engan K, Borhani R, Katsaggelos AK, Orn S, Woie L, et al. Cardiac magnetic resonance image-based classification of the risk of arrhythmias in post-myocardial infarction patients. *Artif Intell Med.* (2015) 64:205–15. doi: 10.1016/j.artmed.2015.06.001
38. Singh A, Sengupta S, Lakshminarayanan V. Explainable deep learning models in medical image analysis. *J Imaging.* (2020) 6:52. doi: 10.3390/jimaging6060052
39. Holzinger A, Biemann C, Pattichis C, Kell D. What do we need to build explainable AI systems for the medical domain? *arXiv preprint arXiv:1712.09923.* (2017).
40. Puyol-Anton E, Chen C, Clough JR, Ruijsink B, Sidhu BS, Gould J, et al. Interpretable deep models for cardiac resynchronisation therapy response prediction. *Med Image Comput Comput Assist Interv.* (2020) 2020:284–93. doi: 10.1007/978-3-030-59710-8\_28
41. Ng M, Guo F, Biswas L, Petersen SE, Piechnik SK, Neubauer S, et al. *Estimating Uncertainty in Neural Networks for Cardiac MRI Segmentation: A Benchmark Study 2020* Available online at: <https://ui.adsabs.harvard.edu/abs/2020arXiv201215772N> (accessed December 01, 2020).
42. Keane PA, Topol EJ. With an eye to AI and autonomous diagnosis. *NPJ Digit Med.* (2018) 1:40. doi: 10.1038/s41746-018-0048-y
43. Tao Q, Yan W, Wang Y, Paiman EHM, Shamonin DP, Garg P, et al. Deep learning-based method for fully automatic quantification of left ventricle function from cine MR images: a multivendor, multicenter study. *Radiology.* (2019) 290:81–8. doi: 10.1148/radiol.2018180513
44. Brocklehurst P, Field D, Greene K, Juszczak E, Keith R, Kenyon S, et al. Computerised interpretation of fetal heart rate during labour (INFANT): a randomised controlled trial. *Lancet.* (2017) 389:1719–29. doi: 10.1016/S0140-6736(17)30568-8
45. Lin H, Li R, Liu Z, Chen J, Yang Y, Chen H, et al. Diagnostic efficacy and therapeutic decision-making capacity of an artificial intelligence platform for childhood cataracts in eye clinics: a multicentre randomized controlled trial. *EClinicalMedicine.* (2019) 9:52–9. doi: 10.1016/j.eclinm.2019.03.001
46. Genin K, Grote T. Randomized controlled trials in medical AI: a methodological critique. *Philos Med.* (2021) 2. doi: 10.5195/phlmed.2021.27
47. Puyol-Antón E, Ruijsink B, Harana JM, Piechnik SK, Neubauer S, Petersen SE, et al. Fairness in cardiac magnetic resonance imaging: assessing sex and racial bias in deep learning-based segmentation. *medRxiv.* (2021). doi: 10.1101/2021.07.19.21260749
48. Saito T, Rehmsmeier M. The precision-recall plot is more informative than the ROC plot when evaluating binary classifiers on imbalanced datasets. *PLoS ONE.* (2015) 10:e0118432. doi: 10.1371/journal.pone.0118432
49. Shah NH, Milstein A, Bagley DS. Making machine learning models clinically useful. *JAMA.* (2019) 322:1351–2. doi: 10.1001/jama.2019.10306
50. Collins GS, Reitsma JB, Altman DG, Moons KG. Transparent reporting of a multivariable prediction model for individual prognosis or diagnosis (TRIPOD): the TRIPOD statement. *BMJ.* (2015) 350:g7594. doi: 10.1136/bmj.g7594
51. Collins GS, Dhiman P, Andaur Navarro CL, Ma J, Hooft L, Reitsma JB, et al. Protocol for development of a reporting guideline (TRIPOD-AI) and risk of bias tool (PROBAST-AI) for diagnostic and prognostic prediction model studies based on artificial intelligence. *BMJ Open.* (2021) 11:e048008. doi: 10.1136/bmjopen-2020-048008
52. Tang S, Modi A, Sjoding M, Wiens J. Clinician-in-the-loop decision making: reinforcement learning with near-optimal set-valued policies. In: Hal D, Aarti S, editors. *Proceedings of the 37th International Conference on Machine Learning; Proceedings of Machine Learning Research.* (2020). p. 9387–96.

**Conflict of Interest:** The authors declare that the research was conducted in the absence of any commercial or financial relationships that could be construed as a potential conflict of interest.

**Publisher's Note:** All claims expressed in this article are solely those of the authors and do not necessarily represent those of their affiliated organizations, or those of the publisher, the editors and the reviewers. Any product that may be evaluated in this article, or claim that may be made by its manufacturer, is not guaranteed or endorsed by the publisher.

Copyright © 2022 Fotaki, Puyol-Antón, Chiribiri, Botnar, Pushparajah and Prieto. This is an open-access article distributed under the terms of the Creative Commons Attribution License (CC BY). The use, distribution or reproduction in other forums is permitted, provided the original author(s) and the copyright owner(s) are credited and that the original publication in this journal is cited, in accordance with accepted academic practice. No use, distribution or reproduction is permitted which does not comply with these terms.



# SGLT2 Inhibition in HFpEF. Do We Need More Quantitative and Load Independent Metrics to Understand the Results of the EMPEROR-Preserved Trial?

Grigorios Korosoglou<sup>1,2\*</sup>, Sorin Giusca<sup>1,2</sup> and Sebastian Kelle<sup>3</sup>

<sup>1</sup> Department of Cardiology, Vascular Medicine and Pneumology, Gesundheitszentrum Rhein-Neckar Hospital Weinheim, Weinheim, Germany, <sup>2</sup> Cardiac Imaging Center Weinheim, Hector Foundation, Weinheim, Germany, <sup>3</sup> Department of Internal Medicine/Cardiology, Deutsches Herzzentrum Berlin, Berlin, Germany

**Keywords:** heart failure, preserved ejection fraction, SGLT2 inhibition, myocardial strain, fast-SENC

## INTRODUCTION

Despite advances in the pharmacologic and interventional treatment of ischemic, myocardial, and valvular heart diseases, heart failure is estimated to affect ~60 million individuals worldwide being associated with high morbidity and mortality rates. In a recent report by Anker and colleagues published in the New England Journal of Medicine, the authors demonstrated that SGLT2 inhibition with empagliflozin leads to relevant clinical outcome improvements, by reducing the relative risk for cardiovascular death and hospitalization for patients with symptomatic heart failure NYHA II-IV and preserved ejection fraction (HFpEF). The results were mainly driven by a reduction in hospitalization rates (1). We congratulate the authors for this article, which is to our knowledge the first randomized study, highlighting the ability of SGLT2 inhibition to improve clinical outcomes in HFpEF. Based on prespecified left ventricular ejection fraction (LVEF) subgroups, however, patients with LVEF ~40–49% mostly benefited from treatment, whereas positive effects were attenuated in patients with LVEF between 50 and 59% and were not statistically significant with LVEF  $\geq 60\%$ .

## PREVIOUS STUDIES WITH SGLT2 INHIBITORS AND UNDERLYING MECHANISMS

Several studies demonstrated the ability of SGLT2 inhibition to reduce cardiovascular endpoints in patients with heart failure and reduced ejection fraction regardless of the presence or absence of type 2 diabetes mellitus (2, 3). Hereby, the exact mechanism of action is still a subject of ongoing research. It has been previously proposed, that SGLT2 inhibition may exert beneficial effects by reducing inflammation, oxidative stress, and blood pressure due to diuresis and natriuresis, resulting in improvement of vascular and kidney function. In addition, beneficial effects in terms of cardiac energy metabolism have been described. Thus, SGLT2 inhibition may improve cardiac energetics and cardiac efficiency, by increasing circulating ketone levels and cardiac ketone oxidation rates, which can act as a thrifty fuel for the undersupplied “starving” failing heart (4). This may improve energy supply of the heart muscle, translating into lower rates of hospitalization due to heart failure symptoms, thus improving clinical outcomes.

## OPEN ACCESS

### Edited by:

Fabrizio Ricci,  
University of Studies G. d'Annunzio  
Chieti and Pescara, Italy

### Reviewed by:

Anna Giulia Pavon,  
Ospedale Regionale di  
Lugano, Switzerland

### \*Correspondence:

Grigorios Korosoglou  
gkorosoglou@hotmail.com

### Specialty section:

This article was submitted to  
Cardiovascular Imaging,  
a section of the journal  
Frontiers in Cardiovascular Medicine

**Received:** 26 November 2021

**Accepted:** 20 December 2021

**Published:** 14 January 2022

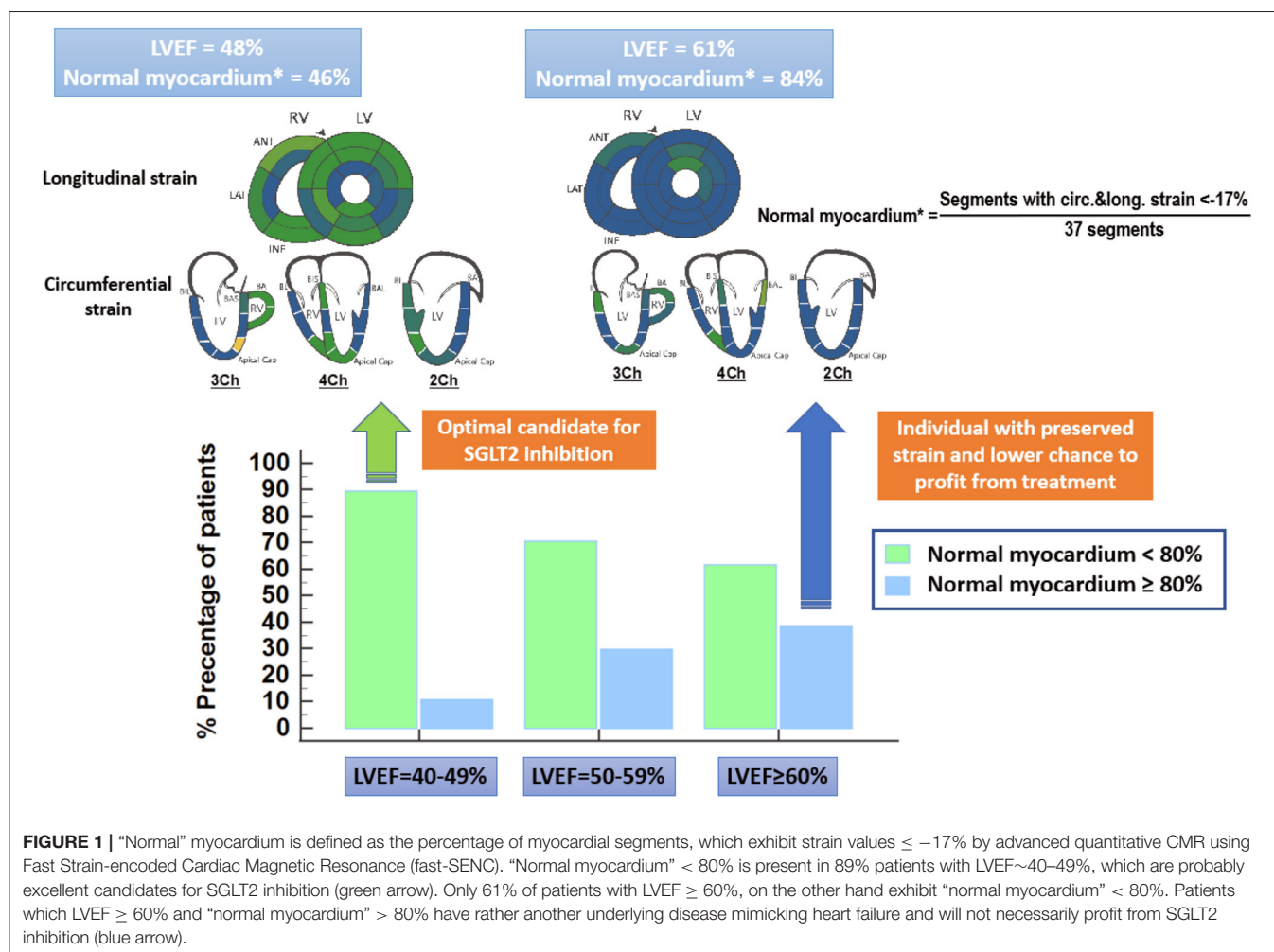
### Citation:

Korosoglou G, Giusca S and Kelle S  
(2022) SGLT2 Inhibition in HFpEF. Do  
We Need More Quantitative and Load  
Independent Metrics to Understand  
the Results of the  
EMPEROR-Preserved Trial?  
Front. Cardiovasc. Med. 8:822968.  
doi: 10.3389/fcvm.2021.822968

## TECHNICAL CONSIDERATIONS AND DISCUSSION

From a pathophysiologic point of view, LVEF is a crude and load-dependent marker for cardiac efficiency (5, 6), whereas myocardial strain by echocardiography and advanced quantitative CMR, recently exhibited important value for the non-invasive assessment of myocardial fibrosis and incremental prognostic value beyond LVEF in heart failure patients (6–8). Thus, global longitudinal strain (GLS) was associated with clinical heart failure status, the level of neurohormonal activation and with long-term cardiac mortality in patients with asymptomatic and symptomatic heart failure (6). In addition, the presence of “normal” myocardium (defined as percentage of myocardial segments exhibiting a strain value  $\leq -17\%$ ) by advanced quantitative CMR using Fast Strain-encoded Cardiac Magnetic Resonance (fast-SENC), recently demonstrated incremental value for the prediction of clinical outcomes beyond LVEF in an all-comer cohort of heart failure patients (7). In this study, more than one third of individuals who were classified just at risk for heart failure by

conventional imaging markers including LVEF, were reclassified to patients with subclinical LV-dysfunction, exhibiting “normal” myocardium  $< 80\%$  (7). Such individuals with “normal” myocardium  $< 80\%$ , who were in most cases asymptomatic at baseline, showed higher rates for all-cause death and hospitalization due heart failure and for new onset of heart failure medications during follow-up (7). Since “normal myocardium” may represent a more valid surrogate marker of impaired myocardial energetics compared to LVEF, it is conceivable that patients with “normal myocardium”  $< 80\%$  are likely to exhibit unfavorable myocardial energetics and benefit from SGLT2 inhibition. In fact, impaired “normal myocardium”  $< 80\%$  was present in 89% patients with LVEF  $\sim 40$ –49% in our recent study, which are probably excellent candidates for SGLT2 inhibition but only in 61% patients with LVEF  $\geq 60\%$ , where SGLT2 inhibition may not necessarily translate to clinical benefits (Figure 1). Although GLS and normal myocardium have not been systematically analyzed in the EMPEROR preserved trial, these load independent metrics may aid in a more precise identification of appropriate candidates for SGLT2 inhibition with preserved LVEF in future trials.



In the same direction, CMR T1 mapping techniques allow for the assessment of interstitial space characteristics and extracellular volume size, which are related to collagen content and interstitial infiltration of myocardial tissue by fibrotic tissue or other molecules, such as amyloid. The ability of such measures for the risk stratification of patients with heart failure, cardiomyopathies or amyloidosis has already been demonstrated (8–11). In addition, recent studies highlighted the ability of such techniques to accurately assess longitudinal changes of myocardial extracellular volume in patients treated with SGLT2 inhibitors (12, 13).

Importantly, metrics such as strain or T1 values can be acquired serially during non-contrast CMR scans, thus without the need for gadolinium administration and without radiation exposure for the patients. Thus, such a direct measure of treatment response in terms of increases in strain and “normal

myocardium” would be feasible in patients receiving SGLT2 inhibitors possibly a couple of weeks after the treatment initiation. Due to the quantitative nature of these parameters smaller populations than the one presented in the EMPEROR preserved trial would be necessary to investigate the direct effects of such drugs on myocardial strain in heart failure patients. Such advanced metrics like “normal myocardium” would therefore decrease trials costs and speed-up transfer of knowledge into clinical use, aiding individualized treatment of heart failure patients or even of asymptomatic individuals with subclinical LV-dysfunction.

## AUTHOR CONTRIBUTIONS

All authors listed have made a substantial, direct, and intellectual contribution to the work and approved it for publication.

## REFERENCES

- Anker SD, Butler J, Filippatos G, Ferreira JP, Bocchi E, Böhm M, et al. Empagliflozin in heart failure with a preserved ejection fraction. *N Engl J Med*. (2021) 385:1451–61. doi: 10.1056/NEJMoa2107038
- McMurray JJV, Solomon SD, Inzucchi SE, Køber L, Kosiborod MN, Martinez FA, et al. Dapagliflozin in patients with heart failure and reduced ejection fraction. *N Engl J Med*. (2019) 381:1995–2008. doi: 10.1056/NEJMoa1911303
- Packer M, Anker SD, Butler J, Filippatos G, Pocock SJ, Carson P, et al. Cardiovascular and renal outcomes with empagliflozin in heart failure. *N Engl J Med*. (2020) 383:1413–24. doi: 10.1056/NEJMoa2022190
- Lopaschuk GD, Verma S. Mechanisms of cardiovascular benefits of sodium glucose co-transporter 2 (SGLT2) inhibitors. *JACC Basic Transl Sci*. (2020) 5:632–44. doi: 10.1016/j.jacbs.2020.02.004
- Pedrizetti G, Lapinskas T, Tonti G, Stoiber L, Zaliunas R, Gebker R, et al. The relationship between EF and strain permits a more accurate assessment of LV systolic function. *JACC Cardiovasc Imaging*. (2019) 12:1893–5. doi: 10.1016/j.jcmg.2019.03.019
- Tröbs S-O, Prochaska JH, Schwuchow-Thonke S, Schulz A, Müller F, Heidorn MW, et al. Association of global longitudinal strain with clinical status and mortality in patients with chronic heart failure. *JAMA Cardiol*. (2021) 6:448–56. doi: 10.1001/jamacardio.2020.7184
- Korosoglou G, Giusca S, Montenbruck M, Patel AR, Lapinskas T, Götze C, et al. Fast strain-encoded cardiac magnetic resonance for diagnostic classification and risk stratification of heart failure patients. *JACC Cardiovasc Imaging*. (2021) 14:1177–88. doi: 10.1016/j.jcmg.2020.10.024
- Mandoli GE, D'Ascenzi F, Vinco G, Benfari G, Ricci F, Focardi M, et al. Novel approaches in cardiac imaging for non-invasive assessment of left heart myocardial fibrosis. *Front Cardiovasc Med*. (2021) 8:614235. doi: 10.3389/fcvm.2021.614235
- Pezel T, Viallon M, Croisille P, Sebbag L, Bochaton T, Garot J, et al. Imaging interstitial fibrosis, left ventricular remodeling, and function in stage A and B heart failure. *JACC Cardiovasc Imaging*. (2021) 14:1038–52. doi: 10.1016/j.jcmg.2020.05.036
- Li S, Zhou D, Sirajuddin A, He J, Xu J, Zhuang B, et al. T1 mapping and extracellular volume fraction in dilated cardiomyopathy: a prognosis study. *JACC Cardiovasc Imaging*. (2021). doi: 10.1016/j.jcmg.2021.07.023. [Epub ahead of print].
- Korosoglou G, Giusca S, André F, Aus dem Siepen F, Nunninger P, et al. Diagnostic work-up of cardiac amyloidosis using cardiovascular imaging: current standards and practical algorithms. *Vasc Health Risk Manag*. (2021) 17:661–73. doi: 10.2147/VHRM.S295376
- Mason T, Coelho-Filho OR, Verma S, Chowdhury B, Zuo F, Quan A, et al. Empagliflozin reduces myocardial extracellular volume in patients with type 2 diabetes and coronary artery disease. *JACC Cardiovasc Imaging*. (2021) 14:1164–1173. doi: 10.1016/j.jcmg.2020.10.017
- Requena-Ibáñez JA, Santos-Gallego CG, Rodriguez-Cordero A, Vargas-Delgado AP, Mancini D, Sartori S, et al. Mechanistic insights of empagliflozin in nondiabetic patients with HFrEF: from the EMPA-TROPISM study. *JACC Heart Fail*. (2021) 9:578–89. doi: 10.1016/j.jchf.2021.04.014

**Conflict of Interest:** SK and GK received research grants from Myocardial Solutions. SK owns stock options of Myocardial Solutions.

The remaining author declares that the research was conducted in the absence of any commercial or financial relationships that could be construed as a potential conflict of interest.

**Publisher's Note:** All claims expressed in this article are solely those of the authors and do not necessarily represent those of their affiliated organizations, or those of the publisher, the editors and the reviewers. Any product that may be evaluated in this article, or claim that may be made by its manufacturer, is not guaranteed or endorsed by the publisher.

Copyright © 2022 Korosoglou, Giusca and Kelle. This is an open-access article distributed under the terms of the Creative Commons Attribution License (CC BY). The use, distribution or reproduction in other forums is permitted, provided the original author(s) and the copyright owner(s) are credited and that the original publication in this journal is cited, in accordance with accepted academic practice. No use, distribution or reproduction is permitted which does not comply with these terms.



# Cardiac MR: From Theory to Practice

**Tevfik F. Ismail<sup>1,2†</sup>, Wendy Strugnell<sup>3†</sup>, Chiara Coletti<sup>4†</sup>, Maša Božić-Iven<sup>4,5†</sup>, Sebastian Weingärtner<sup>4†</sup>, Kerstin Hammernik<sup>6,7†</sup>, Teresa Correia<sup>1,8\*‡</sup> and Thomas Küstner<sup>9\*‡</sup>**

<sup>1</sup> School of Biomedical Engineering and Imaging Sciences, King's College London, London, United Kingdom, <sup>2</sup> Cardiology Department, Guy's and St Thomas' Hospital, London, United Kingdom, <sup>3</sup> Queensland X-Ray, Mater Hospital Brisbane, Brisbane, QLD, Australia, <sup>4</sup> Magnetic Resonance Systems Lab, Delft University of Technology, Delft, Netherlands, <sup>5</sup> Computer Assisted Clinical Medicine, Heidelberg University, Mannheim, Germany, <sup>6</sup> Lab for AI in Medicine, Technical University of Munich, Munich, Germany, <sup>7</sup> Department of Computing, Imperial College London, London, United Kingdom, <sup>8</sup> Centre of Marine Sciences, Faro, Portugal, <sup>9</sup> Medical Image and Data Analysis (MIDAS.lab), Department of Diagnostic and Interventional Radiology, University Hospital of Tübingen, Tübingen, Germany

## OPEN ACCESS

### Edited by:

Andrea Igoren Guaricci,  
Azienda Ospedaliero Universitaria  
Consortiale Policlinico di Bari, Italy

### Reviewed by:

Haikun Qi,  
ShanghaiTech University, China  
Kenichiro Otsuka,  
Massachusetts General Hospital and  
Harvard Medical School,  
United States

### \*Correspondence:

Teresa Correia  
teresa.correia@kcl.ac.uk  
Thomas Küstner  
thomas.kuestner@  
med.uni-tuebingen.de

<sup>†</sup>These authors have contributed  
equally to this work and share first  
authorship

<sup>‡</sup>These authors have contributed  
equally to this work and share last  
authorship

### Specialty section:

This article was submitted to  
Cardiovascular Imaging,  
a section of the journal  
Frontiers in Cardiovascular Medicine

**Received:** 30 November 2021

**Accepted:** 17 January 2022

**Published:** 03 March 2022

### Citation:

Ismail TF, Strugnell W, Coletti C,  
Božić-Iven M, Weingärtner S,  
Hammernik K, Correia T and  
Küstner T (2022) Cardiac MR: From  
Theory to Practice.  
Front. Cardiovasc. Med. 9:826283.  
doi: 10.3389/fcvm.2022.826283

Cardiovascular disease (CVD) is the leading single cause of morbidity and mortality, causing over 17.9 million deaths worldwide per year with associated costs of over \$800 billion. Improving prevention, diagnosis, and treatment of CVD is therefore a global priority. Cardiovascular magnetic resonance (CMR) has emerged as a clinically important technique for the assessment of cardiovascular anatomy, function, perfusion, and viability. However, diversity and complexity of imaging, reconstruction and analysis methods pose some limitations to the widespread use of CMR. Especially in view of recent developments in the field of machine learning that provide novel solutions to address existing problems, it is necessary to bridge the gap between the clinical and scientific communities. This review covers five essential aspects of CMR to provide a comprehensive overview ranging from CVDs to CMR pulse sequence design, acquisition protocols, motion handling, image reconstruction and quantitative analysis of the obtained data. (1) The basic MR physics of CMR is introduced. Basic pulse sequence building blocks that are commonly used in CMR imaging are presented. Sequences containing these building blocks are formed for parametric mapping and functional imaging techniques. Commonly perceived artifacts and potential countermeasures are discussed for these methods. (2) CMR methods for identifying CVDs are illustrated. Basic anatomy and functional processes are described to understand the cardiac pathologies and how they can be captured by CMR imaging. (3) The planning and conduct of a complete CMR exam which is targeted for the respective pathology is shown. Building blocks are illustrated to create an efficient and patient-centered workflow. Further strategies to cope with challenging patients are discussed. (4) Imaging acceleration and reconstruction techniques are presented that enable acquisition of spatial, temporal, and parametric dynamics of the cardiac cycle. The handling of respiratory and cardiac motion strategies as well as their integration into the reconstruction processes is showcased. (5) Recent advances on deep learning-based reconstructions for this purpose are summarized. Furthermore, an overview of novel deep learning image segmentation and analysis methods is provided with a focus on automatic, fast and reliable extraction of biomarkers and parameters of clinical relevance.

**Keywords:** cardiovascular MR, deep learning, CMR protocol, quantitative imaging, image reconstruction, sequence design, imaging acceleration, image processing

## INTRODUCTION

Over the past 40 years, cardiovascular magnetic resonance (CMR) has evolved from an esoteric research tool found in the confines of large academic supraregional tertiary referral centers to being an indispensable clinical tool that routinely changes patient management across the breadth of modern cardiovascular practice (1). Increasing clinical recognition of the transformative role this technology can play in patient care has led to its growing availability in secondary care settings too, although significant barriers remain to its greater adoption world-wide, particularly in Africa.

CMR is a versatile non-invasive and radiation-free imaging modality that provides a comprehensive assessment of multiple parameters of cardiac function and anatomy in a single examination. CMR plays a major role in the diagnosis and management of cardiovascular disease. However, aside from cost, there remain major obstacles for the widespread usage of this technique like: (i) complex underlying physics and technology, (ii) data analysis and interpretation, (iii) large number of pulse sequences and parameters to choose from, (iv) challenges from the inherent cardiac and respiratory motion, and (v) duration of examination. The recent hype around artificial intelligence algorithms designed to overcome these hurdles has raised new questions around the reliability, accuracy, and stability of this technology. Therefore, to help shape the future of CMR, it is essential to bridge the gap between theory and practice, and thus, to promote a bridge of scientific knowledge between the research and clinical communities by improving (maintaining or updating) their knowledge of CMR technical principles and clinical applications.

This review provides an overview of five essential aspects of CMR which have been covered separately in-depth in other review papers (2–11). We address: (1) data acquisition sequences and common artifacts, (2) clinical applications, (3) clinical examination protocols, (4) image acceleration, reconstruction, and motion handling, (5) artificial intelligence-assisted reconstruction and analysis. In addition, this review provides hands-on tutorials and videos that can be found at [ismrm-mit-cmr.github.io](https://ismrm-mit-cmr.github.io). More specifically, Section The Physics Behind Cardiovascular MR describes the key physical principles of CMR, most common pulse sequences and preparation pulses, and the physics behind the most common artifacts. Section Clinical Cardiovascular MR: What do we See and Why do we Need it? covers the clinical application of CMR in the diagnosis of a spectrum of cardiovascular diseases. Section Clinical Cardiovascular MR: How Should we Perform the Examination describes how to complete a comprehensive examination and deal with challenging patients. Section CMR Image Quality: No Free Lunch provides an overview of scan acceleration acquisition and image reconstruction methods while also describing current solutions to overcome challenges from cardiac and respiratory motion. Finally, Section Artificial Intelligence for Cardiovascular MR describes machine learning methods used for automated quantitative analysis of CMR data.

## THE PHYSICS BEHIND CARDIOVASCULAR MR

In this section we aim to provide a brief overview of the physical principles and basic mathematical concepts behind magnetic resonance imaging (MRI) targeted to create the necessary background to understand modern CMR methods. This section will give an overview of the physics of nuclear magnetic resonance and relaxation, essential for describing the concepts behind image formation and the k-space formalism. Furthermore, basic building blocks of MRI are introduced, and common cardiac MR sequences are described.

### Magnetization Formation and Dynamics

MRI is based on a magnetic property that is intrinsic to certain nuclei, some of which can be found all throughout the human body. Nuclei [and (sub)atomic particles] possess an intrinsic quantum mechanical property called spin. Mathematically the spin can be described as the angular momentum of a spinning sphere. As a quantum mechanical quantity, however, the spin can only have a discrete set of states. By convention, the number of spin states are described according to the spin quantum number  $S$  with integer or half-integer values, giving rise to  $2S + 1$  different spin states. In MRI, the nucleus of greatest importance can be found in hydrogen atoms ( $^1\text{H}$ ): It comprises only a single proton with  $S = \frac{1}{2}$  and, thus, two spin states. These are commonly denoted as  $+\frac{1}{2}$  (“spin-up”) and  $-\frac{1}{2}$  (“spin-down”). Due to the classical relationship between angular momentum and magnetic moment of a rotating charged particle, the spin  $S$  is always associated with a magnetic moment  $\mu$  via the particle-specific gyromagnetic ratio  $\gamma$  ([rad/sT]):

$$\mu = \gamma S. \quad (1)$$

In a proton ensemble the magnetic moments of the nuclei are randomly orientated unless an external magnetic field  $B_0$  is applied. In this case, all particles will align depending on their magnetic moment either parallel (“spin-up”) or anti-parallel (“spin-down”) to the applied field. Now, spins parallel to the magnetic field are in a lower energy state compared with those in the opposite direction. Hence, the energy levels of the spin states are separated by  $\Delta E = \gamma \hbar B_0$ , with reduced Planck constant  $\hbar$ . This is also known as the Zeeman effect. Due to the angular momentum, the magnetic moment is also associated with a precession around  $\vec{B}_0$ . The rotational frequency of this precession is called the Larmor frequency  $\omega_L$ :

$$\omega_L = \gamma B_0 \quad (2)$$

For clinical MRI field strengths (0.5T–7T), this frequency is usually found in the radio frequency (RF) range. At thermal equilibrium, there is a slight excess of protons in the “spin-up” state due to its lower energy. Thus, the net magnetization  $\vec{M}$  averaged over all protons will be oriented along and precess around  $\vec{B}_0$ . Following the correspondence principle, this net magnetization  $\vec{M}$  and its precession motion can be described with classical mechanics, where the precession dynamics

resemble those of a spinning top. The net magnetization  $\vec{M}$  can be perturbed if protons are excited from the thermal equilibrium. In the analogy of the spinning top, this would mean tilting its rotation axis to the side. To achieve this, a so-called RF pulse that produces a resonant magnetic field  $\vec{B}_1$  oscillating at  $\omega_L$  needs to be applied. During this RF pulse, energy will be deposited in the spin system and some of the protons will flip to the “spin-down” state. Depending on the duration and strength of the RF pulse, the direction of  $\vec{M}$  progressively tips away from  $\vec{B}_0$  leading to a transverse component perpendicular to  $\vec{B}_0$ . Thereby, the polar angle  $\alpha$  between  $\vec{M}$  and  $\vec{B}_0$  is referred to as flip angle. Assuming that the initial magnetic field  $\vec{B}_0$  is along the  $z$ -axis, then the transverse and longitudinal parts of  $\vec{M}$  are denoted as  $\vec{M}_{xy}$  and  $\vec{M}_z$ , respectively. The above-described phenomenon is called nuclear magnetic resonance and gives MR imaging its name as the underlying physical principle.

## MR Signal and Relaxation: Time to Relax

The precession of  $\vec{M}$  leads to an oscillating magnetic field. We can picture the precessing magnetization as a rotating bar magnet in classical mechanics. This can be detected using a nearby coil where the time-varying magnetic flux induces a measurable electric current via the Faraday-Lenz principle. After the RF pulse has been turned off, the net magnetization continues to precess around  $\vec{B}_0$ . However, over time, the energy transferred to the system dissipates and the magnetization recovers to the thermal equilibrium state  $\vec{M}_0$ . This process is known as longitudinal relaxation and can be described by an exponential growth function with characteristic time constant  $T_1$ :

$$M_z(t) = M_z(0) - (M_z(0) - M_{z,0}) e^{-\frac{t}{T_1}}. \quad (3)$$

Here,  $M_z(0) = M_z(t = 0)$  is the flip angle dependent initial magnetization, and  $M_{z,0}$  the longitudinal magnetization at thermal equilibrium.

Besides the regrowth of  $\vec{M}_z$ , the transverse magnetization is subject to an additional relaxation process: the transverse component  $\vec{M}_{xy}$  is only preserved if all spins precess with the same frequency, i.e., point to the same direction. But, due to differences in the microscopic environment, each spin experiences slightly different magnetic fields. As a result, individual spins precess with slightly different frequencies. Over time, this leads to a dephasing of the spins and to a decrease of  $\vec{M}_{xy}$ . This is referred to as transverse relaxation and can be modeled by an exponential decay with characteristic decay time  $T_2$ :

$$M_{xy}(t) = M_{xy,0} e^{-\frac{t}{T_2}}, \quad (4)$$

where  $M_{xy,0}$  describes the transverse magnetization after excitation. In addition, inhomogeneity of the main magnetic field ( $\Delta B_{0,i}$ ) accelerates dephasing and leads to an effective decay time denoted as  $T_2^* \cdot \frac{1}{T_2^*} = \frac{1}{T_2} + \gamma \Delta B_{0,i}$ . Thus, the actually observed decay time  $T_2^*$  is always equal to or shorter than  $T_2$  and usually shorter than  $T_1$ . Both relaxation processes are influenced by the

atomic and molecular environment of the proton spins, such as type, size, and motion of the particles. Consequently, different tissue types or pathological tissue changes characteristically influence  $T_1$  and  $T_2$  times. In CMR, for example, the  $T_1/T_2$  times of myocardium and native blood at 3T are  $\sim 1,550/45$  ms (12, 13) and  $2,000/250$  ms (12, 14), respectively. Together with the proton density, this contributes to the image contrast in MRI.

The above set of equations was first proposed by Felix Bloch to describe the temporal dynamics of  $\vec{M}$ , and has accordingly been named Bloch equations (15, 16). For the evolution of signal intensities, however, this model is less suitable as it requires solving the individual Bloch equations for all magnetization vectors. Instead, the so-called Extended Phase Graph (EPG) model has been proposed (8, 17–19), where signal dynamics can be expressed efficiently based on a rotation matrix formalism in the Fourier domain (see Sections k-space and View Planning and Image Acquisition).

## Image Acquisition: What Is the Position?

Having established the nuclear origin of the MR signal and how it can be manipulated by RF pulses, the next necessary step for image formation is to spatially localize the signal. This is achieved through spatially varying magnetic fields, the so-called gradients. As described in Equation (2), the precession frequency  $\omega_L$  of a spin is a function of the magnetic field. Thus, by making the magnetic field a function of the location, spins at different spatial locations will have different resonance frequencies. Although various gradient forms can be applied, linear gradients have proven to be the most useful and, thus, will be assumed in the following description. While a linear gradient field is turned on,  $\omega_L$  becomes a function of the spin position  $\vec{r}$  and the field gradient  $\vec{G} = \nabla \vec{B}$ :

$$\omega_L(\vec{r}) = \gamma \vec{G} \cdot \vec{r}. \quad (5)$$

This principle can be used both to select imaging slices within the body as well as to encode positions in-plane within the slice. For simplicity, we will further assume that the imaging slice is in the transverse  $xy$ -plane. Note, however, that arbitrary acquisition angles can be achieved by using a combination of the  $x$ -,  $y$ -, and  $z$ -gradients for the encoding described below.

### Slice Selection (SS)

In slice selection, an additional spatially varying magnetic field gradient  $\vec{G}_z$  can be applied such that the field strength varies along the  $z$ -axis. Thus, the Larmor frequencies of spins will vary along this axis too:  $\omega_L = \gamma (B_0 + G_z z)$ . While the additional gradient field is turned on, spins in different  $xy$ -planes precess with different frequencies, while spins within the same plane all precess with frequency  $\omega_L$ . If the excitation RF pulse is chosen to have just the right frequency bandwidth, only spins in the corresponding  $xy$ -plane are excited. Accordingly, a transverse magnetization will only be created in those.

### In-plane Phase Encoding (PE)

After selecting a two-dimensional (2D) slice, the signal needs to be located within the slice. A phase encoding gradient  $\vec{G}_y$

along the  $y$ -axis is temporarily applied before the readout. During the presence of  $\vec{G}_y$ , spins along the gradient axis precess with different frequencies. After  $\vec{G}_y$  has been turned off, the spins will have accumulated different phases, pointing in different directions, but continue to precess with the same frequency. For one gradient strength, only one phase shift can be achieved. Therefore, multiple PE steps are necessary, which primarily determines the overall scan time. In order to acquire a three-dimensional (3D) volume, a second PE gradient along the slice-selection axis can be applied in the same stepwise manner.

### In-plane Frequency Encoding (FE)

To account for the remaining spatial direction, a gradient  $\vec{G}_x$  is applied, such that spins along the  $x$ -axis will precess with linearly increasing frequencies. Upon Fourier transforming the signal, each obtained frequency can thereby be connected to a position/pixel on the selected axis, usually the  $x$ -axis.

### K-Space

In the presence of linear gradient fields, the MR signal can be conveniently expressed with the so-called k-space formalism. If we consider the precession of  $\vec{M}_{xy}$  in the transverse plane, it can be described as:

$$M_{xy}(t, \vec{r}) = e^{-i\omega t} M_{xy,0}(\vec{r}) \quad (6)$$

with precession frequency  $\omega = \gamma B(\vec{r}) = \gamma (B_0 + \vec{G}(\vec{r}) \cdot \vec{r})$  [Equations (2, 5)]. Given that the acquired signal is the sum of the magnetization of all spins in the imaging volume, it can be described as follows:

$$S(t) \propto e^{-i\gamma B_0 t} \int e^{-i\gamma \vec{G}(\vec{r}) \cdot \vec{r}} M_{xy,0}(\vec{r}) d\vec{r}. \quad (7)$$

The gradient related frequency contribution can be written in terms of the gradient strengths  $G_x$ ,  $G_y$  and  $G_z$ :

$$\begin{aligned} \gamma \vec{G}(\vec{r}) \cdot \vec{r} t &= \gamma (G_x x + G_y y + G_z z) t \\ &= k_x x + k_y y + k_z z \end{aligned} \quad (8)$$

with the spatial frequencies  $k_x$ ,  $k_y$ , and  $k_z$ . If motion is considered,  $\vec{r}$  (spin position) becomes a function of time  $\vec{r}(t)$ . Furthermore, each receiving coil  $j$ , i.e., each receiving channel, has a specific sensitivity  $c_j(\vec{r})$  signal from different spatial points. Combining these with the previous equation yields

$$S_j(t) \propto e^{-i\gamma B_0 t} \iiint e^{-i(k_x x + k_y y + k_z z)} c_j(\vec{r}) M_{xy,0}(\vec{r}) dx dy dz \quad (9)$$

Equation (9) shows that the measured signal in time domain and the magnetization in spatial domain are connected via Fourier transformation. As a consequence of this relation, the spatial frequency ( $k_{xy}$ ) and distance ( $\Delta k_{xy}$ ) of k-space points are associated with image resolution and size (field-of-view, FOV):

$$\text{FOV}_{x/y} = \frac{1}{\Delta k_{x/y}} \text{ and } \frac{\Delta x}{y} = \frac{1}{k_{x/y}}. \quad (10)$$

Image acquisition methods can be distinguished by the proportion of the k-space acquired at once: In so-called single-shot sequences all k-space points are sampled in one acquisition, while in segmented methods the k-space is acquired in subsets during multiple repetitions. The overall scan time is, thus, primarily determined by the number of acquired points in the k-space. In this regard, subsampling techniques offer ways to accelerate image acquisition as described in Section Fast CMR: Speeding up Imaging by Acquiring Less Data.

So far, the MR signal has been treated as a continuous function in both space and time. Actual image acquisition, however, is a discretized process characterized by the data sampling rate and image resolution. Hence, the signal/forward model in Equation (9) can be discretized as:

$$\sigma_j = E_j \vec{\rho} + \vec{\eta}, \quad (11)$$

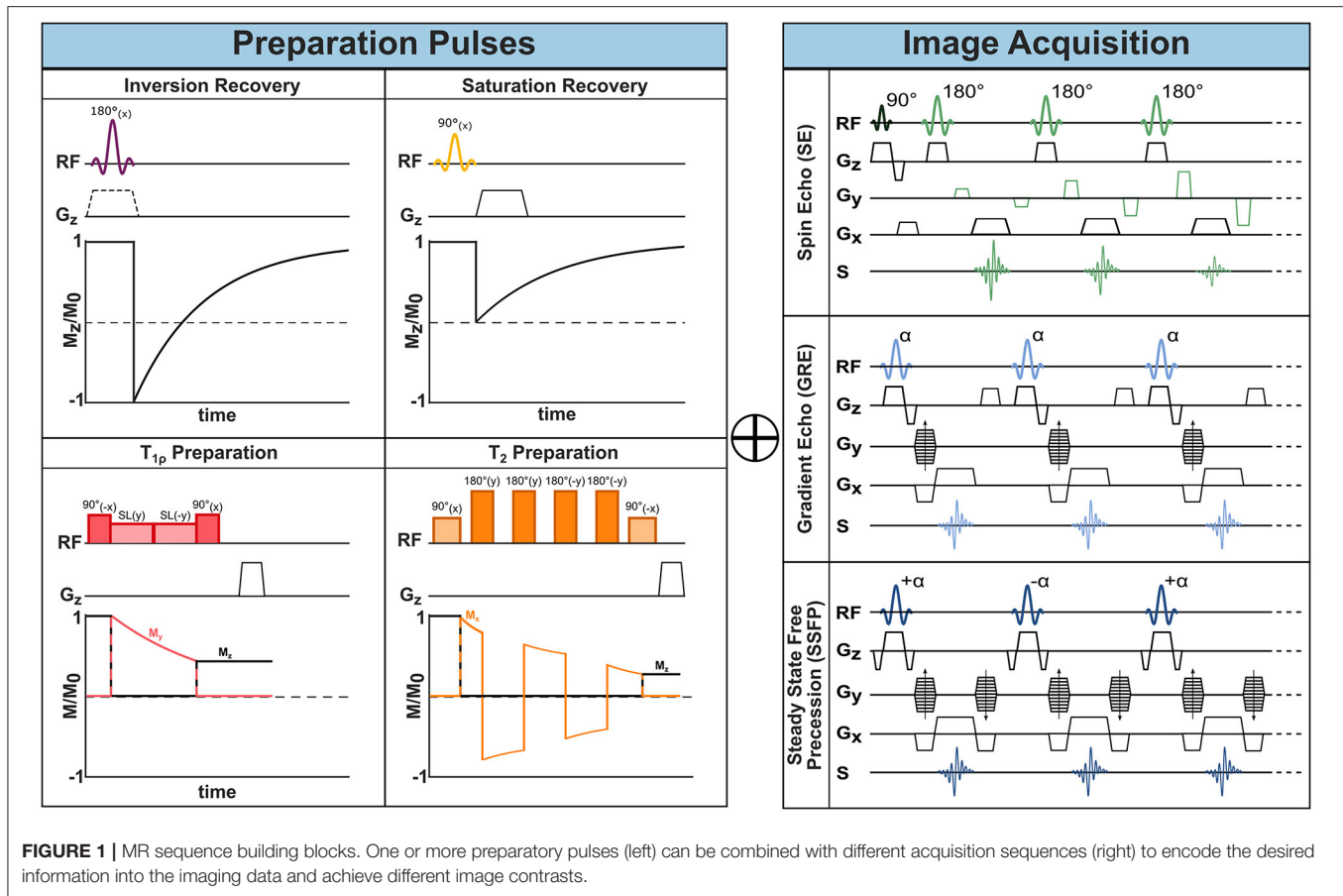
with encoding matrix  $E_j$  for coil  $j$ , initial transverse magnetization  $\vec{\rho}$ , and thermal noise  $\vec{\eta}$  (20). At time point  $\kappa$  and grid point  $\lambda$ ,  $E_j$  is given by  $E_{j\kappa,\lambda} = c_j(\vec{r}) e^{i\Phi(\vec{r}_{\lambda,t_\kappa})}$ . Neglecting relaxation, the phase factor  $\Phi(\vec{r}_{\lambda,t_\kappa})$  accounts for phase accumulation due to time-varying magnetic fields (see Sections Handling motion and Motion Correction).

### Sequence Building Blocks: Time and Order Are Key

By manipulating the timing and strength of RF-pulses and gradients, a plethora of MR sequences can be constructed. Different pulse sequences differ in their acquisition speed, encoded image information, or to which degree image contrast is affected by differences in proton density,  $T_1$ , or  $T_2^*$ , or other properties. CMR sequences are typically described by components for actual image acquisition and components for preparing the magnetization. These elements can be understood as building blocks of MRI sequences. The schematic design of the most common building blocks is shown in **Figure 1**.

### Image Acquisition Methods: Get What You Want Spin Echo

As described in the previous section, after RF excitation the net magnetization is subject to  $T_2^*$  relaxation. Fortunately, part of the dephasing of the transverse magnetization can be recovered with a so-called spin-echo (SE) sequence. In this sequence a second RF pulse is applied, where the simplest form comprises a  $90^\circ$  excitation and  $180^\circ$  refocusing pulse. After the first excitation, the spins dephase and fan out in the transverse  $xy$ -plane. Dephasing caused by temporally invariant field inhomogeneities, however, can be reversed via the second refocusing pulse (21). Its effect is often described as a pancake-flip: The fan of spins is flipped by  $180^\circ$  around the  $x$ - or  $y$ -axis, such that the faster spins now move toward instead of away from the slower rotating spins. After a so-called echo time TE, corresponding to twice the time between the two RF pulses, all dephasing caused by static inhomogeneities is rephased and an echo of the signal is created, as depicted in **Figure 1**. This gives the name to the SE sequence. Consequently,



the contrast in SE, is driven by the  $T_2$  time, which captures the residual dephasing caused by temporally variable factors, such as spin-spin interaction.

### Spoiled Gradient Echo

As opposed to SE, the so-called gradient echo (GRE) sequences retain not the transverse but the longitudinal magnetization. They typically require only one RF excitation pulse after which the frequency encoding gradient is applied (see **Figure 1**). In GRE, however, the positive FE gradient lobe is preceded by an additional negative lobe.

When the areas of the positive and negative lobe are equal, the initially evoked dephasing of spins is reverted—except for  $T_2^*$  decay. This creates a signal which is referred to as a gradient echo and gives name to the GRE sequence (22). In the so-called spoiled GRE (spGRE), remaining transverse magnetization is destroyed at the end of each TR cycle. This can be achieved with strong gradients at the end of the TR and results in  $T_1$  weighted imaging (23). As no additional RF pulses are required, shorter TE and TRs can be achieved in GRE compared to SE allowing for faster image acquisition. In GRE, the echo signal is subject to  $T_2^*$  decay as no rephasing of field inhomogeneities is achieved. Therefore, GRE sequences are less robust in the presence of field inhomogeneities.

### Balanced Steady-State Free Precession

A third common image acquisition sequence in CMR is the so-called Balanced Steady-State Free Precession (bSSFP). It can be understood as a hybrid between SE and GRE. Starting from a GRE sequence, a train of RF pulses is applied with very short TR ( $\ll T_2$ ) such that the magnetization never fully recovers between two consecutive RF pulses and a non-zero net magnetization is present at the next RF pulse. This residual magnetization contributes to the signal of the following TR. Characteristically for bSSFP, the flip angles are alternated every TR between  $+\alpha$  and  $-\alpha$  causing the net magnetization to flip around the  $z$ -axis between TRs (24, 25). This further means that each RF pulse has both an excitation and refocusing effect on the spins and explains the SE nature of bSSFP sequences. For effective refocusing of the magnetization, the gradient moments on all three axes (SS, FE, PE) need to be zero at each TR. This means that the areas of positive and negative gradient lobes on each axis must be equal, as shown in **Figure 1**, which is referred to as balanced gradients. The alternating magnetization progresses through a transient state and after a certain number of TR cycles  $\vec{M}$  reaches a steady state, that is a stationary amplitude. For  $TR \ll T_2$  the contrast in bSSFP sequences is determined by the  $T_2/T_1$  ratio (24). The main advantage of bSSFP lies in the improved signal to noise ratio (SNR) compared with spGRE, due to the recycled transverse magnetization. However, the scheme is

highly sensitive to off-resonances making it a less common choice for high field strength and rarely useful for ultra-high fields (25).

## Preparation Pulses: Be Prepared for the Changes

### Inversion Pulses

So-called inversion pulses, are  $180^\circ$  RF pulses which can be applied before image acquisition in order to flip the initial magnetization along the  $B_0$  axis (26). During the time between inversion and the first imaging RF pulse (inversion time, TI), the longitudinal magnetization recovers along the  $B_0$  axis toward its equilibrium state as depicted in **Figure 1**. At image acquisition, the degree to which  $\vec{M}$  has recovered determines the image contrast and, thus, induces  $T_1$  weighting. This enhances the image contrast based on  $T_1$  properties, which is of interest in many imaging applications. By adjusting TI, imaging can also be timed to the point when the magnetization of specific tissues is crossing the zero point, leading to effective signal suppression (26). For instance, in double inversion black blood imaging (27), a global and slice-selective inversion pulse are applied immediately one after the other such that only the blood outside of the imaging slice is inverted. With an appropriate TI, the signal of blood flowing into the slice can be nulled at image acquisition.

### Saturation Pulses

Intentionally suppressing tissue signal can also be achieved through so-called saturation pulses. These RF pulses flip the magnetization to the transversal plane. Subsequent spoiler gradients dephase the magnetization, thereby nulling the signal from the “saturated” spins. The subsequent recovery of longitudinal magnetization is shown in **Figure 1**. Saturation pulses can be made spatially selective, such that regions in or outside of the image are canceled out. For instance, artifacts due to through-slice flow can be reduced by applying a saturation pulse upstream, parallel to the imaging slice. Furthermore, saturation pulses can be made selective to specific chemical species by adjusting the resonance frequency. The most common example is fat saturation, where RF pulses with carrier frequencies specific to  $\omega_L$  of fat are applied close to the imaging sequence such that only fat but not water signal is nulled. Creating uniform saturation with common rectangular RF pulses is hindered by their high sensitivity to  $B_0$  and  $B_1$  inhomogeneities. To overcome this limit, adiabatic saturation modules—such as composite (28) or  $B_1$  insensitive rotation (BIR) pulses (29)—have been proposed.

### $T_2$ Preparation

$T_2$  contrast can be induced using the so-called  $T_2$  preparation pulses (30, 31). In a  $T_2$  preparation, a first  $90^\circ$  excitation pulse is followed by a series of refocusing pulses and, finally, by a  $90^\circ$  flip-back pulse. To induce robust refocusing, the refocusing pulses are separated by a  $2\tau$  interval, whereas the interval between the  $90^\circ$  pulses and the refocusing pulses is equal to  $\tau$ . The total  $T_2$  preparation time is varied to achieve different echo times. During this time, the refocusing pulses compensate for  $T_2^*$ -decay, resulting in a transverse magnetization decay effectively characterized by the  $T_2$ . The final  $90^\circ$  flip-back pulse brings the

remaining transverse magnetization back to the z-axis, encoding  $T_2$  contrast in the longitudinal magnetization, which is then imaged during acquisition. Several strategies, such as phase cycling following Malcolm Levitt (MLEV) schemes or using composite pulses, are employed in order to make  $T_2$  preparations more robust to field inhomogeneities (32, 33).

### $T_{1\rho}$

The relaxation constant in the rotating frame of reference,  $T_{1\rho}$ , is an additional property of tissues, besides  $T_1$  and  $T_2$  times.  $T_{1\rho}$  contrast can be achieved through spin-lock preparations. A spin-lock module consists of a  $90^\circ$  tip-down pulse followed by a continuous wave RF pulse applied for a certain time  $\tau_{SL}$ . During this time the magnetization is locked on the spin-lock axis, and it relaxes back to its equilibrium value following an exponential  $T_{1\rho}$  decay. Finally, a  $90^\circ$  tip-up pulse is applied after the spin-lock to restore longitudinal magnetization. Spin-lock pulses show high susceptibility to field inhomogeneities. Several compensated schemes, as well as adiabatic spin-lock modules, have been proposed to make  $T_{1\rho}$  preparation more robust to  $B_0$  and  $B_1^+$  variability (34–36).

## Common CMR Sequences: What Are They Made of

The sequence building blocks introduced in the previous sub-sections can be combined to design tailored sequences to assess, for example, cardiac function and viability. These sequences represent powerful tools for the non-invasive characterization of congenital or acquired cardiovascular diseases, including ischemia, valvular diseases and ischemic and non-ischemic cardiomyopathies, as described in Section Clinical Cardiovascular MR: What do we See and Why do we Need it?. Here, we will discuss the physics principles governing the main CMR sequences and introduce some emerging techniques.

### Cine bSSFP

Cardiac function is commonly assessed using bSSFP sequences in cine mode. The structure of bSSFP sequences, described in Section Sequence Building Blocks: Time and Order are Key, allows very short TR values to be achieved and increasing the number of k-space lines acquired in a single heartbeat. At the same time, bSSFP sequences maintain high intrinsic myocardial/blood contrast (37). These characteristics enable the fast acquisition of a single slice across multiple cardiac phases (typically 10–30 phases, also referred to as *frames*). This allows the reconstruction of movies of the beating heart. To achieve good spatial resolution for every frame, the acquisition of each frame is divided among different cardiac cycles, using the so-called segmented acquisition (see Section Handling Motion). During each heartbeat, in fact, only a limited number of k-space lines (or a *segment*) is acquired for each cardiac phase. Therefore, several heartbeats are necessary to acquire all the k-space segments. The acquired images are then assigned to the corresponding heart phases using retrospective gating (see Section Handling Motion). Full heart coverage is achieved by repeating the acquisition of each cine image set for different locations and orientations.

## Late Gadolinium Enhancement CMR

Cardiac viability studies traditionally rely on the use of gadolinium-based contrast agents (see Section Ischemic Heart Disease). These cause enhancement of tissue contrast, with respect to native  $T_1$  contrast. Gadolinium-based contrast agents have the effect of shortening the  $T_1$  of both healthy and diseased myocardium, resulting in their enhancement right after injection. However, healthy and diseased tissues are characterized by different contrast wash-out times: at a certain time point after injection, gadolinium has largely washed out of healthy tissues but is still retained in pathological areas where the extracellular space is expanded.

Late gadolinium enhancement (LGE) imaging is most commonly performed with an inversion-prepared segmented GRE sequence, where the inversion time (TI) is chosen so as to null the signal from healthy myocardium and maximize the contrast. This technique, however, shows high sensitivity to a correctly chosen TI, which is often based on a quick scout acquisition (38). Alternatively, Phase-Sensitive Inversion-Recovery (PSIR) sequences can be used to mitigate the effects of an incorrect TI on the resulting image contrast (39). Unlike traditional IR sequences, PSIR retains the information on the longitudinal magnetization polarity by incorporating the signal phase in the image reconstruction. The reconstructed PSIR images exhibit enhanced contrast between healthy and diseased myocardium. PSIR sequences, however, require the acquisition of a reference image, in addition to the inversion-recovery image, to extract the signal polarity. Nevertheless, the total scan time can be kept constant by acquiring the reference scans during the  $T_1$ -recovery heartbeats.

## First Pass Perfusion CMR

First pass perfusion CMR is becoming essential for measuring myocardial blood flow (MBF) and detecting myocardial ischemia (40), as described in Section Ischemic Heart Disease. In this technique, images are acquired during the first passing of a bolus of contrast agent, which increases the blood signal as described above. To this end, saturation prepared single-shot GRE (1.5T/3T) or bSSFP (1.5T) sequences in multiple slices are usually performed. In consequence, myocardial regions with low perfusion and, hence, low gadolinium concentration, will exhibit lower signal intensities. Moreover, if perfusion data is acquired under stress conditions, myocardial perfusion reserve can be obtained as the ratio of MBF at stress and at rest. Recent first pass perfusion methods can even yield quantitative MBF values by taking the temporal dynamics of the signal into account (41). In clinical practice, first pass and LGE images are often evaluated alongside each other. This provides additional information on cardiac viability.

## Quantitative CMR Techniques

The methods described in the previous section offer powerful tools for the qualitative assessment of cardiac function and viability. Nevertheless, new quantitative MRI biomarkers have recently been introduced, significantly enhancing the diagnostic capabilities of CMR. Here, we provide a general overview of these techniques.

## $T_1$ Mapping

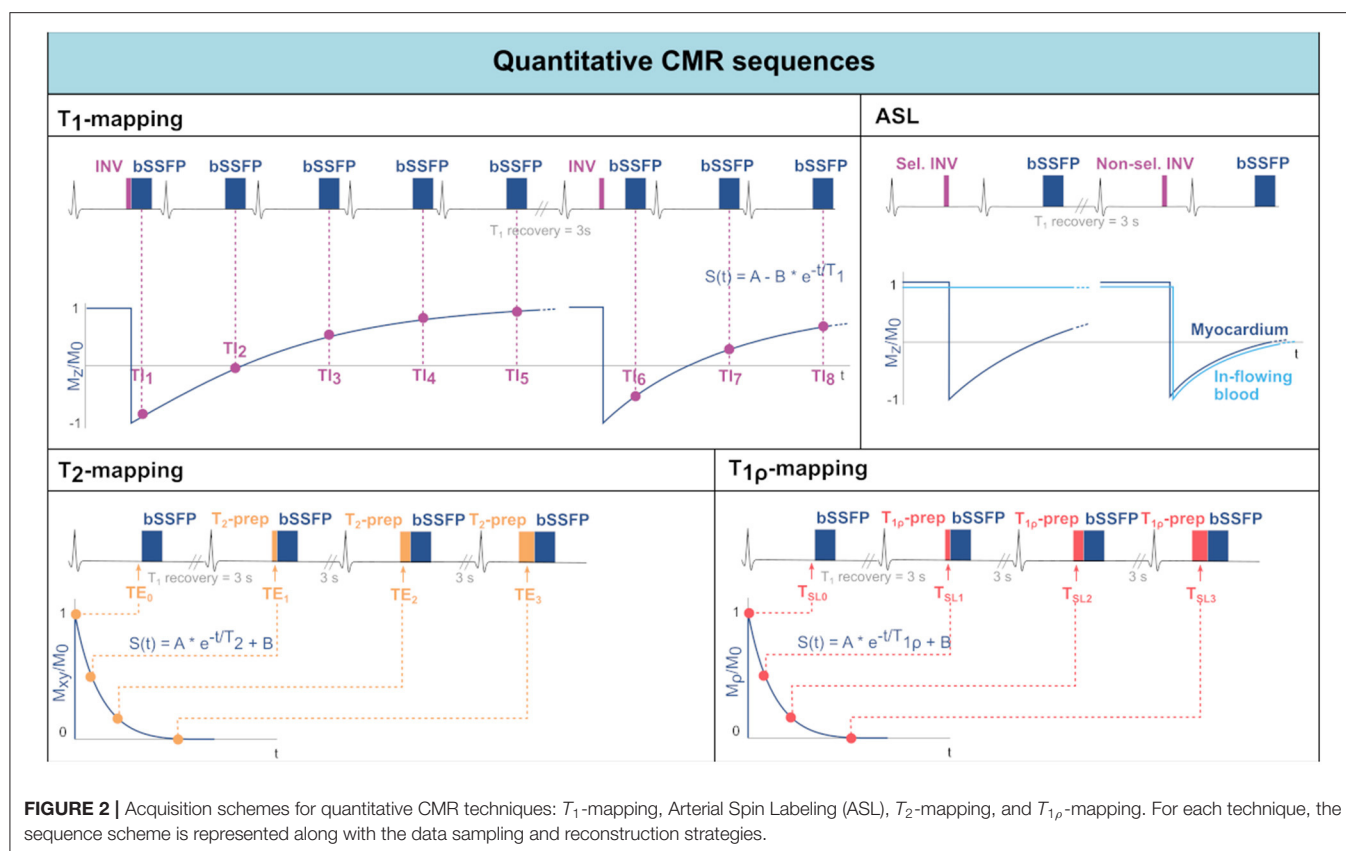
While  $T_1$ -weighted LGE images provide good qualitative characterization of focal myocardial infarction, it becomes less sensitive in the presence of diffuse fibrosis. An emerging alternative is the pixel-by-pixel quantification of  $T_1$  relaxation times (42). By obtaining a healthy reference range, several pathologies can be characterized without the need for healthy reference areas within the image.  $T_1$ -mapping can be performed with or without contrast injection. In the latter case, it is referred to as *native*  $T_1$ -mapping, as opposed to *post-contrast*  $T_1$ -mapping.  $T_1$ -mapping sequences are traditionally based on the Look-Locker technique, which consists in measuring the signal at multiple time points following an inversion preparation pulse (43) (see **Figure 2**). The collected data points, sampling the longitudinal magnetization recovery, are then fit to an exponential curve to derive the  $T_1$  estimates for each pixel. The most commonly used method for myocardial  $T_1$ -mapping is the Modified Look Locker Inversion recovery (MOLLI) sequence. Single-shot bSSFP images are each acquired in the end-diastole phase of consecutive heart beats following the application of an inversion pulse (44). A typical MOLLI pattern is the 5(3s)3 scheme (45), where the first inversion preparation is followed by 5 bSSFP acquisitions in separate heart beats, then 3 s of rest are inserted to allow for  $T_1$  recovery and, finally, a second inversion pulse is followed by the last 3 bSSFP measurements. MOLLI enables precise  $T_1$ -mapping in a single breath-hold.

Saturation recovery has been proposed as an alternative to inversion-recovery techniques. The SATuration recovery single-SHOT Acquisition (SASHA) sequence (46) acquires nine consecutive saturation-prepared single-shot bSSFP images, with variable saturation recovery times, in consecutive heart beats. Saturation recovery-based sequences have the advantages of not requiring rest periods and of acquiring each image independently. As a result, the  $T_1$ -mapping will be less susceptible to biases introduced by  $T_2$ , magnetization transfer, inversion pulse efficiency and magnetic field inhomogeneities, however at the expense of a reduced dynamic range and, thus, reduced precision. Hybrid inversion, saturation recovery sequences have also been proposed to mitigate some loss in precision (47).

## $T_2/T_2^*$ Mapping

$T_2$  relaxation time in the myocardium can be used as a marker for the presence of edema, as mentioned in Section Myocardial Inflammation.  $T_2$ -mapping is most often performed using a  $T_2$ -prepared bSSFP sequence (32), as shown in **Figure 2**. Commonly, the acquisition of each image is interleaved with rest periods to allow for  $T_1$  recovery. Alternatively,  $T_1$  recovery periods can be omitted introducing a saturation pulse at the end of the R wave in every heartbeat (48). The signal is sampled at different TEs by varying the echo time of the  $T_2$ -preparation. Acquired data are then fit to an exponential decay curve to estimate  $T_2$  values.

$T_2^*$ -mapping can also be performed and is used for the identification of iron accumulation (33, 49).  $T_2^*$ -mapping is commonly achieved with multi-echo GRE sequences, with a number of equally-spaced echo times. The resulting signal is then fit to an exponential decay curve to estimate  $T_2^*$  values.



### T<sub>1ρ</sub> Mapping

Myocardial  $T_{1\rho}$ -mapping has been recently introduced as a promising method for assessment of myocardial fibrosis without the need for exogenous contrast agents (50).  $T_{1\rho}$ -mapping is performed through spin-lock-prepared bSSFP sequences acquired for different spin-lock times and interleaved with  $T_1$  recovery periods (Figure 2). The sampled signal is then fit to an exponential decay curve to estimate the relaxation constant  $T_{1\rho}$ . The *in-vivo* applicability of  $T_{1\rho}$ -mapping, however, is hindered by the susceptibility to field inhomogeneities, especially at high field strengths.

### Cardiac Magnetic Resonance Fingerprinting

Obtaining  $T_1/T_2$  values with the techniques described above requires the acquisition and subsequent fit of multiple high-resolution images to exponential decay models. Unfortunately, high-resolution scans can be impractically long, particularly if multiple parameters need to be estimated. On the other hand, magnetic resonance fingerprinting (MRF) offers the possibility to simultaneously quantify multiple tissue parameters in a single scan (51). By varying sequence parameters such as TR and FA throughout the acquisition of highly undersampled images, information on tissue parameters is encoded in the temporal signal of each pixel. These so-called fingerprints are unique to the underlying tissue parameter configuration and can be compared to previously generated dictionaries to infer the model parameters of interest. The dictionary contains simulated

time signals for the chosen sequence parameters for a range of model parameter values. While MRF is well established for studies of the brain, non-static organs such as the heart pose challenges due to high respiratory and cardiac motion (52, 53). Therefore, cardiac MRF is performed in breath-held acquisitions which are ECG triggered to the quiescent, end-diastolic phase of the cardiac cycle (54). More recently, free-breathing cardiac MRF sequences have also been proposed (55). However, since the heart rate varies over time, multiple dictionaries which are simulated with the actual heart rate, are required. To further increase sensitivity to  $T_1/T_2$ , inversion or saturation pulses can be added (54). Although clinical validation is still in its early stages due to complex acquisition and reconstruction as well as relatively long breath-holds, cardiac MRF remains a promising technique for fast multi-parametric mapping.

### Blood Flow

Cardiovascular flow is typically measured through phase contrast methods that are sensitized to through-plane velocities (56). Flow velocity values are obtained by adding bipolar flow-encoding gradients in the slice-selection direction, after the excitation but before read-out. Flow encoding is based on the principle that moving spins, contrary to stationary spins, accumulate a net phase shift proportional to their velocity when subject to bipolar gradients. By toggling the bipolar gradients, the other contributions to the phase shift, such as those caused by field

inhomogeneities, can be neutralized and the blood flow velocity can be quantified.

2D-phase contrast imaging only resolves through-plane flow in 2 spatial dimensions. However, more recently, 4D-flow imaging has been proposed, which combines 3D spatial encoding with 3D directional velocity encoding (57, 58). As a result, 4D-flow MRI offers the possibility to visualize the temporal evolution of complex flow patterns in a 3D volume.

### Arterial Spin Labeling

CMR allows the assessment of myocardial perfusion (40). However, current techniques are based on first pass perfusion imaging which requires the use of contrast agents and, thus, limits the repeatability and clinical applicability. Arterial spin labeling (ASL), on the other hand, relies on endogenous contrast in the form of magnetically labeled blood. The general idea behind ASL is to acquire two images, one with and one without labeled blood. Subsequently, these images are subtracted to obtain the perfusion related signal only. For cardiac applications of ASL, the most commonly used tagging method is Flow-Alternating Inversion Recovery ASL (FAIR-ASL) (59, 60), depicted in **Figure 2**. In FAIR-ASL, spatially selective and non-selective inversion pulses are applied alternately: The selective pulse serves as a preparation for the control image. During image acquisition after the non-selective pulse, however, in-flowing inverted spins reduce the longitudinal magnetization proportionally to the perfusion rate. During reconstruction, the subtracted images are first normalized to the baseline intensity, i.e., an image without any preparation pulse. This difference is then multiplied with the inversion efficiency, the blood water-tissue partition coefficient, and an exponential factor accounting for  $T_1$ -decay to obtain the MBF (61).

### Common CMR Artifacts: Obscured Reality

The complexity of cardiac anatomy, as well as the presence of respiratory motion, cardiac motion, and blood flow, constitute a unique set of challenges for CMR examinations. In this section we recount the most common artifacts in cardiac MR (**Figure 3**) and strategies for mitigating them (see Section CMR Image Quality: No Free Lunch). A comprehensive guide to cardiac MR artifacts can be found in Ferreira et al. (62).

Respiratory motion can cause inconsistencies between different segments of the acquisition. As a result, ghosting artifacts may appear on the reconstructed images. Two approaches are commonly used to avoid breathing-related artifacts: breath-holding and respiratory navigators (both will be described in Section Handling Motion). On the other hand, cardiac motion can cause blurring for long imaging blocks, when the acquisition window includes phases of rapid motion. This effect is commonly tackled by introducing cardiac triggering, which synchronizes the acquisition with the cardiac cycles. Choosing relatively long trigger delays from the R peak of the electrocardiogram (ECG) signal enables acquisition during quiescent cardiac phases, such as mid-diastole.

Blood flow can also be a cause of artifacts in CMR. As already discussed in the blood flow imaging paragraph of Section Quantitative CMR Techniques, motion-induced phase

shifts occur in presence of blood flow, corrupting the spatial phase encoding. Flow-compensated gradients can be employed to minimize these alterations, by nulling the higher-order gradient moments. For instance, 1st order flow compensation consists of nulling the gradients' 1st order moment, minimizing constant flow velocities contributions.

Aliasing artifacts are very common in MRI and specifically in CMR, where the strict time constraints often limit the FOV dimensions. These artifacts manifest as wrap-around ghosts, which can overlap to the anatomical structures under investigation. While aliasing in the frequency-encoding direction can be avoided through oversampling, this is not feasible in the phase encoding direction without increasing scan time. In this case, the FOV must be enlarged at the expense of lower resolution.

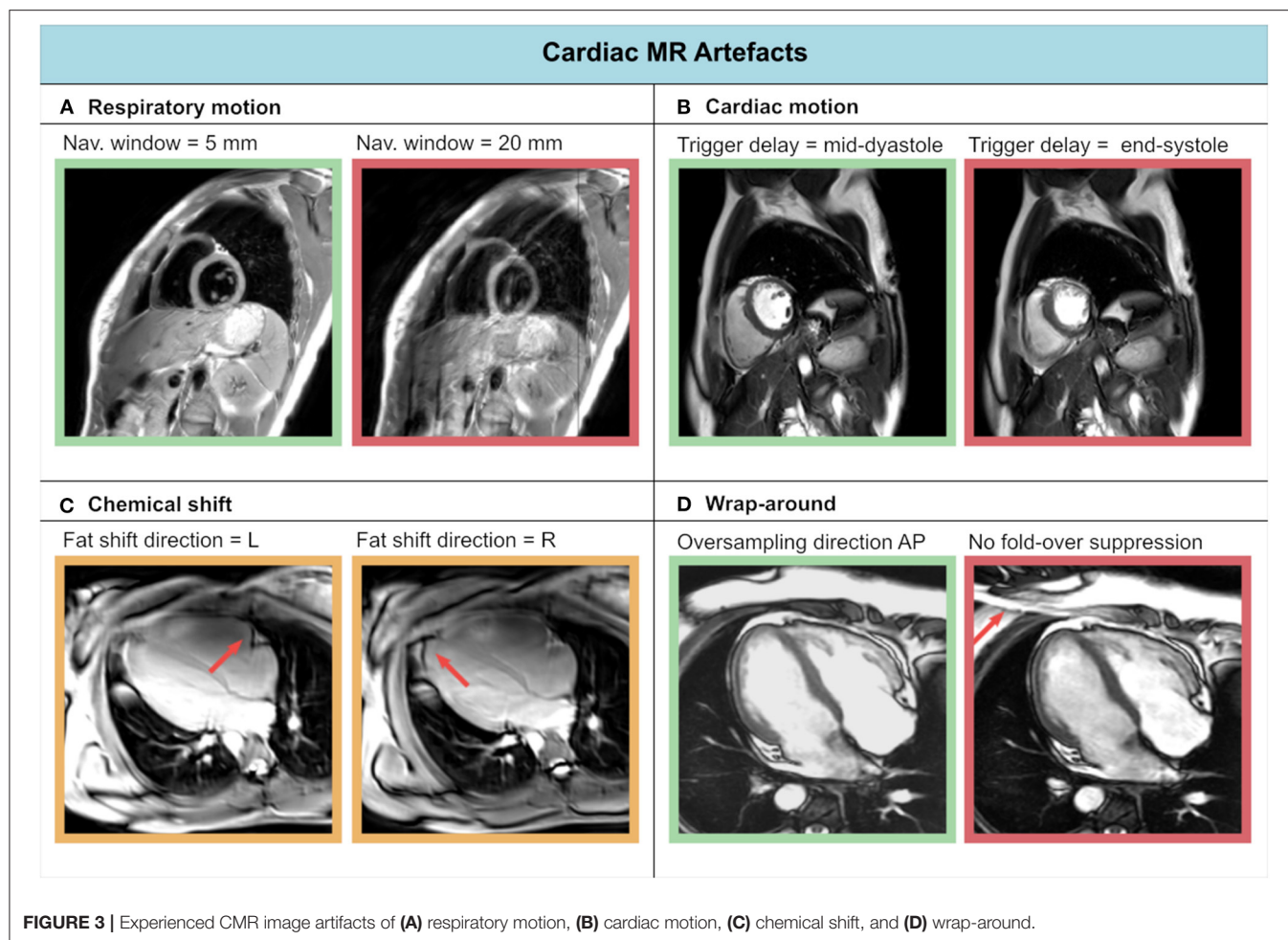
Finally, chemical shift artifacts can manifest in the presence of pericardial fat. These arise because of the different molecular environment of protons in fat and water, whose resonant frequencies differ by approximately 420 Hz (at 3T) as a result. This difference results in a misregistration of fat and water tissues along the frequency encoding direction. Chemical shift artifacts become more evident, for example, when changing the frequency encoding direction. They can be reduced by increasing the signal bandwidth, albeit at the cost of lower SNR.

## CLINICAL CARDIOVASCULAR MR: WHAT DO WE SEE AND WHY DO WE NEED IT?

This section will outline the contributions CMR can make within each of the major cardiovascular subspecialties and set the scene for the remaining sections in this manuscript which focus on image acquisition, reconstruction, and the burgeoning impact of artificial intelligence on all these areas. Where relevant, reference is made to international diagnosis and treatment guidelines and the levels of supporting evidence underpinning recommendations.

### Basic Principles and Advantages of CMR: What You See and What You Get

CMR is widely recognized as the gold-standard for the non-invasive quantification of left ventricular (LV) ejection fraction which remains a cornerstone parameter that guides decision making in various scenarios ranging from the diagnosis of heart failure to determining the need for primary prevention implantable cardioverter defibrillators (ICDs) and the timing of surgical intervention in patients with valvular heart disease (63, 64). For many of these applications, echocardiography remains a first-line investigation, but CMR is particularly valuable for evaluating cardiac structure and function in patients with poor acoustic windows. This is recognized in the recent European society of cardiology (ESC) heart failure guidelines as a class I indication for CMR (Class I: evidence and/or general agreement that a given treatment or procedure is beneficial, useful, or effective) with level of evidence C (consensus opinion of experts and/or small studies, retrospective studies, registries) (63). The ability to non-invasively acquire high spatial and



temporal resolution images in any plane using bSSFP sequences which have high intrinsic  $T_1$  and  $T_2$  contrast affords high endocardial definition enabling chamber volumes and function to be quantified with high accuracy and precision (65). This is achieved by acquiring a contiguous short axis stack parallel to the atrioventricular groove and planned with two and four chamber cine sequences (5, 66), see Section Plan Imaging Accurately and Avoid Common Mistakes.

A key feature of CMR is its ability to non-invasively characterize tissue by exploiting intrinsic differences in nuclear magnetic relaxation characteristics of hydrogen nuclei which are found in abundance in the human body in different chemical environments in the form of water but also bound in large macromolecules such as triglycerides and proteins (**Supplementary Figure 1**). This enables different anatomical structures and pathology to be readily appreciated and differentiated without the need for exogenous contrast. However, the administration of the latter, in the form of large macromolecular chelates of the paramagnetic element gadolinium, augments our ability to detect pathology even further by highlighting the presence of myocardial fibrosis, infiltration, or areas of infarction (67). Gadolinium contrast agents shorten  $T_1$  relaxation times in proportion to their local

concentration. As large positively charged macromolecules, they are unable to penetrate the intact cell membrane and so remain entirely extracellular. As such, in tissues where the extracellular space has been expanded by the presence of fibrosis or infiltrated by exogenous proteins such as for instance in cardiac amyloidosis, gadolinium can accumulate to higher local concentrations. If imaged  $\sim 10$  min after contrast administration using an appropriate inversion recovery prepared  $T_1$ -weighted sequence with an inversion time set to null the signal from healthy myocardium, such areas are illuminated as gadolinium washes out of healthy tissue but remains at higher concentrations in diseased areas, causing faster recovery of signal. Infarcted or non-viable areas of myocardium can be similarly delineated as they are rich in extracellular matrix and proteins, but cell-poor or in the case of acute myocardial injury, may be populated by necrotic cells with disrupted cell membranes (68). The LGE imaging technique (see Section Common CMR Sequences: What are They Made of) plays a pivotal role in phenotyping patients with heart failure, particularly differentiating patients with ischemic from non-ischemic heart failure (Class IIa: conflicting evidence and/or divergence of opinion about the usefulness/efficacy of the given treatment or procedure but weight of evidence/opinion

is in favor of usefulness or efficacy) with level of evidence C (63).

## Ischemic Heart Disease

In patients with ischemic heart disease, occlusion of an epicardial coronary artery tends to cause injury and necrosis of endocardial cells first as these are furthest away from the blood supply, evolving to a wavefront of necrosis that gradually spreads centrifugally toward the epicardium (**Figure 4A**). Areas of LGE extending from the sub-endocardium, particularly if they are regional or in a coronary distribution, denote areas of ischemic infarction. In contrast, non-ischemic pathologies such as dilated cardiomyopathy or myocarditis tend to be associated with LGE in an epicardial or mid-wall distribution, allowing ischemic and non-ischemic etiologies of heart failure to be readily distinguished (**Figure 4B**). CMR is regarded as a class I indication for evaluating acute chest pain or myocardial injury in patients with unobstructed coronary arteries (level of evidence B: moderate quality evidence from one or more well-designed, well-executed non-randomized studies, observational studies or registry studies or meta-analyses of such studies) (69). As well as being diagnostically valuable, it is increasingly being recognized that the presence and/or extent or pattern of LGE may have prognostic significance (70–74).

In patients with ischemic heart disease, the distribution of LGE can localize infarcts to specific coronary territories (**Figure 4A**), and the transmural extent can determine the likelihood of underlying myocardial viability (75). By imaging the first pass of contrast through the myocardium under conditions of vasodilator stress (typically achieved with adenosine or regadenoson), myocardial perfusion abnormalities may be identified which may signify myocardial ischemia (76). When the epicardial coronary arteries are unobstructed, contrast arrives synchronously and homogeneously in all supplied myocardial segments. However, where there is a hemodynamically significant stenosis in a given coronary artery, that vessel will already be maximally vasodilated at baseline. The administration of a vasodilator will thereby augment blood flow (and so the arrival of contrast) to unobstructed coronary arteries, allowing areas of hypoperfusion to be delineated by the delayed and reduced arrival of contrast to the already maximally dilated stenosed vessel (76). This technique can therefore be used to diagnose the presence of coronary disease (77) or where this is already known, determine the functional significance of a given stenosis identified using an anatomical imaging technique such as invasive coronary angiography or CT coronary angiography. As mentioned previously, this technique is frequently used in tandem with LGE imaging to assess for myocardial ischemia and viability and thereby determine the need for or to guide revascularization (76). Recent US chest pain guidelines now regard this as a class I indication for stress CMR (level of evidence B) (69). Advances in sequence design, image processing, and quantification techniques now enable myocardial blood flow to be measured at the voxel level with high in-plane spatial resolution (78–83). The latter allows microvascular dysfunction to be elucidated non-invasively (79, 84, 85) (**Figures 4C,D**), and for ischemic burden to be accurately calculated (81, 86).

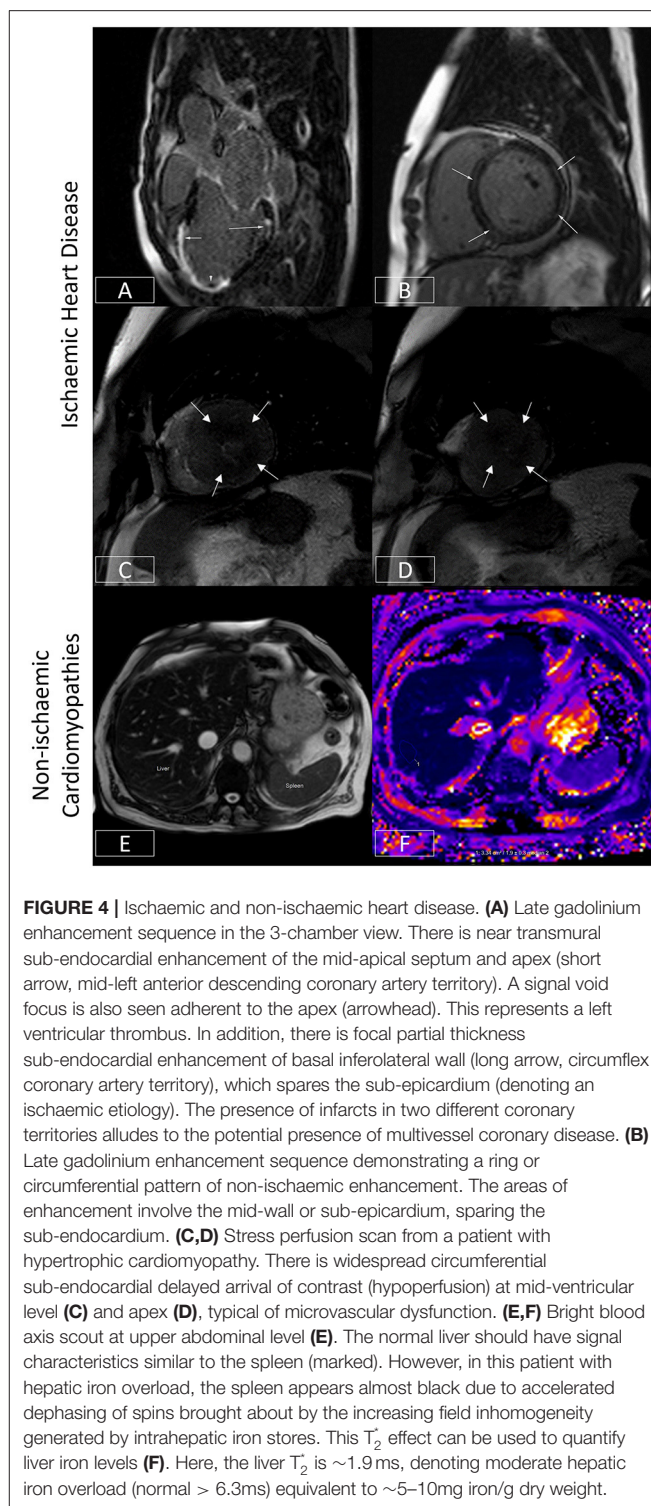
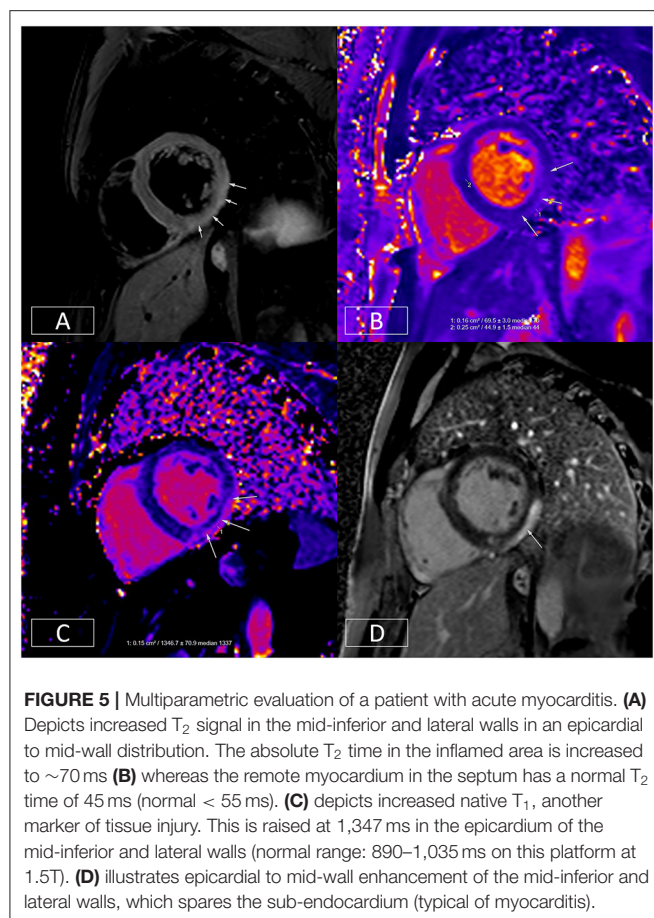


**FIGURE 4 |** Ischaemic and non-ischaemic heart disease. **(A)** Late gadolinium enhancement sequence in the 3-chamber view. There is near transmural sub-endocardial enhancement of the mid-apical septum and apex (short arrow, mid-left anterior descending coronary artery territory). A signal void focus is also seen adherent to the apex (arrowhead). This represents a left ventricular thrombus. In addition, there is focal partial thickness sub-endocardial enhancement of basal inferolateral wall (long arrow, circumflex coronary artery territory), which spares the sub-epicardium (denoting an ischaemic etiology). The presence of infarcts in two different coronary territories alludes to the potential presence of multivessel coronary disease. **(B)** Late gadolinium enhancement sequence demonstrating a ring or circumferential pattern of non-ischaemic enhancement. The areas of enhancement involve the mid-wall or sub-epicardium, sparing the sub-endocardium. **(C,D)** Stress perfusion scan from a patient with hypertrophic cardiomyopathy. There is widespread circumferential sub-endocardial delayed arrival of contrast (hypoperfusion) at mid-ventricular level **(C)** and apex **(D)**, typical of microvascular dysfunction. **(E,F)** Bright blood axis scout at upper abdominal level **(E)**. The normal liver should have signal characteristics similar to the spleen (marked). However, in this patient with hepatic iron overload, the spleen appears almost black due to accelerated dephasing of spins brought about by the increasing field inhomogeneity generated by intrahepatic iron stores. This  $T_2^*$  effect can be used to quantify liver iron levels **(F)**. Here, the liver  $T_2^*$  is  $\sim 1.9$  ms, denoting moderate hepatic iron overload (normal  $> 6.3$  ms) equivalent to  $\sim 5$ – $10$  mg iron/g dry weight.

Quantification techniques also appear to improve the ability to correctly identify multivessel coronary disease (87).

## Non-ischemic Cardiomyopathies

The ability to quantify tissue characteristics has enabled various MR relaxation parameters to be used as biomarkers for diagnosis



and to guide therapy (42, 88). The seminal example of this is the development of  $T_2^*$  imaging (**Figures 4E,F**), which has enabled non-invasive hepatic and myocardial iron quantification (49). By allowing the early diagnosis of iron overload cardiomyopathy and timely initiation and titration of chelation therapy, this has been credited with significantly reducing the risk of death from heart failure in patients with thalassemia (89). The development of  $T_1$  mapping techniques (see Section Quantitative CMR Techniques) has found applications in detecting interstitial fibrosis, and by measuring post-contrast  $T_1$  together with the knowledge of the patient's hematocrit, the estimation of extracellular volume fraction (ECV) has made it possible to track pathologies such as cardiac amyloidosis (42). This is of growing relevance as these conditions are increasingly amenable to novel therapeutics which can stabilize or even potentially partially reverse cardiac amyloid deposition (90). Thus, CMR is regarded as a class I indication for the evaluation of infiltrative disease and suspected iron overload (level of evidence C) (63).

CMR also plays a vital role in the evaluation of patients with heart failure or suspected non-ischemic heart muscle disease. It can be used as a gatekeeper for invasive coronary evaluation (91) but also to accurately evaluate areas of the heart that are difficult to clearly visualize by echocardiography such as the LV apex or the right ventricle. This can be invaluable for the

diagnosis of particularly the apical variants of hypertrophic cardiomyopathy (92) and arrhythmogenic right ventricular (RV) cardiomyopathy (93).

## Myocardial Inflammation

The ESC guidelines regard CMR as a class I indication (level of evidence C) for the evaluation of patients with suspected myocardial inflammation (63). Acute inflammatory processes and tissue injury can increase tissue water content and increase the mobility of tissue water protons (94). This can be exploited with  $T_2$ -weighted imaging techniques and quantitative mapping methodologies (see Section Quantitative CMR Techniques) to diagnose the presence and distribution of myocardial inflammation (**Figure 5**) (88, 94, 95). Myocarditis can be diagnosed when in the appropriate clinical context, there is evidence of tissue oedema and inflammation/injury on one  $T_2$ -based ( $T_2$ -weighted-imaging or  $T_2$ -maps) and one  $T_1$ -based criterion (native  $T_1$  map, LGE imaging, or ECV maps), respectively, in a non-ischemic distribution (96).

## Cardiac Electrophysiology

Within the sphere of cardiac electrophysiology, not only is CMR playing a vital role in the identification of patients at increased risk of arrhythmia (70, 72–74), but it is increasingly being used to plan invasive arrhythmia ablation procedures (97). Atrial fibrillation is the commonest sustained cardiac arrhythmia and an important cause of morbidity and mortality (98). In most patients, the arrhythmia is triggered by electrical activity from the pulmonary veins which can be treated by electrically isolating these through ablation (98). 3D-anatomical and fibrosis imaging sequences can help to define the number of pulmonary veins and the degree of fibrotic remodeling of the atrium which may influence procedural success (**Figure 6**) (99). For patients with malignant ventricular arrhythmias, identifying the precise origin of arrhythmic foci often requires prolonged and tedious pace-mapping of the electrical substrate increasing procedure times and thereby risk to patients (100). This can be considerably facilitated by pre-procedural CMR which can identify areas of scar tissue and help target electrical interrogation of the diseased myocardium (100).

## Congenital Heart Disease

CMR has also revolutionized the care of patients with congenital heart disease, which occurs at a frequency of 6–8 per 1,000 live births (101). Advances in care now mean that more patients are surviving to adulthood and so are forming an important cohort of patients who require regular clinical and imaging evaluation (101–103). The complexity of disease can range from minor anomalies such as a small restrictive ventricular septal defect through to patients with complex cyanotic heart disease with cardiac malformations that require often multiple complex surgeries to correct or palliate. The imaging assessment of such patients requires the ability to image in multiple planes, in 3D, and to quantify blood flow, particularly to diagnose the presence and severity of any intracardiac shunts (101, 103). Importantly, this is achieved without the need for any

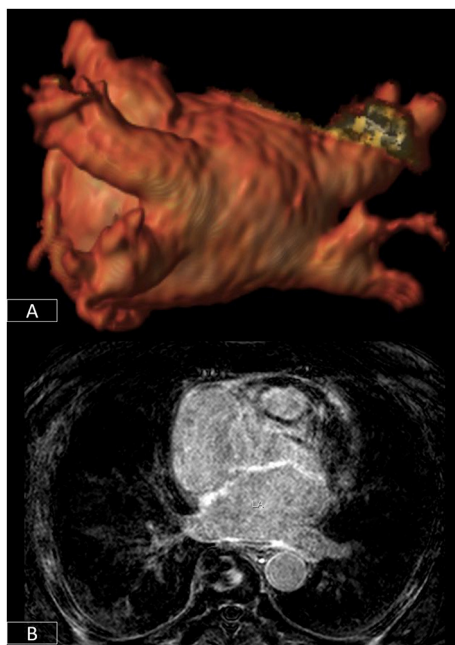


**FIGURE 6 |** 3D-segmentation of the left atrium depicting left atrial anatomy and four pulmonary veins and their tributaries (A). There is extensive fibrosis of the left atrial wall (B) on 3D late enhancement sequences which may reduce the likelihood of successful ablation.

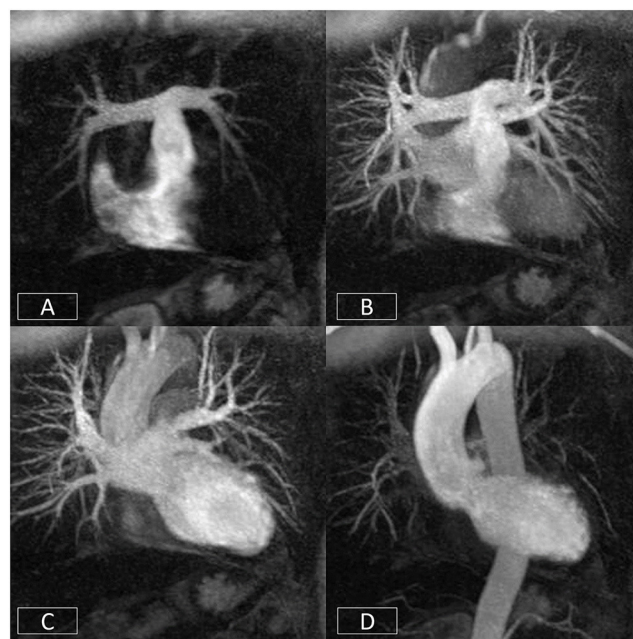


**FIGURE 7 |** Cardiovascular time resolved 3D-angiography. The bolus of contrast is imaged progressively as it passes from the right side of the heart (A) into the pulmonary arteries (B), left atrium/ventricle (C), and thoracic aorta (D). This obviates the need to precisely time the contrast volume and enables the rapid visualization of different parts of the circulation with a single bolus of contrast.

ionizing radiation (which would have a greater impact on this younger cohort of patients who need frequent serial imaging) and unfettered by limitations imposed by acoustic windows as echocardiography often is. This is particularly true for structures such as the right ventricle that are more challenging to image with echocardiography (104). The high accuracy and precision of the measurements of ventricular size and function as well as blood flow enable these parameters to be used to guide the timing for surgical intervention, for instance, pulmonary valve interventions in patients with repaired tetralogy of Fallot (103, 105). The broad utility of CMR in congenital heart disease has been recognized in recent international guidelines (106). The presence of RV scar detected by LGE-CMR has been highlighted as a risk factor for sudden cardiac death and its use for risk stratification is recommended as a class IIa indication (level of evidence C). These guidelines also recognize CMR with physical stress as a class I indication (level of evidence C) for the evaluation patients with coronary anomalies to confirm/exclude myocardial ischemia (106).

## Valvular Heart Disease

While Doppler echocardiography is rightly considered the modality of choice for the evaluation of patients with valvular heart disease, phase-contrast velocity mapping is particularly adept at quantifying regurgitant lesions such as aortic and pulmonary regurgitation (107). It can play a role in corroborating echo findings or in providing accurate

quantification where unfavorable echo windows preclude this, or jet eccentricity can result in underestimation of jet severity (Supplementary Figures 2, 3) (64, 108). As in many other spheres of cardiovascular medicine, an accurate quantification of ventricular ejection fraction may be vital in determining the timing of any intervention (109).

## Angiography and Vascular Disease

CMR also has the added advantage of enabling visualization of the aorta and great vessels which can often need intervention in patients with aortic valve disease, particularly if this is associated with aortopathy such as patients with bicuspid aortic valves. This can be achieved using time-resolved angiographic approaches (110), as well as with 3D-sequences acquired in free-breathing that can increasingly be combined with multiple tissue contrasts (111–113). The former can enable the visualization of multiple vascular beds and structures (systemic venous, pulmonary arterial and venous, and systemic arterial) with a single dose of contrast (Figure 7) (110). This has a range of applications from the evaluation of vascular disease itself to planning interventions.

Advances in rapid imaging techniques, catheter technology, and the development of interventional imaging suites now allows actual invasive procedures to be performed under MR-guidance (114, 115). This brings the principal benefit of minimizing the

need for X-ray fluoroscopy particularly in younger patients who require frequent serial evaluation.

There is also growing interest in leveraging the tissue characterization capabilities of CMR to evaluate coronary plaque characteristics (116, 117). Specifically,  $T_1$ -weighted non-contrast coronary imaging can be used to delineate the presence of methemoglobin, a marker of coronary thrombosis or intraplaque hemorrhage, which has been associated with vulnerable plaque morphology and angina severity (118).

## Cardiac Tumors

Another area where CMR has made significant indispensable contributions to patient care is the evaluation of cardiac tumors (119). While these are thankfully rare, the ability of CMR to provide full-spectrum non-invasive characterization can help to refine the diagnosis and, in many instances, can type specific lesions. Anatomical and cine sequences can localize a lesion and define its geometry and relationship with surrounding structures (119). Sequences with different  $T_1$  and  $T_2$  weighting with and without fat-saturation can be used to delineate tissue characteristics. Imaging of the tumor during the first pass of contrast can depict its vascularity and perfusion (120). Imaging in the early phase after contrast administration can differentiate thrombus from neoplasia or reveal the presence of superadded thrombosis. Imaging in the late phase can provide information on the contrast uptake characteristics of the lesion which again can be valuable in differential diagnosis (119, 120). Such data can increasingly be combined with fluorodeoxyglucose (FDG)-positron emission tomography (PET) and other radiotracer uptake data in hybrid CMR-PET imaging platforms to provide truly multimodal comprehensive evaluation that encompasses tumor metabolic activity (121).

In summary, CMR has found applications within every sphere of cardiovascular medicine and has often had a positive disruptive effect—improving diagnosis and in many cases, changing patient outcomes. In a single comprehensive study, it is now possible to assess and reliably quantify cardiovascular anatomy, function, tissue  $T_1$ ,  $T_2$ ,  $T_2^*$ , ECV, perfusion at stress and rest, late gadolinium enhancement, and blood flow. While many of the necessary sequences are ECG-gated and have been done with breath holding, recent advances now make it possible to acquire most data using free-breathing techniques making CMR more accessible and tolerable for patients with cardiovascular disease who often suffer from breathlessness (see Section Handling Motion). However, although the ability to acquire more and more data has grown over the years, the time available to scan patients (typically 1 h) and report the voluminous imaging data sets that are generated has not. This requires careful protocolling and efficient image acquisition to harness the true benefits of this technology in a value-conscious and efficient way (see Section Clinical Cardiovascular MR: How Should we Perform the Examination). Advances in the application of artificial intelligence to both image reconstruction and interpretation may help offset some of these challenges and are addressed in Section Artificial Intelligence for Cardiovascular MR.

## CLINICAL CARDIOVASCULAR MR: HOW SHOULD WE PERFORM THE EXAMINATION

As new imaging techniques are developed and the clinical applications of CMR expand, implementing efficient workflow practices has become increasingly important in clinical practice. To complete a comprehensive examination in a clinically acceptable timeframe with high quality imaging requires considerable forethought and planning.

Developing and applying a systematic approach to all aspects of the examination can save considerable scanner time, even if the operator is proficient in the placement of imaging planes. In this section, key areas essential to developing an efficient and structured approach to a CMR examination are outlined.

### Clinically-Tailored Protocols: Make It Right for Patients

The vast array of CMR imaging sequences now available has the potential to considerably extend the CMR examination to clinically unrealistic lengths. Therefore, it is important to approach CMR as a modality with a suite of standardized, clinically-targeted protocols rather than a single one-size-fits-all examination. Protocols should be developed to answer the clinical question with a focus on adding value. Resources are available (5) to guide the development of in-house clinical protocols, which can then be modified to suit patient-specific requirements. It is essential to review each patient's clinical history and previous imaging and tailor the protocol to answer the clinical question, focusing on providing the information only CMR can provide. Even reasonably fit patients can become fatigued from multiple breath holds. Removing any sequences from the examination that do not assist in making the diagnosis will increase efficiency and improve patient compliance.

### Template Protocols: Have Them Ready

Before creating comprehensive CMR protocols on the scanner, build a high quality clinically-appropriate template protocol for each of the basic pulse sequence types, e.g., cine bSSFP; phase contrast (PC) flow quantification imaging; dark blood  $T_2$  weighted fast spin echo imaging; and LGE imaging (see Sections Preparation Pulses: Be Prepared for the Changes and Common CMR Sequences: What Are They Made of).

In accordance with field strength and scanner capabilities, each template protocol should be created ensuring the scan times are as short as possible whilst maintaining appropriate spatial and temporal resolution, and without introducing artifacts from undersampling or cutting corners (see Section Common CMR Artifacts: Obscured Reality).

Once created, each pulse sequence template protocol can be used and modified to build plane-specific image acquisitions, for example, the 4-chamber or LV vertical long axis views.

This approach ensures consistency and standardization of image quality across the entire examination and clinical service.

## The Building Blocks of a Successful CMR Exam

Almost all CMR examinations will require the basic building blocks of LV and often RV function. All the basic cardiac planes are aligned relative to the heart and are specific to the patient's anatomy. Each plane is prescribed building on prior knowledge from previous acquisitions. Scanning efficiency can be significantly improved by giving careful thought to the order of acquisition of these basic building block sequences. The sequence order below has been planned to ensure that there is no downtime between acquisitions. All image planes required for planning have been acquired at least one acquisition ahead.

### Imaging Protocol for LV and RV Function

1. Three plane (axial, sagittal, coronal) localizer—centered on heart in three planes.
2. Axial non-cine bSSFP localizer—cover from aortic arch to the inferior border of the heart.
3. LV Vertical Long Axis (VLA) cine bSSFP localizer—use the axial bSSFP localizer to prescribe a single slice through the middle of the mitral valve to the LV apex.
4. Sagittal oblique Main Pulmonary Artery (MPA) cine bSSFP—prescribe one slice through the middle of the MPA and the RV outflow tract (RV OT) using the axial localizer.
5. LV short axis (SAX) single heartbeat multislice localizer—use the axial localizer and LV VLA localizer to prescribe a stack through the atrio-ventricular valve.
6. Coronal oblique MPA cine bSSFP—use Sagittal Oblique MPA to prescribe one slice through middle of MPA, Pulmonary Valve (PV) and RV OT.
7. 4-chamber cine bSSFP—use the basal slice of the LV SAX stack localizer to prescribe one slice through the center of the mitral and tricuspid valves. Cross reference to the LV VLA localizer to ensure the slice is through the center of the mitral valve and the LV apex.
8. LV 2-chamber cine bSSFP—use the 4-chamber to prescribe one slice through the middle of the mitral valve to the LV apex.
9. RV VLA cine bSSFP—use the 4-chamber to prescribe one slice through the middle of tricuspid valve to the RV apex. Cross-reference to LV SAX stack localizer to ensure RV OT and PV are in the plane of the slice.
10. LV SAX cine bSSFP—8 or 6 mm slice thickness with 2 or 4 mm gap, respectively, to make total 10 mm; use both the 2-chamber and 4-chamber diastolic phase images to prescribe a series of slices from the mitral valve annulus to the LV apex. See Section Plan Imaging Accurately and Avoid Common Mistakes for extra positioning tips.
11. Three chamber cine bSSFP—use the basal slice of the LV SAX series and prescribe one slice through the middle of the aortic valve and the left atrium.
12. LV Outflow Tract (LV OT) cine bSSFP—use the 3-chamber to prescribe one slice through the middle of the aorta and the LV OT.
13. RV SAX cine bSSFP—(8/2 or 6/4 mm); use both the sagittal MPA and the RV VLA diastolic phase images to prescribe a series of slices in a plane perpendicular to a line from the pulmonary valve to the apex of the RV. The first slice should be placed at the level of the PV in diastole (122). See Section Plan imaging Accurately and Avoid Common Mistakes for extra positioning tips.
14. Phase Contrast (PC) Flow Aorta—use both the 3-chamber and LV OT diastolic phase images to prescribe a slice perpendicular to the aorta in both planes, at the level of the sino-tubular junction.
15. PC Flow Aortic Valve—use both 3-chamber and LV OT diastolic phase images to prescribe a slice perpendicular to the aorta in both planes, at the level of the aortic valve annulus.
16. PC Flow MPA—use both sagittal and coronal MPA diastolic phase images to prescribe a slice perpendicular to the MPA in both planes, just distal to the valve, through the tubular portion of the MPA, avoiding bifurcation.

### Plan Imaging Accurately and Avoid Common Mistakes

Due to the variability of cardiac morphology and body shape between patients, it can take considerable time to become proficient at localizing cardiac imaging planes. The heart does not lie in an orthogonal plane to the thorax and therefore more than one localizer plane is necessary for accurate and reproducible positioning. Learning to avoid common positioning errors can improve scanning efficiency and diagnostic quality.

#### The 4-Chamber View

The 4-chamber view affords an overall visual assessment of cardiac function. A well-positioned view (**Figure 8A**) will demonstrate the mitral and tricuspid valves and the right and left atria and ventricles. However, frequently the four cardiac chambers and the atrio-ventricular valve planes are not well-visualized due the slice plane being prescribed incorrectly. **Figure 8B** is an example of a poorly positioned 4-chamber with the slice plane prescribed through the LV OT. To successfully position the 4-chamber view requires the use of three views. On the LV VLA view (**Figure 8C**), the operator should ensure the slice plane is prescribed through the center of the mitral valve and the LV apex. On a mid-ventricular LV SAX slice (**Figure 8D**), the plane is tilted down to the RV apex. Finally, the position is cross-checked on a basal LV SAX view (**Figure 8E**) to ensure the slice positioning avoids the LV OT and aortic root.

#### Left Ventricular Short Axis—Accurate Positioning of the Basal Slice

Correct positioning of the basal slice of the LV SAX stack can significantly improve the accuracy and reproducibility of volumetric analysis. A consistent and reproducible method of positioning this slice is critical. As outlined in Section Clinical Cardiovascular MR: What do we See and why do we Need it?, both the LV VLA (**Figure 9A**) and 4-chamber (**Figure 9B**) views must be used to ensure the basal diastolic phase slice is positioned parallel to the mitral valve annulus, avoiding atrium and with an even amount of myocardium around the blood pool (**Figure 9C**).

If the image position is not correct, simple corrections are shown in **Figure 10** (top row). If the basal diastolic phase slice includes atrium (**Figure 10A**), the slice must be repositioned

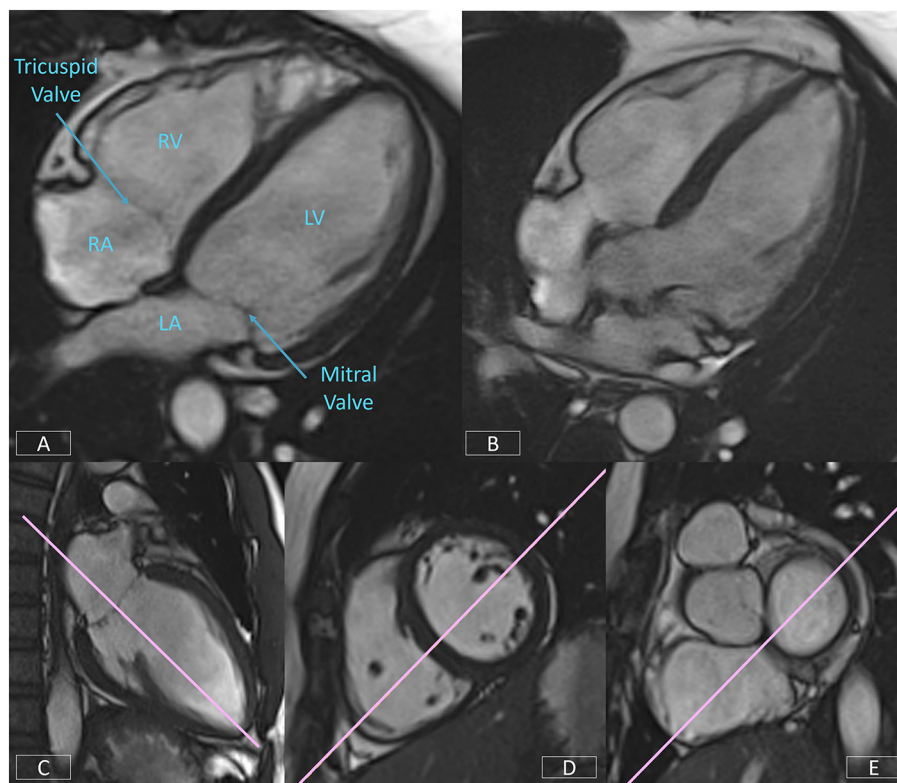


**FIGURE 8 |** Well-positioned 4-chamber view **(A)** demonstrating mitral and tricuspid valves, right and left atria, and ventricles. Incorrect prescription **(B)** with the slice plane prescribed through the LV OT. Accurate positioning of the 4-chamber view requires the use of three views, the LV VLA view **(C)**, mid-ventricular LV SAX slice **(D)**, and the basal LV SAX slice **(E)**.

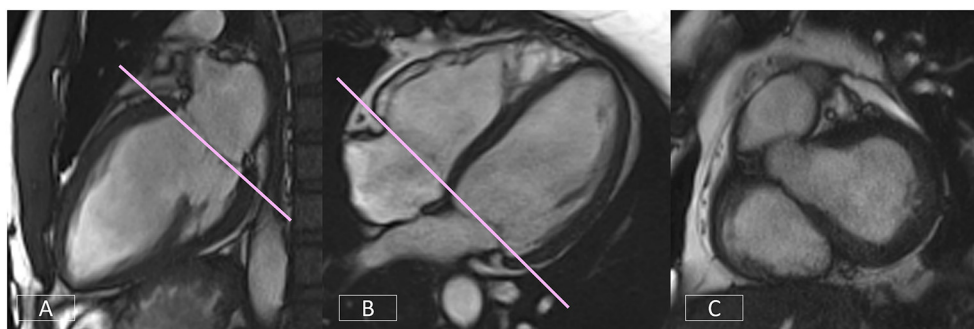


**FIGURE 9 |** Accurate positioning of the basal slice of the LV SAX series requires the use of both the LV VLA **(A)** and the 4-chamber **(B)** views to ensure the basal diastolic phase slice is positioned parallel to the mitral valve annulus, avoiding atrium and with an even amount of myocardium around the blood pool **(C)**.

toward the apex (**Figure 10B**). If there is an inconsistent amount of myocardium (**Figure 10C**), the slice angle is tilted on the LV VLA view (**Figure 10D**).

### Right Ventricular Vertical Long Axis View

The non-geometric shape of the RV increases the complexity of positioning. A well-positioned RV VLA (**Figure 10E**) will enable visualization of the pulmonary and tricuspid valves, the RVOT and the RV apex in one plane. After positioning the slice

on the 4-chamber view (**Figure 10F**) through the RV apex and avoiding the septum, the slice plane is tilted up to the RV OT and pulmonary valve using the basal LV SAX slice (**Figure 10G**).

### Right Ventricular Short Axis

The modified RV short axis series (122) enables more accurate and reproducible planimetry of the ventricular borders making analysis less prone to operator error. A well-positioned RV VLA is key to ensuring correct positioning of the RV SAX.

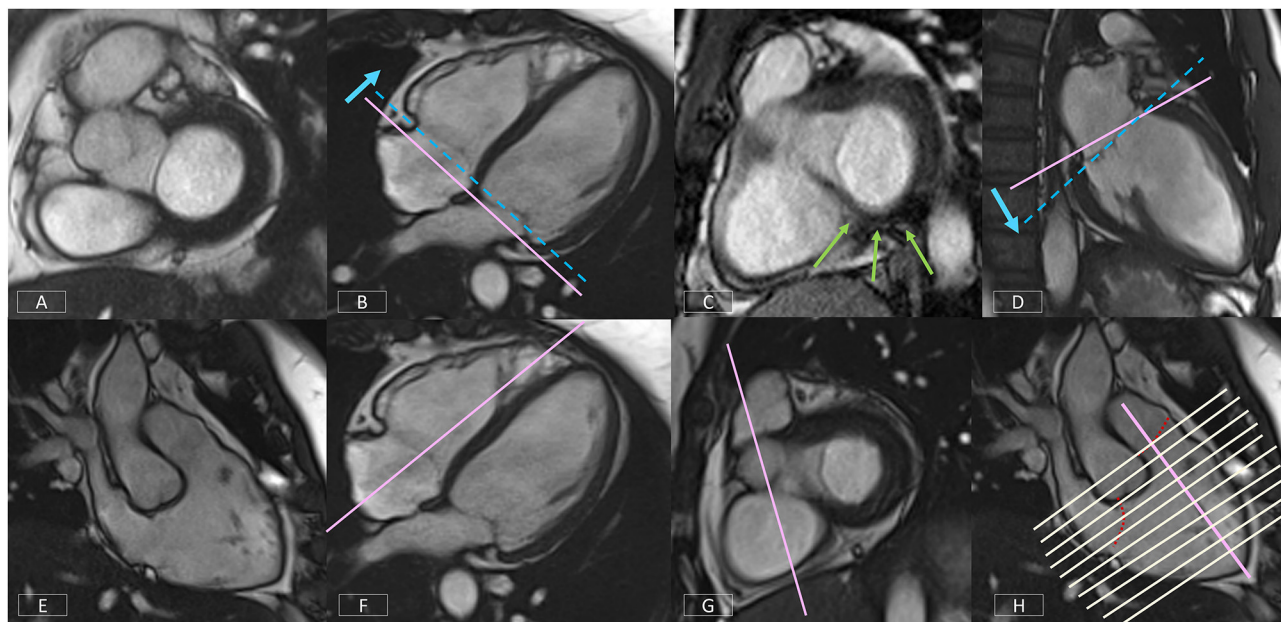


**FIGURE 10 |** Top row: Positioning corrections for the LV SAX series include repositioning the slice more apically (**B**) if the basal diastolic phase slice includes atrium (**A**). If there is an inconsistent amount of myocardium around the blood pool (**C**), the slice angle is tilted on the LV VLA view (**D**). Bottom row: A well-positioned RV VLA (**E**) is achieved by positioning the slice on the 4-chamber view (**F**) through the RV apex and avoiding the septum, then tilting the slice plane up to the RVOT and pulmonary valve on the basal LV SAX slice (**G**). The RV SAX series can then be planned on this view to transect the tricuspid valve at an angle between 45° and 90° (**H**).

**Figure 10H** shows the prescription of the RV SAX slices on the RV VLA. The slices should transect the tricuspid valve at an angle between 45° and 90° to ensure the slices are not prescribed too close to parallel to the valve.

## Building Blocks to a Comprehensive CMR Protocol

As mentioned earlier, the order of image acquisition is important for scanning efficiently. The operator should start by creating scan protocols of the building blocks outlined in Section The Building Blocks of a Successful CMR Exam. Using the template pulse sequence protocol created as per the facility requirements, each individual acquisition can then be built and named accordingly.

This foundation protocol then forms the basis of all the clinical protocols to be built on the scanner.

A general cardiomyopathy protocol can be used for the majority of clinical presentations. Options tailored to specific presentations, such as oedema-weighted imaging and T<sub>2</sub>-mapping for acute presentations, can be selected as required. Advanced imaging techniques, such as T<sub>1</sub>-mapping, should be added as appropriate (see Section Quantitative CMR Techniques). LGE imaging acquisitions should be built with plane specific labels, e.g., LV SAX LGE series, to assist in quickly identifying series when viewing images during reporting. **Supplementary Table 1** is an example of a clinical protocol for the assessment of acute cardiomyopathic diseases such as acute myocarditis.

The next step is to build further indication-specific protocols matched to the facility clinical protocols, such as Hypertrophic Cardiomyopathy, Arrhythmogenic Cardiomyopathy or Tetralogy of Fallot where very specific clinical questions need to be addressed.

Using this method to build a comprehensive CMR protocol library will enhance efficiency, improve patient compliance, and ensure that all required imaging sequences are performed.

## Get Your Patient Ready

Performing an efficient CMR examination is highly dependent on patient cooperation. To optimize scanner time, the patient should be prepared outside the scan room. It is useful for patients to understand the important role they play in the quality of their examination, particularly the importance of consistent breath holding. Coaching breath hold procedures, checking breath hold capacity, and assessing likely compliance with instructions prior to commencing the examination will save valuable scanner time.

A good ECG trace is essential and is achieved by preparing the skin with abrasive gel, shaving if necessary and using low-impedance MRI safe electrodes. The use of an impedance meter to check electrode-to-skin contact and ensure strong lead voltage enables the operator to reposition using new electrodes prior to the patient entering the scan room. Once the patient is in the scanner and connected to the scanner gating system, the ECG trace should be assessed to ensure there is adequate voltage in each lead. If necessary, electrodes should be replaced and repositioned until a reliable ECG trace is obtained. If the poor ECG trace is due to the patient's irregular rhythm, acquisition

strategies must be planned accordingly (see Sections Managing Challenging Patients and Handling Motion).

## Plan, Review, and Correct

Examination time can be reduced by attention to detail during scan preparation. With most CMR sequences requiring one breath hold per slice, it is important to limit the acquisition of any unnecessary slices. When acquiring a multi-slice series, each series should be prescribed carefully to cover only the anatomy needed. Images should be reviewed as they are acquired so that the series can be stopped if the anatomy is covered, rather than completing the full prescribed series.

Equally important is to observe the patient during each acquisition. Display the ECG and respiratory pulse on the console and be alert to patient movement; failure to hold breath for the full length of the scan; ectopic beats or irregular rhythms. It may be necessary to repeat slices with artifact, particularly if the images are part of a series used for quantitative analysis.

As a rule, the use of manual breath hold instructions improves patient compliance with breathing instructions and reduces the need to repeat slices due to breathing artifact.

## Managing Challenging Patients Irregular Rhythms

Learning how to deal with irregular heart rhythms is one of the most important components of becoming a proficient CMR operator. Significant time can be lost if there is no management strategy in place. It is possible to achieve diagnostic images still within a reasonable timeframe by building protocols in advance with appropriate options for each pulse sequence type.

For each clinical protocol in the library, three acquisition strategies should be built: Sinus Rhythm, Mildly Irregular Rhythm, and Severely Irregular Rhythm (**Supplementary Figure 4**). Operators must learn when it is appropriate to change strategies and which strategy is required.

Retrospective gating should only be used for sinus rhythm or where there is a very occasional ectopic beat. The average heart rate range (RR interval) displayed on cine bSSFP images can be used to determine which strategy to use. Generally, if the variability is  $< \pm 40$  ms, retrospective gating can be used (Sinus Rhythm strategy). Where the variability is greater, it will be necessary to change to prospective triggering for cine bSSFP and PC flow imaging (Mildly Irregular Rhythm strategy). Caution should be used when acquiring images used for quantitative analysis (such as parametric tissue mapping) to ensure the integrity and reliability of the data.

In the presence of a severely irregular rhythm, real-time and highly accelerated options will need to be employed (see Section Fast CMR: Speeding up Imaging by Acquiring Less Data).

## Non-compliant Patients

For extremely unwell or claustrophobic patients, a plan for a short, high-value examination is required. Prior to commencing the examination, the clinical history and any previous imaging should be reviewed to determine the most critical clinical question. Generally, this will be information that no other diagnostic imaging test can provide such as tissue

characterization. The imaging protocol is then planned to obtain this information as a priority in case it is necessary to terminate the examination prematurely. Protocols should be trimmed of any unnecessary sequences. For example, if the main question is the presence of myocardial fibrosis, an option would be to inject the contrast prior to moving the patient into the scanner, obtain the LGE first, then acquire any other imaging possible in the remaining time.

## Quantitative CMR: It Is Your Responsibility

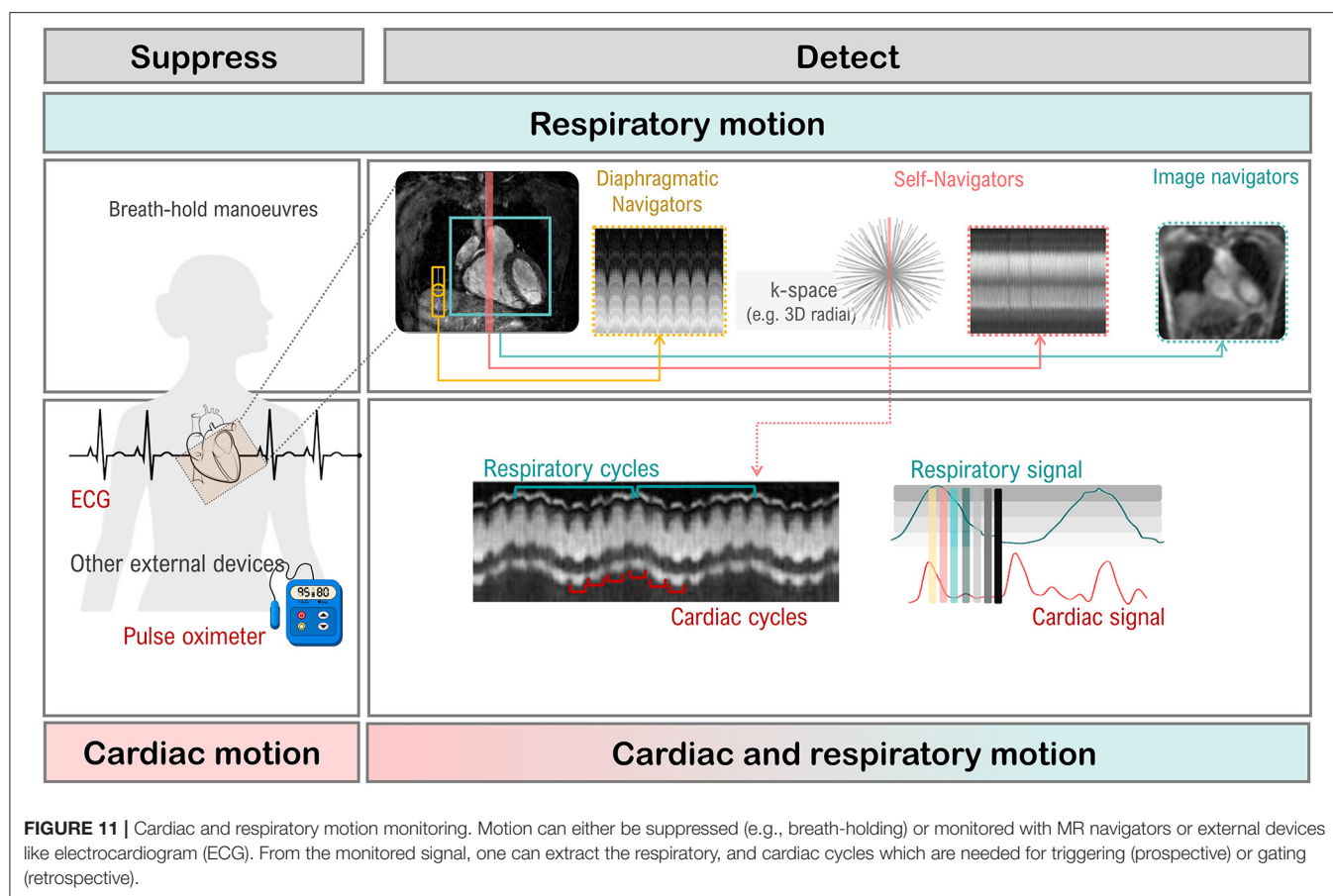
CMR is highly operator and patient dependent and the quality of images obtained directly affects the accuracy and reliability of quantitative data. Surgical, therapeutic, or prognostic decisions are made on this data and attention to detail at every stage of the CMR examination is necessary to ensure the integrity of the results. It is incumbent upon the operator to recognize and report the limitations of the data if necessary.

## CMR IMAGE QUALITY: NO FREE LUNCH

When setting up and optimizing a clinical CMR protocol to obtain the best images possible, the inherent trade-off between spatial and temporal resolution, scan time and signal-to-noise ratio (SNR) must be taken into consideration. For example, imaging at higher spatial resolution will result in lower SNR or longer scan times. Thus, a compromise in this triangle needs to be found in terms of image quality and acquisition time. Moreover, CMR can be impacted from image degradation due to cardiac and respiratory motion. Physiological motion induces aliasing along the phase-encoding direction and/or blurring of the image content (see Section Image Acquisition: What is the Position?), where the appearance depends on the imaging trajectory. Therefore, CMR acquisitions generally require synchronization or handling of the cardiac and respiratory cycles as depicted in **Figure 11**. In CMR, to avoid artifacts related to cardiac motion, it is usually desirable to freeze the heart motion, using gated/triggered acquisitions with  $< 100$  ms temporal resolution. Unfortunately, this comes at the expense of spatial resolution and/or coverage adding further constraints to CMR.

## Handling Motion

Motion artifacts can be mitigated by (a) avoiding motion, i.e., training the patient to perform breath-holds or applying anesthesia and sedation to freeze respiratory motion; (b) reducing motion, i.e., signal averaging to smooth out motion, performing fast imaging to become less sensitive to motion (123–127) or suppressing motion outside the field of view using saturation bands; (c) triggering or gating motion, i.e., monitoring the motion cycle [using, for e.g., MR navigators (128–132), cameras (133), field probes (134), pilot tone (135), respiratory belts or electrocardiogram (136)] and either prospectively trigger on the respective motion (137, 138), meaning only acquiring within a small portion of the motion cycle, or retrospectively gate the motion (139–142), meaning sorting the data into distinct motion states for reconstruction. Motion avoidance [case (a)] requires, however, patient compliance and reduces patient comfort. For highly non-compliant patients (for e.g.,



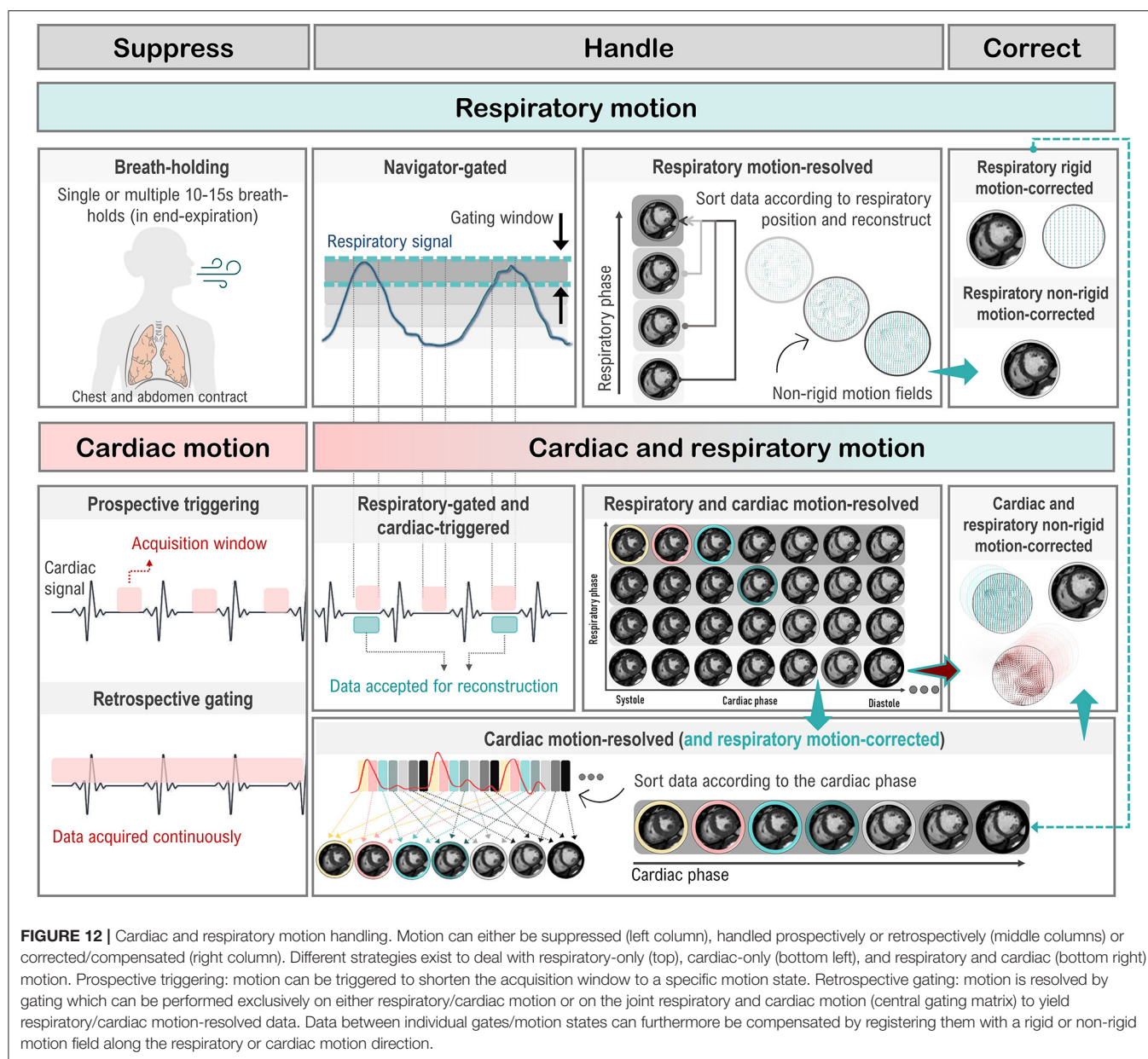
pediatric patients), moderate sedation or general anesthesia can be given which does however require the use of a lung respirator, increasing scan time and costs, and could have potential side effects and complications. Motion reduction [case (b)] can require longer scan times, increases induced radio frequency energy on patient (i.e., tissue heating) and residual motion artifacts can remain in the image. Motion triggering and gating [case (c)] capture only a fraction of the entire dynamic respiratory and cardiac cycle or periodic assumptions of the dynamic cycle are made which may not hold in practice. Thus, a varied range of strategies has been proposed to avoid CMR image degradation due to cardiac and/or respiratory motion, some of which are summarized in **Figure 12**.

### Respiratory Motion: You Can Breathe Normally

**Breath-holding** techniques are commonly used to reduce respiratory motion artifacts. If the patient complies with the breathing instructions this provides a 10–15 s window where artifact-free images can be obtained. A CMR examination requires multiple breath holds (143), which can lead to patient discomfort and fatigue, resulting in poor breath-holding and, consequently, motion artifacts that can impact the downstream analysis (144, 145). In addition, breath-holding can be challenging or impossible for pediatric, critically ill, or uncooperative patients (146). Moreover, some CMR protocols,

such as CMRA and other 3D CMR applications, require acquisition times that are too long for a breath-hold. Free-breathing alternatives that use respiratory triggering or gating based on *diaphragmatic navigators* (that monitor the superior-inferior motion of the diaphragm) are available on most CMR scanners (147–149). Unfortunately, this approach has low scan efficiency, since only data within a small predefined respiratory gating window is used to generate an image, which leads to long and unpredictable scan times (due to irregular breathing patterns). External respiratory monitoring devices, such as bellows around the chest or abdomen, are also often used. More recently, novel tracking devices like pilot tone (135, 150) are being investigated for the usage of a sequence-independent motion monitoring solution.

Free-breathing CMR techniques based on *self-navigation* (151–155) or *image navigators* (130, 156–159) have been proposed to achieve 100% respiratory scan efficiency (no data rejection), by correcting all data for respiratory motion. Thus, allowing for shorter and more predictable scan times. Respiratory self-navigation techniques derive the respiratory-induced motion of the heart directly from the imaging data. Self-navigation is achieved by periodically imaging the central points in k-space and thus do not require any additional interleaving of navigators into the sequence. Typically, self-navigation approaches extract the respiratory signal from 1D projections of the field of



view (in one or more directions). However, signal from static structures, such as chest wall, is also included in 1D self-navigators, which can lead to motion estimation and correction errors. Image-based navigators, which allow separation of static structures from the moving heart, have been proposed as an alternative to 1D self-navigation to reduce motion estimation errors. These methods use low spatial resolution images acquired with sequence interleaved imaging blocks at periodic intervals, prior to the CMR data acquisition, to estimate and correct for 2D or 3D respiratory motion. Free-breathing single shot CMR sequences often rely on retrospective motion correction using image registration methods to correct for respiratory motion between time frames.

Once the respiratory signal has been estimated, image degradation caused by respiratory motion can be reduced

by: (a) correcting for translational motion (directly in k-space) (55, 130, 150, 158, 160–163), (b) separating (or binning) the data into multiple respiratory states to generate respiratory motion-resolved images (164–183), and (c) (using the latter for) correcting for more complex non-rigid motion (113, 157, 184–201).

### Cardiac Motion: Stop Being Triggered

CMR acquisitions are usually synchronized with heart motion through an ECG (with electrodes attached to the chest) to minimize imaging artifacts caused by cardiac motion. Two approaches are typically used: prospective ECG triggering and retrospective ECG gating. *Prospective triggering* uses the R wave from the ECG signal to trigger the data acquisition (and “freeze” the heart) at a specific phase or certain number of

phases of the cardiac cycle (149, 161, 202–206). In *retrospective gating*, data are acquired continuously throughout the cardiac cycle and the ECG signal is recorded simultaneously (140, 143, 144, 207–213). Subsequently, data are reordered and grouped into different cardiac phases according to the ECG signal. However, the ECG can be unreliable in CMR (as described in Sections Clinical Cardiovascular MR: What do we See and why do we Need it? and Clinical Cardiovascular MR: How Should we Perform the Examination), particularly in the case of arrhythmias and ectopic hearts. Finger pulse oximetry can be used as an alternative to ECG, but its signal is delayed relative to the ECG R wave. To overcome these challenges, cardiac *self-gating* approaches have been proposed to estimate an ECG-like signal directly from the acquired data (141, 142, 167, 171). The signal is then used for cardiac gating. More recently, contactless external sensors like pilot tone have also been used to track motion during CMR exams (214).

### Cardiac and Respiratory Motion: No Stopping Now

Several solutions have been developed to eliminate the need for ECG synchronization and breath-holding altogether. This allows continuous acquisition of CMR data, known as *free-running CMR* (55, 167, 169, 170, 179, 197, 215). After acquisition, data is then sorted into multiple cardiac phases (with the desired temporal resolution) and multiple respiratory motion phases based on the cardiac (ECG, self-navigation, pilot tone, etc.) and respiratory (self-navigation, belt, etc.) motion signals to generate a multidimensional dataset for reconstruction. Moreover, the (self-navigation) respiratory signal or, for each cardiac phase, the bin-to-bin (affine) respiratory motion can be estimated and used to correct for respiratory motion directly in k-space (by applying the corresponding phase-shifts in k-space), before the image reconstruction, to generate respiratory motion-corrected cardiac phase-resolved CMR images (170, 182). In addition, these images can be used to generate cardiac motion-corrected images by selecting the cardiac phases with the smallest intra- and interphase motion and then correcting for non-rigid motion (200). The obtained respiratory and/or cardiac motion-gated k-spaces are usually sparsely sampled. During reconstruction, the spatio-temporal information can be exploited by either regularizing the motion dimensions (171, 179), correcting for the motion (216–218) or exploring the low-rankness (see Section CMR Reconstruction: From k-space to image space) of the dynamic processes (219, 220).

*Retrospective gating* assumes a periodicity of the temporal motion evolution which is however not a given for patients with arrhythmias or irregular breathing patterns (221, 222). In these cases, real-time CMR which is based on fast imaging sequences, like spGRE or bSSFP, can provide a viable solution (154, 157, 185, 222–228). Imaging with high (sub-second) temporal resolution makes acquisitions robust to motion, and thus, images can be obtained without gating or binning (220). In combination with efficient sampling trajectories and reconstruction techniques, 2D and 3D imaging with high spatio-temporal resolution can be performed.

### Fast CMR: Speeding up Imaging by Acquiring Less Data

Several approaches have been proposed to speed up CMR acquisitions by reducing the amount of data required for accurate reconstruction, including *parallel imaging* (125, 126), *k-t accelerated imaging* (173, 174, 229, 230), or pseudo-random sub-Nyquist sampling (123, 124, 231). Besides more efficient sampling trajectories, fast imaging sequences like fast low angle shot magnetic resonance imaging (FLASH) (232), bSSFP (24), fast spin-echo imaging (RARE) (233), echo planar imaging (EPI) (234) have enabled fast CMR imaging. Accelerated scans can be used to shorten the imaging time, to shorten breath-holds and improve patient comfort, but can also be used to collect more information (within the same imaging time), to increase temporal or spatial resolution and/or volumetric coverage.

*Parallel imaging* methods, such as (the image-based) SENSitivity Encoding (SENSE) (126) and (k-space-based) GeneRALized Autocalibrating Partial Parallel Acquisition (GRAPPA) (125), are used worldwide for CMR applications, but are limited by the number of receiver coils (see Section k-space) and in practice typically to 2- to 3-fold acceleration. *K-t accelerated imaging* (173, 174, 229, 230) extends these concepts along the dynamic temporal direction. It uses a regular undersampling pattern that is shifted over time. Images are reconstructed using a linear reconstruction approach, which relies on information extracted from low spatial resolution calibration data (with high temporal resolution) to minimize fold-over artifacts.

*Simultaneous multi-slice* (SMS) imaging (235–240) has the potential to acquire multiple slices, i.e., increasing cardiac coverage without sacrificing in-plane spatial resolution. However, pre-calibration scans are required to calibrate the unfolding during reconstruction which increase overall scan time.

On the other hand, reduced spatial coverage but increased dynamic resolution can be obtained with *real-time CMR* (154, 157, 185, 222–228). It relies on fast imaging sequences and trajectories to provide respiratory and cardiac motion-resolved images. Data acquisition is performed under free-breathing with sufficiently fast enough trajectories to capture whole field of view with minimal motion impact.

High acceleration factors can be achieved if the compressibility (or sparsity in a transform domain) of images is exploited as proposed in *Compressed Sensing* (CS) (124) or *Low-Rank* methods (178, 231). In these cases, we seek a (pseudo-) random sub-Nyquist sampling (i.e., undersampling) of the data. The applied sampling induces incoherent noise-like aliasing artifacts in the sparse domain. Thus, to satisfy the incoherence criterion (pseudo-) random Cartesian or non-Cartesian undersampling schemes are used to accelerate scans.

### CMR Trajectories: It Is That Sample

The k-space undersampling patterns to accelerate CMR acquisitions in combination with the selected reconstruction method determine the obtainable image quality. A few exemplar trajectories are shown in **Figure 13**. In parallel imaging, the number of k-space lines is usually reduced using regular

Cartesian undersampling (i.e., sampling below the Nyquist-Shannon sampling limit) (125, 126). In dynamic CMR, the Cartesian sampling patterns can be extended along the dynamic motion direction as used in k-t imaging (173, 174, 229, 230). A different k-space undersampling should be used for each time frame to introduce incoherence along the temporal dimension, and to thus enable exploitation of both spatial and temporal sparsity, as for example performed with a variable-density incoherent spatiotemporal acquisition (VISTA) sampling (241).

Non-Cartesian sampling schemes may be preferred because they are less sensitive to motion (123, 151, 163, 169, 171, 172, 181, 198, 202, 210, 224, 230, 237, 242–253), due to a densely sampled low-frequency range and the repeated sampling of the k-space center enables the extraction of motion signals (self-navigation). Unfortunately, non-Cartesian sampling requires resampling of the acquired data onto a Cartesian grid, which is computationally expensive.

Several Cartesian trajectories that acquire data using a radial or spiral-like pattern on a Cartesian grid have been proposed to overcome the computational complexity of non-Cartesian trajectories, such as Variable-Density sampling and Radial view ordering (VDRad) (254), CIRCular Cartesian UnderSampling (CIRCUS) (255), (Variable-Density) Cartesian acquisition with Spiral Profile ordering (VD-CASPR, CASPR) (201, 207, 256), Golden-angle Cartesian Randomized Time-resolved (GOCART) (257), rotating Cartesian k-space (ROCK) (146), centric reordering (211) or Enhancing Sharpness by Partially Reduced Subsampling Set (ESPRESSo) (258, 259) sampling.

For 3D CMR imaging, non-Cartesian trajectories can be combined with Cartesian sampling, as in, for example, radial stack-of-stars (123, 175, 212, 260, 261) or stack-of-spiral (262) sampling schemes. Alternatively, 3D whole-heart CMR can be achieved using 3D Cartesian trajectories (167, 208, 254, 255), or 3D non-Cartesian sampling patterns, such as radial “koosh-ball” (169, 182, 209) or spiral phyllotaxis (170, 181). Moreover, acquisitions often use a golden-angle ordering scheme for which consecutive k-space spokes are incremented by the golden angle ( $\theta \approx 111.25^\circ$ ) (263, 264), to achieve nearly uniform k-space coverage (also optimal for retrospective binning) and incoherence along both spatial and temporal dimensions.

## CMR Reconstruction: From K-Space to Image Space

The undersampled data requires appropriate reconstruction techniques to recover an aliasing-free image, as illustrated in **Figure 13**. The raw data is linked with the image via the forward model as stated in Equation (11). CS relies on non-linear reconstruction algorithms to reconstruct images from randomly (or pseudo-randomly) undersampled data (124). In CS, the undersampling trajectory should lead to incoherent, noise-like aliasing artifacts which can be corrected for if images can be sparsely represented in a set transform domain (e.g., wavelets). In contrast to fixing the transform domain, *dictionary learning* techniques (265) seek to find the sparsest image representation by learning the sparsifying transform specific to each type of application. CS has the advantage that it does not require any

training data and can achieve high accelerations. It can also be combined with parallel imaging methods (266, 267). However, it depends on application specific hyperparameter optimization, and the iterative algorithms result in long reconstruction times.

*Low-rank matrix completion* methods have extended the idea of CS to matrices (178, 231). These explore the global or local (patches) correlations within CMR images e.g., along the temporal or multi-contrast dimensions (113, 178, 179, 189, 207, 231, 268–278). For dynamic CMR, low-rank methods can act as an implicit motion compensation for any residual motion (after prior triggering/gating) (177, 207). Some methods simultaneously enforce low-rank and sparsity constraints to separate the temporally correlated background and dynamic information in various CMR applications, such as dynamic contrast-enhanced CMR (231, 274, 277). Moreover, *low-rank tensor imaging* has been proposed for multi-dimensional CMR imaging (169, 195, 197, 219, 220, 272, 279–281). These methods explore the spatio-temporal correlations in all dimensions (spatial, contrast, cardiac, and respiratory motion) to generate multi-parametric and motion-resolved CMR images, e.g., cardiac- and respiratory-resolved  $T_1$  and  $T_2$  maps. In addition, motion can be handled implicitly in the low-rank decomposition instead of performing a prior motion gating.

*Model-based reconstruction* approaches have also been proposed to accelerate quantitative CMR imaging (248, 249, 282–285). These methods incorporate the physics of the MR signal into the image reconstruction problem allowing for the direct reconstruction of quantitative maps from the undersampled CMR data, bypassing the intermediate steps of image reconstruction and pixel-wise model fitting. Furthermore, in model-based reconstructions the underlying respiratory and cardiac motion model can be accounted for. Explicit motion compensation can be performed by mapping image data along the temporal direction with the underlying motion model extracted from image registration (187, 216, 217, 284).

Fast reconstruction is essential in a clinical setting. However, non-standard and iterative reconstruction methods often suffer from high computational demands, long computational times and require careful tuning of the algorithm (regularization) parameters. Recently, deep learning-based solutions have been proposed to address some of these shortcomings and which will be covered in more detail in Section Image Reconstruction.

## ARTIFICIAL INTELLIGENCE FOR CARDIOVASCULAR MR

Artificial Intelligence (AI) and Machine Learning (ML), a subclass of AI, have led to a break-through in the last years and have the potential to transform the clinical workflow substantially. CMR imaging leverages a high potential to enhance each individual step of the imaging pipeline (**Figure 14**), from complex CMR acquisition processes, the highly varying imaging protocols, to automated diagnosis. Despite the success of ML and AI, these new techniques should not replace clinicians, but aid clinicians in decision making, facilitate cardiac view-planning, or

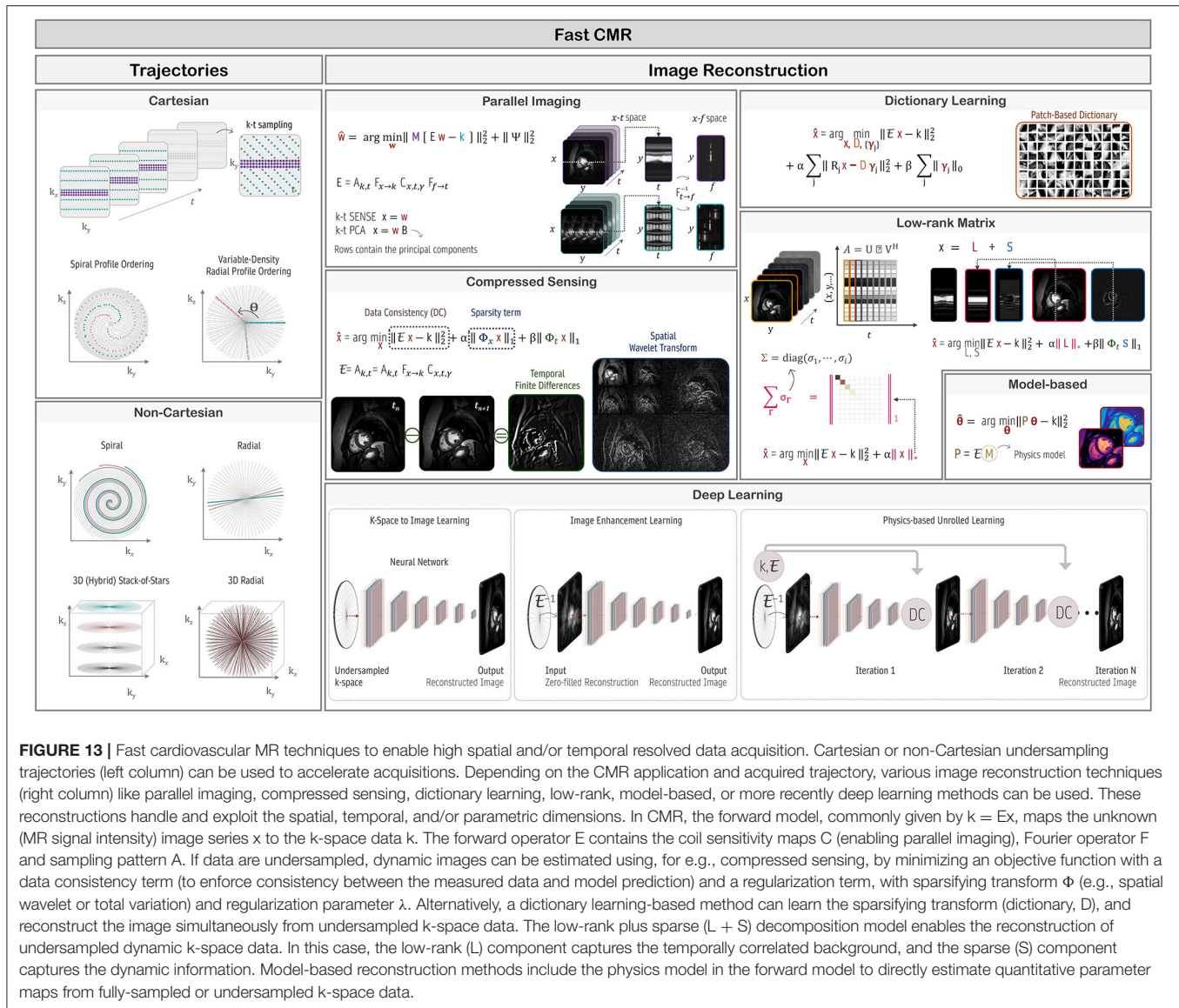


**FIGURE 13 |** Fast cardiovascular MR techniques to enable high spatial and/or temporal resolved data acquisition. Cartesian or non-Cartesian undersampling trajectories (left column) can be used to accelerate acquisitions. Depending on the CMR application and acquired trajectory, various image reconstruction techniques (right column) like parallel imaging, compressed sensing, dictionary learning, low-rank, model-based, or more recently deep learning methods can be used. These reconstructions handle and exploit the spatial, temporal, and/or parametric dimensions. In CMR, the forward model, commonly given by  $k = Ex$ , maps the unknown (MR signal intensity) image series  $x$  to the  $k$ -space data  $k$ . The forward operator  $E$  contains the coil sensitivity maps  $C$  (enabling parallel imaging), Fourier operator  $F$  and sampling pattern  $A$ . If data are undersampled, dynamic images can be estimated using, for e.g., compressed sensing, by minimizing an objective function with a data consistency term (to enforce consistency between the measured data and model prediction) and a regularization term, with sparsifying transform  $\Phi$  (e.g., spatial wavelet or total variation) and regularization parameter  $\lambda$ . Alternatively, a dictionary learning-based method can learn the sparsifying transform (dictionary,  $D$ ), and reconstruct the image simultaneously from undersampled  $k$ -space data. The low-rank plus sparse ( $L + S$ ) decomposition model enables the reconstruction of undersampled dynamic  $k$ -space data. In this case, the low-rank ( $L$ ) component captures the temporally correlated background, and the sparse ( $S$ ) component captures the dynamic information. Model-based reconstruction methods include the physics model in the forward model to directly estimate quantitative parameter maps from fully-sampled or undersampled  $k$ -space data.

support in the tedious task of image segmentation to simplify and speed up quantification of functional cardiac parameters.

In this section, we first provide an overview of the common terminology and building blocks in ML, without the usage of complex mathematical notations. In the second part, we provide an overview on how ML can be used at each individual stage of the imaging pipeline, i.e., cardiac view-planning, image acquisition, image reconstruction, shape analysis, image segmentation, and quantification of biomarkers. Finally, we provide insights into potential pitfalls in using ML in CMR, and an outlook into the future of ML for CMR.

## Breaking Down the Terminology

The terms AI, ML and more recently deep learning (DL) are often used interchangeably. However, there is a huge difference between these terms. AI leverages the potential of machines to mimic the human mind's ability to solve

problems or make decisions. As a sub-branch of AI, ML uses algorithms to learn patterns from data and make predication about a certain task. Pre-defined features are extracted from the input data and are then fed into the (statistical) model. The parameters of this model are then trained using data to make correct predictions for a specific task without human assistance. After model training, predictions from new unseen data can be made using the trained model parameters. While ML in its classic formulation depends on defining hand-crafted discriminative features which are tedious and time-consuming to extract, a further sub-branch of ML called DL directly learns feature representations from data using neural networks (NNs). Although the concept of NNs was established in the late 1980's, DL has flourished since 2015. The break-through of DL came with the availability of Graphics Processing Units (GPUs), large datasets, and advanced architectures.

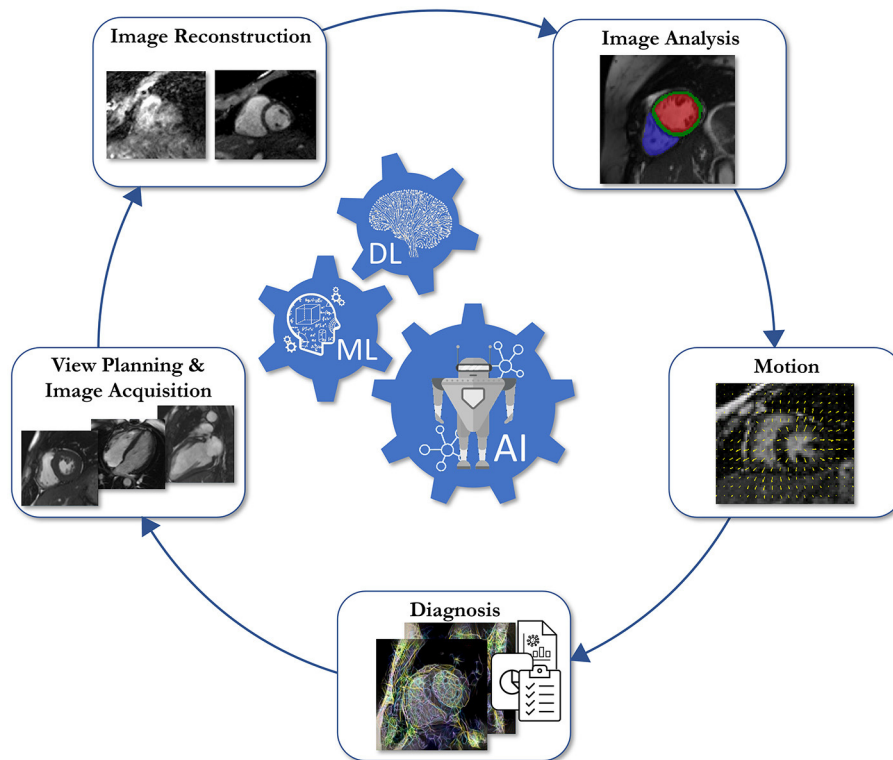


**FIGURE 14 |** Schematic overview of the five areas in which Artificial Intelligence (AI)/Machine Learning (ML)/Deep Learning (DL) assisted operations can support the clinical workflow.

ML has the ability to support in various challenging tasks. In image *classification*, the model takes the input image or already extracted features as input, and outputs a classification label, to predict, e.g., a certain heart disease. The task of assigning an individual label to each input pixel is called *segmentation*. Typical application of image segmentation in the field of cardiac imaging is the segmentation of the heart into four chambers and myocardium. Image-to-image or sensor-to-image translation describe regression tasks that form the third group of important ML tasks. *Regression* tasks can be found in MR image reconstruction from undersampled k-space data, super-resolution, or image enhancement.

### Types of AI: Does It Need Supervision?

Machine Learning can be categorized in three major types: supervised learning, self-supervised learning, and un-supervised learning. Supervised learning methods require a training database with a set of input data and annotated output labels for training. The model tries to make predictions, which are then compared to the correct output labels using a cost function. The error in the cost function then gives an idea how the models' parameters have to be updated in the training loop. In contrast, neither labeled data nor any other prior knowledge on the data is available in unsupervised learning. Hence, the model learns itself how to identify patterns in the data, as in clustering (variational) autoencoders, or Generative Adversarial

Networks. Self-supervised learning is a form of unsupervised learning, where the data provides the supervision.

### Training, Validation, and Testing: Getting It to Work

To update the parameters of the model, the network needs to be *trained* with respective training data. A training database consists of a number of training samples. For each update of the model parameters, a *batch* is drawn from the training samples and passed through the network. This is repeated until all training samples have been processed, defining one *epoch* of training. The network itself is trained for several epochs until convergence. The number of training epochs depends on the selected dataset, the number of training samples, and the selected task. A separate *validation* data set is used to monitor the training process and to tune hyper-parameters (learning rate, architecture parameters etc.). This allows for, e.g., identification of model overfitting. However, the validation data set is not used to update the model parameters of the network. In the *testing* stage, the model is tested on further unseen data and used for the final model evaluation. It is important to note that training data, validation data, and test data are mutually exclusive.

However, in medical imaging, and especially in the context of CMR, only small databases are often available. This requires a thorough study of the robustness of the model to avoid a bias toward selected validation samples. Cross validation provides

a way to study the robustness of models if small datasets are available. For *k*-fold *cross validation*, the database is split into a number of *k* subsets and the networks are trained for training data in *k*-1 folds, and the data in the remaining fold is used for validation/test. This is repeated such that *k* networks are trained, with every fold being used for validation. Deviations in evaluation metrics indicate reduced robustness of the models.

In medical imaging, we often observe another danger when creating our own training databases. In CMR, we often acquire several slices from a single subject. Hence, in case training samples are drawn from multiple subjects with several slices each, we need to make sure that data from the same patient does not appear in training and validation simultaneously to avoid any bias of the models toward specific anatomies or pathologies.

### Database: Does Size Really Matter?

The availability of large training databases is one of the most challenging aspects in ML for CMR. In the context of image reconstruction, publicly available datasets are very rare. In CMR, for example, we found that some data for radial image reconstruction of dynamic cardiac MRI are available (286). For other ML tasks like image classification and image segmentation, tens of thousands of annotated CMR datasets are available in, e.g., UK Biobank (287), M&M (288), or ACDC (289). However, the availability of both raw *k*-space data for image reconstruction and annotations of the same data for image segmentation or cardiac disease classifications are still limited. Hence, in the context of multi-task models, special focus must be given on the datasets, as *k*-space data for image reconstruction tasks are often simulated or only retrospectively undersampled, limiting the application of proposed approaches to clinical workflow.

### Neural Networks and Their Building Blocks: How to Build Your CMR Network From Scratch

The recent success of neural networks not only depends on the availability of training data, but also on the availability of expressive network architectures. The idea of neural networks goes back to the 1957, where an artificial neuron was modeled similar to the neurons in the brain (290). An input signal arrives at the neuron (layer) and is processed by the layer weights. An activation function decides if the neuron should be fired or not. A typical deep neural network consists of several layers, which can be related to modeling the complex wired structures in the brain.

*Convolutional layers* are powerful local feature extractors. The spatially-dependent features are generated by convolving the underlying image with a set of trainable filter kernels, optimized during model training. To extract global features, *fully connected layers* are used, connecting each input pixel with each output pixel. Global features are necessary in, e.g., image classification and segmentation. To emphasize the extracted features, non-linear *activation functions* are applied. Common activation functions for image regression are ReLU and its various variants, e.g., LeakyReLU, PreLU, while for image segmentation and classification tasks bounded activation functions such as tanh, sigmoid, or softmax are used. *Pooling layers* or *strided*

*convolution layers* are used to downsample the spatial features, to increase the receptive field. To increase the resolution, *strided transposed convolution layers* or *upsampling layers* that perform interpolation are common choices. In-between convolution and activation layers, often *normalization layers* are used that are reported to stabilize training and improve training convergence. These are the basic elements to build a deep neural network, however, more detailed building blocks are out of scope of this review paper.

It should be noted that the nature of MR data is complex-valued, but in the core literature only real-valued building blocks are reported. Hence, the real and imaginary plane are handled as a real-valued image with two feature channels. Recent works also focused on the implementation and correct utilization of complex-valued versions of the aforementioned building blocks, and correct network training following Wirtinger calculus (291).

### CMR Applications

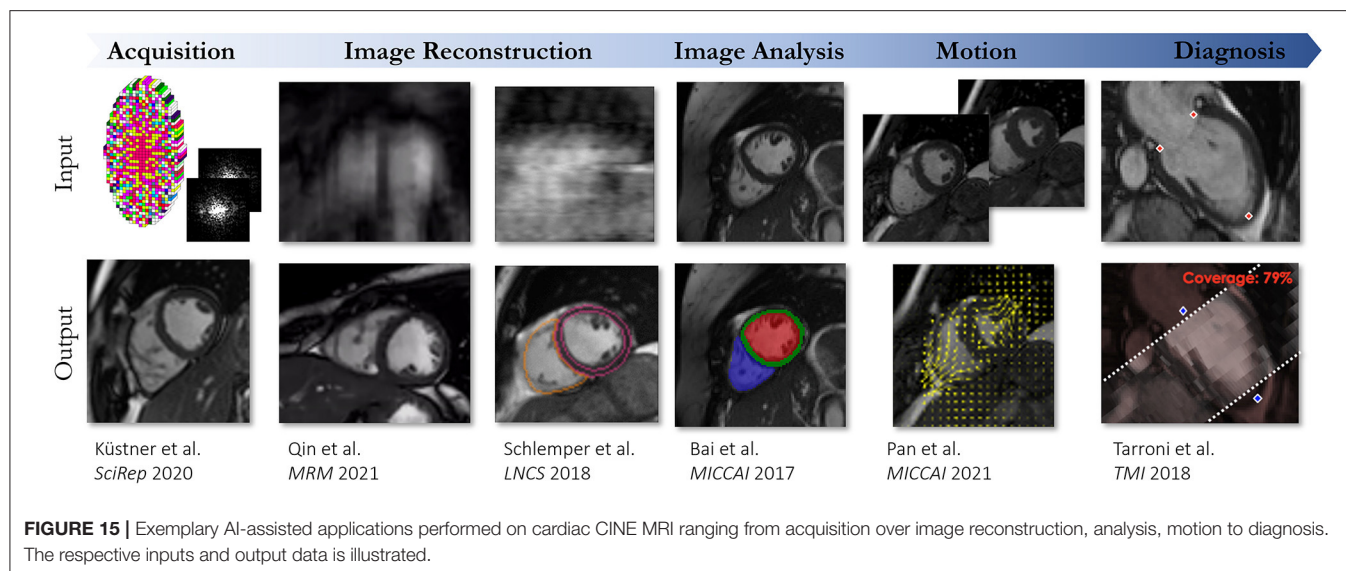
The presented layers and building blocks can be used to form a full network. For CMR, convolutional neural networks are most used, however, no unique network definition exists, and numerous variants have been proposed for various tasks. The targeted application, dimensionality and data availability mainly determine the task definitions and subsequently architectural choices. An exemplary scenario for AI applications for cardiac cine MRI over the various CMR processing steps (**Figure 14**) is depicted in **Figure 15**.

### View Planning and Image Acquisition

A comprehensive CMR exam requires complex and time-consuming scan planning and optimization of acquisition protocols. Thus, the effectiveness and image quality of a CMR scan highly depends on the experience and ability of the operator to adequately prepare patients, tune acquisition parameters, plan cardiac views and shimming, all in a timely fashion (see Section Clinical Cardiovascular MR: How Should we Perform the Examination). Currently, highly trained operators manually plan and conduct clinical CMR exams. Recently, ML methods have been proposed to automate or shorten the scanning process, standardize image acquisition and quality across patients (292–296). Major CMR vendors are now introducing ML solutions to help or automatically optimize and plan exam protocols. Other ML methods have been proposed for assessing image quality, replacing the usually subjective visual inspection, which can detect artifacts, correct acquisition parameters, and trigger a rescan if deemed necessary (297–299). Moreover, ML methods can also be used to learn the optimal sampling pattern for reducing the acquisition time while maximizing image quality (300). Thus, ML-assisted CMR examinations can help operators solve complex decision-making tasks under time pressure.

### Image Reconstruction

In MR image reconstruction, we aim at recovering an image from (undersampled) *k*-space which is corrupted by measurement noise. The acquisition process is thereby approximated and formalized in a linear forward operator, see Equation (11). Depending on the imaging application and signal modeling, the



operator involves Fourier transforms, sampling trajectories, and coil sensitivity maps. Field inhomogeneities, relaxation effects, motion, and diffusion can also be considered.

In ML frameworks, the objective is to learn the sensor-to-image mapping function having learnable parameters. The mapping function can be stated as NNs and can be used in different ways to reconstruct an image from the measured k-space data. All tasks have an image and/or k-space as input but differ in how data is processed and how further MR specific information (meta parameters or other tensors like trajectories and coil sensitivity maps) are handled for the targeted application output. These reconstruction tasks are further described hereafter and depicted in **Figure 13**.

### Image Enhancement Learning

Certain types of undersampling introduce incoherent noise-like aliasing in the zero-filled reconstructed images. Thus, an image enhancement task can be used to reduce the noise-like aliasing in the images. The network performs an image-to-image regression by predicting the output value based on the corrupted input image. The input to the denoising task can be the zero-filled (and noise-affected) MR images or reconstructed MR images that present remaining aliasing or noise amplification for high undersamplings (e.g., images reconstructed with parallel imaging). Instead of learning the denoised image, some approaches learn the residual noise to be removed from the noisy input (301–303). The mapping only acts on the image and does not consider any further information from the acquired k-space. Hence, data consistency to the measured k-space signal cannot be guaranteed. Approaches exist that add additional k-space consistency to the cost function (304) or enforce k-space consistency after image denoising (305, 306).

### K-Space to Image Learning

A different DL-based approach is to reconstruct the MR image directly from the acquired k-space data. With the so-called direct

k-space to image mapping, the k-space data are directly used as the input. Consequently, the network approximates the forward model (see Section CMR Reconstruction: From K-space to Image Space). Learning a direct mapping is especially useful if the forward model or parts of the forward model are not exactly known. In the case of fully sampled MRI under ideal conditions, the learned mapping approximates the Fourier transform (307). However, this becomes computationally very demanding due to fully connected layers which are involved here. Furthermore, consistency with the acquired k-space data cannot be guaranteed.

### Physics-Based Unrolled Learning

Another family of DL-based MR reconstruction methods is referred to as physics-based reconstruction. These approaches integrate the traditional physics-based modeling of the MR encoding (see Section K-space) with DL, ensuring consistency with the acquired data. We can distinguish two classes of problems: (a) learning in k-space domain and (b) iterative optimization in image domain with interleaved data consistency steps. The first approaches are referred as k-space learning whereas the latter one is known as unrolled optimization. These two approaches can be combined to hybrid approaches that learn both a neural network in k-space and image domain.

#### K-Space Learning

A prominent approach for physics-based learning in k-space domain (308) can be viewed as extension of the linear kernel estimation in GRAPPA. A non-linear kernel modeled by the network is learned from the ACS. The missing k-space lines can then be filled using this estimated, non-linear kernel and the data is then transformed to the image space using an Inverse Fourier transform. The final image is obtained by root-sum-of-squares reconstruction of the individual coil images.

#### Hybrid Learning

Hybrid approaches (309–311) combine the advantages of learning in k-space and image domain. These networks

are applied in an alternating manner to obtain the final reconstruction. When designing hybrid approaches, it is important to keep the basic theorems of the Fourier transform in mind: local changes in image domain result in global changes in k-space domain and vice versa, to avoid unexpected behavior.

### **Plug-and-Play Priors**

Trained image denoisers can be also combined with physics-based learning or conventional iterative reconstructions and thus serve as an advanced regularization for a traditional optimization problem. Iterative, image-wise, or patch-wise denoising is performed followed by a subsequent data consistency step, as involved in plug-and-play priors (302, 312–314), regularization by denoising (315) or image restoration (316).

### **Unrolled Optimization**

Physics-based learning, which is modeled as iterative optimization, can be viewed as generalization of iterative SENSE (126, 317) with a learned regularization in image domain. It contains a data-consistency term and a regularization term which imposes prior knowledge on the reconstruction. A gradient descent (318), proximal gradient (319), variable splitting (320), or primal-dual optimization (321) can be used for algorithm unrolling. The iterative optimization scheme is unrolled for a fixed number of iterations. Neural networks replace the gradient of the hand-crafted regularizer by a learned data-driven mapping. Various regularization networks can be used, *e.g.*, variational networks (322) or cascade of convolutional networks (319). In CMR, the dynamic or quantitative dimensions can be incorporated into network architecture design [*e.g.*, recurrent networks (311, 323)], building blocks [*e.g.*, 2D+t (324), 3D+t convolutions (325)], data priors (326), or loss modeling (327). Training several iterations with alternating mapping functions and intermittent data consistencies reflect thus unrolled optimizations (328).

### **Super Resolution**

An alternative approach for accelerating the image acquisition while simultaneously increasing spatial resolution is the usage of DL-based super resolution (SR). Images are acquired at a low-resolution (with or without undersampling) and retrospectively reconstructed to the high-resolution target. This has been studied for cardiac cine (329, 330) and whole-heart CMR (331–336).

### **Image Analysis**

CMR image segmentation and quantitative evaluation can be a challenging, time-consuming and operator intensive task. However, quantitative analysis of myocardial function, perfusion, pathological tissues, provides important diagnostic and prognostic information (66). In recent years, a large number of ML-based methods have been proposed to automatically perform CMR image segmentation and analysis, thereby significantly reducing the time required for CMR image assessment (337). Considerable efforts have been directed toward cine imaging, as it is considered the gold standard for the assessment of cardiac chamber volumes and function (338–341). In this case, DL-based methods automatically segment the

myocardium and cardiac chambers from MRI images, replacing manual approaches that are time-consuming and prone to observer variability, to enable the extraction of quantitative indices, such as LV and RV volumes, mass, and EF. Some frameworks additionally provide myocardial strain measures (299, 342). Automated segmentation methods have also been proposed to quantitatively derive other important markers of cardiovascular disease such as volume of pericardial adipose tissue (343), and scarred tissue areas (from LGE images) (344–348). Moreover, few DL-based methods have proposed to automatically quantify myocardial tissue from native T<sub>1</sub> mapping (349, 350) and myocardial blood flow from contrast-enhanced perfusion CMR (351, 352).

### **Motion Correction**

Motion artifacts due to physiological motion or caused by mis-triggering in the ECG or movements during the examination are a potential source of image degradation. Several approaches using DL exist to correct for motion artifacts in the area of CMR.

Adversarial training strategies as proposed in Zhang et al. (353) aim to correct for the motion in the image domain. A database of motion-corrected and motion-degraded images serve as training database. A generator network predicts motion-corrected images. The discriminator network tries to distinguish if the generated motion-corrected image is from the manifold of real motion-corrected or generated motion-corrected images. The goal of the generator network is to fool the discriminator network to generate images that look like real motion-corrected images. Another method of retrospective motion correction in CMR with adversarial training is proposed in Ghodrati et al. (354). Here, a Variational Autoencoders is trained on healthy subjects and patients with suspected cardiovascular disease to remove respiratory motion.

Instead of addressing MR motion correction in the image domain, Oksuz et al. (355), apply motion correction directly in k-space. Their method uses a generator network that is motivated by Automap (307) to transform the k-space directly to a reconstructed image. Pairs of synthetically motion-corrupted k-space data and artifact-free reconstructed CMR images serve as training database for the proposed adversarial training strategy. Beyond image reconstruction, Oksuz et al. (356) introduced a joint framework for motion artifact detection and correction in k-space and image segmentation. The motion artifact network detects motion-affected lines in k-space, influencing the data consistency term. The motion-corrected image is obtained from a subsequent bi-directional recurrent CNN. The segmentation network is based on a standard UNet architecture (357). Their work showed that end-to-end training outperforms sequential training substantially when trained on UK Biobank data (287), with synthetic motion corruption and synthetically added phase information.

Retrospective motion-correction of reconstructed CMR images is proposed in Huang et al. (358). First, CMR reconstruction is performed with a Convolutional Gated Recurrent Units and a subsequent data consistency layer. Motion fields are then estimated from the reconstructed images using a FlowNet architecture. The estimated motion fields are then

used in a post-processing motion-correction step to improve the final reconstruction.

Large non-rigid motion across multiple temporal frames can occur and in the case of 2D imaging, the existence of through-plane motion complicates the motion estimation process. A fast and reliable motion estimation is therefore required that correlates these short- and long-term correspondences, as proposed by Pan et al. (359) and Küstner et al. (360), and either operates on the image domain (359) or on the accelerated raw data (360).

Joint motion estimation and reconstruction is proposed by Seegolam et al. (361). Here, a motion-estimation UNet is embedded directly in the data consistency term of a dynamic reconstruction network. This approach allows for exploiting the whole temporal information in each cardiac phase, resulting in high-quality reconstruction of extremely undersampled CMR data.

## Multi-Task Networks

Sun et al. (362) proposed a unified deep network architecture for joint image reconstruction and segmentation. Image reconstruction is formulated as a cascaded encoder-decoder network with intermittent data consistency layers to facilitate learning and making use of the acquired k-space data. The reconstruction and segmentation networks share the same encoder, acting as a regularizer for the two tasks, while the decoder is different, and hence, task specific. Their results suggest that training a joint network is beneficial for high-quality segmentation of undersampled k-space data, however, the evaluation was performed on simulated k-space data of the MRBrainS segmentation challenge dataset (363). Similar observations were made in Huang et al. (364) where FR-Net for image reconstruction (inspired by the fast iterative shrinkage-thresholding algorithm), was combined with a UNet for myocardial segmentation. However, this approach was evaluated only on simulated k-space data. While these multi-task networks aim for a reconstructed intermediate image, Schlemper et al. (365) bypassed this step and directly predicted segmentation maps from highly undersampled dynamic CMR images of the UK Biobank data (287). Their results indicate that clinical parameters can be computed within an error of 10% if at least 10 lines are acquired for each cardiac phase, using Cartesian sampling.

Joint learning of motion estimation and segmentation from fully-sampled data was proposed by Qin et al. (366). An extension to undersampled data has been proposed in Qin et al. (367), where the network training is guided by fully-sampled data. The results suggested that an efficient motion estimation network can bypass the need for high-quality reconstructions in order to achieve accurate image segmentation.

The surveyed approaches achieve promising results for end-to-end training. However, to date, none of these approaches have been tested on real k-space data and evaluated for clinical applicability. Furthermore, evaluation of these k-space data also requires the availability of proper training databases with both real k-space data and manual segmentations.

## CHALLENGES AND CONCLUSION

The plethora of CMR sequences available and information offered makes the technique attractive, but also very challenging, particularly for a beginner. This review has provided an overview of the main CMR concepts and techniques, including recent technical advances, which should be useful for anyone wanting to improve, update, or maintain their knowledge and understanding of CMR. Ultimately, the dialogue between the scientific and clinical communities should improve if all users understand CMR terms and use a common language. This review has described the key physical principles underlying the most commonly used (quantitative) CMR sequences and preparation pulses and causes of common image artifacts. This review has explained how and why CMR can (and should) be used for diagnosis and guiding clinical decision making in a range of cardiovascular disease scenarios, such as ischemic heart disease, myocarditis, atrial fibrillation, valvular heart disease, vascular disease, congenital heart disease, and cardiac tumors. This review has also outlined the building blocks of a CMR examination, explained how to perform a comprehensive patient-tailored examination based on these building blocks in a clinically acceptable timeframe and avoid common scanning mistakes. The challenges of CMR associated with acquisition time, SNR, spatial and temporal resolution, cardiac and respiratory motion have been discussed. In addition, popular and recently developed methods of suppressing and handling motion have been described. This review has explained how to speed up CMR scans by acquiring less data (than needed by conventional methods) using (pseudo-)random sampling trajectories and non-linear reconstruction algorithms, such as compressed sensing and low-rank completion, model-based or DL reconstruction approaches. Finally, this review has discussed how DL approaches can potentially help overcome challenges such as time-consuming reconstructions and quantitative analysis.

## AUTHOR CONTRIBUTIONS

TI, WS, SW, CC, MB-I, KH, TC, and TK wrote sections of the manuscript. TC and TK edited the sections and manuscript. All authors contributed to manuscript revision, read, and approved the submitted version.

## FUNDING

This work was supported by the Deutsche Forschungsgemeinschaft (DFG, German Research Foundation) under Germany's Excellence Strategy—EXC 2180 #390900677 and EXC 2064/1 #390727645. This work was part of a project that has received funding from the European Union's Horizon 2020 research and innovation programme under grant agreement No. 867450.

## ACKNOWLEDGMENTS

Caitlin Penny (Queensland X-Ray, Mater Hospital Brisbane, Brisbane, Australia) contributed to the intellectual content of

## Section Clinical Cardiovascular MR: How Should We Perform the Examination.

## SUPPLEMENTARY MATERIAL

The Supplementary Material for this article can be found online at: <https://www.frontiersin.org/articles/10.3389/fcvm.2022.826283/full#supplementary-material>

**Supplementary Figure 1 |** Still from a balanced steady-state free precession 4-chamber cine. This sequence has high intrinsic  $T_1$  and  $T_2$  contrast enabling cardiac chambers and anatomy to be visualized with exquisite clarity. The blood pool appears bright. Fat also appears high signal. Areas where fat and water protons interface appear black in outline due to chemical shift artifact. This allows fibrofatty change (arrows) to be readily visualized in the septum (arrows) and epicardial lateral wall, enabling a diagnosis of arrhythmogenic cardiomyopathy to be made without the need for contrast.

**Supplementary Figure 2 |** Balanced steady-state free precession cine demonstrating a jet of aortic regurgitation (arrow). This cannot be reliably quantified by visual assessment of the jet and once detected should be further evaluated using phase-contrast velocity mapping.

**Supplementary Figure 3 |** Quantification of aortic regurgitation in the patient depicted in **Figure 9** using phase-contrast velocity mapping. The magnitude image on the top right is used to contour a region of interest in the aorta. The phase image on the top left is used to determine flow and plot this against time (bottom). The flow drops below the baseline for the whole of systole. The regurgitant volume is ~67 ml which amounts to a regurgitant fraction of 60%, denoting severe regurgitation.

**Supplementary Figure 4 |** An example of a clinical imaging protocol library built with three acquisition strategies for managing irregular rhythms: Sinus Rhythm; Mildly Irregular Rhythm; Severely Irregular Rhythm.

**Supplementary Table 1 |** A general cardiomyopathy protocol can be modified to assess acute presentations by the addition of imaging sequences sensitive to oedema (highlighted).

## REFERENCES

- Pohost GM. The history of cardiovascular magnetic resonance. *JACC Cardiovasc Imaging*. (2008) 1:672–8. doi: 10.1016/j.jcmg.2008.07.009
- Ridgway JP. Cardiovascular magnetic resonance physics for clinicians: part I. *J Cardiovasc Magn Reson*. (2010) 12:71. doi: 10.1186/1532-429X-12-71
- Biglands JD, Radjenovic A, Ridgway JP. Cardiovascular magnetic resonance physics for clinicians: part II. *J Cardiovasc Magn Reson*. (2012) 14:66. doi: 10.1186/1532-429X-14-66
- Leiner T, Rueckert D, Suinesiaputra A, Baeßler B, Nezafat R, Išgum I, et al. Machine learning in cardiovascular magnetic resonance: basic concepts and applications. *J Cardiovasc Magn Reson*. (2019) 21:61. doi: 10.1186/s12968-019-0575-y
- Kramer CM, Barkhausen J, Bucciarelli-Ducci C, Flamm SD, Kim RJ, Nagel E. Standardized cardiovascular magnetic resonance imaging (CMR) protocols: 2020 update. *J Cardiovasc Magn Reson*. (2020) 22:17. doi: 10.1186/s12968-020-00607-1
- Menchón-Lara R-M, Simmross-Wattenberg F, Casaseca-de-la-Higuera P, Martín-Fernández M, Alberola-López C. Reconstruction techniques for cardiac cine MRI. *Insights Imaging*. (2019) 10:100. doi: 10.1186/s13244-019-0754-2
- Hamilton J, Franson D, Seiberlich N. Recent advances in parallel imaging for MRI. *Prog Nucl Magn Reson Spectrosc*. (2017) 101:71–95. doi: 10.1016/j.pnmrs.2017.04.002
- Feng L, Ma D, Liu F. Rapid MR relaxometry using deep learning: an overview of current techniques and emerging trends. *NMR Biomed*. (2020) 2020:e4416. doi: 10.1002/nbm.4416
- Larkman DJ, Nunes RG. Parallel magnetic resonance imaging. *Phys Med Biol*. (2007) 52:R15–55. doi: 10.1088/0031-9155/52/7/R01
- Kawel-Boehm N, Hetzel SJ, Ambale-Venkatesh B, Captur G, Francois CJ, Jerosch-Herold M, et al. Reference ranges (“normal values”) for cardiovascular magnetic resonance (CMR) in adults and children: 2020 update. *J Cardiovasc Magn Reson*. (2020) 22:87. doi: 10.1186/s12968-020-00683-3
- Sermesant M, Delingette H, Cochet H, Jaïs P, Ayache N. Applications of artificial intelligence in cardiovascular imaging. *Nat Rev Cardiol*. (2021) 18:600–9. doi: 10.1038/s41569-021-00527-2
- Weingärtner S, Meßner NM, Budjan J, Loßnitzer D, Mattler U, Papavassiliu T, et al. Myocardial T(1)-mapping at 3T using saturation-recovery: reference values, precision and comparison with MOLLI. *J Cardiovasc Magn Reson*. (2016) 18:84. doi: 10.1186/s12968-016-0302-x
- von Knobelsdorff-Brenkenhoff F, Prothmann M, Dieringer MA, Wassmuth R, Greiser A, Schwenke C, et al. Myocardial T1 and T2 mapping at 3 T: reference values, influencing factors and implications. *J Cardiovasc Magn Reson*. (2013) 15:53. doi: 10.1186/1532-429X-15-53
- Bush A, Borzage M, Detterich J, Kato RM, Meiselman HJ, Coates T, et al. Empirical model of human blood transverse relaxation at 3 T improves MRI T(2) oximetry. *Magn Reson Med*. (2017) 77:2364–71. doi: 10.1002/mrm.26311
- Bloch F. Nuclear induction. *Phys Rev*. (1946) 70:460. doi: 10.1103/PhysRev.70.460
- Bloch F, Hansen WW, Packard M. The nuclear induction experiment. *Phys Rev*. (1946) 70:474–85. doi: 10.1103/PhysRev.70.474
- Hennig J. Echoes—how to generate, recognize, use or avoid them in MR-imaging sequences. Part I: fundamental and not so fundamental properties of spin echoes. *Concepts Magn Reson*. (1991) 3:125–43. doi: 10.1002/cmr.1820030302
- Hennig J. Echoes—how to generate, recognize, use or avoid them in MR-imaging sequences. Part II: echoes in imaging sequences. *Concepts Magn Reson*. (1991) 3:179–92. doi: 10.1002/cmr.1820030402
- Weigel M. Extended phase graphs: dephasing, RF pulses, and echoes—pure and simple. *J Magn Reson Imaging*. (2015) 41:266–95. doi: 10.1002/jmri.24619
- Wilm BJ, Barmet C, Pavan M, Pruessmann KP. Higher order reconstruction for MRI in the presence of spatiotemporal field perturbations. *Magn Reson Med*. (2011) 65:1690–701. doi: 10.1002/mrm.22767
- Hahn EL. Spin echoes. *Phys Rev*. (1950) 80:580. doi: 10.1103/PhysRev.80.580
- Mansfield P, Maudsley AA. Planar spin imaging by NMR. *J Phys C Solid State Phys*. (1976) 9:L409. doi: 10.1088/0022-3719/9/15/004
- Sekihara K. Steady-state magnetizations in rapid NMR imaging using small flip angles and short repetition intervals. *IEEE Trans Med Imaging*. (1987) 6:157–64. doi: 10.1109/TMI.1987.4307816
- Bieri O, Scheffler K. Fundamentals of balanced steady state free precession MRI. *J Magn Reson Imaging*. (2013) 38:2–11. doi: 10.1002/jmri.24163
- Scheffler K, Lehnhardt S. Principles and applications of balanced SSFP techniques. *Eur Radiol*. (2003) 13:2409–18. doi: 10.1007/s00330-003-1957-x
- Bydder GM, Young IR. MR imaging: clinical use of the inversion recovery sequence. *J Comput Assist Tomogr*. (1985) 9:659–75. doi: 10.1097/00004728-198507010-00002
- Edelman RR, Chien D, Kim D. Fast selective black blood MR imaging. *Radiology*. (1991) 181:655–60. doi: 10.1148/radiology.181.3.1947077
- Levitt MH. Composite pulses. *Prog Nucl Magn Reson Spectrosc*. (1986) 18:61–122. doi: 10.1016/0079-6565(86)80005-X
- Ugurbil K, Garwood M, Bendall MR. Amplitude- and frequency-modulated pulses to achieve 90° plane rotations with inhomogeneous B1 fields. *J Magn Reson*. (1987) 72:177–85. doi: 10.1016/0022-2364(87)90186-7
- Brittain JH, Hu BS, Wright GA, Meyer CH, Macovski A, Nishimura DG. Coronary angiography with magnetization-prepared T2 contrast. *Magn Reson Med*. (1995) 33:689–96. doi: 10.1002/mrm.1910330515

31. Foltz WD, Al-Kwafi O, Sussman MS, Stainsby JA, Wright GA. Optimized spiral imaging for measurement of myocardial T2 relaxation. *Magn Reson Med.* (2003) 49:1089–97. doi: 10.1002/mrm.10467
32. Giri S, Chung Y-C, Merchant A, Mihai G, Rajagopalan S, Raman SV, et al. T2 quantification for improved detection of myocardial edema. *J Cardiovasc Magn Reson.* (2009) 11:1–13. doi: 10.1186/1532-429X-11-56
33. Huang T-Y, Liu Y-J, Stemmer A, Poncelet BP. T2 measurement of the human myocardium using a T2-prepared transient-state TrueFISP sequence. *Magn Reson Med.* (2007) 57:960–6. doi: 10.1002/mrm.21208
34. Gram M, Seethaler M, Gensler D, Oberberger J, Jakob PM, Nordbeck P. Balanced spin-lock preparation for B1-insensitive and B0-insensitive quantification of the rotating frame relaxation time T1. *Magn Reson Med.* (2021) 85:2771–80. doi: 10.1002/mrm.28585
35. Mangia S, Liimatainen T, Garwood M, Michaeli S. Rotating frame relaxation during adiabatic pulses vs. conventional spin lock: simulations and experimental results at 4T. *Magn Reson Imaging.* (2009) 27:1074–87. doi: 10.1016/j.mri.2009.05.023
36. Michaeli S, Sorce DJ, Springer Jr CS, Ugurbil K, Garwood M. T1 MRI contrast in the human brain: modulation of the longitudinal rotating frame relaxation shutter-speed during an adiabatic RF pulse. *J Magn Reson.* (2006) 181:135–47. doi: 10.1016/j.jmr.2006.04.002
37. Carr JC, Simonetti OP, Bundy J, Li D, Pereles S, Finn JP. Cine MR angiography of the heart with segmented true fast imaging with steady-state precession. *Radiology.* (2001) 219 3:828–34. doi: 10.1148/radiology.219.3.r01jn44828
38. Amano Y, Takayama M, Kumita S. Contrast-enhanced myocardial T1-weighted scout (Look-Locker) imaging for the detection of myocardial damages in hypertrophic cardiomyopathy. *J Magn Reson Imaging.* (2009) 30:778–84. doi: 10.1002/jmri.21921
39. Kellman P, Arai AE, McVeigh ER, Aletras AH. Phase-sensitive inversion recovery for detecting myocardial infarction using gadolinium-delayed hyperenhancement. *Magn Reson Med.* (2002) 47:372–83. doi: 10.1002/mrm.20110
40. Qayyum AA, Kastrup J. Measuring myocardial perfusion: the role of PET, MRI and CT. *Clin Radiol.* (2015) 70:576–84. doi: 10.1016/j.crad.2014.12.017
41. Kellman P, Arai AE. Imaging sequences for first pass perfusion—a review. *J Cardiovasc Magn Reson.* (2007) 9:525–37. doi: 10.1080/10976640601187604
42. Haaf P, Garg P, Messroghli DR, Broadbent DA, Greenwood JP, Plein S. Cardiac T1 mapping and extracellular volume (ECV) in clinical practice: a comprehensive review. *J Cardiovasc Magn Reson.* (2017) 18:89. doi: 10.1186/s12968-016-0308-4
43. Look DC, Locker DR. Time saving in measurement of NMR and EPR relaxation times. *Rev Sci Instrum.* (1970) 41:250–1. doi: 10.1063/1.1684482
44. Messroghli DR, Radjenovic A, Kozerke S, Higgins DM, Sivananthan MU, Ridgway JP. Modified look-locker inversion recovery (MOLLI) for high-resolution T1 mapping of the heart. *Magn Reson Med.* (2004) 52:141–6. doi: 10.1002/mrm.20110
45. Kellman P, Hansen MS. T1-mapping in the heart: accuracy and precision. *J Cardiovasc Magn Reson.* (2014) 16:1–20. doi: 10.1186/1532-429X-16-2
46. Chow K, Flewitt JA, Green JD, Pagano JJ, Friedrich MG, Thompson RB. Saturation recovery single-shot acquisition (SASHA) for myocardial T1 mapping. *Magn Reson Med.* (2014) 71:2082–95. doi: 10.1002/mrm.24878
47. Weingärtner S, Akçakaya M, Basha T, Kissinger KV, Goddu B, Berg S, et al. Combined saturation/inversion recovery sequences for improved evaluation of scar and diffuse fibrosis in patients with arrhythmia or heart rate variability. *Magn Reson Med.* (2014) 71:1024–34. doi: 10.1002/mrm.24761
48. Ding H, Fernandez-de-Manuel L, Schär M, Schuleri KH, Halperin H, He L, et al. Three-dimensional whole-heart T2 mapping at 3T. *Magn Reson Med.* (2015) 74:803–16. doi: 10.1002/mrm.25458
49. Anderson LJ, Holden S, Davis B, Prescott E, Charrier CC, Bunce NH, et al. Cardiovascular T2-star (T2\*) magnetic resonance for the early diagnosis of myocardial iron overload. *Eur Heart J.* (2001) 22:2171–9. doi: 10.1053/euhj.2001.2822
50. Witschey WRT, Zsido GA, Koomalsingh K, Kondo N, Minakawa M, Shuto T, et al. In vivo chronic myocardial infarction characterization by spin locked cardiovascular magnetic resonance. *J Cardiovasc Magn Reson.* (2012) 14:1–9. doi: 10.1186/1532-429X-14-37
51. Ma D, Gulani V, Seiberlich N, Liu K, Sunshine JL, Duerk JL, et al. Magnetic resonance fingerprinting. *Nature.* (2013) 495:187–92. doi: 10.1038/nature11971
52. Liu Y, Hamilton J, Rajagopalan S, Seiberlich N. Cardiac magnetic resonance fingerprinting: technical overview and initial results. *JACC Cardiovasc Imaging.* (2018) 11:1837–53. doi: 10.1016/j.jcmg.2018.08.028
53. Cruz G, Jaubert O, Botnar RM, Prieto C. Cardiac magnetic resonance fingerprinting: technical developments and initial clinical validation. *Curr Cardiol Rep.* (2019) 21:1–10. doi: 10.1007/s11886-019-1181-1
54. Hamilton JJ, Jiang Y, Chen Y, Ma D, Lo WC, Griswold M, et al. MR fingerprinting for rapid quantification of myocardial T1, T2, and proton spin density. *Magn Reson Med.* (2017) 77:1446–58. doi: 10.1002/mrm.26216
55. Cruz G, Jaubert O, Qi H, Bustin A, Milotta G, Schneider T, et al. 3D free-breathing cardiac magnetic resonance fingerprinting. *NMR Biomed.* (2020) 33:e4370. doi: 10.1002/nbm.4370
56. Bryant DJ, Payne JA, Firmin DN, Longmore DB. Measurement of flow with NMR imaging using a gradient pulse and phase difference technique. *J Comput Assist Tomogr.* (1984) 8:588–93. doi: 10.1097/00004728-198408000-00002
57. Markl M, Frydrychowicz A, Kozerke S, Hope M, Wieben O. 4D flow MRI. *J Magn Reson Imaging.* (2012) 36:1015–36. doi: 10.1002/jmri.23632
58. Wigström L, Sjöqvist L, Wranne B. Temporally resolved 3D phase-contrast imaging. *Magn Reson Med.* (1996) 36:800–3. doi: 10.1002/mrm.1910360521
59. Kober F, Jao T, Troalen T, Nayak KS. Myocardial arterial spin labeling. *J Cardiovasc Magn Reson.* (2016) 18:1–16. doi: 10.1186/s12968-016-0235-4
60. Zun Z, Wong EC, Nayak KS. Assessment of myocardial blood flow (MBF) in humans using arterial spin labeling (ASL): feasibility and noise analysis. *Magn Reson Med.* (2009) 62:975–83. doi: 10.1002/mrm.22088
61. Buxton RB, Frank LR, Wong EC, Siewert B, Warach S, Edelman RR. A general kinetic model for quantitative perfusion imaging with arterial spin labeling. *Magn Reson Med.* (1998) 40:383–96. doi: 10.1002/mrm.1910400308
62. Ferreira PF, Gatehouse PD, Mohiaddin RH, Firmin DN. Cardiovascular magnetic resonance artefacts. *J Cardiovasc Magn Reson.* (2013) 15:1–39. doi: 10.1186/1532-429X-15-41
63. McDonagh TA, Metra M, Adamo M, Gardner RS, Baumbach A, Bohm M, et al. 2021 ESC Guidelines for the diagnosis and treatment of acute and chronic heart failure. *Eur Heart J.* (2021) 42:3599–726. doi: 10.1093/eurheartj/ehab368
64. Vahanian A, Beyersdorf F, Praz F, Milojevic M, Baldus S, Bauersachs J, et al. 2021 ESC/EACTS guidelines for the management of valvular heart disease: developed by the task force for the management of valvular heart disease of the European society of cardiology (ESC) and the European association for cardio-thoracic surgery (EACTS). *Eur J Card Thorac Surg.* (2021) 60:727–800. doi: 10.1093/eurheartj/ehab395
65. Pennell DJ. Cardiovascular magnetic resonance: twenty-first century solutions in cardiology. *Clin Med.* (2003) 3:273–8. doi: 10.7861/clinmedicine.3-3-273
66. Schulz-Menger J, Bluemke DA, Bremerich J, Flamm SD, Fogel MA, Friedrich MG, et al. Standardized image interpretation and post-processing in cardiovascular magnetic resonance - 2020 update: society for cardiovascular magnetic resonance (SCMR): board of trustees task force on standardized post-processing. *J Cardiovasc Magn Reson.* (2020) 22:19. doi: 10.1186/s12968-020-00610-6
67. Bing R, Dweck MR. Myocardial fibrosis: why image, how to image and clinical implications. *Heart.* (2019) 105:1832–40. doi: 10.1136/heartjnl-2019-315560
68. Mahrholdt H, Wagner A, Judd RM, Sechtem U, Kim RJ. Delayed enhancement cardiovascular magnetic resonance assessment of non-ischaemic cardiomyopathies. *Eur Heart J.* (2005) 26:1461–74. doi: 10.1093/eurheartj/ehi258
69. Gulati M, Levy PD, Mukherjee D, Amsterdam E, Bhatt DL, Birtcher KK, et al. 2021 AHA/ACC/ASE/CHEST/SAEM/SCCT/SCMR guideline for the evaluation and diagnosis of chest pain: executive summary: a report of the American college of cardiology/American heart association joint committee on clinical practice guidelines. *Circulation.* (2021) 144:e368–454. doi: 10.1161/CIR.0000000000001030

70. Ismail TF, Prasad SK, Pennell DJ. Prognostic importance of late gadolinium enhancement cardiovascular magnetic resonance in cardiomyopathy. *Heart*. (2012) 98:438–42. doi: 10.1136/heartjnl-2011-300814
71. Halliday BP, Gulati A, Ali A, Guha K, Newsome S, Arzanauskaite M, et al. Association between midwall late gadolinium enhancement and sudden cardiac death in patients with dilated cardiomyopathy and mild and moderate left ventricular systolic dysfunction. *Circulation*. (2017) 135:2106–15. doi: 10.1161/CIRCULATIONAHA.116.026910
72. Gulati A, Japp AG, Raza S, Halliday BP, Jones DA, Newsome S, et al. Absence of myocardial fibrosis predicts favorable long-term survival in new-onset heart failure. *Circ Cardiovasc Imaging*. (2018) 11:e007722. doi: 10.1161/CIRCIMAGING.118.007722
73. Gulati A, Jabbour A, Ismail TF, Guha K, Khwaja J, Raza S, et al. Association of fibrosis with mortality and sudden cardiac death in patients with nonischemic dilated cardiomyopathy. *JAMA*. (2013) 309:896–908. doi: 10.1001/jama.2013.1363
74. Georgiopoulos G, Figliozzi S, Sanguineti F, Aquaro GD, di Bella G, Stamatiopoulos K, et al. Prognostic impact of late gadolinium enhancement by cardiovascular magnetic resonance in myocarditis: a systematic review and meta-analysis. *Circ Cardiovasc Imaging*. (2021) 14:e011492. doi: 10.1161/CIRCIMAGING.120.011492
75. Kim RJ, Wu E, Rafael A, Chen EL, Parker MA, Simonetti O, et al. The use of contrast-enhanced magnetic resonance imaging to identify reversible myocardial dysfunction. *N Engl J Med*. (2000) 343:1445–53. doi: 10.1056/NEJM200011163432003
76. Patel AR, Salerno M, Kwong RY, Singh A, Heydari B, Kramer CM. Stress cardiac magnetic resonance myocardial perfusion imaging: JACC review topic of the week. *J Am Coll Cardiol*. (2021) 78:1655–68. doi: 10.1016/j.jacc.2021.08.022
77. Leiner T, Bogaert J, Friedrich MG, Mohiaddin R, Muthurangu V, Myerson S, et al. SCMR position paper (2020) on clinical indications for cardiovascular magnetic resonance. *J Cardiovasc Magn Reson*. (2020) 22:76. doi: 10.1186/s12968-020-00682-4
78. Arai AE, Hsu LY. Global developments in stress perfusion cardiovascular magnetic resonance. *Circulation*. (2020) 141:1292–4. doi: 10.1161/CIRCULATIONAHA.120.045967
79. Gulati A, Ismail TF, Ali A, Hsu LY, Goncalves C, Ismail NA, et al. Microvascular dysfunction in dilated cardiomyopathy: a quantitative stress perfusion cardiovascular magnetic resonance study. *JACC Cardiovasc Imaging*. (2019) 12 (8 Pt. 2):1699–708. doi: 10.1016/j.jcmg.2018.10.032
80. Hsu LY, Jacobs M, Benovoy M, Ta AD, Conn HM, Winkler S, et al. Diagnostic performance of fully automated pixel-wise quantitative myocardial perfusion imaging by cardiovascular magnetic resonance. *JACC Cardiovasc Imaging*. (2018) 11:697–707. doi: 10.1016/j.jcmg.2018.01.005
81. Sammut EC, Villa ADM, Di Giovine G, Dancy L, Bosio F, Gibbs T, et al. Prognostic value of quantitative stress perfusion cardiac magnetic resonance. *JACC Cardiovasc Imaging*. (2018) 11:686–94. doi: 10.1016/j.jcmg.2017.07.022
82. Zarinabad N, Chiribiri A, Hautvast GL, Ishida M, Schuster A, Cvetkovic Z, et al. Voxel-wise quantification of myocardial perfusion by cardiac magnetic resonance. Feasibility and methods comparison. *Magn Reson Med*. (2012) 68:1994–2004. doi: 10.1002/mrm.24195
83. Tourais J, Schneider T, Scannell C, Franks R, Sanchez-Gonzalez J, Doneva M, et al. editors. *Free-Breathing High-Resolution Quantitative First-Pass Perfusion Cardiac MR using Dual-Echo Dixon*. ISMRM (2021).
84. Villa AD, Sammut E, Zarinabad N, Carr-White G, Lee J, Bettencourt N, et al. Microvascular ischemia in hypertrophic cardiomyopathy: new insights from high-resolution combined quantification of perfusion and late gadolinium enhancement. *J Cardiovasc Magn Reson*. (2016) 18:4. doi: 10.1186/s12968-016-0223-8
85. Ismail TF, Hsu LY, Greve AM, Goncalves C, Jabbour A, Gulati A, et al. Coronary microvascular ischemia in hypertrophic cardiomyopathy - a pixel-wise quantitative cardiovascular magnetic resonance perfusion study. *J Cardiovasc Magn Reson*. (2014) 16:49. doi: 10.1186/s12968-014-0049-1
86. Hsu LY, Groves DW, Aletras AH, Kellman P, Arai AE. A quantitative pixel-wise measurement of myocardial blood flow by contrast-enhanced first-pass CMR perfusion imaging: microsphere validation in dogs and feasibility study in humans. *JACC Cardiovasc Imaging*. (2012) 5:154–66. doi: 10.1016/j.jcmg.2011.07.013
87. Patel AR, Antkowiak PF, Nandalur KR, West AM, Salerno M, Arora V, et al. Assessment of advanced coronary artery disease: advantages of quantitative cardiac magnetic resonance perfusion analysis. *J Am Coll Cardiol*. (2010) 56:561–9. doi: 10.1016/j.jacc.2010.02.061
88. Messroghli DR, Moon JC, Ferreira VM, Grosse-Wortmann L, He T, Kellman P, et al. Clinical recommendations for cardiovascular magnetic resonance mapping of T1, T2, T2\* and extracellular volume: a consensus statement by the society for cardiovascular magnetic resonance (SCMR) endorsed by the European association for cardiovascular imaging (EACVI). *J Cardiovasc Magn Reson*. (2017) 19:75. doi: 10.1186/s12968-017-0389-8
89. Modell B, Khan M, Darlison M, Westwood MA, Ingram D, Pennell DJ. Improved survival of thalassaemia major in the UK and relation to T2\* cardiovascular magnetic resonance. *J Cardiovasc Magn Reson*. (2008) 10:42. doi: 10.1186/1532-429X-10-42
90. Kittleson MM, Maurer MS, Ambardekar AV, Bullock-Palmer RP, Chang PP, Eisen HJ, et al. Cardiac amyloidosis: evolving diagnosis and management: a scientific statement from the American heart association. *Circulation*. (2020) 142:e7–22. doi: 10.1161/CIR.0000000000000792
91. Assomull RG, Shakespeare C, Kalra PR, Lloyd G, Gulati A, Strange J, et al. Role of cardiovascular magnetic resonance as a gatekeeper to invasive coronary angiography in patients presenting with heart failure of unknown etiology. *Circulation*. (2011) 124:1351–60. doi: 10.1161/CIRCULATIONAHA.110.011346
92. Maron BJ, Maron MS. The remarkable 50 years of imaging in HCM and how it has changed diagnosis and management: from M-mode echocardiography to CMR. *JACC Cardiovasc Imaging*. (2016) 9:858–72. doi: 10.1016/j.jcmg.2016.05.003
93. te Riele AS, Tandri H, Bluemke DA. Arrhythmogenic right ventricular cardiomyopathy (ARVC): cardiovascular magnetic resonance update. *J Cardiovasc Magn Reson*. (2014) 16:50. doi: 10.1186/s12968-014-0050-8
94. Eitel I, Friedrich MG. T2-weighted cardiovascular magnetic resonance in acute cardiac disease. *J Cardiovasc Magn Reson*. (2011) 13:13. doi: 10.1186/1532-429X-13-13
95. Bustin A, Hua A, Milotta G, Jaubert O, Hajhosseiny R, Ismail TF, et al. High-Spatial-Resolution 3D whole-heart MRI t2 mapping for assessment of myocarditis. *Radiology*. (2021) 298:578–86. doi: 10.1148/radiol.202101630
96. Ferreira VM, Schulz-Menger J, Holmvang G, Kramer CM, Carbone I, Sechtem U, et al. Cardiovascular magnetic resonance in nonischemic myocardial inflammation: expert recommendations. *J Am Coll Cardiol*. (2018) 72:3158–76. doi: 10.1016/j.jacc.2018.09.072
97. Kollandaivelu A, Lardo AC, Halperin HR. Cardiovascular magnetic resonance guided electrophysiology studies. *J Cardiovasc Magn Reson*. (2009) 11:21. doi: 10.1186/1532-429X-11-21
98. Michaud GF, Stevenson WG. Atrial fibrillation. *N Engl J Med*. (2021) 384:353–61. doi: 10.1056/NEJMc2023658
99. Chubb H, Karim R, Mukherjee R, Williams SE, Whitaker J, Harrison J, et al. A comprehensive multi-index cardiac magnetic resonance-guided assessment of atrial fibrillation substrate prior to ablation: prediction of long-term outcomes. *J Cardiovasc Electrophysiol*. (2019) 30:1894–903. doi: 10.1111/jce.14111
100. Soto-Iglesias D, Penela D, Jauregui B, Acosta J, Fernandez-Armenta J, Linhart M, et al. Cardiac magnetic resonance-guided ventricular tachycardia substrate ablation. *JACC Clin Electrophysiol*. (2020) 6:436–47. doi: 10.1016/j.jacep.2019.11.004
101. Ntsinjana HN, Hughes ML, Taylor AM. The role of cardiovascular magnetic resonance in pediatric congenital heart disease. *J Cardiovasc Magn Reson*. (2011) 13:51. doi: 10.1186/1532-429X-13-51
102. Marelli AJ, Mackie AS, Ionescu-Ittu R, Rahme E, Pilote L. Congenital heart disease in the general population: changing prevalence and age distribution. *Circulation*. (2007) 115:163–72. doi: 10.1161/CIRCULATIONAHA.106.627224
103. Babu-Narayan SV, Giannakoulas G, Valente AM, Li W, Gatzoulis MA. Imaging of congenital heart disease in adults. *Eur Heart J*. (2016) 37:1182–95. doi: 10.1093/eurheartj/ehv519
104. Gulati A, Ismail TF, Jabbour A, Alpendurada F, Guha K, Ismail NA, et al. The prevalence and prognostic significance of right ventricular systolic dysfunction in nonischemic dilated cardiomyopathy. *Circulation*. (2013) 128:1623–33. doi: 10.1161/CIRCULATIONAHA.113.002518

105. Rashid I, Mahmood A, Ismail TF, O'Meagher S, Kutty S, Celermajer D, et al. Right ventricular systolic dysfunction but not dilatation correlates with prognostically significant reductions in exercise capacity in repaired tetralogy of fallot. *Eur Heart J Cardiovasc Imaging*. (2020) 21:906–13. doi: 10.1093/ehjci/jez245
106. Baumgartner H, De Backer J. The ESC clinical practice guidelines for the management of adult congenital heart disease 2020. *Eur Heart J*. (2020) 41:4153–4. doi: 10.1093/eurheartj/ehaa701
107. Cawley PJ, Maki JH, Otto CM. Cardiovascular magnetic resonance imaging for valvular heart disease: technique and validation. *Circulation*. (2009) 119:468–78. doi: 10.1161/CIRCULATIONAHA.107.742486
108. Myerson SG. Heart valve disease: investigation by cardiovascular magnetic resonance. *J Cardiovasc Magn Reson*. (2012) 14:7. doi: 10.1186/1532-429X-14-7
109. Myerson SG, d'Arcy J, Mohiaddin R, Greenwood JP, Karamitsos TD, Francis JM, et al. Aortic regurgitation quantification using cardiovascular magnetic resonance: association with clinical outcome. *Circulation*. (2012) 126:1452–60. doi: 10.1161/CIRCULATIONAHA.111.083600
110. Lohan DG, Krishnam M, Tomasian A, Saleh R, Finn JP. Time-resolved MR angiography of the thorax. *Magn Reson Imaging Clin N Am*. (2008) 16:235–48, viii. doi: 10.1016/j.mric.2008.02.015
111. Ginami G, Neji R, Rashid I, Chiribiri A, Ismail TF, Botnar RM, et al. 3D whole-heart phase sensitive inversion recovery CMR for simultaneous black-blood and bright-blood gadolinium enhancement and bright-blood coronary CMR angiography. *J Cardiovasc Magn Reson*. (2017) 19:94. doi: 10.1186/s12968-017-0405-z
112. Correia T, Ginami G, Rashid I, Nordio G, Hajhosseiny R, Ismail TF, et al. Accelerated high-resolution free-breathing 3D whole-heart T2-prepared black-blood and bright-blood cardiovascular magnetic resonance. *J Cardiovasc Magn Reson*. (2020) 22:88–. doi: 10.1186/s12968-020-00691-3
113. Bustin A, Ginami G, Cruz G, Correia T, Ismail TF, Rashid I, et al. Five-minute whole-heart coronary MRA with sub-millimeter isotropic resolution, 100% respiratory scan efficiency, and 3D-PROST reconstruction. *Magn Reson Med*. (2019) 81:102–15. doi: 10.1002/mrm.27354
114. Velasco Forte MN, Roujol S, Ruijsink B, Valverde I, Duong P, Byrne N, et al. MRI for guided right and left heart cardiac catheterization: a prospective study in congenital heart disease. *J Magn Reson Imaging*. (2021) 53:1446–57. doi: 10.1002/jmri.27426
115. Knight DS, Kotecha T, Martinez-Naharro A, Brown JT, Bertelli M, Fontana M, et al. Cardiovascular magnetic resonance-guided right heart catheterization in a conventional CMR environment - predictors of procedure success and duration in pulmonary artery hypertension. *J Cardiovasc Magn Reson*. (2019) 21:57. doi: 10.1186/s12968-019-0569-9
116. Botnar RM, Kim WY. Coronary MR imaging: moving from lumenography to plaque assessment. *JACC Cardiovasc Imaging*. (2015) 8:1153–5. doi: 10.1016/j.jcmg.2015.08.003
117. Noguchi T, Nakao K, Asaumi Y, Morita Y, Otsuka F, Kataoka Y, et al. Noninvasive coronary plaque imaging. *J Atheroscler Thromb*. (2018) 25:281–93. doi: 10.5551/jat.RV17019
118. Matsumoto K, Ehara S, Hasegawa T, Sakaguchi M, Otsuka K, Yoshikawa J, et al. Localization of coronary high-intensity signals on t1-weighted mr imaging: relation to plaque morphology and clinical severity of angina pectoris. *JACC Cardiovasc Imaging*. (2015) 8:1143–52. doi: 10.1016/j.jcmg.2015.06.013
119. Motwani M, Kidambi A, Herzog BA, Uddin A, Greenwood JP, Plein S. MR imaging of cardiac tumors and masses: a review of methods and clinical applications. *Radiology*. (2013) 268:26–43. doi: 10.1148/radiol.13121239
120. Tyebally S, Chen D, Bhattacharyya S, Mughrabi A, Hussain Z, Manisty C, et al. Cardiac tumors: JACC cardiooncology state-of-the-art review. *JACC Cardio Oncol*. (2020) 2:293–311. doi: 10.1016/j.jacc.2020.05.009
121. Nazir MS, Ismail TF, Reyes E, Chiribiri A, Kaufmann PA, Plein S. Hybrid positron emission tomography-magnetic resonance of the heart: current state of the art and future applications. *Eur Heart J Cardiovasc Imaging*. (2018) 19:962–74. doi: 10.1093/ehjci/jey090
122. Strugnell WE, Slaughter RE, Riley RA, Trotter AJ, Bartlett H. Modified RV short axis series—a new method for cardiac MRI measurement of right ventricular volumes. *J Cardiovasc Magn Reson*. (2005) 7:769–74. doi: 10.1080/10976640500295433
123. Block KT, Uecker M, Frahm J. Undersampled radial MRI with multiple coils. Iterative image reconstruction using a total variation constraint. *MRM*. (2007) 57:1086–98. doi: 10.1002/mrm.21236
124. Lustig M, Donoho D, Pauly JM. Sparse MRI: the application of compressed sensing for rapid MR imaging. *Magn Reson Med*. (2007) 58:1182–95. doi: 10.1002/mrm.21391
125. Griswold MA, Jakob PM, Heidemann RM, Nittka M, Jellus V, Wang J, et al. Generalized autocalibrating partially parallel acquisitions (GRAPPA). *Magn Reson Med*. (2002) 47:1202–10. doi: 10.1002/mrm.10171
126. Pruessmann KP, Weiger M, Scheidegger MB, Boesiger P. SENSE: sensitivity encoding for fast MRI. *Magn Reson Med*. (1999) 42:952–62. doi: 10.1002/(SICI)1522-2594(199911)42:5<952::AID-MRM16>3.0.CO;2-S
127. Otazo R, Kim D, Axel L, Sodickson DK. Combination of compressed sensing and parallel imaging for highly accelerated first-pass cardiac perfusion MRI. *Magn Reson Med*. (2010) 64:767–76. doi: 10.1002/mrm.22463
128. Ehman RL, Felmlee JP. Adaptive technique for high-definition MR imaging of moving structures. *Radiology*. (1989) 173:255–63. doi: 10.1148/radiology.173.1.2781017
129. Van der Kouwe AJ, Benner T, Dale AM. Real-time rigid body motion correction and shimming using cloverleaf navigators. *Magn Reson Med*. (2006) 56:1019–32. doi: 10.1002/mrm.21038
130. Henningsson M, Koken P, Stehning C, Razavi R, Prieto C, Botnar RM. Whole-heart coronary MR angiography with 2D self-navigated image reconstruction. *Magn Reson Med*. (2012) 67:437–45. doi: 10.1002/mrm.23027
131. Kawaji K, Spincemaille P, Nguyen TD, Thimmappa N, Cooper MA, Prince MR, et al. Direct coronary motion extraction from a 2D fat image navigator for prospectively gated coronary MR angiography. *Magn Reson Med*. (2014) 71:599–607. doi: 10.1002/mrm.24698
132. Nguyen TD, Spincemaille P, Cham MD, Weinsaft JW, Prince MR, Wang Y. Free-breathing 3D steady-state free precession coronary magnetic resonance angiography: Comparison of diaphragm and cardiac fat navigators. *J Magn Reson Imaging*. (2008) 28:509–14. doi: 10.1002/jmri.21439
133. Maclaren J, Herbst M, Speck O, Zaitsev M. Prospective motion correction in brain imaging: a review. *MRM*. (2013) 69:621–36. doi: 10.1002/mrm.24314
134. De Zanche N, Barmet C, Nordmeyer-Massner JA, Pruessmann KP. NMR probes for measuring magnetic fields and field dynamics in MR systems. *Magn Reson Med*. (2008) 60:176–86. doi: 10.1002/mrm.21624
135. Vahle T, Bacher M, Rigie D, Fenchel M, Speier P, Bollenbeck J, et al. Respiratory motion detection and correction for MR using the pilot tone: applications for MR and simultaneous PET/MR exams. *Invest Radiol*. (2020) 55:153. doi: 10.1097/RLI.0000000000000619
136. Zaitsev M, Maclaren J, Herbst M. Motion artifacts in MRI: a complex problem with many partial solutions. *JMRI*. (2015) 42:887–901. doi: 10.1002/jmri.24850
137. Aletras AH, Ding S, Balaban RS, Wen H. DENSE: displacement encoding with stimulated echoes in cardiac functional MRI. *J Magn Reson*. (1999) 137:247. doi: 10.1006/jmre.1998.1676
138. Wang Y, Christy PS, Korosec FR, Alley MT, Grist TM, Polzin JA, et al. Coronary MRI with a respiratory feedback monitor: the 2D imaging case. *Magn Reson Med*. (1995) 33:116–21. doi: 10.1002/mrm.1910330118
139. Nagel E, Bornstedt A, Schnackenburg B, Hug J, Oswald H, Fleck E. Optimization of realtime adaptive navigator correction for 3D magnetic resonance coronary angiography. *Magn Reson Med*. (1999) 42:408–11. doi: 10.1002/(SICI)1522-2594(199908)42:2<408::AID-MRM24>3.0.CO;2-U
140. Atkinson DJ, Edelman R. Cineangiography of the heart in a single breath hold with a segmented turboFLASH sequence. *Radiology*. (1991) 178:357–60. doi: 10.1148/radiology.178.2.1987592
141. Crowe ME, Larson AC, Zhang Q, Carr J, White RD, Li D, et al. Automated rectilinear self-gated cardiac cine imaging. *Magn Reson Med*. (2004) 52:782–8. doi: 10.1002/mrm.20212
142. Larson AC, White RD, Laub G, McVeigh ER, Li D, Simonetti OP. Self-gated cardiac cine MRI. *Magn Reson Med*. (2004) 51:93–102. doi: 10.1002/mrm.10664
143. Bluemke DA, Boxerman JL, Atalar E, McVeigh ER. Segmented K-space cine breath-hold cardiovascular MR imaging: Part 1. Principles and technique.

- AJR Am J Roentgenol.* (1997) 169:395–400. doi: 10.2214/ajr.169.2.9242742
144. Sievers B, Addo M, Kirchberg S, Bakan A, John-Puthenveetil B, Franken U, et al. Impact of the ECG gating method on ventricular volumes and ejection fractions assessed by cardiovascular magnetic resonance imaging. *J Cardiovasc Magn Reson.* (2005) 7:441–6. doi: 10.1081/JCMR-200053515
  145. Leiner T, Katsimaglis G, Yeh EN, Kissinger KV, van Yperen G, Eggers H, et al. Correction for heart rate variability improves coronary magnetic resonance angiography. *J Magn Reson Imaging.* (2005) 22:577–82. doi: 10.1002/jmri.20399
  146. Han F, Zhou Z, Han E, Gao Y, Nguyen KL, Finn JP, et al. Self-gated 4D multiphase, steady-state imaging with contrast enhancement (MUSIC) using rotating cartesian K-space (ROCK): validation in children with congenital heart disease. *MRM.* (2017) 78:472–83. doi: 10.1002/mrm.26376
  147. Weiger M, Börner P, Proksa R, Schäffter T, Haase A. Motion-adapted gating based on k-space weighting for reduction of respiratory motion artifacts. *Magn Reson Med.* (1997) 38:322–33. doi: 10.1002/mrm.1910380223
  148. Wang Y, Ehman RL. Retrospective adaptive motion correction for navigator-gated 3D coronary MR angiography. *J Magn Reson Imaging.* (2000) 11:208–14. doi: 10.1002/(SICI)1522-2586(200002)11:2<208::AID-JMRI20>3.0.CO;2-9
  149. Wang Y, Watts R, Mitchell IR, Nguyen TD, Bezanson JW, Bergman GW, et al. Coronary MR angiography: selection of acquisition window of minimal cardiac motion with electrocardiography-triggered navigator cardiac motion prescanning—initial results. *Radiology.* (2001) 218:580–5. doi: 10.1148/radiology.218.2.r01fe46580
  150. Ludwig J, Speier P, Seifert F, Schaeffter T, Kolbitsch C. Pilot tone-based motion correction for prospective respiratory compensated cardiac cine MRI. *Magn Reson Med.* (2021) 85:2403–16. doi: 10.1002/mrm.28580
  151. Stehning C, Börner P, Nehrke K, Eggers H, Stuber M. Free-breathing whole-heart coronary MRA with 3D radial SSFP and self-navigated image reconstruction. *Magn Reson Med.* (2005) 54:476–80. doi: 10.1002/mrm.20557
  152. Sachs TS, Meyer CH, Pauly JM, Hu BS, Nishimura DG, Macovski A. The real-time interactive 3-D-DVA for robust coronary MRA. *IEEE Trans Med Imaging.* (2000) 19:73–9. doi: 10.1109/42.836367
  153. Larson AC, Kellman P, Arai A, Hirsch GA, McVeigh E, Li D, et al. Preliminary investigation of respiratory self-gating for free-breathing segmented cine MRI. *Magn Reson Med.* (2005) 53:159–68. doi: 10.1002/mrm.20331
  154. Uribe S, Muthurangu V, Boubertakh R, Schaeffter T, Razavi R, Hill DL, et al. Whole-heart cine MRI using real-time respiratory self-gating. *Magn Reson Med.* (2007) 57:606–13. doi: 10.1002/mrm.21156
  155. Pipe JG. Motion correction with PROPELLER MRI: application to head motion and free-breathing cardiac imaging. *Magn Reson Med.* (1999) 42:963–9. doi.org/10.1002/(SICI)1522-2594(199911)42:5<963::AID-MRM17>3.0.CO;2-L
  156. Kellman P, Ched'hotel C, Lorenz CH, Mancini C, Arai AE, McVeigh ER. Fully automatic, retrospective enhancement of real-time acquired cardiac cine MR images using image-based navigators and respiratory motion-corrected averaging. *Magn Reson Med.* (2008) 59:771–8. doi: 10.1002/mrm.21509
  157. Hansen MS, Sørensen TS, Arai AE, Kellman P. Retrospective reconstruction of high temporal resolution cine images from real-time MRI using iterative motion correction. *Magn Reson Med.* (2012) 68:741–50. doi: 10.1002/mrm.23284
  158. Wu HH, Gurney PT, Hu BS, Nishimura DG, McConnell MV. Free-breathing multiphase whole-heart coronary MR angiography using image-based navigators and three-dimensional cones imaging. *Magn Reson Med.* (2013) 69:1083–93. doi: 10.1002/mrm.24346
  159. Nordio G, Schneider T, Cruz G, Correia T, Bustin A, Prieto C, et al. Whole-heart T1 mapping using a 2D fat image navigator for respiratory motion compensation. *Magn Reson Med.* (2020) 83:178–87. doi: 10.1002/mrm.27919
  160. Keegan J, Gatehouse PD, Yang GZ, Firmin DN. Non-model-based correction of respiratory motion using beat-to-beat 3D spiral fat-selective imaging. *J Magn Reson Imaging.* (2007) 26:624–9. doi: 10.1002/jmri.20941
  161. Van Heeswijk RB, Piccini D, Feliciano H, Hullin R, Schwitter J, Stuber M. Self-navigated isotropic three-dimensional cardiac T2 mapping. *Magn Reson Med.* (2015) 73:1549–54. doi: 10.1002/mrm.25258
  162. Addy NO, Ingle RR, Wu HH, Hu BS, Nishimura DG. High-resolution variable-density 3D cones coronary MRA. *Magn Reson Med.* (2015) 74:614–21. doi: 10.1002/mrm.25803
  163. Malavé MO, Baron CA, Addy NO, Cheng JY, Yang PC, Hu BS, et al. Whole-heart coronary MR angiography using a 3D cones phyllotaxis trajectory. *Magn Reson Med.* (2019) 81:1092–103. doi: 10.1002/mrm.27475
  164. Sussman MS, Stainsby JA, Robert N, Merchant N, Wright GA. Variable-density adaptive imaging for high-resolution coronary artery MRI. *Magn Reson Med.* (2002) 48:753–64. doi: 10.1002/mrm.10275
  165. Hardy CJ, Saranathan M, Zhu Y, Darrow RD. Coronary angiography by real-time MRI with adaptive averaging. *Magn Reson Med.* (2000) 44:940–6. doi: 10.1002/1522-2594(200012)44:6<940::AID-MRM16>3.0.CO;2-F
  166. Lai P, Larson AC, Park J, Carr JC, Li D. Respiratory self-gated four-dimensional coronary MR angiography: a feasibility study. *Magn Reson Med.* (2008) 59:1378–85. doi: 10.1002/mrm.21617
  167. Küstner T, Bustin A, Jaubert O, Hajhosseiny R, Masci PG, Neji R, et al. Fully self-gated free-running 3D Cartesian cardiac CINE with isotropic whole-heart coverage in less than 2 min. *NMR Biomed.* (2020) 2020:e4409. doi: 10.1002/nbm.4409
  168. Piccini D, Monney P, Sierro C, Coppo S, Bonanno G, Van Heeswijk RB, et al. Respiratory self-navigated postcontrast whole-heart coronary MR angiography: initial experience in patients. *Radiology.* (2014) 270:378–86. doi: 10.1148/radiol.13132045
  169. Qi H, Jaubert O, Bustin A, Cruz G, Chen H, Botnar R, et al. Free-running 3D whole heart myocardial T1 mapping with isotropic spatial resolution. *Magn Reson Med.* (2019) 82:1331–42. doi: 10.1002/mrm.27811
  170. Coppo S, Piccini D, Bonanno G, Chaptin J, Vincenti G, Feliciano H, et al. Free-running 4D whole-heart self-navigated golden angle MRI: initial results. *Magn Reson Med.* (2015) 74:1306–16. doi: 10.1002/mrm.25523
  171. Feng L, Axel L, Chandarana H, Block KT, Sodickson DK, Otazo R. XD-GRASP: Golden-angle radial MRI with reconstruction of extra motion-state dimensions using compressed sensing. *Magn Reson Med.* (2016) 75:775–88. doi: 10.1002/mrm.25665
  172. Seiberlich N, Ehse P, Duerk J, Gilkeson R, Griswold M. Improved radial GRAPPA calibration for real-time free-breathing cardiac imaging. *Magn Reson Med.* (2011) 65:492–505. doi: 10.1002/mrm.22618
  173. Tsao J, Boesiger P, Pruessmann KP. k-t BLAST and k-t SENSE: dynamic MRI with high frame rate exploiting spatiotemporal correlations. *Magn Reson Med.* (2003) 50:1031–42. doi: 10.1002/mrm.10611
  174. Huang F, Akao J, Vijayakumar S, Duensing GR, Limkeman M. k-t GRAPPA: A k-space implementation for dynamic MRI with high reduction factor. *Magn Reson Med.* (2005) 54:1172–84. doi: 10.1002/mrm.20641
  175. Liu J, Nguyen TD, Zhu Y, Spincemaille P, Prince MR, Weinsaft JW, et al. Self-Gated free-breathing 3D coronary cine imaging with simultaneous water and fat visualization. *PLoS ONE.* (2014) 9:e89315. doi: 10.1371/journal.pone.0089315
  176. Asif MS, Hamilton L, Brummer M, Romberg J. Motion-adaptive spatiotemporal regularization for accelerated dynamic MRI. *Magn Reson Med.* (2013) 70:800–12. doi: 10.1002/mrm.24524
  177. Mohsin YQ, Lingala SG, DiBella E, Jacob M. Accelerated dynamic MRI using patch regularization for implicit motion compensation. *Magn Reson Med.* (2017) 77:1238–48. doi: 10.1002/mrm.26215
  178. Chen X, Salerno M, Yang Y, Epstein FH. Motion-compensated compressed sensing for dynamic contrast-enhanced MRI using regional spatiotemporal sparsity and region tracking: block low-rank sparsity with motion-guidance (BLOSM). *Magn Reson Med.* (2014) 72:1028–38. doi: 10.1002/mrm.25018
  179. Ma LE, Yerly J, Piccini D, Sopra LD, Roy CW, Carr JC, et al. 5D flow MRI: a fully self-gated, free-running framework for cardiac and respiratory motion-resolved 3D hemodynamics. *Radiol Cardiothorac Imaging.* (2020) 2:e200219. doi: 10.1148/ryct.2020200219
  180. Küstner T, Würslin C, Schwartz M, Martirosian P, Gatidis S, Brendle C, et al. Self-navigated 4D cartesian imaging of periodic motion in the body trunk using partial k-space compressed sensing. *MRM.* (2017) 78:632–44. doi: 10.1002/mrm.26406

181. Piccini D, Littmann A, Nielles-Vallespin S, Zenge MO. Spiral phyllotaxis: the natural way to construct a 3D radial trajectory in MRI. *Magn Reson Med.* (2011) 66:1049–56. doi: 10.1002/mrm.22898
182. Pang J, Sharif B, Fan Z, Bi X, Arsanjani R, Berman DS, et al. ECG and navigator-free four-dimensional whole-heart coronary MRA for simultaneous visualization of cardiac anatomy and function. *Magn Reson Med.* (2014) 72:1208–17. doi: 10.1002/mrm.25450
183. Correia T, Ginami G, Cruz G, Neji R, Rashid I, Botnar RM, et al. Optimized respiratory-resolved motion-compensated 3D cartesian coronary MR angiography. *Magn Reson Med.* (2018) 80:2618–29. doi: 10.1002/mrm.27208
184. Cheng JY, Zhang T, Ruangwattanapaisarn N, Alley MT, Uecker M, Pauly JM, et al. Free-breathing pediatric MRI with nonrigid motion correction and acceleration. *J Magn Reson Imaging.* (2015) 42:407–20. doi: 10.1002/jmri.24785
185. Xue H, Kellman P, Larocca G, Arai AE, Hansen MS. High spatial and temporal resolution retrospective cine cardiovascular magnetic resonance from shortened free breathing real-time acquisitions. *J Cardiovasc Magn Reson.* (2013) 15:102–. doi: 10.1186/1532-429X-15-102
186. Usman M, Atkinson D, Odille F, Kolbitsch C, Vaillant G, Schaeffter T, et al. Motion corrected compressed sensing for free-breathing dynamic cardiac MRI. *Magn Reson Med.* (2013) 70:504–16. doi: 10.1002/mrm.24463
187. Royuela-del-Val J, Cordero-Grande L, Simmross-Wattenberg F, Martín-Fernández M, Alberola-López C. Nonrigid groupwise registration for motion estimation and compensation in compressed sensing reconstruction of breath-hold cardiac cine MRI. *Magn Reson Med.* (2016) 75:1525–36. doi: 10.1002/mrm.25733
188. Tolouee A, Alirezaie J, Babyn P. Nonrigid motion compensation in compressed sensing reconstruction of cardiac cine MRI. *Magn Reson Imaging.* (2018) 46:114–20. doi: 10.1016/j.mri.2017.11.004
189. Liu F, Li D, Jin X, Qiu W, Xia Q, Sun B. Dynamic cardiac MRI reconstruction using motion aligned locally low rank tensor (MALLRT). *Magn Reson Imaging.* (2020) 66:104–15. doi: 10.1016/j.mri.2019.07.002
190. Ahmed AH, Qureshi IM, Shah JA, Zaheer M. Motion correction based reconstruction method for compressively sampled cardiac MR imaging. *Magn Reson Imaging.* (2017) 36:159–66. doi: 10.1016/j.mri.2016.10.008
191. Lingala SG, DiBella E, Jacob M. Deformation corrected compressed sensing (DC-CS): A novel framework for accelerated dynamic MRI. *IEEE Trans Med Imaging.* (2015) 34:72–85. doi: 10.1109/TMI.2014.2343953
192. Roujol S, Foppa M, Weingartner S, Manning WJ, Nezafat R. Adaptive registration of varying contrast-weighted images for improved tissue characterization (ARCTIC): application to T1 mapping. *Magn Reson Med.* (2015) 73:1469–82. doi: 10.1002/mrm.25270
193. Xue H, Shah S, Greiser A, Guetter C, Littmann A, Jolly MP, et al. Motion correction for myocardial T1 mapping using image registration with synthetic image estimation. *Magn Reson Med.* (2012) 67:1644–55. doi: 10.1002/mrm.23153
194. Bustin A, Milotta G, Ismail TF, Neji R, Botnar RM, Prieto C. Accelerated free-breathing whole-heart 3D T2 mapping with high isotropic resolution. *Magn Reson Med.* (2020) 83:988–1002. doi: 10.1002/mrm.27989
195. Serry FM, Ma S, Mao X, Han F, Xie Y, Han H, et al. Dual flip-angle IR-FLASH with spin history mapping for B1+ corrected T1 mapping: application to T1 cardiovascular magnetic resonance multitasking. *Magn Reson Med.* (2021) 86:3182–91. doi: 10.1002/mrm.28935
196. Chow K, Yang Y, Shaw P, Kramer CM, Salerno M. Robust free-breathing SASHA T1 mapping with high-contrast image registration. *J Cardiovasc Magn Reson.* (2016) 18:47. doi: 10.1186/s12968-016-0267-9
197. Shaw JL, Yang Q, Zhou Z, Deng Z, Nguyen C, Li D, et al. Free-breathing, non-ECG, continuous myocardial T1 mapping with cardiovascular magnetic resonance multitasking. *Magn Reson Med.* (2019) 81:2450–63. doi: 10.1002/mrm.27574
198. Kolbitsch C, Bastkowski R, Schaeffter T, Prieto Vasquez C, Weiss K, Maintz D, et al. Respiratory motion corrected 4D flow using golden radial phase encoding. *Magn Reson Med.* (2020) 83:635–44. doi: 10.1002/mrm.27918
199. Cruz G, Atkinson D, Henningsson M, Botnar RM, Prieto C. Highly efficient nonrigid motion-corrected 3D whole-heart coronary vessel wall imaging. *Magn Reson Med.* (2017) 77:1894–908. doi: 10.1002/mrm.26274
200. Pang J, Chen Y, Fan Z, Nguyen C, Yang Q, Xie Y, et al. High efficiency coronary MR angiography with nonrigid cardiac motion correction. *Magn Reson Med.* (2016) 76:1345–53. doi: 10.1002/mrm.26332
201. Correia T, Cruz G, Schneider T, Botnar RM, Prieto C. Technical note: Accelerated nonrigid motion-compensated isotropic 3D coronary MR angiography. *Med Phys.* (2018) 45:214–22. doi: 10.1002/mp.12663
202. Chen Y, Lo W-C, Hamilton JI, Barkauskas K, Saybasili H, Wright KL, et al. Single breath-hold 3D cardiac T1 mapping using through-time spiral GRAPPA. *NMR Biomed.* (2018) 31:e3923. doi: 10.1002/nbm.3923
203. Nordio G, Bustin A, Henningsson M, Rashid I, Chiribiri A, Ismail T, et al. 3D SASHA myocardial T1 mapping with high accuracy and improved precision. *MAGMA.* (2019) 32:281–9. doi: 10.1007/s10334-018-0703-y
204. Guo R, Chen Z, Wang Y, Herzka DA, Luo J, Ding H. Three-dimensional free breathing whole heart cardiovascular magnetic resonance T1 mapping at 3 T. *J Cardiovasc Magn Reson.* (2018) 20:64. doi: 10.1186/s12968-018-0487-2
205. Kozerke S, Scheidegger MB, Pedersen EM, Boesiger P. Heart motion adapted cine phase-contrast flow measurements through the aortic valve. *Magn Reson Med.* (1999) 42:970–8. doi: 10.1002/(SICI)1522-2594(199911)42:5<970::AID-MRM18>3.0.CO;2-I
206. Kozerke S, Schwitter J, Pedersen EM, Boesiger P. Aortic and mitral regurgitation: Quantification using moving slice velocity mapping. *J Magn Reson Imaging.* (2001) 14:106–12. doi: 10.1002/jmri.1159
207. Küstner T, Bustin A, Jaubert O, Hajhosseiny R, Masci PG, Neji R, et al. Isotropic 3D cartesian single breath-hold CINE MRI with multi-bin patch-based low-rank reconstruction. *Magn Reson Med.* (2020) 84:2018–33. doi: 10.1002/mrm.28267
208. Wetzl J, Schmidt M, Pontana F, Longere B, Lugauer F, Maier A, et al. Single-breath-hold 3-D CINE imaging of the left ventricle using cartesian sampling. *MAGMA.* (2018) 31:19–31. doi: 10.1007/s10334-017-0624-1
209. Feng L, Coppo S, Piccini D, Yerly J, Lim RP, Masci PG, et al. 5D whole-heart sparse MRI. *Magn Reson Med.* (2018). 79:826–38. doi: 10.1002/mrm.26745
210. Liu J, Spincemaille P, Codella NC, Nguyen TD, Prince MR, Wang Y. Respiratory and cardiac self-gated free-breathing cardiac CINE imaging with multiecho 3D hybrid radial SSFP acquisition. *Magn Reson Med.* (2010) 63:1230–7. doi: 10.1002/mrm.22306
211. Moghari MH, Barthur A, Amaral ME, Geva T, Powell AJ. Free-breathing whole-heart 3D cine magnetic resonance imaging with prospective respiratory motion compensation. *Magn Reson Med.* (2018) 80:181–9. doi: 10.1002/mrm.27021
212. Spincemaille P, Liu J, Nguyen T, Prince MR, Wang Y. Z intensity-weighted position self-respiratory gating method for free-breathing 3D cardiac CINE imaging. *Magn Reson Imaging.* (2011) 29:861–8. doi: 10.1016/j.mri.2011.02.011
213. Uribe S, Beerbaum P, Sørensen TS, Rasmussen A, Razavi R, Schaeffter T. Four-dimensional (4D) flow of the whole heart and great vessels using real-time respiratory self-gating. *Magn Reson Med.* (2009) 62:984–92. doi: 10.1002/mrm.22090
214. Schroeder L, Wetzl J, Maier A, Lauer L, Bollenbeck J, Fenchel M, et al. editors. A novel method for contact-free cardiac synchronization using the pilot tone navigato. In: *International Society for Magnetic Resonance Medicine (ISMRM).* Singapore (2016).
215. Jaubert O, Cruz G, Bustin A, Schneider T, Koken P, Doneva M, et al. Free-running cardiac magnetic resonance fingerprinting: joint T1/T2 map and cine imaging. *Magn Reson Imaging.* (2020) 68:173–82. doi: 10.1016/j.mri.2020.02.005
216. Batchelor PG, Atkinson D, Irarrazaval P, Hill DL, Hajnal J, Larkman D. Matrix description of general motion correction applied to multishot images. *Magn Reson Med.* (2005) 54:1273–80. doi: 10.1002/mrm.20656
217. Odille F, Vuissoz PA, Marie PY, Felblinger J. Generalized reconstruction by inversion of coupled systems (GRICS) applied to free-breathing MRI. *Magn Reson Med.* (2008) 60:146–57. doi: 10.1002/mrm.21623
218. Atkinson D, Hill DLG, Stoyle PNR, Summers PE, Keevil SF, editors. *An Autofocus Algorithm for the Automatic Correction of Motion Artifacts in MR Images.* Berlin: Springer (1997). doi: 10.1007/3-540-63046-5\_26
219. Christodoulou AG, Shaw JL, Nguyen C, Yang Q, Xie Y, Wang N, et al. Magnetic resonance multitasking for motion-resolved

- quantitative cardiovascular imaging. *Nat Biomed Eng.* (2018) 2:215–26. doi: 10.1038/s41551-018-0217-y
220. Ong F, Zhu X, Cheng JY, Johnson KM, Larson PEZ, Vasanawala SS, et al. Extreme MRI: large-scale volumetric dynamic imaging from continuous non-gated acquisitions. *Magn Reson Med.* (2020) 84:1763–80. doi: 10.1002/mrm.28235
  221. Unterberg-Buchwald C, Fasshauer M, Sohns JM, Staab W, Schuster A, Voit D, et al. Real time cardiac MRI and its clinical usefulness in arrhythmias and wall motion abnormalities. *J Cardiovasc Magn Reson.* (2014) 16:1–2. doi: 10.1186/1532-429X-16-S1-P34
  222. Allen BD, Carr ML, Markl M, Zenge MO, Schmidt M, Nadar MS, et al. Accelerated real-time cardiac MRI using iterative sparse SENSE reconstruction: comparing performance in patients with sinus rhythm and atrial fibrillation. *Eur Radiol.* (2018) 28:3088–96. doi: 10.1007/s00330-017-5283-0
  223. Bassett EC, Kholmovski EG, Wilson BD, DiBella EV, Dosdall DJ, Ranjan R, et al. Evaluation of highly accelerated real-time cardiac cine MRI in tachycardia. *NMR Biomed.* (2014) 27:175–82. doi: 10.1002/nbm.3049
  224. Haji-Valizadeh H, Rahsepar AA, Collins JD, Bassett E, Isakova T, Block T, et al. Validation of highly accelerated real-time cardiac cine MRI with radial k-space sampling and compressed sensing in patients at 1.5T and 3T. *Magn Reson Med.* (2018) 79:2745–51. doi: 10.1002/mrm.26918
  225. Voit D, Zhang S, Unterberg-Buchwald C, Sohns JM, Lotz J, Frahm J. Real-time cardiovascular magnetic resonance at 1.5 T using balanced SSFP and 40 ms resolution. *J Cardiovasc Magn Reson.* (2013) 15:79. doi: 10.1186/1532-429X-15-79
  226. Körperich H, Gieseke J, Barth P, Hooijveen R, Esdorn H, Peterschröder A, et al. Flow volume and shunt quantification in pediatric congenital heart disease by real-time magnetic resonance velocity mapping: a validation study. *Circulation.* (2004) 109:1987–93. doi: 10.1161/01.CIR.0000126494.66859.A2
  227. Kowallick JT, Joseph AA, Unterberg-Buchwald C, Fasshauer M, van Wijk K, Merboldt KD, et al. Real-time phase-contrast flow MRI of the ascending aorta and superior vena cava as a function of intrathoracic pressure (Valsalva manoeuvre). *Br J Radiol.* (2014) 87:20140401. doi: 10.1259/bjr.20140401
  228. Feng L, Srichai MB, Lim RP, Harrison A, King W, Adluru G, et al. Highly accelerated real-time cardiac cine MRI using k-t SPARSE-SENSE. *Magn Reson Med.* (2013) 70:64–74. doi: 10.1002/mrm.24440
  229. Kozerke S, Tsao J, Razavi R, Boesiger P. Accelerating cardiac cine 3D imaging using k-t BLAST. *Magn Reson Med.* (2004) 52:19–26. doi: 10.1002/mrm.20145
  230. Jung H, Park J, Yoo J, Ye JC. Radial k-t FOCUSS for high-resolution cardiac cine MRI. *Magn Reson Med.* (2010) 63:68–78. doi: 10.1002/mrm.22172
  231. Otazo R, Candes E, Sodickson DK. Low-rank plus sparse matrix decomposition for accelerated dynamic MRI with separation of background and dynamic components. *Magn Reson Med.* (2015) 73:1125–36. doi: 10.1002/mrm.25240
  232. Frahm J, Haase A, Matthaei D. Rapid NMR imaging of dynamic processes using the FLASH technique. *Magn Reson Med.* (1986) 3:321–7. doi: 10.1002/mrm.1910030217
  233. Hennig J, Nauert H, Friedburg H. RARE imaging: a fast imaging method for clinical MR. *Magn Reson Med.* (1986) 3:823–33. doi: 10.1002/mrm.1910030602
  234. Mansfield P. Multi-planar image formation using NMR spin echoes. *J Phys C Solid State Phys.* (1977) 10:L55. doi: 10.1088/0022-3719/10/3/004
  235. Bornstedt A, Nagel E, Schalla S, Schnackenburg B, Klein C, Fleck E. Multi-slice dynamic imaging: complete functional cardiac MR examination within 15 seconds. *J Magn Reson Imaging.* (2001) 14:300–5. doi: 10.1002/jmri.1186
  236. Kim YC, Proctor MI, Narayanan SS, Nayak KS. Improved imaging of lingual articulation using real-time multislice MRI. *J Magn Reson Imaging.* (2012) 35:943–8. doi: 10.1002/jmri.23510
  237. Feng X, Blemker SS, Inouye J, Pelland CM, Zhao L, Meyer CH. Assessment of velopharyngeal function with dual-planar high-resolution real-time spiral dynamic MRI. *Magn Reson Med.* (2018) 80:1467–74. doi: 10.1002/mrm.27139
  238. Nayak KS, Pauly JM, Nishimura DG, Hu BS. Rapid ventricular assessment using real-time interactive multislice MRI. *Magn Reson Med.* (2001) 45:371–5. doi: 10.1002/1522-2594(200103)45:3<371::AID-MRM1048>3.0.CO;2-Z
  239. Nazir MS, Neji R, Speier P, Reid F, Stäb D, Schmidt M, et al. Simultaneous multi slice (SMS) balanced steady state free precession first-pass myocardial perfusion cardiovascular magnetic resonance with iterative reconstruction at 1.5 T. *J Cardiovasc Magn Reson.* (2018) 20:84. doi: 10.1186/s12968-018-0502-7
  240. Stäb D, Ritter CO, Breuer FA, Weng AM, Hahn D, Köstler H. CAIPIRINHA accelerated SSFP imaging. *Magn Reson Med.* (2011) 65:157–64. doi: 10.1002/mrm.22600
  241. Ahmad R, Xue H, Giri S, Ding Y, Craft J, Simonetti OP. Variable density incoherent spatiotemporal acquisition (VISTA) for highly accelerated cardiac MRI. *Magn Reson Med.* (2015) 74:1266–78. doi: 10.1002/mrm.25507
  242. Adluru G, Chen L, Kim SE, Burgon N, Kholmovski EG, Marrouche NF, et al. Three-dimensional late gadolinium enhancement imaging of the left atrium with a hybrid radial acquisition and compressed sensing. *J Magn Reson Imaging.* (2011) 34:1465–71. doi: 10.1002/jmri.22808
  243. Haji-Valizadeh H, Feng L, Ma LE, Shen D, Block KT, Robinson JD, et al. Highly accelerated, real-time phase-contrast MRI using radial k-space sampling and GROG-GRASP reconstruction: a feasibility study in pediatric patients with congenital heart disease. *NMR Biomed.* (2020) 33:e4240. doi: 10.1002/nbm.4240
  244. Kramer M, Herrmann KH, Biermann J, Reichenbach JR. Retrospective reconstruction of cardiac cine images from golden-ratio radial MRI using one-dimensional navigators. *J Magn Reson Imaging.* (2014) 40:413–22. doi: 10.1002/jmri.24364
  245. Li YY, Rashid S, Cheng YJ, Schapiro W, Gliganic K, Yamashita AM, et al. Real-time cardiac MRI with radial acquisition and k-space variant reduced-FOV reconstruction. *Magn Reson Imaging.* (2018) 53:98–104. doi: 10.1016/j.mri.2018.07.008
  246. Rank CM, Heußer T, Buzan MTA, Wetscherek A, Freitag MT, Dinkel J, et al. 4D respiratory motion-compensated image reconstruction of free-breathing radial MR data with very high undersampling. *Magn Reson Med.* (2017) 77:1170–83. doi: 10.1002/mrm.26206
  247. Rosenzweig S, Scholand N, Holme HCM, Uecker M. Cardiac and respiratory self-gating in radial MRI using an adapted singular spectrum analysis (SSA-FARY). *IEEE Trans Med Imaging.* (2020) 39:3029–41. doi: 10.1109/TMI.2020.2985994
  248. Wang X, Kohler F, Unterberg-Buchwald C, Lotz J, Frahm J, Uecker M. Model-based myocardial T1 mapping with sparsity constraints using single-shot inversion-recovery radial FLASH cardiovascular magnetic resonance. *J Cardiovasc Magn Reson.* (2019) 21:60. doi: 10.1186/s12968-019-0570-3
  249. Wang X, Rosenzweig S, Scholand N, Holme HCM, Uecker M. Model-based reconstruction for simultaneous multi-slice T1 mapping using single-shot inversion-recovery radial FLASH. *Magn Reson Med.* (2021) 85:1258–71. doi: 10.1002/mrm.28497
  250. Shin T, Lustig M, Nishimura DG, Hu BS. Rapid single-breath-hold 3D late gadolinium enhancement cardiac MRI using a stack-of-spirals acquisition. *J Magn Reson Imaging.* (2014) 40:1496–502. doi: 10.1002/jmri.24494
  251. Wang J, Yang Y, Weller DS, Zhou R, Van Houten M, Sun C, et al. High spatial resolution spiral first-pass myocardial perfusion imaging with whole-heart coverage at 3 T. *Magn Reson Med.* (2021) 86:648–62. doi: 10.1002/mrm.28701
  252. Yang Y, Meyer CH, Epstein FH, Kramer CM, Salerno M. Whole-heart spiral simultaneous multi-slice first-pass myocardial perfusion imaging. *Magn Reson Med.* (2019) 81:852–62. doi: 10.1002/mrm.27412
  253. Qi H, Bustin A, Cruz G, Jaubert O, Chen H, Botnar RM, et al. Free-running simultaneous myocardial T1/T2 mapping and cine imaging with 3D whole-heart coverage and isotropic spatial resolution. *Magn Reson Imaging.* (2019) 63:159–69. doi: 10.1016/j.mri.2019.08.008
  254. Cheng JY, Zhang T, Alley MT, Lustig M, Vasanawala SS, Pauly JM, editors. Variable-density radial view-ordering and sampling for time-optimized 3D Cartesian imaging. In: *Proceedings of the ISMRM Workshop on Data Sampling and Image Reconstruction*. Sedona, AZ (2013).
  255. Liu J, Saloner D. Accelerated MRI with Circular Cartesian UnderSampling (CIRCUS): a variable density cartesian sampling strategy for compressed sensing and parallel imaging. *Quant Imaging Med Surg.* (2014) 4:57–67. doi: 10.3978/j.issn.2223-4292.2014.02.01

256. Prieto C, Doneva M, Usman M, Henningsson M, Greil G, Schaeffter T, et al. Highly efficient respiratory motion compensated free-breathing coronary mra using golden-step cartesian acquisition. *J Magn Reson Imaging*. (2015) 41:738–46. doi: 10.1002/jmri.24602
257. Zhu Y, Guo Y, Lingala SG, Lebel RM, Law M, Nayak KS. GOCART: Golden-angle CArtesian randomized time-resolved 3D MRI. *Magn Reson Imaging*. (2016) 34:940–50. doi: 10.1016/j.mri.2015.12.030
258. Kustner T, Wurslin C, Gatidis S, Martirosian P, Nikolaou K, Schwenzer NF, et al. MR image reconstruction using a combination of compressed sensing and partial fourier acquisition: ESPReSSo. *IEEE Trans Med Imaging*. (2016) 35:2447–58. doi: 10.1109/TMI.2016.2577642
259. Küstner T, Schwartz M, Martirosian P, Gatidis S, Seith F, Gilliam C, et al. MR-based respiratory and cardiac motion correction for PET imaging. *Med Image Anal*. (2017) 42:129–44. doi: 10.1016/j.media.2017.08.002
260. Park J, Larson AC, Zhang Q, Simonetti O, Li D. 4D radial coronary artery imaging within a single breath-hold: cine angiography with phase-sensitive fat suppression (CAPS). *Magn Reson Med*. (2005) 54:833–40. doi: 10.1002/mrm.20627
261. Grimm R, Fürst S, Souvatzoglou M, Forman C, Hutter J, Dregely I, et al. Self-gated MRI motion modeling for respiratory motion compensation in integrated PET/MRI. *Med Image Anal*. (2015) 19:110–20. doi: 10.1016/j.media.2014.08.003
262. Thedens DR, Irrazaval P, Sachs TS, Meyer CH, Nishimura DG. Fast magnetic resonance coronary angiography with a three-dimensional stack of spirals trajectory. *Magn Reson Med*. (1999) 41:1170–9. doi: 10.1002/(SICI)1522-2594(199906)41:6<1170::AID-MRM13>3.0.CO;2-J
263. Winkelmann S, Schaeffter T, Koehler T, Eggers H, Doessel O. An optimal radial profile order based on the golden ratio for time-resolved MRI. *IEEE Trans Med Imaging*. (2007) 26:68–76. doi: 10.1109/TMI.2006.885337
264. Wundrak S, Paul J, Ulrici J, Hell E, Geibel MA, Bernhardt P, et al. Golden ratio sparse MRI using tiny golden angles. *Magn Reson Med*. (2016) 75:2372–8. doi: 10.1002/mrm.25831
265. Ravishanker S, Bresler Y. MR image reconstruction from highly undersampled k-space data by dictionary learning. *IEEE Trans Med Imaging*. (2011) 30:1028–41. doi: 10.1109/TMI.2010.2090538
266. Uecker M, Lai P, Murphy MJ, Virtue P, Elad M, Pauly JM, et al. ESPIRiT—an eigenvalue approach to autocalibrating parallel MRI: where SENSE meets GRAPPA. *Magn Reson Med*. (2014) 71:990–1001. doi: 10.1002/mrm.24751
267. Lustig M, Pauly JM. SPIRiT: iterative self-consistent parallel imaging reconstruction from arbitrary k-space. *Magn Reson Med*. (2010) 64:457–71. doi: 10.1002/mrm.22428
268. Chen J, Liu S, Huang M. Low-Rank and sparse decomposition model for accelerating dynamic MRI reconstruction. *J Healthc Eng*. (2017) 2017:9856058–. doi: 10.1155/2017/9856058
269. Haldar JP. Low-rank modeling of local k-space neighborhoods (LORAKS) for constrained MRI. *IEEE Trans Med Imaging*. (2014) 33:668–81. doi: 10.1109/TMI.2013.2293974
270. Lingala SG, Hu Y, DiBella E, Jacob M. Accelerated dynamic MRI exploiting sparsity and low-rank structure: k-t SLR. *IEEE Trans Med Imaging*. (2011) 30:1042–54. doi: 10.1109/TMI.2010.2100850
271. Miao X, Lingala SG, Guo Y, Jao T, Usman M, Prieto C, et al. Accelerated cardiac cine MRI using locally low rank and finite difference constraints. *Magn Reson Imaging*. (2016) 34:707–14. doi: 10.1016/j.mri.2016.03.007
272. Moeller S, Weingartner S, Akcakaya M. Multi-scale locally low-rank noise reduction for high-resolution dynamic quantitative cardiac MRI. *Annu Int Conf IEEE Eng Med Biol Soc*. (2017) 2017:1473–6. doi: 10.1109/EMBC.2017.8037113
273. Nakarmi U, Wang Y, Lyu J, Liang D, Ying L. A kernel-based low-rank (KLR) model for low-dimensional manifold recovery in highly accelerated dynamic MRI. *IEEE Trans Med Imaging*. (2017) 36:2297–307. doi: 10.1109/TMI.2017.2723871
274. Roohi SF, Zonoobi D, Kassim AA, Jaremko JL. Multi-dimensional low rank plus sparse decomposition for reconstruction of under-sampled dynamic MRI. *Pattern Recognit*. (2017) 63:667–79. doi: 10.1016/j.patcog.2016.09.040
275. Tremoulheac B, Dikaos N, Atkinson D, Arridge SR. Dynamic MR image reconstruction-separation from undersampled (k,t)-space via low-rank plus sparse prior. *IEEE Trans Med Imaging*. (2014) 33:1689–701. doi: 10.1109/TMI.2014.2321190
276. Yoon H, Kim KS, Kim D, Bresler Y, Ye JC. Motion adaptive patch-based low-rank approach for compressed sensing cardiac cine MRI. *IEEE Trans Med Imaging*. (2014) 33:2069–85. doi: 10.1109/TMI.2014.2330426
277. Zhu Y, Liu Y, Ying L, Peng X, Wang YJ, Yuan J, et al. SCOPE: signal compensation for low-rank plus sparse matrix decomposition for fast parameter mapping. *Phys Med Biol*. (2018) 63:185009. doi: 10.1088/1361-6560/aadb09
278. Bustin A, Lima da Cruz G, Jaubert O, Lopez K, Botnar RM, Prieto C. High-dimensionality undersampled patch-based reconstruction (HD-PROST) for accelerated multi-contrast MRI. *Magn Reson Med*. (2019) 81:3705–19. doi: 10.1002/mrm.27694
279. Hamilton JI, Jiang Y, Ma D, Chen Y, Lo WC, Griswold M, et al. Simultaneous multislice cardiac magnetic resonance fingerprinting using low rank reconstruction. *NMR Biomed*. (2019) 32:e4041. doi: 10.1002/nbm.4041
280. Lima da Cruz G, Bustin A, Jaubert O, Schneider T, Botnar RM, Prieto C. Sparsity and locally low rank regularization for MR fingerprinting. *Magn Reson Med*. (2019) 81:3530–43. doi: 10.1002/mrm.27665
281. Yaman B, Weingartner S, Kargas N, Sidiropoulos ND, Akcakaya M. Low-Rank tensor models for improved multi-dimensional MRI: application to dynamic cardiac T1 mapping. *IEEE Trans Comput Imaging*. (2019) 6:194–207. doi: 10.1109/TCI.2019.2940916
282. Becker KM, Schulz-Menger J, Schaeffter T, Kolbitsch C. Simultaneous high-resolution cardiac T1 mapping and cine imaging using model-based iterative image reconstruction. *Magn Reson Med*. (2019) 81:1080–91. doi: 10.1002/mrm.27474
283. Correia T, Schneider T, Chiribiri A. *Model-Based Reconstruction for Highly Accelerated First-Pass Perfusion Cardiac MRI*. Shenzhen: Springer (2019). doi: 10.1007/978-3-030-32245-8\_57
284. Odille F, Uribe S, Batchelor PG, Prieto C, Schaeffter T, Atkinson D. Model-based reconstruction for cardiac cine MRI without ECG or breath holding. *Magn Reson Med*. (2010) 63:1247–57. doi: 10.1002/mrm.22312
285. Velikina JV, Samsonov AA. Reconstruction of dynamic image series from undersampled MRI data using data-driven model consistency condition (MOCCO). *Magn Reson Med*. (2015) 74:1279–90. doi: 10.1002/mrm.25513
286. El-Rewaady H. Multi-domain convolutional neural network (MD-CNN) for radial reconstruction of dynamic cardiac MRI. *Magn Reson Med*. (2021) 85:1195–208. doi: 10.1002/mrm.28485
287. Olliver W, Sprosen T, Peakman T. UK Biobank: from concept to reality. *Pharmacogenomics*. (2005) 6:639–46. doi: 10.2217/14622416.6.6.639
288. Campello VM, Gkontra P, Izquierdo C, Martín-Isla C, Sojoudi A, Full PM, et al. Multi-Centre, multi-vendor and multi-disease cardiac segmentation: the M&Ms challenge. *IEEE Trans Med Imaging*. (2021) 40:3543–54. doi: 10.1109/TMI.2021.3090082
289. Bernard O, Lalonde A, Zotti C, Cervenansky F, Yang X, Heng PA, et al. Deep learning techniques for automatic mri cardiac multi-structures segmentation and diagnosis: is the problem solved? *IEEE Trans Med Imaging*. (2018) 37:2514–25. doi: 10.1109/TMI.2018.2837502
290. Rosenblatt F. The perceptron: a probabilistic model for information storage and organization in the brain. *Psychol Rev*. (1958) 65:386. doi: 10.1037/h0042519
291. Virtue P, Stella XY, Lustig M, editors. Better than real: complex-valued neural nets for MRI fingerprinting. In: *2017 IEEE International Conference on Image Processing (ICIP)*. Beijing: IEEE (2017). doi: 10.1109/ICIP.2017.8297024
292. Frick M, Paetsch I, den Harder C, Kouwenhoven M, Heese H, Dries S, et al. Fully automatic geometry planning for cardiac MR imaging and reproducibility of functional cardiac parameters. *J Magn Reson Imaging*. (2011) 34:457–67. doi: 10.1002/jmri.22626
293. Hayes C, Daniel D, Lu X, Jolly M-P, Schmidt M. Fully automatic planning of the long-axis views of the heart. *J Cardiovasc Magn Reson*. (2013) 15:1–2. doi: 10.1186/1532-429X-15-S1-O54
294. Edalati M, Zheng Y, Watkins MP, Chen J, Liu L, Zhang S, et al. Implementation and prospective clinical validation of AI-based planning and shimming techniques in cardiac MRI. *Med Phys*. (2022) 49:129–43. doi: 10.1002/mp.15327

295. Blansit K, Retson T, Masutani E, Bahrami N, Hsiao A. Deep learning-based prescription of cardiac MRI planes. *Radiol Artif Intell.* (2019) 1:e180069. doi: 10.1148/ryai.2019180069
296. Lu X, Jolly M-P, Georgescu B, Hayes C, Speier P, Schmidt M, et al. editors. Automatic view planning for cardiac MRI acquisition. In: *International Conference on Medical Image Computing and Computer-Assisted Intervention*. Toronto, ON: Springer (2011).
297. Jiang W, Addy O, Overall W, Santos J, Hu B, editors. Automatic artifacts detection as operative scan-aided tool in an autonomous MRI environment. In: *CMR 2018—A Joint 2347 EuroCMR/SCMR Meeting Abstract Supplement*. Barcelona (2018).
298. Tarroni G, Oktay O, Bai W, Schuh A, Suzuki H, Passerat-Palmbach J, et al. Learning-based quality control for cardiac MR images. *IEEE Trans Med Imaging.* (2018) 38:1127–38. doi: 10.1109/TMI.2018.2878509
299. Ruijsink B, Puyol-Antón E, Oksuz I, Sinclair M, Bai W, Schnabel JA, et al. Fully automated, quality-controlled cardiac analysis from CMR: validation and large-scale application to characterize cardiac function. *Cardiovasc Imaging.* (2020) 13:684–95. doi: 10.1016/j.jcmg.2019.05.030
300. Jin KH, Unser M, Yi KM. Self-supervised deep active accelerated MRI. *arXiv preprint arXiv:190104547* (2019).
301. Han YS, Yoo J, Ye JC. Deep residual learning for compressed sensing ct reconstruction via persistent homology analysis. *arXiv preprint arXiv:161106391* (2016).
302. Kofler A, Dewey M, Schaeffter T, Wald C, Kolbitsch C. Spatio-Temporal deep learning-based undersampling artefact reduction for 2D radial cine MRI with limited training data. *IEEE Trans Med Imaging.* (2020) 39:703–17. doi: 10.1109/TMI.2019.2930318
303. Hauptmann A, Arridge S, Lucka F, Muthurangu V, Steeden JA. Real-time cardiovascular MR with spatio-temporal artifact suppression using deep learning—proof of concept in congenital heart disease. *Magn Reson Med.* (2019) 81:1143–56. doi: 10.1002/mrm.27480
304. Yang G, Yu S, Dong H, Slabaugh G, Dragotti PL, Ye X, et al. DAGAN: deep de-aliasing generative adversarial networks for fast compressed sensing MRI reconstruction. *IEEE Trans Med Imaging.* (2017) 37:1310–21. doi: 10.1109/TMI.2017.2785879
305. Hyun CM, Kim HP, Lee SM, Lee SM, Seo JK. Deep learning for undersampled MRI reconstruction. *Phys Med Biol.* (2018) 63:135007–. doi: 10.1088/1361-6560/aac71a
306. Liu F, Samsonov A, Chen L, Kijowski R, Feng L. SANTIS: sampling-augmented neural network with incoherent structure for MR image reconstruction. *Magn Reson Med.* (2019) 82:1890–904. doi: 10.1002/mrm.27827
307. Zhu B, Liu JZ, Cauley SF, Rosen BR, Rosen MS. Image reconstruction by domain-transform manifold learning. *Nature.* (2018) 555:487–92. doi: 10.1038/nature25988
308. Akçakaya M, Moeller S, Weingärtner S, Ugurbil K. Scan-specific robust artificial-neural-networks for k-space interpolation (RAKI) reconstruction: database-free deep learning for fast imaging. *Magn Reson Med.* (2019) 81:439–53. doi: 10.1002/mrm.27420
309. Eo T, Jun Y, Kim T, Jang J, Lee HJ, Hwang D. KIKI-net: cross-domain convolutional neural networks for reconstructing undersampled magnetic resonance images. *Magn Reson Med.* (2018) 80:2188–201. doi: 10.1002/mrm.27201
310. Wang S, Ke Z, Cheng H, Jia S, Ying L, Zheng H, et al. DIMENSION: dynamic MR imaging with both k-space and spatial prior knowledge obtained via multi-supervised network training. *NMR Biomed.* (2019) 2019:e4131. doi: 10.1002/nbm.4131
311. Qin C, Duan J, Hammernik K, Schlemper J, Küstner T, Botnar R, et al. Complementary time-frequency domain networks for dynamic parallel MR image reconstruction. *Magn Reson Med.* (2021) 86:3274–91. doi: 10.1002/mrm.28917
312. Ahmad R, Bouman CA, Buzzard GT, Chan S, Liu S, Reehorst ET, et al. Plug-and-Play methods for magnetic resonance imaging: using denoisers for image recovery. *IEEE Signal Process Mag.* (2020) 37:105–16. doi: 10.1109/MSP.2019.2949470
313. Lempitsky V, Vedaldi A, Ulyanov D, editors. Deep image prior. In: *Proceedings of the IEEE Computer Society Conference on Computer Vision and Pattern Recognition* (2018). doi: 10.1109/CVPR.2018.00984
314. Meinhardt T, Moeller M, Hazirbas C, Cremers D, editors. Learning proximal operators: using denoising networks for regularizing inverse imaging problems. In: *IEEE International Conference on Computer Vision*. Venedig: Institute of Electrical and Electronics Engineers Inc. (2017). doi: 10.1109/ICCV.2017.198
315. Romano Y, Elad M, Milanfar P. The little engine that could: regularization by denoising (RED). *SIAM J Imaging Sci.* (2017) 10:1804–44. doi: 10.1137/16M1102884
316. Lehtinen J, Munkberg J, Hasselgren J, Laine S, Karras T, Aittala M, et al. Noise2Noise: learning image restoration without clean data. In: *35th International Conference on Machine Learning, ICML*. Stockholm (2018). p. 4620–31.
317. Pruessmann KP, Weiger M, Boernert P, Boesiger P. Advances in sensitivity encoding with arbitrary k-space trajectories. *Magn Reson Med.* (2001) 46:638–51. doi: 10.1002/mrm.1241
318. Aggarwal HK, Mani MP, Jacob M. MoDL: model-based deep learning architecture for inverse problems. *IEEE Trans Med Imaging.* (2019) 38:394–405. doi: 10.1109/TMI.2018.2865356
319. Schlemper J, Caballero J, Hajnal JV, Price AN, Rueckert D. A deep cascade of convolutional neural networks for dynamic MR image reconstruction. *IEEE Trans Med Imaging.* (2018) 37:491–503. doi: 10.1109/TMI.2017.2760978
320. Duan J, Schlemper J, Qin C, Ouyang C, Bai W, Biffi C, et al. editors. Vs-net: Variable splitting network for accelerated parallel MRI reconstruction. In: *Lecture Notes in Computer Science*. Shenzhen: Springer (2019). doi: 10.1007/978-3-030-32251-9\_78
321. Adler J, Öktem O. Learned primal-dual reconstruction. *IEEE Trans Med Imaging.* (2018) 37:1322–32. doi: 10.1109/TMI.2018.2799231
322. Fuin N, Bustin A, Küstner T, Oksuz I, Clough J, King AP, et al. A multi-scale variational neural network for accelerating motion-compensated whole-heart 3D coronary MR angiography. *Magn Reson Imaging.* (2020) 70:155–67. doi: 10.1016/j.mri.2020.04.007
323. Qin C, Schlemper J, Caballero J, Price AN, Hajnal JV, Rueckert D. Convolutional recurrent neural networks for dynamic MR image reconstruction. *IEEE Trans Med Imaging.* (2018) 38:280–90. doi: 10.1109/TMI.2018.2863670
324. Sandino CM, Lai P, Vasanaawala SS, Cheng JY. Accelerating cardiac cine MRI using a deep learning-based ESPIRiT reconstruction. *Magn Reson Med.* (2021) 85:152–67. doi: 10.1002/mrm.28420
325. Küstner T, Fuin N, Hammernik K, Bustin A, Qi H, Hajhosseiny R, et al. CINENet: deep learning-based 3D cardiac CINE MRI reconstruction with multi-coil complex-valued 4D spatio-temporal convolutions. *Sci Rep.* (2020) 10:1–13. doi: 10.1038/s41598-020-70551-8
326. Biswas S, Aggarwal HK, Jacob M. Dynamic MRI using model-based deep learning and STORM priors: MoDL-STORM. *Magn Reson Med.* (2019) 82:485–94. doi: 10.1002/mrm.27706
327. Liu F, Feng L, Kijowski R. MANTIS: model-augmented neural network with incoherent k-space sampling for efficient MR parameter mapping. *Magn Reson Med.* (2019) 82:174–88. doi: 10.1002/mrm.27707
328. Gregor K, Lecun Y, editors. Learning fast approximations of sparse coding. In: *Proceedings of the International Conference on Machine Learning*. Haifa (2010).
329. Lin J-Y, Chang Y-C, Hsu WH. Efficient and phase-aware video super-resolution for cardiac MRI. *arXiv preprint.* (2020) arXiv:2005.10626. doi: 10.1007/978-3-030-59719-1\_7
330. Bastý N, Grau V, editors. *Super Resolution of Cardiac Cine MRI Sequences Using Deep Learning*. Cham: Springer International Publishing (2018). doi: 10.1007/978-3-030-00946-5\_3
331. Oktay O, Bai W, Lee M, Guerrero R, Kamnitsas K, Caballero J, et al. editors. Multi-input cardiac image super-resolution using convolutional neural networks. In: *International Conference on Medical Image Computing and Computer-Assisted Intervention*. Athens: Springer (2016). doi: 10.1007/978-3-319-46726-9\_29
332. Xie Y, Lin R, Chen Y, Zhang Y, Shi F, Fei Y, et al. editors. *Super Resolution MRI Using 3D Generative Adversarial Network: Towards Single Breath-Hold Coronary MR Angiography*. Paris: ISMRM (2018).

333. Ishida M, Nakayama R, Uno M, Ito T, Goto Y, Ichikawa Y, et al. Learning-based super-resolution technique significantly improves detection of coronary artery stenoses on 1.5T whole-heart coronary MRA. *J Cardiovasc Magn Reson.* (2014) 16:P218. doi: 10.1186/1532-429X-16-S1-P218
334. Zhao M, Liu X, Liu H, Wong KKL. Super-resolution of cardiac magnetic resonance images using laplacian pyramid based on generative adversarial networks. *Comput Med Imaging Graph.* (2020) 80:101698. doi: 10.1016/j.compmedimag.2020.101698
335. Steeden JA, Quail M, Gotschy A, Mortensen KH, Hauptmann A, Arridge S, et al. Rapid whole-heart CMR with single volume super-resolution. *J Cardiovasc Magn Reson.* (2020) 22:56. doi: 10.1186/s12968-020-00651-x
336. Küstner T, Munoz C, Psenicny A, Bustin A, Fuin N, Qi H, et al. Deep-learning based super-resolution for 3D isotropic coronary MR angiography in less than a minute. *Magn Reson Med.* (2021) 86:2837–52. doi: 10.1002/mrm.28911
337. Chen C, Qin C, Qiu H, Tarroni G, Duan J, Bai W, et al. Deep learning for cardiac image segmentation: a review. *Front Cardiovasc Med.* (2020) 7:25. doi: 10.3389/fcvm.2020.00025
338. Bai W, Sinclair M, Tarroni G, Oktay O, Rajchl M, Vaillant G, et al. Automated cardiovascular magnetic resonance image analysis with fully convolutional networks. *J Cardiovasc Magn Reson.* (2018) 20:65. doi: 10.1186/s12968-018-0471-x
339. Tao Q, Yan W, Wang Y, Paiman EH, Shamonin DP, Garg P, et al. Deep learning-based method for fully automatic quantification of left ventricle function from cine MR images: a multivendor, multicenter study. *Radiology.* (2019) 290:81–8. doi: 10.1148/radiol.2018180513
340. Poudel RP, Lamata P, Montana G. Recurrent fully convolutional neural networks for multi-slice MRI cardiac segmentation. In: *Reconstruction, Segmentation, and Analysis of Medical Images*. Cham: Springer (2016). p. 83–94. doi: 10.1007/978-3-319-52280-7\_8
341. Lourenço A, Kerfoot E, Dibblin C, Alskaf E, Anjari M, Bharath AA, et al. editors. Left atrial ejection fraction estimation using SEGANet for fully automated segmentation of CINE MRI. In: *International Workshop on Statistical Atlases and Computational Models of the Heart*. Cham: Springer (2020). doi: 10.1007/978-3-030-68107-4\_14
342. Morales MA, van den Boomen M, Nguyen C, Kalpathy-Cramer J, Rosen BR, Stultz CM, et al. DeepStrain: a deep learning workflow for the automated characterization of cardiac mechanics. *Front Cardiovasc Med.* (2021) 8:730316. doi: 10.3389/fcvm.2021.730316
343. Bard A, Raisi-Estabragh Z, Ardissino M, Lee AM, Pugliese F, Dey D, et al. Automated quality-controlled cardiovascular magnetic resonance pericardial fat quantification using a convolutional neural network in the UK biobank. *Front Cardiovasc Med.* (2021) 8:677574. doi: 10.3389/fcvm.2021.677574
344. Fahmy AS, Rausch J, Neisius U, Chan RH, Maron MS, Appelbaum E, et al. Automated cardiac MR scar quantification in hypertrophic cardiomyopathy using deep convolutional neural networks. *JACC Cardiovasc Imaging.* (2018) 11:1917–8. doi: 10.1016/j.jcmg.2018.04.030
345. Chen J, Yang G, Gao Z, Ni H, Angelini E, Mohiaddin R, et al. editors. Multiview two-task recursive attention model for left atrium and atrial scars segmentation. In: *International Conference on Medical Image Computing and Computer-Assisted Intervention*. Cham: Springer (2018). doi: 10.1007/978-3-030-00934-2\_51
346. Zabihollahy F, White JA, Ukwatta E, editors. Myocardial scar segmentation from magnetic resonance images using convolutional neural network. In: *Medical Imaging 2018: Computer-Aided Diagnosis*. Orlando, FL: International Society for Optics and Photonics (2018). doi: 10.1117/12.2293518
347. Moccia S, Banali R, Martini C, Muscogiuri G, Pontone G, Pepi M, et al. Development and testing of a deep learning-based strategy for scar segmentation on CMR-LGE images. *Magn Reson Mater Phys Biol Med.* (2019) 32:187–95. doi: 10.1007/s10334-018-0718-4
348. Yue Q, Luo X, Ye Q, Xu L, Zhuang X, editors. Cardiac segmentation from LGE MRI using deep neural network incorporating shape and spatial priors. In: *International Conference on Medical Image Computing and Computer-Assisted Intervention*. Cham: Springer (2019). doi: 10.1007/978-3-030-32245-8\_62
349. Puyol-Antón E, Ruijsink B, Baumgartner CF, Masci P-G, Sinclair M, Konukoglu E, et al. Automated quantification of myocardial tissue characteristics from native T1 mapping using neural networks with uncertainty-based quality-control. *J Cardiovasc Magn Reson.* (2020) 22:1–15. doi: 10.1186/s12968-020-00650-y
350. Fahmy AS, El-Rewaify H, Nezafat M, Nakamori S, Nezafat R. Automated analysis of cardiovascular magnetic resonance myocardial native T1 mapping images using fully convolutional neural networks. *J Cardiovasc Magn Reson.* (2019) 21:1–12. doi: 10.1186/s12968-018-0516-1
351. Xue H, Brown LA, Nielles-Vallespin S, Plein S, Kellman P. Automatic in-line quantitative myocardial perfusion mapping: processing algorithm and implementation. *Magn Reson Med.* (2020) 83:712–30. doi: 10.1002/mrm.27954
352. Scannell CM, Veta M, Villa AD, Sammut EC, Lee J, Breeuwer M, et al. Deep-learning-based preprocessing for quantitative myocardial perfusion MRI. *J Magn Reson Imaging.* (2020) 51:1689–96. doi: 10.1002/jmri.26983
353. Zhang Y, Zhang W, Zhang Q, Yang J, Chen X, Zhao S. CMR motion artifact correction using generative adversarial nets. *arXiv preprint.* (2019) arXiv:190211121.
354. Ghodrati V, Bydder M, Ali F, Gao C, Prosper A, Nguyen KL, et al. Retrospective respiratory motion correction in cardiac cine MRI reconstruction using adversarial autoencoder and unsupervised learning. *NMR Biomed.* (2021) 34:e4433. doi: 10.1002/nbm.4433
355. Oksuz I, Clough J, Bustin A, Cruz G, Prieto C, Botnar R, et al. Cardiac MR motion artefact correction from k-space using deep learning-based reconstruction. In: *International Workshop on Machine Learning for Medical Image Reconstruction*. Cham: Springer (2018). doi: 10.1007/978-3-030-00129-2\_3
356. Oksuz I, Clough JR, Ruijsink B, Anton EP, Bustin A, Cruz G, et al. Deep learning-based detection and correction of cardiac MR motion artefacts during reconstruction for high-quality segmentation. *IEEE Trans Med Imaging.* (2020) 39:4001–10. doi: 10.1109/TMI.2020.3008930
357. Ronneberger O, Fischer P, Brox T, editors. U-net: convolutional networks for biomedical image segmentation. In: *International Conference on Medical Image Computing and Computer-Assisted Intervention*. Munich: Springer (2015). doi: 10.1007/978-3-319-24574-4\_28
358. Huang Q, Yang D, Qu H, Yi J, Wu P, Metaxas D, editors. Dynamic MRI reconstruction with motion-guided network. In: *International Conference on Medical Imaging with Deep Learning*. London (2019).
359. Pan J, Rueckert D, Küstner T, Hammernik K, editors. Efficient image registration network for non-rigid cardiac motion estimation. In: *International Workshop on Machine Learning for Medical Image Reconstruction*. Springer (2021). doi: 10.1007/978-3-030-88552-6\_2
360. Küstner T, Pan J, Qi H, Cruz G, Gilliam C, Blu T, et al. LAPNet: non-rigid registration derived in k-space for magnetic resonance imaging. *IEEE Trans Med Imaging.* (2021) 40:3686–97. doi: 10.1109/TMI.2021.3096131
361. Seegoolam G, Schlemper J, Qin C, Price A, Hajnal J, Rueckert D, et al. Exploiting motion for deep learning reconstruction of extremely-undersampled dynamic MRI. In: *International Conference on Medical Image Computing and Computer-Assisted Intervention*. Cham: Springer (2019). doi: 10.1007/978-3-030-32251-9\_77
362. Sun L, Fan Z, Ding X, Huang Y, Paisley J. Joint CS-MRI reconstruction and segmentation with a unified deep network. In: *Lecture Notes in Computer Science*. Hong Kong: Springer (2019). p. 492–504. doi: 10.1007/978-3-030-20351-1\_38
363. Mendrik AM, Vincken KL, Kuijff HJ, Breeuwer M, Bouvy WH, Bresser JD, et al. MRBrainS challenge. *Comput Intell Neurosci.* (2015) 2015:16. doi: 10.1155/2015/813696
364. Huang Q, Yang D, Yi J, Axel L, Metaxas D. FR-Net: joint reconstruction and segmentation in compressed sensing cardiac MRI. In: *Lecture Notes in Computer Science*. Bordeaux: Springer (2019). p. 352–60. doi: 10.1007/978-3-030-21949-9\_38
365. Schlemper J, Oktay O, Bai W, Castro DC, Duan J, Qin C, et al. Cardiac MR segmentation from undersampled k-space using deep latent representation learning. In: *Lecture Notes in*

- Computer Science* (2018). p. 259–67. doi: 10.1007/978-3-030-00928-1\_30
366. Qin C, Bai W, Schlemper J, Petersen SE, Piechnik SK, Neubauer S, et al. Joint learning of motion estimation and segmentation for cardiac MR image sequences. In: *Lecture Notes in Computer Science*. Granada: Springer (2018). p. 472–80. doi: 10.1007/978-3-030-00934-2\_53
367. Qin C, Bai W, Schlemper J, Petersen SE, Piechnik SK, Neubauer S, et al. Joint motion estimation and segmentation from undersampled cardiac MR image. In: *Lecture Notes in Computer Science*. Granada: Springer (2018). p. 55–63. doi: 10.1007/978-3-030-00129-2\_7

**Conflict of Interest:** The authors declare that the research was conducted in the absence of any commercial or financial relationships that could be construed as a potential conflict of interest.

**Publisher's Note:** All claims expressed in this article are solely those of the authors and do not necessarily represent those of their affiliated organizations, or those of the publisher, the editors and the reviewers. Any product that may be evaluated in this article, or claim that may be made by its manufacturer, is not guaranteed or endorsed by the publisher.

Copyright © 2022 Ismail, Strugnell, Coletti, Božić-Iven, Weingärtner, Hammernik, Correia and Küstner. This is an open-access article distributed under the terms of the Creative Commons Attribution License (CC BY). The use, distribution or reproduction in other forums is permitted, provided the original author(s) and the copyright owner(s) are credited and that the original publication in this journal is cited, in accordance with accepted academic practice. No use, distribution or reproduction is permitted which does not comply with these terms.



# Automatic Detection of Secundum Atrial Septal Defect in Children Based on Color Doppler Echocardiographic Images Using Convolutional Neural Networks

## OPEN ACCESS

### Edited by:

Daniel Rueckert,  
Technical University of Munich,  
Germany

### Reviewed by:

Hideaki Suzuki,  
Tohoku University Hospital, Japan  
Andrew Gilbert,  
GE Healthcare, Norway

### \*Correspondence:

Yuqi Zhang  
changyuqi@hotmail.com  
Xiaoqing Liu  
xiaoqing.liu@ieee.org  
Liebin Zhao  
zhaoliebin@126.com

† These authors have contributed  
equally to this work and share first  
authorship

### Specialty section:

This article was submitted to  
Cardiovascular Imaging,  
a section of the journal  
Frontiers in Cardiovascular Medicine

**Received:** 07 January 2022

**Accepted:** 24 February 2022

**Published:** 06 April 2022

### Citation:

Hong W, Sheng Q, Dong B, Wu L,  
Chen L, Zhao L, Liu Y, Zhu J, Liu Y,  
Xie Y, Yu Y, Wang H, Yuan J, Ge T,  
Zhao L, Liu X and Zhang Y (2022)  
Automatic Detection of Secundum  
Atrial Septal Defect in Children Based  
on Color Doppler Echocardiographic  
Images Using Convolutional Neural  
Networks.  
Front. Cardiovasc. Med. 9:834285.  
doi: 10.3389/fcvm.2022.834285

Wenjing Hong<sup>1†</sup>, Qiuyang Sheng<sup>2†</sup>, Bin Dong<sup>3,4†</sup>, Lanping Wu<sup>1</sup>, Lijun Chen<sup>1</sup>,  
Leisheng Zhao<sup>1</sup>, Yiqing Liu<sup>1</sup>, Junxue Zhu<sup>1</sup>, Yiman Liu<sup>1</sup>, Yixin Xie<sup>1</sup>, Yizhou Yu<sup>2</sup>,  
Hansong Wang<sup>3,4</sup>, Jiajun Yuan<sup>3,4</sup>, Tong Ge<sup>3,4</sup>, Liebin Zhao<sup>4\*</sup>, Xiaoqing Liu<sup>2\*</sup> and  
Yuqi Zhang<sup>1\*</sup>

<sup>1</sup> Department of Pediatric Cardiology, Shanghai Children's Medical Center, School of Medicine, Shanghai Jiao Tong University, Shanghai, China, <sup>2</sup> Deepwise Artificial Intelligence Laboratory, Beijing, China, <sup>3</sup> Pediatric Artificial Intelligence Clinical Application and Research Center, Shanghai Children's Medical Center, School of Medicine, Shanghai Jiao Tong University, Shanghai, China, <sup>4</sup> Shanghai Engineering Research Center of Intelligence Pediatrics (SERCIP), Shanghai, China

Secundum atrial septal defect (ASD) is one of the most common congenital heart diseases (CHDs). This study aims to evaluate the feasibility and accuracy of automatic detection of ASD in children based on color Doppler echocardiographic images using convolutional neural networks. In this study, we propose a fully automatic detection system for ASD, which includes three stages. The first stage is used to identify four target echocardiographic views (that is, the subcostal view focusing on the atrium septum, the apical four-chamber view, the low parasternal four-chamber view, and the parasternal short-axis view). These four echocardiographic views are most useful for the diagnosis of ASD clinically. The second stage aims to segment the target cardiac structure and detect candidates for ASD. The third stage is to infer the final detection by utilizing the segmentation and detection results of the second stage. The proposed ASD detection system was developed and validated using a training set of 4,031 cases containing 370,057 echocardiographic images and an independent test set of 229 cases containing 203,619 images, of which 105 cases with ASD and 124 cases with intact atrial septum. Experimental results showed that the proposed ASD detection system achieved accuracy, recall, precision, specificity, and F1 score of 0.8833, 0.8545, 0.8577, 0.9136, and 0.8546, respectively on the image-level averages of the four most clinically useful echocardiographic views. The proposed system can automatically and accurately identify ASD, laying a good foundation for the subsequent artificial intelligence diagnosis of CHDs.

**Keywords:** artificial intelligence, convolutional neural networks, automatic detection, secundum atrial septal defect, echocardiogram

## INTRODUCTION

Congenital heart diseases (CHDs) are one of the most common congenital birth defects. The incidence of CHD is about 0.9% among the newborns born in China (1). Atrial septal defect (ASD) is considered to be one of the most common CHDs, and the estimated prevalence of ASD is 0.88 per 1,000 patients. The most common type of ASD is the secundum ASD, which accounts for approximately 80% of ASD (2). Echocardiography is noninvasive, nonradioactive, and can comprehensively evaluate the structure and function of the heart and blood vessels, and is widely used in the diagnosis and treatment of cardiovascular malformations. In China, because of the large pediatric population, there is a huge demand for echocardiography specialists for CHD diagnosis. Echocardiographic diagnosis relies on the operator to collect video streams from different perspectives and observe the morphology of organs and tissues from multiple views. Accurate diagnosis is largely affected by the operator's personal technical skills. However, due to the long training time to be an echocardiography expert, it is difficult to diagnose CHDs accurately for most of primary hospitals lacking experienced echocardiography experts. Therefore, there is an urgent need to develop an automatic diagnostic system based on echocardiographic analysis that can quickly and accurately diagnose CHDs and assist echocardiography operators to reduce misdiagnosis caused by artificial factors.

In recent years, with the development of artificial intelligence (AI) technology, deep learning methods based on convolutional neural networks (CNNs) have been applied to various medical image analysis tasks, including lesion detection, organ segmentation, and disease diagnosis. Recent studies have shown that object detection technology can be used to detect lesions of knee joint (3), thyroid (4), breast (5), pancreas (6), and other diseases. However, there are very few reports on detection of abnormal cardiac structures. The U-Net based architecture has also been widely applied in many segmentation tasks, such as liver (7, 8), lung (9), tumor segmentation (10, 11), and prostate (12, 13). U-Net has also attracted many attentions in the field of ultrasonic images such as segmentation of ovary (14), fetal head (15), and breast (16). As for CHD diagnosis, it has also been reported that AI-based automatic auscultation may improve the accuracy of CHD screening (17). However, the application of automatic auscultation in the diagnosis of CHD is limited since it cannot accurately diagnose the type of CHDs, measure the size of the defect, and, further evaluate hemodynamics (such as shunt direction).

Advances in the digitization, standardization, and storage of echocardiograms have led to recent interest in the automatic interpretation of echocardiograms based on deep learning. Current research on echocardiographic analysis focused on detecting abnormal ventricular function and locating ventricular wall motion (18–20). Nevertheless, existing work of ventricular segmentation (21), cardiac phase detection (22), ejection fraction assessment (23), and other tasks still cannot meet the needs of accurate diagnosis of CHDs. Standard view recognition based on echocardiography is a prerequisite for clinical diagnosis of heart diseases. Baumgartner et al. (24) proposed a two-dimensional

CNN containing six convolutional modules, which can recognize 12 standard views of fetal ultrasound with an average accuracy of 0.69 and an average recall rate of 0.80. Sridar et al. (25) used the pre-trained AlexNet to identify 14 views of fetuses and achieved a precision of 0.76 and a recall of 0.75 on average. Madani et al. (26) and Howard et al. (27) also trained CNN-based models to classify 15 standard echocardiographic views with reasonable results. However, these tasks used large networks with high computational complexity to achieve high performance and require high-standard hardware configurations, which may not meet the real-time requirements of CHD diagnosis in practice. Recent advances on CNNs have also led to rapid progress in multiple standard view recognition for echocardiography (26, 28, 29), with an overall accuracy of 97 or 98%. However, these works were for adults and may not be suitable for ASD detection in children.

In this study, we proposed an automatic ASD detection system which can perform image-level ASD detection based on color Doppler echocardiographic images using CNNs. The proposed automatic ASD detection system consists of four modules, namely the standard view identification module, the cardiac anatomy segmentation module, the ASD candidate detection module and the detection refinement module. In clinical diagnosis, due to the complexity of the heart structure and the limitations of two-dimensional echocardiographic scanning of ASDs, especially posterior inferior border defect detection, clinicians need to examine the heart from different views. In addition, some clinical signs can only be observed from certain views. We used multiple sites (subxiphoid, apical, and parasternal) and multiple views to simulate the diagnosis by sonographers in real clinical scenarios instead of using a single view. The standard view identification module is designed to identify four clinical meaningful echocardiographic views (that is, the subcostal view focusing on the atrium septum, the apical four-chamber view, the low parasternal four-chamber view, and the parasternal short-axis view) that are most useful for diagnosing ASD. The cardiac anatomy segmentation module aims to segment the left atrium (LA) and the right atrium (RA) from the images of the four target standard views, since ASD occurs in the septal area between LA and RA. The ASD candidate detection module finds all ASD candidates, and finally the detection refinement module applies deterministic spatial analysis to further refine the ASD detection results based on the information derived from the output of the cardiac anatomy segmentation. The proposed ASD detection system was developed and validated using a training set of 4,031 cases containing 370,057 echocardiographic images and an independent test set of 229 cases containing 203,619 images. Experimental results show the proposed system can automatically and accurately detect ASD, paving the way for the automatic diagnosis of CHD.

The main contributions of this study include: firstly, to our knowledge, a fully automatic CNN-based ASD detection system was proposed for the first time; secondly, we established a data set consists of a training set of 370,057 images of 4,031 cases and a test set of 203,619 images of 229 cases, that meets the requirements of ASD clinical diagnosis and is

the largest dataset reported so far; thirdly, our standard view identification model has achieved the state of the art recognition performance with an the average accuracy of 0.9942 and F1 score of 0.9377 for the four target views of ASD diagnosis while using a small network through knowledge distillation which meet the real-time requirements of CHD diagnosis in practice; fourthly, the newly introduced dense dual attention mechanism in the cardiac anatomy segmentation can improve segmentation performance by simultaneously aggregating context and location information; and finally experimental results proved that the proposed detection refinement module can effectively improve the detection precision while keep the recall rate basically unchanged.

## MATERIALS AND METHODS

### Participants

The subject of this retrospective study is color Doppler echocardiographic images of pediatric patients undergoing ASD examination at Shanghai Children's Medical Center. The time period for these examinations is from September 2018 to April 2021. These cases include patients diagnosed as positive and negative. Among them, positive cases were diagnosed as ASD with a diameter greater than 5 mm, and negative cases were diagnosed as intact atrial septum.

### Data Collection

The study has been approved by the Institutional Review Board of Shanghai Children's Medical Center (Approval No. SCMCIRB-W2021058) and a patient exemption has been applied for. All patients were examined with echocardiography using Philips iE33, EPIQ 7C, and GE Vivid E95 ultrasound systems with S5-1, S8-3, M5Sc, and 6S transducers. Standard imaging techniques were used for two-dimensional, M-mode, and Color Doppler echocardiography in accordance with the recommendations of the American Society of Echocardiography (30). All data used in this study were randomly selected cases from Shanghai Children's Medical Center's PACS database and these cases were collected by different doctors on different ultrasound machines. All data were strictly desensitized to protect patient privacy. The original data format of echocardiography was DICOM video stored in the PACS database. In order to facilitate program processing, DICOM video was divided frame-by-frame into a series of JPEG images. The human heart is not a static organ, it is constantly contracting and expanding. ASD size and shunts also vary with the cardiac cycle. Therefore, we dynamically sample and collect a series of image frames from different cardiac cycles. Five junior clinicians were recruited to manually label the data, including view types, outlines of cardiac structures, and ASD diagnostic annotations. Diagnosis was made by analyzing the heart using image segments from different views (subcostal-, apex-, parasternal-, and suprasternal views, etc.). All manually annotated data were further reviewed and confirmed as the gold standard by two senior clinicians. During systole, diastole, and torsion of the heartbeat, the position of the atrial septum changes to some extent. The atrial septum may be blurred (especially in

**TABLE 1** | Summary of the training and validation data sets.

|                                | Training set    |                  | Validation set  |                  |
|--------------------------------|-----------------|------------------|-----------------|------------------|
|                                | Number of cases | Number of images | Number of cases | Number of images |
| Standard view identification   | 3,409           | 247,750          | 96              | 102,904          |
| Cardiac anatomy segmentation   | 237             | 7,500            | 101             | 2,185            |
| Atrial septal defect detection | 150             | 8,355            | 38              | 1,363            |

the subxiphoid view) due to motion artifacts. In this study, images with motion blur were excluded after expert review.

### Training/Validation Dataset

A total of 4,031 cases (370,057 images) were used as the training set of the standard view recognition module, the cardiac anatomy segmentation module and the ASD detection module. Since our training set is large enough to adequately represent the data distribution, we sample and collect image frames using fewer cardiac cycles for each case. The dataset was randomly divided into training and validation sets and selectively annotated as shown in **Table 1**. Since the data are collected from a real clinical practice, the view distribution is basically the same as the daily diagnosis.

### Test Dataset

Additional 105 ASD patients (32 male, median age of 1.80 years) and 124 normal controls with intact atrial septum (45 male, median age of 2.09 years) were enrolled as an independent test data set for the final ASD detection evaluation (**Table 2**). In order to thoroughly test the performance of the model, we sampled and collected image frames with more cardiac cycles for each case. As a result, a total of 203,619 echocardiography images were included (92,616 images in the ASD group and 111,003 images in the normal group). **Table 2** shows the view distribution as well as clinical characteristics of the two groups of the test dataset. According to the recognition results of the standard view identification module, the data of the four target standard views were used to evaluate the performance of ASD detection. As shown in **Table 2**, there are a total of 40,264 images, including 18,338 images from ASD patients and 21,926 images from a normal control groups.

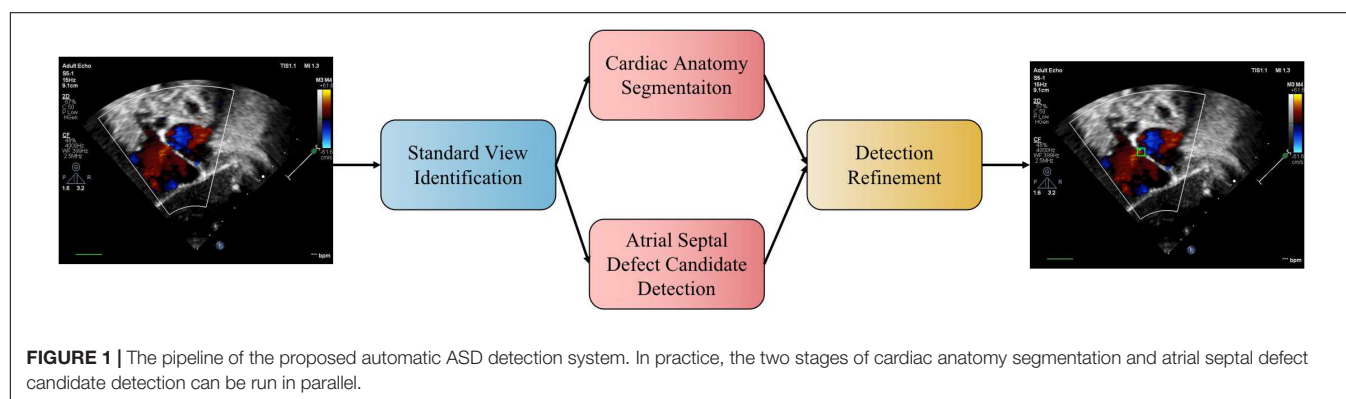
## Proposed Method

We propose a three-stage ASD detection system, which includes four modules, namely, standard view identification, cardiac anatomy segmentation, ASD detection, and detection refinement, as shown in **Figure 1**. The first stage is the identification of standard view module, aiming to extract four target standard views, namely, the subcostal view focusing on the atrium septum (subAS), the apical four-chamber view (A4C), the low parasternal four-chamber view (LPS4C), and the sax-basal view, from frames of dynamic videos. The second stage includes cardiac anatomy segmentation and ASD detection modules. The former is to segment the target cardiac anatomy, and the latter is to detect candidate ASDs. The input of these two modules is the image of the target standard view extracted in the first stage. The third

**TABLE 2 |** Clinical characteristic and view distribution comparisons between the ASD group and the normal group of the test data set.

|                                     | ASD group (n = 105)                       | Normal group (n = 124)   | p-Value/total |
|-------------------------------------|---|--|---------------|
| Age (years)                         | 1.80 (0.04–14.46)                         | 2.09 (0.11–14.61)  | $p = 0.25$    |
| Female/male                         | 73/32                                     | 79/45  | $p = 0.40$    |
| Weight (kg)                         | 11.00 (3.45–52.00)                        | 12.50 (4.30–50.00)   | $p = 0.082$   |
| Height (cm)                         | 80.00 (45.00–162.00)                      | 90.00 (51.00–152.00)   | $p = 0.073$   |
| Size of ASD (mm)                    | 12.1 ± 5.2                                | /  |               |
| Associated cardiac conditions       | PDA (n = 2)<br>VSD (n = 11)<br>PS (n = 4) | Small PDA (n = 3)<br>VSD (n = 6)<br>Post PDA occlusion (n = 4) |               |
| subAS (ASD detection/total) (n)     | 7,503/8,079                               | 8,498/8,790  | 16,001/16,869 |
| A4C (ASD detection/total) (n)       | 2,942/3,078                               | 3,840/4,003  | 6,782/7,081   |
| LPS4C (ASD detection/total) (n)     | 4,410/4,798                               | 4,714/5,159  | 9,124/9,957   |
| Sax-basal (ASD detection/total) (n) | 3,483/4,245                               | 4,874/5,689  | 8,357/9,934   |
| Other (n)                           | 72,416                                    | 87,362   | 159,778       |
| Total (n)                           | 92,616                                    | 111,003  | 203,619       |

ASD, atrial septal defect; VSD, ventricular septal defect; PDA, patent ductus arteriosus; PS, pulmonary stenosis; subAS, subcostal atrium septum; A4C, apical four-chamber; LPS4C, low parasternal four-chamber.



stage is the detection refinement module, which combines the results of the second stage to obtain refined detection results.

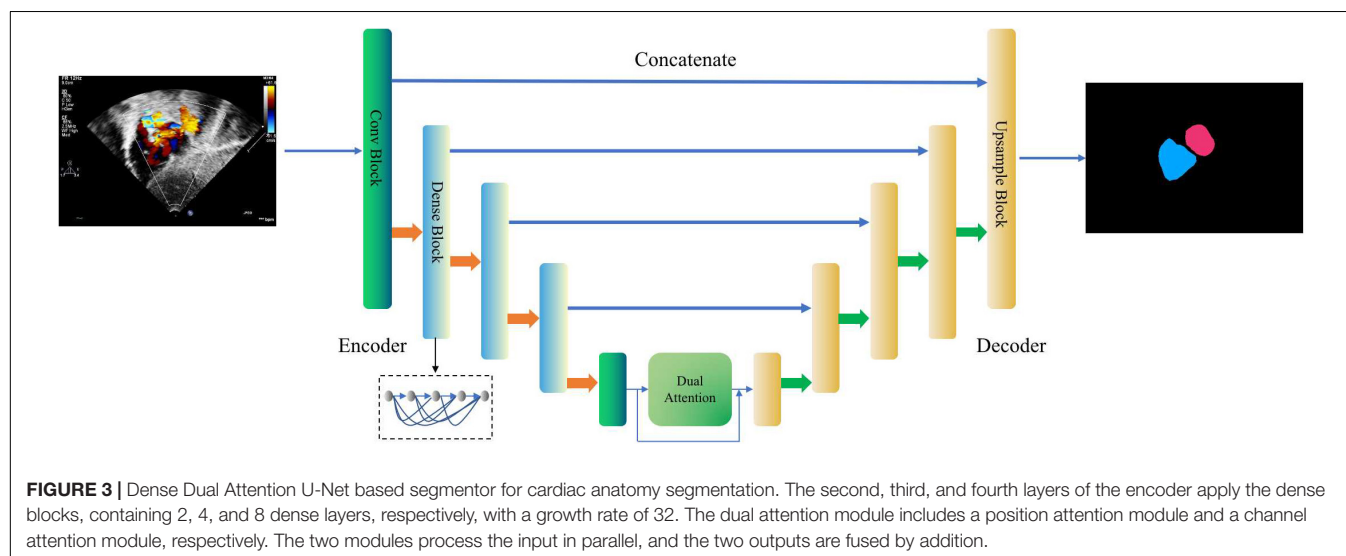
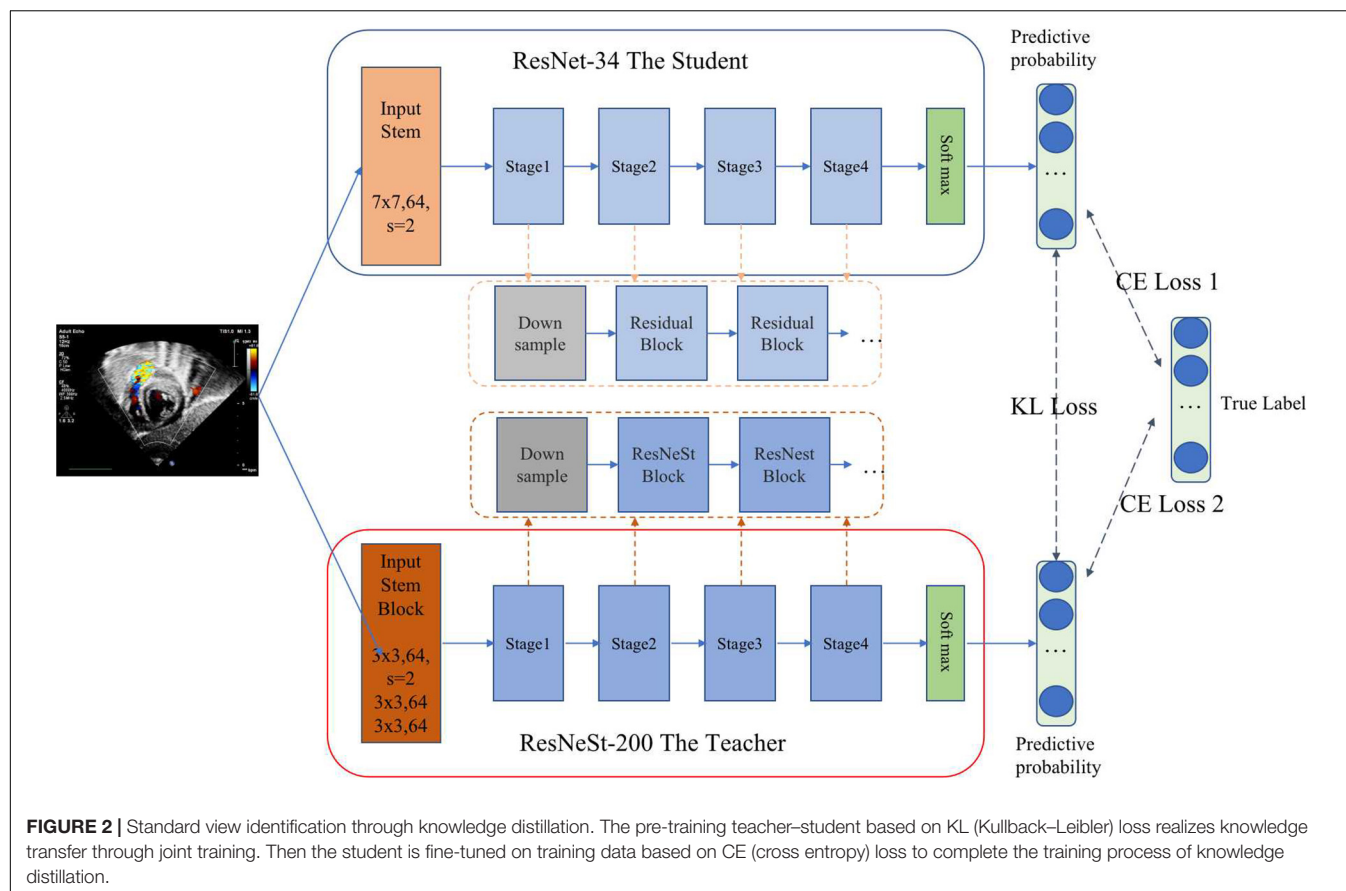
### Standard View Identification

Standard echocardiographic view recognition is a prerequisite for clinical diagnosis of heart disease. Our standard view identification model is based on our previous work (31), where we recognized 24 classes of standard views with high accuracy. Since the purpose of this study is to detect ASD, we only focus on four target views (i.e., subAS, A4C, LPS4C, and sax-basal) and refer to all other views as “other.” As shown in **Figure 2**, a knowledge distillation (32) method was applied to train the standard view identification model, in which we applied ResNet-34 (33) as the student model and ResNeSt-200 (34) as the teacher model. We first trained a ResNeSt-200 network with a large amount of parameters, and then transferred the “knowledge” to a ResNet-34 network with a small amount of parameters through knowledge distillation. By minimizing the Kullback–Leibler divergence between the probability distributions of teacher and student models, knowledge transfer was achieved through joint training. During the training process, data augmentation methods were also applied, including horizontal random flip, vertical random flip, and polar coordinate rotation. It needs

to be noted that the teacher model was only used during the training phase, and the small student model ResNet34 was used for inference.

### Cardiac Anatomy Segmentation

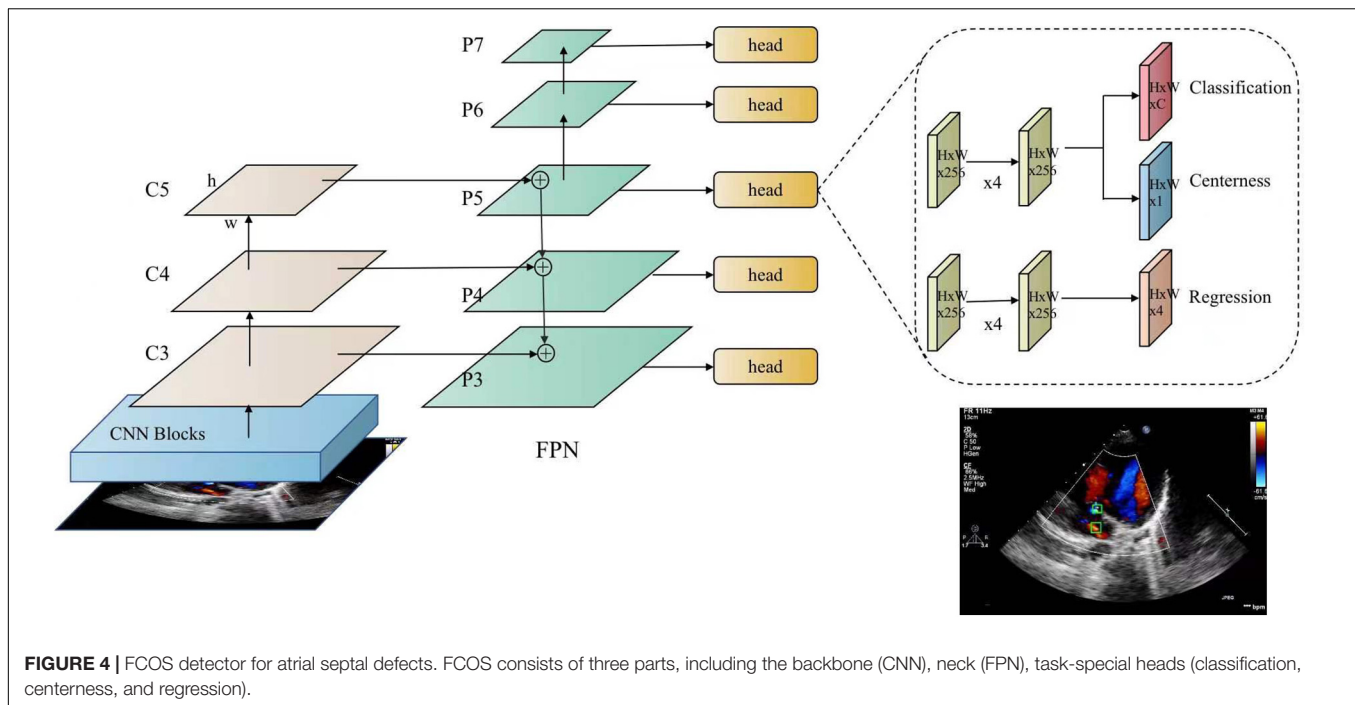
This module is designed to segment the LA and the RA from the images of the four target standard views. As shown in **Figure 3**, a new encoder-decoder network called Dense Dual Attention U-Net is proposed as the atrium segmentor. The encoder gradually extracts features from the input image to obtain a high-dimensional representation of the image. The decoder reconstructs the image according to the high dimensional feature representation, and then outputs the segmentation mask. Jumping out of the tradition of U-Net (35), the hierarchical output features of the encoder are input to the decoder one by one through the “skip connection” mechanism for feature fusion. The convolutional layers of Dense Dual Attention U-Net adopts “dense connection” (36), and the encoder also uses “dual attention” (37), which are spatial-based and channel-based attentions, respectively. The dense dual attention mechanism introduced in the U-Net architecture can improve segmentation performance by simultaneously aggregating context and location information.



### Atrial Septal Defect Candidate Detection

This module aims to detect ASD candidates from the images of the four target standard views and mark the detected ASD candidates with confidence values. In this study, a fully convolutional single-stage object detector, known as FCOS (38) is applied as the ASD detector. As shown in **Figure 4**, FCOS has two output heads. The classification head outputs the class

probability of the detected ASD candidate, i.e., the confidence of the detected ASD candidate, and the regression head outputs the coordinates of the candidate ASD area. The size of ASD varies greatly. The detection of large ASD relies on a large receptive field while the detection of small ASD relies on a high-resolution feature map. The feature pyramid network (FPN) (39) module in FCOS can handle this problem. In addition, FCOS



has achieved a good balance between detection accuracy and computational complexity, meeting the real-time requirements of the proposed system.

### Detection Refinement

The basic rule of ASD diagnosis is that ASD occurs in the septum area between LA and RA. Theoretically, the ASD candidates detected by the FCOS detector may appear in any area of the image. Therefore, detection refinement is necessary to filtered out false positives detected. Based on the outputs of the cardiac anatomy segmentation, the septum area can be extracted through deterministic spatial analysis. More specifically, we first need to find the smallest convex hull of LA and RA, and then the difference between the convex hull and the area of LA and RA is the septum area. As shown in **Figure 5**, considering the decision margin, morphological dilation techniques can be used to expand the septum area. Finally, ASD candidates detected outside the septum area are regarded as false positives and filtered, as shown in **Figure 6**.

### Environment Configuration

All codes were implemented using Python 3.7 and Pytorch 1.4.0. The experiment was conducted on a workstation platform with 8 NVIDIA TITAN RTX GPUs, 24 GB GPU memory, 256 G RAM, and 80 Intel(R) Xeon(R) Gold 6248 CPU @ 2.50 GHz, using Ubuntu 16.04.

## RESULTS

### Performance Evaluation

We use Accuracy, Recall, Precision, Specificity, and F1 Score to evaluate the performance of view identification and ASD

detection and apply *Dice Similarity Coefficient (DSC)* as the performance evaluation metric for cardiac anatomical segmentation. They are defined as follows:

$$\text{Accuracy} = \frac{TP + TN}{TP + FP + FN + TN} \quad (1)$$

$$\text{Recall} = \text{Sensitivity} = \frac{TP}{TP + FN} \quad (2)$$

$$\text{Precision} = \frac{TP}{TP + FP} \quad (3)$$

$$\text{Specificity} = \frac{TN}{TN + FP} \quad (4)$$

$$\text{F1 Score} = 2 \times \frac{\text{Precision} \times \text{Recall}}{\text{Precision} + \text{Recall}} \quad (5)$$

$$\text{DSC} = \frac{2 \times |A \cap B|}{|A| + |B|} \quad (6)$$

Among them, TP, FP, TN, and FN are the counts of true positive, false positive, true negative, and false negative, respectively. TP and TN represent the positives and negatives of correct predictions with respect to the ground truth. FP and FN represent positives and negatives of incorrect predictions with respect to the ground truth. F1 score is the harmonic average of Precision and Recall with a value ranged in (0–1). The higher value, the better the model performance. A is defined as the ground truth area, and B is defined as the segmented area.

The receiver operating characteristic (ROC) curve is plotted by using *1-Specificity* as the X-axis and *Sensitivity* as the Y-axis.

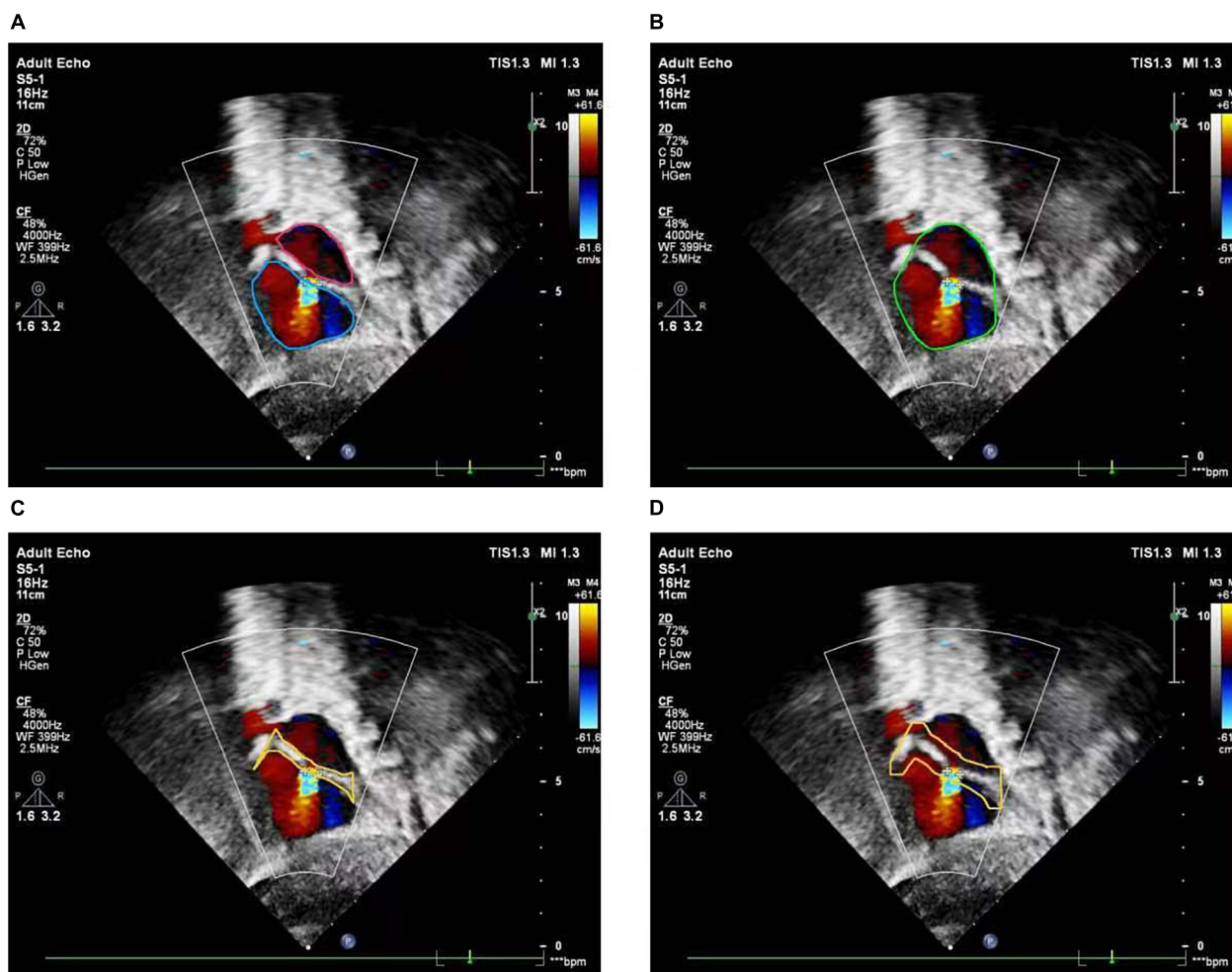


**FIGURE 5 |** Atrial septal region extraction. (A) Segmented left and right atria, (B) convex hull embracing segmented left and right atria, (C) region differences between (A) and (B), (D) morphologically dilated atrial septum.

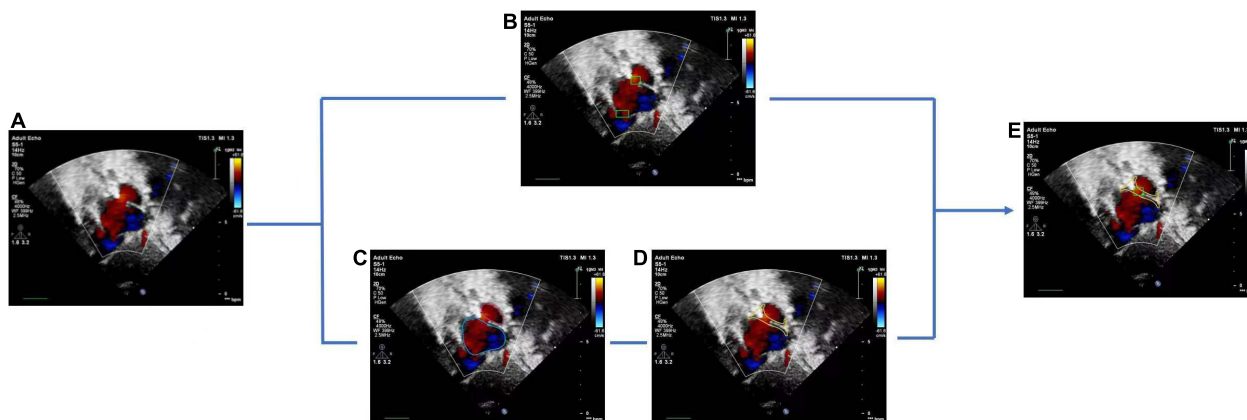


**FIGURE 6 |** Atrial septal defect detection refinement. (A) Input image with a target view, (B) detected ASD candidates, (C) segmentation result of cardiac anatomy, (D) extraction of atrial septal region based on (C), (E) final refined result of ASD detection.

**TABLE 3 |** Performance results of standard view identification.

| View               | Accuracy               | Recall                 | Precision              | Specificity            | F1 score               |
|--------------------|------------------------|------------------------|------------------------|------------------------|------------------------|
| subAS (95% CI)     | 0.9965 (0.9962–0.9969) | 0.9485 (0.9452–0.9519) | 0.9985 (0.9979–0.9991) | 0.9999 (0.9998–0.9999) | 0.9729 (0.9729–0.9729) |
| A4C (95% CI)       | 0.9975 (0.9972–0.9978) | 0.9444 (0.9391–0.9497) | 0.9788 (0.9754–0.9822) | 0.9993 (0.9991–0.9994) | 0.9613 (0.9613–0.9613) |
| LPS4C (95% CI)     | 0.9908 (0.9902–0.9914) | 0.9163 (0.9109–0.9218) | 0.8971 (0.8912–0.9031) | 0.9946 (0.9943–0.9949) | 0.9066 (0.9066–0.9067) |
| Sax-basal (95% CI) | 0.9919 (0.9913–0.9924) | 0.8413 (0.8341–0.8484) | 0.9908 (0.9887–0.9928) | 0.9996 (0.9995–0.9997) | 0.9099 (0.9099–0.9099) |
| Mean               | 0.9942                 | 0.9126                 | 0.9663                 | 0.9983                 | 0.9377                 |

subAS, subcostal atrium septum; A4C, apical four-chamber; LPS4C, low parasternal four-chamber.

The area under the curve (AUC) is calculated based on the trapezoidal method to measure the detection performance. The best confidence cut-off point is determined according to the *Youden Index* defined as follows:

$$\text{Youden Index} = \text{Sensitivity} + \text{Specificity} - 1 \quad (7)$$

## Performance of Standard View Identification

The performance of the standard view recognition was evaluated on 203,619 echocardiographic images in the test data set. As shown in **Table 3**, our standard view identification model achieved excellent performance. For the four target views (i.e., subAS, A4C, LPS4C, and PSAX), the averages of accuracy, recall, precision, specificity, and F1 score were 0.9942, 0.9126, 0.9663, 0.9983, and 0.9377, respectively. The parameters of our model are about 21.3 M, which is less than 1/3 of the parameters of the teacher ResNeSt-200 model (approximately 70.2 M). In terms of computational complexity, the FLOPs of our model is about 3.7 G, which is only 1/5 of the FLOPs of ResNeSt-200 (about 13.48 G). Through knowledge distillation, it significantly reduced the computational cost while maintained the precision of network classification.

## Performance of Cardiac Anatomy Segmentation

The performance of the cardiac anatomical segmentation was evaluated on 101 cases with 2,185 echocardiographic images in the validation data set. In this study, we categorized the verification data into four groups. More specifically, data containing only LA and RA was considered as A2C; data containing LA, RA, left ventricle, and right ventricle was regarded as A2C-V2C; data containing atrium and left ventricle was classified as A2C-LV; and data containing LA, RA, and right ventricle was categorized as A2C-RV. The number distribution of each group and the corresponding segmentation results were shown in **Table 4**, where we only focused on the segmentation results of the LA and the RA. **Table 5** also demonstrated the ablation experimental results of the proposed Dense Dual Attention U-Net, which incorporated two additional modules, namely the Dense block and the Dual Attention modules. As shown in **Table 5**, both the Dense block and the Dual Attention had positive impacts on the segmentation performance of the U-Net. **Figure 7** also demonstrated some of the example results of cardiac anatomical segmentation with high, medium and low performance.

## Performance of Atrial Septal Defect Detection

The ROC Curve of the ASD detection model on the four target echocardiographic views was illustrated in **Figure 8**. The AUC of subAS was the highest, reaching 0.8965, and the AUCs of the other three views were roughly at the same level, indicating that the model had a stronger ASD detection ability in the view of subAS. In this study, the optimal cut-point was determined by calculating the maximum value of *Youden Index*. According to the analysis of AUC curves, the optimal cut-point was 0.95. Therefore, cases that are not detected or have a confidence level lower than 0.95 were considered as negatives and cases with a confidence level greater than or equal to 0.95 were regarded as positives. **Figure 9** also showed example successful and failure cases of ASD detection. The ASD detection performances of before and after the detection refinement were compared in **Table 6**. The average values of *Accuracy*, *Recall*, *Precision*, *Specificity*, and *F1 Score* for image-level ASD detection before

**TABLE 4 |** Performance results of cardiac anatomy segmentation.

|            | Number of images | Left atrium (DSC) | Right atrium (DSC) | Mean (DSC) |
|------------|------------------|-------------------|--------------------|------------|
| A2C        | 993              | 0.8960            | 0.9089             | 0.9025     |
| A2C-V2C    | 731              | 0.8987            | 0.9239             | 0.9113     |
| A2C-LV     | 31               | 0.8908            | 0.8816             | 0.8862     |
| A2C-RV     | 430              | 0.8638            | 0.9171             | 0.8905     |
| Total/mean | 2,185            | 0.8873            | 0.9079             | 0.8976     |

A2C, image containing left and right atria only; A2C-V2C, image containing left and right atria and left and right ventricles; A2C-LV, image containing left and right atria and only left ventricle; A2C-RV, image containing left and right atria and only right ventricle.

**TABLE 5 |** Performance of U-Net with different modules.

|         | U-Net  | U-Net w/dense block | U-Net w/dual attention | Dense dual attention U-Net |
|---------|--------|---------------------|------------------------|----------------------------|
| A2C     | 0.8860 | 0.8969              | 0.8973                 | <b>0.9025</b>              |
| A2C-V2C | 0.8889 | 0.9044              | 0.9018                 | <b>0.9113</b>              |
| A2C-LV  | 0.8814 | 0.8837              | 0.8716                 | <b>0.8862</b>              |
| A2C-RV  | 0.8548 | <b>0.8932</b>       | 0.8705                 | 0.8905                     |
| Mean    | 0.8778 | 0.8945              | 0.8853                 | <b>0.8976</b>              |

A2C, image containing left and right atria only; A2C-V2C, image containing left and right atria and left and right ventricles; A2C-LV, image containing left and right atria and only left ventricle; A2C-RV, image containing left and right atria and only right ventricle.

Numbers in bold font indicate better performance in each category.

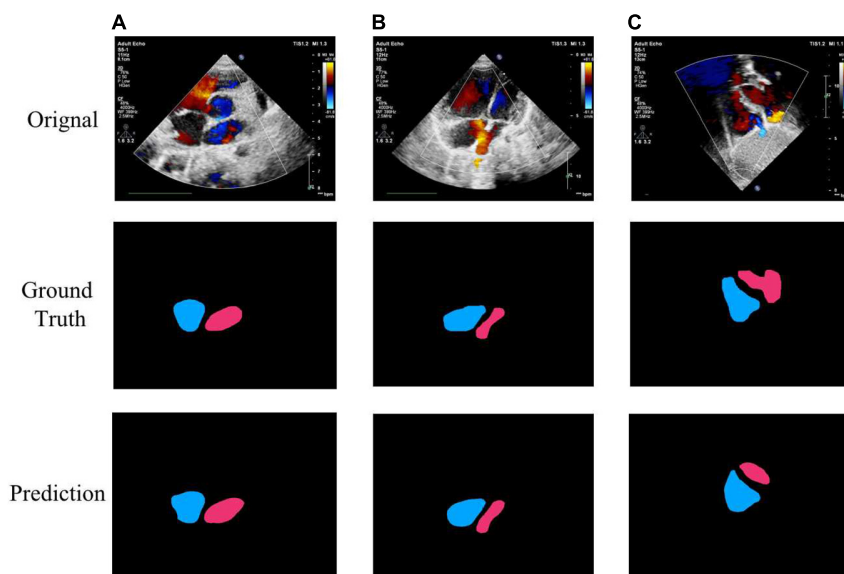


**FIGURE 7 |** Example segmentation results of cardiac anatomy. **(A)** High precision segmentation of DSC 0.9517; **(B)** medium precision segmentation of DSC 0.9115; **(C)** poor segmentation performance of DSC 0.7347.

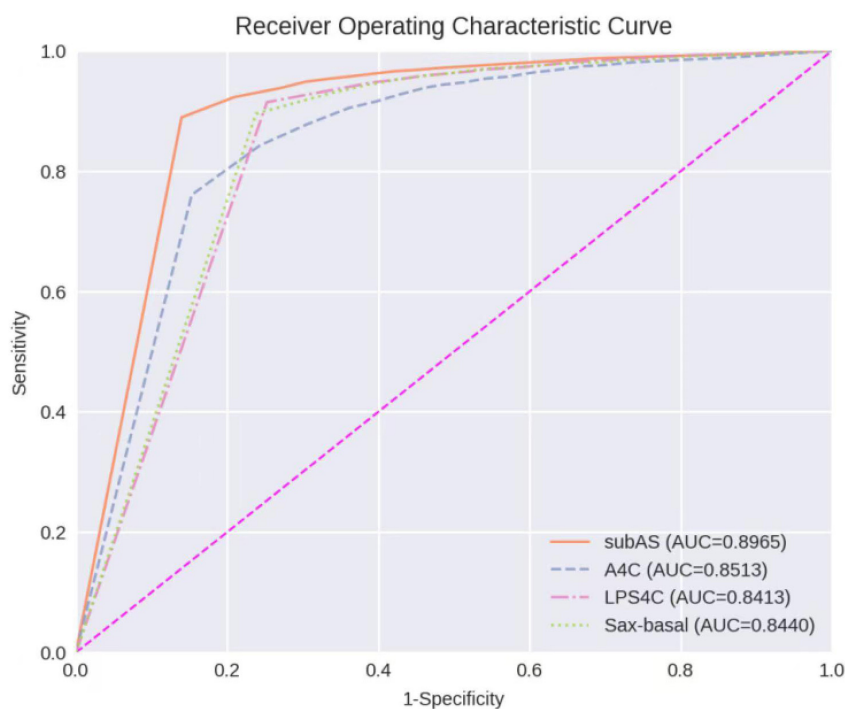


**FIGURE 8 |** Receiver operating characteristic curves of ASD detection on four target echocardiographic views.

the detection refinement were 0.8699, 0.8608, 0.8208, 0.8744, and 0.8397, respectively, while the average values of *Accuracy*, *Recall*, *Precision*, *Specificity*, and *F1 Score* for image-level ASD detection after the detection refinement were 0.8833, 0.8545, 0.8577, 0.9136, and 0.8546, respectively. It can be seen that *Accuracy*, *Precision*, *Specificity*, and *F1 Score* have increased by 1.34, 3.69, 3.92, and 1.49%, respectively, while the recall rate

has been reduced by only 0.63%. The *p*-values of the *t*-test indicated statistically significant differences in ASD detection before and after the refinement module for all performance metrics in all other views except the LPS4C view. As for view LPS4C, the differences in ASD detection before and after the refinement module were statistically significant in terms of recall, precision, and specificity, but not in terms of accuracy and F1

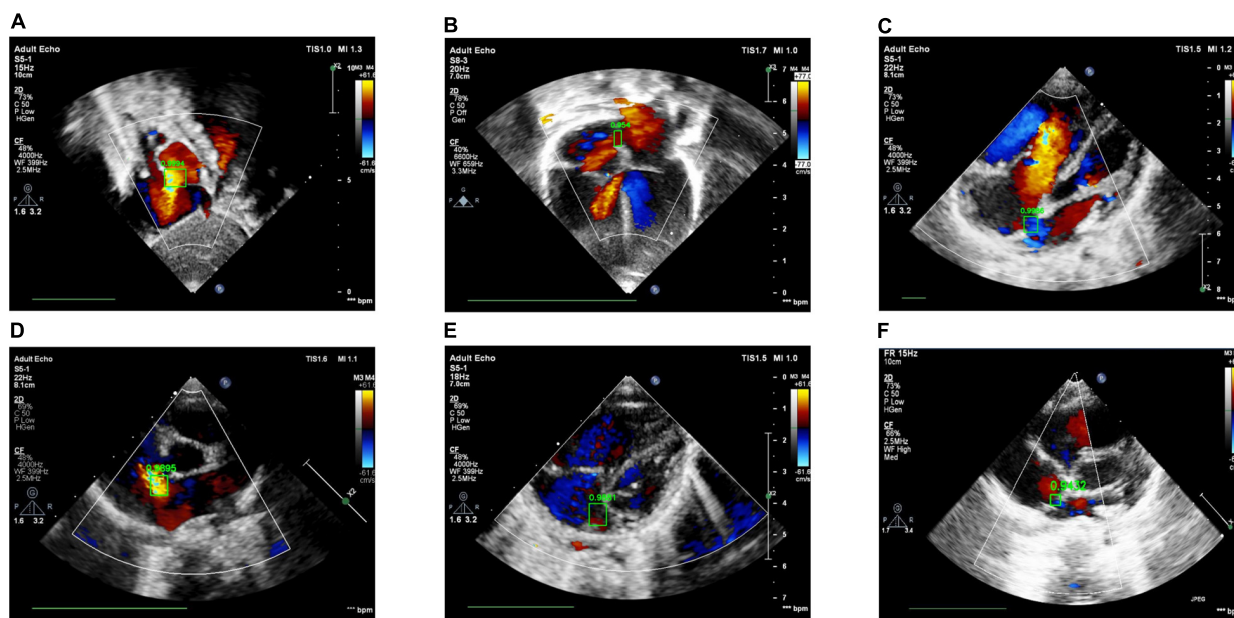


**FIGURE 9 |** Examples of success and failure cases. **(A)** ASD detected in the subAS view: bright red shows the transeptal flow with left-to-right shunt, **(B)** ASD detected in the A4C view: dark red in the center of the atrial septum indicates the occurrence of left-to-right shunt flow, **(C)** ASD detected in the LPS4C view: blue regions represent the transeptal flow with right-to-left shunt, **(D)** ASD detected in the PSAX view: bright red shows the transeptal flow with left-to-right shunt. **(E)** ASD detection of false positive, due to the confusion of similar structures and the failure of the cardiac anatomy segmentation stage; **(F)** ASD detection of true negative, due to the low confidence ( $0.9432 < 0.95$ ).

score. In addition, a preliminary case-level study has also been conducted where a threshold of 0.6 was used based on a prior from experienced physicians. As shown in **Table 6**, the average values of Accuracy, Recall, Precision, Specificity, and F1 Score for case-level ASD detection before the detection refinement were 0.9888, 0.8381, 0.8786, 0.9214, and 0.9072, respectively, while the average values of Accuracy, Recall, Precision, Specificity, and F1 Score for case-level ASD detection after the detection refinement were 0.9897, 0.9143, 0.9318, 0.9563, and 0.9505, respectively. A thorough grid-search based approach can be performed to find the optimal threshold in future studies when larger test sets are available.

## DISCUSSION

In this study, we proposed a CNN-based ASD detection system, which consists of three stages. In the first stage, four target standard views are extracted from the echocardiographic video frames. In the second stage, the cardiac anatomy and ASD candidates are obtained, separately. Finally, the third stage combines the two results of the second stage to refine and obtain the final ASD detection result. In practice, the cardiac anatomy segmentation and ASD candidate detection in the second stage can be run in parallel to meet the real-time requirements of CHD diagnosis. In our study, the floating point operations per second (FLOPs) of the ResNet-34 standard view identification module, the Dense Dual Attention U-Net, and the FCOS ASD detector were about 3.7 G, 130.28, and 219.25 G, respectively.

The proposed ASD detection system was developed using a training set of 4,031 cases containing 370,057 echocardiograms. The experimental results on an independent test set of 229 cases showed that the proposed system can accurately identify ASD in color Doppler echocardiographic images, which provides a good preparation for subsequent AI-based CHD diagnosis. Ideally, we should conduct additional ablation studies on the impact of each module on the final ASD detection. However, currently, due to the huge cost of data labeling, currently, our independent test data only has ASD labels for each image without segmentation ground truth. Therefore, we take this as one of the limitations and future work. As for the standard view identification module, since the overall accuracy of 0.9942 is high enough, the impact of failure cases of this module should be negligible.

Based on our clinical experience, small defects may close spontaneously in childhood, while large defects may cause hemodynamic abnormalities and clinical symptoms if they are not repaired in time. In addition, the hemodynamics of long-term left-to-right shunt significantly increase the possibility of late clinical complications, including functional decline, atrial arrhythmia, and pulmonary hypertension. Therefore, in this study, we have selected cases with a defect size of more than 5 mm as our research object. These cases may have abnormal hemodynamics and require surgery or transcatheter closure.

The *F1 Score* of ASD detection for images of the A4C view is relatively low compared to images of the other three views. Atrial septum is a relatively thin structure, especially in the fossa ovalis area. According to clinical expertise, subcostal, and the parasternal views are particularly useful for ASD

**TABLE 6 |** Performance results of ASD detection before vs after refinement.

| View               | Accuracy  | Recall   | Precision   | Specificity   | F1 score  |
|--------------------|---|--|---|---|---|
| subAS (95% CI)     | 0.8958 (0.8912–0.9005)/ <b>0.9030</b><br>(0.8985–0.9075) ( $p < 0.0001$ ) | <b>0.8755</b> (0.8678–0.8832)/0.8742<br>(0.8656–0.8828) ( $p < 0.0001$ ) | 0.8771 (0.8694–0.8848)/ <b>0.8909</b><br>(0.8827–0.8991) ( $p < 0.0001$ ) | 0.9106 (0.9049–0.9163)/ <b>0.9329</b><br>(0.9277–0.9381) ( $p < 0.0001$ ) | 0.8763 (0.8762–0.8764)/ <b>0.8825</b><br>(0.8824–0.8825) ( $p < 0.0001$ ) |
| A4C (95% CI)       | 0.8220 (0.8132–0.8309)/ <b>0.8500</b><br>(0.8418–0.8583) ( $p < 0.0001$ ) | <b>0.7540</b> (0.7375–0.7705)/0.7352<br>(0.7153–0.7552) ( $p < 0.0001$ ) | 0.7601 (0.7437–0.7765)/ <b>0.8461</b><br>(0.8286–0.8636) ( $p = 0.00$ )   | 0.8616 (0.8515–0.8717)/ <b>0.9388</b><br>(0.9314–0.9461) ( $p = 0.00$ )   | 0.7570 (0.7568–0.7572)/ <b>0.7868</b><br>(0.7866–0.7870) ( $p < 0.0001$ ) |
| LPS4C (95% CI)     | 0.8860 (0.8798–0.8922)/ <b>0.8990</b><br>(0.8931–0.9049) ( $p = 0.38$ )   | 0.9080 (0.8995–0.9166)/0.9080<br>(0.8984–0.9176) ( $p < 0.0001$ )        | 0.8447 (0.8344–0.8550)/ <b>0.8734</b><br>(0.8626–0.8842) ( $p < 0.0001$ ) | 0.8687 (0.8598–0.8775)/ <b>0.9020</b><br>(0.8935–0.9106) ( $p < 0.0001$ ) | 0.8752 (0.8751–0.8753)/ <b>0.8904</b><br>(0.8902–0.8905) ( $p = 0.62$ )   |
| Sax-basal (95% CI) | 0.8758 (0.8693–0.8824)/ <b>0.8813</b><br>(0.8750–0.8877) ( $p < 0.0001$ ) | <b>0.9058</b> (0.8965–0.9151)/0.9005<br>(0.8897–0.9113) ( $p = 0.0016$ ) | 0.8013 (0.7894–0.8132)/ <b>0.8203</b><br>(0.8071–0.8335) ( $p < 0.0001$ ) | 0.8567 (0.8478–0.8656)/ <b>0.8808</b><br>(0.8717–0.8898) ( $p < 0.0001$ ) | 0.8504 (0.8502–0.8505)/ <b>0.8585</b><br>(0.8584–0.8587) ( $p < 0.0001$ ) |
| Mean               | 0.8699/ <b>0.8833</b>   | <b>0.8608</b> /0.8545  | 0.8208/ <b>0.8577</b>   | 0.8744/ <b>0.9136</b>   | 0.8397/ <b>0.8546</b>   |
| Case-level         | 0.9888/ <b>0.9897</b>   | 0.8381/ <b>0.9143</b>  | 0.8786/ <b>0.9318</b>   | 0.9214/ <b>0.9563</b>   | 0.9072/ <b>0.9505</b>   |

subAS, subcostal atrium septum; A4C, apical four-chamber; LPS4C, low parasternal four-chamber. A  $p$ -value ( $p < 0.05$ ) indicates statistically significant. Numbers in bold font indicate better performance in each category.

diagnosis, because in these views, the septum is aligned almost perpendicular to the ultrasound beam. The thin area of the atrial septum and the color shunt flow can be particularly well resolved in these views. On the other hand, because the atrial septum is aligned parallel to the ultrasound beam in the A4C view, it is challenging to diagnose ASD with certainty in this view. Therefore, our experimental results are consistent with clinical practice.

Our model was trained and tested based on the Asian children. Although there is no literature evidence for differences in ASD by ethnicity, we may evaluate our model performance of different ethnic groups as one of the possible future studies. The acoustic window degenerates with age, especially in the subcostal view. It is not clear whether the proposed method can detect small ASD in adults, which will be further explored in future studies.

In our study, we found that ASD shunt blood flow was not present in every frame of the cardiac cycle due to the contraction, relaxation and torsion of the heartbeat. Image-level detection is the basis for case-level diagnosis. This research was the first attempt to identify ASD in children at the image level. A preliminary case-level study has also been conducted where a threshold of 0.6 was used based on a prior from experienced physicians. A thorough grid-search based approach can be performed to find the optimal threshold value in future studies when larger test sets are available. In addition, future research may also be to discover hidden patterns embedded in the cardiac cycle and to design case-level diagnostic models for ASD. It is well known that echocardiography cannot avoid the influence of color noise and the system performance largely depends on the quality of the original images. How to integrate the proposed system into the actual clinical diagnosis of ASD will be another direction of future research.

## DATA AVAILABILITY STATEMENT

The raw data supporting the conclusions of this article will be made available for research purposes only upon request.

## ETHICS STATEMENT

Study approval was granted by the Institutional Review Board of Shanghai Children's Medical Center (SCMCIRB-W2021058). The procedures were performed in accordance with the Declaration of Helsinki and International Ethical Guidelines for Biomedical Research Involving Human Subjects. Written informed consent to participate in this study was provided by the participants' legal guardian/next of kin.

## AUTHOR CONTRIBUTIONS

WH, YZ, XL, and YY: conception and design. YZ, YY, and LiZ: administrative support. WH, LW, and LC: provision of study materials or patients, and collection and assembly of data. QS, XL, WH, and YY: data analysis and interpretation. All authors wrote and final approval of manuscript.

## FUNDING

This work was supported by the Zhejiang Provincial Key Research and Development Program (No. 2020C03073), Science and Technology Innovation – Biomedical Supporting

Program of Shanghai Science and Technology Committee (19441904400), and Program for Artificial Intelligence Innovation and Development of Shanghai Municipal Commission of Economy and Informatization (2020-RGZN-02048).

## REFERENCES

- Zhao QM, Liu F, Wu L, Ma XJ, Niu C, Huang GY. Prevalence of congenital heart disease at live birth in China. *J Pediatr*. (2019) 204:53–8. doi: 10.1016/j.jpeds.2018.08.040
- Bradley EA, Zaidi AN. Atrial septal defect. *Cardiol Clin*. (2020) 38:317–24. doi: 10.1016/j.ccl.2020.04.001
- Liu F, Zhou Z, Samsonov A, Blankenbaker D, Larison W, Kanarek A, et al. Deep learning approach for evaluating knee MR images: achieving high diagnostic performance for cartilage lesion detection. *Radiology*. (2018) 289:160–9. doi: 10.1148/radiol.2018172986
- Ma J, Wu F, Jiang T, Zhu J, Kong D. Cascade convolutional neural networks for automatic detection of thyroid nodules in ultrasound images. *Med Phys*. (2017) 44:1678–91. doi: 10.1002/mp.12134
- Cao Z, Duan L, Yang G, Yue T, Chen Q. An experimental study on breast lesion detection and classification from ultrasound images using deep learning architectures. *BMC Med Imaging*. (2019) 19:51. doi: 10.1186/s12880-019-0349-x
- Chu LC, Park S, Kawamoto S, Wang Y, Zhou Y, Shen W, et al. Application of deep learning to pancreatic cancer detection: lessons learned from our initial experience. *J Am Coll Radiol*. (2019) 16(9 Pt B):1338–42. doi: 10.1016/j.jacr.2019.05.034
- Seo H, Huang C, Bassenne M, Xiao R, Xing L. Modified U-net (mU-Net) with incorporation of object-dependent high level features for improved liver and liver-tumor segmentation in CT images. *IEEE Trans Med Imaging*. (2020) 39:1316–25. doi: 10.1109/TMI.2019.2948320
- Jin Q, Meng Z, Sun C, Cui H, Su R. RA-UNet: a hybrid deep attention-aware network to extract liver and tumor in CT scans. *Front Bioeng Biotechnol*. (2020) 23:605132. doi: 10.3389/fbioe.2020.605132
- Yahyatabar M, Jouvett P, Cheriet F. Dense-Unet: a light model for lung fields segmentation in chest X-ray images. *Annu Int Conf IEEE Eng Med Biol Soc*. (2020) 2020:1242–5. doi: 10.1109/EMBC44109.2020.9176033
- Meng Z, Fan Z, Zhao Z, Su F. ENS-Unet: end-to-end noise suppression U-net for brain tumor segmentation. *Annu Int Conf IEEE Eng Med Biol Soc*. (2018) 2018:5886–9. doi: 10.1109/EMBC.2018.8513676
- Yang T, Zhou Y, Li L, Zhu C. DCU-net: multi-scale U-net for brain tumor segmentation. *J Xray Sci Technol*. (2020) 28:709–26. doi: 10.3233/XST-200650
- Aldoj N, Biavati F, Michallek F, Stober S, Dewey M. Automatic prostate and prostate zones segmentation of magnetic resonance images using denseNet-like U-net. *Sci Rep*. (2020) 10:14315. doi: 10.1038/s41598-020-71080-0
- Machireddy A, Meermeier N, Coakley F, Song X. Malignancy detection in prostate multi-parametric MR images using U-net with attention. *Annu Int Conf IEEE Eng Med Biol Soc*. (2020) 2020:1520–3. doi: 10.1109/EMBC44109.2020.9176050
- Li H, Fang J, Liu S, Liang X, Yang X, Mai Z, et al. CR-Unet: a composite network for ovary and follicle segmentation in ultrasound images. *IEEE J Biomed Health Inform*. (2020) 24:974–83. doi: 10.1109/JBHI.2019.2946092
- Ashkani Chenarlogh V, Ghelich Oghli M, Shabanzadeh A, Sirjani N, Akhavan A, Shiri I, et al. Fast and accurate U-net model for fetal ultrasound image segmentation. *Ultrasound Imaging*. (2022) 6:1617346211069882. doi: 10.1177/01617346211069882
- Amiri M, Brooks R, Behboodi B, Rivaz H. Two-stage ultrasound image segmentation using U-net and test time augmentation. *Int J Comput Assist Radiol Surg*. (2020) 15:981–8. doi: 10.1007/s11548-020-02158-3
- Thompson WR, Reinisch AJ, Unterberger MJ, Schriebl AJ. Artificial intelligence-assisted auscultation of heart murmurs: validation by virtual clinical trial. *Pediatr Cardiol*. (2019) 40:623–9. doi: 10.1007/s00246-018-2036-z
- Sudarshan V, Acharya UR, Ng EY, Meng CS, Tan RS, Ghista DN. Automated identification of infarcted myocardium tissue characterization using ultrasound images: a review. *IEEE Rev Biomed Eng*. (2015) 8:86–97. doi: 10.1109/RBME.2014.2319854
- Kusunose K, Abe T, Haga A, Fukuda D, Yamada H, Harada M, et al. A deep learning approach for assessment of regional wall motion abnormality from echocardiographic images. *JACC Cardiovasc Imaging*. (2020) 13(2 Pt 1):374–81. doi: 10.1016/j.jcmg.2019.02.024
- Kusunose K, Haga A, Yamaguchi N, Abe T, Fukuda D, Yamada H, et al. Deep learning for assessment of left ventricular ejection fraction from echocardiographic images. *J Am Soc Echocardiogr*. (2020) 33:632–5.e1. doi: 10.1016/j.echo.2020.01.009
- Yu L, Guo Y, Wang Y, Yu J, Chen P. Segmentation of fetal left ventricle in echocardiographic sequences based on dynamic convolutional neural networks. *IEEE Trans Biomed Eng*. (2017) 64:1886–95. doi: 10.1109/TBME.2016.2628401
- Taheri Dezaki F, Liao Z, Luong C, Girgis H, Dhungel N, Abdi AH, et al. Cardiac phase detection in echocardiograms with densely gated recurrent neural networks and global extrema loss. *IEEE Trans Med Imaging*. (2019) 38:1821–32. doi: 10.1109/TMI.2018.2888807
- Jafari MH, Girgis H, Van Woudenberg N, Liao Z, Rohling R, Gin K, et al. Automatic biplane left ventricular ejection fraction estimation with mobile point-of-care ultrasound using multi-task learning and adversarial training. *Int J Comput Assist Radiol Surg*. (2019) 14:1027–37. doi: 10.1007/s11548-019-01954-w
- Baumgartner CF, Kamnitsas K, Matthew J, Fletcher TP, Smith S, Koch LM, et al. SonoNet: real-time detection and localisation of fetal standard scan planes in freehand ultrasound. *IEEE Trans Med Imaging*. (2017) 36:2204–15. doi: 10.1109/TMI.2017.2712367
- Sridar P, Kumar A, Quinton A, Nanan R, Kim J, Krishnakumar R. Decision fusion-based fetal ultrasound image plane classification using convolutional neural networks. *Ultrasound Med Biol*. (2019) 45:1259–73. doi: 10.1016/j.ultrasmedbio.2018.11.016
- Madani A, Arnaout R, Mofrad M, Arnaout R. Fast and accurate view classification of echocardiograms using deep learning. *NPJ Digit Med*. (2018) 1:6. doi: 10.1038/s41746-017-0013-1
- Howard JP, Tan J, Shun-Shin MJ, Mahdi D, Nowbar AN, Arnold AD, et al. Improving ultrasound video classification: an evaluation of novel deep learning methods in echocardiography. *J Med Artif Intell*. (2020) 25:4. doi: 10.21037/jmai.2019.10.03
- Østvik A, Smistad E, Aase SA, Haugen BO, Lovstakken L. Real-time standard view classification in transthoracic echocardiography using convolutional neural networks. *Ultrasound Med Biol*. (2019) 45:374–84. doi: 10.1016/j.ultrasmedbio.2018.07.024
- Zhang J, Gajjala S, Agrawal P, Tison GH, Hallock LA, Beussink N, et al. Fully automated echocardiogram interpretation in clinical practice. *Circulation*. (2018) 138:1623–35. doi: 10.1161/CIRCULATIONAHA.118.034338
- Lopez L, Colan SD, Frommelt PC, Ensing GJ, Kendall K, Younoszai AK, et al. Recommendations for quantification methods during the performance of a pediatric echocardiogram: a report from the pediatric measurements writing group of the American society of echocardiography pediatric and congenital heart disease council. *J Am Soc Echocardiogr*. (2010) 23:465–95; quiz 576–7. doi: 10.1016/j.echo.2010.03.019
- Wu L, Dong B, Liu X, Hong W, Chen L, Gao K, et al. Standard echocardiographic view recognition in diagnosis of congenital heart defects in children using deep learning based on knowledge distillation. *Front Pediatr*. (2022) 9:770182. doi: 10.3389/fped.2021.770182
- Passalis N, Tzelepi M, Tefas A. Probabilistic knowledge transfer for lightweight deep representation learning. *IEEE Trans Neural Netw Learn Syst*. (2021) 32:2030–9. doi: 10.1109/TNNLS.2020.2995884
- He K, Zhang X, Ren S, Sun J. Deep residual learning for image recognition. In: *Proceedings of the 2016 IEEE Conference on Computer Vision and Pattern*

- Recognition (CVPR)*. Las Vegas, NV (2016). p. 770–8. doi: 10.1109/CVPR.2016.90
34. Zhang H, Wu C, Zhang Z, Zhu Y, Zhang Z, Lin H, et al. Resnest: split-attention networks. *arXiv [Preprint]*. (2020). arXiv:2004.08955. doi: 10.3390/s21134612
  35. Ronneberger O, Philipp F, Thomas B. U-net: convolutional networks for biomedical image segmentation. In: *Proceedings of the International Conference on Medical Image Computing and Computer-Assisted Intervention (MICCAI)*. Munich (2015). p. 234–41. doi: 10.1007/978-3-319-24574-4\_28
  36. Huang G, Liu Z, Van Der Maaten L, Weinberger K. Densely connected convolutional networks. In: *Proceedings of the 2017 IEEE Conference on Computer Vision and Pattern Recognition (CVPR)*. Honolulu, HI (2017). p. 4700–8. doi: 10.1109/CVPR.2017.243
  37. Fu J, Liu J, Jiang J, Li Y, Bao Y, Lu H. Scene segmentation with dual relation-aware attention network. *IEEE Trans Neural Netw Learn Syst*. (2021) 32:2547–60. doi: 10.1109/TNNLS.2020.3006524
  38. Tian Z, Shen C, Chen H, He T. FCOS: a simple and strong anchor-free object detector. *IEEE Trans Pattern Anal Mach Intell*. (2020) 19:1922–33. doi: 10.1109/TPAMI.2020.3032166
  39. Lin T, Dollár P, Girshick R, He K, Hariharan B, Belongie S. Feature pyramid networks for object detection. In: *Proceedings of the 2017 IEEE Conference on Computer Vision and Pattern Recognition (CVPR)*. Honolulu, HI (2017). p. 936–44. doi: 10.1109/CVPR.2017.106
- Conflict of Interest:** The authors declare that the research was conducted in the absence of any commercial or financial relationships that could be construed as a potential conflict of interest.
- Publisher's Note:** All claims expressed in this article are solely those of the authors and do not necessarily represent those of their affiliated organizations, or those of the publisher, the editors and the reviewers. Any product that may be evaluated in this article, or claim that may be made by its manufacturer, is not guaranteed or endorsed by the publisher.

Copyright © 2022 Hong, Sheng, Dong, Wu, Chen, Zhao, Liu, Zhu, Liu, Xie, Yu, Wang, Yuan, Ge, Zhao, Liu and Zhang. This is an open-access article distributed under the terms of the Creative Commons Attribution License (CC BY). The use, distribution or reproduction in other forums is permitted, provided the original author(s) and the copyright owner(s) are credited and that the original publication in this journal is cited, in accordance with accepted academic practice. No use, distribution or reproduction is permitted which does not comply with these terms.



# Imaging Assessment of Endothelial Function: An Index of Cardiovascular Health

Anum S. Minhas<sup>1,2</sup>, Erin Goerlich<sup>1</sup>, Mary C. Corretti<sup>1</sup>, Armin Arbab-Zadeh<sup>1</sup>, Sebastian Kelle<sup>3</sup>, Thorsten Leucker<sup>1</sup>, Amir Lerman<sup>4</sup> and Allison G. Hays<sup>1\*</sup>

<sup>1</sup> Division of Cardiology, Department of Medicine, The Johns Hopkins University School of Medicine, Baltimore, MD, United States, <sup>2</sup> Department of Epidemiology, Johns Hopkins Bloomberg School of Public Health, Baltimore, MD, United States, <sup>3</sup> Department of Internal Medicine and Cardiology, German Heart Center Berlin, Berlin, Germany, <sup>4</sup> Division of Ischemic Heart Disease and Critical Care, Department of Cardiovascular Medicine, Mayo Clinic, Rochester, MN, United States

## OPEN ACCESS

### Edited by:

Luis Lopes,  
University College London,  
United Kingdom

### Reviewed by:

Konstantin V. Zavadovsky,  
Cardiology Research Institute, Tomsk  
National Research Medical Center  
(RAS), Russia  
Miguel Mota Carmo,  
NOVA Medical School, Portugal

### \*Correspondence:

Allison G. Hays  
ahays2@jhmi.edu

### Specialty section:

This article was submitted to  
Cardiovascular Imaging,  
a section of the journal  
Frontiers in Cardiovascular Medicine

**Received:** 17 September 2021

**Accepted:** 28 February 2022

**Published:** 15 April 2022

### Citation:

Minhas AS, Goerlich E,  
Corretti MC, Arbab-Zadeh A, Kelle S,  
Leucker T, Lerman A and Hays AG  
(2022) Imaging Assessment  
of Endothelial Function: An Index  
of Cardiovascular Health.  
Front. Cardiovasc. Med. 9:778762.  
doi: 10.3389/fcvm.2022.778762

Endothelial dysfunction is a key early mechanism in a variety of cardiovascular diseases and can be observed in larger conduit arteries as well as smaller resistance vessels (microvascular dysfunction). The presence of endothelial dysfunction is a strong prognosticator for cardiovascular events and mortality, and assessment of endothelial function can aid in selecting therapies and testing their response. While the gold standard method of measuring coronary endothelial function remains invasive angiography, several non-invasive imaging techniques have emerged for investigating both coronary and peripheral endothelial function. In this review, we will explore and summarize the current invasive and non-invasive modalities available for endothelial function assessment for clinical and research use, and discuss the strengths, limitations and future applications of each technique.

**Keywords:** coronary MRI, endothelial function, CAD, CMR, vascular disease

## INTRODUCTION

Despite declines in cardiovascular disease (CVD) mortality rates over the past few decades, CVD still remains the leading cause of morbidity and mortality in the United States (1). Endothelial dysfunction contributes to atherosclerosis development and progression, which may ultimately lead to plaque rupture and cardiovascular events. Although the vascular endothelium serves many important functions including maintaining vasomotor tone and barrier functions, the most readily detectable means to define endothelial pathology or dysfunction in humans is by quantifying vasomotor responses to endothelial dependent stressors. The development in recent years of imaging strategies to measure endothelial function of the coronary and peripheral vessels has provided insights into important contributors of coronary artery disease (CAD) and the vascular response to therapeutic intervention. In this review, we will briefly examine mechanisms relating endothelial function and atherosclerosis, review imaging strategies, both invasive and non-invasive, to quantify endothelial function of the coronary and peripheral circulation, and discuss recent insights from human endothelial function studies.

## OVERVIEW: THE VASCULAR ENDOTHELIUM

Dysfunction of the vascular endothelium is increasingly recognized as serving a prominent role in CVD pathology. The endothelium regulates vascular tone, smooth muscle cell proliferation,

thrombosis, and leukocyte adhesion and platelet aggregation (2). Endothelial dysfunction, or alteration in normal function, often precedes the development of anatomic atherosclerotic disease progression and clinical manifestation. Examination of endothelial function can enhance risk stratification, improve early detection of disease and be used to assess the vascular response to therapeutic intervention (3).

Healthy endothelial cells respond to local and systemic factors by producing and releasing vasoactive molecules to maintain vascular tone, a balance between vasodilation and vasoconstriction (4). A defining feature of endothelium-dependent relaxation is the release of nitric oxide (NO), which diffuses to vascular smooth muscle cells and results in cGMP-mediated vasodilation (4). NO is released in response to a variety of signals, such as adenosine, serotonin, catecholamines, ischemia, and shear stress (5). Conversely, systemic inflammation and increased reactive oxygen species (ROS) tend to counter the effects of NO, and can result in chronic endothelial dysfunction (6). Cardiovascular risk factors such as hyperlipidemia, hypertension, and diabetes may result in dysregulation of endothelial nitric oxide synthase (eNOS) and ROS (7), leading to endothelial dysfunction, one of the earliest steps in the atherosclerotic disease process (8). Although dysfunctional endothelium is characterized by increased vascular inflammation, permeability and thrombosis, it is impaired vasodilation in response to stressors that increase NO that is the most readily measurable response in humans and detectable by imaging.

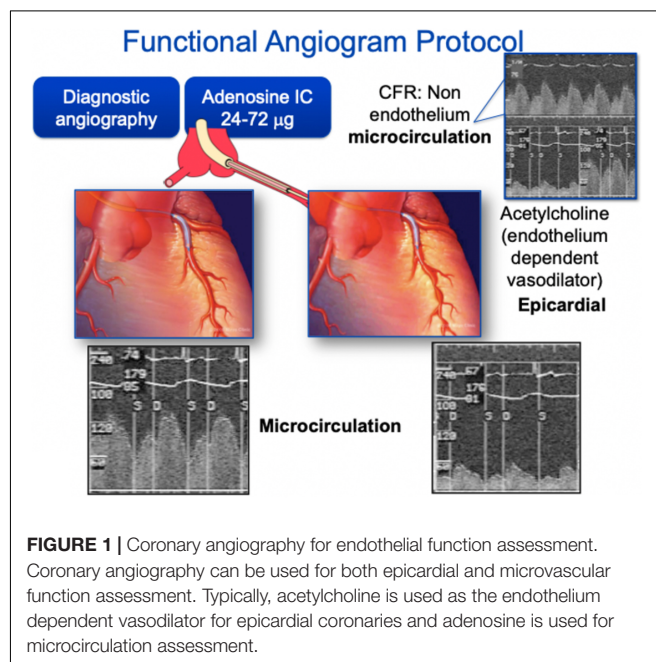
In the peripheral conduit vessels, endothelial function is typically evaluated in the brachial artery due to its accessibility, and measures can be performed invasively (forearm plethysmography) or non-invasively (brachial ultrasound for flow mediated dilation) by evaluating the vasomotor response to endothelial dependent stressors (9). Measuring endothelial function of the coronary arteries is more challenging but important as the clinical impact of coronary endothelial dysfunction is greater than other vascular beds. Coronary endothelial function (CEF) is typically examined through invasive measures during coronary angiography. Coronary arteries are prone to atherosclerosis and studying CEF provides new information about the heterogeneity of endothelial function and contributors to plaque formation in patients with, or at risk for coronary artery disease. However, the invasive measurement of CEF carries procedural risk and preclude studies in lower risk patients over time. Newer non-invasive measures of CEF including with magnetic resonance imaging (MRI) and positron emission tomography (PET) promise new insights into the pathophysiology of CVD in low risk and other populations not undergoing invasive angiography and can assess response to therapy. Finally, microcirculatory assessment of smaller vessels, comprised of pre-arterioles, arterioles, capillaries and venules, investigates endothelial function in vascular resistance, which mediates blood pressure and blood flow. The measure of endothelial function of the larger (conduit) or smaller (microvessels) provides important and complementary information which can

help gauge CV risk and provide prognostic information for patients (10).

## TECHNIQUES TO MEASURE ENDOTHELIAL FUNCTION IN HUMANS: INVASIVE CORONARY ENDOTHELIAL FUNCTION ASSESSMENT

The measurement of human endothelial function primarily focuses on vasoreactivity testing, as this is the most clinically demonstrable function of the vascular endothelium (11). Coronary endothelial dysfunction predicts cardiovascular events and remains the most important vascular bed studied in vasoreactivity (10, 12, 13). The gold standard for coronary endothelial functional assessment is via invasive quantitative angiography to detect luminal changes in response to vasoactive stimuli, either pharmacologic or physiologic, that increase the endothelial release of NO (**Figure 1**) (14, 15).

Coronary angiography for epicardial arterial dimension measurement is often performed with intracoronary infusion of acetylcholine. Acetylcholine is an endothelial-dependent vasodilator that is suitable for intracoronary infusion and is the most commonly used drug for the purposes of invasive vasomotor testing. Healthy endothelium should result in coronary arterial vasodilation and increased blood flow (by > 50%) in response to low dose acetylcholine, while dysfunctional endothelium may lead to diminished blood flow response and even to paradoxical vasoconstriction. At higher doses, acetylcholine can result in constriction of small arteries via direct effect on smooth muscle cells, and may be used to evaluate microvascular function (16). Less commonly, other agents used in endothelial-dependent vasomotor testing have



included bradykinin, papaverine and Substance P (17). In addition, adenosine has partial endothelial dependent effects (18). These vasoactive agents act on coronary microvasculature through vasodilation and increased flow, resulting in NO release and proximal coronary artery vasodilation, or flow-mediated dilation (FMD) (19, 20), permitting the study of epicardial endothelial function.

Coronary microvascular function can be studied invasively by measuring coronary blood flow changes and thereby coronary flow reserve using a Doppler wire. Generally, this is accomplished by placement of a Doppler-tipped guide wire into the coronary artery of interest, whereby continuous blood flow velocity is measured both at baseline and during intracoronary infusion of vasoactive substances (acetylcholine, adenosine, or papaverine) through the guiding catheter (17, 21, 22).

Further, invasive CEF assessment can also be performed by cold pressor testing (CPT) or exercise testing, both endothelial-dependent stressors (23). Exercise stress testing can be performed while supine using a bicycle ergometer with concurrent hemodynamic monitoring (24). Healthy coronary arteries dilate in response to these stressors, while paradoxical vasoconstriction occurs in diseased coronary arteries, suggesting underlying endothelial dysfunction.

Endothelial dysfunction diagnosed by invasive methods has been reported in several cardiometabolic disease states and is associated with future atherosclerosis and other adverse outcomes (13, 25–27). These techniques have also been used in the assessment of endothelial dysfunction reversal with treatment therapies (28). The advantages of catheter-based methods of coronary endothelial assessment include the precision and accuracy of results obtained using this gold standard of testing, particularly in comparison to techniques that rely on surrogate measures of coronary arterial function (17). With this approach, however, come the limitations of an invasive procedure with intra-arterial injection of vasoactive medications that can have systemic adverse effects, along with exposure to radiation and contrast. Given these risks, repeat evaluation is often not performed. Invasive techniques are therefore largely limited to patients undergoing coronary angiography for clinical reasons. Additionally, in patients with CAD, vessel area measurements may be limited in coronary segments with atherosclerosis.

## NON-INVASIVE EVALUATION OF EPICARDIAL CORONARY ENDOTHELIAL FUNCTION

### Magnetic Resonance Imaging for Assessment of Coronary Endothelial Function

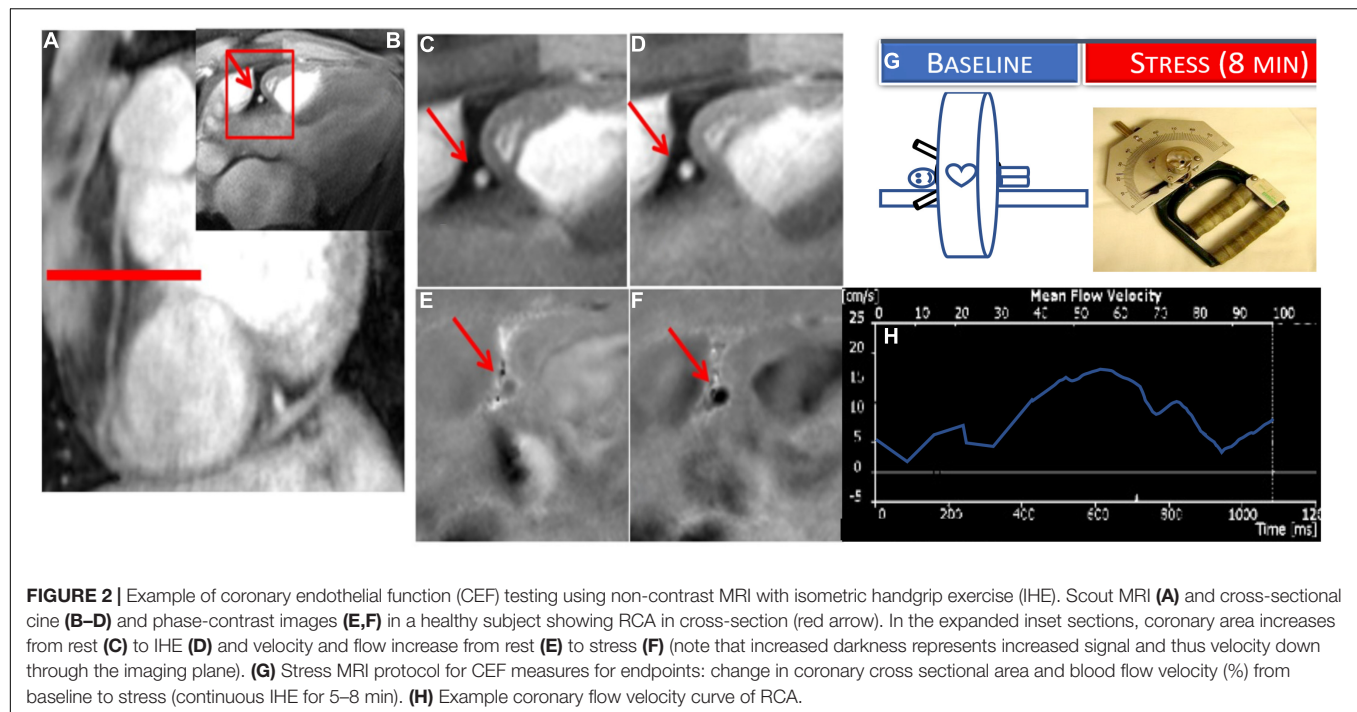
Magnetic resonance imaging provides a reproducible and safe means to measure CEF non-invasively without contrast and with high spatial resolution. In addition, MRI offers the ability to quantify coronary blood flow velocity and determine blood flow, important in the assessment of microvascular endothelial vasoreactivity, as well as measures of vessel wall remodeling,

important in the detection of early atherosclerosis. MR measures of coronary area and blood flow velocity have been validated and compared to invasive measures using quantitative coronary angiography with Doppler techniques in response to stress (29–31). However, MRI has not been exploited to investigate coronary endothelial-dependent vasomotor responses in healthy and diseased states until more recently.

To measure CEF non-invasively, coronary MRI has been combined with isometric handgrip exercise (IHE), a known endothelial-dependent stressor to quantify IHE-induced coronary cross sectional area and blood flow change as quantitative measures of CEF (32). Using these MRI-IHE methods, initial studies showed impaired CEF in patients with CAD (32, 33) and separately in people living with HIV compared to risk factor matched control participants (34–36). MR images were taken perpendicular to a proximal or middle straight segment of the coronary artery best identified on scout images (**Figure 2**) and all quantifications were performed during a period of least cardiac motion as previously described (32, 37, 38). Both anatomical (cross sectional area) and velocity-encoded (for coronary velocity and flow) images were quantified at baseline and during approximately 5 min of continuous isometric handgrip exercise while under direct supervision to ensure compliance. In addition, endothelial independent coronary vasoreactivity was assessed in a subset of healthy volunteers and CAD patients who additionally received sublingual nitroglycerin, and imaging was repeated (32). Moreover, the degree of coronary artery luminal stenosis in a given CAD patient was compared to local CEF within the same segment. In this initial study, normal, physiologic coronary vasodilation and increased coronary velocity and blood flow were observed in healthy subjects in response to handgrip, but not in CAD patients. Nitroglycerin, an endothelial-independent stressor induced normal vasodilation in patients with CAD, indicating preservation of vascular smooth muscle relaxation in the same segments where endothelial function was abnormal (32). Importantly, local CEF was more severely impaired in areas with significant luminal stenosis and early coronary wall thickening than that in minimally diseased vessels (32, 33). Furthermore, reproducibility (including intra-interobserver and interscan) on the same day and over time (8 weeks) was robust, important for designing future intervention studies using this technique (32, 39). Therefore, these MRI methods to non-invasively and reproducibly characterize CEF provide an opportunity to allow the monitoring of interventions aimed at an early stage of coronary disease. The main limitation of the technique is lack of widespread availability and that the 2D approach does not permit CEF measurements of the entire coronary tree. Finally, because the protocol involves serial breath holds, the study may be difficult in sicker patients with respiratory problems.

### Vascular Insights of Coronary Endothelial Function Studies

Important for any new study measuring endothelial function is to demonstrate that the vasoreactive response being measured



truly reflects NO-mediated endothelial function. The normal coronary vasoreactive response to IHE detected by MRI was quantified before and during the infusion of the NO synthase inhibitor, NG-monomethyl-L-arginine (L-NMMA), to determine if the coronary response to IHE is NO-mediated, the defining feature of endothelial function (39). In this study, L-NMMA infusion blocked the normal coronary vasodilatory response and coronary blood flow increase with IHE in healthy participants, demonstrating that IHE is a primarily NO-dependent endothelial coronary stressor that can be combined with MRI to measure CEF. In addition, similar approaches were employed to quantify endothelial function of the internal mammary artery (IMA), a systemic vessel that rarely develops atherosclerosis, is often used as a coronary artery bypass graft, and has been previously used to study systemic endothelial function (38). These initial studies showed that the IMA response to IHE was NO-dependent and reproducible, was impaired in patients with CAD compared to healthy subjects and differed from the endothelial response of the coronary arteries in a given patient. In summary, MRI promises a non-invasive assessment of coronary vascular health that can be safely applied to low- and medium risk populations without the risks of invasive angiography.

## POSITRON EMISSION TOMOGRAPHY/COMPUTED TOMOGRAPHY FOR ASSESSMENT OF CORONARY ENDOTHELIAL FUNCTION

Nuclear imaging methods can be used to evaluate myocardial blood flow and response to endothelial-dependent stressors.

PET can be used to estimate coronary flow reserve and myocardial regional perfusion using intravenously injected tracers ( $^{15}\text{O}$ xygen-labeled water,  $^{13}\text{N}$ itrogen-ammonia, and  $^{82}\text{Rb}$ idium), and studies have revealed abnormalities in endothelial function prior to visible atherosclerosis on angiography (40, 41). These techniques have been successfully combined with CPT to assess CEF. CPT protocols typically involve immersion of the subject's hand or foot into an ice bath at  $2^{\circ}\text{C}$  for at least 1 min prior to radioactive tracer injection and PET scan (42). CPT functions to increase myocardial oxygen demand via sympathetic activation, which should cause vasodilation and an endothelial-dependent increase in coronary blood flow in healthy subjects (43). Using these principles, cardiac PET during CPT has been shown to reflect epicardial vasomotor dysfunction in subjects at high risk for CAD (44). Abnormalities in myocardial blood flow on PET, regardless of concurrent CAD, appear to confer an increased relative risk of death and heart failure (42, 45). It is important to recognize that myocardial blood flow is affected by epicardial coronary vasomotor tone and microvascular function, making it challenging by PET imaging alone to determine whether changes in flow are related to conduit or resistance vessels (41).

The addition of computed tomography (CT) to PET can further enhance the sensitivity for atherosclerosis detection (46). A hybrid PET/CT approach has the ability to quantify changes in coronary cross-sectional area in response to stress, global, and relative myocardial perfusion, left ventricular functional performance, and coronary calcium score. This non-invasive tool for assessing coronary vascular health may represent a clinically relevant evaluation that can be performed in early disease or to predict downstream risk, however, its use has been primarily research-related (47).

# NON-INVASIVE EVALUATION OF MYOCARDIAL BLOOD FLOW RESERVE AS A MEASURE OF CORONARY MICROVASCULAR FUNCTION

## Positron Emission Tomography

Among the currently available non-invasive methods for measuring myocardial blood flow and myocardial flow reserve with stress, PET is the most well studied and validated test (48). Images are obtained at rest and vasodilator-induced stress following injection of a radiotracer. Post-processing of images is then performed to quantify regional and global myocardial blood flow (ml/min/g of myocardium) (45, 49). Myocardial flow reserve (MFR) is calculated as the ratio of stress to rest myocardial blood flow (MBF). MBF is affected by myocardial oxygen demand, contractility, heart rate, blood pressure and preload, resulting in a reported resting MBF ranging from 0.4 to 1.4 ml/g/min (50). Typically,  $MFR < 2.0$  is considered abnormal and consistent with microvascular dysfunction in the absence of significance epicardial disease as changes in MFR can be due to epicardial and/or microvascular changes in blood flow (50). A representative image is provided showing rest and stress images with PET in a patient with microvascular dysfunction and no CAD on invasive angiography (**Figure 3**).

Multiple studies have evaluated the prognostic implications of MFR by PET. Studies have demonstrated that dysfunction

seen on PET can identify individuals at high risk for major adverse cardiac events and cardiovascular death in those with and without obstructive CAD (51–53). Moreover, PET has been shown to reclassify risk in about one third of patients when compared to only traditional cardiovascular risk factors (54). The benefits of PET in prognosticating cardiac death may be particularly evident in specific groups such as those with cardiometabolic diseases (55, 56). Notably, abnormal MFR on PET has also been shown to be predictive of hospitalizations for heart failure in patients with heart failure with preserved ejection fraction (57). Despite several studies enhancing risk assessment using PET, there are limited studies using PET measures to evaluate therapeutic interventions and response, likely due to concerns about radiation exposure. Prior studies using PET imaging have examined the therapeutic response to statins and bariatric surgery (45, 58, 59).

Ultimately, the advantages of dynamic PET myocardial imaging include validation by microsphere blood flow studies in preclinical animal models and human studies (60, 61). PET also offers better spatial resolution and lower radiation exposure compared to single-photon-emission-computed-tomography (SPECT) perfusion (60). However, PET imaging is associated with high cost, limited radiotracer availability and advanced equipment, which can be a limitation to routine and widespread use.

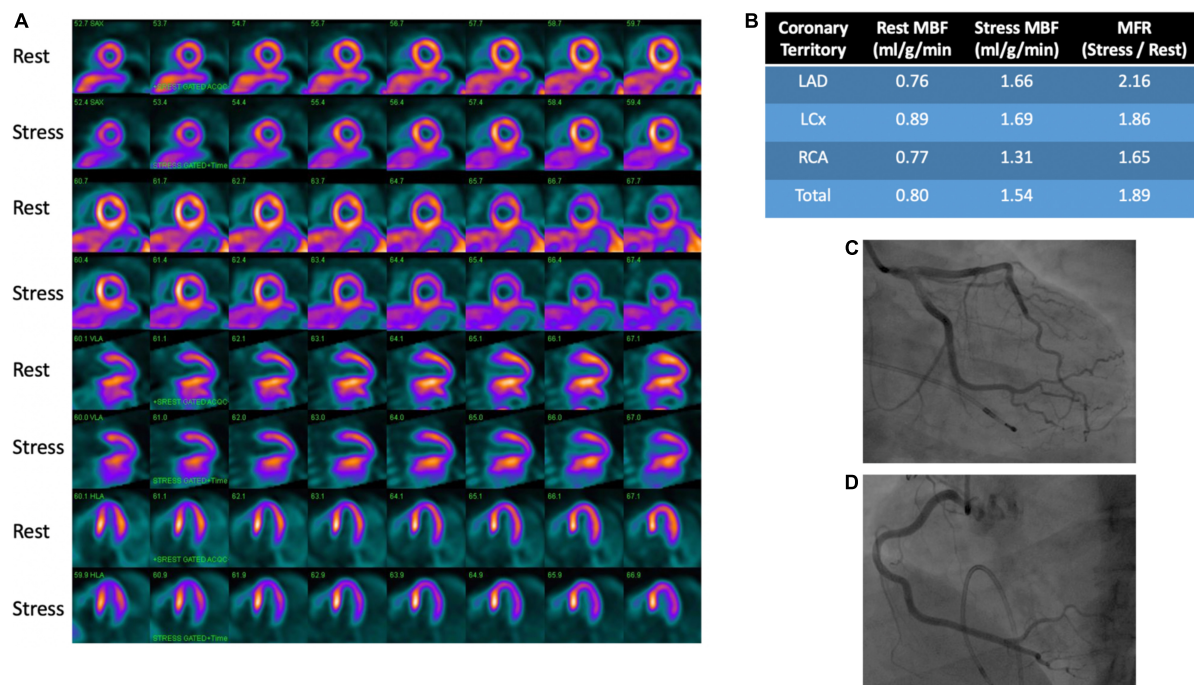


**FIGURE 3 |** PET rest/stress images and coronary angiography in a patient with microvascular dysfunction. **(A)** Perfusion images demonstrate no evidence of stress (regadenoson)-induced myocardial ischemia. **(B)** Provides quantitative myocardial perfusion analysis with an overall reduced coronary flow reserve of 1.89, indicative of mild diffuse microvascular disease. The functional analysis for this patient showed normal wall motion. No obstructive coronary artery disease was seen on angiography of the left anterior descending **(C)**, left circumflex **(C)** and right coronary **(D)** arteries.

## CARDIOVASCULAR MAGNETIC RESONANCE PERFUSION IMAGING

Non-invasive assessment of impaired myocardial blood flow, which contributes to ischemia in patients with CAD and cardiomyopathy, can be performed using stress perfusion cardiovascular magnetic resonance (CMR), which may be especially helpful for serial examinations evaluating treatment success (62). Stress perfusion CMR, distinct from coronary vasoreactivity approaches mentioned above, typically uses vasodilator stress (i.e., adenosine) to detect macrovascular (i.e., coronary stenosis) and microvascular differences in myocardial blood flow in response to stress. Recently, studies have employed fully quantitative stress myocardial perfusion techniques in patients with no obstructive CAD and detected reduced myocardial perfusion reserve, not explained by cardiac hypertrophy or fibrosis (63). The ability of CMR to study ventricular function/structure and fibrosis make it well-suited to be used in combination with stress perfusion techniques, especially in patients with left ventricular hypertrophy.

Stress perfusion CMR techniques have also been employed to evaluate patients at risk for microvascular dysfunction. Clinical guidelines have recently added microvascular dysfunction to epicardial stenosis and epicardial coronary spasm as one of the mechanisms of myocardial ischemia in patients with CAD (64). One study used stress CMR techniques and showed that myocardial perfusion reserve index was impaired in women with no obstructive CAD on coronary angiography, reflecting microvascular dysfunction compared to reference controls (65). A randomized trial in this setting showed that medical therapy with ranolazine improved angina and reduced ischemic burden in woman with myocardial ischemia detected by stress CMR in the absence of obstructive CAD, suggesting a possible use of MRI for therapeutic assessment (66). Additionally, in patients with infiltrative heart disease such as amyloidosis, it has been demonstrated that impaired myocardial perfusion is related to abnormalities in myocardial structure and function not only at stress, but also at rest (67). Taken together, studies support the use of stress perfusion CMR to investigate myocardial perfusion reserve, which reflects microvascular dysfunction in the absence of CAD. In addition, stress CMR has already demonstrated high prognostic value and cost-effectiveness compared to invasive strategies (68, 69). While classically, limitations of this technique included the need for highly specialized equipment and providers, recent technical developments now allow quantitative and fully automated assessment of myocardial ischemia using stress CMR, which may enable the broad use of this modality outside of specialized centers (70).

## COMPUTED TOMOGRAPHY ANGIOGRAPHY

The homogeneity of myocardial perfusion can be readily assessed by its uptake of iodine contrast medium and its associated X-ray attenuation. George et al. demonstrated that myocardial perfusion can be quantified using CT and that reversible perfusion defects can be identified after vasodilator challenge

analogous to nuclear imaging techniques (71). CT scanning is performed using injection of an iodinated contrast agent with prospective electrocardiographic gating. Microvascular function may be assessed by determining MBF at rest and after vasodilator challenge with abnormal flow reserve typically defined as a ratio of  $<2.0$  (60). In the absence of obstructive CAD and local myocardial perfusion defects, reduced MFR can be attributed to microvascular dysfunction. **Figure 4** shows an imaging example of a patient with a severe myocardial perfusion defect in the lateral and posterolateral walls post infarct.

Advantages of CT include faster image acquisition than with nuclear techniques and markedly superior spatial resolution. Directly compared to nuclear myocardial perfusion imaging using exercise or vasodilator challenge, CT myocardial perfusion yields at least equivalent accuracy for identifying patients with CAD (72). Another major advantage of cardiac CT is the assessment of both coronary arterial anatomy and myocardium. Using contemporary technology, rest-vasodilator CT for coronary angiography and myocardial perfusion imaging can be performed with radiation doses lower than standard nuclear perfusion imaging using SPECT, though requiring two contrast applications of approximately 60 ml each (72). Determining MBF and coronary flow reserve by CT myocardial perfusion imaging is possible using dynamic imaging, i.e., continued imaging over several cardiac cycles (73).

Application of dynamic CT imaging had been hindered by high associated radiation exposure to the patient but new protocols have been developed using lower tube settings which have reduced radiation to levels similar to that by conventional rest-vasodilator myocardial perfusion protocols (73). Comparison to PET revealed high accuracy of dynamic CT for detecting abnormal MBF using a mean radiation dose of 8.4 mSv (74). Further radiation dose reductions are feasible using intermittent instead of continuous scanning, thus overcoming one of the major limitations of dynamic CT perfusion imaging and opening the possibility of comprehensive coronary arterial and myocardial assessment.

## PERIPHERAL ENDOTHELIAL FUNCTION ASSESSMENT

### Brachial Artery Flow Mediated Dilatation

In the early 1990s, high-resolution B-mode ultrasound and Doppler emerged as a non-invasive tool to measure brachial artery diameter and flow changes in response to vasomotor stimuli in research investigations of endothelial function, and remain as such currently (9, 75). Specifically, flow-mediated vasodilatation (FMD) of the brachial artery (or forearm radial artery) measures a focal segment of the artery to dilate in response to NO release induced by a 5 min blood pressure cuff occlusion and release (hyperemic stimulus). Oral nitroglycerin is typically used as the non-endothelium dependent vasoactive stimulus. Calculation of the % FMD is the percent change in arterial diameter post-stimulus compared to the baseline diameter, measured manually or with edge-detection software (76). Doppler velocity of the artery is also acquired at baseline, and upon immediate and 2 min post cuff release. Baseline and

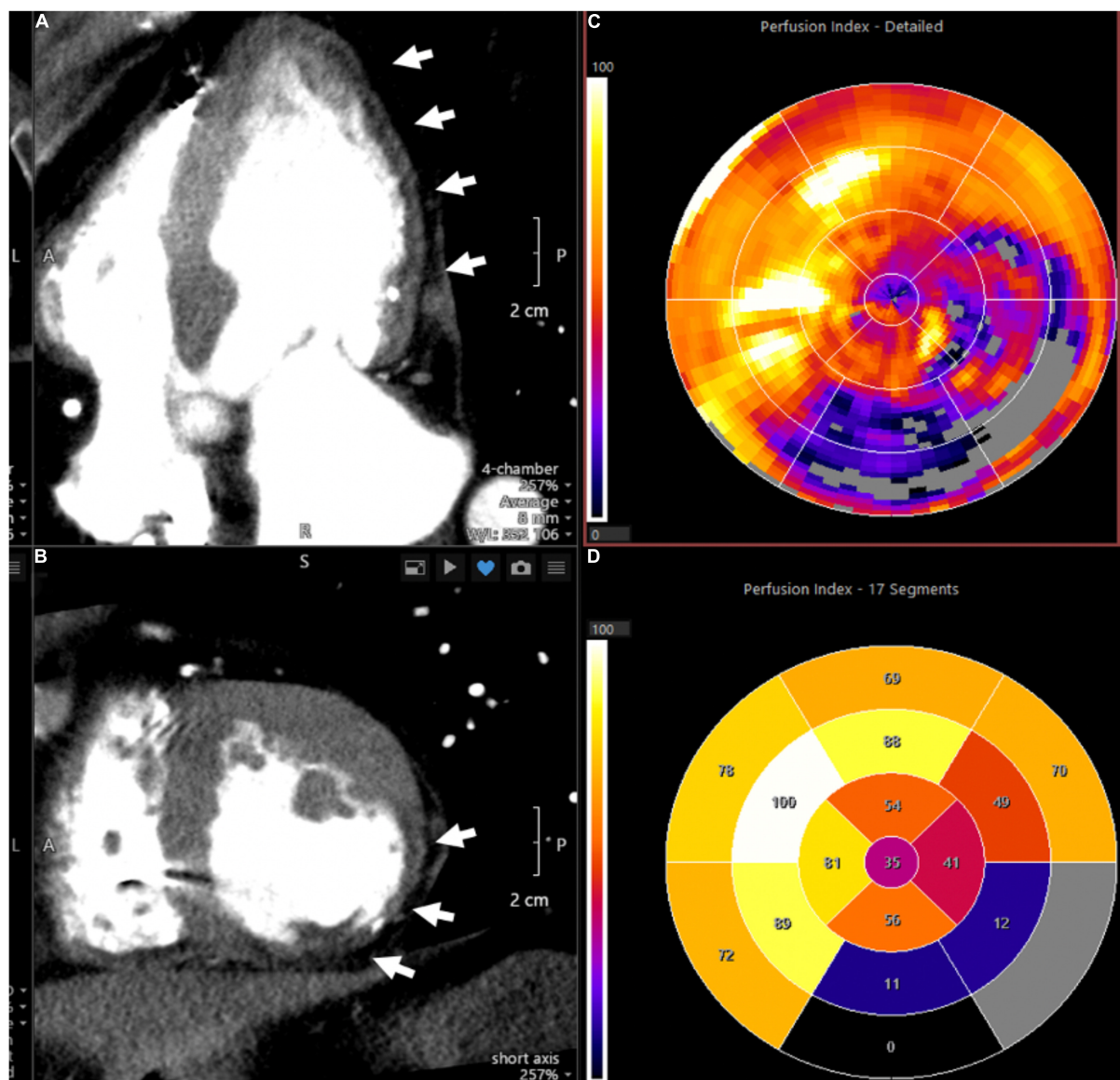


**FIGURE 4 |** Representative CT perfusion images and polar plots. Images demonstrate severe myocardial perfusion abnormalities in the lateral and posterolateral walls in a patient with history of myocardial infarction. **(A)** Depicts a cardiac four-chamber view with arrows pointing to hypodense areas in the subendocardial and mid myocardial levels, representing perfusion defects. In addition, thinning of the myocardium is consistent with prior infarct. **(B)** Provides a cross-sectional assessment of the same case. **(C)** (Polar plot) shows the corresponding perfusion indices, with the affected myocardial segments provided in **(D)**.

hyperemic blood flow are calculated from the time-averaged pulsed Doppler spectral trace time-velocity integral (NOVA Medical School) from the onset of one waveform to the beginning of the next waveform. A representative image is shown in **Figure 5** (9). Over the course of time, there have been some modifications of the technical method and exam protocol, but studies relying on this technique provide insight into endothelial function at the imaging site, the time course of diameter changes and flow, and the role of distal microvascular physiology (75, 77).

Advantages of the FMD technique include relative cost-effectiveness, easy access, availability, and validated digital

software for more automated analyses. In addition there is robust reproducibility in experienced labs and importantly, strong evidence that endothelial dysfunction measured with FMD predicts cardiovascular events (78). However, optimal acquisition of the vessel images and Doppler in a time-sensitive manner is technically challenging, with a significant learning curve to achieve and maintain high-quality, consistent performance and reproducibility in data acquisition and interpretation. Differences in methodological technique and exam protocols also limit the comparability, accuracy, validity, and reproducibility. Nevertheless, brachial FMD methods provide a validated non-invasive assessment of endothelial function.

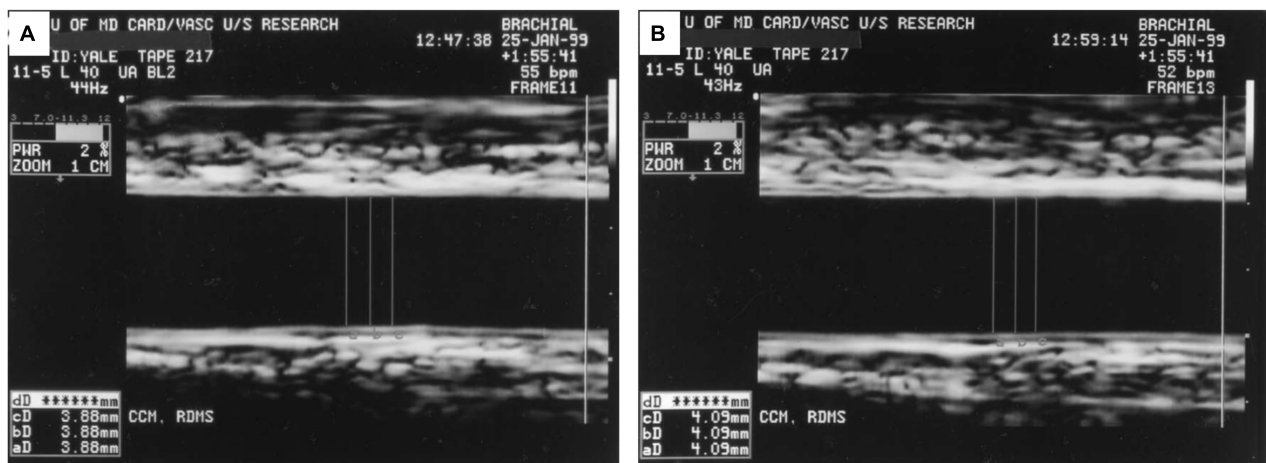


**FIGURE 5 |** Ultrasound Images Demonstrating Brachial Flow-Mediated Dilatation. **(A)** Shows the brachial artery at rest with arterial diameter of 3.88 mm. **(B)** Shows the artery 1 min after hyperemic stimulus with arterial diameter of 4.09 mm. Figure reproduced with permission from Corretti et al. (9) copyright JACC (Elsevier).

**TABLE 1 |** Comparison of the invasive and non-invasive methods for assessing endothelial function.

| Modality                                      | Strengths  | Limitations  |
|---|--|--|
| Coronary angiography                          | <ul style="list-style-type: none"> <li>Gold standard method</li> <li>Direct visualization and quantitation of endothelial function</li> <li>Able to assess dose-response</li> <li>Precise and accurate results</li> </ul>          | <ul style="list-style-type: none"> <li>Invasive</li> <li>Expensive</li> <li>Vasoactive medications can have systemic effects</li> <li>Largely limited to clinical studies</li> </ul>   |
| Brachial artery flow mediated dilatation      | <ul style="list-style-type: none"> <li>Non-invasive</li> <li>Cost-effective</li> <li>Validated software for automated analyses</li> <li>Well correlated with coronary endothelial function</li> </ul>                              | <ul style="list-style-type: none"> <li>Operator dependent</li> <li>Technically challenging to obtain optimal images</li> <li>Variable measurements, which limit comparability and reproducibility</li> </ul>   |
| Forearm plethysmography/Applanation tonometry | <ul style="list-style-type: none"> <li>Minimal training required</li> <li>Inexpensive</li> <li>Portable</li> <li>Well tolerated</li> <li>Can provide indirect information on the structure of small resistance arteries</li> </ul> | <ul style="list-style-type: none"> <li>No clear cutoff values</li> <li>Used mostly for mechanistic research studies</li> <li>Limited reproducibility</li> <li>Requires specialized training for standardization</li> <li>Findings may not reflect endothelial function only</li> </ul> |
| Venous occlusion plethysmography              | <ul style="list-style-type: none"> <li>Validated technique</li> <li>Reproducible</li> <li>Easier to access than coronary arteries</li> </ul>   | <ul style="list-style-type: none"> <li>Invasive</li> <li>Limited ability to compare application between individuals or groups</li> </ul>   |
| Positron emission tomography                  | <ul style="list-style-type: none"> <li>Well-validated in animal and human studies</li> <li>Automated software for quantitative analysis</li> </ul>   | <ul style="list-style-type: none"> <li>Radiation exposure</li> <li>Expensive</li> <li>Lack of easy access</li> </ul>   |
| Computed tomography                           | <ul style="list-style-type: none"> <li>Good spatial resolution</li> <li>Relatively cost-effective</li> <li>Fast image acquisition</li> </ul>   | <ul style="list-style-type: none"> <li>Radiation exposure</li> <li>Image may be compromised by increased heart rate</li> <li>Calcium related beam hardening may result in artifacts</li> </ul>   |
| Magnetic resonance imaging                    | <ul style="list-style-type: none"> <li>High spatial and temporal resolution</li> <li>No ionizing radiation</li> <li>Cardiac structure and function assessment included</li> </ul>  | <ul style="list-style-type: none"> <li>Limited availability</li> <li>Expensive</li> <li>Long study length</li> <li>Limited use in patients with arrhythmias, claustrophobia or implanted devices</li> </ul>  |

## Venous and Arterial Plethysmography

Venous occlusion plethysmography is an invasive, extensively used research technique to study human vascular physiology and pharmacology *in vivo*. The technique indirectly measures microvascular function as forearm blood flow in response to an intra-arterial infusion of a vasoactive substance such

as acetylcholine, adenosine, or nitroglycerin into either the brachial or radial artery, or alternatively to reactive hyperemia induced by increased shear stress. The contralateral arm is used as the control, and the results are expressed as the ratio of the changes in flow measured in both arms (79). Training is essential to ensure standardization and

quality control. The technique is validated, reliable, and highly reproducible (79). However, its invasive nature precludes application for routine clinical use. Additionally, the various anatomic, physiologic and technical factors involved with venous plethysmography limit its application to study changes between individuals, groups or in large populations. A limitation to plethysmography and applanation tomography include lack of standardization. Nonetheless, it remains a valuable research tool to evaluate the pathologic mechanisms underlying endothelial dysfunction, the effect of various therapeutic interventions and risk factor modifications.

Similarly, finger plethysmography (peripheral arterial/amplitude tonometry) can be used to assess peripheral endothelial function in the digital microvasculature (75, 80). Pulse amplitude tonometry (commercially available as Endo-PAT2000 (Pulse Arterial Tone), Itamar Medical) is an FDA approved product that records pulse amplitude in the individual's fingertip at rest and during reactive hyperemia (81). Hyperemia is induced by occluding blood flow through the brachial artery for 5 min using an inflatable cuff. Hyperemia in the fingertip increases the pulse amplitude. Proprietary software is applied to obtain the net response is expressed as the reactive hyperemia pulse amplitude tonometry index (RHI), considered a marker of endothelial function. The endothelium-mediated change in the PAT signal, elicited by the downstream hyperemic response, is calculated automatically by the system. A PAT ratio is then created using the post and pre occlusion values normalized to measurements from the contralateral arm (control). Importantly, studies have shown that peripheral microvascular dysfunction predicts future cardiovascular events (82, 83).

## Endothelial Function in the Coronary vs. Peripheral Circulation

Although abnormal systemic and coronary endothelial function are predictors of cardiovascular events, vasoreactivity across different vascular beds are not always closely associated. Studies comparing to coronary systemic endothelial function have shown that the correlation between the two may be modest (38, 84). Further, other studies have shown that endothelial dysfunction is not always uniform across vascular regions or even within the coronary tree of the same individual (32, 38). These regional differences in endothelial function may be due differences in local shear, downstream resistance vessels, neurohormonal regulation or propensity to develop atherosclerosis and plaque rupture. Taken together, endothelial function measures of different vascular beds may provide complementary information, each with unique strengths and limitations (Table 1). However, further studies are need to elucidate the relative role of endothelial measures in different vessels.

## CLINICAL STUDIES AND APPLICATIONS

Both established and newer cardiovascular risk factors can adversely affect endothelial function, including obesity, diabetes, smoking, and inflammation/oxidative stress (7, 8). To this end,

the measurement of endothelial vasoreactivity serves as an index of the sum total effects of environmental and genetic factors on the vasculature. Furthermore endothelial dysfunction is a marker for subclinical disease, an independent predictor of adverse cardiovascular events, and a potential target for medical interventions (78, 82). One study using PET showed that cigarette smokers have reduced MFR, with improvement seen with smoking cessation (85). Similarly, initiation of antihypertensives can result in improved endothelial function in patients with hypertension (86). Obese patients were reported to demonstrate impaired MBF with improvement after bariatric surgery (59). In addition, MFR is reduced in patients with diabetes, with some suggestion that endothelial function (measured by FMD) may improve with dapagliflozin (55, 87).

Recently, coronary microvascular dysfunction has been implicated in multiple disease processes including microvascular angina, a common encountered disorder which can lead to ischemia or myocardial infarction, even in the absence of obstructive coronary artery disease (60). Microvascular angina due to ischemia with non-obstructive coronary arteries (INOCA) can be challenging to diagnose, with a heterogenous approach to patients and many knowledge gaps with regards to treatment. The CorMicA trial showed that guiding therapy by invasive provocative coronary testing in patients with INOCA identified to have microvascular dysfunction may be of clinical benefit (88). Recent methods using stress perfusion CMR are being employed in the CorCMR study to evaluate whether a non-invasive approach to assess coronary microvascular dysfunction in INOCA patients improves cardiovascular risk and anginal symptoms (89). The results of study may have important

**TABLE 2 |** Range of normal values for coronary flow reserve (invasive) and myocardial flow or perfusion reserve (non-invasive) with different imaging modalities.

| Modality                    | Values used to diagnose CMD  |
|-----------------------------|--|
| <b>Invasive methods</b>     |  |
| Angiography + adenosine     | CFR: abnormal <2.0 (94)  |
| Angiography + acetylcholine | CFR: abnormal <1.5 (95)  |
| <b>Non-invasive methods</b> |  |
| CMR + adenosine             | MFR: definite CMD <1.5, borderline CMD 1.5–2.6 (96)<br>MPRI: abnormal <1.84 (97), $\leq 1.47$ predicts MACE (98)<br>Global stress MBF without visual perfusion defects: abnormal $\leq 2.25$ ml/g/min (70) |
| PET + adenosine             | MFR: definite CMD <1.5, borderline CMD 1.5–2.6 (96)  |
| CT-perfusion                | MFR: abnormal <2 (60)  |
| Forearm plethysmography     | No established cutoff  |
| Finger plethysmography      | RHI: <1.6–1.75 portends high risk for cardiovascular events (99)   |

*CMD, coronary microvascular disease; CFR, coronary flow reserve; MFR, myocardial flow reserve; MPRI, myocardial perfusion reserve index; MACE, major adverse cardiac events; MBF, myocardial blood flow; RHI, reactive hyperemic index. Non-invasive measures of MFR reflect CMD if significant contribution of reduced from epicardial coronaries has been ruled out.*

clinical implications in this patient population, where there is less evidence in terms of diagnostic testing and treatment. Furthermore, using these approaches to quantify coronary microvascular function may provide clinically meaningful information beyond what is possible using standard anatomic and ischemia assessment with the ultimate goal of improving patient outcomes. It is important to note that many of the techniques described in this review (PET, specialized CMR, and CT perfusion) are not yet widely available clinically, however, may play an important role in the evaluation of patients with INOCA and to test early therapies to justify larger clinical trials with hard end points.

Both coronary and systemic endothelial function measures have been used as endpoints in clinical intervention trials after the techniques were shown to be reproducible in the short and intermediate term (90). Studies using endothelial function as an endpoint enable the assessment of the vascular impact of emerging treatment strategies and can guide novel drug development, such as approaches to target oxidative stress or inflammation. Studies targeting the xanthine oxidase (XO) system, a significant source of vascular oxidative stress, or systemic inflammation using colchicine have used CEF testing as a surrogate imaging endpoint over time in randomized placebo-controlled clinical trials (90, 91). Recently, impaired CEF in people with HIV and dyslipidemia improved with short term treatment with the PCSK9 inhibitor, evolocumab, indicating that the MRI-CEF technique can detect rapid improvements in CEF in response to treatment (92). Therefore, this approach enables future studies focused on repeated CEF measures in healthy and lower risk populations over time.

## CONCLUSION

Endothelial dysfunction is now a well-established gauge of cardiovascular risk and predicts future adverse events. Recently, endothelial dysfunction has been implicated as a contributor to a variety of cardiovascular diseases including INOCA, stress cardiomyopathy, preeclampsia and heart failure with preserved ejection fraction among others (26, 93). We have summarized multiple methods that are available for probing coronary and peripheral endothelial, each with specific strengths and weaknesses, and different values for defining pathology (Table 2).

## REFERENCES

1. Virani SS, Alonso A, Benjamin EJ, Bittencourt MS, Callaway CW, Carson AP, et al. Heart disease and stroke statistics—2020 update: a report from the American heart association. *Circulation*. (2020) 141:e139–596. doi: 10.1161/CIR.0000000000000757
2. Vita JA, Keaney JF. Endothelial function: a barometer for cardiovascular risk? *Circulation*. (2002) 106:640–2. doi: 10.1161/01.cir.0000028581.07992.56
3. Flammer AJ, Anderson T, Celermajer DS, Creager MA, Deanfield J, Ganz P, et al. The assessment of endothelial function: from research into clinical practice. *Circulation*. (2012) 126:753–67. doi: 10.1161/CIRCULATIONAHA.112.093245
4. Deanfield JE, Halcox JP, Rabelink TJ. Endothelial function and dysfunction: testing and clinical relevance. *Circulation*. (2007) 115:1285–95. doi: 10.1161/CIRCULATIONAHA.106.652859

Currently available endothelial testing methods are helpful for mechanistic understanding of disease and for risk stratification and prognostication. It is important to recognize, though, that using a pharmacological stressor for imaging to assess endothelial function will often detect function in response to a combination of endothelial and non-endothelial dependent mechanisms, and depending on the stressor and imaging modality, this should be considered. Increasingly endothelial function testing is being explored for clinical management and evaluation of therapeutic response, although there are currently no guidelines recommending use of endothelial function in routine patient management. Nonetheless, evidence continues to grow in the role of the vascular endothelium in disease pathophysiology and ongoing large-scale studies are essential for the evaluation of therapies targeting endothelial function.

## AUTHOR CONTRIBUTIONS

AM, EG, MC, AA-Z, SK, and AH drafted the manuscript. TL and AL edited the manuscript. All authors contributed to the article and approved the submitted version.

## FUNDING

AM was supported by National Heart, Lung, and Blood Institute training grant T32HL007024, the Johns Hopkins University Lou and Nancy Grasmick Research Fellowship and the Marie-Josée and Henry R. Kravis Endowed Fellowship in Honor of Dr. James L. Weiss. AH was supported by the NIH/NHLBI 1R01HL147660. EG was supported by the Ruth L. Kirschstein Institutional National Research Service Award T32HL007227. TL received a Career Development Award from the American Heart Association (19CDA34760040) and Clinician Scientist Career Development Award from the Johns Hopkins School of Medicine. AA-Z has received research support from Canon Medical Systems. SK was supported by a grant from Philips Healthcare and received funding by the German Ministry of Education and Research and was funded by the Deutsche Forschungsgemeinschaft (DFG, German Research Foundation) – SFB-1470 – B06.

5. Moncada S, Erusalimsky JD. Does nitric oxide modulate mitochondrial energy generation and apoptosis? *Nat Rev Mol Cell Biol*. (2002) 3:214–20. doi: 10.1038/nrm762
6. Rhee SG. Cell signaling. H<sub>2</sub>O<sub>2</sub>, a necessary evil for cell signaling. *Science*. (2006) 312:1882–3. doi: 10.1126/science.1130481
7. Celermajer DS, Sorensen KE, Bull C, Robinson J, Deanfield JE. Endothelium-dependent dilation in the systemic arteries of asymptomatic subjects relates to coronary risk factors and their interaction. *J Am Coll Cardiol*. (1994) 24:1468–74. doi: 10.1016/0735-1097(94)90141-4
8. Ross R. Atherosclerosis—an inflammatory disease. *N Engl J Med*. (1999) 340:115–26.
9. Corretti MC, Anderson TJ, Benjamin EJ, Celermajer D, Charbonneau F, Creager MA, et al. Guidelines for the ultrasound assessment of endothelial-dependent flow-mediated vasodilation of the brachial artery. *J Am Coll Cardiol*. (2002) 39:257–65. doi: 10.1016/s0735-1097(01)01746-6

10. Halcox JPJ, Schenke WH, Zalos G, Mincemoyer R, Prasad A, Waclawiw MA, et al. Prognostic value of coronary vascular endothelial dysfunction. *Circulation*. (2002) 106:653–8. doi: 10.1161/01.cir.0000025404.78001.d8
11. Hasdai D, Lerman A. The assessment of endothelial function in the cardiac catheterization laboratory in patients with risk factors for atherosclerotic coronary artery disease. *Herz*. (1999) 24:544–7. doi: 10.1007/BF03044226
12. Schächinger V, Britten MB, Zeiher AM. Prognostic impact of coronary vasodilator dysfunction on adverse long-term outcome of coronary heart disease. *Circulation*. (2000) 101:1899–906. doi: 10.1161/01.cir.101.16.1899
13. Schindler TH, Hornig B, Buser PT, Olschewski M, Magosaki N, Pfisterer M, et al. Prognostic value of abnormal vasoreactivity of epicardial coronary arteries to sympathetic stimulation in patients with normal coronary angiograms. *Arterioscler Thromb Vasc Biol*. (2003) 23:495–501. doi: 10.1161/01.ATV.0000057571.03012.F4
14. Zeiher AM, Drexler H, Wollschläger H, Just H. Modulation of coronary vasomotor tone in humans. Progressive endothelial dysfunction with different early stages of coronary atherosclerosis. *Circulation*. (1991) 83:391–401. doi: 10.1161/01.cir.83.2.391
15. Drexler H, Zeiher AM. Progression of coronary endothelial dysfunction in man and its potential clinical significance. In: Drexler H, Zeiher AM, Bassenge E, Just H, editors. *Endothelial Mechanisms of Vasomotor Control*. Heidelberg: Steinkopff (1991). p. 223–32. doi: 10.1007/978-3-642-72461-9\_22
16. Ludmer PL, Selwyn AP, Shook TL, Wayne RR, Mudge GH, Alexander RW, et al. Paradoxical vasoconstriction induced by acetylcholine in atherosclerotic coronary arteries. *N Engl J Med*. (1986) 315:1046–51. doi: 10.1056/NEJM198610233151702
17. Niccoli G, Scalone G, Crea F. Coronary functional tests in the catheterization laboratory – pathophysiological and clinical relevance. *Circ J*. (2015) 79:676–84. doi: 10.1253/circj.CJ-15-0201
18. Smits P, Williams SB, Lipson DE, Banitt P, Rongen GA, Creager MA. Endothelial release of nitric oxide contributes to the vasodilator effect of adenosine in humans. *Circulation*. (1995) 92:2135–41. doi: 10.1161/01.cir.92.8.2135
19. Cox DA, Vita JA, Treasure CB, Fish RD, Alexander RW, Ganz P, et al. Atherosclerosis impairs flow-mediated dilation of coronary arteries in humans. *Circulation*. (1989) 80:458–65. doi: 10.1161/01.cir.80.3.458
20. Drexler H, Zeiher AM, Wollschläger H, Meinertz T, Just H, Bonzel T. Flow-dependent coronary artery dilatation in humans. *Circulation*. (1989) 80:466–74. doi: 10.1161/01.cir.80.3.466
21. Raitakari OT, Celermajer DS. Testing for endothelial dysfunction. *Ann Med*. (2000) 32:293–304. doi: 10.3109/07853890008995931
22. Treasure CB, Klein JL, Vita JA, Manoukian SV, Renwick GH, Selwyn AP, et al. Hypertension and left ventricular hypertrophy are associated with impaired endothelium-mediated relaxation in human coronary resistance vessels. *Circulation*. (1993) 87:86–93. doi: 10.1161/01.cir.87.1.86
23. Nabel EG, Ganz P, Gordon JB, Alexander RW, Selwyn AP. Dilation of normal and constriction of atherosclerotic coronary arteries caused by the cold pressor test. *Circulation*. (1988) 77:43–52. doi: 10.1161/01.cir.77.1.43
24. Gordon JB, Ganz P, Nabel EG, Fish RD, Zebede J, Mudge GH, et al. Atherosclerosis influences the vasomotor response of epicardial coronary arteries to exercise. *J Clin Invest*. (1989) 83:1946–52. doi: 10.1172/JCI114103
25. Houghton JL, Smith VE, Strogatz DS, Hennesch LF, Breisblatt WM, Carr AA. Effect of African-American race and hypertensive left ventricular hypertrophy on coronary vascular reactivity and endothelial function. *Hypertension*. (1997) 29:706–14. doi: 10.1161/01.hyp.29.3.706
26. Verna E, Provasoli S, Ghiringhelli S, Morandi F, Salerno-Uriarte J. Abnormal coronary vasoreactivity in transient left ventricular apical ballooning (takotsubo) syndrome. *Int J Cardiol*. (2018) 250:4–10. doi: 10.1016/j.ijcard.2017.07.032
27. Cosson E, Pham I, Valensi P, Paries J, Attali J-R, Nitenberg A. Impaired Coronary endothelium-dependent vasodilation is associated with microalbuminuria in patients with type 2 diabetes and angiographically normal coronary arteries. *Diabetes Care*. (2006) 29:107–12. doi: 10.2337/diacare.29.1.107
28. Treasure CB, Klein JL, Weintraub WS, Talley JD, Stillabower ME, Kosinski AS, et al. Beneficial effects of cholesterol-lowering therapy on the coronary endothelium in patients with coronary artery disease. *N Engl J Med*. (1995) 332:481–7. doi: 10.1056/NEJM199502233320801
29. Bluemke DA, Achenbach S, Budoff M, Gerber TC, Gersh B, Hillis LD, et al. Noninvasive coronary artery imaging: magnetic resonance angiography and multidetector computed tomography angiography: a scientific statement from the American heart association committee on cardiovascular imaging and intervention of the council on cardiovascular radiology and intervention, and the councils on clinical cardiology and cardiovascular disease in the young. *Circulation*. (2008) 118:586–606. doi: 10.1161/CIRCULATIONAHA.108.189695
30. Yoon YE, Kitagawa K, Kato S, Ishida M, Nakajima H, Kurita T, et al. Prognostic value of coronary magnetic resonance angiography for prediction of cardiac events in patients with suspected coronary artery disease. *J Am Coll Cardiol*. (2012) 60:2316–22. doi: 10.1016/j.jacc.2012.07.060
31. Hundley WG, Lange RA, Clarke GD, Meshack BM, Payne J, Landau C, et al. Assessment of coronary arterial flow and flow reserve in humans with magnetic resonance imaging. *Circulation*. (1996) 93:1502–8. doi: 10.1161/01.cir.93.8.1502
32. Hays AG, Hirsch GA, Kelle S, Gerstenblith G, Weiss RG, Stuber M. Noninvasive visualization of coronary artery endothelial function in healthy subjects and in patients with coronary artery disease. *J Am Coll Cardiol*. (2010) 56:1657–65. doi: 10.1016/j.jacc.2010.06.036
33. Hays AG, Iantorno M, Schär M, Mukherjee M, Stuber M, Gerstenblith G, et al. Local coronary wall eccentricity and endothelial function are closely related in patients with atherosclerotic coronary artery disease. *J Cardiovasc Magn Reson*. (2017) 19:51. doi: 10.1186/s12968-017-0358-2
34. Iantorno M, Schär M, Soleimanifard S, Brown TT, Moore R, Barditch-Crovo P, et al. Coronary artery endothelial dysfunction is present in HIV-positive individuals without significant coronary artery disease. *AIDS*. (2017) 31:1281–9. doi: 10.1097/QAD.0000000000001469
35. Iantorno M, Soleimanifard S, Schär M, Brown TT, Bonanno G, Barditch-Crovo P, et al. Regional coronary endothelial dysfunction is related to the degree of local epicardial fat in people with HIV. *Atherosclerosis*. (2018) 278:7–14. doi: 10.1016/j.atherosclerosis.2018.08.002
36. Leucker TM, Weiss RG, Schär M, Bonanno G, Mathews L, Jones SR, et al. Coronary endothelial dysfunction is associated with elevated serum PCSK9 levels in people with HIV independent of low-density lipoprotein cholesterol. *J Am Heart Assoc*. (2018) 7:e009996. doi: 10.1161/JAHA.118.009996
37. Hays AG, Kelle S, Hirsch GA, Soleimanifard S, Yu J, Agarwal HK, et al. Regional coronary endothelial function is closely related to local early coronary atherosclerosis in patients with mild coronary artery disease: pilot study. *Circ Cardiovasc Imaging*. (2012) 5:341–8. doi: 10.1161/CIRCIMAGING.111.969691
38. Iantorno M, Hays AG, Schär M, Krishnaswamy R, Soleimanifard S, Steinberg A, et al. Simultaneous noninvasive assessment of systemic and coronary endothelial function. *Circ Cardiovasc Imaging*. (2016) 9:e003954. doi: 10.1161/CIRCIMAGING.115.003954
39. Hays AG, Iantorno M, Soleimanifard S, Steinberg A, Schär M, Gerstenblith G, et al. Coronary vasomotor responses to isometric handgrip exercise are primarily mediated by nitric oxide: a noninvasive MRI test of coronary endothelial function. *Am J Physiol Heart Circ Physiol*. (2015) 308:H1343–50. doi: 10.1152/ajpheart.00023.2015
40. Beanlands RS, Muzik O, Melon P, Sutor R, Sawada S, Muller D, et al. Noninvasive quantification of regional myocardial flow reserve in patients with coronary atherosclerosis using nitrogen-13 ammonia positron emission tomography. Determination of extent of altered vascular reactivity. *J Am Coll Cardiol*. (1995) 26:1465–75. doi: 10.1016/0735-1097(95)00359-2
41. Iantorno M, Weiss RG. Using advanced noninvasive imaging techniques to probe the links between regional coronary artery endothelial dysfunction and atherosclerosis. *Trends Cardiovasc Med*. (2014) 24:149–56. doi: 10.1016/j.tcm.2013.10.001
42. Schindler TH, Nitzsche EU, Schelbert HR, Olschewski M, Sayre J, Mix M, et al. Positron emission tomography-measured abnormal responses of myocardial blood flow to sympathetic stimulation are associated with the risk of developing cardiovascular events. *J Am Coll Cardiol*. (2005) 45:1505–12. doi: 10.1016/j.jacc.2005.01.040
43. Zeiher AM, Drexler H, Wollschlaeger H, Saurbier B, Just H. Coronary vasomotion in response to sympathetic stimulation in humans: importance of the functional integrity of the endothelium. *J Am Coll Cardiol*. (1989) 14:1181–90. doi: 10.1016/0735-1097(89)90414-2

44. Schindler TH, Facta AD, Prior JO, Campisi R, Inubushi M, Kreissl MC, et al. PET-measured heterogeneity in longitudinal myocardial blood flow in response to sympathetic and pharmacologic stress as a non-invasive probe of epicardial vasomotor dysfunction. *Eur J Nucl Med Mol Imaging*. (2006) 33:1140–9. doi: 10.1007/s00259-006-0069-7
45. Schindler TH, Schelbert HR, Quercioli A, Dilsizian V. Cardiac PET imaging for the detection and monitoring of coronary artery disease and microvascular health. *JACC Cardiovasc Imaging*. (2010) 3:623–40. doi: 10.1016/j.jcmg.2010.04.007
46. Ziadi MC. Myocardial flow reserve (MFR) with positron emission tomography (PET)/computed tomography (CT): clinical impact in diagnosis and prognosis. *Cardiovasc Diagn Ther*. (2017) 7:206–18. doi: 10.21037/cdt.2017.04.10
47. Al Badarin F, Aljazeera A, Almasoudi F, Al-Mallah MH. Assessment of myocardial blood flow and coronary flow reserve with positron emission tomography in ischemic heart disease: current state and future directions. *Heart Fail Rev*. (2017) 22:441–53. doi: 10.1007/s10741-017-9625-4
48. Taqueti VR, Di Carli MF. Coronary microvascular disease pathogenic mechanisms and therapeutic options. *J Am Coll Cardiol*. (2018) 72:2625–41. doi: 10.1016/j.jacc.2018.09.042
49. Schindler TH, Zhang X-L, Vincenti G, Mhiri L, Lerch R, Schelbert HR. Role of PET in the evaluation and understanding of coronary physiology. *J Nucl Cardiol*. (2007) 14:589–603. doi: 10.1016/j.nuclcard.2007.05.006
50. Schindler TH, Dilsizian V. Coronary microvascular dysfunction. *JACC Cardiovasc Imaging*. (2020) 13:140–55.
51. Gupta A, Taqueti VR, van de Hoef TP, Bajaj NS, Bravo PE, Murthy VL, et al. Integrated noninvasive physiological assessment of coronary circulatory function and impact on cardiovascular mortality in patients with stable coronary artery disease. *Circulation*. (2017) 136:2325–36. doi: 10.1161/CIRCULATIONAHA.117.029992
52. Herzog BA, Husmann L, Valenta I, Gaemperli O, Siegrist PT, Tay FM, et al. Long-term prognostic value of <sup>13</sup>N-ammonia myocardial perfusion positron emission tomography added value of coronary flow reserve. *J Am Coll Cardiol*. (2009) 54:150–6. doi: 10.1016/j.jacc.2009.02.069
53. Ziadi MC, Dekemp RA, Williams KA, Guo A, Chow BJW, Renaud JM, et al. Impaired myocardial flow reserve on rubidium-82 positron emission tomography imaging predicts adverse outcomes in patients assessed for myocardial ischemia. *J Am Coll Cardiol*. (2011) 58:740–8. doi: 10.1016/j.jacc.2011.01.065
54. Murthy VL, Naya M, Foster CR, Hainer J, Gaber M, Di Carli G, et al. Improved cardiac risk assessment with noninvasive measures of coronary flow reserve. *Circulation*. (2011) 124:2215–24. doi: 10.1161/CIRCULATIONAHA.111.050427
55. Murthy VL, Naya M, Foster CR, Gaber M, Hainer J, Klein J, et al. Association between coronary vascular dysfunction and cardiac mortality in patients with and without diabetes mellitus. *Circulation*. (2012) 126:1858–68. doi: 10.1161/CIRCULATIONAHA.112.120402
56. Taqueti VR, Shaw LJ, Cook NR, Murthy VL, Shah NR, Foster CR, et al. Excess cardiovascular risk in women relative to men referred for coronary angiography is associated with severely impaired coronary flow reserve not obstructive disease. *Circulation*. (2017) 135:566–77. doi: 10.1161/circulationaha.116.023266
57. Taqueti VR, Solomon SD, Shah AM, Desai AS, Goarke JD, Osborne MT, et al. Coronary microvascular dysfunction and future risk of heart failure with preserved ejection fraction. *Eur Heart J*. (2018) 39:840–9. doi: 10.1093/eurheartj/ehx721
58. Yokoyama I. Impaired myocardial vasodilatation during hyperaemic stress is improved by simvastatin but not by pravastatin in patients with hypercholesterolaemia. *Eur Heart J*. (2004) 25:671–9. doi: 10.1016/j.ehj.2004.02.017
59. Quercioli A, Montecucco F, Pataky Z, Thomas A, Ambrosio G, Staub C, et al. Improvement in coronary circulatory function in morbidly obese individuals after gastric bypass-induced weight loss: relation to alterations in endocannabinoids and adipocytokines. *Eur Heart J*. (2013) 34:2063–73. doi: 10.1093/eurheartj/ehx085
60. Feher A, Sinusas AJ. Quantitative assessment of coronary microvascular function: dynamic single-photon emission computed tomography, positron emission tomography, ultrasound, computed tomography, and magnetic resonance imaging. *Circ Cardiovasc Imaging*. (2017) 10:e006427. doi: 10.1161/CIRCIMAGING.117.006427
61. Bergmann SR, Fox KA, Rand AL, McElvany KD, Welch MJ, Markham J, et al. Quantification of regional myocardial blood flow in vivo with H<sub>2</sub><sup>15</sup>O. *Circulation*. (1984) 70:724–33. doi: 10.1161/01.cir.70.4.724
62. Crea F, Camici PG, Bairey Merz CN. Coronary microvascular dysfunction: an update. *Eur Heart J*. (2014) 35:1101–11. doi: 10.1093/eurheartj/ehx513
63. Zorach B, Shaw PW, Bourque J, Kuruvilla S, Balfour PC, Yang Y, et al. Quantitative cardiovascular magnetic resonance perfusion imaging identifies reduced flow reserve in microvascular coronary artery disease. *J Cardiovasc Magn Reson*. (2018) 20:14. doi: 10.1186/s12968-018-0435-1
64. Knuuti J, Wijns W, Saraste A, Capodanno D, Barbato E, Funck-Brentano C, et al. ESC scientific document group. 2019 ESC guidelines for the diagnosis and management of chronic coronary syndromes. *Eur Heart J*. (2020) 41:407–77. doi: 10.1093/eurheartj/ehz425
65. Shufelt CL, Thomson LEJ, Goykhman P, Agarwal M, Mehta PK, Sedlak T, et al. Cardiac magnetic resonance imaging myocardial perfusion reserve index assessment in women with microvascular coronary dysfunction and reference controls. *Cardiovasc Diagn Ther*. (2013) 3:153–60. doi: 10.3978/j.issn.2223-3652.2013.08.02
66. Mehta PK, Goykhman P, Thomson LEJ, Shufelt C, Wei J, Yang Y, et al. Ranolazine improves angina in women with evidence of myocardial ischemia but no obstructive coronary artery disease. *JACC Cardiovasc Imaging*. (2011) 4:514–22. doi: 10.1016/j.jcmg.2011.03.007
67. Dorbala S, Vangala D, Bruyere J, Quarta C, Kruger J, Padera R, et al. Coronary microvascular dysfunction is related to abnormalities in myocardial structure and function in cardiac amyloidosis. *JACC Heart Fail*. (2014) 2:358–67. doi: 10.1016/j.jchf.2014.03.009
68. Kelle S, Nagel E, Voss A, Hofmann N, Gitsioudis G, Buss SJ, et al. A bi-center cardiovascular magnetic resonance prognosis study focusing on dobutamine wall motion and late gadolinium enhancement in 3,138 consecutive patients. *J Am Coll Cardiol*. (2013) 61:2310–2. doi: 10.1016/j.jacc.2013.02.063
69. Petrov G, Kelle S, Fleck E, Wellnhofer E. Incremental cost-effectiveness of dobutamine stress cardiac magnetic resonance imaging in patients at intermediate risk for coronary artery disease. *Clin Res Cardiol*. (2015) 104:401–9. doi: 10.1007/s00392-014-0793-0
70. Kotecha T, Martinez-Naharro A, Boldrini M, Knight D, Hawkins P, Kalra S, et al. Automated pixel-wise quantitative myocardial perfusion mapping by CMR to detect obstructive coronary artery disease and coronary microvascular dysfunction. *JACC Cardiovasc Imaging*. (2019) 12:1958–69. doi: 10.1016/j.jcmg.2018.12.022
71. George RT, Jerosch-Herold M, Silva C, Kitagawa K, Bluemke DA, Lima JAC, et al. Quantification of myocardial perfusion using dynamic 64-detector computed tomography. *Invest Radiol*. (2007) 42:815–22. doi: 10.1097/RLI.0b013e318124a884
72. George RT, Mehra VC, Chen MY, Kitagawa K, Arbab-Zadeh A, Miller JM, et al. Myocardial CT perfusion imaging and SPECT for the diagnosis of coronary artery disease: a head-to-head comparison from the CORE320 multicenter diagnostic performance study. *Radiology*. (2014) 272:407–16. doi: 10.1148/radiol.14140806
73. Nieman B, Balla S. Dynamic CT myocardial perfusion imaging. *J Cardiovasc Comput Tomogr*. (2020) 14:303–6.
74. Alessio AM, Bindschadler M, Busey JM, Shuman WP, Caldwell JH, Branch KR. Accuracy of myocardial blood flow estimation from dynamic contrast-enhanced cardiac CT compared with PET. *Circ Cardiovasc Imaging*. (2019) 12:e008323. doi: 10.1161/CIRCIMAGING.118.008323
75. Blumenthal RS, Foody JM, Wong ND, Braunwald E, editors. *Preventive Cardiology: a Companion to Braunwald's Heart Disease*. Philadelphia, PA: Elsevier/Saunders (2011).
76. Haluska B, Sutherland A, Case C, Kennedy R, Marwick TH. Automated edge-detection technique for measurement of brachial artery reactivity: a comparison of concordance with manual measurements. *Ultrasound Med Biol*. (2001) 27:1285–9. doi: 10.1016/s0301-5629(01)00406-9
77. Sorensen KE, Celermajor DS, Spiegelhalter DJ, Georgakopoulos D, Robinson J, Thomas O, et al. Non-invasive measurement of human endothelium

- dependent arterial responses: accuracy and reproducibility. *Heart*. (1995) 74:247–53. doi: 10.1136/hrt.74.3.247
78. Matsuzawa Y, Kwon T, Lennon RJ, Lerman LO, Lerman A. Prognostic value of flow-mediated vasodilation in brachial artery and fingertip artery for cardiovascular events: a systematic review and meta-analysis. *J Am Heart Assoc*. (2015) 4:e002270. doi: 10.1161/JAHA.115.002270
  79. Wilkinson IB, Webb DJ. Venous occlusion plethysmography in cardiovascular research: methodology and clinical applications. *Br J Clin Pharmacol*. (2001) 52:631–46. doi: 10.1046/j.0306-5251.2001.01495.x
  80. Kuvin JT, Patel AR, Sliney KA, Pandian NG, Sheffy J, Schnall RP, et al. Assessment of peripheral vascular endothelial function with finger arterial pulse wave amplitude. *Am Heart J*. (2003) 146:168–74. doi: 10.1016/S0002-8703(03)00094-2
  81. Axtell AL, Gomari FA, Cooke JP. Assessing endothelial vasodilator function with the Endo-PAT 2000. *J Vis Exp*. (2010) 44:2167. doi: 10.3791/2167
  82. Heitzer T, Schlinzig T, Krohn K, Meinertz T, Münzel T. Endothelial dysfunction, oxidative stress, and risk of cardiovascular events in patients with coronary artery disease. *Circulation*. (2001) 104:2673–8. doi: 10.1161/hc4601.099485
  83. Rubinshtein R, Kuvin JT, Soffler M, Lennon RJ, Lavi S, Nelson RE, et al. Assessment of endothelial function by non-invasive peripheral arterial tonometry predicts late cardiovascular adverse events. *Eur Heart J*. (2010) 31:1142–8. doi: 10.1093/eurheartj/ehq010
  84. Anderson TJ, Uehata A, Gerhard MD, Meredith IT, Knab S, Delagrangue D, et al. Close relation of endothelial function in the human coronary and peripheral circulations. *J Am Coll Cardiol*. (1995) 26:1235–41. doi: 10.1016/0735-1097(95)00327-4
  85. Morita K, Tsukamoto T, Naya M, Noriyasu K, Inubushi M, Shiga T, et al. Smoking cessation normalizes coronary endothelial vasomotor response assessed with 15O-water and PET in healthy young smokers. *J Nucl Med*. (2006) 47:1914–20.
  86. Modena MG, Bonetti L, Coppi F, Bursi F, Rossi R. Prognostic role of reversible endothelial dysfunction in hypertensive postmenopausal women. *J Am Coll Cardiol*. (2002) 40:505–10. doi: 10.1016/s0735-1097(02)01976-9
  87. Shigiyama F, Kumashiro N, Miyagi M, Ikehara K, Kanda E, Uchino H, et al. Effectiveness of dapagliflozin on vascular endothelial function and glycemic control in patients with early-stage type 2 diabetes mellitus: DEFENCE study. *Cardiovasc Diabetol*. (2017) 16:84. doi: 10.1186/s12933-017-0564-0
  88. Ford TJ, Stanley B, Good R, Rocchiccioli P, McEntegart M, Watkins S, et al. Stratified medical therapy using invasive coronary function testing in angina: the CorMicA trial. *J Am Coll Cardiol*. (2018) 72:2841–55. doi: 10.1016/j.jacc.2018.09.006
  89. Corcoran D, Ford TJ, Hsu L-Y, Chiribiri A, Orchard V, Mangion K, et al. Rationale and design of the coronary microvascular angina cardiac magnetic resonance imaging (CorCMR) diagnostic study: the CorMicA CMR sub-study. *Open Heart*. (2018) 5:e000924. doi: 10.1136/openhrt-2018-000924
  90. Hays AG, Iantorno M, Schär M, Lai S, Czarny M, Breton E, et al. The influence of febuxostat on coronary artery endothelial dysfunction in patients with coronary artery disease: a phase 4 randomized, placebo-controlled, double-blind, crossover trial. *Am Heart J*. (2018) 197:85–93. doi: 10.1016/j.ahj.2017.11.006
  91. Hays AG, Schär M, Barditch-Crovo P, Bagchi S, Bonanno G, Meyer J, et al. A randomized, placebo-controlled, double-blinded clinical trial of colchicine to improve vascular health in people living with HIV. *AIDS*. (2021) 35:1041–50. doi: 10.1097/QAD.0000000000002845
  92. Leucker TM, Gerstenblith G, Schär M, Brown TT, Jones SR, Afework Y, et al. Evolocumab, a PCSK9-monoclonal antibody, rapidly reverses coronary artery endothelial dysfunction in people living with HIV and people with dyslipidemia. *J Am Heart Assoc*. (2020) 9:e016263. doi: 10.1161/JAHA.120.016263
  93. Shah SJ, Lam CSP, Svedlund S, Saraste A, Hage C, Tan R-S, et al. Prevalence and correlates of coronary microvascular dysfunction in heart failure with preserved ejection fraction: PROMIS-HFpEF. *Eur Heart J*. (2018) 39:3439–50. doi: 10.1093/eurheartj/ehy531
  94. Beltrame JF, Crea F, Kaski JC, Ogawa H, Ong P, Sechtem U, et al. International standardization of diagnostic criteria for vasospastic angina. *Eur Heart J*. (2015) 38:ehv351. doi: 10.1093/eurheartj/ehv351
  95. Rahman H, Demir OM, Ryan M, McConkey H, Scannell C, Ellis H, et al. Optimal use of vasodilators for diagnosis of microvascular angina in the cardiac catheterization laboratory. *Circ Cardiovasc Interv*. (2020) 13:e009019. doi: 10.1161/CIRCINTERVENTIONS.120.009019
  96. Löffler AI, Bourque JM. Coronary microvascular dysfunction, microvascular angina, and management. *Curr Cardiol Rep*. (2016) 18:1. doi: 10.1007/s11886-015-0682-9
  97. Thomson LEJ, Wei J, Agarwal M, Haft-Baradaran A, Shufelt C, Mehta PK, et al. Cardiac magnetic resonance myocardial perfusion reserve index is reduced in women with coronary microvascular dysfunction: a national heart, lung, and blood institute-sponsored study from the women's ischemia syndrome evaluation. *Circ Cardiovasc Imaging*. (2015) 8:10. doi: 10.1161/CIRCIMAGING.114.002481
  98. Zhou W, Lee JCY, Leung ST, Lai A, Lee T-F, Chiang JB, et al. Long-term prognosis of patients with coronary microvascular disease using stress perfusion cardiac magnetic resonance. *JACC Cardiovasc Imaging*. (2021) 14:602–11. doi: 10.1016/j.jcmg.2020.09.034
  99. Matsue Y, Suzuki M, Nagahori W, Ohno M, Matsumura A, Hashimoto Y, et al. Endothelial dysfunction measured by peripheral arterial tonometry predicts prognosis in patients with heart failure with preserved ejection fraction. *Int J Cardiol*. (2013) 168:36–40. doi: 10.1016/j.ijcard.2012.09.021

**Conflict of Interest:** AA-Z has received research support from Canon Medical Systems. AL serves as a consultant for Itamar Medical.

The remaining authors declare that the research was conducted in the absence of any commercial or financial relationships that could be construed as a potential conflict of interest.

**Publisher's Note:** All claims expressed in this article are solely those of the authors and do not necessarily represent those of their affiliated organizations, or those of the publisher, the editors and the reviewers. Any product that may be evaluated in this article, or claim that may be made by its manufacturer, is not guaranteed or endorsed by the publisher.

Copyright © 2022 Minhas, Goerlich, Corretti, Arbab-Zadeh, Kelle, Leucker, Lerman and Hays. This is an open-access article distributed under the terms of the Creative Commons Attribution License (CC BY). The use, distribution or reproduction in other forums is permitted, provided the original author(s) and the copyright owner(s) are credited and that the original publication in this journal is cited, in accordance with accepted academic practice. No use, distribution or reproduction is permitted which does not comply with these terms.



# Regional Fat Distributions Are Associated With Subclinical Right Ventricular Dysfunction in Adults With Uncomplicated Obesity

Jing Liu<sup>1†</sup>, Jing Li<sup>2†</sup>, Jianqun Yu<sup>1</sup>, Chunchao Xia<sup>1</sup>, Huaxia Pu<sup>1</sup>, Wenzhang He<sup>1</sup>, Xue Li<sup>1</sup>, Xiaoyue Zhou<sup>3</sup>, Nanwei Tong<sup>2\*</sup> and Liqing Peng<sup>1\*</sup>

<sup>1</sup> Department of Radiology, West China Hospital, Sichuan University, Chengdu, China, <sup>2</sup> Department of Endocrinology and Metabolism, West China Hospital, Sichuan University, Chengdu, China, <sup>3</sup> MR Collaboration, Siemens Healthineers Ltd., Shanghai, China

## OPEN ACCESS

### Edited by:

Alexander Meyer,  
German Heart Center Berlin, Germany

### Reviewed by:

Radu Tanacli,  
German Heart Center Berlin, Germany  
Philippe Obert,  
University of Avignon, France

### \*Correspondence:

Nanwei Tong  
tongnw@scu.edu.cn  
Liqing Peng  
pengliqing@wchscu.cn

<sup>†</sup>These authors have contributed  
equally to this work and share first  
authorship

### Specialty section:

This article was submitted to  
Cardiovascular Imaging,  
a section of the journal  
Frontiers in Cardiovascular Medicine

Received: 13 November 2021

Accepted: 22 March 2022

Published: 25 April 2022

### Citation:

Liu J, Li J, Yu J, Xia C, Pu H, He W,  
Li X, Zhou X, Tong N and Peng L  
(2022) Regional Fat Distributions Are  
Associated With Subclinical Right  
Ventricular Dysfunction in Adults With  
Uncomplicated Obesity.  
Front. Cardiovasc. Med. 9:814505.  
doi: 10.3389/fcvm.2022.814505

**Objective:** Obesity is a prominent public health problem that has increased cardiovascular mortality risks. However, the specific effects of obesity, independent of comorbidities, on cardiac structure and function have not been well clarified, especially those effects on the right ventricle (RV). Cardiovascular magnetic resonance (CMR) tissue tracking can assess detailed RV mechanical features. This study aimed to evaluate RV strain using CMR in uncomplicated obese adults and assess its association with fat distributions.

**Methods:** A total of 49 obese patients and 30 healthy controls were included. The RV global systolic function and strain parameters based on CMR were assessed. Body fat distributions were measured with dual X-ray absorptiometry. RV function indices of obese patients were compared with those of healthy controls. Correlations among related body fat distribution parameters and RV function indices were conducted with multivariable linear regression.

**Results:** Compared with healthy controls, the obese group had impaired RV strain with lower global longitudinal peak strain (PS), longitudinal peak systolic strain rate (PSSR), circumferential and longitudinal peak diastolic strain rates (PDSR) (all  $P < 0.05$ ), while LV and RV ejection fractions were not significantly different between the two groups ( $P > 0.05$ ). Multivariable linear regression analysis demonstrated that android fat% was independently associated with longitudinal PS ( $\beta = -0.468$ , model  $R^2 = 0.219$ ), longitudinal PDSR ( $\beta = -0.487$ , model  $R^2 = 0.237$ ), and circumferential PSSR ( $\beta = -0.293$ , model  $R^2 = 0.086$ ). Trunk fat% was independently associated with longitudinal PSSR ( $\beta = -0.457$ , model  $R^2 = 0.209$ ). In addition, the strongest correlations of circumferential PDSR were BMI and gynoid fat% ( $\beta = -0.278$ ,  $\beta = 0.369$ , model  $R^2 = 0.324$ ).

**Conclusions:** Extensive subclinical RV dysfunction is found in uncomplicated obese adults. BMI, as an index of overall obesity, is independently associated with subclinical RV dysfunction. In addition, central obesity (android fat and trunk fat distributions) has

a negative effect on subclinical RV function, while peripheral obesity (gynoid fat distribution) may have a positive effect on it.

**Clinical Trials Registration:** Effect of lifestyle intervention on metabolism of obese patients based on smart phone software (ChiCTR1900026476).

**Keywords:** regional fat distributions, cardiovascular magnetic resonance, right ventricular, obesity, strain

## INTRODUCTION

Overweight and obesity have rapidly increased global disease burden over the last decades. To date, no country has successfully reversed this obesity epidemic (1, 2). Since the beginning of the 21st century, obesity has become an epidemic in China caused by rapid economic growth with an estimated increase in prevalence of obesity of 0.32% per year (3). Obesity-related comorbidities, such as diabetes, hypertension, and coronary heart disease, are major risk factors that contribute to heart failure. However, in obese subjects with no clinically apparent cardiovascular risk factors, subclinical structural and functional changes can also be noted, which predisposes these individuals to heart failure at some point (4, 5). Previous studies examining cardiac function and the cardiovascular system have mainly focused on obese patients with comorbidities, while only few researches have focused on obese subjects without clinical signs or comorbidities. Specific right ventricular (RV) functional changes on CMR have not been studied in this subset of obese patients.

RV function assessment has been known to provide a prognostic role in several cardiac diseases (6). Previous echocardiographic studies evaluated RV functional strain in obese adults (4, 5, 7, 8). However, a review compared cardiac strain evaluations using cardiac magnetic resonance (CMR) and speckle tracking echocardiography (STE) and found that the STE technique had a major limitation, which greatly depended on image quality. Indeed, compared with CMR, echocardiographic images had lower signal-to-noise ratio (SNR) and inadequate imaging of some myocardial segments, especially in the distal part of the ultrasound sector (9). In obese subjects, signal interference due to excessive adiposity makes echocardiography more challenging. The advantages of CMR include larger fields of view, higher SNR, and 3-dimensional imaging of the heart, enabling the assessment of ventricular geometry and function with high accuracy and reproducibility (10). In clinical practice, ejection fraction (EF) is most widely used in evaluating global ventricular function; however, EF might not be a sensitive indicator of early RV dysfunction in obese subjects (7). Currently, the CMR tissue tracking technique is widely used as a subclinical myocardial dysfunction indicator for its high sensitivity when measuring global and regional cardiac mechanics through tracking myocardial motion (11). According to our literature search, only one article on children with uncomplicated obesity using CMR was identified. That article indicated that obese/overweight children had greater RV mass indices and lower RV free wall longitudinal strain (12). Until now, no studies have documented RV strain changes in obese adults with no clinical signs or comorbidities using CMR tissue tracking.

Body mass index (BMI) is the most widely used index of general obesity and is associated with other cardiovascular disease risks. Previous studies have found that different regions of fat deposition have various effects on the heart. For example, one study showed that visceral fat rather than subcutaneous fat was significantly associated with decreased RV strain (13). Dual X-ray absorptiometry (DXA) has also been extensively applied as it allows to accurately assess regional fat distributions, such as fat of the android, gynoid, trunk, upper and lower extremities, and visceral regions. A study examining the relationship between regional body fat and LV subendocardial viability ratios indicated that subjects with abdominal fat distribution (android-to-gynoid fat mass ratio) had poorer LV function (14). To our knowledge, no studies have focused on the association between regional fat distributions on RV function in obese individuals with no clinical signs or comorbidities. We aimed to evaluate RV functional changes seen on CMR in obese adults with no clinical signs or comorbidities and the association between RV strain and fat distributions.

## METHODS AND MATERIALS

### Study Population

We prospectively recruited 49 obese subjects defined by a BMI  $\geq 27.5$  kg/m<sup>2</sup> (ranging from 27.5 to 34.9 kg/m<sup>2</sup>) and 30 healthy volunteers ( $18.5 \leq \text{BMI} \leq 23.0$  kg/m<sup>2</sup>) between 18 and 60 years old from September 2019 to September 2021. Subjects were excluded if they had any of the following conditions: hypertension or diabetes measured by oral glucose tolerance; history of cardiovascular diseases or history of any cardiovascular procedures; major systemic diseases that could affect the myocardium, such as connective tissue diseases and sarcoidosis; endocrine disease, such as hyperthyroidism and hypothyroidism; metabolic diseases, such as a history of alcohol abuse or amyloidosis; obstructive sleep apnea; any contraindication to CMR imaging. The study complied with the Declaration of Helsinki and was approved by the Institutional Review Board of the West China Hospital in Sichuan University. Written informed consent was obtained from all study participants.

### Baseline Data Collection

Baseline data of the participants were collected, including medical history, anthropometric measurements (weight and height), heart rate, and blood pressure. Fasting blood glucose and serum lipid profiles, including triglycerides, total cholesterol, high-density lipoprotein (HDL), and low-density lipoprotein (LDL), were also measured.

## Assessment of Obesity

Waist circumference (WC) was measured at the midway between the last rib and the iliac crest, and hip circumference (HC) was measured at the largest diameter of the hip. WC and HC were measured to the nearest 0.5 cm. The waist-to-hip ratio and waist-to-height ratio were calculated. Body mass index (BMI) ( $\text{kg}/\text{m}^2$ ) was calculated as weight (kg) divided by height squared ( $\text{m}^2$ ). According to the Chinese criteria, BMI was categorized into the following three groups: healthy weight ( $18.5\text{--}23.0 \text{ kg}/\text{m}^2$ ), overweight ( $23.0\text{--}27.5 \text{ kg}/\text{m}^2$ ), and obese ( $\geq 27.5 \text{ kg}/\text{m}^2$ ) (15). Total fat, android fat, gynoid fat, trunk fat, upper and lower extremities fat, and visceral fat mass (g) were measured using DXA (Lunar iDXA, GE Medical Systems Lunar, Madison, USA). Specifically, the region of interest (ROI) of android fat distribution was defined from the pelvic cut (lower boundary) to above the pelvis cut by 20% of the distance between the iliac crest and chin (upper boundary). The gynoid fat distribution ROI upper boundary was 1.5 times the height of the android ROI below the iliac crest to a line equal to twice the height of the android fat distribution ROI (lower boundary) (16). Percentage of fat mass in android, gynoid, trunk, peripheral, upper extremities and lower extremities, and visceral regions reflect fat deposition in the corresponding regions, relative to total fat mass. Peripheral fat mass was calculated as the sum of upper and lower extremities fat mass. Percentage of fat mass in trunk, android, and visceral regions (also expressed as trunk fat%, android fat%, and visceral fat%) were indices predictive of central obesity. While Percentage of fat mass in gynoid, peripheral, upper extremities and lower extremities regions (also expressed as gynoid fat%, peripheral fat%, upper extremities fat%, and lower extremities fat%) were indices predictive of peripheral obesity.

## CMR Protocol

CMR examinations were performed using a 3 Tesla whole-body scanner (MAGNETOM Skyra, Siemens Healthcare, Erlangen, Germany) with an 18-channel phased-array body coil on patients in a supine position. With a standard ECG-triggering device, data was acquired during the end-expiratory breath-hold period. A segmented breath-hold balanced steady-state free precession (bSSFP) sequence was used to obtain 8–14 contiguous cine images from the base to the apex in the short-axis view and the two- and four-chamber cine images in the long-axis view. The bSSFP parameters are as follows  $\text{TR}/\text{TE} = 3.3/1.22 \text{ ms}$ , flip angle =  $41^\circ$ , slice thickness = 8 mm, field of view =  $360 \times 320 \text{ mm}^2$ , matrix size =  $208 \times 166$ , and a temporal resolution = 39.34 ms.

## CMR Image Analysis

All CMR data was imported to commercially available software (CVI 42 version 5.11.3, Circle Cardiovascular Imaging Inc., Calgary, Canada). Two radiologists with more than 3 years of CMR experience analyzed the measurements and were blinded to the subject status (obesity vs. control).

## Epicardial Adipose Tissue Quantification

Epicardial adipose tissue (EAT) represents high-signal intensity region between the myoepicardium and parietal pericardium.

The EAT volume was measured on the short-axis cine slices during the end-diastolic phase. The myoepicardial and parietal pericardial contours were manually delineated per slice, extending from the mitral valve hinge down to the ventricular apex. High-signal intensity regions between the myoepicardium and parietal pericardium were semi-automatically traced and calculated, excluding blood vessels.

## Global Ventricular Geometry and Function

The endocardial and epicardial contours of the right ventricle (RV) and left ventricle (LV) myocardium on the short-axis cine images were manually traced during the end-diastolic and end-systolic phases of the CVI42 short-3D module software. The global conventional functional parameters, namely EF, end-diastolic volume (EDV), end-systolic volume (ESV), and LV mass at end-diastole, were automatically computed. In addition, the average LV regional values for 16 myocardial segment thicknesses (American Heart Association standard segmentation model) were also automatically computed. Finally, the LV thickness and interventricular septal (IVS) thickness averages were calculated.

## RV and LV Strain

The long-axis 4-chamber, 2-chamber and short-axis cine slices were transferred to the three-dimensional tissue tracking module for RV and LV myocardial strain analysis. The endocardial and epicardial contours were manually delineated per slice during the end-diastolic phase in all series, and the papillary muscles and moderator bands were excluded (Figure 1). Strain is defined as the degree of myocardial deformation from its initial length ( $L_0$ , in end-diastole) to its maximum length ( $L$ , in end-systole):  $\text{myocardial strain} = (L - L_0)/L_0$ . Strain rate represents the rate of length shortening (17). For different directions of myocardial deformation, the RV and LV global myocardial strain parameters, including the radial, circumferential, and longitudinal peak strains (PS), peak systolic strain rates (PSSR), and peak diastolic strain rates (PDSR) can be calculated. Since RV radial deformation values had low reproducibility and high variability due to the complex morphologic structure and relatively thin ventricular wall, the related parameters (radial PS, PSSR, and PDSR) were excluded.

## Reproducibility

Intra- and inter-observer variabilities for the EAT and RV myocardial strain indices were analyzed in 20 random subjects, including 12 obese patients and 8 healthy controls. To determine intra-observer variability, one radiologist measured the same image within a 1-month interval. To evaluate the inter-observer variability, the second radiologist, who was blinded to the first observer's results, re-analyzed the measurements.

## Statistical Analysis

All statistical analyses were performed using SPSS software (version 23, IBM, Armonk, Armonk, New York, USA). Continuous data with normal distributions were compared between the obese and healthy groups with the student's  $t$ -test and were expressed as the mean  $\pm$  SD. Binary variables were analyzed using the cross tabs Chi-square test. Correlations

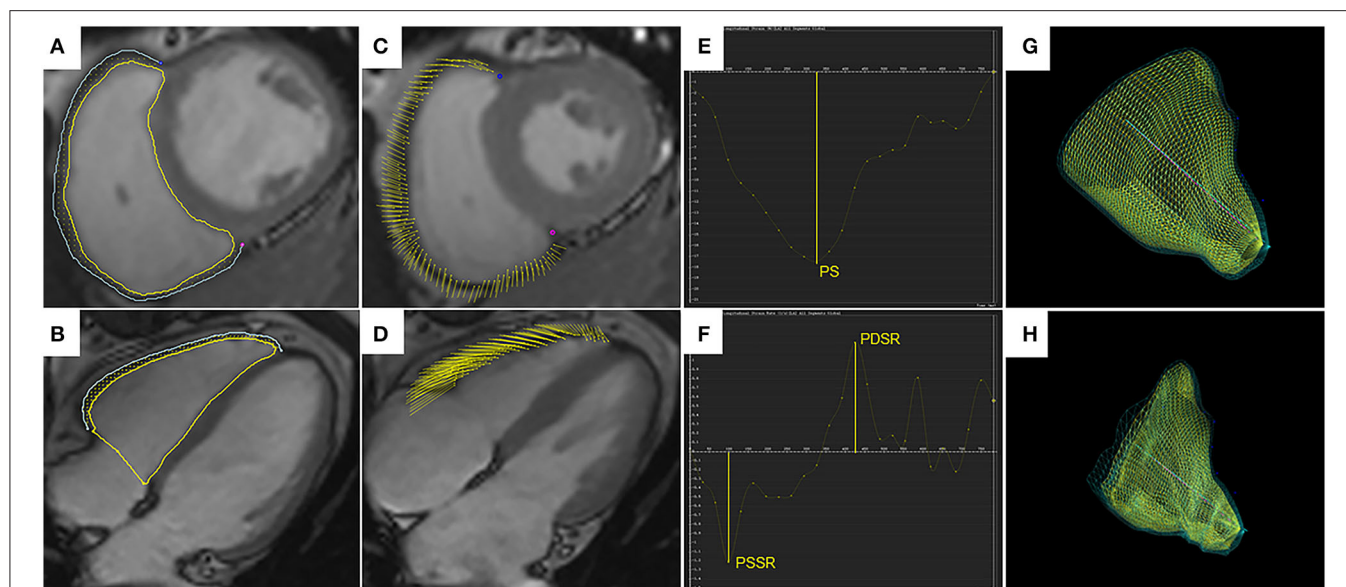


**FIGURE 1 |** Right ventricular tissue tracking using cardiac magnetic resonance imaging. Right ventricular (RV) contours are delineated on the short-axis SSFP image (A) and the four-chamber image (B), shown for the end-diastolic phase. Yellow and blue lines represent RV endocardial and epicardial borders, and yellow dots between the borders represent myocardial points. (C,D) demonstrate myocardial points motion from the end-diastolic phase to the end-systolic phase using tissue tracking. (E,F) show strain curve and strain rate curve. The peak strain (PS) and strain rates (PSSR and PDSR) can be acquired in the curves. 3D models of the RV in the end-diastolic phase (G) and the end-systolic phase (H). SSFP, steady-state free precession; PS, peak strain; PSSR, peak systolic strain rate; PDSR, peak diastolic strain rate; 3D, three-dimensional.

between RV functional parameters and LVEF and LV geometry (mass and thickness) and IVS thickness were assessed in obese patients. Pearson's correlation coefficient was used to determine the correlations between regional fat, blood lipids, and RV functional parameters (global function and strain indices) in whole population. Stepwise multivariable linear regression was used to estimate the associations between regional fat distributions and RV functional parameters in whole population. Related fat distribution, including android fat%, gynoid fat%, trunk fat%, peripheral fat%, visceral fat%, EAT were entered in univariable analyses. Variables with statistical significance in the univariable analyses were then included in a stepwise multivariable analysis. In order to determine the association between obesity and RV function independent of growth differences, age and sex were added in multivariable analyses. The intraclass correlation coefficient (ICC) was used to evaluate both inter- and intra-observer variabilities. A  $P < 0.05$  indicated statistical significance.

## RESULTS

### Baseline Characteristics

This study included 49 obese subjects ( $\text{BMI } 29.9 \pm 2.0 \text{ kg/m}^2$ ) and 30 healthy controls ( $19.7 \pm 1.1 \text{ kg/m}^2$ ), and the baseline characteristics of the patients are shown in **Table 1**. Mean age, height, male proportion, and heart rate were compared and the differences between the two groups were not statistically significant. Compared with healthy controls, obese subjects had

higher blood pressure, although it was within the normal range. For blood parameters, the obese group had higher fasting blood glucose, triglycerides, total cholesterol, and LDL, and lower HDL compared with the healthy group. The obese group had greater conventional fat indexes, including WC, HC, waist-to-hip ratio, and waist-to-height ratio compared to healthy group. Additionally, the obese group had greater DXA-related central fat deposition indexes, including trunk fat%, visceral fat%, and android fat% compare those of healthy group. In contrast, they had lower DXA-related peripheral fat deposition indexes including gynoid fat%, peripheral fat%, and lower extremities fat% compared with healthy individuals. The obese group had greater EAT than those of healthy group.

### Comparison of CMR Findings Between the Obese Subjects and Healthy Controls

The RVEF and LVEF were within the normal range ( $\text{RVEF} > 40\%$  and  $\text{LVEF} > 50\%$ ) for all obese patients and neither were statistically different between the two groups ( $51.2 \pm 4.3\%$  vs.  $50.9 \pm 4.6\%$ ,  $P = 0.087$ ;  $60.9 \pm 4.5\%$  vs.  $62.7 \pm 4.6\%$ ,  $P = 0.091$ , respectively) compared with the controls. Compared with the healthy controls, obese patients exhibited greater RV sizes (RVEDV, RVESV), LV sizes (LVEDV, LVESV), LV geometric parameters (LV mass and LV average thickness), and IVS average thickness. For RV strain, the obese group showed lower global longitudinal PS, PSSR and PDSR, circumferential PDSR, and preserved circumferential PS and PSSR compared with the control group (**Figure 2**). For LV strain, the obese group showed

**TABLE 1** | Baseline characteristics of the study cohort.

| Variables                      | Controls<br>(n = 30) | Obese<br>patients<br>(n = 49) | P-value |
|--------------------------------|----------------------|-------------------------------|---------|
| Demographics                   |                      |                               |         |
| Male, n (%)                    | 10 (33.3)            | 27 (55.1)                     | 0.06    |
| Age (years)                    | 28.8 ± 7.1           | 32.6 ± 8.8                    | 0.05    |
| Height (cm)                    | 164.4 ± 8.1          | 167.6 ± 9.4                   | 0.130   |
| Weight (kg)                    | 53.2 ± 5.3           | 84 ± 11                       | <0.001* |
| BMI (kg/m <sup>2</sup> )       | 19.7 ± 1.1           | 29.9 ± 2.0                    | <0.001* |
| Hemodynamic variables          |                      |                               |         |
| Heart rate (bpm)               | 73.4 ± 8.1           | 73.7 ± 9.6                    | 0.860   |
| SBP (mmHg)                     | 104 ± 12             | 123.5 ± 9.9                   | <0.001* |
| DBP (mmHg)                     | 70.4 ± 8.1           | 78.9 ± 6.5                    | <0.001* |
| Laboratory data                |                      |                               |         |
| Fasting blood glucose (mmol/L) | 4.7 ± 0.3            | 5.4 ± 0.7                     | <0.001* |
| Plasma triglycerides (mmol/L)  | 0.6 ± 0.2            | 1.9 ± 1.4                     | <0.001* |
| Total cholesterol (mmol/L)     | 3.9 ± 0.7            | 4.9 ± 1.1                     | <0.001* |
| HDL (mmol/L)                   | 1.6 ± 0.3            | 1.3 ± 0.3                     | <0.001* |
| LDL (mmol/L)                   | 2.1 ± 0.6            | 2.7 ± 0.8                     | <0.001* |
| Fat distribution               |                      |                               |         |
| EAT (cm <sup>3</sup> )         | 20.6 ± 7.9           | 48 ± 14                       | <0.001* |
| Total fat (kg)                 | 12.0 ± 3.0           | 29.3 ± 5.7                    | <0.001* |
| Android fat%                   | 5.7 ± 1.1            | 9.8 ± 1.5                     | <0.001* |
| Gynoid fat%                    | 18.4 ± 2.9           | 14.9 ± 2.0                    | <0.001* |
| Trunk fat%                     | 44.9 ± 4.6           | 57.7 ± 4.7                    | <0.001* |
| Peripheral fat%                | 47.5 ± 5.1           | 38.5 ± 5.0                    |         |
| Upper extremities fat%         | 11.1 ± 0.2           | 10.5 ± 0.2                    | 0.08    |
| Lower extremities fat%         | 36.4 ± 4.9           | 28.0 ± 4.2                    | <0.001* |
| Visceral fat%                  | 2.0 ± 1.4            | 4.9 ± 2.5                     | <0.001* |
| Waist circumference (cm)       | 72.1 ± 4.7           | 100 ± 11                      | <0.001* |
| Hip circumference (cm)         | 92.1 ± 3.9           | 107.3 ± 4.1                   | <0.001* |
| Waist-to-height ratio          | 0.78 ± 0.05          | 0.93 ± 0.09                   | <0.001* |
| Waist-to-hip ratio             | 0.4 ± 0.2            | 0.60 ± 0.06                   | <0.001* |

BMI, body mass index; SBP, systolic blood pressure; DBP, diastolic blood pressure; HDL, high-density lipoprotein; LDL, low-density lipoprotein; EAT, epicardial adipose tissue.

\* $P < 0.05$ .

lower global longitudinal and circumferential PS and preserved radial PS compared with the control group (Table 2).

## Associations Between RV Strain Parameters, Biventricular Geometries, and Global Systolic Function in Obese Individuals

Among obese subjects, the RVEF had a positive correlation with the circumferential PS and longitudinal PS ( $r = 0.419$  and  $r = 0.328$ ); whereas RV size (RVEDV and RVESV), LV size (LVEDV and LVESV), LV mass, LV average thickness, and ISV average thickness showed weak-moderate negative correlations with RV strain indices ( $r = -0.3$  to  $-0.5$ ). Among them, LV average thickness was strongest for the longitudinal PS ( $r = -0.504$ ). In addition, LVEF was positively correlated with RV longitudinal PS, PSSR, and PDSR ( $r = 0.3$  to  $0.4$ );

LV longitudinal, circumferential, and radial PS had positive correlations with the RV strain parameters ( $r = 0.3$  to  $0.4$ ) (Table 3).

## Association Between Regional Fat Distributions and Cardiovascular Risk Factors in Whole Population

BMI, EAT, android fat%, and trunk fat% were positively correlated with fasting blood glucose, triglycerides, total cholesterol, and LDL ( $r = 0.3$  to  $0.6$ ), while were negatively correlated with HDL ( $r = -0.4$  to  $-0.6$ ). In contrast, gynoid fat% had negative associations with triglycerides, total cholesterol, and LDL ( $-0.2$  to  $-0.5$ ), while had a positive association with HDL ( $r = 0.484$ ); peripheral fat% was negatively associated with fasting blood glucose and total cholesterol ( $r = -0.236$ ;  $r = -0.232$ ) (Table 4).

## Association Between Adiposity and RV Functional Parameter in Whole Population

Univariable analysis showed that BMI, android fat% and trunk fat% were negatively associated with longitudinal PS, longitudinal and circumferential strain rate (PSSR and PDSR) ( $r = -0.3$  to  $-0.5$ ). Visceral fat% and EAT were negatively associated with circumferential PDSR and longitudinal PS, PSSR and PDSR ( $r = -0.3$  to  $-0.4$ ). In contrast, gynoid fat% and peripheral fat% were positively associated with circumferential PDSR, and longitudinal PS, PSSR and PDSR ( $r = 0.4$  to  $0.5$ ); gynoid fat% was positively associated with RVEF ( $r = 0.264$ ) (Table 5 and Figure 3).

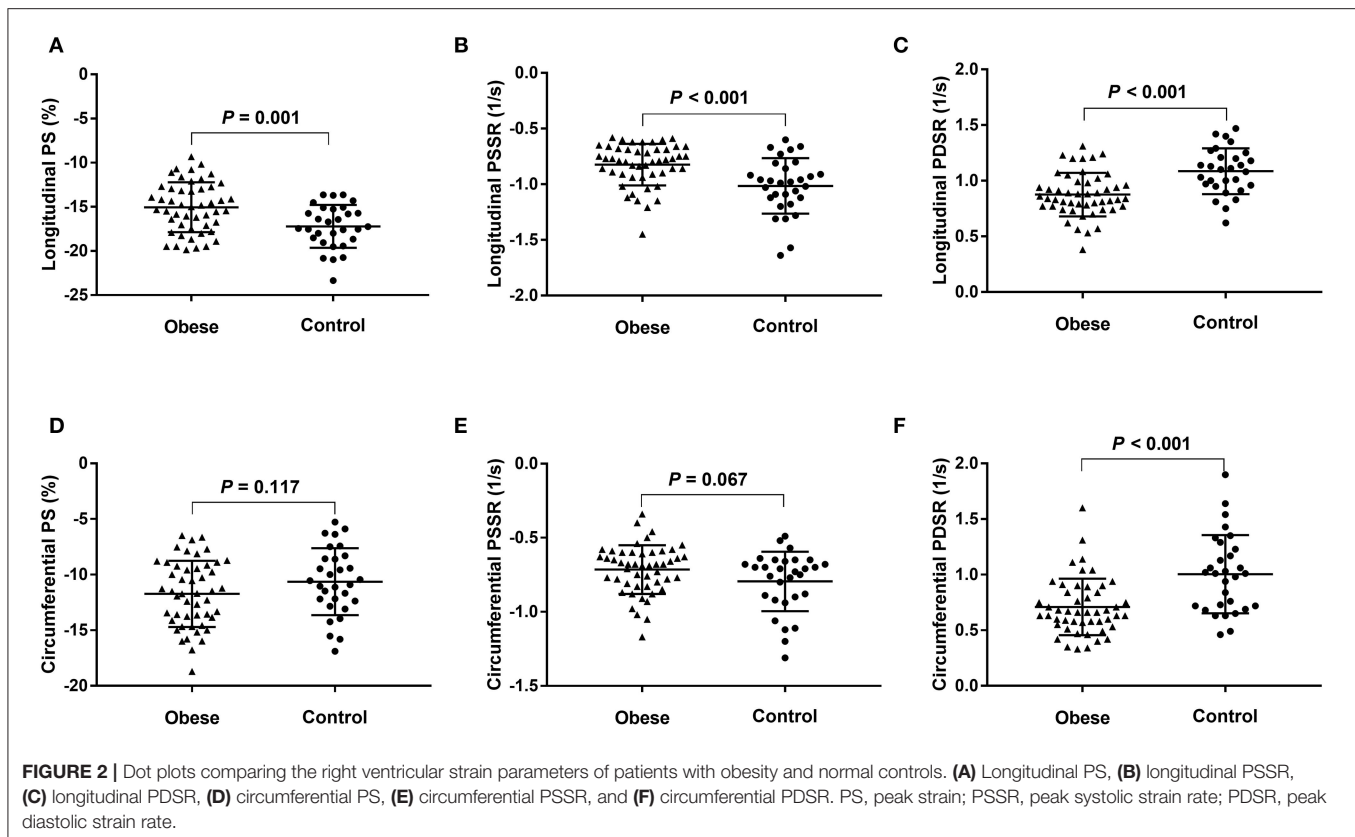
Multivariable linear regression analysis demonstrated that android fat% was independently associated with longitudinal PS ( $\beta = -0.468$ ,  $P < 0.001$ , model  $R^2 = 0.219$ ), longitudinal PDSR ( $\beta = -0.487$ ,  $P < 0.001$ , model  $R^2 = 0.237$ ), and circumferential PSSR ( $\beta = -0.293$ ,  $P = 0.009$ , model  $R^2 = 0.086$ ). Trunk fat% was independently associated with longitudinal PSSR ( $\beta = -0.457$ ;  $P < 0.001$ , model  $R^2 = 0.209$ ). In addition, the strongest correlates of circumferential PDSR were BMI and gynoid fat% ( $\beta = -0.278$ ,  $P = 0.016$ ;  $\beta = 0.369$ ,  $P = 0.002$ ; model  $R^2 = 0.324$ ) (Table 6).

## Intra-observer and Inter-observer Variability

The intra- and inter-observer variability for EAT quantifications and strain parameters are summarized in Table 7. The ICCs for intra- and inter-observer variability were 0.833 and 0.790 for EAT, respectively. There were good intra- and inter-observer agreements for the RV strain parameters (ICC = 0.794–0.921 and 0.773–0.920, respectively), and circumferential and longitudinal strains had better repeatability than the strain rates.

## DISCUSSION

In this study, we compared RV functional parameters in adults with uncomplicated obesity with those in normal controls using CMR and assessed associations between fat distributions and RV function in whole population. The main findings were as follows:



(1) although the RVEF was within the normal range in both groups, the subjects with obesity had impaired RV myocardial contractility manifested by lower longitudinal PS, longitudinal PSSR, and circumferential and longitudinal PDSR; (2) Decreased LV longitudinal and circumferential PS and preserved LVEF in obese group compared with healthy group. (3) the individuals with obesity had cardiac remodeling with greater RV size, LV size, LV myocardial mass, and LV wall thickness compared with controls; (4) the impaired subclinical RV function was associated with cardiac remodeling; (5) BMI, as an index of overall obesity, was independently associated with subclinical RV dysfunction. In addition, central fat distribution indicators (android fat% and trunk fat%) were negatively correlated with subclinical RV function, whereas peripheral fat distribution indicator (gynoid fat%) was positively correlated with it. Until now, no studies have documented RV strain changes in obese adults with no clinical signs or comorbidities using CMR tissue tracking and the associations between DXA-related fat distributions and RV function.

## Obesity and RV Dysfunction

Our study revealed no statistical differences for RVEFs between the two groups, indicating a lack of global right ventricular systolic functional impairment. This result is consistent with that of previous echocardiographic studies of obese adults without known cardiovascular diseases (4, 7). Nevertheless, a CMR study exhibited lower RVEF in obese group compared with the

control group, in which partial participants were diagnosed with hypertension or diabetes (18). The difference between two CMR studies may be attributed to the multi-ethnic participants that were older in age (ranging from 45 to 84 years old) and had obesity-related complications in previous study. Furthermore, our study showed decreased RV longitudinal PS and strain rates (PSSR and PDSR) of obese participants compared with those of normal controls. These results are similar with those of several other echocardiographic studies in obese adults (4, 5, 7, 8). There are only subendocardial and subepicardial layers in the RV myocardium. Longitudinal deformation is primarily caused by the shortening of longitudinal myocardial fibers located in the subendocardial layer (17). Obesity can alter myocardial perfusion, resulting in myocardial ischemia, and meanwhile the subendocardial layer is vulnerable to microvascular ischemia (19). Moreover, our study also revealed impaired circumferential RV mechanics, represented by decreased circumferential PDSR in obese group compared with those in healthy group, which has not been previously reported. Notably, the differences in circumferential PS and PSSR between two groups were not statistically significant, confirming that PDSR is more sensitive to subclinical myocardial dysfunction than either PS or PSSR in obesity. Circumferential strain largely reflects the circumferentially oriented myofibers in the subepicardial layer (20) which might indicate that the myocardial injury is not only in the subendocardial layer but also in the subepicardial layer of the RV myocardium in obese patients. In summary, subclinical

**TABLE 2 |** Comparison of cardiac magnetic resonance parameters between two groups.

| Variables                  | Controls<br>(n = 30) | Obese<br>patients<br>(n = 49) | P-value |
|----------------------------|----------------------|-------------------------------|---------|
| RV global function         |                      |                               |         |
| RVEF                       | 51.2 ± 4.3           | 50.9 ± 4.6                    | 0.087   |
| RVEDV (ml)                 | 136 ± 30             | 163 ± 38                      | <0.001* |
| RVESV (ml)                 | 67 ± 18              | 81 ± 24                       | <0.001* |
| RV strain                  |                      |                               |         |
| Circumferential PS (%)     | -10.6 ± 3.0          | -11.7 ± 3.0                   | 0.117   |
| Circumferential PSSR (1/s) | -0.8 ± 0.2           | -0.7 ± 0.2                    | 0.067   |
| Circumferential PDSR (1/s) | 1.0 ± 0.3            | 0.7 ± 0.3                     | <0.001* |
| Longitudinal PS (%)        | -17.2 ± 2.4          | -15.1 ± 2.8                   | 0.001*  |
| Longitudinal PSSR (1/s)    | -1 ± 0.4             | -0.8 ± 0.2                    | <0.001* |
| Longitudinal PDSR (1/s)    | 1.1 ± 0.2            | 0.9 ± 0.2                     | <0.001* |
| LV global function         |                      |                               |         |
| LVEF                       | 60.9 ± 4.5           | 62.7 ± 4.6                    | 0.091   |
| LVEDV (ml)                 | 120 ± 24             | 158 ± 28                      | <0.001* |
| LVESV (ml)                 | 49.1 ± 9.6           | 60 ± 14                       | <0.001* |
| LV mass (g)                | 73 ± 16              | 91 ± 20                       | <0.001* |
| LV average thickness (mm)  | 5.6 ± 0.7            | 6.0 ± 0.8                     | 0.016*  |
| IVS average thickness (mm) | 5.7 ± 0.4            | 6.7 ± 0.9                     | <0.001* |
| LV strain                  |                      |                               |         |
| Longitudinal PS (%)        | -15.8 ± 1.9          | -13.5 ± 2.9                   | <0.001* |
| Circumferential PS (%)     | -20.7 ± 1.9          | -19.6 ± 2.0                   | 0.018*  |
| Radial PS (%)              | 34.6 ± 5.5           | 32.1 ± 5.5                    | 0.057   |

RV, right ventricular; EF, ejection fraction; EDV, end diastolic volume; ESV, end systolic volume; PS, peak strain; PSSR, peak systolic strain rate; PDSR, peak diastolic strain rate; LV, left ventricular; IVS, interventricular septum.

\*P < 0.05.

RV functional impairment occurred before decrease in RVEF in obese participants.

In addition, obese participants had greater RV volumes (RVESV and RVEDV) compared with those of the normal subjects in our study. A echocardiographic study demonstrated that RV volumes significantly increased only in the severely obese group (BMI = 46.8 ± 11 kg/cm<sup>2</sup>), but not in mild-to-moderate obesity (7). Another echocardiographic study showed no changes in RV volumes in mild obese group (4). The results indicate that CMR is more sensitive than echocardiography to measure RV volume. In fact, echocardiography with limited acoustic window, low spatial resolutions, and compromised geometric assumptions, is inaccurate for RV geometric parameter evaluations (21). Meanwhile, RV volumes were negatively associated with RV strain and strain rates in our study. RV dilation is caused by increased total blood volume and cardiac output due to the high metabolic activity of obesity (22). RV dilation can result in contractility impairments due to increased ventricular wall stress (23).

Our study might find ventricular-ventricular interactions in obese individuals. LV myocardial remodeling (greater chamber size, wall thickness, and mass occurred) in obese adults. LV

**TABLE 3 |** Association (correlation coefficients) between cardiac geometry, function, and RV strains in obese patients.

|                       | RV Circumferential |          |          | RV Longitudinal |          |          |
|-----------------------|--------------------|----------|----------|-----------------|----------|----------|
|                       | PS                 | PSSR     | PDSR     | PS              | PSSR     | PDSR     |
| RVEF                  | 0.419**            | 0.252    | 0.154    | 0.328*          | 0.136    | 0.249    |
| RVEDV                 | -0.439**           | -0.395** | -0.398** | -0.365*         | -0.178   | -0.319*  |
| RVESV                 | -0.472**           | -0.401** | -0.362*  | -0.381**        | -0.190   | -0.339*  |
| LVEF                  | 0.130              | 0.112    | 0.007    | 0.311*          | 0.323*   | 0.366**  |
| LVEDV                 | -0.315*            | -0.232   | -0.313*  | -0.213          | -0.295*  | -0.248   |
| LVESV                 | -0.319*            | -0.281   | -0.251   | -0.351*         | -0.397** | -0.417** |
| LV mass               | -0.292*            | -0.223   | -0.333*  | -0.412**        | -0.311*  | -0.185   |
| LV thickness          | -0.362*            | -0.228   | -0.369** | -0.504**        | -0.266   | -0.198   |
| IVS thickness         | -0.295*            | -0.147   | -0.289*  | -0.444**        | -0.201   | -0.192   |
| LV longitudinal PS    | 0.303*             | 0.326*   | 0.286*   | 0.186           | 0.270    | 0.257    |
| LV circumferential PS | 0.301*             | 0.357*   | 0.154    | 0.217           | 0.271    | 0.310*   |
| LV radial PS          | 0.438**            | 0.440**  | 0.224    | 0.375**         | 0.423**  | 0.348*   |

Longitudinal/circumferential PS and PSSR are calculated as absolute values. RV, right ventricular; EF, ejection fraction; EDV, end diastolic volume; ESV, end systolic volume; LV, left ventricular; IVS, interventricular septum; PS, peak strain; PSSR, peak systolic strain rate; PDSR, peak diastolic strain rate.

\*P < 0.05 and \*\*P < 0.01.

**TABLE 4 |** Association between regional fat distributions and cardiovascular risk factors in whole population.

|                 | Fasting<br>blood<br>glucose | Plasma<br>triglycerides | Total<br>cholesterol | HDL      | LDL     |
|-----------------|-----------------------------|-------------------------|----------------------|----------|---------|
| BMI             | 0.445**                     | 0.548**                 | 0.403**              | -0.509** | 0.296** |
| EAT             | 0.446**                     | 0.457**                 | 0.359**              | -0.387** | 0.335** |
| Android fat%    | 0.415**                     | 0.637**                 | 0.429**              | -0.549** | 0.336** |
| Gynoid fat%     | -0.209                      | -0.530**                | -0.305**             | 0.484**  | -0.227* |
| Trunk fat%      | 0.354**                     | 0.644**                 | 0.444**              | -0.554** | 0.334** |
| Peripheral fat% | -0.236*                     | -0.204                  | -0.232*              | 0.076    | -0.178  |
| Visceral fat%   | 0.202                       | 0.531**                 | 0.372**              | -0.474** | 0.301** |

LDL, low-density lipoprotein; HDL, high-density lipoprotein; BMI, body mass index; EAT, epicardial adipose tissue.

\*P < 0.05 and \*\*P < 0.01.

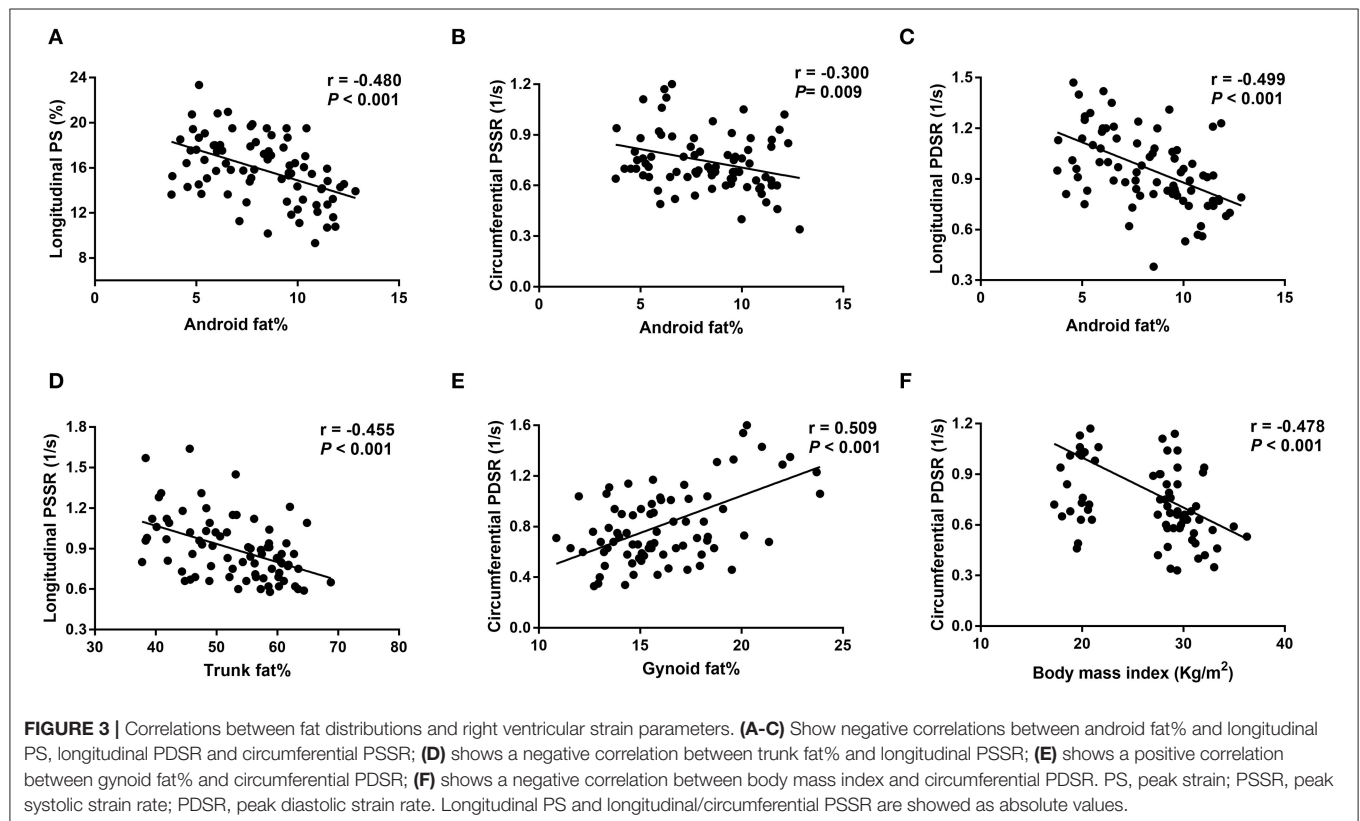
myocardial remodeling was negatively associated with the RV strain parameters, which indicated that RV function could be impacted by LV myocardial remodeling through ventricular-ventricular interactions. Similar results were also reported in a CMR study with uncomplicated obese children (12). In an experimental study of dogs, the RV free wall was electrically isolated and showed that despite stopping the RV free wall pacing in diastole, more than half of the RV systolic pressure and pulmonary flow were obtained in the subsequent heart beat (24). Another study demonstrated that LV shortening contributed to RV stroke exertion when the RV free wall was replaced with a non-contractile patch (25). In other words, LV contraction directly impacts RV function. In our study, LV global longitudinal and circumferential PS decreased in obese group compared with healthy group, indicating LV contraction

**TABLE 5 |** Association between regional fat distributions and RVEF and strain parameters in whole population.

|                 | RVEF   | RV Circumferential |          |          | RV Longitudinal |          |          |
|-----------------|--------|--------------------|----------|----------|-----------------|----------|----------|
|                 |        | PS                 | PSSR     | PDSR     | PS              | PSSR     | PDSR     |
| BMI             | −0.045 | 0.118              | −0.287*  | −0.478** | −0.380**        | −0.428** | −0.464** |
| EAT             | 0.040  | 0.235              | −0.088   | −0.335** | −0.370**        | −0.327** | −0.442** |
| Android fat%    | −0.090 | 0.041              | −0.300** | −0.485** | −0.480**        | −0.476** | −0.499** |
| Gynoid fat%     | 0.264* | 0.060              | 0.174    | 0.509**  | 0.394**         | 0.367**  | 0.391**  |
| Trunk fat%      | −0.130 | 0.037              | −0.279*  | −0.450** | −0.455**        | −0.455** | −0.462** |
| Peripheral fat% | 0.216  | 0.016              | 0.216    | 0.431**  | 0.451**         | 0.440**  | 0.446**  |
| Visceral fat%   | −0.139 | 0.083              | −0.044   | −0.271*  | −0.362**        | −0.340** | −0.372** |

Longitudinal/circumferential PS and PSSR are calculated as absolute values. RV, right ventricular; EF, ejection fraction; PS, peak strain; PSSR, peak systolic strain rate; PDSR, peak diastolic strain rate; BMI, body mass index; EAT, epicardial adipose tissue.

\* $P < 0.05$  and \*\* $P < 0.01$ .



impairment. In general, our results showed that LV myocardial remodeling and contraction impairment in obese patients were responsible for RV subclinical dysfunction.

## Regional Fat Distributions and RV Dysfunction

Our study described the linear relationships between regional fat distributions and RV functional assessments, and the results showed that central fat distribution indicators (android fat% and trunk fat%) had deleterious effects on subclinical RV function, whereas peripheral fat distribution indicator (gynoid fat%) had a positive effect on it. Notably,

our result showed that visceral fat and EAT volume were negatively associated with RV strain in univariate analysis, while no linear relationship with RV strain parameter in multivariate analysis. Previous CMR studies on obesity with no complications have reported that visceral fat, EAT volume or area had linear relationships with LV subclinical dysfunction in multivariate analysis (26, 27). However, whether EAT could predict RV subclinical dysfunction in these patients is still unclear. Additionally, different from the previous studies, we added DXA-related regional fat distributions (android fat, gynoid fat, trunk fat, peripheral fat) into multivariate analysis and they may attenuate

**TABLE 6 |** Multivariable linear regression analysis of association between regional fat distributions and RV strains in whole population.

| Independent variables | Factors in models | R square | Adjusted R square | B      | $\beta$ | P-value |
|-----------------------|-------------------|----------|-------------------|--------|---------|---------|
| Longitudinal PS       | Android fat%      | 0.219    | 0.209             | −0.549 | −0.468  | <0.001  |
| Longitudinal PSSR     | Trunk fat%        | 0.209    | 0.199             | −0.013 | −0.457  | <0.001  |
| Longitudinal PDSR     | Android fat%      | 0.237    | 0.227             | −0.048 | −0.487  | <0.001  |
| Circumferential PSSR  | Android fat%      | 0.086    | 0.074             | −0.022 | −0.293  | 0.009   |
| Circumferential PDSR  | BMI               | 0.324    | 0.306             | −0.017 | −0.278  | 0.016   |
|                       | Gynoid fat%       |          |                   | 0.042  | 0.369   | 0.002   |

Longitudinal PS and longitudinal/circumferential PSSR are showed as absolute values. RV, right ventricular; PS, peak strain; PSSR, peak systolic strain rate; PDSR, peak diastolic strain rate; BMI, body mass index.

**TABLE 7 |** Comparison of inter- and intra-observer variability among epicardial adipose tissue and RV peak strain parameters.

|                      | Intra-observer (n = 20) |             | Inter-observer (n = 20) |             |
|----------------------|-------------------------|-------------|-------------------------|-------------|
|                      | ICC                     | 95% CI      | ICC                     | 95% CI      |
| EAT                  | 0.883                   | 0.705-0.957 | 0.790                   | 0.577-0.923 |
| Circumferential PS   | 0.921                   | 0.864-0.955 | 0.920                   | 0.862-0.976 |
| Longitudinal PS      | 0.906                   | 0.839-0.946 | 0.891                   | 0.808-0.939 |
| Circumferential PSSR | 0.840                   | 0.609-0.941 | 0.782                   | 0.490-0.917 |
| Longitudinal PSSR    | 0.794                   | 0.513-0.922 | 0.773                   | 0.468-0.914 |
| Circumferential PDSR | 0.851                   | 0.627-0.945 | 0.819                   | 0.555-0.933 |
| Longitudinal PDSR    | 0.889                   | 0.711-0.960 | 0.774                   | 0.474-0.914 |

EAT, epicardial adipose tissue; PS, peak strain; PSSR, peak systolic strain rate; PDSR, peak diastolic strain rate; ICC, intraclass correlation coefficient; CI, confidence interval. All  $P < 0.001$ .

the effects of EAT and visceral fat on the RV function. In other words, instead of EAT and visceral fat, trunk fat, android fat or gynoid fat were better predictors of RV subclinical function.

One explanation for the different effects of regional fat distributions on RV function was dyslipidemia. Our study revealed that central obesity parameters (android fat and trunk fat) were positively correlated with triglycerides, total cholesterol, and LDL, while were negatively correlated with HDL. The result is consistent with previous researches which demonstrated that central obesity parameters (android fat or trunk fat distributions) had positive associations with triglycerides and LDL levels, while they had negative associations with HDL levels (28–30). In contrast, we found that gynoid fat distribution had negative associations with triglycerides, total cholesterol, and LDL, while had a positive association with HDL. A previous study has also indicated that gynoid fat% had a negative association with hypertriglyceridemia (31, 32). It is well known that high HDL levels are considered as cardiovascular protective factors, while triglycerides, cholesterol, and LDL levels are considered cardiovascular risk factors. Obesity has also been shown to be associated with increased oxidized lipid levels (33), and oxidized LDL levels and oxidized lipid

derivatives were shown to cause myocardial dysfunction and cardiomyopathy by inducing inflammation, apoptosis, and endoplasmic reticulum stress (34). Anti-oxidation proteins, such as platelet activating factor acetyl hydrolase and paraoxonase, are primarily included in HDL and might mitigate LDL oxidation and remove lipid oxidation products (35). Android fat and trunk fat have also been shown to be important risk factors for insulin resistance (30, 36). A previous study reported that insulin resistance was only found in the women with android obesity, rather than those with gynoid obesity (37). A study on sucrose-fed rats suggested that insulin resistance directly induced cardiac contractile impairments (38), and a clinical study in obese female subjects showed that its link with myocardial fatty acid metabolism could reduce myocardial contractile function (39). Adipokines and chronic inflammatory factors have also been implicated in obesity. Trunk fat and android fat were inversely correlated with adiponectin (40, 41), whereas correlated with increased leptin (42, 43). The leg fat was positively correlated with adiponectin (44). Adiponectin and leptin are proteins secreted by adipose tissue. Adiponectin is associated with antidiabetic and antiatherogenic properties, which mediates insulin-sensitizing effects and reduce hyperlipidemia (45, 46). It is well known that the leptin has beneficial effects on the inhibition of food intake and insulin sensitivity enhancements. However, high circulating leptin levels in obese individuals were mainly caused by leptin resistance, which was associated with increased insulin resistance (47, 48). The individuals with android obesity had elevated necrosis factor alpha- $\alpha$  (TNF- $\alpha$ ) (49). The trunk fat% or android fat% was positively associated with TNF- $\alpha$ , while lower-body fat% or gynoid fat% was negatively associated with it (50). Leg fat was negatively associated with inflammatory markers including interleukin-6 (IL-6), C-reactive protein (CRP), and TNF- $\alpha$  (44, 51). CRP and TNF- $\alpha$  are associated with insulin resistance and atherosclerosis (45, 46, 52). IL-6 has been shown to have a critical role in aldosterone-induced macrophage recruitment and infiltration of myocardial macrophages, which play an important role in myocardial fibrosis (53).

In addition, android fat was correlated with higher blood pressure (29, 41), while the leg fat mass was negatively correlated with SBP (44). A study observing

the relationship between blood pressure and RV function using STE demonstrated that subclinical RV function, assessed by strain, was impaired by increased blood pressure even though blood pressure was within the normal range (54).

## Limitations

There are several limitations in this study. First, this was a cross-sectional study, and we could not determine whether subtle RV contractile impairments cause heart failure with obesity progression and whether these changes can be reversed. Therefore, longitudinal studies are needed to examine dynamic cardiac changes and explore the underlying factors that reverse these changes. Second, past studies have indicated that multiple key inflammatory mediators and insulin resistance are consistently associated with obesity and obesity-related comorbidities. However, we did not examine inflammatory markers and insulin resistance in this study. These laboratory data should be measured and discussed in subsequent studies to clarify the mechanisms of myocardial damage in obese patients.

## CONCLUSIONS

Extensive subclinical RV dysfunction is found in uncomplicated obese adults. BMI, as an index of overall obesity, is independently associated with subclinical RV dysfunction. In addition, central obesity (android fat and trunk fat distributions) has a negative effect on subclinical RV function, while peripheral obesity (gynoid fat distribution) may have a positive effect on it.

## REFERENCES

1. Collaborators GBDO, Afshin A, Forouzanfar MH, Reitsma MB, Sur P, Estep K, et al. Health effects of overweight and obesity in 195 countries over 25 years. *N Engl J Med.* (2017) 377:13-27. doi: 10.1056/NEJMoa1614362
2. Swinburn BA, Kraak VI, Allender S, Atkins VJ, Baker PI, Bogard JR, et al. The global syndemic of obesity, undernutrition, and climate change: the lancet commission report. *Lancet.* (2019) 393:791-846. doi: 10.1016/S0140-6736(18)32822-8
3. Tian Y, Jiang C, Wang M, Cai R, Zhang Y, He Z, et al. BMI, leisure-time physical activity, and physical fitness in adults in China: results from a series of national surveys, 2000-14. *Lancet Diabetes Endocrinol.* (2016) 4:487-97. doi: 10.1016/S2213-8587(16)00081-4
4. Unlu S, Tacoy G. Early adulthood obesity is associated with impaired left ventricular and right ventricular functions evaluated by speckle tracking and 3D echocardiography. *Turk Kardiyol Dern Ars.* (2021) 49:312-20. doi: 10.5543/tkda.2021.57336
5. Orhan AL, Uslu N, Dayi SU, Nurkalem Z, Uzun F, Erer HB, et al. Effects of isolated obesity on left and right ventricular function: a tissue doppler and strain rate imaging study. *Echocardiogr J Card.* (2010) 27:236-43. doi: 10.1111/j.1540-8175.2009.01024.x
6. DeFaria Yeh D, Stefanescu Schmidt AC, Eisman AS, Serfas JD, Naqvi M, Youniss MA, et al. Impaired right ventricular reserve predicts adverse cardiac outcomes in adults with congenital right heart disease. *Heart.* (2018) 104:2044-50. doi: 10.1136/heartjnl-2017-312572

## DATA AVAILABILITY STATEMENT

The raw data supporting the conclusions of this article will be made available by the authors, without undue reservation.

## ETHICS STATEMENT

The studies involving human participants were reviewed and approved by the Institutional Review Board of the West China Hospital in Sichuan University. The patients/participants provided their written informed consent to participate in this study.

## AUTHOR CONTRIBUTIONS

JLiu, JLi, LP, and NT: conception and design and provision of study materials or patients. LP and NT: administrative support and final approval of manuscript. JLiu, JLi, LP, HP, WH, XL, and XZ: collection and assembly of data. JLiu, JLi, and LP: manuscript writing. All authors: data analysis and interpretation.

## FUNDING

This work was supported by the National Natural Science Foundation of China (Grant Number 81601462), the Key Research & Development Project of Science and Technology of Sichuan Province (Grant Number 2021YFS0142), and 1.3.5. project for disciplines of excellence, West China Hospital, Sichuan University (Grant Number ZYGD18017).

7. Wong CY, O'Moore-Sullivan T, Leano R, Hukins C, Jenkins C, Marwick TH. Association of subclinical right ventricular dysfunction with obesity. *J Am Coll Cardiol.* (2006) 47:611-6. doi: 10.1016/j.jacc.2005.11.015
8. Nakanishi K, Daimon M, Yoshida Y, Ishiwata J, Sawada N, Hirokawa M, et al. Relation of body mass index to adverse right ventricular mechanics. *Am J Cardiol.* (2021) 144:137-42. doi: 10.1016/j.amjcard.2020.12.069
9. Pedrizzetti G, Claus P, Kilner PJ, Nagel E. Principles of cardiovascular magnetic resonance feature tracking and echocardiographic speckle tracking for informed clinical use. *J Cardiovasc Magn Reson.* (2016) 18:51. doi: 10.1186/s12968-016-0269-7
10. Grothues F, Smith GC, Moon JC, Bellenger NG, Collins P, Klein HU, et al. Comparison of interstudy reproducibility of cardiovascular magnetic resonance with two-dimensional echocardiography in normal subjects and in patients with heart failure or left ventricular hypertrophy. *Am J Cardiol.* (2002) 90:29-34. doi: 10.1016/S0002-9149(02)02381-0
11. Claus P, Omar AMS, Pedrizzetti G, Sengupta PP, Nagel E. Tissue tracking technology for assessing cardiac mechanics: principles, normal values, and clinical applications. *JACC Cardiovasc Imaging.* (2015) 8:1444-60. doi: 10.1016/j.jcmg.2015.11.001
12. Jing LY, Pulenthiran A, Nevius CD, Mejia-Spiegler A, Suever JD, Wehner GJ, et al. Impaired right ventricular contractile function in childhood obesity and its association with right and left ventricular changes: a cine DENSE cardiac magnetic resonance study. *J Cardiovasc Magn Reson.* (2017) 19:49. doi: 10.1186/s12968-017-0363-5

13. Sawada N, Nakanishi K, Daimon M, Yoshida Y, Ishiwata J, Hirokawa M, et al. Influence of visceral adiposity accumulation on adverse left and right ventricular mechanics in the community. *Eur J Prev Cardiol.* (2020) 27:2006-15. doi: 10.1177/2047487319891286
14. Gonzales JU, Hadri O. Role of heart rate in the relation between regional body fat and subendocardial viability ratio in women. *Clin Exp Pharmacol Physiol.* (2016) 43:789-94. doi: 10.1111/1440-1681.12597
15. Chen YJ, Peng Q, Yang Y, Zheng SS, Wang Y, Lu WL. The prevalence and increasing trends of overweight, general obesity, and abdominal obesity among Chinese adults: a repeated cross-sectional study. *BMC Public Health.* (2019) 19:1293. doi: 10.1186/s12889-019-7633-0
16. Petak S, Barbu CG, Yu EW, Fielding R, Mulligan K, Sabowitz B, et al. The Official Positions of the International Society for Clinical Densitometry: body composition analysis reporting. *J Clin Densitom.* (2013) 16:508-19. doi: 10.1016/j.jocd.2013.08.018
17. Scatteia A, Baritussio A, Bucciarelli-Ducci C. Strain imaging using cardiac magnetic resonance. *Heart Fail Rev.* (2017) 22:465-76. doi: 10.1007/s10741-017-9621-8
18. Chahal H, McClelland RL, Tandri H, Jain A, Turkbey EB, Hundley WG, et al. Obesity and right ventricular structure and function: the MESA-Right Ventricle Study. *Chest.* (2012) 141:388-95. doi: 10.1378/chest.11-0172
19. Selthofer-Relatic K, Bosnjak I, Kibel A. Obesity related coronary microvascular dysfunction: from basic to clinical practice. *Cardiol Res Pract.* (2016) 2016:8173816. doi: 10.1155/2016/8173816
20. Kovacs A, Lakatos B, Tokodi M, Merkely B. Right ventricular mechanical pattern in health and disease: beyond longitudinal shortening. *Heart Fail Rev.* (2019) 24:511-20. doi: 10.1007/s10741-019-09778-1
21. Chuang ML, Danias PG, Riley MF, Hibberd MG, Manning WJ, Douglas PS. Effect of increased body mass index on accuracy of two-dimensional echocardiography for measurement of left ventricular volume, ejection fraction, and mass. *Am J Cardiol.* (2001) 87:371-4, A10. doi: 10.1016/S0002-9149(00)01383-7
22. Alpert MA, Karthikeyan K, Abdullah O, Ghadban R. Obesity and cardiac remodeling in adults: mechanisms and clinical implications. *Prog Cardiovasc Dis.* (2018) 61:114-23. doi: 10.1016/j.pcad.2018.07.012
23. Alpert MA. Obesity cardiomyopathy: pathophysiology and evolution of the clinical syndrome. *Am J Med Sci.* (2001) 321:225-36. doi: 10.1097/0000441-200104000-00003
24. Damiano RJ Jr, La Follette P Jr, Cox JL, Lowe JE, Santamore WP. Significant left ventricular contribution to right ventricular systolic function. *Am J Physiol.* (1991) 261:H1514-24. doi: 10.1152/ajpheart.1991.261.5.H1514
25. Hoffman D, Sisto D, Frater RW, Nikolic SD. Left-to-right ventricular interaction with a noncontracting right ventricle. *J Thorac Cardiovasc Surg.* (1994) 107:1496-502. doi: 10.1016/S0022-5223(12)70150-2
26. Lan Z, Shengjia G, Qingrou W, Xiaoyue Z, Simin W, Caixia F, et al. Left ventricular myocardial deformation: a study on diastolic function in the Chinese male population and its relationship with fat distribution. *Quant Imaging Med Surg.* (2020) 10:634-45. doi: 10.21037/qims.2020.01.16
27. Jing L, Binkley CM, Suever JD, Umasankar N, Haggerty CM, Rich J, et al. Cardiac remodeling and dysfunction in childhood obesity: a cardiovascular magnetic resonance study. *J Cardiovasc Magn Reson.* (2016) 18:28. doi: 10.1186/s12968-016-0247-0
28. Latt E, Maestu J, Jurimae J. Longitudinal associations of android and gynoid fat mass on cardiovascular disease risk factors in normal weight and overweight boys during puberty. *Am J Hum Biol.* (2018) 30:e23171. doi: 10.1002/ajhb.23171
29. Daniels SR, Morrison JA, Sprecher DL, Khoury P, Kimball TR. Association of body fat distribution and cardiovascular risk factors in children and adolescents. *Circulation.* (1999) 99:541-5. doi: 10.1161/01.CIR.99.4.541
30. He F, Rodriguez-Colon S, Fernandez-Mendoza J, Vgontzas AN, Bixler EO, Berg A, et al. Abdominal obesity and metabolic syndrome burden in adolescents—Penn State Children Cohort study. *J Clin Densitom.* (2015) 18:30-6. doi: 10.1016/j.jocd.2014.07.009
31. Wiklund P, Toss F, Weinehall L, Hallmans G, Franks PW, Nordstrom A, et al. Abdominal and gynoid fat mass are associated with cardiovascular risk factors in men and women. *J Clin Endocrinol Metab.* (2008) 93:4360-6. doi: 10.1210/jc.2008-0804
32. Wiklund P, Toss F, Jansson JH, Eliasson M, Hallmans G, Nordstrom A, et al. Abdominal and gynoid adipose distribution and incident myocardial infarction in women and men. *Int J Obes.* (2010) 34:1752-8. doi: 10.1038/ijo.2010.102
33. Marin MT, Dasari PS, Tryggstad JB, Aston CE, Teague AM, Short KR. Oxidized HDL and LDL in adolescents with type 2 diabetes compared to normal weight and obese peers. *J Diabetes Complications.* (2015) 29:679-85. doi: 10.1016/j.jdiacomp.2015.03.015
34. Hajri T. Effects of oxidized lipids and lipoproteins on cardiac function. *Front Biosci.* (2018) 23:1822-47. doi: 10.2741/4675
35. Kontush A, de Faria EC, Chantepie S, Chapman MJ. Antioxidative activity of HDL particle subspecies is impaired in hyperalphalipoproteinemia: relevance of enzymatic and physicochemical properties. *Arterioscler Thromb Vasc Biol.* (2004) 24:526-33. doi: 10.1161/01.ATV.0000118276.87061.00
36. Aucouturier J, Meyer M, Thivel D, Taillardat M, Duche P. Effect of android to gynoid fat ratio on insulin resistance in obese youth. *Arch Pediatr Adolesc Med.* (2009) 163:826-31. doi: 10.1001/archpediatrics.2009.148
37. Orbetzova MM, Koleva DI, Mitkov MD, Atanassova IB, Nikolova JG, Atanassova PK, et al. Adipocytokines, neuropeptide Y and insulin resistance in overweight women with gynoid and android type of adipose tissue distribution. *Folia Med.* (2012) 54:22-9. doi: 10.2478/v10153-011-0093-7
38. Hintz KK, Aberle NS, Ren J. Insulin resistance induces hyperleptinemia, cardiac contractile dysfunction but not cardiac leptin resistance in ventricular myocytes. *Int J Obes Relat Metab Disord.* (2003) 27:1196-203. doi: 10.1038/sj.ijo.0802389
39. Peterson LR, Herrero P, Schechtman KB, Racette SB, Waggoner AD, Kisrieva-Ware Z, et al. Effect of obesity and insulin resistance on myocardial substrate metabolism and efficiency in young women. *Circulation.* (2004) 109:2191-6. doi: 10.1161/01.CIR.0000127959.28627.F8
40. Kouda K, Nakamura H, Ohara K, Fujita Y, Iki M. Increased ratio of trunk-to-appendicular fat and decreased adiponectin: a population-based study of school children in Hamamatsu, Japan. *J Clin Densitom.* (2017) 20:66-72. doi: 10.1016/j.jocd.2015.10.004
41. Miazgowski T, Safranow K, Krzyzanowska-Swiniarska B, Iskierska K, Widecka K. Adiponectin, visfatin and regional fat depots in normal weight obese premenopausal women. *Eur J Clin Invest.* (2013) 43:783-90. doi: 10.1111/eci.12106
42. Scott HA, Gibson PG, Garg ML, Pretto JJ, Morgan PJ, Callister R, et al. Relationship between body composition, inflammation and lung function in overweight and obese asthma. *Respir Res.* (2012) 13:10. doi: 10.1186/1465-9921-13-10
43. Cho BA, Iyengar NM, Zhou XK, Mendieta H, Winston L, Falcone DJ, et al. Increased trunk fat is associated with altered gene expression in breast tissue of normal weight women. *NPJ Breast Cancer.* (2022) 8:15. doi: 10.1038/s41523-021-00369-8
44. Samouda H, De Beaufort C, Stranges S, Hirsch M, Van Nieuwenhuysse JP, Doms G, et al. Cardiometabolic risk: leg fat is protective during childhood. *Pediatr Diabetes.* (2016) 17:300-8. doi: 10.1111/pedi.12292
45. Noordam R, Boersma V, Verkouter I, le Cessie S, Christen T, Lamb HJ, et al. The role of C-reactive protein, adiponectin and leptin in the association between abdominal adiposity and insulin resistance in middle-aged individuals. *Nutra Metab Cardiovasc Dis.* (2020) 30:1306-14. doi: 10.1016/j.numecd.2020.04.021
46. Lau WB, Ohashi K, Wang Y, Ogawa H, Murohara T, Ma XL, et al. Role of adipokines in cardiovascular disease. *Circ J.* (2017) 81:920-8. doi: 10.1253/circj.CJ-17-0458
47. Thorand B, Zierer A, Baumert J, Meisinger C, Herder C, Koenig W. Associations between leptin and the leptin / adiponectin ratio and incident

- Type 2 diabetes in middle-aged men and women: results from the MONICA / KORA Augsburg study 1984-2002. *Diabet Med.* (2010) 27:1004-11. doi: 10.1111/j.1464-5491.2010.03043.x
48. Sainz N, Barrenetxe J, Moreno-Aliaga MJ, Martinez JA. Leptin resistance and diet-induced obesity: central and peripheral actions of leptin. *Metabolism.* (2015) 64:35-46. doi: 10.1016/j.metabol.2014.10.015
  49. Bal Y, Adas M, Helvacı A. Evaluation of the relationship between insulin resistance and plasma tumor necrosis factor-alpha, interleukin-6 and C-reactive protein levels in obese women. *Bratisl Lek Listy.* (2010) 111:200-4. doi: 10.3357/ASEM.21011.2010
  50. Wu B, Huang J, Fukuo K, Suzuki K, Yoshino G, Kazumi T. Different associations of trunk and lower-body fat mass distribution with cardiometabolic risk factors between healthy middle-aged men and women. *Int J Endocrinol.* (2018) 2018:1289485. doi: 10.1155/2018/1289485
  51. Koster A, Stenholm S, Alley DE, Kim LJ, Simonsick EM, Kanaya AM, et al. Body fat distribution and inflammation among obese older adults with and without metabolic syndrome. *Obesity.* (2010) 18:2354-61. doi: 10.1038/oby.2010.86
  52. Borst SE. The role of TNF-alpha in insulin resistance. *Endocrine.* (2004) 23:177-82. doi: 10.1385/ENDO:23:2-3:177
  53. Liao CW, Chou CH, Wu XM, Chen ZW, Chen YH, Chang YY, et al. Interleukin-6 plays a critical role in aldosterone-induced macrophage recruitment and infiltration in the myocardium. *Biochim Biophys Acta Mol Basis Dis.* (2020) 1866:165627. doi: 10.1016/j.bbdis.2019.165627
  54. Pedrinelli R, Canale ML, Giannini C, Talini E, Dell'Omo G, Di Bello V. Abnormal right ventricular mechanics in early systemic hypertension: a two-dimensional strain imaging study. *Eur J Echocardiogr.* (2010) 11:738-42. doi: 10.1093/ejehocardiography/jeq059

**Conflict of Interest:** XZ was employed by Siemens Healthineers Ltd.

The remaining authors declare that the research was conducted in the absence of any commercial or financial relationships that could be construed as a potential conflict of interest.

**Publisher's Note:** All claims expressed in this article are solely those of the authors and do not necessarily represent those of their affiliated organizations, or those of the publisher, the editors and the reviewers. Any product that may be evaluated in this article, or claim that may be made by its manufacturer, is not guaranteed or endorsed by the publisher.

Copyright © 2022 Liu, Li, Yu, Xia, Pu, He, Li, Zhou, Tong and Peng. This is an open-access article distributed under the terms of the Creative Commons Attribution License (CC BY). The use, distribution or reproduction in other forums is permitted, provided the original author(s) and the copyright owner(s) are credited and that the original publication in this journal is cited, in accordance with accepted academic practice. No use, distribution or reproduction is permitted which does not comply with these terms.



# Left Heart Chamber Volumetric Assessment by Automated Three-Dimensional Echocardiography in Heart Transplant Recipients

## OPEN ACCESS

### Edited by:

Sebastian Kelle,  
Deutsches Herzzentrum Berlin,  
Germany

### Reviewed by:

Valeria Pergola,  
University Hospital of Padua, Italy  
Qiangjun Cai,  
University of Texas Medical Branch  
at Galveston, United States

### \*Correspondence:

Li Zhang  
zli429@hust.edu.cn  
Mingxing Xie  
xiemx@hust.edu.cn

<sup>†</sup>These authors have contributed  
equally to this work and share first  
authorship

### Specialty section:

This article was submitted to  
Cardiovascular Imaging,  
a section of the journal  
Frontiers in Cardiovascular Medicine

**Received:** 16 February 2022

**Accepted:** 04 April 2022

**Published:** 27 April 2022

### Citation:

Zhang Y, Wu C, Sun W, Zhu S,  
Zhang Y, Xie Y, Zhu Y, Zhang Z,  
Zhao Y, Li Y, Xie M and Zhang L  
(2022) Left Heart Chamber Volumetric  
Assessment by Automated  
Three-Dimensional Echocardiography  
in Heart Transplant Recipients.  
Front. Cardiovasc. Med. 9:877051.  
doi: 10.3389/fcvm.2022.877051

Yiwei Zhang<sup>1,2†</sup>, Chun Wu<sup>1,2†</sup>, Wei Sun<sup>1,2†</sup>, Shuangshuang Zhu<sup>1,2†</sup>, Yanting Zhang<sup>1,2</sup>,  
Yuji Xie<sup>1,2</sup>, Ye Zhu<sup>1,2</sup>, Zisang Zhang<sup>1,2</sup>, Yang Zhao<sup>1,2</sup>, Yuman Li<sup>1,2</sup>, Mingxing Xie<sup>1,2\*</sup> and  
Li Zhang<sup>1,2\*</sup>

<sup>1</sup> Department of Ultrasound Union Hospital, Tongji Medical College, Huazhong University of Science and Technology, Wuhan, China, <sup>2</sup> Hubei Province Key Laboratory of Molecular Imaging, Wuhan, China

**Background:** Recently, a new automated software (Heart Model) was developed to obtain three-dimensional (3D) left heart chamber volumes. The aim of this study was to verify the feasibility and accuracy of the automated 3D echocardiographic algorithm in heart transplant (HTx) patients. Conventional manual 3D transthoracic echocardiographic (TTE) tracings and cardiac magnetic resonance (CMR) images were used as a reference for comparison.

**Methods:** This study enrolled 103 healthy HTx patients prospectively. In protocol 1, left ventricular end-diastolic volume (LVEDV), LV end-systolic volume (LVESV), left atrial max volume (LAVmax), LA minimum volume (LAVmin) and LV ejection fraction (LVEF) were obtained using the automated 3D echocardiography (3DE) and compared with corresponding values obtained through the manual 3DE. In protocol 2, 28 patients' automated 3DE measurements were compared with CMR reference values. The impacts of contour edit and surgical technique were also tested.

**Results:** Heart Model was feasible in 97.1% of the data sets. In protocol 1, there was strong correlation between 3DE and manual 3DE for all the parameters ( $r = 0.77$  to  $0.96$ ,  $p < 0.01$ ). Compared to values obtained through manual measurements, LV volumes and LVEF were overestimated by the automated algorithm and LA volumes were underestimated. All the biases were small except for that of LAVmin. After contour adjustment, the biases reduced and all the limits of agreement were clinically acceptable. In protocol 2, the correlations for LV and LA volumes were strong between automated 3DE with contour edit and CMR ( $r = 0.74$  to  $0.93$ ,  $p < 0.01$ ) but correlation for LVEF remained moderate ( $r = 0.65$ ,  $p < 0.01$ ). Automated 3DE overestimated LV volumes but underestimated LVEF and LA volumes compared with CMR. The limits of agreement were clinically acceptable only for LVEDV and LAVmax.

**Conclusion:** Simultaneous quantification of left heart volumes and LVEF with the automated Heart Model program is rapid, feasible and to a great degree it is accurate in HTx recipients. Nevertheless, only LVEDV and LAVmax measured by automated 3DE with contour edit seem applicable for clinical practice when compared with CMR. Automated 3DE for HTx recipients is a worthy attempt, though further verification and optimization are needed.

**Keywords:** 3D echocardiography, heart transplant, heart model, left atrial volume, left ventricular function, left ventricular volume

## INTRODUCTION

Orthotopic heart transplantation (HTx) is one of the most effective treatments for patients with end-stage heart disease. With improvement in operative techniques and postoperative surveillance and therapy, the median survival after adult heart transplants has increased to 12.5 years (1–4). Previous studies have shown that the volume of left ventricular (LV) and left atrial (LA) are crucially related to overall left heart function (5–7), which is of great importance for the assessment of transplanted heart. Echocardiography has become post-transplantation annual routine follow-up for its convenience and accuracy and usually used for the assessment of heart volumes. 3-dimensional (3D) transthoracic echocardiographic (TTE) measurements of cardiac chamber volumes are proved superior to 2-dimensional (2D) techniques in accuracy and reproducibility, due to avoidance of geometric assumptions and foreshortened views (5–7). However, widespread use of 3D TTE for LA and LV volume assessments has not become a clinical reality, as time and training are required to obtain accurate and reproducible 3DE volumetric measurements (5, 8, 9).

Heart Model is a novel automated 3DE software with the ability of simultaneous quantification of heart chamber volumes and LV ejection fraction (LVEF) within few seconds. Previous studies have shown the feasibility and accuracy of Heart Model in measuring left heart volumes and LVEF in multiple cohorts (10–12). Nevertheless, this automated adaptive analytics algorithm relies on the 3DE database comprised of morphologies derived from a ‘training’ population, which may not adequately encompass the HTx recipients cohort, whose heart geometry is usually grossly distorted (13).

Thus, the aim of this study was to explore the accuracy and reproducibility of the Heart Model program for automated measurement of LV, LA volumes and LVEF from 3DE datasets in the HTx recipients, using expert manual 3DE and cardiac magnetic resonance (CMR) as references.

## MATERIALS AND METHODS

### Study Population

A total of 103 HTx patients at Union Hospital in Wuhan, China, were prospectively enrolled in this study between January 2018 and January 2020.

In Protocol 1, we prospectively included 103 HTx patients referred to the echocardiography laboratory for their routine follow-up examination. All of them presented as clinically well and underwent 2D and 3D TTE. 3 of the 103 patients were excluded for poor 3D-echocardiographic image quality unsuitable for automated analysis. LV end-diastolic volume (LVEDV), LV end-systolic volume (LVESV), LVEF, LA max volume (LAV max) and LA minimum volume (LAV min) derived from automated 3DE were compared with the manual 3DE and 2D biplane Simpson method measurements.

In Protocol 2, 28 of the 103 HTx recipients who agreed to undergo CMR examination within the following 24 h after echocardiographic examination were enrolled. The automated 3D echocardiographic measurements of LVEDV, LVESV, LVEF, and LAV were compared with the CMR values. 28 participants were divided into biatrial group and bicaval group according to the surgical technique and the correlation coefficients between automated 3DE measurements and CMR measurements of the two groups were compared.

Weight, height, heart rate, primary diagnosis, surgical technique and time since HTx of every patients were recorded. The study was approved by the Ethics Committee of Tongji Medical College, Huazhong University of Science and Technology. Written informed consent of all participants have been obtained.

### Echocardiographic Image Acquisition

All echocardiographic examinations were performed by an experienced echocardiographic doctor using EPIQ 7C (Philips Medical Systems) and an X5-1 matrix probe (Philips Medical Systems) with the patient breath-holding. 2D echocardiographic (2DE) images were acquired from the parasternal short-axis view at the apical four-, three-, and two- chamber views. Foreshortening of the left ventricle and left atrium has been avoided. 3D echocardiographic acquisitions were recorded from the four-chamber apical view in heart model mode, and were gathered over four cardiac cycles, during a breath-hold lasting for a few seconds (14). The volume rate was adjusted above 18 Hz when 3D echocardiographic acquisition was performed. Imaging settings were optimized for visualizing endocardium before every acquisition.

### Two-Dimensional Echocardiography Analysis

LV end-diastolic volume (LVEDV), LV end-systolic volume (LVESV), LVEF, LA max volume (LAV max) and LA minimum

volume (LAV min) were calculated using the biplane Simpson method, by means of a commercially available software (QLAB-2DQ, Philips Healthcare). The papillary muscles were included in the LV cavity when tracking the endocardial contours.

### Manual (Semiautomated) Three-Dimensional Echocardiography Analysis

For manual 3D echocardiographic analysis, a semi-automatically derived 3D echocardiographic method was used. Operators used commercially available software (QLAB-3DQadv, Philips Healthcare) to measure LVEDV, LVESV, LVEF, LAVmax and LAVmin. Firstly, the multiplanar views were adjusted to optimize the horizontal and vertical lines in the middle of LV chamber. Then the operator placed reference points at the end-diastolic and end-systolic frames: two points to identify the mitral valve annulus and the apex in four- and two- chamber view. For LA, this included two points to identify the mitral valve annulus in each of the two apical views, and one point to identify the center of the posterior wall in either view. Finally, the software automatically identified LV and LA endocardial border and created a 3D model of left cardiac chamber to calculate LV, LA volumes and LVEF.

### Automated Three-Dimensional Echocardiography Analysis

3D echocardiographic acquisitions were also analyzed by the HeartModel software. This algorithm is able to automatically detect LV and LA endocardial borders at end-diastole and end-systole and measure LVEDV, LVESV, LVEF, LAVmax and LAVmin (**Figure 1**). Observers can freely move the adjustable slider to optimize cardiac chamber border identification according to their preference, including global and regional editing.

### Cardiac Magnetic Resonance Imaging

Cardiac magnetic resonance was performed in 28 of 103 patients within 24 hours of the echocardiography by 1.5-Tesla system (MAGNETOM Aera, Siemens Healthineers, Erlangen, Germany). In each patient, the long axis of the heart was identified by retrospective electrocardiogram-gated localizing spin-echo sequences. Steady state free-precession dynamic gradient echo cine loops of the left ventricle and left atrium were then acquired during 10- to 15-second breath-holds. The cine image parameters in our study were obtained as follows: slice thickness of 8 mm, matrix of 205 × 256 pixels, and flip angle of 80°.

### Cardiac Magnetic Resonance Analysis

Cardiac magnetic resonance images were analyzed using commercial software (Argus, Siemens Healthineers). Left cardiac volumetric and functional parameters were derived by manual delineation of the endocardial contours on the continuous LV and LA short-axis cine images at the end-diastolic frame and end-systolic frame. Papillary

muscles and trabeculations were included in the LV cavity, while pulmonary veins and LA appendage were excluded from the LA cavity.

### Reproducibility

Of the 100 participants in protocol 1, 20 participants were selected randomly for the evaluation of the reproducibility of manual 3DE and automated 3DE. For test-retest variability, the same observer analyzed 3D echocardiographic data sets of each patient. For intraobserver variability, the same observer analyzed the 3D echocardiographic data set 2 weeks later after the first analysis, blinded to the previous measurements. For interobserver variability, two blinded and independent observers analyzed the 3D echocardiographic data set.

### Statistical Analysis

Continuous variables were presented as mean ± SD. and nominal variables as percentages. 2D and 3D echocardiographic images were analyzed offline by a single investigator who was blind to the values of echocardiographic and CMR measurements. CMR measurements were performed by an observer experienced in CMR analysis, who was not allowed to view the echocardiographic results. Pearson's or Spearman's correlation coefficient and Bland-Altman analysis were used to test the correlation and agreement between two sets of measurements by calculating the bias (mean difference) and the limits of agreement (LOA; 1.96 SDs around the mean difference). The descriptions of the strength of correlations were based on the following standard: *r* value between 0.7 and 0.9 was considered strong correlation; *r* value between 0.5 and 0.69 was considered moderate correlation; and *r* value between 0.3 and 0.5 was considered weak correlation. For LV and LA volumes, the relative bias and the percentage error of the LOA were also calculated. The reference method in protocol 1 and protocol 2 was manual 3DE and CMR, respectively. The LOA is used to estimate the precision or random error of the measurements around the bias. A percentage error of the LOA below 30% was considered clinically acceptable.

For 3D echocardiographic measurements, intraobserver, and interobserver variability was examined and expressed as coefficient of variation (the absolute difference between two measurements in percentage of their mean in each patient and then averaged over the entire study group). Comparisons of correlation coefficients were performed on MedCalc version 18.2.1 (MedCalc Software, Ostend, Belgium). All statistical analyses were performed on SPSS version 22.0 (Statistical Package for the Social Sciences, Chicago, Illinois), GraphPad Prism version 8.0.1 and MedCalc version 18.2.1 (MedCalc Software, Ostend, Belgium). A *P*-value <0.05 was considered statistically significant.

## RESULTS

### Study Population

103 HTx recipients (80 male, 23 female) were included in protocol 1. 3 of them were excluded from analysis because

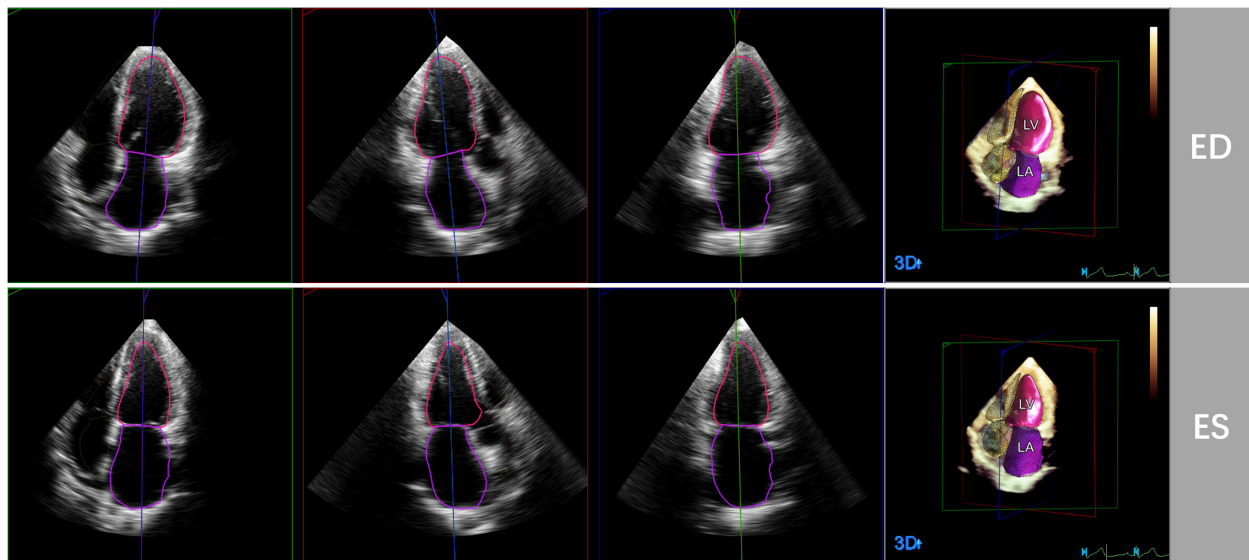


**FIGURE 1 |** Representative case of automated 3D echocardiographic analysis for left heart chamber quantification. Left heart chambers' endocardial borders were automatically detected by the Heart Model software at end-diastole (ED) and end-systole (ES) in apical four-, three-, and two chamber sections.

of failure to be analyzed by automated 3D echocardiographic system, with the remaining 100 participants included in the final analysis. The feasibility of automated 3D echocardiographic system in protocol 1 was 97.1%, and feasibility of 2D echocardiographic analysis and manual 3D echocardiographic analysis were both 100.0%. 28 HTx recipients (20 male, 8 female) were enrolled in protocol 2. The feasibility of both automated 3D echocardiographic system and CMR in protocol 2 were 100.0%. The baseline clinical characteristics of all participants, including those in protocol 1 and protocol 2, are summarized in **Table 1**. The mean values of LVEDV, LVESV, LVEF, LAVmax and LAVmin measured by different methods are presented in **Table 2**.

## Automated Three-Dimensional Echocardiography Versus Manual Three-Dimensional Echocardiography

There were strong correlations for LVEDV, LVESV, LAVmax and LAVmin between automated 3DE and manual 3DE ( $r = 0.87$ ,  $r = 0.84$ ,  $r = 0.90$  and  $r = 0.83$ , respectively,  $P < 0.01$  for all). The automated 3DE measurements of LVEF correlated moderately with the reference value measured by manual 3DE ( $r = 0.79$ ,  $P < 0.01$ ). After contour edit, the correlations for volumes and LVEF were all excellent ( $r = 0.95$  for LVEDV,  $r = 0.92$  for LVESV,  $r = 0.77$  for LVEF,  $r = 0.96$  for LAVmax, and  $r = 0.94$  for LAVmin,  $P < 0.01$  for all). Results are presented in **Table 3**.

Compared with the manual 3DE reference values, LVEDV, LVESV, LVEF, and LAVmax, without contour edit, were overestimated by the automated 3DE, with tolerable biases (10.1 mL for LVEDV, 1.3 mL for LVESV, 2.9% for LVEF, and 0.0 mL for LAVmax) between the two methods (**Figure 2**). Automated 3DE without contour adjustment underestimated

**TABLE 1 |** Clinical characteristics of the study subjects.

| Variable                           | Protocol 1  | Protocol 2  |
|------------------------------------|-------------|-------------|
| Number of patients                 | 100         | 28          |
| Gender, male                       | 79 (79)     | 20 (71)     |
| Age, years                         | 47.3 ± 12.7 | 45.6 ± 13.5 |
| BSA, m <sup>2</sup>                | 1.69 ± 0.17 | 1.64 ± 0.17 |
| Heart rate, bpm                    | 87 ± 9      | 88 ± 7      |
| <b>Primary diagnosis</b>           |             |             |
| DCM                                | 56 (56)     | 13 (46)     |
| CAD                                | 15 (15)     | 5 (18)      |
| VHD                                | 8 (8)       | 1 (4)       |
| Others                             | 21 (21)     | 9 (32)      |
| <b>Surgical technique</b>          |             |             |
| Biatrinal                          | 39 (39)     | 12 (43)     |
| Bicaval                            | 61 (61)     | 16 (57)     |
| Time since transplantation, months | 22.2 ± 24.1 | 19.3 ± 28.1 |
| %HM feasibility                    | 97.1        | 100.0       |

DCM, dilated cardiomyopathy; CAD, coronary artery disease; VHD, valvular heart disease; HM, automated 3DE by Heart Model.

LAVmin compared with manual 3DE, with small bias (−5.3 mL). When there was no contour adjustment, the automated 3DE measurements of LVEDV were on average 12.1% higher than values derived by manual 3DE, while automated 3DE-derived LAVmax was on average 0.7% lower than values obtained by manual 3DE (relative biases). The LOA for both were clinically acceptable (percentage error of the LOA < 30%), while that of LVESV and LAVmin were not (**Table 3**).

After contour edit, the biases and LOA for LVEDV, LVESV, LVEF and LAVmin between automated 3DE and manual 3DE were reduced (**Figure 3**). The automated 3DE

**TABLE 2** | Mean of LV volumes, LVEF and LA volumes obtained by the different methods.

| Method               | n   | LVEDV (mL)   | LVESV (mL)  | LVEF (%)   | LAVmax (mL) | LAVmin (mL) |
|----------------------|-----|--------------|-------------|------------|-------------|-------------|
| <b>Protocol 1</b>    |     |              |             |            |             |             |
| 2DE                  | 103 | 86.9 ± 20.8  | 34.3 ± 9.4  | 60.5 ± 5.1 | 88.0 ± 24.3 | 53.3 ± 19.6 |
| <b>Automated 3DE</b> |     |              |             |            |             |             |
| Without contour edit | 100 | 100.1 ± 23.3 | 37.4 ± 11.6 | 62.9 ± 5.8 | 84.0 ± 28.6 | 51.7 ± 23.1 |
| With contour edit    | 100 | 94.9 ± 21.9  | 37.0 ± 10.4 | 61.0 ± 5.1 | 85.6 ± 25.0 | 56.5 ± 20.8 |
| Manual 3DE           | 103 | 90.0 ± 21.2  | 36.1 ± 10.2 | 60.0 ± 5.0 | 83.9 ± 23.6 | 57.0 ± 20.0 |
| <b>Protocol 2</b>    |     |              |             |            |             |             |
| <b>Automated 3DE</b> |     |              |             |            |             |             |
| Without contour edit | 28  | 97.8 ± 23.6  | 39.0 ± 13.1 | 60.8 ± 5.6 | 75.3 ± 23.8 | 46.1 ± 15.3 |
| With contour edit    | 28  | 88.4 ± 20.8  | 35.5 ± 11.8 | 60.0 ± 6.2 | 84.5 ± 22.6 | 57.2 ± 17.4 |
| CMR                  | 28  | 85.2 ± 21.0  | 33.9 ± 12.0 | 60.8 ± 6.3 | 89.3 ± 23.6 | 76.7 ± 22.4 |

**TABLE 3** | Comparison of LV volumes, LVEF, and LA volumes measured by 2DE, automated 3DE against manual 3D echocardiographic measurements.

| Method               | Parameter   | r     | P     | Bias ± LOA  | Relative bias (%) | Percentage error (%) |
|----------------------|-------------|-------|-------|-------------|-------------------|----------------------|
| 2DE                  |             |       |       |             |                   |                      |
|                      | LVEDV (mL)  | 0.88  | <0.01 | −3.1 ± 17.8 | −3.0              | 20.1                 |
|                      | LVESV (mL)  | 0.82  | <0.01 | −1.9 ± 10.7 | 3.9               | 30.4                 |
|                      | LVEF (%)    | 0.67  | <0.01 | 0.5 ± 7.9   | —                 | —                    |
|                      | LAVmax (mL) | 0.91  | <0.01 | 4.0 ± 19.8  | 5.5               | 23.0                 |
|                      | LAVmin (mL) | 0.88  | <0.01 | −3.8 ± 18.9 | 5.1               | 34.3                 |
| <b>Automated 3DE</b> |             |       |       |             |                   |                      |
| Without contour edit | LVEDV (mL)  | 0.87  | <0.01 | 10.1 ± 21.9 | 12.1              | 23.0                 |
|                      | LVESV (mL)  | 0.84  | <0.01 | 1.3 ± 11.1  | 3.9               | 30.2                 |
|                      | LVEF (%)    | 0.79  | <0.01 | 2.9 ± 6.5   | —                 | —                    |
|                      | LAVmax (mL) | 0.90  | <0.01 | 0.0 ± 24.0  | 0.7               | 28.6                 |
|                      | LAVmin (mL) | 0.83  | <0.01 | −5.3 ± 24.6 | −9.8              | 45.3                 |
| With contour edit    | LVEDV (mL)  | 0.95* | <0.01 | 4.8 ± 11.7  | 5.7               | 12.7                 |
|                      | LVESV (mL)  | 0.92* | <0.01 | 0.9 ± 7.2   | 3.1               | 19.7                 |
|                      | LVEF (%)    | 0.77  | <0.01 | 1.0 ± 5.6   | —                 | —                    |
|                      | LAVmax (mL) | 0.96* | <0.01 | 1.7 ± 14.2  | 1.9               | 16.7                 |
|                      | LAVmin (mL) | 0.94* | <0.01 | −0.6 ± 14.1 | −0.7              | 24.8                 |

Relative bias = (parameter<sub>method</sub> − parameter<sub>manual 3DE</sub>) / parameter<sub>manual 3DE</sub>. Percentage error = LOA / mean value of parameter measured by studied method and manual 3DE. \*,  $p < 0.05$  compared with 2DE.

measurements of LV volumes and LVEF were overestimated compared with those of manual 3DE, with small biases (biases, 4.8 ml for LVEDV, 0.9 ml for LVESV, and 1.0% for LVEF; relative bias, 5.7% for LVEDV, 3.1% for LVESV of manual 3DE values). LAVmin obtained by automated 3DE was underestimated, with negligible bias (bias, −0.6 ml, relative bias, −0.7% of manual 3D echocardiographic values). However, bias for LAVmax compared with manual 3DE increased when contour edit was performed. LAVmax obtained by automated 3DE with contour adjustment was slightly overestimated with small bias (1.7 ml). All the LOA were clinically acceptable (Table 3).

## Two-Dimensional Echocardiography Versus Manual Three-Dimensional Echocardiography

Detailed results are presented in Table 3. The correlations for LV, LA volumes between 2DE and manual 3DE were both

strong with no significant difference between automated 3DE measurements and manual 3DE ones ( $P > 0.05$ ). However, when contour adjustments were performed, the correlations for left cardiac chamber volumes between automated 3DE and manual 3DE were significantly stronger than those between 2DE and manual 3DE. 2DE measured LVEF correlated moderately with values derived from manual 3DE, while the correlations for LVEF between automated 3DE and manual 3DE, with or without contour adjustment, were strong. There was no significant difference between those correlations.

Compared with manual 3DE, 2DE underestimated LVEDV, LVESV, and LAVmin but overestimated LVEF and LAVmax. In general, the biases in measurements of LVESV, LAVmax were smaller for automated 3DE than 2DE. For automated 3DE with contour edit, the biases in measurements of all parameters were smaller than 2DE, except for LVEDV and LVEF. The LOA of automated 3DE with contour edit were tighter than those derived from 2DE.

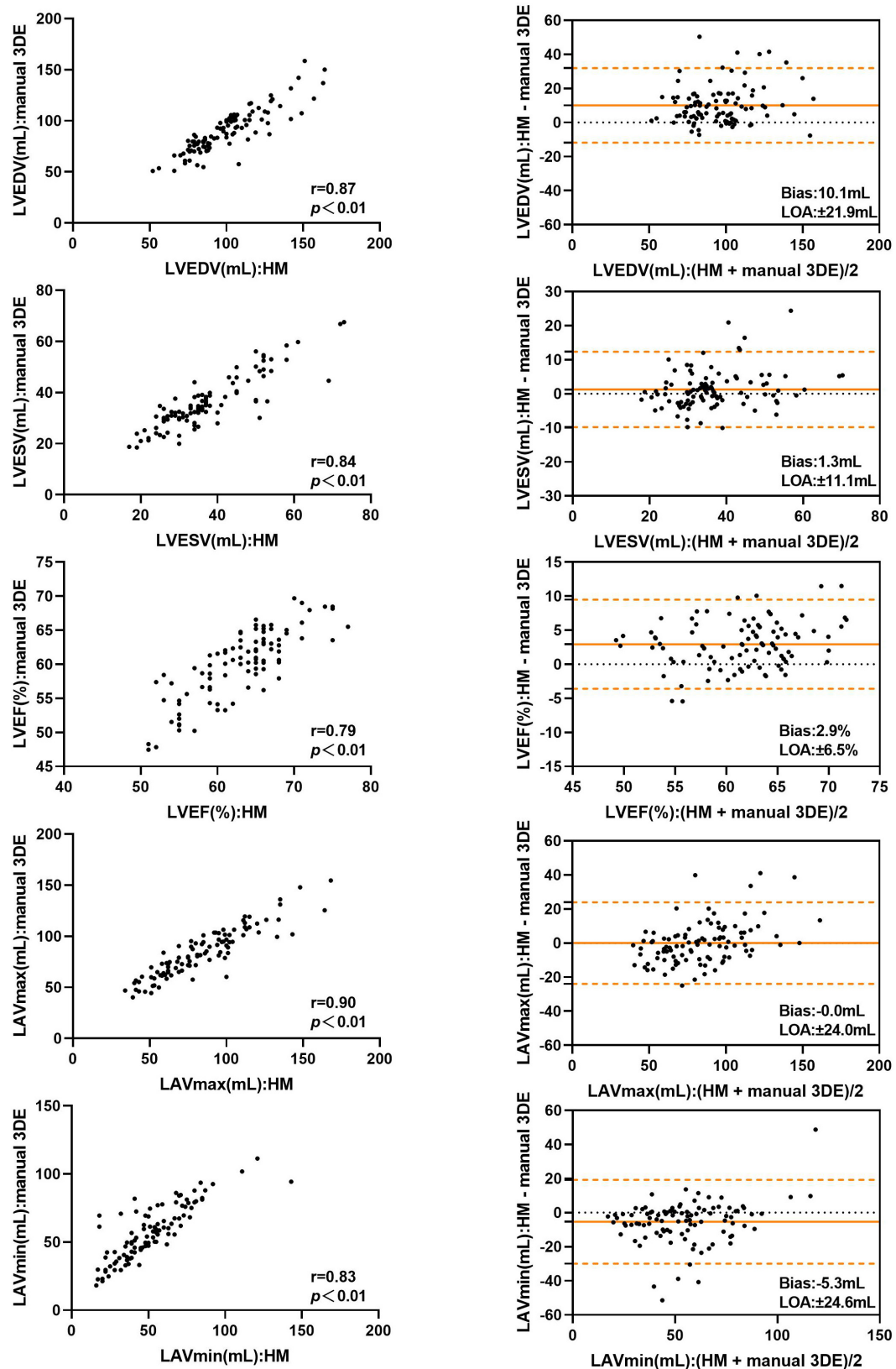


**FIGURE 2 |** Comparison between automated 3DE without contour adjustment and manual 3DE of left heart volumes and ejection fraction: correlation and Bland-Altman analysis. HM: Automated 3DE by Heart Model without contour adjustment.

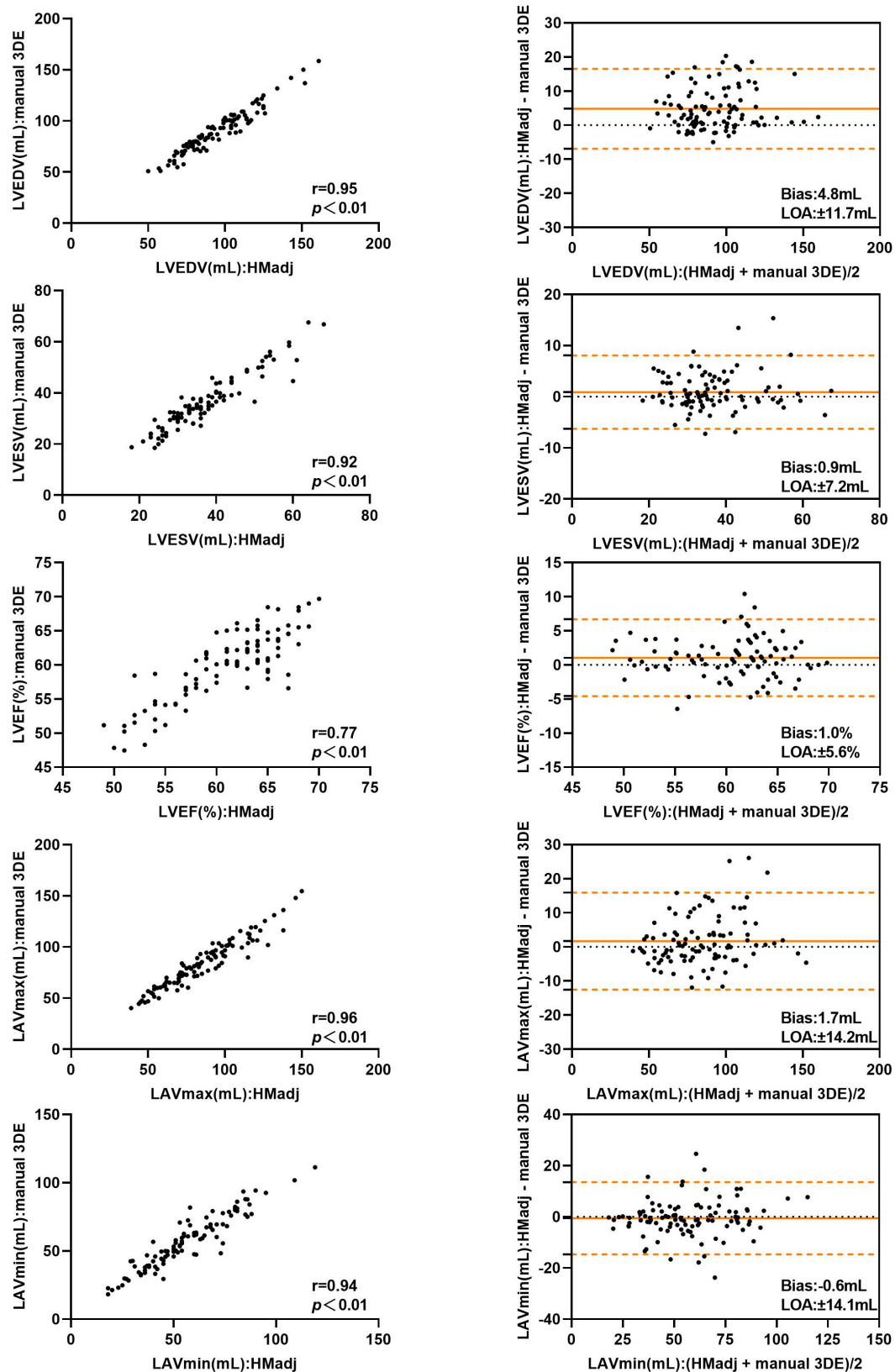


**FIGURE 3 |** Comparison between automated 3DE with contour adjustment and manual 3DE of left heart volumes and ejection fraction: correlation and Bland-Altman analysis. HMadj: Automated 3DE by Heart Model with contour adjustment.

**TABLE 4** | Comparison of LV volumes, LVEF, and LAV measured by automated 3DE against CMR measurements.

| Method               | Parameter   | r     | P     | Bias ± LOA   | Relative bias (%) | Percentage error (%) |
|----------------------|-------------|-------|-------|--------------|-------------------|----------------------|
| <b>Automated 3DE</b> |             |       |       |              |                   |                      |
| Without contour edit | LVEDV (mL)  | 0.68  | <0.01 | 12.6 ± 30.4  | 17.0              | 33.2                 |
|                      | LVESV (mL)  | 0.63  | <0.01 | 5.1 ± 18.5   | 19.9              | 54.7                 |
|                      | LVEF (%)    | 0.62  | <0.01 | 0.0 ± 10.2   | —                 | —                    |
|                      | LAVmax (mL) | 0.77  | <0.01 | −14.1 ± 31.6 | −15.4             | 38.4                 |
|                      | LAVmin (mL) | 0.64  | <0.01 | −30.6 ± 33.9 | −38.9             | 55.1                 |
| With contour edit    | LVEDV (mL)  | 0.92* | <0.01 | 3.2 ± 13.7   | 4.5               | 15.8                 |
|                      | LVESV (mL)  | 0.74  | <0.01 | 1.6 ± 12.7   | 8.0               | 36.7                 |
|                      | LVEF (%)    | 0.65  | <0.01 | −0.8 ± 10.2  | —                 | —                    |
|                      | LAVmax (mL) | 0.93* | <0.01 | −4.8 ± 17.0  | −5.0              | 19.5                 |
|                      | LAVmin (mL) | 0.79  | <0.01 | −19.5 ± 27.1 | −24.7             | 40.5                 |

Relative bias = (parameter<sub>method</sub> − parameter<sub>CMR</sub>) / parameter<sub>CMR</sub>. Percentage error = LOA / mean value of parameter measured by studied method and CMR. \**p* < 0.05 compared with without contour edit group.

## Automated Three-Dimensional Echocardiography Versus Cardiac Magnetic Resonance

**Table 4** represents the details of the comparisons between the automated 3DE echocardiographic measurements and the corresponding values obtained by CMR. There was strong correlation for LAVmax and modest correlations for LVEDV, LVESV, LVEF, and LAVmin between automated 3DE without contour edit and CMR ( $r = 0.77$ ,  $r = 0.68$ ,  $r = 0.63$ ,  $r = 0.62$ , and  $r = 0.64$ , respectively,  $P < 0.01$  for all). The correlations for LV and LA volumes were strong between automated 3DE with contour edit and CMR ( $r = 0.92$  for LVEDV,  $r = 0.74$  for LVESV,  $r = 0.93$  for LAVmax,  $r = 0.79$  for LAVmin,  $P < 0.01$  for all), while correlation for LVEF remained moderate ( $r = 0.65$ ,  $P < 0.01$ ).

The LVEDV and LVESV derived by automated 3DE without contour edit were overestimated compared with CMR reference values, with small bias. The LAVmax and LAVmin obtained by automated 3DE without contour edit were underestimated with big bias (**Figure 4**). The LOA were wide for all (**Table 4**).

With contour adjustment of automated 3DE values, the bias for LV and LA volumes compared with CMR were reduced (**Figure 5**). Automated 3DE with contour edit slightly overestimated LVEDV and LVESV (biases, 3.2 ml for LVEDV, 1.6 ml for LVESV; relative bias, 4.5% for LVEDV, 8.0% for LVESV of CMR values). The LAVmax and LAVmin were underestimated by automated 3DE with contour edit (biases, −4.8 ml for LAVmax, −19.5 ml for LAVmin; relative bias, −5.0% for LAVmax, −24.7% for LAVmin of CMR values). The LOA for LV and LA volumes were also reduced but were clinically acceptable only for LVEDV and LAVmax (**Table 4**).

When the impact of surgical technique was assessed, the biatrial group's correlations of LVESV and LVEF derived from automated 3DE with CMR reference values were stronger than those of bicaval group with contour edit, and the difference was statistically significant (**Table 5**).

## Reproducibility of Three-Dimensional Echocardiographic Measurements

Intraobserver and interobserver (with or without contour edit) variability for 3D echocardiographic measurements of LV, LA volumes and LVEF is summarized in **Table 6**.

Intraobserver and interobserver reproducibility of automated 3DE was high without contour edit (variability value <10%). When contour adjustment was performed, the variability values increased, however, those of LVEDV and LVEF remained low. As for manual 3DE, variability values of intraobserver and interobserver were higher than that of automated 3DE, no matter whether the contour adjustment was performed or not.

## DISCUSSION

To the best of our knowledge, this is the first study to assess the automated 3D echocardiographic algorithm (Heart Model) for quantification of left cardiac chamber volumes and LVEF in HTx recipients. Previous studies have demonstrated feasibility and reproducibility of automated 3DE in measuring left heart chamber and its function. In these studies, automated 3DE measurements have shown strong correlations with values derived from 2DE, manual 3DE, and CMR (11, 15, 16). These results were widely verified in adults, children, healthy population, and patients with specific diseases, including mitral regurgitation or atrial fibrillation (10, 17, 18). However, a transplanted heart is different from a normal one in cardiac anatomy, including its special location and structure after the orthotopic transplantation. Therefore, we tested the feasibility and accuracy of the automated 3DE technique, HeartModel, in HTx recipients.

Our major findings are as follows: in HTx recipients, (1) the correlations for LV and LA volumes between automated 3DE and manual 3DE were strong, while the correlation of LVEF between the two was moderate. After contour adjustment, all the values derived from automated 3DE

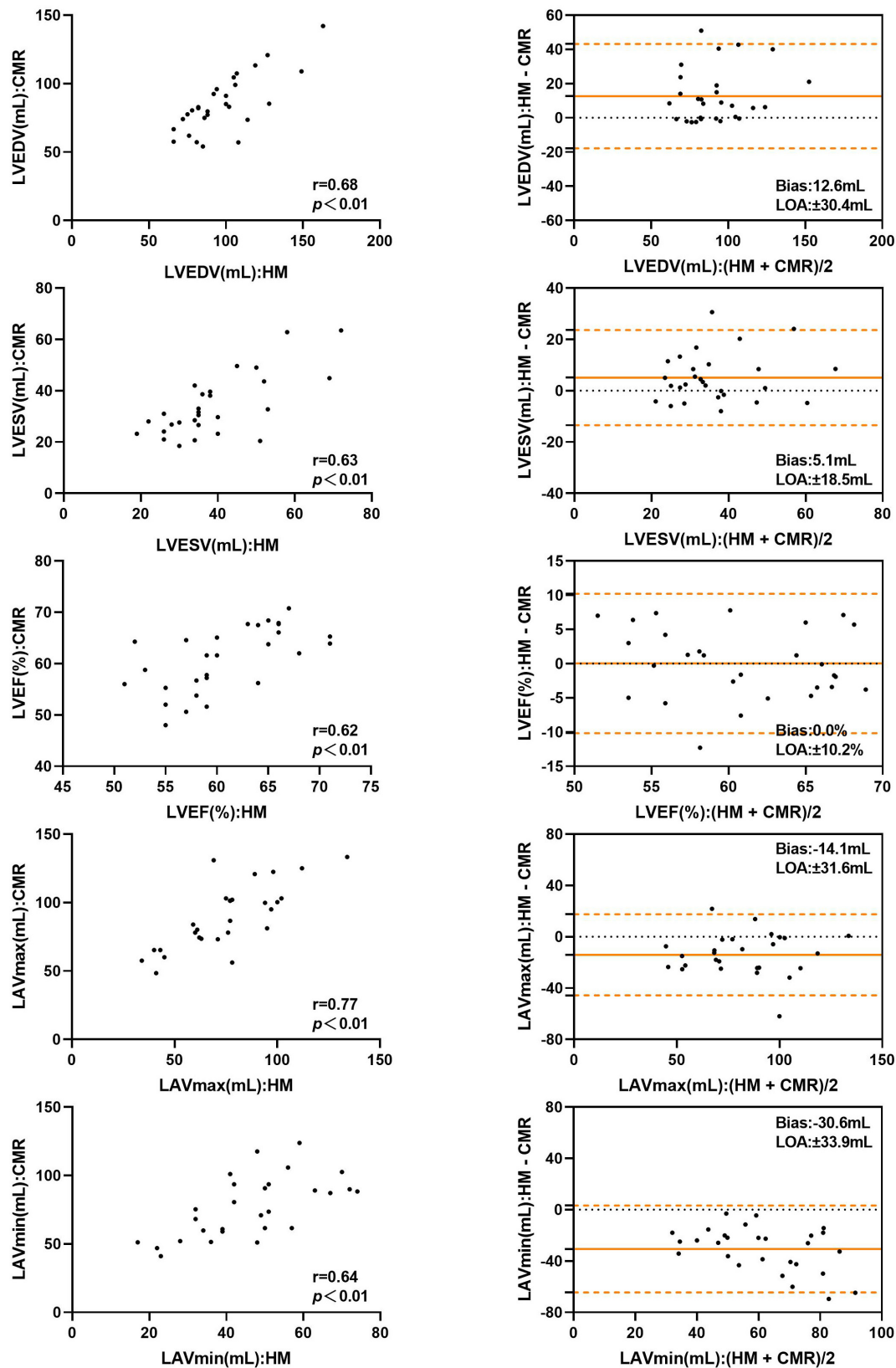


**FIGURE 4 |** Comparison between automated 3DE without contour adjustment and CMR of left heart volumes and ejection fraction: correlation and Bland-Altman analysis. HM: Automated 3DE by Heart Model without contour adjustment.

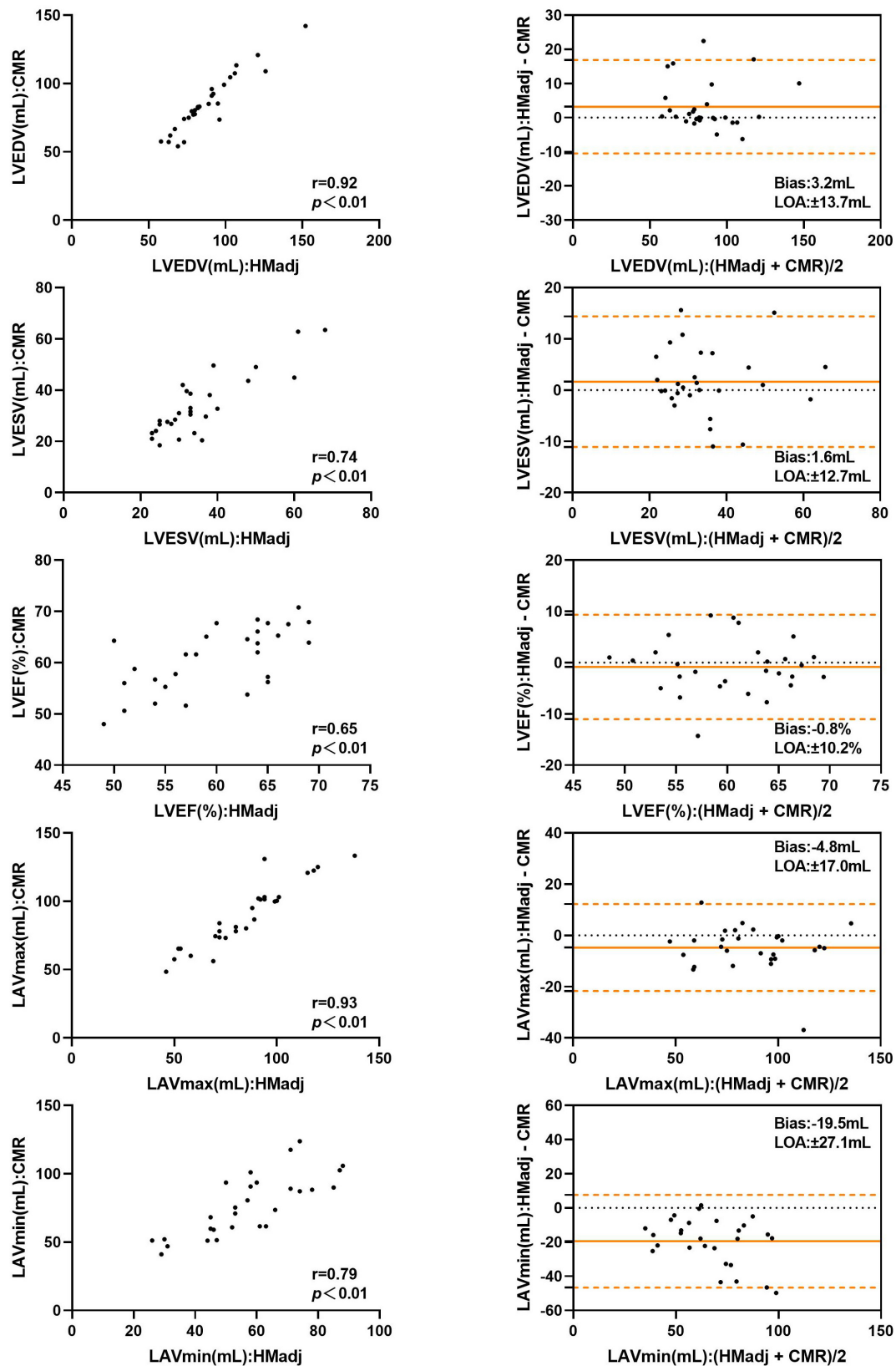


**FIGURE 5 |** Comparison between automated 3DE with contour adjustment and CMR of left heart volumes and ejection fraction: correlation and Bland-Altman analysis. HMadj: Automated 3DE by Heart Model with contour adjustment.

**TABLE 5 |** Effect of surgical technique on measurements from the automated 3DE compared with CMR measurements.

|                             | n  | Automated 3DE | CMR         | r                 | Bias ± LOA   |
|-----------------------------|----|---------------|-------------|-------------------|--------------|
| <b>LVEDV (mL)</b>           |    |               |             |                   |              |
| <b>Without contour edit</b> |    |               |             |                   |              |
| Biatrial                    | 12 | 94.5 ± 19.1   | 85.9 ± 15.5 | 0.75              | −8.6 ± 24.9  |
| Bicaval                     | 16 | 100.3 ± 26.9  | 84.7 ± 24.8 | 0.78              | −15.6 ± 33.7 |
| <b>With contour edit</b>    |    |               |             |                   |              |
| Biatrial                    | 12 | 86.6 ± 15.4   | 85.9 ± 15.5 | 0.98              | −0.7 ± 6.0   |
| Bicaval                     | 16 | 89.8 ± 24.5   | 84.7 ± 24.8 | 0.94              | −5.1 ± 16.6  |
| <b>LVESV (mL)</b>           |    |               |             |                   |              |
| <b>Without contour edit</b> |    |               |             |                   |              |
| Biatrial                    | 12 | 37.3 ± 11.2   | 33.7 ± 11.2 | 0.82              | −3.6 ± 13.6  |
| Bicaval                     | 16 | 40.3 ± 14.6   | 34.0 ± 12.9 | 0.68              | −6.2 ± 21.7  |
| <b>With contour edit</b>    |    |               |             |                   |              |
| Biatrial                    | 12 | 34.3 ± 11.1   | 33.7 ± 11.2 | 0.95 <sup>*</sup> | −0.6 ± 6.4   |
| Bicaval                     | 16 | 36.4 ± 12.6   | 34.0 ± 12.9 | 0.66              | −2.4 ± 16.0  |
| <b>LVEF (%)</b>             |    |               |             |                   |              |
| <b>Without contour edit</b> |    |               |             |                   |              |
| Biatrial                    | 12 | 61.3 ± 5.6    | 61.2 ± 7.8  | 0.74              | −0.1 ± 10.3  |
| Bicaval                     | 16 | 60.5 ± 5.7    | 60.5 ± 5.1  | 0.52              | −0.0 ± 10.4  |
| <b>With contour edit</b>    |    |               |             |                   |              |
| Biatrial                    | 12 | 60.5 ± 7.1    | 61.2 ± 7.8  | 0.93 <sup>*</sup> | 0.7 ± 5.6    |
| Bicaval                     | 16 | 59.6 ± 5.7    | 60.5 ± 5.1  | 0.28              | 0.9 ± 12.8   |
| <b>LAVmax (mL)</b>          |    |               |             |                   |              |
| <b>Without contour edit</b> |    |               |             |                   |              |
| Biatrial                    | 12 | 89.1 ± 22.5   | 99.7 ± 19.6 | 0.82              | 10.6 ± 25.1  |
| Bicaval                     | 16 | 64.9 ± 19.4   | 81.5 ± 23.9 | 0.67              | 16.6 ± 35.6  |
| <b>With contour edit</b>    |    |               |             |                   |              |
| Biatrial                    | 12 | 96.5 ± 20.2   | 99.7 ± 19.6 | 0.97              | 3.2 ± 9.6    |
| Bicaval                     | 16 | 75.6 ± 20.5   | 81.5 ± 23.9 | 0.90              | 5.9 ± 20.9   |
| <b>LAVmin (mL)</b>          |    |               |             |                   |              |
| <b>Without contour edit</b> |    |               |             |                   |              |
| Biatrial                    | 12 | 49.1 ± 12.9   | 85.8 ± 19.2 | 0.60              | 36.7 ± 25.6  |
| Bicaval                     | 16 | 43.9 ± 16.9   | 69.9 ± 22.7 | 0.64              | 26.0 ± 34.6  |
| <b>With contour edit</b>    |    |               |             |                   |              |
| Biatrial                    | 12 | 60.0 ± 13.7   | 85.8 ± 19.2 | 0.72              | 25.8 ± 25.9  |
| Bicaval                     | 16 | 55.1 ± 19.9   | 69.9 ± 22.7 | 0.83              | 14.78 ± 24.9 |

\**p* < 0.05 compared with bicaval group.**TABLE 6 |** Test-retest, intraobserver, interobserver variability (coefficients of variation) for the automated and manual 3D echocardiographic measurements of LV volumes, LVEF and LA volumes.

|        | Automated 3DE                        |                                   |  |                                     | Manual 3DE        |                   |
|--------|--------------------------------------|-----------------------------------|--|-------------------------------------|-------------------|-------------------|
|        | Test-retest without contour edit (%) | Test-retest with contour edit (%) | Interobserver without contour edit (%) | Interobserver with contour edit (%) | Intraobserver (%) | Interobserver (%) |
| LVEDV  | 4.0 ± 5.3                            | 9.4 ± 7.9                         | 4.9 ± 5.6                              | 8.0 ± 8.9                           | 10.9 ± 11.3       | 10.3 ± 13.6       |
| LVESV  | 8.5 ± 11.3                           | 12.7 ± 8.8                        | 6.2 ± 9.0                              | 11.7 ± 10.4                         | 13.9 ± 14.5       | 17.1 ± 13.9       |
| LVEF   | 3.6 ± 5.7                            | 5.6 ± 4.6                         | 4.1 ± 3.9                              | 5.6 ± 4.5                           | 8.4 ± 7.0         | 7.9 ± 5.6         |
| LAVmax | 8.3 ± 10.1                           | 11.5 ± 9.4                        | 8.3 ± 9.9                              | 9.8 ± 10.0                          | 13.1 ± 12.0       | 14.8 ± 13.7       |
| LAVmin | 7.1 ± 9.0                            | 13.5 ± 12.5                       | 6.4 ± 8.8                              | 15.8 ± 10.2                         | 13.4 ± 11.6       | 15.6 ± 9.8        |

showed strong correlations with manual 3DE reference values; (2) All the automated 3DE measurements had stronger correlations with manual 3DE reference values than 2DE-derived values except for LVEF; (3) LV volumes, LAVmin, and LVEF derived from automated 3DE were moderately correlated with CMR reference values, but

the automated 3DE measurements of LAVmax correlated strongly with CMR reference values. When contour edit was performed, all the correlations became strong except for LVEF; and (4) surgical techniques had no impact on the correlations for most left cardiac chamber volumes between automated 3DE and CMR whether or not contour edit was performed. Only the biatrial group's correlations for LVESV and LVEF between automated 3DE and CMR were stronger than those of bicaval group after contour edit.

In our study, automated 3DE presented a high degree of feasibility in HTx recipients, which was in line with previous studies performed in unselected patients. Although the position of the transplanted heart is more or less different from that of the normal heart, HeartModel can overcome this barrier in its automatic analysis.

However, the correlations between automated 3DE measurements and manual 3DE measurements for left heart chamber and LVEF in our cohort were lower than those obtained in previous studies. Contour adjustment can improve the correlations but it is hard to reach the level found in patients without HTx. Nevertheless, the correlations for left cardiac chamber volumes between automated 3DE and manual 3DE were stronger than those between 2DE and manual 3DE. 3DE is independent of geometric assumptions, which makes it more reliable than 2DE, and this can explain the stronger correlations between automated 3DE measurements and manual 3DE ones.

When automated 3DE was compared with the gold standard, CMR, only the accuracy of automated 3DE measurements of LVEDV and LAVmax was similar to that of previous studies after the contour edit (11). We believe this poor precision could be explained by the workflow of Heart Model and the distorted anatomy of transplanted hearts. The first step of Heart Model's automated analysis is knowledge-based identification, which is trained to use approximately 1000 echo images from a wide variety of heart shapes and sizes. The software screens the cardiac chamber shapes, including the overall morphological size, shape, curvature, and volume of the 3DE data, to select the best "matching" shapes (11). However, a transplanted heart was made up of the donor's and part of the recipient heart. It is hard to find an appropriate "matching" shape in the database. The moderate precision of automated 3DE for LVESV measurements can explain the moderate correlation for LVEF between automated 3DE and CMR. This was also reported in some previous publications (15, 17). In our cohort, LA volumes were underestimated by automated 3DE, which was consistent with previous studies (11). Contrary to what was found in previous publications (11, 19), automated 3DE overestimated LV volumes compared with CMR. As is mentioned above, the automated analysis software will select a best "matching" shape for the analyzed heart in its database, which is made up of various heart shapes. The surgical techniques used in our study entailed anastomoses at the mid-level of the left and right atria or at the base of the left atrial appendage (13), which makes the atria of transplanted heart bigger

than the normal one. To match the big atria, the software had to choose a bigger shape than the best matching for ventricle. The biatrial group demonstrated stronger correlations for LVESV and LVEF than bicaval group after contour edit. Bicaval anastomosis technique results in varying degrees of enlargement of the two atriums, and thus the transplanted heart of the bicaval group was more twisty than the biatrial group. Therefore, it is more difficult for the software to match a suitable model and make appropriate adaption for the heart to be analyzed. We believe the difference between correlations for LVEF can be explained by the different correlations for LVESV. However, it cannot explain the similarity of the correlations for LVEDV and LA volumes between the two groups.

Our study demonstrated intraobserver and interobserver variability for LV and LA indices' manual 3D echocardiographic measurements, which was consistent with previous studies. For automated 3DE in patients without HTx, test-retest with or without contour edit, intraobserver, and interobserver variability values were similar to or slightly higher than those in previous studies (10–12, 19–21).

## LIMITATIONS

First, this was a single-center study performed in clinically well HTx recipients, and the sample size was small. Though the number of patients was enough in comparisons with the reference techniques to reach statistical significance, multi-centered studies with larger sample size are desirable to further validate the findings. In addition, the HeartModel algorithm we used was based on heart contours of patients without heart transplantation, which would inevitably hamper the accuracy of our results. We hope the database of the algorithm could add a 3DE data set of cardiac chamber images from a large cohort of HTx recipients, which could improve its feasibility and accuracy. Furthermore, lower spatial and temporal resolution in 3DE may explain in part some of the discrepancies in our results. But the mean 3DE volume rate which was 20 Hz is acceptable for the analysis of chamber morphologies.

## CONCLUSION

In HTx recipients, automated 3DE is feasible to a great degree. It is both reproducible and faster can be achieved than manual 3DE. Meanwhile, it is comparable with manual 3DE for measurements of left heart volumes, along with slight overestimation of LVEDV and underestimation of LAVmax, a large overestimation of LVESV and underestimation of LAVmin. But the inaccuracies for LVESV and LAVmin can be improved with manual contour edit. Although there is a good correlation between CMR and automated 3DE in LV and LA volumes from the echocardiograms of HTx recipients using the HeartModel, only LVEDV and LAVmax measured by automated 3DE with contour edit seems sufficiently

accurate for clinical practice. There was slight overestimation of LVEDV and underestimation of LAVmax, but with clinically acceptable precision.

## DATA AVAILABILITY STATEMENT

The original contributions presented in the study are included in the article/supplementary material, further inquiries can be directed to the corresponding authors.

## ETHICS STATEMENT

The study was approved by the Ethics Committee of Tongji Medical College, Huazhong University of Science and Technology. Furthermore, we obtained written informed consent from all participants.

## REFERENCES

1. Dipchand AI, Edwards LB, Kucheryavaya AY, Benden C, Dobbels F, Levvey BJ, et al. The registry of the international society for heart and lung transplantation: seventeenth official pediatric heart transplantation report—2014; focus theme: retransplantation. *J Heart Lung Transplant.* (2014) 33:985–95. doi: 10.1016/j.healun.2014.08.002
2. Hunt SA, Haddad F. The changing face of heart transplantation. *J Am Coll Cardiol.* (2008) 52:587–98. doi: 10.1016/j.jacc.2008.05.020
3. Eleid MF, Caracciolo G, Cho EJ, Scott RL, Steidley DE, Wilansky S, et al. Natural history of left ventricular mechanics in transplanted hearts: relationships with clinical variables and genetic expression profiles of allograft rejection. *JACC Cardiovasc Imaging.* (2010) 3:989–1000. doi: 10.1016/j.jcmg.2010.07.009
4. Khush KK, Cherikh WS, Chambers DC, Harhay MO, Hayes D Jr, Hsieh E, et al. The international thoracic organ transplant registry of the international society for heart and lung transplantation: thirty-sixth adult heart transplantation report – 2019. Focus theme: donor and recipient size match. *J Heart Lung Transplant.* (2019) 38:1056–66. doi: 10.1016/j.healun.2019.08.004
5. Mor-Avi V, Jenkins C, Kuhl HP, Nesser HJ, Marwick T, Franke A, et al. Real-time 3-dimensional echocardiographic quantification of left ventricular volumes: multicenter study for validation with magnetic resonance imaging and investigation of sources of error. *JACC Cardiovasc Imaging.* (2008) 1:413–23. doi: 10.1016/j.jcmg.2008.02.009
6. Sugeng L, Mor-Avi V, Weinert L, Niel J, Ebner C, Steringer-Mascherbauer R, et al. Quantitative assessment of left ventricular size and function: side-by-side comparison of real-time three-dimensional echocardiography and computed tomography with magnetic resonance reference. *Circulation.* (2006) 114:654–61. doi: 10.1161/CIRCULATIONAHA.106.626143
7. Mor-Avi V, Yodanis C, Jenkins C, Kuhl H, Nesser HJ, Marwick TH, et al. Real-time 3d echocardiographic quantification of left atrial volume: multicenter study for validation with CMR. *JACC Cardiovasc Imaging.* (2012) 5:769–77. doi: 10.1016/j.jcmg.2012.05.011
8. Muraru D, Badano LP, Ermacor D, Piccoli G, Iliceto S. Sources of variation and bias in assessing left ventricular volumes and dyssynchrony using three-dimensional echocardiography. *Int J Cardiovasc Imaging.* (2012) 28:1357–68. doi: 10.1007/s10554-011-9985-0
9. Tsang W, Kenny C, Adhya S, Kapetanakis S, Weinert L, Lang RM, et al. Interinstitutional measurements of left ventricular volumes, speckle-tracking strain, and dyssynchrony using three-dimensional echocardiography. *J Am Soc Echocardiogr.* (2013) 26:1253–7. doi: 10.1016/j.echo.2013.07.023

## AUTHOR CONTRIBUTIONS

YwZ, CW, YL, LZ, and MX: conception and design of the study. YwZ, CW, WS, SZ, YeZ, and YaZ: acquisition of data. YwZ and YTZ: analysis and interpretation of data. YwZ, YX, and ZZ: drafting the article. LZ: revising the article. LZ and MX: finale approval of the article. All authors listed have made a substantial, direct, and intellectual contribution to the work, and approved it for publication.

## FUNDING

This work was supported by the National Natural Science Foundation of China (Nos. 81922033 and 82171964) and Outstanding Youth Foundation of Hubei Province of China (2021CFA046).

10. Otani K, Nakazono A, Salgo IS, Lang RM, Takeuchi M. Three-dimensional echocardiographic assessment of left heart chamber size and function with fully automated quantification software in patients with atrial fibrillation. *J Am Soc Echocardiogr.* (2016) 29:955–65. doi: 10.1016/j.echo.2016.06.010
11. Tsang W, Salgo IS, Medvedofsky D, Takeuchi M, Prater D, Weinert L, et al. Transthoracic 3d echocardiographic left heart chamber quantification using an automated adaptive analytics algorithm. *JACC Cardiovasc Imaging.* (2016) 9:769–82. doi: 10.1016/j.jcmg.2015.12.020
12. Spitzer E, Ren B, Soliman OI, Zijlstra F, Van Mieghem NM, Geleijnse ML. Accuracy of an automated transthoracic echocardiographic tool for 3d assessment of left heart chamber volumes. *Echocardiography.* (2017) 34:199–209. doi: 10.1111/echo.13436
13. Badano LP, Miglioranza MH, Edvardsen T, Colafranceschi AS, Muraru D, Bacal F, et al. European association of cardiovascular imaging/cardiovascular imaging department of the Brazilian society of cardiology recommendations for the use of cardiac imaging to assess and follow patients after heart transplantation. *Eur Heart J Cardiovasc Imaging.* (2015) 16:919–48. doi: 10.1093/ehjci/jev139
14. Lang RM, Badano LP, Mor-Avi V, Afilalo J, Armstrong A, Ernande L, et al. Recommendations for cardiac chamber quantification by echocardiography in adults: an update from the american society of echocardiography and the european association of cardiovascular imaging. *J Am Soc Echocardiogr.* (2015) 28:1–39.e14. doi: 10.1016/j.echo.2014.10.003
15. Medvedofsky D, Mor-Avi V, Byku I, Singh A, Weinert L, Yamat M, et al. Three-dimensional echocardiographic automated quantification of left heart chamber volumes using an adaptive analytics algorithm: feasibility and impact of image quality in nonselected patients. *J Am Soc Echocardiogr.* (2017) 30:879–85. doi: 10.1016/j.echo.2017.05.018
16. Tamborini G, Piazzese C, Lang RM, Muratori M, Chiorino E, Mapelli M, et al. Feasibility and accuracy of automated software for transthoracic three-dimensional left ventricular volume and function analysis: comparisons with two-dimensional echocardiography, three-dimensional transthoracic manual method, and cardiac magnetic resonance imaging. *J Am Soc Echocardiogr.* (2017) 30:1049–58. doi: 10.1016/j.echo.2017.06.026
17. Amadiou R, Hadeed K, Jaffro M, Karsenty C, Ratsimandresy M, Dulac Y, et al. Feasibility of new transthoracic three-dimensional echocardiographic automated software for left heart chamber quantification in children. *J Am Soc Echocardiogr.* (2019) 32: 121–34.e1. doi: 10.1016/j.echo.2018.08.001
18. Levy F, Marechaux S, Iacuzio L, Schouder ED, Castel AL, Toledano M, et al. Quantitative assessment of primary mitral regurgitation using left ventricular volumes obtained with new automated three-dimensional transthoracic echocardiographic software: a comparison with 3-tesla cardiac magnetic

- resonance. *Arch Cardiovasc Dis.* (2018) 111:507–17. doi: 10.1016/j.acvd.2017.10.008
19. Levy F, Dan Schouver E, Iacuzio L, Civaia F, Rusek S, Dommerc C, et al. Performance of new automated transthoracic three-dimensional echocardiographic software for left ventricular volumes and function assessment in routine clinical practice: comparison with 3 tesla cardiac magnetic resonance. *Arch Cardiovasc Dis.* (2017) 110:580–9. doi: 10.1016/j.acvd.2016.12.015
  20. Luo XX, Fang F, So HK, Liu C, Yam MC, Lee AP. Automated left heart chamber volumetric assessment using three-dimensional echocardiography in Chinese adolescents. *Echo Res Pract.* (2017) 4:53–61. doi: 10.1530/ERP-17-0028
  21. Medvedofsky D, Mor-Avi V, Amzulescu M, Fernandez-Golfin C, Hinojar R, Monaghan MJ, et al. Three-dimensional echocardiographic quantification of the left-heart chambers using an automated adaptive analytics algorithm: multicentre validation study. *Eur Heart J Cardiovasc Imaging.* (2018) 19:47–58. doi: 10.1093/ehjci/jew328

**Conflict of Interest:** The authors declare that the research was conducted in the absence of any commercial or financial relationships that could be construed as a potential conflict of interest.

**Publisher's Note:** All claims expressed in this article are solely those of the authors and do not necessarily represent those of their affiliated organizations, or those of the publisher, the editors and the reviewers. Any product that may be evaluated in this article, or claim that may be made by its manufacturer, is not guaranteed or endorsed by the publisher.

Copyright © 2022 Zhang, Wu, Sun, Zhu, Zhang, Xie, Zhu, Zhang, Zhao, Li, Xie and Zhang. This is an open-access article distributed under the terms of the Creative Commons Attribution License (CC BY). The use, distribution or reproduction in other forums is permitted, provided the original author(s) and the copyright owner(s) are credited and that the original publication in this journal is cited, in accordance with accepted academic practice. No use, distribution or reproduction is permitted which does not comply with these terms.



# High-Resolution Free-Breathing Quantitative First-Pass Perfusion Cardiac MR Using Dual-Echo Dixon With Spatio-Temporal Acceleration

## OPEN ACCESS

### Edited by:

Sebastian Kelle,  
Deutsches Herzzentrum  
Berlin, Germany

### Reviewed by:

Vivek Muthurangu,  
University College London,  
United Kingdom  
Theo Pezel,  
Hôpital Lariboisière, France  
Otávio R. Coelho-Filho,  
State University of Campinas, Brazil

### \*Correspondence:

Teresa Correia  
teresa.correia@kcl.ac.uk

†These authors have contributed  
equally to this work

### Specialty section:

This article was submitted to  
Cardiovascular Imaging,  
a section of the journal  
Frontiers in Cardiovascular Medicine

Received: 25 February 2022

Accepted: 04 April 2022

Published: 29 April 2022

### Citation:

Tourais J, Scannell CM, Schneider T,  
Alskaf E, Crawley R, Bosio F,  
Sanchez-Gonzalez J, Doneva M,  
Schülke C, Meineke J, Keupp J,  
Smink J, Breeuwer M, Chiribiri A,  
Henningsson M and Correia T (2022)  
High-Resolution Free-Breathing  
Quantitative First-Pass Perfusion  
Cardiac MR Using Dual-Echo Dixon  
With Spatio-Temporal Acceleration.  
Front. Cardiovasc. Med. 9:884221.  
doi: 10.3389/fcvm.2022.884221

Joao Tourais<sup>1,2,3†</sup>, Cian M. Scannell<sup>4†</sup>, Torben Schneider<sup>5</sup>, Ebrahim Alskaf<sup>4</sup>,  
Richard Crawley<sup>4</sup>, Filippo Bosio<sup>4</sup>, Javier Sanchez-Gonzalez<sup>6</sup>, Mariya Doneva<sup>7</sup>,  
Christophe Schülke<sup>7</sup>, Jakob Meineke<sup>7</sup>, Jochen Keupp<sup>7</sup>, Jouke Smink<sup>1</sup>,  
Marcel Breeuwer<sup>1,2</sup>, Amedeo Chiribiri<sup>4</sup>, Markus Henningsson<sup>4,8,9†</sup> and Teresa Correia<sup>4,10\*†</sup>

<sup>1</sup> Department of Biomedical Engineering, Eindhoven University of Technology, Eindhoven, Netherlands, <sup>2</sup> Department of MR R&D – Clinical Science, Philips Healthcare, Best, Netherlands, <sup>3</sup> Department of Imaging Physics, Magnetic Resonance Systems Lab, Delft University of Technology, Delft, Netherlands, <sup>4</sup> School of Biomedical Engineering and Imaging Sciences, King's College London, London, United Kingdom, <sup>5</sup> Philips Healthcare, Guildford, United Kingdom, <sup>6</sup> Philips Healthcare Iberia, Madrid, Spain, <sup>7</sup> Philips Research, Hamburg, Germany, <sup>8</sup> Division of Cardiovascular Medicine, Department of Medical and Health Sciences, Linköping University, Linköping, Sweden, <sup>9</sup> Center for Medical Image Science and Visualization (CMIV), Linköping University, Linköping, Sweden, <sup>10</sup> Centre for Marine Sciences (CCMAR), Faro, Portugal

**Introduction:** To develop and test the feasibility of free-breathing (FB), high-resolution quantitative first-pass perfusion cardiac MR (FPP-CMR) using dual-echo Dixon (FOSTERS; Fat-water separation for mOtion-corrected Spatio-TEmporally accelerated myocardial perFuSion).

**Materials and Methods:** FOSTERS was performed in FB using a dual-saturation single-bolus acquisition with dual-echo Dixon and a dynamically variable Cartesian k-t undersampling (8-fold) approach, with low-rank and sparsity constrained reconstruction, to achieve high-resolution FPP-CMR images. FOSTERS also included automatic in-plane motion estimation and T<sub>2</sub>\* correction to obtain quantitative myocardial blood flow (MBF) maps. High-resolution (1.6 × 1.6 mm<sup>2</sup>) FB FOSTERS was evaluated in eleven patients, during rest, against standard-resolution (2.6 × 2.6 mm<sup>2</sup>) 2-fold SENSE-accelerated breath-hold (BH) FPP-CMR. In addition, MBF was computed for FOSTERS and spatial wavelet-based compressed sensing (CS) reconstruction. Two cardiologists scored the image quality (IQ) of FOSTERS, CS, and standard BH FPP-CMR images using a 4-point scale (1–4, non-diagnostic – fully diagnostic).

**Results:** FOSTERS produced high-quality images without dark-rim and with reduced motion-related artifacts, using an 8x accelerated FB acquisition. FOSTERS and standard BH FPP-CMR exhibited excellent IQ with an average score of 3.5 ± 0.6 and 3.4 ± 0.6 (no statistical difference, *p* > 0.05), respectively. CS images exhibited severe artifacts and high levels of noise, resulting in an average IQ score of 2.9 ± 0.5. MBF values obtained with FOSTERS presented a lower variance than those obtained with CS.

**Discussion:** FOSTERS enabled high-resolution FB FPP-CMR with MBF quantification. Combining motion correction with a low-rank and sparsity-constrained reconstruction results in excellent image quality.

**Keywords:** myocardial perfusion, high-resolution, free-breathing, quantitative myocardial blood flow, Dixon, motion correction

## INTRODUCTION

First-pass perfusion cardiac MR (FPP-CMR) enables non-invasive detection of ischemic heart disease (1–3). Typically, assessment is based on visual comparison of relative contrast enhancement in different myocardial segments, which requires highly trained readers (4). Quantitative FPP-CMR (QFPP-CMR) provides an objective assessment by estimating pixel-wise myocardial blood flow (MBF) (5) and has high diagnostic and prognostic value (6–10). However, there are several technical challenges that can negatively impact the image quality and the diagnostic yield. Since MBF quantification is based on modeling the signal intensity during the first pass of a contrast agent bolus, sources of motion must be minimized to ensure that the same anatomy is depicted for a given pixel across time. In particular, the duration of the first pass, approximately 30–50 s, does not fit into a breath-hold and therefore, respiratory motion poses a significant challenge (11). Free-breathing QFPP-CMR can be performed with retrospective respiratory motion correction using image registration, yet the localized strong image contrast changes can hamper the performance of conventional signal intensity-based registration algorithms (12, 13). FPP-CMR images are also commonly affected by the dark-rim artifact which mimics perfusion defects and is exacerbated by a low spatial resolution (14, 15). The signal from subcutaneous, epicardial, or intramyocardial fat may also adversely impact quantification and image quality. While fat-selective saturation prepulses can be employed, in practice they are limited to centric phase encoding sampling which can cause blurring and reduced contrast. Finally, MBF quantification may be biased by signal nonlinearities at very high contrast agent concentrations due to  $T_1$  saturation and  $T_2^*$ -related signal loss (5, 16–18).

Recently, a dual-bolus multi-echo Dixon QFPP-CMR framework has been proposed to address in-plane respiratory motion,  $T_2^*$ -related signal loss, and fat suppression (19). This method provides fat-only images, which were used to estimate respiratory motion, while motion-corrected water-only images were used for visual assessment and MBF quantification. In this work, a framework titled “Fat-water separation for motion-corrected Spatio-TEmporally accelerated myocardial perFuSion” (FOSTERS) is proposed. FOSTERS extends the previous work by combining a dynamic variable undersampled dual-echo Dixon acquisition with a motion-corrected reconstruction with low-rank and sparsity constraints to achieve high-resolution FPP-CMR images. Additionally, the high-resolution acquisition is interleaved with a low-resolution image with a low  $T_1$  sensitivity for estimating the arterial input function (AIF) (20). As before, echo images were used for correcting the AIF for  $T_2^*$ -related signal losses to further improve MBF quantification. The

performance of FOSTERS is compared to a standard compressed sensing reconstruction as well as the corresponding clinical standard-resolution breath-hold FPP-CMR. This comparison assessed the variability of MBF, the image sharpness, and the image quality scores of expert readers.

## MATERIALS AND METHODS

### FOSTERS Framework

#### Pulse Sequence

The FOSTERS pipeline (shown in **Figure 1**) comprises an electrocardiogram-triggered multi-slice dual-saturation (21) single-bolus acquisition with dual-echo gradient-echo imaging to allow for water-fat separation and  $T_2^*$  correction. In each cardiac cycle, to measure the AIF, the dual-echo acquisition is preceded by a low-resolution image with a short saturation time (20). A variable density Poisson distribution undersampled Cartesian acquisition was employed (22), where the center of k-space is more densely sampled than the periphery, to achieve an incoherent artifact distribution. In addition, the  $k_y$  pattern was pseudo-randomly varied individually for each time point ( $k$ -t acceleration).

#### Image Reconstruction and Motion Correction

The FOSTERS image reconstruction and motion correction were implemented in the Recon 2.0 environment (Philips, Best, The Netherlands) to allow for inline scanner integration. First, a Dixon reconstruction with compressed sensing (CS) using low-rank (time-domain) and sparsity (spatial domain) constraints (23) was performed with 10 iterations (empirically determined), which generates water- and fat-only images from  $k$ -t undersampled data with sufficient quality for in-plane respiratory motion estimation using image registration.

Thresholding, followed by dilation, was then employed to create a binary mask from the water images. From this binary mask, a bounding box was automatically placed around the epicardial fat and was used to estimate rigid respiratory motion using the Fast Elastic Image Registration (FEIR) toolbox (24) with normalized gradient fields as an image similarity measure. Fat images were used as a stable reference for the anatomy because they do not show contrast uptake-related image intensity changes, as proposed by Scannell et al. (19). A reference time frame, with superior-inferior (SI) motion displacement closest to the mean SI position, was selected. This translational motion information was used to correct rigidly the dual-echo data by applying a linear phase shift in  $k$ -space. Rigid motion only was estimated in this step due to the sparse signal of the fat images being unsuitable for non-rigid motion estimation. A non-rigid refinement step is performed at a later stage.

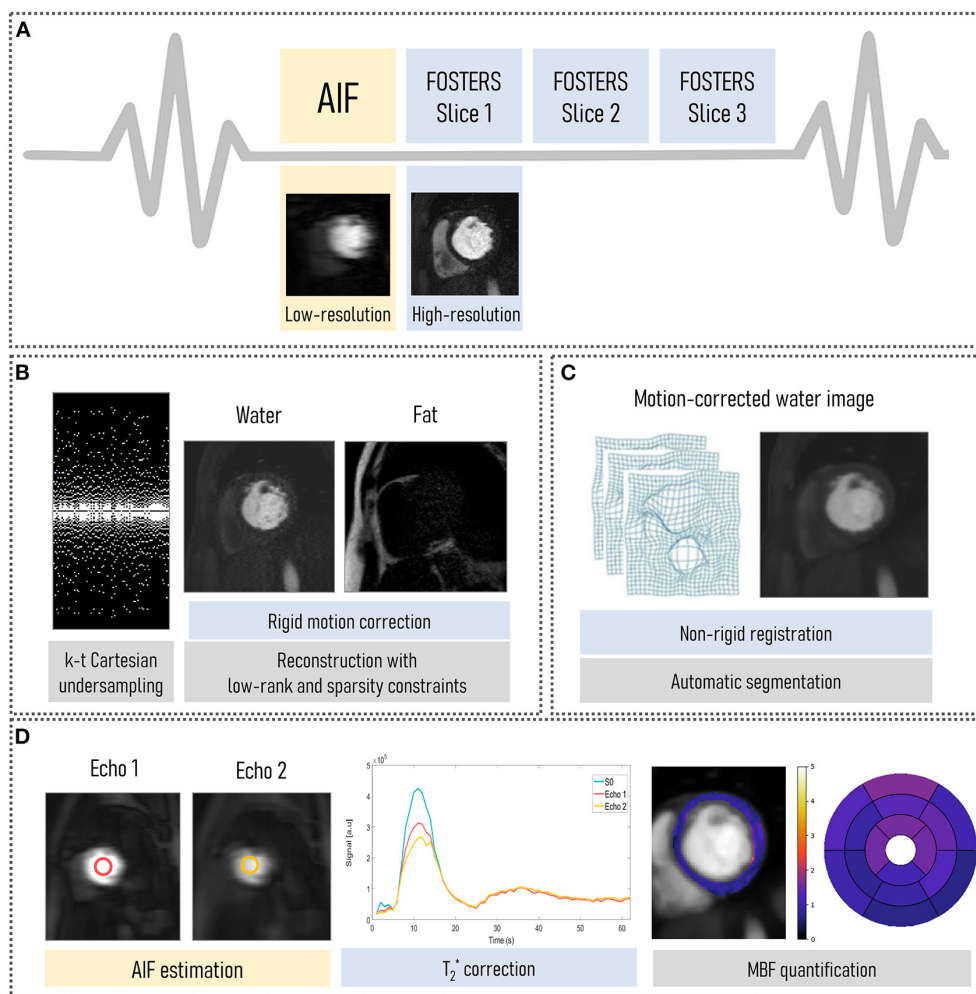


**FIGURE 1 |** FOSTERS framework: **(A)** A dual-saturation dual-echo Dixon FPP-CMR sequence was used to acquire low-resolution arterial input function (AIF) and high-resolution myocardial images. **(B)** Water- and fat-only images were obtained from k-t undersampled data using a fast low-rank and sparsity constrained reconstruction method with 10 iterations. Fat-only images were used to estimate in-plane respiratory motion. Then, rigidly motion-corrected images were generated using the same fast low-rank and sparsity regularized reconstruction method with 50 iterations. **(C)** The rigidly motion-corrected water-only images were fine-tuned using non-rigid registration and were automatically segmented to an AHA 16-segment model. **(D)** AIF echoes were used to correct for  $T_2^*$  decay and quantitative myocardial blood flow (MBF) maps were automatically obtained.

Finally, motion-corrected water-only images were generated using a CS reconstruction with low-rank and sparsity constraints after 50 iterations. Images were reconstructed using a fast sparsity and nuclear norm regularization method (23), which solved the following minimization problem:

$$\hat{x} = \arg \min_x \left\{ \frac{1}{2} \|Ex - k\|_2^2 + \alpha \|x\|_* + \beta \|\Psi x\|_1 \right\},$$

where  $x$  are the dynamic images,  $k$  is the dynamic time-series data (after translational motion correction),  $E$  is the SENSE encoding operator,  $\Psi$  is the spatial anisotropic total variation operator,  $\alpha$  and  $\beta$  are regularization parameters,  $\|\bullet\|_*$  is the nuclear norm (sum of singular values) and  $\|\bullet\|_1$  is the L1-norm. The regularization parameters were selected empirically and set at  $\alpha = 1$  and  $\beta = 0.005$  for all subjects.

### Post-processing: $T_2^*$ Correction and Quantification of Myocardial Blood Flow

The rigidly motion-corrected dynamic water-only images were fine-tuned using non-rigid registration to a corresponding motionless synthetic image series, generated with principal component analysis (12). FPP-CMR images were automatically segmented to an AHA 16-segment model using a deep learning-based method, as previously published (25). This model comprises four neural networks applied sequentially: a convolutional neural network (CNN) to detect the time-frame with peak left ventricle (LV) enhancement, a CNN to select a bounding box that encompasses the LV cavity and myocardium, a U-Net to segment the myocardium, and a U-Net to detect the right ventricle insertion points that define the 16 AHA-segments. In addition, the dual-echo images were used for estimating the AIF and  $T_2^*$ -related signal loss by

fitting the mean signal magnitude to an exponential decay model (19). Quantitative MBF values were estimated on a pixel-wise level by fitting the observed AIF and myocardial tissue curves to a two-compartment exchange model, using Bayesian inference (26). MBF quantification was performed using only the dynamic contrast-enhanced data corresponding to the first pass of the contrast bolus (approximately 20 sec of data).

## In vivo Experiments

All acquisitions reported in this study were performed on a 3.0T Achieva scanner (Philips, Best, The Netherlands) using a 32-channel cardiac coil. The study was approved by the National Research Ethics Service (15/NS/0030) and written informed consent was obtained from each participant according to institutional guidelines. All the patients enrolled in this study underwent a CMR examination for clinical nonstress function and viability assessment with known or suspected heart disease. Patients were required to be  $\geq 18$  years of age and have no contraindications to gadolinium contrast, inclusive of an estimated glomerular filtration rate  $\leq 60$  ml/min/1.73 m<sup>2</sup>.

Eleven patients (baseline characteristics in **Supplementary Table 1**) with suspected cardiovascular disease were scanned during rest with 8-fold k-t accelerated FOSTERS during the first pass of a contrast bolus injection (0.075 mmol/kg of Gadobutrol at 4 ml/s followed by 25 ml saline flush). Three short-axis slices (basal, mid, and apical) were acquired with the following parameters: FOV = 320 × 300 mm<sup>2</sup>, matrix size = 200 × 186, acquired/reconstructed in-plane resolution = 1.6 × 1.6 / 1.43 × 1.43 mm<sup>2</sup>, slice thickness = 10 mm, TR/TE1/TE2 = 2.8/1.1/1.9 ms, acceleration factor (R) = 8, saturation time (short TS / long TS) = 23.5/100 ms, flip angle = 15°, acquisition window = 65.4 ms, temporal resolution = 145 ms, bandwidth = 2,083.3 Hz, 54–87 dynamic frames, and scan time = 60 s. Apart from the previously mentioned saturation time and acquired in-plane resolution, all imaging parameters were kept constant between the AIF and the dual-echo images. The dual-echo FPP-CMR datasets were also reconstructed with the vendor's commercially available inline CS wavelet-based reconstruction (only spatial sparsity constraints with the default parameters) (27) and non-rigid motion correction. A BH standard-resolution 2D FPP-CMR acquisition (referred here as standard BH) (20) was acquired for the same eleven subjects with identical imaging parameters to FOSTERS except for in-plane resolution = 2.6 × 2.6 mm<sup>2</sup>, TR/TE = 2.2/1 ms, temporal resolution = 160 ms, SENSE = 2 and partial Fourier = 0.75. The standard BH and FOSTERS scans were performed with individual contrast injections and were separated by 5–7 min to allow for contrast washout.

To assess the motion correction performance of FOSTERS in different circumstances, one patient (baseline characteristics in **Supplementary Table 1**) was scanned separately with FOSTERS both in free-breathing (FB) and breath-hold (BH) during the same CMR examination. The scan parameters were kept identical for both acquisitions, and the BH-FOSTERS was acquired 11 min after the FB-FOSTERS.

## Image Evaluation and Statistical Analysis

FOSTERS, CS, and standard BH were processed, including the non-rigid motion compensation, following the procedure described in section 2.1.3. The MBF values estimated with FOSTERS were compared to those obtained with CS. The FOSTERS MBF values were not compared directly with the standard BH MBF values as the standard BH acquisition was the second contrast injection and the MBF values are biased by the residual contrast from the first injection. The presence of dark-rim artifacts and the image quality (IQ) of the three slices acquired with FOSTERS, CS, and standard BH were assessed jointly by two experienced cardiologists in a randomized setup, blinded to the patient information and imaging. IQ was graded on a scale of 1 to 4, in consensus: where (1) was non-diagnostic IQ; (2) was diagnostic IQ with major artifacts; (3) diagnostic IQ with minor artifacts; and (4) was fully diagnostic IQ with no artifacts. For each dataset (FOSTERS, CS, and standard BH) the total combined IQ score was calculated as the average score of the three slices. Quantitative image sharpness was calculated for FOSTERS, CS, and standard BH. For each patient, the three acquired slices were selected for sharpness analysis. In each image, a profile was manually selected between the left ventricle blood pool and the endocardium, as shown in **Supplementary Figure 1**. The sharpness was defined as the distance in pixels between 20% and 80% of the pixel intensity range of the profile, and a lower pixel distance indicates a sharper border (28). For FOSTERS, CS, and standard BH, the total image sharpness was calculated as the average of the three slices. For all statistical comparisons a *p*-value cut-off level of 0.05 was chosen to indicate significance and was performed using the Wilcoxon signed-rank test (IQ) and the Mann-Whitney U-test (sharpness).

## RESULTS

**Figure 2** shows the comparison of FB and BH FOSTERS on a single patient. Three-time frames are displayed for each slice together with 16-segment bullseye plots. Good image quality was achieved with both approaches, with FB-FOSTERS exhibiting overall sharper image features, while BH-FOSTERS presented some residual ghosting artifacts in some timeframes. In addition, FB-FOSTERS ( $0.7 \pm 0.1$  mL/min/g) yielded MBF values with 4-fold lower variation when compared to BH-FOSTERS ( $0.8 \pm 0.4$  mL/min/g).

All 11 patient scans were completed, reconstructed, and the in-plane motion was estimated successfully for all slices. **Figure 3** displays a comparison between the water-only images (middle slice) obtained with FB-FOSTERS, spatial wavelet-based CS, and standard BH for two representative patients (patients 5 and 7). **Supplementary Videos 1, 2** contain animations of these datasets for all approaches. Three different FOSTERS timeframes are displayed, demonstrating high image quality with no visible motion artifacts and clear myocardial depiction. Conversely, CS exhibited degraded image quality with high levels of noise. These differences between FOSTERS and CS are also visible in the fat-only images and the temporal profile as shown in **Supplementary Figure 2** and **Supplementary Video 3**. Standard

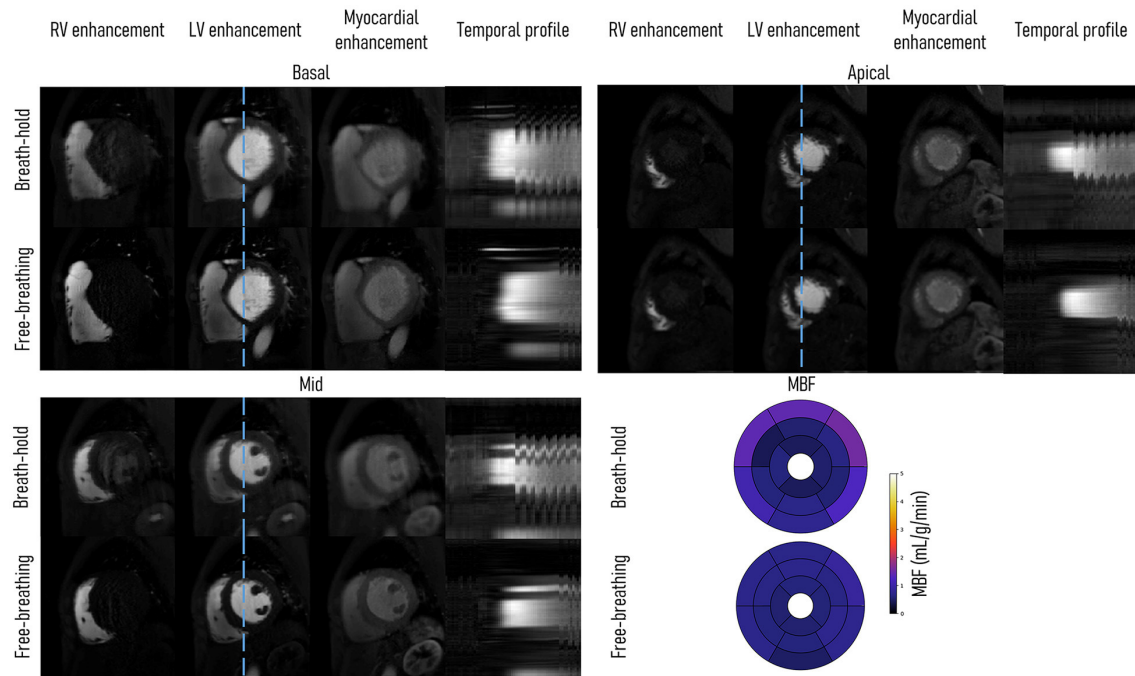


**FIGURE 2 |** Single patient (diagnosed with dilated cardiomyopathy) comparison between breath-hold (BH) and free-breathing (FB) FOSTERS. Right ventricle (RV), left ventricle (LV), myocardial enhancement timeframes, and a temporal profile (blue dashed line) are displayed for the acquired three short-axis slices (basal, mid, and apical). FB-FOSTERS images exhibit excellent quality with no visible motion artifacts, despite some visible motion in the final part of the acquisition, as shown in the temporal profile. In some timeframes, BH-FOSTERS displays residual ghosting artifacts, due to unsuccessful motion correction. This can be explained by the more regular respiratory motion during FB which is easier to correct than the large amplitude motion that may occur due to incomplete breath-holding. The 16-segment bullseye plot shows that the myocardial blood flow (MBF) values were more uniform for FB- than for BH-FOSTERS (average  $\pm$  SD for the 16 segments of  $0.7 \pm 0.1$  and  $0.8 \pm 0.4$  mL/min/g, respectively). The reconstruction parameters were kept identical for both approaches.

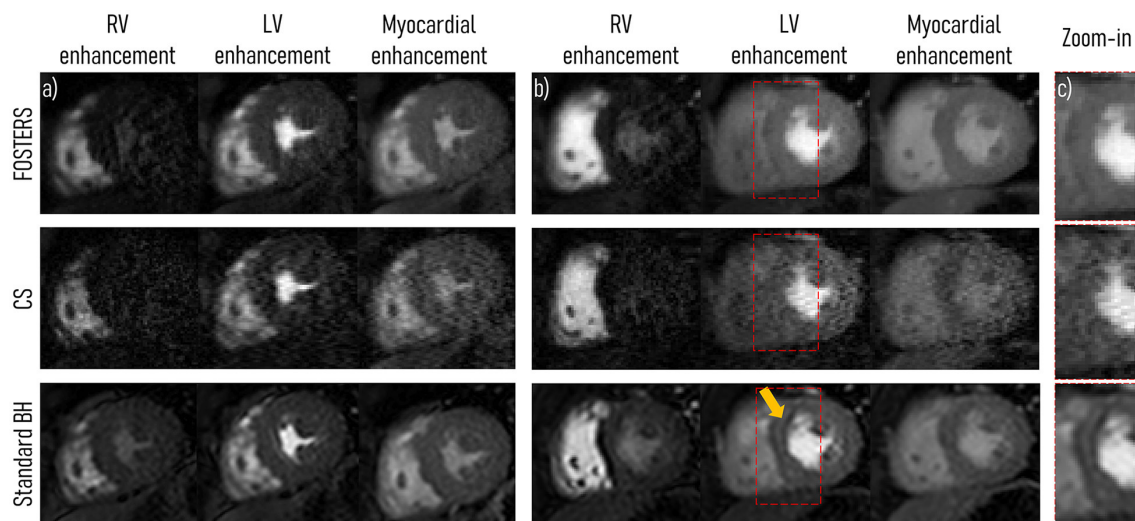


**FIGURE 3 |** A single short-axis view at mid-ventricular level is displayed during right ventricle (RV), left ventricle (LV), and myocardial enhancement for two representative patients (middle slice for **(A)** patient 5 and **(B)** 7). High-resolution free-breathing water-only FPP-CMR FOSTERS and spatial wavelet-based compressed sensing (CS) reconstruction in addition to standard-resolution FPP-CMR (Standard BH) are displayed. Overall, CS FPP-CMR exhibits a higher level of noise and artifacts compared to FOSTERS and standard BH. **(C)** In the zoom-in region (red rectangle), a dark-rim artifact can be seen in the standard BH images (arrow), which were not visible in the FOSTERS and CS images. **Supplementary Videos 1, 2** contains an animation of these datasets for all approaches.

BH FPP-CMR achieved excellent image sharpness (**Figure 3**), but dark-rim artifacts were still present in 7 out of the 33 cases (3 acquired slices for 11 patients). These were not visible in the FOSTERS and CS images.

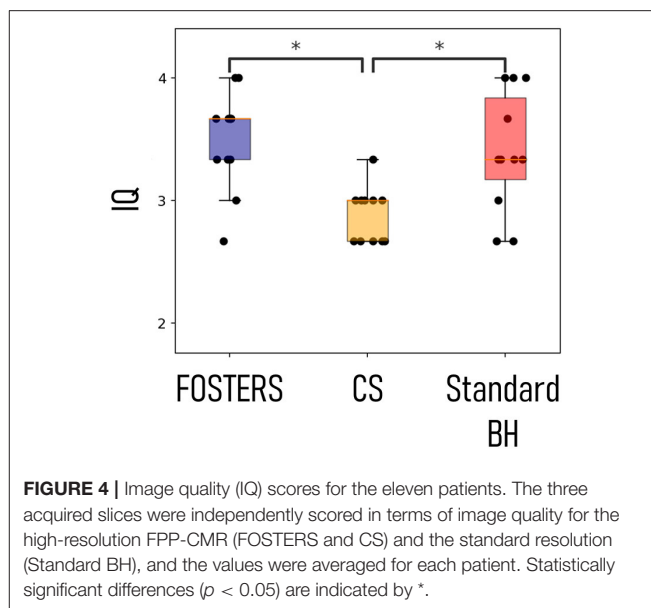
**Figure 4** shows the image quality score for all the patients, as an average score for the three slices, using FB-FOSTERS, CS, and standard BH. FOSTERS scored the highest ( $3.5 \pm 0.6$ ), followed by standard BH ( $3.4 \pm 0.6$ ) and CS ( $2.9 \pm 0.5$ ). The differences between FOSTERS and CS and between standard BH and CS were statistically significant ( $p = 0.004$  and  $0.02$ , respectively). There was no significant difference between the FOSTERS and standard BH images ( $p = 0.72$ ). The mean blood-myocardium sharpness  $\pm$  standard deviation was  $4.8 \pm 1.8$  for FOSTERS,  $3.2 \pm 2.1$  for CS, and  $4.9 \pm 2.4$  for standard BH. For the blood-myocardium sharpness measurements, no statistically significant differences were found between FOSTERS and CS ( $p = 0.08$ ), between FOSTERS and standard BH ( $p = 0.68$ ), and between CS and standard BH ( $p = 0.25$ ).

The 16-segment MBF plots for the FB-FOSTERS and CS approaches for all eleven patients are displayed in **Figure 5**. FOSTERS provides uniform MBF maps whereas CS results in MBF values with higher variation, which could be attributed to residual artifacts unresolved by the reconstruction algorithm and high levels of noise. These artifacts will affect the motion estimation performance,  $T_2^*$  correction of the AIF, and accuracy of the MBF estimation. The mean MBF ( $\pm$  SD) values were  $1.0 (\pm 0.3)$  and  $1.3 (\pm 0.6)$  mL/min/g for FOSTERS and CS, respectively. FOSTERS also resulted in a lower SD ( $0.4$  mL/min/g) when compared to CS ( $0.6$  mL/min/g). Significant differences ( $p = 0.01$ ) in MBF were found between the two methods. **Figure 6** shows representative slices of the pixel-wise MBF maps acquired with Standard BH, CS, and FOSTERS in three subjects. When compared to FOSTERS, the MBF maps obtained with Standard BH and CS exhibited a higher level of noise, resulting in a larger variation in the MBF values. MBF values obtained with the standard BH are higher due to the residual contrast from the FOSTERS acquisition, this is visible in the first row of **Figure 6**.

## DISCUSSION

Here, the feasibility of high-resolution QFPP-CMR imaging during FB was demonstrated by using a dual-saturation dual-echo Dixon water-fat separation, a compressed sensing reconstruction with low-rank and sparsity constraints, and respiratory motion correction. The dynamically varying 8-fold Cartesian k-t undersampling allowed to obtain a short temporal resolution ( $< 150$  ms) while maintaining the desired high in-plane resolution ( $1.6 \times 1.6$  mm<sup>2</sup>), making FOSTERS suitable for patients with heart rates up to 110 bpm. High-spatial resolution imaging is beneficial for minimizing dark-rim artifacts and detecting subtle sub-endocardial ischemia associated with coronary microvascular dysfunction (29) and is likely to improve the diagnostic yield of the modality.

As a proof-of-principle, to assess the performance of FOSTERS respiratory motion correction and MBF quantification, a comparison between FB- and BH-FOSTERS was performed in one patient (**Figure 2**). Fat-only images produced by the dual-echo Dixon acquisition allowed for

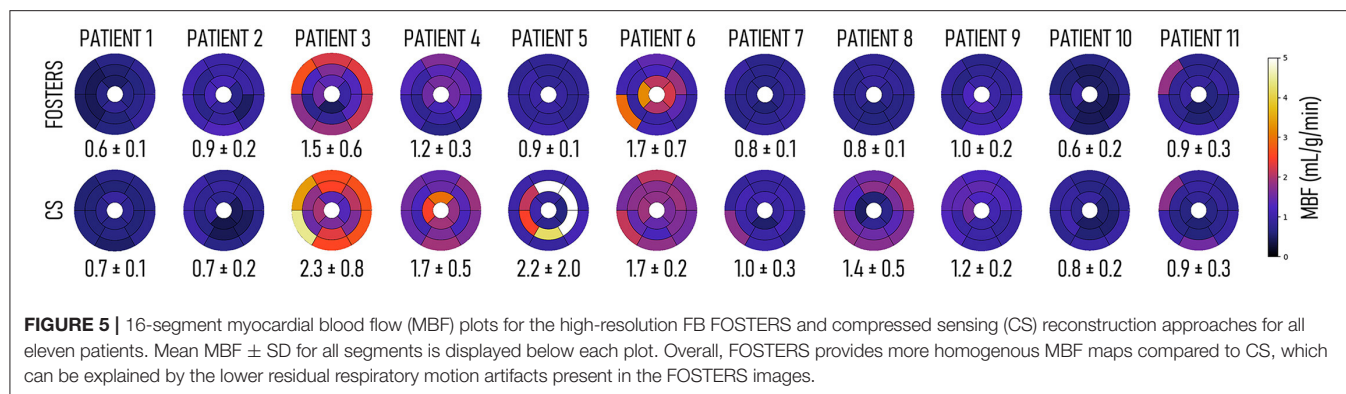


accurate in-plane motion estimation during free-breathing. Moreover, FB-FOSTERS resulted in FPP-CMR images with excellent sharpness of the cardiac structures and more uniform MBF maps compared to BH-FOSTERS. This can be explained by an incomplete BH, which resulted in high MBF values observed in the anterior and lateral walls of the basal slices.

In the image quality evaluation, FB-FOSTERS was ranked the highest. In the representative cases displayed in **Figure 3**, FOSTERS presented an excellent depiction of the myocardium with minimal residual motion-related artifacts in the FPP-CMR images. Standard BH also exhibited excellent image quality, but the need for the BH significantly impacted the subject's comfort, which can lead to images with insufficient diagnostic quality. In addition, dark-rim artifacts were observed in standard BH images but were not visible in FOSTERS water-only FPP-CMR images because of the higher image resolution of FOSTERS compared to standard BH ( $1.6 \times 1.6$  and  $2.6 \times 2.6$  mm<sup>2</sup>, respectively). The image quality using spatial wavelet-based CS was scored the lowest due to the high level of image artifacts and noise. On the other hand, image quality of k-t undersampled reconstruction is known to be sensitive to respiratory motion, which negatively affects the spatio-temporal correlations. The addition of a rigid motion correction step (translational motion) in combination with a non-rigid motion correction results in robust FB acquisitions, as previously demonstrated by Scannell et al. (19).

Overall, FOSTERS provided more homogenous MBF maps compared to CS for the eleven patients included in this work. This may be due to the higher respiratory motion artifacts present in the CS images, which result in higher values and variance in the measured MBF.

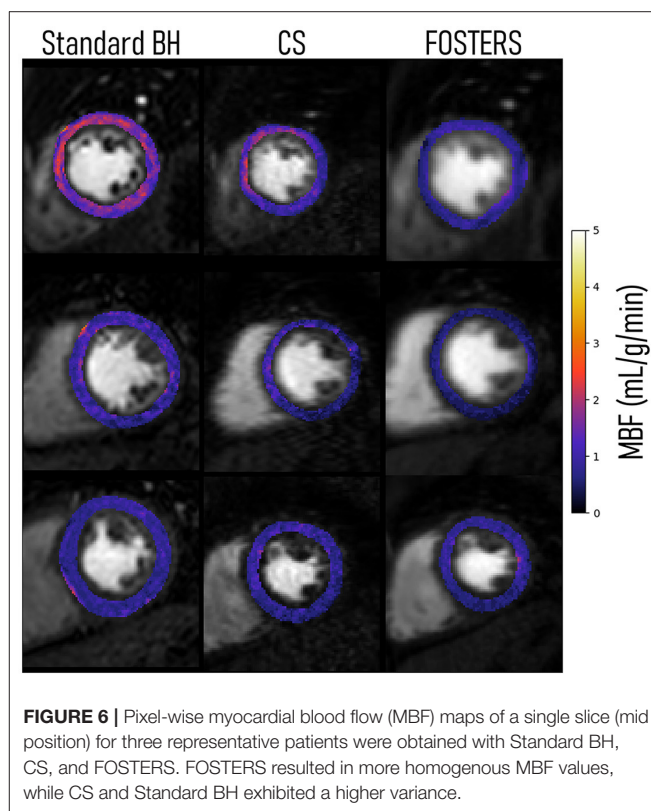
Compared to the multi-echo Dixon QFPP-CMR introduced by Scannell et al. (19), FB-FOSTERS is substantially accelerated using k-t undersampling and acquiring two, rather than three, echo images. Shortening the acquisition time window



is necessary to allow the acquisition of three high-resolution slices in the short RR intervals associated with (stress) FPP-CMR imaging and allows higher in-plane spatial resolution. In addition, a dual-saturation strategy was employed, rather than a dual-bolus, allowing for the acquisition of AIF and myocardial tissue information in the same cardiac cycle and after injection of a single bolus.

Several other approaches have been proposed to accelerate FPP-CMR acquisitions to increase the in-plane spatial resolution (30–35), minimize dark-rim artifacts, improve the detection of subendocardial ischemia, and/or increase cardiac coverage and slice resolution [e.g., simultaneous multi-slice, SMS (36–40), or 3D whole-heart acquisitions (41–47)]. To minimize respiratory motion artifacts, motion compensation strategies (22, 48–51) and non-Cartesian sampling schemes (43, 44, 52–54) have been proposed. However, FB-FOSTERS offers several advantages. FOSTERS estimates rigid in-plane respiratory motion from the fat-only image, while most methods use the dynamic contrast-enhanced time series, which is prone to image registration errors due to changes in image intensity during contrast passage (13, 16, 22, 55, 56). Moreover, FOSTERS also eliminates signal contributions from the chest and body fat that have detrimental effects on motion estimation and MBF quantification (19). Incomplete fat suppression can lead to partial volume effects at the myocardial-epicardial border, which affects the MBF quantification accuracy. FOSTERS corrects for in-plane rigid motion during the inline reconstruction, thus avoiding geometric distortions and blurring caused by non-rigid methods in the presence of large respiratory displacements. The reconstructed FB-FOSTERS images show very small residual motion such that non-rigid motion registration can be successfully and efficiently applied before MBF quantification (12). A further benefit of FOSTERS is the inclusion of a low-resolution, low-saturation-time slice to measure the AIF for accurate MBF quantification (20). The low-saturation-time slice was used to account for  $T_1$  and  $T_2^*$ -related signal loss in the AIF, in addition to the high-resolution dual-echo images. Furthermore, FOSTERS can be combined with non-Cartesian sampling, SMS, and 3D whole-heart acquisitions, which will be the focus of future work.

FOSTERS shows promise for future clinical stress/rest perfusion studies due to its robustness to in-plane motion, high IQ, as well as inline reconstruction implementation. The short



acquisition window, together with the removal of breath-holding, can enable acquisition in patients with short RR intervals. In this study, only rest FPP-CMR scans were performed, but future studies will aim to validate FOSTERS in a larger cohort of patients with coronary artery disease during stress and rest FPP-CMR.

This study has several limitations that warrant discussion. First, 2D imaging was used and no through-plane motion correction was performed, which may influence the estimated MBF values. However, in this patient group, no severe through-plane motion was identified in FB-FOSTERS acquisitions, likely associated with the regularity of shallower breathing - reducing the risk of motion that can occur at the start or end of a long BH. In addition, in this patient group, sufficient fat content was

present in the fat-only images, but more studies are warranted to assess the performance of the motion estimation in patients with low levels of fat around the heart. Additionally in future work, FOSTERS should be tested in a heterogeneous patient cohort that includes different patient profiles, to assess the impact of subcutaneous, epicardial, or intramyocardial fat content. Due to practical reasons, FOSTERS and standard BH scans were acquired with a relatively short pause between scans (5–7 min), so baseline contrast contamination was observed in some standard BH datasets. In addition, a randomized order of sequences was not performed, with FOSTERS always preceding the standard BH FPP-CMR images. Finally, myocardial coverage was limited to three slices, but whole-heart coverage could be of high diagnostic utility (46).

## CONCLUSION

FOSTERS, a k-t accelerated dual-saturation dual-echo Dixon FPP-CMR framework, enables free-breathing and high-resolution quantitative FPP-CMR and improved MBF quantification, with automatic in-plane respiratory motion correction and  $T_2^*$  correction. When compared to standard-resolution breath-hold FPP-CMR, no statistical differences were found in the image quality score, and substantially reduced dark-rim artifacts were observed in the FOSTERS FPP-CMR images. Future studies will aim to test FOSTERS in patients with coronary artery disease during stress.

## DATA AVAILABILITY STATEMENT

The raw data supporting the conclusions of this article will be made available by the authors, without undue reservation.

## ETHICS STATEMENT

The studies involving human participants were reviewed and approved by National Research Ethics Service (15/NS/0030). The patients/participants provided their written informed consent to participate in this study.

## AUTHOR CONTRIBUTIONS

JT and CMS implemented the sequence and the reconstruction framework, performed data analysis and interpretation, statistical analysis, and drafted the main manuscript. TS contributed to study design and contributed to pulse sequence and

reconstruction algorithms. EA, RC, FB, and AC contributed to patient recruitment, CMR imaging and performed image quality scoring. JS-G, MD, CS, JM, JK, JS, and MB contributed to pulse sequence and reconstruction algorithms. MH and TC contributed substantially to the conception and design of the study, data analysis and interpretation, and drafted the main manuscript. All authors read, revised, and approved the final manuscript.

## FUNDING

This work was supported by the Wellcome/EPSRC Center for Medical Engineering [WT 203148/Z/16/Z], the Swedish Research Council [grant 2018-04164], and the European Commission within the Horizon 2020 Framework through the MSCA-ITN-ETN European Training Networks (project number 642458).

## SUPPLEMENTARY MATERIAL

The Supplementary Material for this article can be found online at: <https://www.frontiersin.org/articles/10.3389/fcvm.2022.884221/full#supplementary-material>

**Supplementary Table 1 |** Patients Characteristics.

**Supplementary Video 1 |** First-pass perfusion cardiac MR obtained from patient 5 using FOSTERS, CS, and standard BH.

**Supplementary Video 2 |** First-pass perfusion cardiac MR obtained from patient 7 using FOSTERS, CS, and standard BH.

**Supplementary Video 3 |** Fat- and water-only dynamic images were obtained from one representative patient using FOSTERS and CS. A temporal profile in the foot-head direction (yellow dashed line) is also shown.

**Supplementary Figure 1 |** Example of myocardium-to-blood border sharpness analysis in the mid-short-axis slices of two representative patients. One profile (red line) is manually drawn perpendicular to the myocardium-blood interface, avoiding myocardial trabeculations. Image sharpness is defined as the pixel distance ( $d$ ) between 20% and 80% of the maximum intensity range ( $r$ ). For each approach (FOSTERS, CS, and standard BH), the final image sharpness value was calculated as the average sharpness across the three acquired slices.

**Supplementary Figure 2 |** Fat- and water-only dynamic images were obtained from one representative patient using FOSTERS and spatial wavelet-based compressed sensing (CS). A single slice (mid-slice) for three different dynamic timeframes and a temporal profile in the foot-head direction (yellow dashed line) are shown. The FOSTERS fat-only images contain enough structural information to allow in-plane motion estimation and were less affected by the contrast bolus. The CS fat-only images still contain a high level of noise which hampers the motion estimation performance resulting in lower quality water-only images. Supplementary Video 3 contains an animation of this dataset for both approaches.

## REFERENCES

1. Hamirani YS, Kramer CM. Cardiac MRI assessment of myocardial perfusion. *Fut Cardiol.* (2014) 10:349–58. doi: 10.2217/fca.14.18
2. Greenwood JP, Ripley DP, Berry C, McCann GP, Plein S, Bucciarelli-Ducci C, et al. Effect of care guided by cardiovascular magnetic resonance, myocardial perfusion scintigraphy, or NICE guidelines on subsequent unnecessary angiography rates: the CE-MARC 2 randomized clinical trial. *JAMA.* (2016) 316:1051–60. doi: 10.1001/jama.2016.12680
3. Nagel E, Greenwood JP, McCann GP, Bettencourt N, Shah AM, Hussain ST, et al. Magnetic resonance perfusion or fractional flow reserve in coronary disease. *N Engl J Med.* (2019) 380:2418–28. doi: 10.1056/NEJMoa1716734
4. Villa ADM, Corsinovi L, Ntulas I, Milidonis X, Scannell C, Di Giovine G, et al. Importance of operator training and rest perfusion on the diagnostic accuracy of stress perfusion cardiovascular magnetic resonance. *J Cardiovasc Magn Reson.* (2018) 20:74. doi: 10.1186/s12968-018-0493-4
5. Jerosch-Herold M. Quantification of myocardial perfusion by cardiovascular magnetic resonance. *J Cardiovasc Magn Reson.* (2010) 12:57. doi: 10.1186/1532-429X-12-57

6. Lockie T, Ishida M, Perera D, Chiribiri A, De Silva K, Kozerke S, et al. High-resolution magnetic resonance myocardial perfusion imaging at 3.0-Tesla to detect hemodynamically significant coronary stenoses as determined by fractional flow reserve. *J Am Coll Cardiol.* (2011) 57:70–5. doi: 10.1016/j.jacc.2010.09.019
7. Hsu LY, Jacobs M, Benovoy M, Ta AD, Conn HM, Winkler S, et al. Diagnostic performance of fully automated pixel-wise quantitative myocardial perfusion imaging by cardiovascular magnetic resonance. *JACC Cardiovasc Imaging.* (2018) 11:697–707. doi: 10.1016/j.jcmg.2018.01.005
8. Rahman H, Scannell CM, Demir OM, Ryan M, McConkey H, Ellis H, et al. High-resolution cardiac magnetic resonance imaging techniques for the identification of coronary microvascular dysfunction. *JACC Cardiovasc Imaging.* (2021) 14:978–86. doi: 10.1016/j.jcmg.2020.10.015
9. Knott KD, Seraphim A, Augusto JB, Xue H, Chacko L, Aung N, et al. The prognostic significance of quantitative myocardial perfusion: an artificial intelligence-based approach using perfusion mapping. *Circulation.* (2020) 141:1282–91. doi: 10.1161/CIRCULATIONAHA.119.044666
10. Sammut EC, Villa ADM, Di Giovine G, Dancy L, Bosio F, Gibbs T, et al. Prognostic value of quantitative stress perfusion cardiac magnetic resonance. *JACC Cardiovasc Imaging.* (2018) 11:686–94. doi: 10.1016/j.jcmg.2017.07.022
11. Gupta V, Kirisli HA, Hendriks EA, van der Geest RJ, van de Giessen M, Niessen W, et al. Cardiac MR perfusion image processing techniques: a survey. *Med Image Anal.* (2012) 16:767–85. doi: 10.1016/j.media.2011.12.005
12. Scannell CM, Villa ADM, Lee J, Breeuwer M, Chiribiri A. Robust non-rigid motion compensation of free-breathing myocardial perfusion MRI Data. *IEEE Trans Med Imaging.* (2019) 38:1812–20. doi: 10.1109/TMI.2019.2897044
13. Wollny G, Kellman P, Santos A, Ledesma-Carbayo MJ. Automatic motion compensation of free breathing acquired myocardial perfusion data by using independent component analysis. *Med Image Anal.* (2012) 16:1015–28. doi: 10.1016/j.media.2012.02.004
14. Di Bella EV, Parker DL, Sinusas AJ. On the dark rim artifact in dynamic contrast-enhanced MRI myocardial perfusion studies. *Magn Reson Med.* (2005) 54:1295–9. doi: 10.1002/mrm.20666
15. Sharif B, Dharmakumar R, LaBounty T, Arsanjani R, Shufelt C, Thomson L, et al. Towards elimination of the dark-rim artifact in first-pass myocardial perfusion MRI: removing Gibbs ringing effects using optimized radial imaging. *Magn Reson Med.* (2014) 72:124–36. doi: 10.1002/mrm.24913
16. Kellman P, Hansen MS, NIELLES-Vallespin S, Nickander J, Themudo R, Ugander M, et al. Myocardial perfusion cardiovascular magnetic resonance: optimized dual sequence and reconstruction for quantification. *J Cardiovasc Magn Reson.* (2017) 19:43. doi: 10.1186/s12968-017-0355-5
17. Hsu LY, Kellman P, Arai AE. Nonlinear myocardial signal intensity correction improves quantification of contrast-enhanced first-pass MR perfusion in humans. *J Magn Reson Imaging.* (2008) 27:793–801. doi: 10.1002/jmri.21286
18. Kellman P, Aletras AH, Hsu LY, McVeigh ER, Arai AE. T2\* measurement during first-pass contrast-enhanced cardiac perfusion imaging. *Magn Reson Med.* (2006) 56:1132–4. doi: 10.1002/mrm.21061
19. Scannell CM, Correia T, Villa ADM, Schneider T, Lee J, Breeuwer M, et al. Feasibility of free-breathing quantitative myocardial perfusion using multi-echo Dixon magnetic resonance imaging. *Sci Rep.* (2020) 10:12684. doi: 10.1038/s41598-020-69747-9
20. Sanchez-Gonzalez J, Fernandez-Jimenez R, Nothnagel ND, Lopez-Martin G, Fuster V, Ibanez B. Optimization of dual-saturation single bolus acquisition for quantitative cardiac perfusion and myocardial blood flow maps. *J Cardiovasc Magn Reson.* (2015) 17:21. doi: 10.1186/s12968-015-0116-2
21. Gatehouse PD, Elkington AG, Ablitt NA, Yang GZ, Pennell DJ, Firmin DN. Accurate assessment of the arterial input function during high-dose myocardial perfusion cardiovascular magnetic resonance. *J Magn Reson Imaging.* (2004) 20:39–45. doi: 10.1002/jmri.20054
22. Zhou R, Huang W, Yang Y, Chen X, Weller DS, Kramer CM, et al. Simple motion correction strategy reduces respiratory-induced motion artifacts for k-t accelerated and compressed-sensing cardiovascular magnetic resonance perfusion imaging. *J Cardiovasc Magn Reson.* (2018) 20:6. doi: 10.1186/s12968-018-0427-1
23. Yao J, Xu Z, Huang X, Huang J. An efficient algorithm for dynamic MRI using low-rank and total variation regularizations. *Med Image Anal.* (2018) 44:14–27. doi: 10.1016/j.media.2017.11.003
24. Kabus S, Lorenz C. *Fast Elastic Image Registration. Proc Medical Image Analysis for the Clinic—A Grand Challenge MICCAI.* (2010). pp. 81–89.
25. Scannell CM, Veta M, Villa ADM, Sammut EC, Lee J, Breeuwer M, et al. Deep-learning-based preprocessing for quantitative myocardial perfusion MRI. *J Magn Reson Imaging.* (2020) 51:1689–96. doi: 10.1002/jmri.26983
26. Scannell CM, Chiribiri A, Villa ADM, Breeuwer M, Lee J. Hierarchical bayesian myocardial perfusion quantification. *Med Image Anal.* (2020) 60:101611. doi: 10.1016/j.media.2019.101611
27. Geerts-Ossevoort L, de Weerd E, Duijndam A, et al. Compressed sense. speed done right every time. *Philips Field Strength Mag.* (2018):6619.
28. Bratis K, Henningsson M, Grigoratos C, Dell'Omodarme M, Chasapides K, Botnar R, et al. Image-navigated 3-dimensional late gadolinium enhancement cardiovascular magnetic resonance imaging: feasibility and initial clinical results. *J Cardiovasc Magn Reson.* (2017) 19:97. doi: 10.1186/s12968-017-0418-7
29. Rahman H, Ryan M, Lumley M, Modi B, McConkey H, Ellis H, et al. Coronary microvascular dysfunction is associated with myocardial ischemia and abnormal coronary perfusion during exercise. *Circulation.* (2019) 140:1805–16. doi: 10.1161/CIRCULATIONAHA.119.041595
30. Lingala SG, Hu Y, DiBella E, Jacob M. Accelerated dynamic MRI exploiting sparsity and low-rank structure: k-t SLR. *IEEE Trans Med Imaging.* (2011) 30:1042–54. doi: 10.1109/TMI.2010.2100850
31. Motwani M, Maredia N, Fairbairn TA, Kozerke S, Radjenovic A, Greenwood JP, et al. High-resolution versus standard-resolution cardiovascular MR myocardial perfusion imaging for the detection of coronary artery disease. *Circ Cardiovasc Imaging.* (2012) 5:306–13. doi: 10.1161/CIRCIMAGING.111.971796
32. Lingala SG, DiBella E, Adluru G, McGann C, Jacob M. Accelerating free breathing myocardial perfusion MRI using multi coil radial k-t SLR. *Phys Med Biol.* (2013) 58:7309–27. doi: 10.1088/0031-9155/58/20/7309
33. Sharif B, Arsanjani R, Dharmakumar R, Bairey Merz CN, Berman DS, Li D. All-systolic non-ECG-gated myocardial perfusion MRI: feasibility of multi-slice continuous first-pass imaging. *Magn Reson Med.* (2015) 74:1661–74. doi: 10.1002/mrm.25752
34. Otazo R, Candes E, Sodickson DK. Low-rank plus sparse matrix decomposition for accelerated dynamic MRI with separation of background and dynamic components. *Magn Reson Med.* (2015) 73:1125–36. doi: 10.1002/mrm.25240
35. Naresh NK, Haji-Valizadeh H, Aouad PJ, Barrett MJ, Chow K, Ragin AB, et al. Accelerated, first-pass cardiac perfusion pulse sequence with radial k-space sampling, compressed sensing, and k-space weighted image contrast reconstruction tailored for visual analysis and quantification of myocardial blood flow. *Magn Reson Med.* (2019) 81:2632–43. doi: 10.1002/mrm.27573
36. Stab D, Wech T, Breuer FA, Weng AM, Ritter CO, Hahn D, et al. High resolution myocardial first-pass perfusion imaging with extended anatomic coverage. *J Magn Reson Imaging.* (2014) 39:1575–87. doi: 10.1002/jmri.24303
37. Wang H, Adluru G, Chen L, Kholmovski EG, Bangerter NK, DiBella EV. Radial simultaneous multi-slice CAIPI for ungated myocardial perfusion. *Magn Reson Imaging.* (2016) 34:1329–36. doi: 10.1016/j.mri.2016.07.015
38. Nazir MS, Neji R, Speier P, Reid F, Stab D, Schmidt M, et al. Simultaneous multi slice (SMS) balanced steady state free precession first-pass myocardial perfusion cardiovascular magnetic resonance with iterative reconstruction at 1.5 T. *J Cardiovasc Magn Reson.* (2018) 20:84. doi: 10.1186/s12968-018-0502-7
39. Yang Y, Meyer CH, Epstein FH, Kramer CM, Salerno M. Whole-heart spiral simultaneous multi-slice first-pass myocardial perfusion imaging. *Magn Reson Med.* (2019) 81:852–62. doi: 10.1002/mrm.27412
40. McElroy S, Ferrazzi G, Nazir MS, Kunze KP, Neji R, Speier P, et al. Combined simultaneous multislice bSSFP and compressed sensing for first-pass myocardial perfusion at 1.5 T with high spatial resolution and coverage. *Magn Reson Med.* (2020) 84:3103–16. doi: 10.1002/mrm.28345
41. Fair MJ, Gatehouse PD, DiBella EV, Firmin DN. A review of 3D first-pass, whole-heart, myocardial perfusion cardiovascular magnetic resonance. *J Cardiovasc Magn Reson.* (2015) 17:68. doi: 10.1186/s12968-015-0162-9
42. Vitanis V, Manka R, Giese D, Pedersen H, Plein S, Boesiger P, et al. High resolution three-dimensional cardiac perfusion imaging using compartment-based k-t principal component analysis. *Magn Reson Med.* (2011) 65:575–87. doi: 10.1002/mrm.22620

43. Chen L, Adluru G, Schabel MC, McGann CJ, Dibella EV. Myocardial perfusion MRI with an undersampled 3D stack-of-stars sequence. *Med Phys.* (2012) 39:5204–11. doi: 10.1118/1.4738965
44. Shin T, Nayak KS, Santos JM, Nishimura DG, Hu BS, McConnell MV. Three-dimensional first-pass myocardial perfusion MRI using a stack-of-spirals acquisition. *Magn Reson Med.* (2013) 69:839–44. doi: 10.1002/mrm.24303
45. Motwani M, Kidambi A, Sourbron S, Fairbairn TA, Uddin A, Kozerke S, et al. Quantitative three-dimensional cardiovascular magnetic resonance myocardial perfusion imaging in systole and diastole. *J Cardiovasc Magn Reson.* (2014) 16:19. doi: 10.1186/1532-429X-16-19
46. Manka R, Wissmann L, Gebker R, Jogiya R, Motwani M, Frick M, et al. Multicenter evaluation of dynamic three-dimensional magnetic resonance myocardial perfusion imaging for the detection of coronary artery disease defined by fractional flow reserve. *Circ Cardiovasc Imaging.* (2015) 8:e003061. doi: 10.1161/CIRCIMAGING.114.003061
47. Mendes JK, Adluru G, Likhite D, Fair MJ, Gatehouse PD, Tian Y, et al. Quantitative 3D myocardial perfusion with an efficient arterial input function. *Magn Reson Med.* (2020) 83:1949–63. doi: 10.1002/mrm.28050
48. Schmidt JE, Wissmann L, Manka R, Kozerke S. Iterative k-t principal component analysis with nonrigid motion correction for dynamic three-dimensional cardiac perfusion imaging. *Magn Reson Med.* (2014) 72:68–79. doi: 10.1002/mrm.24894
49. Chen X, Salerno M, Yang Y, Epstein FH. Motion-compensated compressed sensing for dynamic contrast-enhanced MRI using regional spatiotemporal sparsity and region tracking: block low-rank sparsity with motion-guidance (BLOSM). *Magn Reson Med.* (2014) 72:1028–38. doi: 10.1002/mrm.25018
50. Lingala SG, DiBella E, Jacob M. Deformation corrected compressed sensing (DC-CS): a novel framework for accelerated dynamic MRI. *IEEE Trans Med Imaging.* (2015) 34:72–85. doi: 10.1109/TMI.2014.2343953
51. Mohsin YQ, Lingala SG, DiBella E, Jacob M. Accelerated dynamic MRI using patch regularization for implicit motion compensation. *Magn Reson Med.* (2017) 77:1238–48. doi: 10.1002/mrm.26215
52. Kholmovski EG, DiBella EV. Perfusion MRI with radial acquisition for arterial input function assessment. *Magn Reson Med.* (2007) 57:821–7. doi: 10.1002/mrm.21210
53. Salerno M, Sica C, Kramer CM, Meyer CH. Improved first-pass spiral myocardial perfusion imaging with variable density trajectories. *Magn Reson Med.* (2013) 70:1369–79. doi: 10.1002/mrm.24569
54. Wang J, Yang Y, Weller DS, Zhou R, Van Houten M, Sun C, et al. High spatial resolution spiral first-pass myocardial perfusion imaging with whole-heart coverage at 3 T. *Magn Reson Med.* (2021) 86:648–62. doi: 10.1002/mrm.28701
55. Benovoy M, Jacobs M, Cheriet F, Dahdah N, Arai AE, Hsu LY. Robust universal nonrigid motion correction framework for first-pass cardiac MR perfusion imaging. *J Magn Reson Imaging.* (2017) 46:1060–72. doi: 10.1002/jmri.25659
56. Mooiweer R, Neji R, McElroy S, Nazir MS, Razavi R, Chiribiri A, et al. A fast navigator (fastNAV) for prospective respiratory motion correction in first-pass myocardial perfusion imaging. *Magn Reson Med.* (2021) 85:2661–71. doi: 10.1002/mrm.28617

**Conflict of Interest:** JT, TS, JS-G, JS, and MB are Philips Healthcare employees. MD, CS, JM, and JK are employees of Philips Research Europe.

The remaining authors declare that the research was conducted in the absence of any commercial or financial relationships that could be construed as a potential conflict of interest.

**Publisher's Note:** All claims expressed in this article are solely those of the authors and do not necessarily represent those of their affiliated organizations, or those of the publisher, the editors and the reviewers. Any product that may be evaluated in this article, or claim that may be made by its manufacturer, is not guaranteed or endorsed by the publisher.

Copyright © 2022 Tourais, Scannell, Schneider, Alskaf, Crawley, Bosio, Sanchez-Gonzalez, Doneva, Schülke, Meineke, Keupp, Smink, Breeuwer, Chiribiri, Henningson and Correia. This is an open-access article distributed under the terms of the Creative Commons Attribution License (CC BY). The use, distribution or reproduction in other forums is permitted, provided the original author(s) and the copyright owner(s) are credited and that the original publication in this journal is cited, in accordance with accepted academic practice. No use, distribution or reproduction is permitted which does not comply with these terms.



# Radiomics and Machine Learning for Detecting Scar Tissue on CT Delayed Enhancement Imaging

Hugh O'Brien<sup>1\*</sup>, Michelle C. Williams<sup>2\*</sup>, Ronak Rajani<sup>1,3</sup> and Steven Niederer<sup>1</sup>

<sup>1</sup> School of Biomedical Engineering and Imaging Sciences, King's College London, London, United Kingdom, <sup>2</sup> Centre for Cardiovascular Science, University of Edinburgh, Edinburgh, United Kingdom, <sup>3</sup> Cardiology Department, Guy's and St Thomas' NHS Foundation Trust, London, United Kingdom

## OPEN ACCESS

### Edited by:

Marcus R. Makowski,  
Technical University of  
Munich, Germany

### Reviewed by:

Lennart Tautz,  
Fraunhofer Institut für Bildgestützte  
Medizin (MEVIS), Germany  
Fu-Zong Wu,  
Kaohsiung Veterans General  
Hospital, Taiwan

### \*Correspondence:

Hugh O'Brien  
hugh.o'brien@kcl.ac.uk  
Michelle C. Williams  
michelle.williams@ed.ac.uk

### Specialty section:

This article was submitted to  
Cardiovascular Imaging,  
a section of the journal  
Frontiers in Cardiovascular Medicine

**Received:** 03 January 2022

**Accepted:** 21 February 2022

**Published:** 12 May 2022

### Citation:

O'Brien H, Williams MC, Rajani R and  
Niederer S (2022) Radiomics and  
Machine Learning for Detecting Scar  
Tissue on CT Delayed Enhancement  
Imaging.  
Front. Cardiovasc. Med. 9:847825.  
doi: 10.3389/fcvm.2022.847825

**Background:** Delayed enhancement CT (CT-DE) has been evaluated as a tool for the detection of myocardial scar and compares well to the gold standard of MRI with late gadolinium enhancement (MRI-LGE). Prior work has established that high performance can be achieved with manual reading; however, few studies have looked at quantitative measures to differentiate scar and healthy myocardium on CT-DE or automated analysis.

**Methods:** Eighteen patients with clinically indicated MRI-LGE were recruited for CT-DE at multiple 80 and 100 kV post contrast imaging. Left ventricle segmentation was performed on both imaging modalities, along with scar segmentation on MRI-LGE. Segmentations were registered together and scar regions were estimated on CT-DE. 93 radiomic features were calculated and analysed for their ability to differentiate between scarred and non-scarred myocardium regions. Machine learning (ML) classifiers were trained using the strongest set of radiomic features to classify segments containing scar on CT-DE. Features and classifiers were compared across both tube voltages and combined-energy images.

**Results:** There were 59 and 51 statistically significant features in the 80 and 100 kV images respectively. Combined-energy imaging increased this to 63 with more features having area under the curve (AUC) above 0.9. The 10 highest AUC features for each image were used in the ML classifiers. The 100 kV images produced the best ML classifier, a support vector machine with an AUC of 0.88 (95% CI 0.87–0.90). Comparable performance was achieved with both the 80 kV and combined-energy images.

**Conclusions:** CT-DE can be quantitatively analyzed using radiomic feature calculations. These features may be suitable for ML classification techniques to prospectively identify AHA segments with performance comparable to previously reported manual reading. Future work on larger CT-DE datasets is warranted to establish optimum imaging parameters and features.

**Keywords:** radiomics analysis, machine learning, delayed enhancement cardiac computed tomography, scar imaging, computed tomography

## INTRODUCTION

Imaging of myocardial fibrosis is routinely used for patient diagnosis, prognosis and procedure planning. The clinical gold standard is cardiac magnetic resonance imaging (MRI) with late gadolinium enhancement (LGE) (1). As an alternative to MRI-LGE, delayed enhancement CT (CT-DE) has been proposed in those patients who are unable to undergo MRI scanning owing to

availability, cost, claustrophobia, the presence of metallic implants or body size. CT is both cheaper and more widely available than MRI. Even with a delayed enhancement protocol, a cardiac CT scan is much shorter to perform than MRI-LGE, while also providing a higher spatial resolution.

Previous research studies have established that CT-DE can identify myocardial scar using MRI-LGE as a reference standard, in both animal models (2) and patients (3–5). Expert delineated myocardial scar on CT-DE also has a good agreement with invasive electro-mapping of scar (6). Previous studies have shown that visual assessment by expert readers can identify segments containing scar on CT-DE, with accuracy as high as 90% (3). However, there remain questions about the optimal acquisition parameters for CT-DE, and whether using combined-energy imaging can improve scar detection.

Quantitative analysis and the potential for automated analysis of CT-DE has been less well-explored. Radiomic features have been shown to be useful in other quantitative evaluations of CT, such as coronary plaque vulnerability (7) and identification of myocardial infarction (8). One previous study has attempted to assess radiomic features of scar on CT-DE (9), but only used first order parameters and did not use scar confirmation with a reference modality.

The aim of this study was therefore to extract radiomic features which indicate myocardial scar on CT-DE, as determined by the clinical gold standard of MRI-LGE, and to investigate their potential to identify regions with myocardial scar. We also compare multiple energy levels for their suitability for CT-DE scar radiomic analysis.

## METHODS

### Study Design

In a single center study we recruited 18 patients who had MRI proven late gadolinium enhancement on MRI imaging performed for clinical indications. The study was approved by the local ethics committee and patients provided written informed consent.

### Image Acquisition

Magnetic resonance imaging was performed as part of the patient's clinical care on a 1.5 Tesla scanner (Siemens Healthineers) at the Edinburgh Heart Center. Sequences were acquired according to the clinical indication, but included localisers, axial HASTE images, and standard breath-held and electrocardiogram-gated CINE sequences. Delayed enhancement images (gradient echo inversion recovery sequences) were performed 10 min after injection of gadolinium contrast agent (0.2 mmol/kg).

Patients underwent cardiac CT imaging using a 320 multidetector scanner (Aquilion One, Canon Medical Systems) at Edinburgh Imaging, University of Edinburgh. Participants with a heart rate of greater than 60 beats/min received intravenous beta blockade prior to CT imaging. Sublingual glyceryl trinitrate was administered prior to CT imaging, unless contraindicated. Electrocardiogram-gated CT was performed 4 min after injection of 100 ml of iodinated contrast (Iomeron

400). Patients underwent CT using four tube voltages in rapid succession (80, 100, 120, and 135 kV). Only the 80 and 100 kV images were used in this study. Tube current was automatically set based on scout image attenuation. Mean radiation dose of 80 kV images was  $1.6 \pm 0.4$  millisievert (mSv) and 100 kV images was  $2.6 \pm 1.2$  mSv (conversion factor 0.028 mSv/mGy.cm).

### Myocardial Scar Region Estimation

The MRI-LGE scans were used to generate image masks for scar regions on the CT-DE scans. Images from both modalities were segmented separately using Siemens Healthineers prototype software, which was previously described by Behar et al. (10). CT-DE segmentation for both 80 and 100 kV as well as MRI CINE segmentation was automatic for the left ventricle. The MRI-LGE scar region segmentation was performed using the same tool. Scar was segmented initially using the full width at half maximum method, with manual corrections by an operator with 3 years experience at this task.

The resulting left ventricle meshes were registered using iterative closest point (ICP) registration performed in custom software using the VTK C++ library (11). Registration was performed in three steps. First the major axis of each mesh is calculated and then registered together. Then the right ventricle insertion points, which are outputted by the segmentation tool, are registered to correctly rotate the LVs from the two modalities. Finally, the whole endocardium meshes are registered to fine tune the registration. The resulting registration transform is applied to the MRI-LGE scar mesh to generate a scar mesh registered to the CT anatomy.

Registrations were assessed manually for correctness by matching the aortic valves and apex in both meshes. 60 short-axis slices were then obtained across the CT left ventricle, with myocardium and scar masks calculated from the meshes (Figure 1). The mesh registration and slicing software can be made available on request. All scar regions, regardless of their transmural, were labeled as transmural to account for differences in phase between the MRI and CT.

### Radiomic Analysis

Radiomic features were calculated using the open-source PyRadiomics package (12) (version 3.0.1). 93 features were calculated for both 80 and 100 kV images. A full list can be found in **Supplementary Table S1**. These were 18 first order statistics, 24 gray level co-occurrence matrix (GLCM) features, 14 gray level dependence matrix (GLDM) features, 16 gray level size zone matrix (GLSZM) features, 16 gray level run length matrix (GLRLM) features and 5 neighboring gray tone difference matrix (NGTDM) features. Details of the parameters used are included in the **Supplementary Methods**.

Each feature was tested for discrimination ability using two methods. Statistical difference between scar and non-scar region feature values was determined using a two-sided Student's *t*-test. Linear regression was performed using patient-wise stratified 5-fold cross validation. From this receiver operating characteristic metrics were calculated, with confidence intervals calculated using bootstrapping on 1,000 samples with replacement.

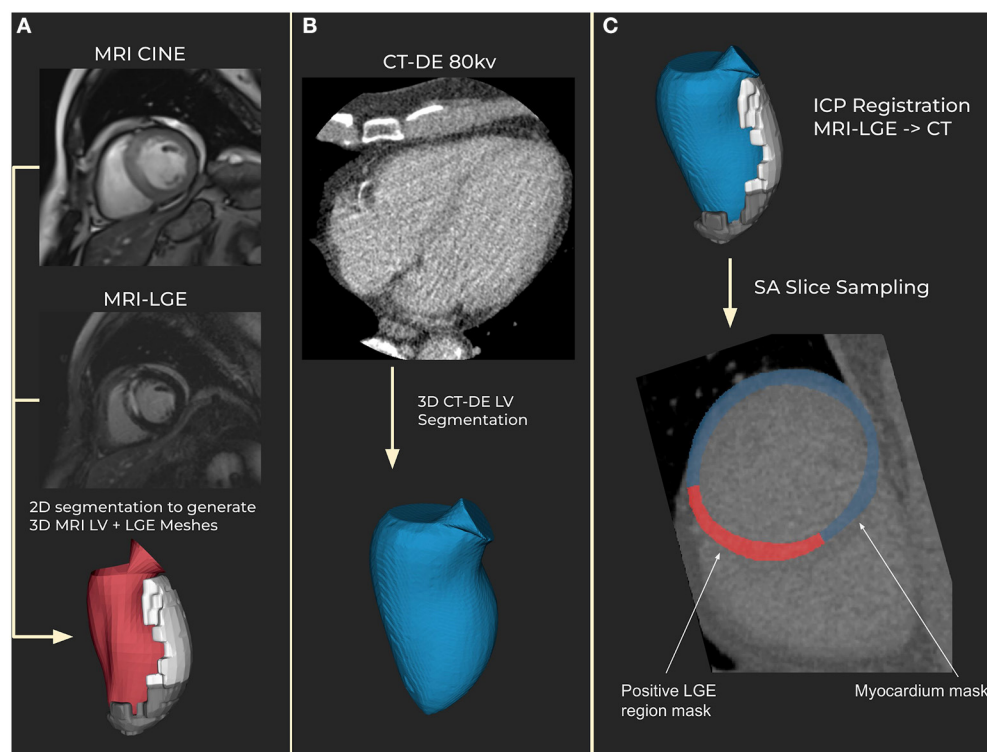


**FIGURE 1 |** Segmentation and registration. **(A)** Magnetic resonance imaging (MRI) segmentation using CINE MRI for anatomical 3D mesh and MRI late gadolinium enhancement (LGE) for scar mesh. Endocardial (red) and scar meshes (white) shown **(B)** Delayed enhancement computed tomography (CT-DE) segmentation to generate a 3D mesh of left ventricle from CT. CT endocardial mesh is shown in blue. **(C)** CT scar mesh generated by iterative closest point (ICP) registration from the MRI to CT left ventricle anatomical meshes. Applying the resulting transform to the MRI-LGE mesh produces a CT aligned scar mesh. This provides locations to mask for scar on the CT-DE.

## Combined-Energy Radiomic Analysis

Features were also calculated on combined-energy images, by combining the 100 kV and 80 kV images. Three combinations were considered, with the 100 kV images contributing 40, 50, and 60% to the final image.

Combined-energy images were generated by registering the 100 kV images to the 80 kV using the open source Medical Image Registration Toolkit (MIRTK). The resulting registered 100 kV image was added to corresponding 80 kV images at the three contribution levels to generate the final images.

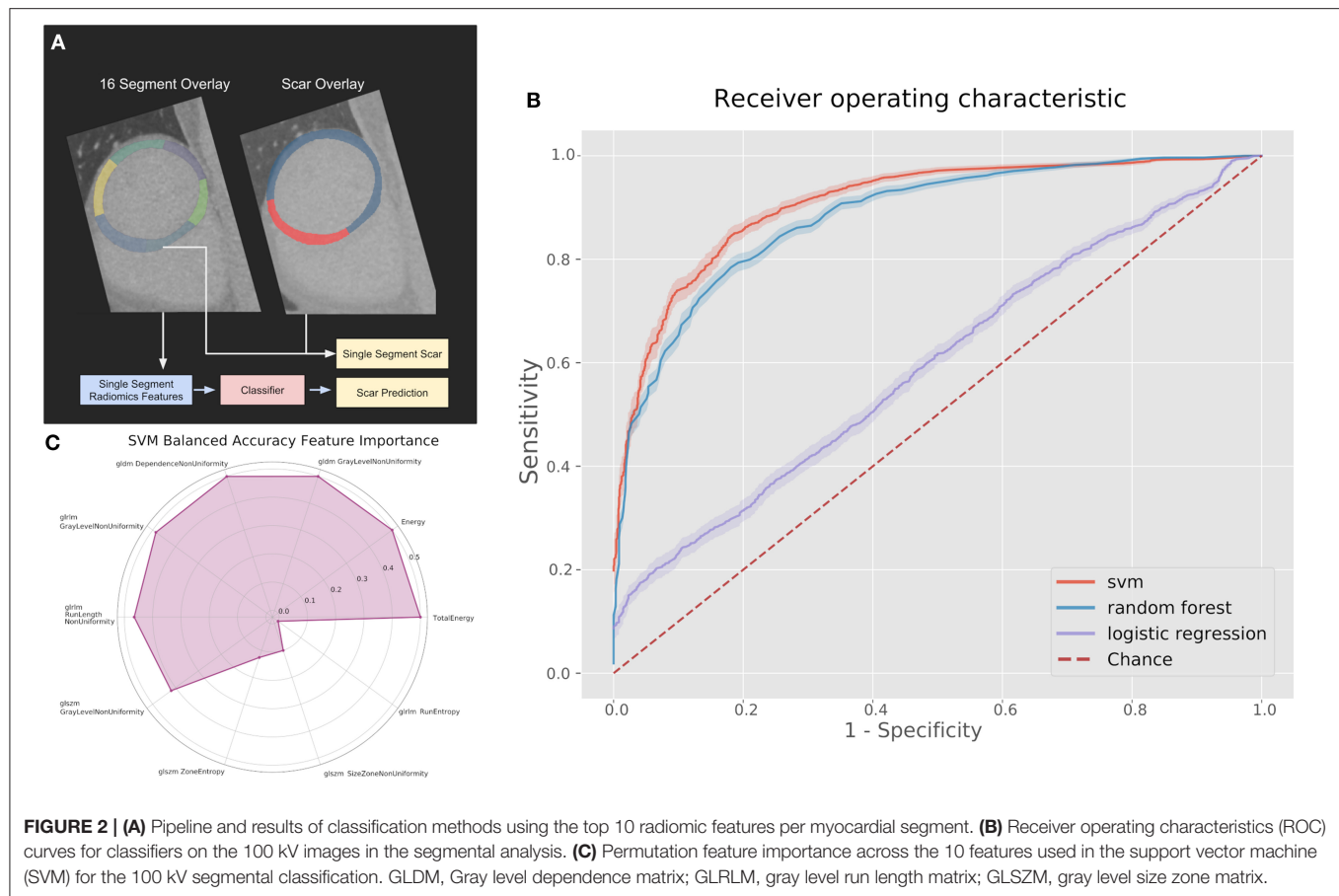
Features were calculated using the 80 kV segmentation and registered scar meshes from the main analysis. Comparisons with the single-energy images were made by comparing area under receiver operator characteristic curves (AUC) across significant features, which were determined using the same method.

## Per Segment Scar Classification

To demonstrate possible clinical usage of these radiomic features we trained classifiers to identify myocardial segments as scar or non-scar. Myocardial segments were defined according to the American Heart Association (AHA) 16 segment model. Myocardial scar ground truths were determined by the percentage of the total segment volume which had scar present.

Scar thresholds of 10, 20, and 30% total volume were compared as ground truths. This was determined by the MRI-LGE registration and as a proportion of the total region size (**Figure 2**). This was considered important as a low threshold could produce radiomic features too close to normal myocardium and a higher threshold would miss substantial scar regions. While the previous radiomic analysis compared the whole scar region to healthy myocardium, these classification experiments aim to assess the ability to predict scar using known radiomic features on a meaningful region for evaluating scar burden. Classifiers were compared also across 80 kV, 100 kV, and the best combined-energy level image.

We compared support vector machine (SVM), logistic regression and random forest classifiers implemented with the open source Scikit-learn (13) Python library (version 1.0.1). Parameters were optimized with grid search and 5-fold cross-validation was used. The 10 radiomic features which showed the largest difference between healthy and scarred myocardium from the radiomic analysis were used as input features to the classifiers after being scaled to unit length. Feature importance was calculated using the Scikit-learn implementation of permutation importance, which determines the importance of each input feature by re-calculating accuracy metrics after removing each feature.



## RESULTS

### Study Population

Of the 18 available cases, 16 cases had good MRI-LGE segmentation and were suitable for registration. Exclusions were due to a missing or unsuitable short-axis sequence in MRI. 15 cases were used for the 80 kV analysis, with one being excluded due to low contrast between the left ventricle myocardium and the blood pool resulting in a poor wall segmentation. 14 were used for the 100 kV analysis, with poor segmentation results meaning two cases were excluded.

Mean age of the included patients was  $62 \pm 8.8$  and 90% were male. 11 patients had a history of previous myocardial infarction (8 ST elevation and three non-ST elevation myocardial infarction). One patient had previously undergone coronary artery bypass graft surgery.

### Radiomic Analysis

For the 80 kV analysis there were 15 patients with 431 valid slices to perform radiomic analysis and for the 100 kV analysis there were 14 patients with 388 valid slices. The combined-energy analysis included 13 patients with 321 slices.

For the 80 kV images, 59 out of the 93 (63%) features were statistically significant predictors of the presence of myocardial scar, whereas 51 (54%) were statistically significant for the 100 kV images. Many of these had low AUCs below 0.7. Above an

AUC of 0.7 there were 16 (17%) and 29 (31%) features for the 80 and 100 kV images, respectively. Above 0.8 this was 11 and 10, respectively. There was a clear overlap in features which presented a significant difference between energy levels. **Figure 3** displays the AUC values across all features per energy level. The best five AUC values are shown in **Figures 4, 5**.

The best metric for both 80 and 100 kV was gray level dependence matrix (GLDM) gray level non-uniformity, where the scar region metric was significantly lower than the normal myocardium, indicating greater similarity within scar regions. Other highly significant metrics which were used for the classifier inputs were GLDM dependence non-uniformity, gray level run length matrix (GLRLM) gray level non-uniformity, gray level size zone matrix (GLSZM) size zone non-uniformity, gray level run length matrix (GLRLM) run-length non-uniformity, total energy, energy, GLSZM gray level non-uniformity, GLSZM zone entropy and GLRLM run entropy. Full results for each metric are listed in the **Supplementary Methods**. These results support a measurable difference in texture in scar overlap regions as compared to normal myocardium.

### Combined-Energy Image Analysis

For the segmental classification analysis there were 1,922 segments (628 with scar) at 80 kV, 1,806 (659 with scar) at 100 kV, and 1,766 (522 with scar) for the combined-energy images.

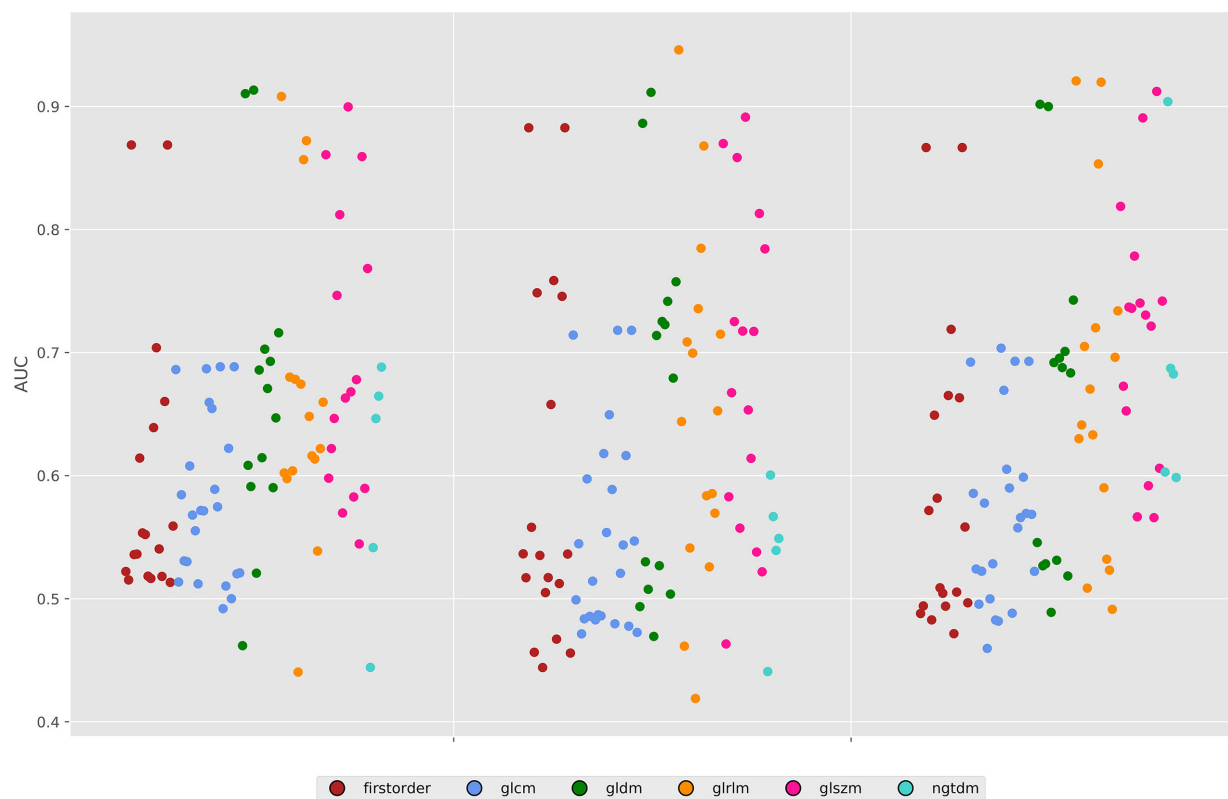


**FIGURE 3 |** Area under the ROC curves for all features across both energy levels and the 50% combined image. GLDM, Gray level dependence matrix; GLCM, gray Level Co-occurrence matrix; GLRLM, gray level run length matrix; GLSZM, gray level size zone matrix; NGTDM, neighboring gray tone difference matrix.

The 50% 100 kV combined-energy image had the highest number of statistically significant radiomic features to predict scar with 63 significant features (68%). Compared to the other energy levels and combined-energy combinations it also had the highest AUC features, with five above an AUC of 0.9, against three for 80 kV, 2 for 100 kV, and two for both other combined-energy settings. Across high AUC features, the 50% combined-energy images outperformed the other proposed combinations. The top features matched the single-energy images except for NGTDM coarseness, which measures the average difference between a center pixel and its neighborhood. This was significant for all the combined-energy image variations with high AUCs ( $>0.9$ ); whereas it was only significant for the 100 kV single-energy images with a relatively low AUC (0.6).

## Classification of Scar Using Radiomic Features

Based on radiomic analysis the 10 best features were calculated to identify, *per segment*, CT-DE scar for the 100 kV, 80 kV, and combined-energy 50% images.

The best performing classifier across all images was the SVM. **Table 1** shows the AUCs and sensitivities for the SVM at each image level and scar threshold. The 20% scar threshold performed the best for all combinations. The results were similar across image types with slightly higher results for the 100 kV

images. SVM was the best performing classification method with a best AUC of 0.88 (95% CI 0.87–0.90) with a sensitivity of 0.79 and specificity of 0.83. The random forest had a comparable AUC with the best being of 0.88 (CI 0.87–0.9) but a worse sensitivity of 0.59 and specificity of 0.92. The logistic regression had a poor AUC with the best being on the 80 kV images at 0.65 (CI 0.62–0.67) with a sensitivity of 0.57 and specificity of 0.61. On this small sample size, these results serve as a proof of concept for the potential to automatically identify scar areas from CT-DE.

**Figure 2C** displays the feature permutation importance for 100 kV images at a 20% threshold, which displays a strong importance across 7 of the 10 included features in terms of changes to balanced accuracy, with the most important feature being first order total energy.

## DISCUSSION

In this study we have demonstrated the ability of radiomic features extracted from CT-DE to predict myocardial scar regions compared to the gold standard assessment of MRI-LGE. Similar features were identified as predictors of myocardial scar and non-scar regions in all examined single-energy and combined-energy images. Good performance was obtained using machine learning methods to classify myocardial segments as scar or non-scar

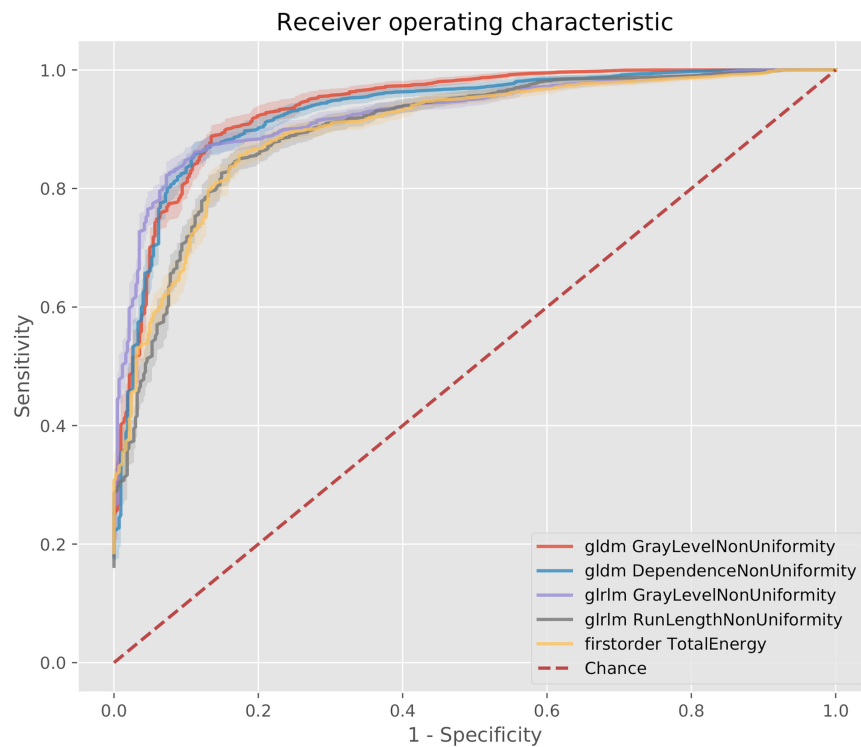


**FIGURE 4 |** ROC curves for the best 5 AUC values on the 80 kV images. GLDM, Gray level dependence matrix; GLRLM, gray level run length matrix.

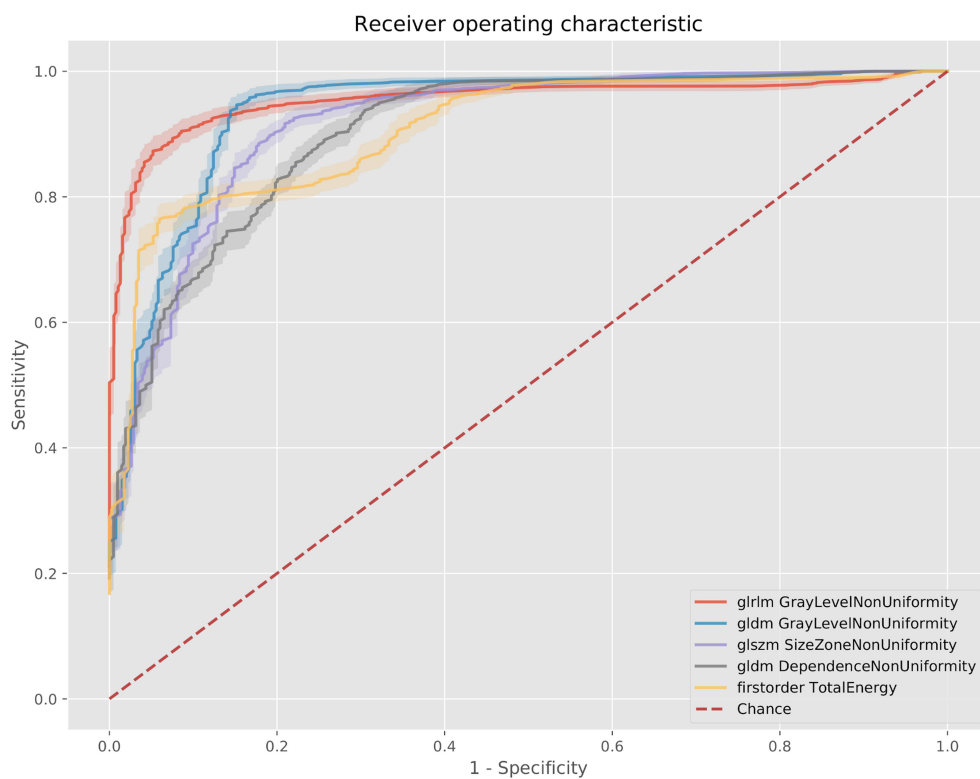


**FIGURE 5 |** ROC curves for the best 5 AUC values on the 100 kV images. GLDM, Gray level dependence matrix; GLSZM, gray level size zone matrix.

**TABLE 1** | Area under ROC curve, sensitivity and specificity for the classifiers at all three energy levels and three scar thresholds.

|                            | 10% Threshold |             |             | 20% Threshold |             |             | 30% Threshold |             |             |
|----------------------------|---------------|-------------|-------------|---------------|-------------|-------------|---------------|-------------|-------------|
|                            | AUC           | Sensitivity | Specificity | AUC           | Sensitivity | Specificity | AUC           | Sensitivity | Specificity |
| <b>SVM</b>                 |               |             |             |               |             |             |               |             |             |
| 80 kV                      | 0.86          | 0.74        | 0.82        | 0.87          | 0.76        | 0.82        | 0.85          | 0.74        | 0.85        |
| 100 kV                     | 0.88          | 0.77        | 0.82        | <b>0.88</b>   | <b>0.79</b> | <b>0.83</b> | 0.88          | 0.77        | 0.78        |
| 50% combined Image         | 0.85          | 0.73        | 0.85        | 0.86          | 0.73        | 0.86        | 0.85          | 0.72        | 0.88        |
| <b>Random forest</b>       |               |             |             |               |             |             |               |             |             |
| 80 kV                      | 0.88          | 0.61        | 0.9         | 0.88          | 0.57        | 0.94        | 0.88          | 0.51        | 0.94        |
| 100 kV                     | 0.87          | 0.66        | 0.89        | 0.88          | 0.59        | 0.92        | 0.88          | 0.63        | 0.91        |
| 50% combined image         | 0.88          | 0.63        | 0.92        | 0.87          | 0.56        | 0.94        | 0.87          | 0.52        | 0.95        |
| <b>Logistic regression</b> |               |             |             |               |             |             |               |             |             |
| 80 kV                      | 0.62          | 0.54        | 0.6         | 0.64          | 0.57        | 0.61        | 0.63          | 0.54        | 0.61        |
| 100 kV                     | 0.57          | 0.57        | 0.5         | 0.55          | 0.52        | 0.53        | 0.56          | 0.52        | 0.54        |
| 50% combined image         | 0.67          | 0.61        | 0.62        | 0.68          | 0.62        | 0.63        | 0.67          | 0.61        | 0.63        |

based on three thresholds of scar coverage, with a slightly better performance for the 100 k images.

The ability of visual assessment of CT-DE to act as an alternative to MRI-LGE for expert readers has been established (2, 3, 5). However, quantitative analysis of CT-DE could improve accuracy and repeatability of assessments and reduce the time to report CT-DE. Here we show a path forward for future standardization and automation of scar detection using CT-DE. Our results correspond well with those of Antunes et al. (9), who found that energy, a first order radiomic statistic, was a statistically significant predictor to identify myocardial scar on CT-DE. However, we have assessed a larger number of radiomic features, and have established the top 10 best radiomic features that can identify scarred compared to non-scarred myocardium. In future, it may be possible to use these features to prospectively identify scar on CT-DE.

Scar in this study was determined using a 3D mesh registration between MRI-LGE and CT-DE. This provides us with a more accurate delimitation of the scar region compared to previous studies, which used *per segment* classification (2–4). This means that in our radiomic analysis we have calculated the most important features without the overlap of healthy tissue within a segment. This also means that we were able to perform the segmental classification with assessment of different levels of scar volume.

The performance of our method is in line with previously shown manual reading (3). We did not find any clear advantage of combined-energy images or large differences between energy levels in the single-energy images. Previous studies have used either 80 kV or 100 kV images for CT-DE assessment. Visually 80 kV images provides a higher difference between areas of contrast enhancement and non-enhancement compared to 100 kV images, but this is at the expense of image noise. Interestingly we found that the 80 and 100 kV images share similar radiomic features in areas of myocardial scar. However, we showed that there may be a small advantage of 100 kV when using radiomic features. Thus, the choice of 80 or 100 kV for CT-DE images

should be made based on the whether visual or quantitative assessment will be performed.

## Study Limitations

This was a single center study with a small number of cases and larger cohort studies with external validation would be required. Our study did not differentiate between ischaemic and non-ischaemic scar or determine the transmural of myocardial scar.

We used an automated segmentation tool with some user corrections to establish areas of myocardial scar. As we were working with large regions of myocardial scar and radiomic features calculated across them, small segmentation errors would not have greatly affected the results. Nevertheless, more accurate automatic or manual segmentations may produce stronger radiomic features and resulting classifiers. While segmental analyses are clinically useful, with additional datasets it may be possible to produce a more specific classification of scar regions. Convolutional neural networks have been shown capable of this task for MRI with LGE (14) and could be applied here instead of calculating radiomic features.

## CONCLUSION

This study showed that CT-DE can identify myocardial scar using radiomic features and machine learning methods, with good accuracy compared to the gold standard of MRI-LGE. Further large prospective studies are required to evaluate the use of this technique in clinical practice.

## DATA AVAILABILITY STATEMENT

The data analyzed in this study was subject to the following licenses/restrictions: The data used for this study was imaging data from an NHS hospital for which ethics was acquired for specific use in this study. The mesh registration and slice generation software can be made available on request to the authors. Requests to access these datasets should be directed to hugh.o'brien@kcl.ac.uk.

## ETHICS STATEMENT

The studies involving human participants were reviewed and approved by the local ethics committee. The patients/participants provided their written informed consent to participate in this study.

## AUTHOR CONTRIBUTIONS

HO'B, MW, and SN: conception and design. HO'B and MW: analysis and interpretation of data. All authors were involved in drafting of the manuscript or revising it for content and approved the final manuscript submitted.

## FUNDING

MW (FS/ICRF/20/26002) was supported by the British Heart Foundation. HO'B would like to acknowledge funding from

the EPSRC Centre for Doctoral Training in Medical Imaging (EP/L015226/1). The study was funded by Edinburgh & Lothians Health Foundation (49–187), and by core funding from the Wellcome/EPSCRC Centre for Medical Engineering [WT203148/Z/16/Z]. For the purpose of Open Access, the author has applied a CC BY public copyright license to any Author Accepted Manuscript version arising from this submission. The software used for segmenting MRI and CTA datasets was provided by Siemens Healthineers. The software is currently in a prototype stage and commercial availability can't be guaranteed.

## SUPPLEMENTARY MATERIAL

The Supplementary Material for this article can be found online at: <https://www.frontiersin.org/articles/10.3389/fcvm.2022.847825/full#supplementary-material>

## REFERENCES

- Flett AS, Hasleton J, Cook C, Hausenloy D, Quarta G, Ariti C, et al. Evaluation of techniques for the quantification of myocardial scar of differing etiology using cardiac magnetic resonance. *JACC: Cardiovasc Imag.* (2011) 4:150–6. doi: 10.1016/j.jcmg.2010.11.015
- Truong QA, Thai WE, Wai B, Cordaro K, Cheng T, Beaudoin J, et al. Myocardial scar imaging by standard single-energy and dual-energy late enhancement computed tomography: comparison to pathology and electroanatomical map in an experimental chronic infarct porcine model. *J Cardiovasc Comp Tomograp.* (2015) 9:313–20. doi: 10.1016/j.jcct.2015.03.003
- Bettencourt N, Ferreira ND, Leite D, Carvalho M, Ferreira WD, Schuster A, et al. CAD detection in patients with intermediate-high pre-test probability: low-dose CT delayed enhancement detects ischemic myocardial scar with moderate accuracy but does not improve performance of a stress-rest CT perfusion protocol. *JACC: Cardiovasc Imag.* (2013) 6:1062–71. doi: 10.1016/j.jcmg.2013.04.013
- Bettencourt N, Ferreira ND, Leite D, Carvalho M, Ferreira WD, Schuster A, et al. Assessment of myocardial delayed enhancement with cardiac computed tomography in cardiomyopathies: a prospective comparison with delayed enhancement cardiac magnetic resonance imaging. *Intern J Cardiovasc Imag.* (2017) 33:577–84. doi: 10.1007/s10554-016-1024-8
- Palmisano A, Vignale D, Benedetti G, Del Maschio A, De Cobelli F, Esposito A. Late iodine enhancement cardiac computed tomography for detection of myocardial scars: impact of experience in the clinical practice. *La RadioLogia Medica.* (2020) 125:128–36. doi: 10.1007/s11547-019-01108-7
- Esposito A, Palmisano A, Antunes S, Maccabelli G, Colantoni C, Rancoita et al. Cardiac CT with delayed enhancement in the characterization of ventricular tachycardia structural substrate. *JACC: Cardiovasc Imag.* (2016) 9:822–32. doi: 10.1016/j.jcmg.2015.10.024
- Kolossváry M, Park J, Bang JI, Zhang J, Lee JM, Paeng JC, et al. Identification of invasive and radionuclide imaging markers of coronary plaque vulnerability using radiomic analysis of coronary computed tomography angiography. *Eur Heart J - Cardiovasc Imag.* (2019) 20:1250–8. doi: 10.1093/ehjci/jez033
- Manoj Mannil, Jochen von Spiczak, Robert Manka, Hatem Alkadhi. Texture analysis and machine learning for detecting myocardial infarction in noncontrast low-dose computed tomography. *Invest Radiol.* (2018) 53:338–43. doi: 10.1097/RLI.0000000000000448
- Antunes S, Esposito A, Palmisano A, Colantoni C, De Cobelli F, Del Maschio A. Characterization of normal and scarred myocardium based on texture analysis of cardiac computed tomography images. In: *2016 38th Annual International Conference of the IEEE Engineering in Medicine and Biology Society (EMBC)*. Orlando, FL (2016):4161. doi: 10.1109/EMBC.2016.7591643
- Behar JM, Mountney P, Toth D, Reiml S, Panayiotou M, Brost A, et al. Real-time X-MRI-guided left ventricular lead implantation for targeted delivery of cardiac resynchronization therapy. *JACC: Clin Electrophysiol.* (2016) 3:803–14. doi: 10.1016/j.jacep.2017.01.018
- Schroeder W, Martin K, Lorensen B. *The Visualization Toolkit*: Prentice-Hall, Inc. (1998). Available online at: <https://dl.acm.org/citation.cfm?id=272980>
- Van Griethuysen JJ, Fedorov A, Parmar C, Hosny A, Aucoin N, Narayan V, et al. Computational radiomics system to decode the radiographic phenotype. *Cancer Research.* (2017) 77:e104–7. doi: 10.1158/0008-5472.CAN-17-0339
- Pedregosa F, Varoquaux G, Gramfort A, Michel V, Thirion B, Grisel O, et al. Scikit-learn: machine learning in python. *J Mac Learn Res.* (2011) 12:2825–30.
- Zhuang X, Xu J, Luo X, Chen C, Ouyang C, Rueckert D, et al. Cardiac segmentation on late gadolinium enhancement MRI: a benchmark study from multi-sequence cardiac MR segmentation challenge. (2020). Available online at: <http://arxiv.org/abs/2006.12434>. arXiv: 2006.12434

**Conflict of Interest:** MW - Speaker bureau for Canon Medical Systems.

The remaining authors declare that the research was conducted in the absence of any commercial or financial relationships that could be construed as a potential conflict of interest.

**Publisher's Note:** All claims expressed in this article are solely those of the authors and do not necessarily represent those of their affiliated organizations, or those of the publisher, the editors and the reviewers. Any product that may be evaluated in this article, or claim that may be made by its manufacturer, is not guaranteed or endorsed by the publisher.

Copyright © 2022 O'Brien, Williams, Rajani and Niederer. This is an open-access article distributed under the terms of the Creative Commons Attribution License (CC BY). The use, distribution or reproduction in other forums is permitted, provided the original author(s) and the copyright owner(s) are credited and that the original publication in this journal is cited, in accordance with accepted academic practice. No use, distribution or reproduction is permitted which does not comply with these terms.



# Deep Learning for Detection of Exercise-Induced Pulmonary Hypertension Using Chest X-Ray Images

Kenya Kusunose<sup>1\*</sup>, Yukina Hirata<sup>2</sup>, Natsumi Yamaguchi<sup>2</sup>, Yoshitaka Kosaka<sup>1</sup>, Takumasa Tsuji<sup>3</sup>, Jun'ichi Kotoku<sup>3</sup> and Masataka Sata<sup>1</sup>

## OPEN ACCESS

### Edited by:

Sebastian Kelle,  
Deutsches Herzzentrum Berlin,  
Germany

### Reviewed by:

Ismini Lourentzou,  
Virginia Tech, United States  
Ozgur Kasapcopur,  
Istanbul University-Cerrahpasa,  
Turkey  
Himanshu Buckchash,  
UIT The Arctic University of Norway,  
Norway

### \*Correspondence:

Kenya Kusunose  
kusunosek@tokushima-u.ac.jp

### Specialty section:

This article was submitted to  
Cardiovascular Imaging,  
a section of the journal  
Frontiers in Cardiovascular Medicine

**Received:** 08 March 2022

**Accepted:** 12 May 2022

**Published:** 15 June 2022

### Citation:

Kusunose K, Hirata Y,  
Yamaguchi N, Kosaka Y, Tsuji T,  
Kotoku J and Sata M (2022) Deep  
Learning for Detection  
of Exercise-Induced Pulmonary  
Hypertension Using Chest X-Ray  
Images.  
Front. Cardiovasc. Med. 9:891703.  
doi: 10.3389/fcvm.2022.891703

<sup>1</sup> Department of Cardiovascular Medicine, Tokushima University Hospital, Tokushima, Japan, <sup>2</sup> Ultrasound Examination Center, Tokushima University Hospital, Tokushima, Japan, <sup>3</sup> Department of Radiological Technology, Graduate School of Medical Care and Technology, Teikyo University, Tokyo, Japan

**Background:** Stress echocardiography is an emerging tool used to detect exercise-induced pulmonary hypertension (EIPH). However, facilities that can perform stress echocardiography are limited by issues such as cost and equipment.

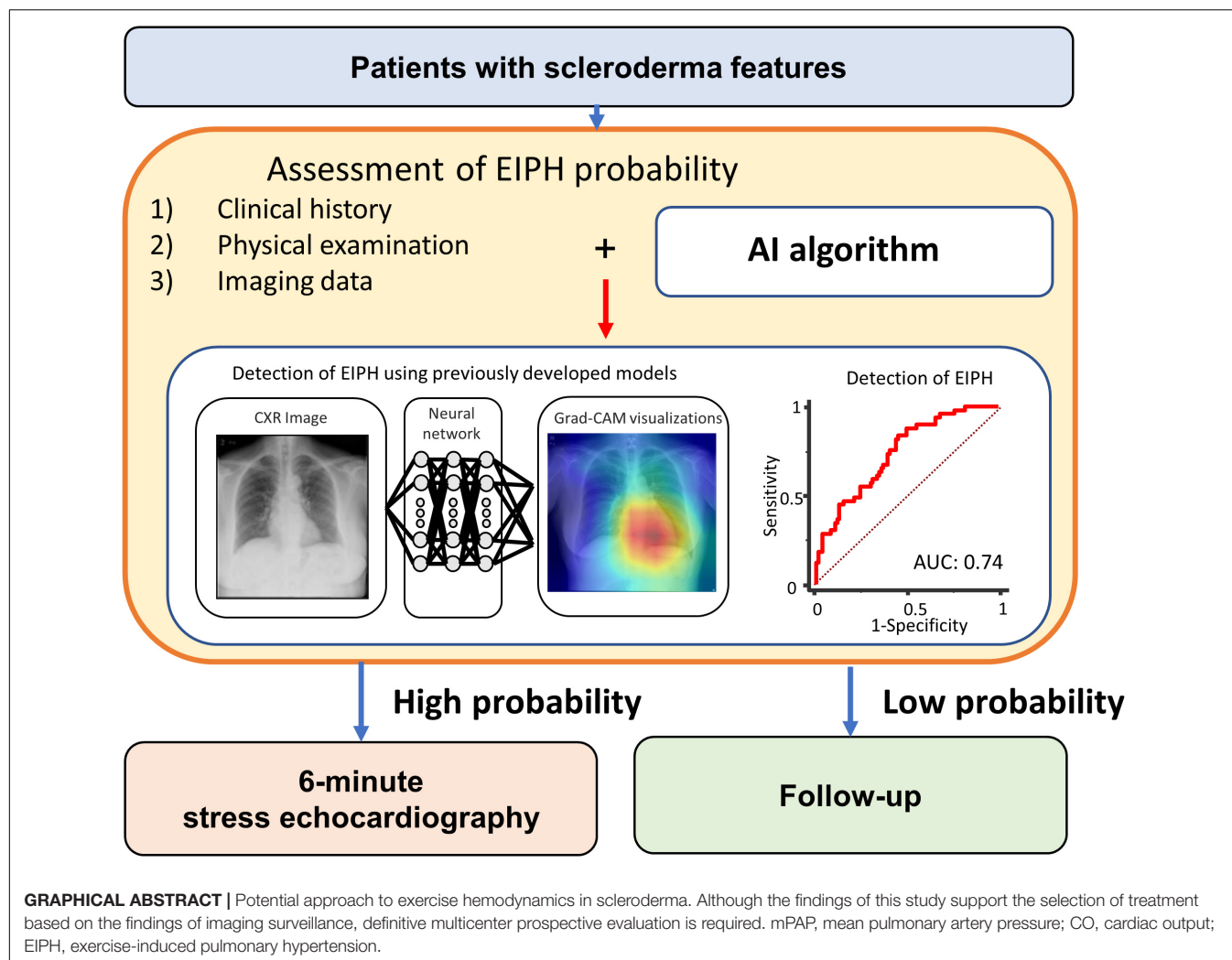
**Objective:** We evaluated the usefulness of a deep learning (DL) approach based on a chest X-ray (CXR) to predict EIPH in 6-min walk stress echocardiography.

**Methods:** The study enrolled 142 patients with scleroderma or mixed connective tissue disease with scleroderma features who performed a 6-min walk stress echocardiographic test. EIPH was defined by abnormal cardiac output (CO) responses that involved an increase in mean pulmonary artery pressure (mPAP). We used the previously developed AI model to predict PH and calculated PH probability in this cohort.

**Results:** EIPH defined as  $\Delta\text{mPAP}/\Delta\text{CO} > 3.3$  and exercise mPAP  $> 25$  mmHg was observed in 52 patients, while non-EIPH was observed in 90 patients. The patients with EIPH had a higher mPAP at rest than those without EIPH. The probability of PH based on the DL model was significantly higher in patients with EIPH than in those without EIPH. Multivariate analysis showed that gender, mean PAP at rest, and the probability of PH based on the DL model were independent predictors of EIPH. A model based on baseline parameters (age, gender, and mPAP at rest) was improved by adding the probability of PH predicted by the DL model (AUC: from 0.65 to 0.74;  $p = 0.046$ ).

**Conclusion:** Applying the DL model based on a CXR may have a potential for detection of EIPH in the clinical setting.

**Keywords:** artificial intelligence, connective tissue disease, echocardiography, exercise pulmonary hypertension, scleroderma (SSc)



## INTRODUCTION

Pulmonary hypertension (PH) is a major cause of mortality in patients with scleroderma. Early detection of PH remains a clinical challenge despite several diagnostic tools developed. Because the elevated mean pulmonary artery pressure (mPAP) during exercise can be a cause of dyspnea and fatigue, the exercise-induced PH (EIPH) has been promised as a potential useful status for the early identification at the risk of developing resting PH (1). Right heart catheter (RHC) is the gold standard for defining the mPAP during exercise. However, RHC is an invasive procedure and we need the non-invasive tests to screen PH in the clinical setting. Exercise stress echocardiography has been used to screen scleroderma patients in an attempt to identify those with EIPH as an indicator of early-stage PH (2). Several recent studies have suggested that abnormal cardiac output (CO) responses to increments in mPAP have the potential to assess the state of disease and functional class of patients (3, 4). We have shown previously that the pressure-flow relationship between mPAP and CO measurement

predicted future development of overt PH and was helpful for making treatment decisions regarding pulmonary arterial hypertension (PAH)-specific medications (5, 6). EIPH defined by  $\Delta\text{mPAP}/\Delta\text{CO}$  indicates an abnormal pulmonary vascular response to exercise due to impaired pulmonary vascular capacity. This index is important for detecting early pulmonary vascular disease in at-risk patients, such as those with scleroderma.

However, the use of exercise echocardiography to diagnose EIPH may be limited by issues of cost and equipment in health care facilities. Identifying resting parameters that can predict EIPH therefore has important clinical implications. Recently, artificial intelligence (AI) including deep learning (DL) has been applied to sophisticated recognition of understated

**Abbreviations:** PH, pulmonary hypertension; mPAP, mean pulmonary artery pressure; EIPH, exercise-induced pulmonary hypertension; RHC, right heart catheter; CO, cardiac output; PAH, pulmonary arterial hypertension; AI, artificial intelligence; DL, deep learning; CXR, chest x-ray; SS, scleroderma; MCTD, mixed connective tissue disease; LV, left ventricular; GLS, Global longitudinal strain; RV, right ventricular; 6MW, Six-minute walk; AUC, area under the curve; PAWP, pulmonary artery wedge pressure.

patterns in medical images (7, 8). We reported that a DL model based on chest X-ray (CXR) analysis, predicted elevated pulmonary artery pressure in patients who underwent right-sided heart catheterization (9). We suspected the DL model can detect the known pathological effects of PH at early stage on the CXR images. Thus, we hypothesized that a previously developed application of the CXR-based DL algorithm could also be used to predict EIPH in patients with scleroderma (SSc) or mixed connective tissue disease (MCTD) with scleroderma features. The objectives of the current study were (1) to assess the baseline clinical and echocardiographic predictors at rest of EIPH in at-risk patients, and (2) to evaluate whether the predictive value for the presence of EIPH is increased when an AI model for PH is added to clinical and echocardiographic parameters at rest.

## MATERIALS AND METHODS

### Study Population

The study enrolled patients with SSc or MCTD with scleroderma features treated at our hospital. The definitions of these two diseases were based on the American College of Rheumatology diagnostic criteria (10). Patients who underwent a 6-min walk stress echocardiographic study and had a normal range of mean PAP (<25 mmHg) at rest were recruited consecutively from patients referred to our echocardiographic examination center between January 2013 and December 2017. Patients with moderate or severe valvular disease, atrial fibrillation/flutter, left ventricular (LV) ejection fraction <50%, significant shunts, significant interstitial lung disease, known coronary artery disease, or thromboembolism were excluded from the study. Eight patients at rest and four patients during stress were excluded due to lack of a measurable tricuspid regurgitant jet. The study was approved by the local ethics committee and Institutional Review Board of the University of Tokushima (protocol: 1095-2).

### Echocardiographic Assessment

Transthoracic echocardiography was performed by experienced sonographers/doctors using a commercially-available ultrasound machine (Vivid 9, GE Vingmed, Horten, Norway). The measurements and recordings were obtained according to the recommendations of the American Society of Echocardiography (11). Systolic PAP was measured from the maximal continuous-wave Doppler velocity of the tricuspid regurgitant jet using the systolic trans-tricuspid pressure gradient calculated by the modified Bernoulli equation. Right atrial pressure was estimated from the inferior vena cava diameter and collapsibility (12). Mean PAP was calculated as  $0.6 \times \text{systolic PAP} + 2$  (13). Peak systolic longitudinal strain measurements were obtained from gray-scale images recorded in the apical four-chamber, two-chamber, and long-axis views. The frame rate was maintained at >40 frame/s. All the measurements of strain were analyzed offline using speckle tracking vendor-independent software (EchoInsight, Epsilon Imaging, Ann Arbor, MI, United States). Global longitudinal strain (GLS) was calculated by averaging

all the segmental strain values from the apical four-chamber, two-chamber, and long-axis views. In the right ventricular (RV) longitudinal strain analysis of the RV focused apical four-chamber view, the interventricular septum was included in the region-of-interest for speckle-tracking echocardiography. Only the free wall strain values were included and the septal strain values were discarded to avoid LV interaction.

### Six-Min Walk Stress Echocardiography

Six-min walk (6MW) tests were performed according to the American Thoracic Society guidelines (14). Transcutaneous arterial oxygen saturation was determined by pulse oximetry. The peak tricuspid regurgitation jet observed by echocardiography was obtained immediately after the 6MW test (i.e., within 10 s). CO was also determined at the same time using electric cardiometry (Aesculon Electrical Velocimetry, Osypka Medical GmbH, Berlin, Germany). We calculated the PAP—cardiac output relationship as mPAP divided by CO (mPAP/CO), and calculated the slope of mPAP/CO in individual patients ( $\Delta\text{mPAP}/\Delta\text{CO}$ ). Patients with EIPH were diagnosed based on our previous work that used a  $\Delta\text{mPAP}/\Delta\text{CO} > 3.3$  and exercise mPAP >25 mmHg (5). The reproducibility of  $\Delta\text{mPAP}/\Delta\text{CO}$  obtained by echocardiography, expressed as the coefficient of variation, has been reported by our group as  $5.6 \pm 3.8\%$  and  $7.2 \pm 5.1\%$  for intra-observer and inter-observer variation, respectively (5).

Right heart catheter was performed using a Swan-Ganz catheter. Pressure measurements were obtained at rest and during supine bicycle ergometry. Thermodilution CO was analyzed after averaging the sum of three measurements collected at rest and during exercise. Pulmonary vascular resistance was calculated as  $(\text{mPAP} - \text{PAWP})/\text{CO}$ . In our cohort using invasive data ( $n = 29$ ) we showed that there was a good correlation between invasive and non-invasive (electric cardiometry and echocardiography) values of  $\Delta\text{mPAP}/\Delta\text{CO}$  ( $r = 0.61$ ;  $p < 0.001$ ) (Supplementary Figure 1).

### Artificial Intelligence Model for Detection of Pulmonary Hypertension

We used the previously developed AI model to predict PH in this study (9). We defined PH using the AI model using the mean PAP >20 mmHg because we need an early detection of pulmonary vascular dysfunction for screening purposes. The area under the curve (AUC) of the AI model for prediction of elevated PAP was 0.71 in the test cohort (9). We briefly describe the model as follows. Data were divided into 10 groups, 9 of the groups were used as a training and validation to create a model, and the rest were used to test the model so that the 900 total cases were split with 90 cases  $\times$  10 groups. Also, the images of the training dataset were augmented by using gamma correction, horizontal flipping, rotation, and pixel shift. Then, we have done nested-cross validation (Supplementary Figure 2) and tuned hyperparameters using grid-search. A capsule-network-based model was constructed with the addition of some residual blocks to detect PH (15). Each residual block contained two convolution layers, two batch normalizations, a rectified linear

unit (ReLU), and a skip connection. Details are shown in **Supplementary Figure 3**. The network consisted of six residual blocks, six convolution layers, and six batch normalizations. All activation functions were set to ReLU functions. The highest elements in the likelihood vector were defined as the output label (mean PAP > 20 mmHg). The proposed network architecture is presented in **Supplementary Figure 4**. We pre-trained the model using a CXR dataset, which is published by RSNA Pneumonia Detection Challenge in Kaggle.<sup>1</sup> Then, we performed fine-tuning with the pre-trained model and nested 10-fold cross-validation. The batch size was set to 16 and an Adam optimizer used for training. We constructed the proposed network model on a computer (Xeon CPUs; Intel Corp. and Tesla P100 16GB GPU; NVIDIA Corp.) using a Chainer (ver. 7.2.0) deep learning framework. We also performed gradient-weighted class activation mapping (Grad-CAM) to visualize how our model detected abnormalities from a CXR of each case. The averaged analysis time is  $2 \pm 1$  min for each case.

## Statistical Analysis

The continuous variables were expressed as mean  $\pm$  SD of the normal distribution, while the non-normal continuous variables were expressed as median (interquartile range). Wilcoxon W test or Kruskal Wallis test was used to assess the differences among groups. We performed a univariate logistic regression analysis to evaluate the correlation between EIPH and clinical variables, laboratory data, echocardiographic data, and probability of PH calculated by the AI model. The independence of the association between the variables was tested using multiple logistic regression analysis. The predictive performance was evaluated using receiver operating characteristic (ROC) analysis and pairwise comparisons of the AUC according to the DeLong method (16). To evaluate the effectiveness of the AI model to predict EIPH, two models were constructed and compared using ROC curve analysis. Model 1, the basic model, consisted of age, gender, blood pressure and mean PAP at rest, while Model 2 included the variables in model 1 plus the probability of PH calculated using the AI algorithm. The statistical analyses were performed using standard statistical software packages (SPSS

software 21.0; SPSS Inc., Chicago, IL, United States and MedCalc Software 17; Mariakerke, Belgium). Statistical significance was defined as a  $p$ -value < 0.05.

## RESULTS

### Patient Characteristics

The baseline characteristics of the study group are shown in **Table 1**. The study population consisted of 142 patients [ $58 \pm 13$  years; 17 (12%) male] who underwent 6-min stress echocardiography. Of the 142 patients, 90 (63%) had non-EIPH and 52 (37%) had EIPH (**Figure 1**). Patients with EIPH had higher diastolic blood pressure, lower SpO<sub>2</sub> post-6MW, higher mPAP, higher exercise mPAP, and lower exercise cardiac output than that observed in patients with non-EIPH. **Table 2** shows the invasive hemodynamic data in the patients with EIPH ( $\Delta$ mPAP/ $\Delta$ CO > 3.3 mmHg/L/min and exercise mPAP  $\geq$  25 mmHg by echocardiography) who received explanations for exercise RHC. We obtained informed consent for exercise RHC in 29 patients with EIPH and referred them to our catheter laboratory for assessment of exercise pulmonary hemodynamics. Twenty-three patients refused exercise RHC due to the risk of RHC. In the 29 patients who underwent exercise RHC, 28 fulfilled the catheter criteria of EIPH described in a previous report (17). Based on this finding we considered that diagnosing EIPH using 6-min stress echocardiography was acceptable in the clinical setting.

### The Value of Clinical Parameters and the AI Model for Predicting EIPH

The results of the univariate and multivariate logistic analyses are shown in **Table 3**. In univariate analyses, the presence of EIPH was associated with diastolic blood pressure, mean PAP, and PH probability by the AI model. After adjustment for age, gender, diastolic blood pressure, and mean PAP at baseline, EIPH was also associated with the probability of PH predicted by the AI model.

The results of the ROC analysis for detection of EIPH are summarized in **Figure 2**. In this cohort, the AUC of the AI model was 0.71 (95% CI: 0.62–0.78). For mPAP at rest measured

<sup>1</sup><https://www.kaggle.com/c/rsna-pneumonia-detection-challenge>

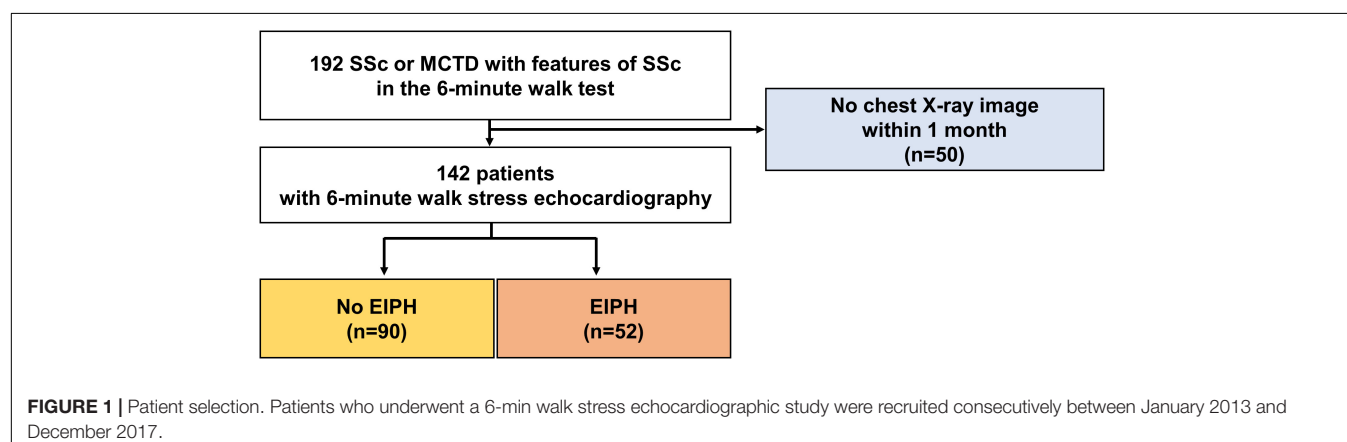


**TABLE 1 |** Clinical characteristics in the entire study cohort: of the 142 patients, 90 (63%) had non-EIPH and 52 (37%) had EIPH.

|                                     | All           | Non-EIPH      | EIPH          | p-value |
|-------------------------------------|---------------|---------------|---------------|---------|
| Number                              | 142           | 90            | 52            |         |
| Age, year                           | 58 ± 13       | 57 ± 13       | 60 ± 14       | 0.30    |
| Male, %                             | 17 (12)       | 8 (9)         | 9 (17)        | 0.17    |
| Body surface area, m <sup>2</sup>   | 1.52 ± 0.14   | 1.53 ± 0.14   | 1.51 ± 0.15   | 0.30    |
| WHO Class I or II/III or IV         | 125/17        | 82/8          | 43/9          | 0.17    |
| <b>History</b>                      |               |               |               |         |
| SSc, %                              | 110 (77)      | 69 (77)       | 41 (79)       | 0.76    |
| MCTD with SSc features, %           | 32 (23)       | 21 (23)       | 11 (21)       | 0.76    |
| <b>Medication</b>                   |               |               |               |         |
| Antihypertensive drugs, %           | 1 (1)         | 1 (1)         | 0 (0)         | 0.33    |
| Diuretic, %                         | 3 (2)         | 1 (1)         | 2 (4)         | 0.35    |
| Anticoagulants, %                   | 0 (0)         | 0 (0)         | 0 (0)         | –       |
| <b>Respiratory function</b>         |               |               |               |         |
| %EFV1, %                            | 82 ± 21       | 86 ± 16       | 80 ± 24       | 0.42    |
| %FVC, %                             | 102 ± 22      | 103 ± 27      | 102 ± 21      | 0.91    |
| %DLCO                               | 76 ± 22       | 77 ± 22       | 75 ± 23       | 0.79    |
| <b>Baseline hemodynamics</b>        |               |               |               |         |
| HR, bpm                             | 71 ± 12       | 71 ± 13       | 71 ± 12       | 0.81    |
| Systolic BP, mmHg                   | 122 ± 20      | 120 ± 21      | 125 ± 18      | 0.14    |
| Diastolic BP, mmHg                  | 70 ± 16       | 68 ± 15       | 74 ± 17       | 0.06    |
| SpO <sub>2</sub> , %                | 97 ± 2        | 98 ± 1        | 97 ± 2        | 0.13    |
| <b>Post 6-min walk hemodynamics</b> |               |               |               |         |
| HR, bpm                             | 94 ± 18       | 95 ± 18       | 92 ± 19       | 0.50    |
| Systolic BP, mmHg                   | 129 ± 25      | 128 ± 25      | 130 ± 27      | 0.67    |
| Diastolic BP, mmHg                  | 72 ± 11       | 71 ± 12       | 74 ± 10       | 0.10    |
| SpO <sub>2</sub> , %                | 96 ± 3        | 96 ± 3        | 95 ± 4        | 0.05    |
| 6MW distance, meter                 | 450 (400–500) | 425 (385–499) | 451 (400–501) | 0.48    |
| <b>Echocardiographic variables</b>  |               |               |               |         |
| LVEDVi, ml/m <sup>2</sup>           | 49 ± 12       | 48 ± 10       | 50 ± 14       | 0.59    |
| LVESVi, ml/m <sup>2</sup>           | 17 ± 5        | 17 ± 4        | 17 ± 5        | 0.52    |
| LVEF, %                             | 65 ± 3        | 65 ± 3        | 65 ± 3        | 0.47    |
| LV-GLS, %                           | 20 ± 2        | 19 ± 2        | 20 ± 3        | 0.65    |
| LVMi, g/m <sup>2</sup>              | 77 ± 17       | 76 ± 16       | 79 ± 19       | 0.41    |
| LAVi, ml/m <sup>2</sup>             | 26 ± 8        | 26 ± 6        | 27 ± 10       | 0.61    |
| E/e'                                | 7.0 ± 2.5     | 6.7 ± 2.1     | 7.4 ± 3.0     | 0.15    |
| RVFAC, %                            | 41 ± 12       | 41 ± 12       | 41 ± 12       | 0.81    |
| TAPSE, mm                           | 22 ± 4        | 21 ± 3        | 22 ± 4        | 0.83    |
| RV-GLS, %                           | 22 ± 4        | 22 ± 4        | 21 ± 5        | 0.62    |
| <b>Pulmonary hemodynamics</b>       |               |               |               |         |
| Mean PAP, mmHg                      | 18 ± 3        | 17 ± 3        | 19 ± 3        | 0.003   |
| CO, l/min                           | 4.0 ± 1.3     | 4.1 ± 1.2     | 3.9 ± 1.4     | 0.39    |
| Exercise mean PAP, mmHg             | 24 ± 5        | 22 ± 3        | 29 ± 5        | –       |
| Exercise cardiac output, l/min      | 6.3 ± 2.3     | 6.8 ± 2.4     | 5.5 ± 1.7     | <0.001  |
| ΔmPAP/ΔCO, mmHg/l/min               | 2.9 (1.6–5.3) | 1.8 (1.2–2.7) | 6.4 (4.4–8.3) | –       |
| <b>AI model</b>                     |               |               |               |         |
| PH probability (%)                  | 20 (5–58)     | 11 (3–35)     | 37 (21–76)    | <0.001  |

Data are expressed as the number of patients (percentage) and mean ± SD or median (interquartile range).

EIPH, exercise-induced pulmonary hypertension; SSc, scleroderma; MCTD, mixed connective tissue disease; %FEV1, percent forced expiratory volume in 1 s; %FVC, percent forced vital capacity; %DLCO, diffusing capacity for carbon monoxide; HR, heart rate; BP, blood pressure; SpO<sub>2</sub>, percutaneous oxygen saturation; LVEDVi, left ventricular end-diastolic volume index; LVESVi, left ventricular end-systolic volume index; LVEF, left ventricular ejection fraction; GLS, global longitudinal strain; LVMi, left ventricular mass index; LAVi, left atrial volume index; E, early diastolic transmitral flow velocity; e', early diastolic mitral annular motion; RVEA, right ventricular end-diastolic area; RVESA, right ventricular end-systolic area; RVFAC, right ventricular functional area change; TAPSE, tricuspid annular plane systolic excursion; mPAP, mean pulmonary artery pressure; CO, cardiac output.

**TABLE 2 |** Invasive hemodynamic data in the patients with EIPH by exercise stress echocardiography who received exercise RHC.

| Invasive hemodynamic data                    |           |
|--|-----------|
| Number                                       | 29        |
| <b>Baseline</b>                              |           |
| Heart rate, bpm                              | 70 ± 13   |
| Systolic blood pressure, mmHg                | 132 ± 21  |
| Mean pulmonary artery pressure, mmHg         | 20 ± 4    |
| Mean pulmonary arterial wedge pressure, mmHg | 9 ± 3     |
| Mean right atrial pressure, mmHg             | 6 ± 4     |
| Pulmonary vascular resistance, wood unit     | 2.1 ± 1.1 |
| CO, l/min                                    | 5.5 ± 1.9 |
| <b>Peak exercise</b>                         |           |
| Heart rate, bpm                              | 107 ± 26  |
| Systolic blood pressure, mmHg                | 162 ± 30  |
| Mean pulmonary arterial pressure, mmHg       | 40 ± 9    |
| Mean pulmonary artery wedge pressure, mmHg   | 18 ± 4    |
| Mean right atrial pressure, mmHg             | 6 ± 2     |
| Pulmonary vascular resistance, wood unit     | 2.6 ± 1.2 |
| CO, l/min                                    | 9.2 ± 2.6 |
| ΔmPAP/ΔCO, mmHg/l/min                        | 6.2 ± 3.0 |

EIPH, exercise-induced pulmonary hypertension; RHC, right heart catheter; CO, cardiac output; mPAP, mean pulmonary artery pressure.

by echocardiography, the AUC was 0.64 (95% CI: 0.56–0.72). **Figure 3** shows the ROC analysis of the combination of clinical variables (age, gender, blood pressure and mean PAP at rest) and the AI model. Importantly, the predictive potential of the model based on these variables (age, gender, blood pressure and mean PAP at rest) was improved by adding the DL model (increase in AUC from 0.65 to 0.74,  $p = 0.046$ ). We checked the precision, recall, f-score values, and confusion matrix for performance evaluation of the AI model. Importantly, the recall of AI algorithm for detecting EIPH was 94.5% using the cut off value of 21% for AI estimated probability (**Supplementary Table 1**). AI assessment may be considered an option to check the need of RHC in patients with suspected EIPH.

## Assessment of Gradient-Weighted Class Activation Mapping

To help explain the AI assessment, we analyzed the images to determine where AI was focused (**Figure 4**). In many cases, Grad-CAM showed that our model focused on the cardiac area in patients with EIPH. Interestingly, in patients without EIPH, the focus was on the area in the right middle lung field. The resulting AI model may provide new insights to appropriately discern differences using CXR images.

## DISCUSSION

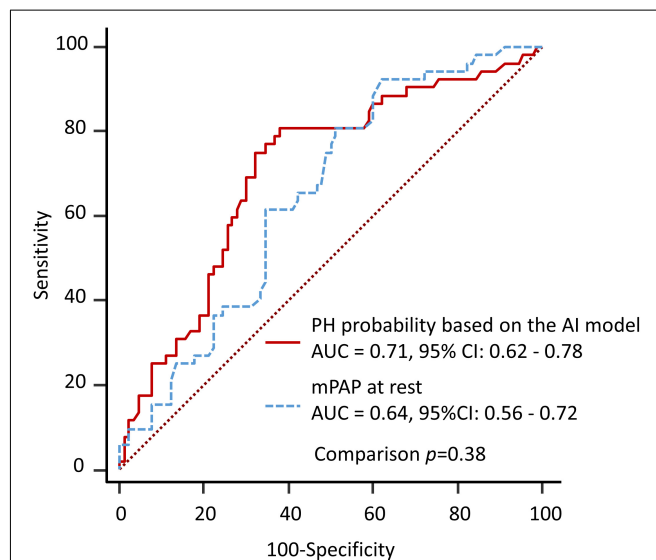
We demonstrated that 52 of 142 patients (37%) with high-risk PAH (SSc or MCTD with SSc features) and normal resting echocardiographic findings had EIPH based on an elevated ΔmPAP/ΔCO measured by 6MW stress echocardiography. Mean PAP at rest was a significant predictor of EIPH after

**TABLE 3 |** Univariate and multivariate associations of EIPH.

|                           | Univariate model |           |         | Multivariate model |            |         |
|---------------------------|------------------|-----------|---------|--------------------|------------|---------|
|                           | OR               | 95% CI    | p-value | OR                 | 95% CI     | p-value |
| <b>Clinical variables</b> |                  |           |         |                    |            |         |
| Age, year                 | 1.04             | 0.99–1.04 | 0.29    | 1.02               | 0.98–1.05  | 0.33    |
| Male, %                   | 2.15             | 0.77–5.96 | 0.14    | 3.27               | 1.01–10.55 | 0.05    |
| Diastolic BP, mmHg        | 1.03             | 0.99–1.06 | 0.05    | 1.02               | 0.98–1.05  | 0.38    |
| <b>Echocardiography</b>   |                  |           |         |                    |            |         |
| Mean PAP, mmHg            | 1.22             | 1.06–1.41 | 0.002   | 1.02               | 1.00–1.39  | 0.04    |
| <b>AI model</b>           |                  |           |         |                    |            |         |
| PH probability (per 1%)   | 1.02             | 1.01–1.03 | <0.001  | 1.02               | 1.01–1.04  | 0.002   |

After adjustment for clinical variables, EIPH was associated significantly with the probability of PH calculated by the AI model.

BP, blood pressure; PAP, pulmonary artery pressure; PH, pulmonary hypertension.

**FIGURE 2 |** Diagnostic ability to predict EIPH using a single variable. The area under the curve by AI model for detection of EIPH was similar to the AUC by measurement of mPAP at rest.

adjustment for age and gender, whereas parameters of respiratory function were not. Furthermore, the combination of the DL model significantly improved the ability to predict EIPH compared to that achieved by combining clinical parameters. To our knowledge, this is the first study to demonstrate the clinical utility of a DL algorithm based on standard CXRs to estimate EIPH in at risk patients.

## Prognostic Importance of Exercise-Induced Pulmonary Hypertension

The management of the PAH high risk cohort remains a matter of debate because of limited data on prognosis. The pathological findings in the pulmonary vasculature that characterize PAH include initial proliferation and fibrosis, medial hypertrophy, and thrombosis (18). The large capacity of the pulmonary circulation results in PH usually being diagnosed late in its course, with

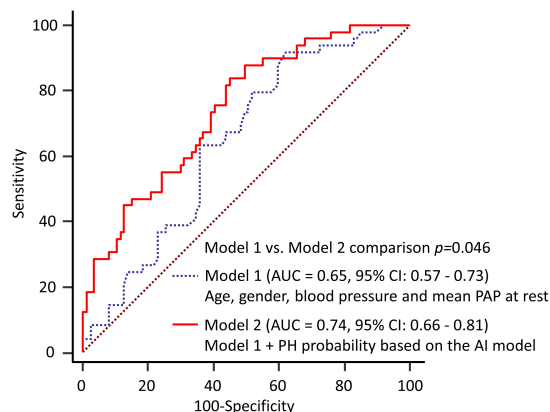


**FIGURE 3 |** Diagnostic ability to predict EIPH using multiple variables. The predictive potential of the model based on these variables was improved by adding the DL model (increase in AUC from 0.65 to 0.74,  $p = 0.046$ ). Model 1 = age, gender, blood pressure and mean PAP at rest; Model 2 = Model 1 plus DL model.

an asymptomatic stage preceding onset (19). Therefore, patients with early PH may present with an almost normal resting mPAP, but have an abnormal exercise mPAP as a result of increased pulmonary blood flow. From the perspective of the pulmonary circulation during exercise, the clinical utility of mPAP-CO assessment has been described in several previous studies (3–5). Several investigators have also reported that the benefit of treatment for EIPH was an improvement in pulmonary vascular response to exercise within 1 year (6, 20–23). Therefore, EIPH is an important clinical condition in patients with a high risk of developing PAH. However, cardiovascular institutes that can perform stress echocardiography may be limited by issues related to cost and equipment. The detection of EIPH using minimally invasive or non-invasive approaches at rest therefore has important clinical implications.

## Exercise-Induced Pulmonary Hypertension and Artificial Intelligence Model

Chest x-ray is a simple and economical screening method for assessing PH. The American College of Chest Physicians has recommended obtaining a CXR in patients who are suspected of having PH in order to reveal features supportive of this diagnosis (24). Recently, we developed an AI application for CXRs to identify the patients with a high-risk of developing PH. In the current study, we tested the ability of this model to predict EIPH in the study cohort. The results showed that the DL model provided an additive value for predicting EIPH compared to that achieved by clinical parameters. During the 6th World Symposium on Pulmonary Hypertension in 2018, a working group proposed revising the hemodynamic definition of PH by lowering the threshold from  $\geq 25$  mmHg to  $>20$  mmHg in order to identify patients in the early stage of PH (2). EIPH is a similar concept for detecting early stage PH. In our previous study on a large patient cohort ( $n = 243$ ), mean PAP was higher in patients with EIPH ( $19 \pm 3$  mmHg, around 20 mmHg) than in those with non-EIPH ( $17 \pm 3$  mmHg). One possible reason why the model performed well in this cohort is that the AI model had been trained using a cut-off mean PAP value of 20 mmHg. There is a problem of DL regarding the “black box” algorithm. To understand our model’s recognition of CXR, we adopted Grad-CAM. According to the results of the heat map analysis, our model focused on structures in the cardiac area in patients with EIPH. These findings may help to understand the images of EIPH on CXR.

## Exercise-Induced Pulmonary Hypertension and Clinical Variables

In our analysis, most of the resting echocardiographic measurements were similar in the EIPH and non-EIPH

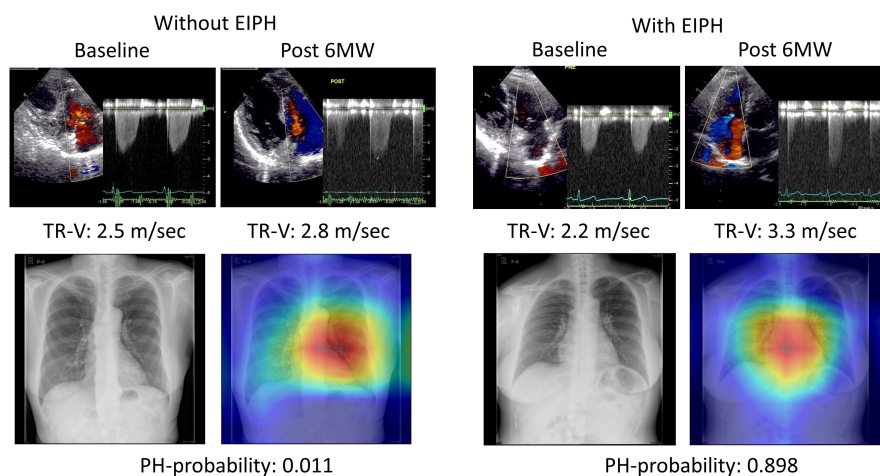


**FIGURE 4 |** Examples of gradient-weighted class activation mapping visualizations (grad-CAM). Chest X-rays were visualized using grad-CAM, with the yellow and red areas showing regions that the deep learning model considered important for detecting EIPH.

groups. This result emphasizes the importance of stress echocardiography to identify EIPH. In our cohort, only a higher mean PAP at rest was found to be associated with a higher risk of EIPH. This increase in mean PAP at rest can be considered as an indicator for EIPH in stress echocardiography. Several studies have reported a correlation between respiratory parameters and EIPH (25, 26). In the present study, no respiratory parameter was a significant predictor of EIPH. We speculate that the respiratory parameters in the patients may not have decreased at the time of the study because many were in the early stage of PH. Moreover, PH related to SSc can sometimes be associated with occult left-side diastolic dysfunction (27). The spectrum of PH is therefore wide and includes several etiologies (28). For example, during the development of PAH and heart failure with PH, some patients may have pulmonary vascular disease and some elements of occult left-sided heart failure. In our cohort, there were small differences in  $E/e'$  between the EIPH and non-EIPH groups ( $p = 0.15$ ). All patients had an  $E/e' < 15$  (surrogate of left ventricular end-diastolic pressure by echocardiography, mean,  $7 \pm 3$ ) at baseline, while 29 patients on RHC had a pulmonary artery wedge pressure (PAWP)  $\leq 15$  mmHg (mean,  $9 \pm 3$ ) and exercise PAWP  $< 25$  mmHg (mean,  $17 \pm 3$ ). Therefore, we could exclude patients with secondary PH due to left heart involvement from our patient cohort.

One major concern in the present study was that not all patients had been confirmed as having EIPH by exercise RHC, although 97% of the cases of EIPH diagnosed by 6MW stress echocardiography were identified by exercise RHC. We gathered a high-risk EIPH cohort including SSc or MCTD with scleroderma features. Thus, there were smaller sample for the male population. There was a significant bias and we should apply this model to the high-risk cohort for EIPH in the further study. Natriuretic peptides were not measured consistently in our study cohort. Some cases of unobtainable tricuspid regurgitation may be problematic. The specific X-ray parameters used by the convolutional neural network to classify patients with PH are not well-described because of a “black box” algorithm. Because of these limitations, these data should be considered as hypothesis-generating and we consider that larger prospective multicenter studies are warranted to validate our findings.

## Summary Points and Clinical Implications

EIPH should be diagnosed by stress echocardiography to improve the prognosis of patients with PH. On the other hand, many institutes are unable to easily perform stress echocardiography due to cost and equipment limitations. Therefore, developing a tool to predict EIPH in advance is clinically important. Our

DL algorithm based on standard CXRs can estimate EIPH in at risk patients. Graphical Abstract shows a potential pathway for detecting EIPH in patients with scleroderma. In the high-risk cohort detected by the AI algorithm, the use of 6MW stress echocardiography might be considered to assess pulmonary vascular function and act as a guide for treatment in this high-risk cohort.

## CONCLUSION

Applying the DL model based on a CXR may have a potential for detection of EIPH in the clinical setting.

## DATA AVAILABILITY STATEMENT

The original contributions presented in this study are included in the article/**Supplementary Material**, further inquiries can be directed to the corresponding author.

## ETHICS STATEMENT

The study was approved by the Local Ethics Committee and Institutional Review Board of the University of Tokushima (protocol: 1095-2). The ethics committee waived the requirement of written informed consent for participation.

## AUTHOR CONTRIBUTIONS

KK conceived the idea for this study and produced the initial draft of the manuscript. YH, TT, and JK conducted the data analyses. All authors were involved in interpreting the results, writing the manuscript, read, and approved the final manuscript.

## FUNDING

This work was partially supported by the JSPS Kakenhi Grants (Number 21K12706 to YH) and the Takeda Science Foundation (to KK).

## SUPPLEMENTARY MATERIAL

The Supplementary Material for this article can be found online at: <https://www.frontiersin.org/articles/10.3389/fcvm.2022.891703/full#supplementary-material>

## REFERENCES

1. Codullo V, Caporali R, Cuomo G, Ghio S, D'Alto M, Fusetti C, et al. Stress Doppler echocardiography in systemic sclerosis: evidence for a role in the prediction of pulmonary hypertension. *Arthritis Rheum.* (2013) 65:2403–11. doi: 10.1002/art.38043
2. Simonneau G, Montani D, Celermajer DS, Denton CP, Gatzoulis MA, Krowka M, et al. Haemodynamic definitions and updated clinical classification of pulmonary hypertension. *Eur Respir J.* (2019) 53:1801913. doi: 10.1183/13993003.01913-2018
3. Argiento P, Vanderpool RR, Mule M, Russo MG, D'Alto M, Bossone E, et al. Exercise stress echocardiography of the pulmonary circulation: limits of

- normal and sex differences. *Chest*. (2012) 142:1158–65. doi: 10.1378/chest.12-0071
4. Lau EM, Vanderpool RR, Choudhary P, Simmons LR, Corte TJ, Argiento P, et al. Dobutamine stress echocardiography for the assessment of pressure-flow relationships of the pulmonary circulation. *Chest*. (2014) 146:959–66. doi: 10.1378/chest.13-2300
  5. Kusunose K, Yamada H, Hotchi J, Bando M, Nishio S, Hirata Y, et al. Prediction of future overt pulmonary hypertension by 6-min walk stress echocardiography in patients with connective tissue disease. *J Am Coll Cardiol*. (2015) 66:376–84. doi: 10.1016/j.jacc.2015.05.032
  6. Kusunose K, Yamada H, Nishio S, Hirata Y, Saijo Y, Torii Y, et al. Pulmonary artery hypertension-specific therapy improves exercise tolerance and outcomes in exercise-induced pulmonary hypertension. *JACC Cardiovasc Imaging*. (2019) 12:2576–9. doi: 10.1016/j.jcmg.2019.07.002
  7. Kusunose K, Abe T, Haga A, Fukuda D, Yamada H, Harada M, et al. A deep learning approach for assessment of regional wall motion abnormality from echocardiographic images. *JACC Cardiovasc Imaging*. (2019) 13:374–81. doi: 10.1016/j.jcmg.2019.02.024
  8. Kusunose K, Haga A, Abe T, Sata M. Utilization of Artificial Intelligence in Echocardiography. *Circ J*. (2019) 83:1623–9. doi: 10.1253/circj.CJ-19-0420
  9. Kusunose K, Hirata Y, Tsuji T, Kotoku J, Sata M. Deep learning to predict elevated pulmonary artery pressure in patients with suspected pulmonary hypertension using standard chest X ray. *Sci Rep*. (2020) 10:19311. doi: 10.1038/s41598-020-76359-w
  10. Hochberg MC. Updating the American College of Rheumatology revised criteria for the classification of systemic lupus erythematosus. *Arthritis Rheum*. (1997) 40:1725. doi: 10.1002/art.1780400928
  11. Lang RM, Badano LP, Mor-Avi V, Afilalo J, Armstrong A, Ernande L, et al. Recommendations for cardiac chamber quantification by echocardiography in adults: an update from the American Society of Echocardiography and the European Association of Cardiovascular Imaging. *J Am Soc Echocardiogr*. (2015) 28:1–39.e14.
  12. Milan A, Magnino C, Veglio F. Echocardiographic indexes for the non-invasive evaluation of pulmonary hemodynamics. *J Am Soc Echocardiogr*. (2010) 23:225–39. doi: 10.1016/j.echo.2010.01.003
  13. Chemla D, Castelain V, Humbert M, Hebert JL, Simonneau G, Lecarpentier Y, et al. New formula for predicting mean pulmonary artery pressure using systolic pulmonary artery pressure. *Chest*. (2004) 126:1313–7. doi: 10.1378/chest.126.4.1313
  14. ATS Committee on Proficiency Standards for Clinical Pulmonary Function Laboratories. ATS statement: guidelines for the six-minute walk test. *Am J Respir Crit Care Med*. (2002) 166:111–7.
  15. Xiong Y, Berisha V, Chakrabarti C. Residual+ capsule networks (ResCap) for simultaneous single-channel overlapped keyword recognition. In: *Proceedings of the Annual Conference of the International Speech Communication Association, INTERSPEECH*. Baixas: International Speech Communication Association (2019). p. 3337–41.
  16. DeLong ER, DeLong DM, Clarke-Pearson DL. Comparing the areas under two or more correlated receiver operating characteristic curves: a nonparametric approach. *Biometrics*. (1988) 44:837–45.
  17. Herve P, Lau EM, Sitbon O, Savale L, Montani D, Godinas L, et al. Criteria for diagnosis of exercise pulmonary hypertension. *Eur Respir J*. (2015) 46:728–37. doi: 10.1183/09031936.00021915
  18. Waxman AB. Exercise physiology and pulmonary arterial hypertension. *Prog Cardiovasc Dis*. (2012) 55:172–9.
  19. Lau EM, Manes A, Celermajor DS, Galie N. Early detection of pulmonary vascular disease in pulmonary arterial hypertension: time to move forward. *Eur Heart J*. (2011) 32:2489–98. doi: 10.1093/eurheartj/ehrl160
  20. Wallace WD, Nouraei M, Chan SY, Risbano MG. Treatment of exercise pulmonary hypertension improves pulmonary vascular distensibility. *Pulm Circ*. (2018) 8:2045894018787381. doi: 10.1177/2045894018787381
  21. Saggat R, Khanna D, Shapiro S, Furst DE, Maranian P, Clements P, et al. Brief report: effect of ambrisentan treatment on exercise-induced pulmonary hypertension in systemic sclerosis: a prospective single-center, open-label pilot study. *Arthritis Rheum*. (2012) 64:4072–7. doi: 10.1002/art.34614
  22. Kovacs G, Maier R, Aberer E, Brodmann M, Graninger W, Kqiku X, et al. Pulmonary arterial hypertension therapy may be safe and effective in patients with systemic sclerosis and borderline pulmonary artery pressure. *Arthritis Rheum*. (2012) 64:1257–62. doi: 10.1002/art.33460
  23. Yagi S, Akaike M, Iwase T, Kusunose K, Niki T, Yamaguchi K, et al. Bosentan ameliorated exercise-induced pulmonary arterial hypertension complicated with systemic sclerosis. *Intern Med*. (2010) 49:2309–12. doi: 10.2169/internalmedicine.49.3812
  24. McGoon M, Gutterman D, Steen V, Barst R, McCrory DC, Fortin TA, et al. Screening, early detection, and diagnosis of pulmonary arterial hypertension: ACCP evidence-based clinical practice guidelines. *Chest*. (2004) 126:14S–34S. doi: 10.1378/chest.126.1\_suppl.14S
  25. Callejas-Rubio JL, Moreno-Escobar E, de la Fuente PM, Perez LL, Fernandez RR, Sanchez-Cano D, et al. Prevalence of exercise pulmonary arterial hypertension in scleroderma. *J Rheumatol*. (2008) 35:1812–6.
  26. Loth DW, Lahousse L, Leening MJG, Krijthe BP, Felix JF, Gall H, et al. Pulmonary function and diffusion capacity are associated with pulmonary arterial systolic pressure in the general population: the rotterdam study. *Respir Med*. (2017) 132:50–5. doi: 10.1016/j.rmed.2017.09.009
  27. Fox BD, Shimony A, Langleben D, Hirsch A, Rudski L, Schlesinger R, et al. High prevalence of occult left heart disease in scleroderma-pulmonary hypertension. *Eur Respir J*. (2013) 42:1083–91. doi: 10.1183/09031936.00091212
  28. Borlaug BA, Obokata M. Is it time to recognize a new phenotype? Heart failure with preserved ejection fraction with pulmonary vascular disease. *Eur Heart J*. (2017) 38:2874–8. doi: 10.1093/eurheartj/ehx184

**Conflict of Interest:** The authors declare that the research was conducted in the absence of any commercial or financial relationships that could be construed as a potential conflict of interest.

**Publisher's Note:** All claims expressed in this article are solely those of the authors and do not necessarily represent those of their affiliated organizations, or those of the publisher, the editors and the reviewers. Any product that may be evaluated in this article, or claim that may be made by its manufacturer, is not guaranteed or endorsed by the publisher.

Copyright © 2022 Kusunose, Hirata, Yamaguchi, Kosaka, Tsuji, Kotoku and Sata. This is an open-access article distributed under the terms of the Creative Commons Attribution License (CC BY). The use, distribution or reproduction in other forums is permitted, provided the original author(s) and the copyright owner(s) are credited and that the original publication in this journal is cited, in accordance with accepted academic practice. No use, distribution or reproduction is permitted which does not comply with these terms.



## OPEN ACCESS

EDITED BY  
Sebastian Kelle,  
German Heart Center Berlin, Germany

REVIEWED BY  
Mingxing Xie,  
Huazhong University of Science  
and Technology, China  
Omid Memarian Sorkhabi,  
University of Isfahan, Iran

\*CORRESPONDENCE  
Bharath Ambale-Venkatesh  
✉ bambale1@jhmi.edu

†These authors have contributed equally to this work and share first authorship

SPECIALTY SECTION  
This article was submitted to  
Cardiovascular Imaging,  
a section of the journal  
Frontiers in Cardiovascular Medicine

RECEIVED 14 May 2022  
ACCEPTED 16 January 2023  
PUBLISHED 07 February 2023

CITATION  
Cong C, Kato Y, Vasconcellos HDD,  
Ostovaneh MR, Lima JAC and  
Ambale-Venkatesh B (2023) Deep  
learning-based end-to-end automated  
stenosis classification and localization on  
catheter coronary angiography.  
*Front. Cardiovasc. Med.* 10:944135.  
doi: 10.3389/fcvm.2023.944135

COPYRIGHT  
© 2023 Cong, Kato, Vasconcellos, Ostovaneh,  
Lima and Ambale-Venkatesh. This is an  
open-access article distributed under the terms  
of the [Creative Commons Attribution License  
\(CC BY\)](https://creativecommons.org/licenses/by/4.0/). The use, distribution or reproduction in  
other forums is permitted, provided the original  
author(s) and the copyright owner(s) are  
credited and that the original publication in this  
journal is cited, in accordance with accepted  
academic practice. No use, distribution or  
reproduction is permitted which does not  
comply with these terms.

# Deep learning-based end-to-end automated stenosis classification and localization on catheter coronary angiography

Chao Cong<sup>1,2†</sup>, Yoko Kato<sup>1†</sup>, Henrique Doria De Vasconcellos<sup>1</sup>,  
Mohammad R. Ostovaneh<sup>1</sup>, Joao A. C. Lima<sup>1</sup> and  
Bharath Ambale-Venkatesh<sup>3\*</sup>

<sup>1</sup>Division of Cardiology, Johns Hopkins University, Baltimore, MD, United States, <sup>2</sup>School of Electrical and Electronic Engineering, Chongqing University of Technology, Chongqing, China, <sup>3</sup>Division of Radiology, Johns Hopkins University, Baltimore, MD, United States

**Background:** Automatic coronary angiography (CAG) assessment may help in faster screening and diagnosis of stenosis in patients with atherosclerotic disease. We aimed to provide an end-to-end workflow that separates cases with normal or mild stenoses from those with higher stenosis severities to facilitate safety screening of a large volume of the CAG images.

**Methods:** A deep learning-based end-to-end workflow was employed as follows: (1) Candidate frame selection from CAG videograms with Convolutional Neural Network (CNN) + Long Short Term Memory (LSTM) network, (2) Stenosis classification with Inception-v3 using 2 or 3 categories (<25%, >25%, and/or total occlusion) with and without redundancy training, and (3) Stenosis localization with two methods of class activation map (CAM) and anchor-based feature pyramid network (FPN). Overall 13,744 frames from 230 studies were used for the stenosis classification training and fourfold cross-validation for image-, artery-, and per-patient-level. For the stenosis localization training and fourfold cross-validation, 690 images with > 25% stenosis were used.

**Results:** Our model achieved an accuracy of 0.85, sensitivity of 0.96, and AUC of 0.86 in per-patient level stenosis classification. Redundancy training was effective to improve classification performance. Stenosis position localization was adequate with better quantitative results in anchor-based FPN model, achieving global-sensitivity for left coronary artery (LCA) and right coronary artery (RCA) of 0.68 and 0.70.

**Conclusion:** We demonstrated a fully automatic end-to-end deep learning-based workflow that eliminates the vessel extraction and segmentation step in coronary artery stenosis classification and localization on CAG images. This tool may be useful to facilitate safety screening in high-volume centers and in clinical trial settings.

## KEYWORDS

stenosis localization, stenosis classification, catheter coronary angiography, end-to-end workflow, deep learning, redundancy training

# Introduction

Coronary artery disease (CAD) is the leading cause of morbidity and mortality worldwide (1). X-ray coronary angiography (CAG) is the current gold standard imaging technique for CAD diagnosis. Expert CAG interpretation requires considerable “hands-on” training both visually and cognitively. In clinical practice and also for quality control purposes in research settings, screening CAG studies visually to distinguish cases with normal or mild stenosis from those with higher stenosis severity is a time-consuming process even for experienced readers. Developing an automatic CAG assessment tool to exclude normal or mild stenosis cases would facilitate diagnosis and treatment and enable the screening of large data sets for quality control purposes.

Recent studies confirmed the feasibility of using deep learning methods for CAG stenosis detection. Generally, the method consists of multiple steps. The most widely used vessel-based workflow starts from the visual or automatic selection of candidate frames (2–4) or regions (5, 6) from a CAG video. This is followed by the artery extraction using image segmentation algorithms (7) like center-tracking (8, 9), model-based (10), or Convolutional Neural Network (CNN) (11–15). Finally, individual stenotic lesion localization and classification is performed in two ways: patch-wise (16–18) and image-wise (2, 3, 6).

However, there are limitations in previous CAG stenosis classification and detection methods. One of the main drawbacks is that the vessel shape and characterization (19, 20) were not well exploited from a multi-view CAG study, causing a relatively low accuracy in detecting the stenotic lesions, especially in curved or bifurcation regions in the vascular tree (21, 22). Another limitation is that there are numerous pre-processing stages (manually or automatically) in some methods (15, 18, 23), such as detecting keyframes/region/views from a CAG sequence, or annotating segmentation for vessels, or preparing patches and labels for training procedure. The need for extensive human interaction during image data and training label preparation, in addition to addressing problems of sampling imbalance during supervised-learning, has led to algorithms that are commonly evaluated on small datasets prone to overfitting (7). Clinically speaking, those studies generally aimed to differentiate significant stenosis from non-significant stenosis in CAG images while developing a tool to facilitate safety screening of a large volume of CAG images by separating cases with normal or mild stenoses from those with higher stenosis severities have not been targeted (24).

In this study, we propose a fully automatic, deep learning-based end-to-end CAG stenosis detection method to achieve efficient safety screening and precise localization of stenoses. Our method consists of following unique steps that (1) it eliminates the vessel extraction and segmentation step for supervised learning; (2) the CNN + LSTM structure is designed for automatic detection of candidate frames from CAG sequences to improve training efficiency and reduce overfitting; (3) a multi-view analyzing architecture is established to train CNNs for different angle-views and generate classification results in artery-level and patient-level; (4) the redundancy training strategy is proposed to eliminate the negative effect of background and unnecessary features in training; and (5) the unsupervised- and supervised-learning methods are explored to localize the coronary stenoses in CAG images, which includes an anchor-based feature pyramid network (FPN).

# Materials and methods

## Study population

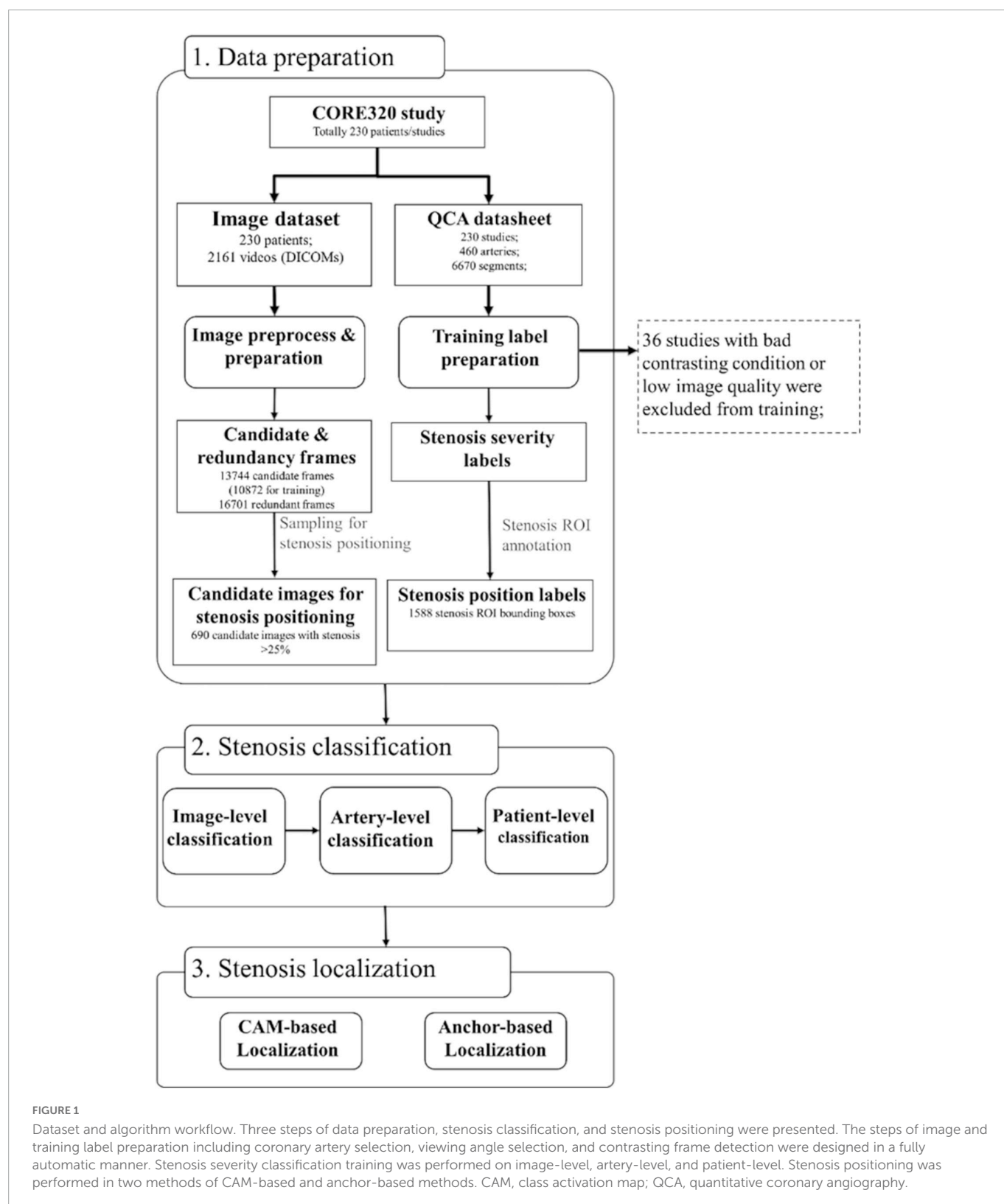
This research was retrospectively performed on 230 participants with available data from a “Combined Non-invasive Coronary Angiography and Myocardial Perfusion Imaging Using 320 Detector Computed Tomography (CORE320)” study (NCT00934037),<sup>1</sup> a prospective, multicenter, international study that assessed the performance of combined 320-row CTA and myocardial CT perfusion imaging (CTP) in comparison with the combination of invasive CAG and single-photon emission computed tomography myocardial perfusion imaging (SPECT-MPI) for detecting myocardial perfusion defects and luminal stenosis in patients with suspected CAD (25, 26). For the stenosis classification, 36 studies out of 230 were excluded from the training due to the low image quality or contrasting condition. These images, however, were included for evaluation. The original CORE320 study was approved by central and local institutional review boards, and written informed consent was obtained from all participants (25, 26). Given the retrospective and ancillary nature of the data, the current study is covered by the original CORE320 study IRB.

## Candidate frame selection

The entire study workflow is summarized in **Figure 1**. All the CAG studies were saved in the universal DICOM format with a resolution of  $512 \times 512$ , 15 fps, typically 60–200 frames per view. The detailed imaging parameters were summarized in **Supplementary Table 1**. Coronary type (left and right coronary artery, LCA, and RCA) was classified initially by experts in a small subset (19 patients). This was then leveraged by training an inception-V3 classifier (27) for automated coronary selection (100% classification accuracy was obtained). To identify the angle views of the CAG images, DICOM tags were used. Overall 4 angles for LCA [left anterior oblique (LAO) Cranial, LAO Caudal, right anterior oblique (RAO) Cranial, and RAO Caudal] and 3 angles for RCA (LAO, straight RAO, and shallow LAO/RAO Cranial) were used based on the optimal view map (OVM) (20).

A CNN + Long Short Term Memory (LSTM) network was implemented for the candidate frame selection from 19 patients (146 videos in total, and 18,688 frames overall). A candidate frame was defined as an image with good quality, full contrasting, clear vessel border, and anatomical significance of stenosis (if it had stenosis) in a video frame. Inception-v3 was employed as a basic classifier to recognize full-contrasting frames and non-contrasting frames as candidates or redundancy frames. Then, the fully connection layer of inception-v3 was output to a bi-directional LSTM with 32 time-steps (units), and also concatenated with the output of forward and backward LSTM units. The concatenation result was connected with a multi-layer perceptron (MLP, with one hidden layer) and a binary activation layer (sigmoid). The detailed structure of inception-v3 and LSTM is provided in **Supplementary Figure 1**. The inception model was initialized by ImageNet weights and then pre-trained for 200 epochs with the initial learning rate (LR) of  $1e^{-4}$  with the loss

<sup>1</sup> <https://clinicaltrials.gov/ct2/show/NCT00934037>



function as binary entropy. The LSTM was initialized using Xavier uniform method for kernels and orthogonal matrix for recurrent weights, then trained for 100 epochs with  $LR = 4e^{-5}$  with the loss function of convolutional F1 score. Typically, this strategy selected 5–10 candidate frames per video.

The performance of candidate frame detection was tested with 582 videos from 175 patients using mean error and standard

deviations of beginning contrasting frame (BCF) and ending contrasting frame (ECF) between ground-truth and prediction. The acceptance and error rates were also calculated with average differences of BCF and ECF in a pre-defined range (2), in which accept rate with the error  $\leq 3$  frames and error rate with the error  $\geq 10$  frames. Performance was reported using classification accuracy, F1, and Kappa.

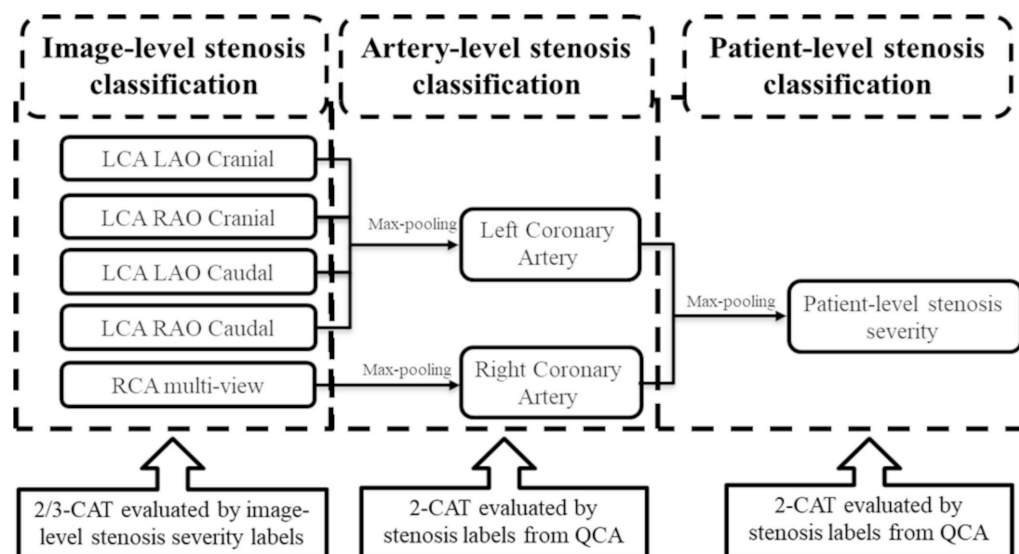


FIGURE 2

The architecture of the output of the stenosis classification inception model. A max-pooling layer was added to the output of inception to evaluate the artery-level stenosis prediction and the patient-level stenosis prediction. LCA, left coronary artery; LAO, left anterior oblique; RAO, right anterior oblique; RCA, right coronary artery; QCA, quantitative coronary angiography.

## Stenosis classification

For the stenosis classification, the quantitative coronary angiography (QCA) results previously documented per segmental level in the CORE320 study were utilized as a reference (25, 26, 28). In the current study, in order to accommodate with our study goals (separating cases with normal coronary arteries or mild stenoses from that with higher stenosis severities), coronary stenosis severities were re-categorized into the per-coronary artery, i.e., per LCA or RCA, and grouped into three categories of < 25%, 25–99%, and total occlusion in 3-categories (CAT), or two groups of < 25 and  $\geq$  25% in 2-CAT. It is known that there is a mismatch between the coronary stenosis severity and functional significance. Even the intermediate stenosis lesion can present functionally significant stenosis by fractional flow reserve (29, 30). Since we aimed to develop a safety screening tool for a large volume of the CAG images, we selected a stenosis threshold with high specificity to correctly separate cases that does and does not need further functional stenosis assessment.

Different CNN architectures of ResNet-50, ResNet-101, Inception-v3 and InceptionResNet-v2 were employed for the image-level stenosis classification training and prediction. And the inception-v3 was employed finally in image-level, artery- and patient-level stenosis prediction, since it has a good balance in transfer timing, parameter size and performance. The training was performed on 4 models of LCA for each angle view and one model of RCA combining the three angle views due to the complicated features of LCA when compared to the RCA (31).

The classification prediction of artery-level and patient-level was implemented by a multi-view analyzing architecture, as described in Figure 2. For artery-level prediction, CNN scores from 4, or, 3 angle-views were combined and fed into a max pooling layer to generate LCA/RCA classification results, respectively. Similarly, the patient-level prediction scores were generated by feeding LCA and RCA scores into another max pooling layer (Figure 2). For the image-level labeling, 2 or 3-CAT stenosis categories were assigned in each

angle view. For the artery-level labeling, 2-CAT stenosis categories were assigned in each coronary artery, i.e., in the LCA and the RCA. Overall 10,872 frames from 194 studies were used for image-level stenosis classification training and 13,744 frames from 230 studies were used for the fourfold cross-validation. The distribution of the cases in the image-, artery-, and patient-levels are summarized in Table 1. Performance of image-level classification on 3- CAT and 2- CAT with and without redundancy training was reported using accuracy, sensitivity, F1, Kappa, and area under the curve (AUC). Performance of artery-level and per-patient level classification was assessed on the 2-CAT with redundancy training image-level results and reported using accuracy, sensitivity, and AUC.

## Redundancy training

In the image-level stenosis classification training, the redundancy frames were accessorially added to the training dataset but not in the validation set. A redundancy frame was defined as a background frame without any contrasting agent in arteries. Thereafter, the redundancy categories were comprised of background frames with the roughly same amount of samples as the target categories in training dataset. Subsequently, there are 12,351 redundancy frames combined with 10,872 candidate frames in 3- and 2- CAT image-level training, namely redundancy training, as the similar methods used before (3, 32). It is expected that the use of redundancy frames can hedge against the invalid feature learning and reduce the train/test overfitting.

## Stenosis localization

For the stenosis positioning, two methods were investigated: (1) class activation map (CAM) (33) based on the back-propagation from the stenosis classification decision and (2) anchor-based FPN. The

TABLE 1 Distribution of the cases in each stenosis severity category used for the image view, artery, and patient-levels validation.

| Stenosis severity | Image level (LCA—LAO Cranial) | Image level (LCA—RAO Cranial) | Image level (LCA—LAO Caudal) | Image level (LCA—RAO Caudal) | Image level (RCA) | Coronary artery level (LCA) | Coronary artery level (RCA) | Per-patient level |
|-------------------|-------------------------------|-------------------------------|------------------------------|------------------------------|-------------------|-----------------------------|-----------------------------|-------------------|
| <25%              | 624 (32.7%)                   | 752 (33.0%)                   | 673 (43.8%)                  | 789 (34.7%)                  | 2,292 (39.9%)     | 57 (24.8%)                  | 84 (36.5%)                  | 46 (20.0%)        |
| 25–99%            | 1,123 (58.9%)                 | 1,393 (61.1%)                 | 673 (43.8%)                  | 1,333 (58.5%)                | 3,181 (55.4%)     | 132 (57.4%)                 | 118 (51.3%)                 | 127 (55.2%)       |
| 100%              | 160 (8.4%)                    | 135 (6.0%)                    | 189 (12.3%)                  | 155 (6.8%)                   | 272 (4.7%)        | 41 (17.8%)                  | 28 (12.2%)                  | 57 (24.8%)        |

Overall 13,744 frames from 230 studies were used for the image level validation. Each of the coronary artery level and per-patient level validations were performed on 230 cases. LCA, left coronary artery; LAO, left anterior oblique; RAO, right anterior oblique; RCA, right coronary artery.

anchor-based FPN model is developed from RetinaNet (34) and FPNs (35), using the pre-trained inception-V3 as backbone. The network structure is demonstrated as **Supplementary Figure 2**. The 1st, 2nd, and 3rd feature map in the pyramid were derived from the output of the concatenate feature before the 1st, 2nd, and 3rd pooling layer, respectively. The 4th and 5th feature maps were down sampled from the previous layers. For FPN inputs, 1,588 positioning boxes with a minimal size of  $35 \times 35$  pixels were annotated by two independent expert cardiologists. The shapes of anchor were preset by K-Means clustering method with seven different groups of height and width. The anchor-based model was trained with Learning Rate =  $1e^{-4}$  over 500 epochs. Then FPN was built on the feature maps of pre-trained classification models. The same reader-annotated bounding boxes were also used for the evaluation of the CAM-based localization technique. For the positioning training and fourfold evaluation, 690 frames with > 25% stenosis were used (**Figure 1**).

The performances of the two stenosis localization methods were assessed by the metrics of global-sensitivity, per-stenosis-sensitivity (Sens\_s), per-stenosis-specificity (Spec\_s), and mean square error (MSE). Global-sensitivity was defined as the recall of localization for the most significant stenosis in the images, which is similar to  $AR^{\wedge}(\max = 1)$  in COCO benchmark (21). Sens\_s and Spec\_s were defined as the recall rate of all stenosis localizations in the images. MSE was assessed in  $512 \times 512$  images for the CAM-based model and the anchor-based models. Due to the lower resolution, metrics for the CAM-based model were calculated with Intersection over Union (IoU) > 0.2 in the CAM-based model whereas IoU > 0.5 for the anchor-based model.

TABLE 2 Clinical characteristics of the study participants.

| Characteristic                            | Included (n = 230) |
|---|--------------------|
| Age (years)                               | 62 (55, 69)        |
| Age ≥ 60 years                            | 134 (58%)          |
| Male sex                                  | 160 (70%)          |
| Race                                      |                    |
| White                                     | 103 (45%)          |
| Black                                     | 18 (8%)            |
| Asian                                     | 105 (46%)          |
| Other                                     | 4 (2%)             |
| Body mass index (BMI, kg/m <sup>2</sup> ) | 26 (24, 29)        |
| Obesity (BMI ≥ 30 kg/m <sup>2</sup> )     | 51 (22%)           |
| Hypertension                              | 188 (82%)          |
| Diabetes mellitus                         | 80 (35%)           |
| Dyslipidemia                              | 159 (71%)          |
| Current smoker                            | 35 (16%)           |
| Family history of CAD                     | 88 (41%)           |
| Diamond-forrester risk score              |                    |
| Low                                       | 4 (2%)             |
| Intermediate                              | 164 (71%)          |
| High                                      | 62 (27%)           |
| Previous cerebrovascular accident         | 9 (4%)             |

A total of 230 individuals were included in our analysis. The median age was 62 years (IQR 55, 69), 70% were men, 45% were white, 82% had hypertension, 71% had dyslipidemia, 16% were current smokers, and 27% had a high pretest probability of obstructive coronary artery disease.

TABLE 3 The image-level stenosis classification performance for the 2-category and 3-category severity levels.

|         | 3-CAT (<25, 25–99, 100% stenosis) |             |             |             |      | 2-CAT (<25, >25% stenosis) |             |             |             |      |
|---------|-----------------------------------|-------------|-------------|-------------|------|----------------------------|-------------|-------------|-------------|------|
|         | Acc.                              | Sensitivity | F1          | $\kappa$    | AUC  | Acc.                       | Sensitivity | F1          | $\kappa$    | AUC  |
| LCA     | 0.71 ± 0.02                       | 0.78 ± 0.04 | 0.65 ± 0.05 | 0.50 ± 0.07 | 0.77 | 0.77 ± 0.01                | 0.90 ± 0.06 | 0.71 ± 0.06 | 0.46 ± 0.04 | 0.80 |
| LCA w/R | 0.70 ± 0.06                       | 0.72 ± 0.04 | 0.70 ± 0.06 | 0.44 ± 0.10 | 0.82 | 0.79 ± 0.02                | 0.89 ± 0.04 | 0.74 ± 0.07 | 0.51 ± 0.06 | 0.84 |
| RCA     | 0.83 ± 0.02                       | 0.82 ± 0.01 | 0.81 ± 0.04 | 0.70 ± 0.04 | 0.86 | 0.84 ± 0.01                | 0.92 ± 0.02 | 0.77 ± 0.01 | 0.56 ± 0.03 | 0.83 |
| RCA w/R | 0.77 ± 0.02                       | 0.81 ± 0.04 | 0.77 ± 0.03 | 0.59 ± 0.04 | 0.90 | 0.83 ± 0.01                | 0.90 ± 0.01 | 0.80 ± 0.03 | 0.63 ± 0.03 | 0.89 |

The classification performance with and without the redundancy training is presented. The performance of image-level stenosis classification results of LCA was reported as a combined result of four angles. Performance is assessed using accuracy, sensitivity, F1-score, kappa, and AUC.

LCA, left coronary artery; RCA, right coronary artery; LCA w/R, LCA with redundancy training; RCA w/R, RCA with redundancy training; Acc., accuracy; F1, weighted F1-score;  $\kappa$ , Cohen's Kappa; AUC, area under the curve.

## Statistical analysis

All the statistical evaluation was performed in Python (version 3.6; Python Software Foundation, Wilmington, Del).<sup>2</sup> In this study, the calculation for diagnostic performance was based on a per-patient approach, including image-level severity classification. Accuracy, f1-score, and Cohen's Kappa were calculated for image-level stenosis classification; receiver operating characteristic (ROC) analysis and areas under the curves (AUC) were used to further evaluate the image-/artery-/patient-level diagnostic performance. Stenosis positioning was evaluated by sensitivity, specificity, and MSE as described above. The CNN, LSTM, CAM, and anchor-based models were performed on TensorFlow (version 2.4.0), Python (version 3.6), and the Ubuntu system (version 20.04). All metrics were computed using Scikit-learn, version 0.19.1. Continuous variables that were normally distributed were summarized and reported as means  $\pm$  standard deviations.

## Results

### Patient characteristics

The study participants' characteristics are given in **Table 2**. A total of 230 individuals were included in our analysis. The median age was 62 years (IQR 55, 69), 70% were men, 45% were white, 82% had hypertension, 71% had dyslipidemia, 16% were current smokers, and 27% had a high pretest probability of obstructive CAD.

### Candidate frame selection

The automatic model achieved a mean error of 2.05 and 2.27 in BCF and ECF detection, respectively. The acceptance and error rates were 83% and 5.0%. A common feature of misclassified cases was a relatively short contrast duration in the video (typically < 5 frames with adequate vessel-to-background contrast). The network did not adequately handle this type of condition because the training dataset had very few instances of short-duration contrasting frames.

### Stenosis classification

The stenosis classification results in 3-CAT and 2-CAT with and without redundancy training models are summarized in **Table 3** and **Figure 3**. In brief, the image-level classification performance was better in 2-CAT than 3-CAT for the LCA while not significantly different for the RCA. The redundancy training improved the AUC values for both 2-CAT and 3-CAT, as well as the accuracy, F1-score, and kappa score in 2-CAT. Based on the better performance in 2-CAT as well as our aim to separate normal coronary/mild stenoses from higher severity of stenosis, 2-CAT evaluation was performed for artery-level (LCA and RCA) and patient-level classification. The accuracies were 0.83, 0.81, 0.85, the sensitivities were 0.94, 0.90, and 0.96 and AUCs were 0.87, 0.88, and 0.86 at the artery-level; LCA and RCA, and at the per-patient level, respectively. A representative image

<sup>2</sup> <https://www.python.org>

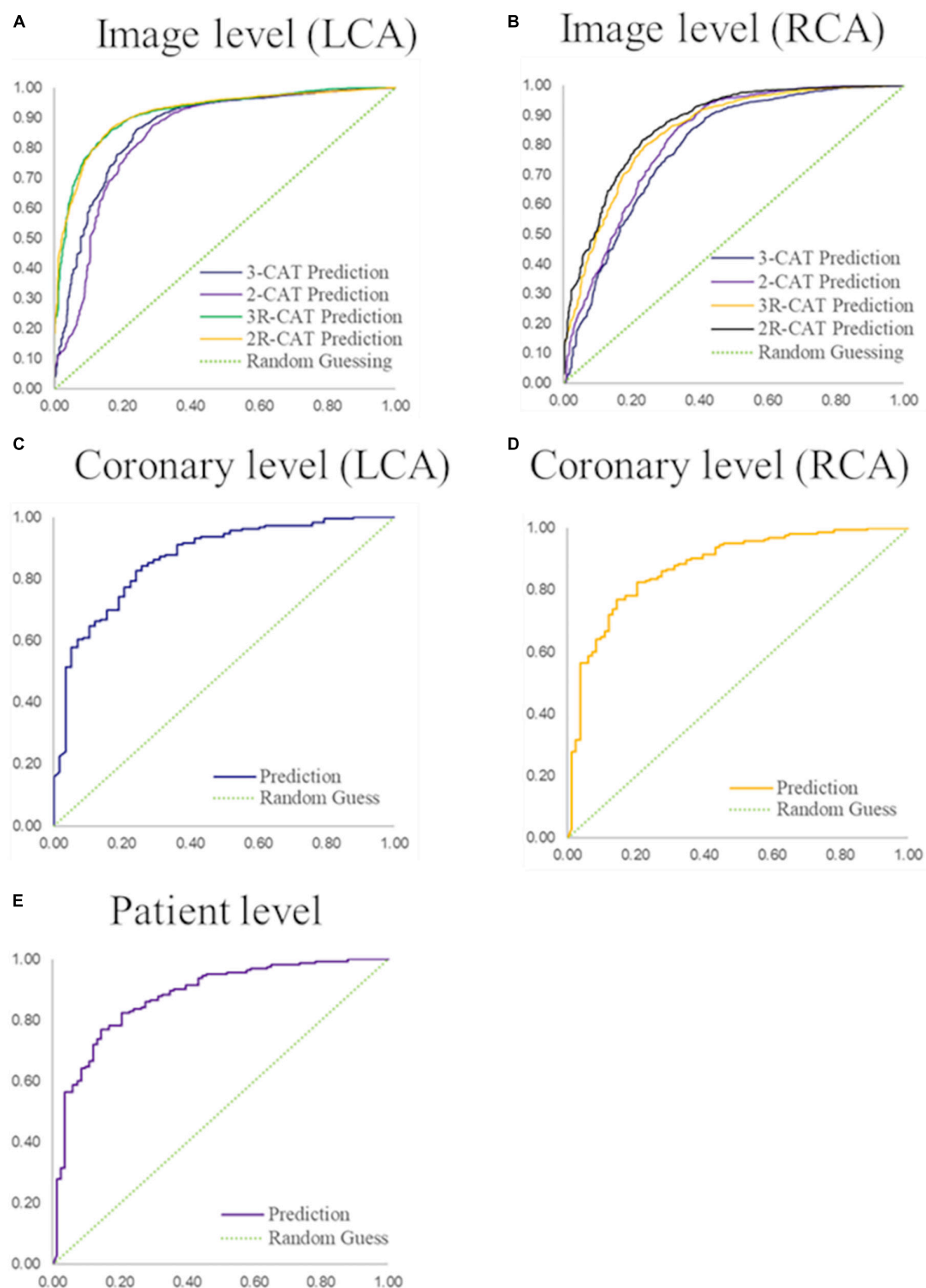


FIGURE 3

Performance of coronary stenosis classifications in image, coronary artery, and patient levels. (A,B) ROC curves of image-level classification on 3-CAT and 2-CAT with and without redundancy training on LCA and RCA. (C,D) ROC curves of coronary artery level classification on LCA and RCA. (E) ROC curve of patient-level classification. The AUC values are summarized in [Table 3](#). RCA, right coronary artery; LCA, left coronary artery; AUC, area under the curve.

illustrating the effect of the redundancy training is demonstrated in [Figure 4](#) with visualization aided by a heatmap. The overfitting caused by background structures is markedly reduced, likely resulting in the improvement in classification performance.

Additionally, the image-level classification performances of different CNN models of ResNet-50, ResNet-101, Inception-v3 and InceptionResNet-v2 were compared in [Table 4](#). The comparative result suggests that Inception-v3 is the most suitable one among all

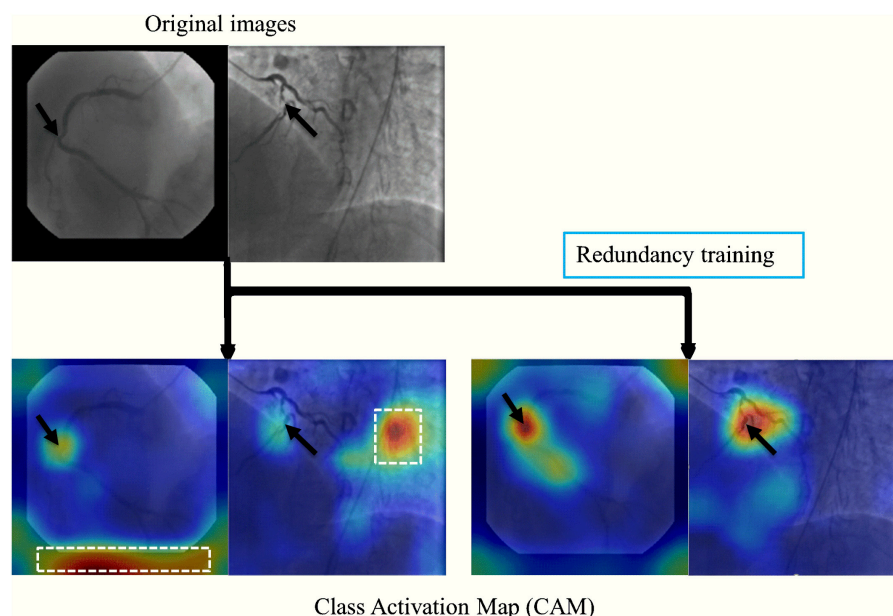


FIGURE 4

A representative image of the effect of the redundancy training demonstrated in a heatmap style. In the original training, the model had mid-to-high level attention on background regions. The redundancy training reduced the overfitting caused by background structures and improved the performance of stenosis classification.

four models, because of its fast inference speed, small size, and high accuracy in many tasks.

## Stenosis localization

Quantitative results were summarized in **Table 5**. In brief, the anchor-based FPN method showed better performance than the CAM-based method by all the metrics studied. Both the localization techniques performed better for RCA images than for LCA images. In both methods, Sensitivity was low due to the many annotations that highlighted small lesions that had ambiguous feature patterns in the arteries. Performance was also lower when there were multiple stenoses in distal coronary arteries or branches (see **Figure 5** for illustration).

## Discussion

In this study, we developed a CAG stenosis detection and localization tool to facilitate safety screening of a large volume of the CAG images. The main findings from the present study are summarized as follows: (1) the fully automatic, end-to-end workflow, which eliminated the vessel extraction and segmentation step for supervised-learning was developed; (2) the multi-view CAG analyzing architecture for artery- and patient-level stenosis classification, achieving an accuracy of 0.85, a sensitivity of 0.96 and an AUC of 0.86 at the per-patient level; (3) redundancy training improved classification performance, hedged against the invalid feature learning and reduced the error between the training and validation sets; (4) stenosis localization was investigated with two methods of CAM-based and anchor-based models, with superior quantitative results with the anchor-based models.

End-to-end workflow is advantageous in reducing human interaction steps. In our proposed workflow, once applied to the CAG videos, the model automatically selects the optimal frames, performs stenosis classification and localizes stenosis positions, providing robust results at both the artery and patient levels. Our workflow is advantageous in a large volume clinical setting or quality control purposes because the timely screening of many CAG videos to identify cases with normal or only mild stenoses consequences to secure more time on the cases with higher stenosis severities, which can translate into improved productivity and facilitated safety screening. Additionally, by providing stenosis classification and localization, the reader/physician can quickly focus on the lesion and perform quantitative CAG in an efficient manner.

The candidate frame selection performance presented here was better than previous publication by another group (4), likely due to the use of the bi-directional CNN + LSTM network to effectively extract high dimensional features of contrast flows from images, so that the network can effectively detect the changing trend in temporal sequences and find the contrast frames with higher accuracy than the RNN-only method (4). The stenosis classification results in the current study are encouraging that are comparable and sometimes outperforming when compared to the methods reported in previous studies; in which the image-based stenosis classification methods (5, 36) presented patient-level 2-CAT sensitivity of 0.80, 0.87; other three vessel- and patch-based studies (6, 9, 17) presented accuracies of 0.94, 0.97, and 0.92, respectively. We attribute our favorable results to addressing different aspects of a typical CAG study such as multiple angle views, background frames, and visually insignificant features of vessel stenoses through redundancy training to reduce overfitting in classification training.

Redundancy training is an effective tool for improving classification accuracy and reducing the error between the training and validation sets. In the original training, CNNs may be activated

TABLE 4 The comparative study of different CNN models in image-level stenosis classification performance.

| Method             | LCA w/R 3-CAT |      | RCA w/R 3-CAT |      | LCA w/R 2-CAT |      | RCA w/R 2-CAT |      | FLOPS   |  | Parameter memory |  | Inference time |
|--------------------|---------------|------|---------------|------|---------------|------|---------------|------|---------|--|------------------|--|----------------|
|                    | Acc.          | AUC  | Acc.          | AUC  | Acc.          | AUC  | Acc.          | AUC  |         |  |                  |  |                |
| Inception V3       | 0.73          | 0.82 | 0.79          | 0.90 | 0.81          | 0.84 | 0.84          | 0.89 | 5.72 G  |  | 91 M             |  | 13.93 ms       |
| ResNet-50          | 0.67          | 0.76 | 0.64          | 0.75 | 0.76          | 0.80 | 0.71          | 0.64 | 3.87 G  |  | 98 M             |  | 12.30 ms       |
| ResNet-101         | 0.58          | 0.78 | 0.63          | 0.87 | 0.81          | 0.78 | 0.76          | 0.71 | 7.6 G   |  | 170 M            |  | 15.33 ms       |
| Inception ResNetV2 | 0.75          | 0.83 | 0.80          | 0.92 | 0.80          | 0.83 | 0.82          | 0.88 | 13.18 G |  | 214 M            |  | 18.16 ms       |

The comparative study of different CNN models is presented by the performance of image-level stenosis classification. Performance is assessed using accuracy (Acc.) and AUC (> 25% stenosis vs. < 25% stenosis). The metrics of floating-point operations (FLOPS), parameter memory (unit: byte) are referred from the following website: <https://github.com/Coderx7/SimpleNet>. Acc., accuracy; LCA w/R 3-CAT, LCA with redundancy training in three category classification; RCA w/R 3-CAT, RCA with redundancy training in three category classification; LCA w/R 2-CAT, LCA with redundancy training in two category classification; RCA w/R 2-CAT, RCA with redundancy training in two category classification; AUC, area under the curve; FLOPS, floating-point Operations.

by invalid features such as image background and artifacts, which can be visualized from CAM heatmap. Comparatively, the redundancy frames were introduced as new categories in redundancy training, therefore the stenosis features were more activated on effective features such as vessel morphology, intensity change and narrow characteristics.

The comparison between 2-CAT and 3-CAT classification implies extra characteristics in stenoses analyzing. From the experimental result, the image-level classification performance is better in 2-CAT than 3-CAT for the LCA (accuracy = 0.77 vs. 0.71) while not significantly different for the RCA (accuracy = 0.84 vs. 0.83). One possible reason is that LCA anatomy presents itself with more variation than RCA (31), causing adverse factors against the CNN models to detect vascular blockage and occlusion in 3-CAT classification. Another explanation is that there are slightly imbalanced category distributions in 3-CAT classification than in 2-CAT, resulting in reduced accuracy (in LCA) and sensitivities (both in LCA and RCA).

Our study also explores a solution to the stenosis localization problem *via* an object detection framework. Two different stenosis localization methods of CAM and FPN were compared. The CAM-based model has the strength of employing a simple derivation that uses stenosis classification as a backbone model. However, as the activation map should be calculated by feature maps in deep layers from CNNs, CAM method is unfavorable for fine-grained and multiple object detection, such as small blood vessel stenoses in the same CAG image. In contrast, anchor-based model showed a better performance for stenosis positioning, since the different scales of features can be well exploited by feature pyramid structure. The trade-off is that the additional annotations and supervised-learning procedure were necessary for training the anchor-based model. Additionally, the comparison of the stenosis localization performances between RCA and LCA also support our viewpoint that the complexity of morphology and structure of angiographic vessels may be a severely adverse factor to the accuracy of the algorithms (classification and localization). In LCA angle views, two main arteries (LAD and LCX) may interlap on the 2-dimensional CAG image and twist with each other, raising difficulties in stenosis visualization. In some cases, there are multiple lesions in separate vessels or segments in LCA (such as second diagonal, second obtuse marginal or posterolateral), with vague and insignificant visual characteristics. By comparison, RCA has clearer vessel shapes and simpler morphologic characteristics so that more significant stenosis features. Therefore, all the above factors lead to better localization performances with both methods for RCA than for LCA.

Future work will aim at the following aspects. (1) We could perform an external validation in different studies as a means to generalize our technique and further improve performance. We believe that the proposed method will achieve good results with new images. Considering that the new dataset may have different imaging parameters (angle views, phase intervals, and FOVs), we may have to adjust the image pre-processing algorithm to accommodate the new images. Furthermore, transfer learning in a small subset could also improve performance. (2) Application in a variety of clinical or investigative scenarios beyond safety screening with different clinical goals such as fine-grained stenosis classification/localization.

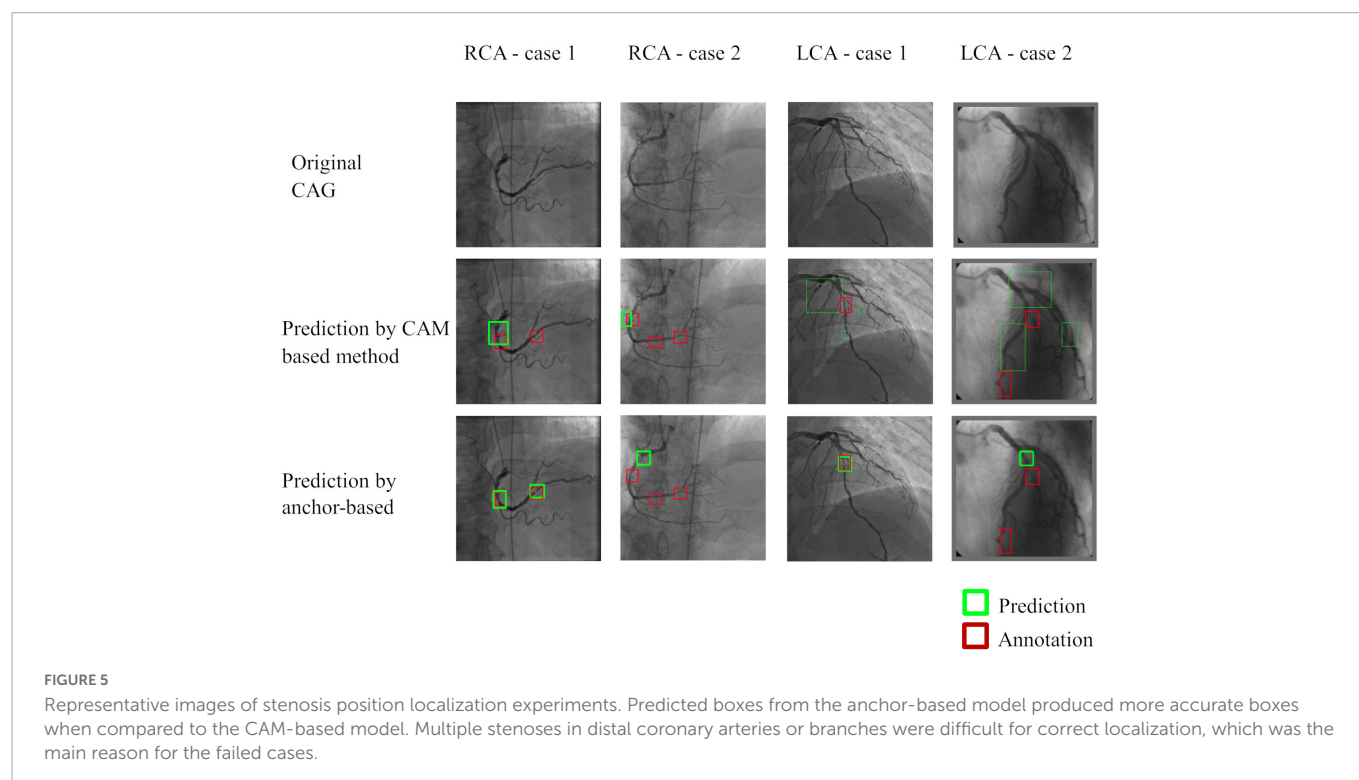
Our study had a few important limitations. Training and evaluation were performed in the same cohort. A validation

**TABLE 5** Performance of the stenosis localization algorithms for the LCA and RCA.

|     | CAM-based          |                   |                   |                 | Anchor-based       |                   |                   |                 |
|-----|--------------------|-------------------|-------------------|-----------------|--------------------|-------------------|-------------------|-----------------|
|     | Global-sensitivity | Sens <sub>s</sub> | Spec <sub>s</sub> | MSE (deviation) | Global-sensitivity | Sens <sub>s</sub> | Spec <sub>s</sub> | MSE (deviation) |
| LCA | 0.59               | 0.25              | 0.43              | 103.3 (71.18)   | 0.68               | 0.44              | 0.68              | 39.3 (40.00)    |
| RCA | 0.61               | 0.17              | 0.51              | 79.5 (47.21)    | 0.70               | 0.51              | 0.77              | 37.6 (51.63)    |

Results are presented as the global sensitivity, sensitivity, specificity, and MSE for the two techniques presented—the CAM-based model and the anchor-based model. Global-sensitivity was defined as the sensitivity of one most severe stenosis localization per image. Due to the low resolution, metrics (Sens, Sens<sub>s</sub>, Spec<sub>s</sub>) for the CAM-based model were calculated with IoU > 0.2 whereas the metrics for the anchor-based model were calculated with IoU > 0.5.

LCA, left coronary artery; RCA, right coronary artery; Sens<sub>s</sub>, per-stenosis sensitivity; Spec<sub>s</sub>, per-stenosis specificity; MSE, mean square error; CAM, class activation map; IoU, intersection over union.



study using an external cohort is needed to accurately assess the performance of our techniques. Stenosis classification was simply categorized into three groups of < 25, 25–99%, and total occlusion for 3-CAT while < 25 and 25–100% stenosis for 2-CAT. Our aim was to develop a tool that identifies normal and mild stenosis cases within a large cohort. In this regard, more granular categories for mild to moderate stenosis may be considered for different clinical or investigational purposes, such as the detection of hemodynamically significant stenosis.

## Conclusion

In conclusion, a fully automatic end-to-end deep learning-based workflow for CAG images that eliminates the vessel extraction and segmentation step was accomplished. Our redundancy-based algorithm showed high accuracy for stenosis classification, and accurate localization was achieved by an anchor-based model. This end-to-end approach may facilitate safety screening in high-volume centers and in clinical trial settings.

## Data availability statement

The raw data supporting the conclusions of this article will be made available by the authors, without undue reservation.

## Ethics statement

The studies involving human participants were reviewed and approved by the Johns Hopkins Institutional Review Board. The patients/participants provided their written informed consent to participate in this study.

## Author contributions

CC and YK contributed to conception and design of the study, data analysis, manuscript drafting, and revisions. HV, MO, JL, and BA-V participated in the design and coordination of the study as well as manuscript revisions. All authors have read and approved the final manuscript.

# Funding

This study was supported by Master Research Agreement 09–115 and Artificial Intelligence Health Information Exchange (AIHEX).

# Conflict of interest

JL reported receipt of grant support from Canon Medical Systems.

The remaining authors declare that the research was conducted in the absence of any commercial or financial relationships that could be construed as a potential conflict of interest.

# Publisher's note

All claims expressed in this article are solely those of the authors and do not necessarily represent those of their affiliated organizations, or those of the publisher, the editors and the reviewers. Any product that may be evaluated in this article, or claim that may

be made by its manufacturer, is not guaranteed or endorsed by the publisher.

# Supplementary material

The Supplementary Material for this article can be found online at: <https://www.frontiersin.org/articles/10.3389/fcvm.2023.944135/full#supplementary-material>

## SUPPLEMENTARY FIGURE 1

The detailed structure of inception-v3 and LSTM. Inception-v3 was employed as a basic classifier to recognize full-contrasting frames and non-contrasting frames as candidates or redundancy frames. Then, the fully connection layer of inception-v3 was output to a bi-directional LSTM with 32 time-steps (units), and also concatenated with the output of forward and backward LSTM units. The concatenation result was connected with a multi-layer perception (MLP, with one hidden layer) and a binary activation layer (sigmoid).

## SUPPLEMENTARY FIGURE 2

The architecture of the anchor-based feature pyramid network for stenosis localization. The 1st, 2nd, and 3rd feature map in the pyramid were derived from the output of the concatenate feature before the 1st, 2nd, and 3rd pooling layer, respectively. The 4th and 5th feature maps were down sampled from the previous layers. The shapes of anchor were preset by K-Means clustering method with seven different groups of height and width.

# References

1. Tsao C, Aday A, Almarzooq Z, Alonso A, Beaton A, Bittencourt M, et al. Heart disease and stroke statistics—2022 update: a report from the American heart association. *Circulation*. (2022) 145:e153–639. doi: 10.1161/CIR.0000000000001052
2. Pang K, Ai D, Fang H, Fan J, Song H, Yang J. Stenosis-dtnet: sequence consistency-based stenosis detection for X-Ray coronary angiography. *Comput Med Imaging Grap*. (2021) 89:101900. doi: 10.1016/j.compmedimag.2021.101900
3. Cong C, Kato Y, Vasconcellos H, Lima J, Venkatesh B editors. *Automated stenosis detection and classification in x-ray angiography using deep neural network*. 2019 IEEE international conference on bioinformatics and biomedicine (BIBM). Piscataway, NJ: IEEE (2019).
4. Ma H, Ambrosini P, van Walsum T editors. s. Fast Prospective Detection of Contrast Inflow in X-Ray Angiograms with Convolutional Neural Network and Recurrent Neural Network. *International conference on medical image computing and computer-assisted intervention*. Berlin: Springer (2017).
5. Wu W, Zhang J, Xie H, Zhao Y, Zhang S, Gu L. Automatic detection of coronary artery stenosis by convolutional neural network with temporal constraint. *Comput Biol Med*. (2020) 118:103657. doi: 10.1016/j.compbiomed.2020.103657
6. Moon J, Cha W, Chung M, Lee K, Cho B, Choi J. Automatic stenosis recognition from coronary angiography using convolutional neural networks. *Comput Methods Programs Biomed*. (2021) 198:105819. doi: 10.1016/j.cmpb.2020.105819
7. Moccia S, De Momi E, El Hadji S, Mattos L. Blood vessel segmentation algorithms — review of methods, datasets and evaluation metrics. *Comput Methods Programs Biomed*. (2018) 158:71–91. doi: 10.1016/j.cmpb.2018.02.001
8. Compas C, Syeda-Mahmood T, McNeillie P, Beymer D editors. Automatic Detection of Coronary Stenosis in X-Ray Angiography through Spatio-Temporal Tracking. 2014 IEEE 11th international symposium on biomedical imaging (ISBI). Piscataway, NJ: IEEE (2014).
9. Wan T, Feng H, Tong C, Li D, Qin Z. Automated identification and grading of coronary artery stenoses with X-Ray angiography. *Comput Methods Programs Biomed*. (2018) 167:13–22. doi: 10.1016/j.cmpb.2018.10.013
10. Hernandez-Vela A, Gatta C, Escalera S, Igual L, Martin-Yuste V, Sabate M, et al. Accurate coronary centerline extraction, caliber estimation, and catheter detection in angiographies. *IEEE Trans Inform Technol Biomed*. (2012) 16:1332–40. doi: 10.1109/TITB.2012.2220781
11. Yang S, Kweon J, Roh J, Lee J, Kang H, Park L, et al. Deep learning segmentation of major vessels in X-Ray coronary angiography. *Sci Rep*. (2019) 9:16897. doi: 10.1038/s41598-019-53254-7
12. Nasr-Esfahani E, Samavi S, Karimi N, Soroushmehr S, Ward K, Jafari M, et al. editors. Vessel Extraction in X-Ray Angiograms Using Deep Learning. 2016 38th Annual international conference of the IEEE engineering in medicine and biology society (EMBC). Piscataway, NJ: IEEE (2016).
13. Nasr-Esfahani E, Karimi N, Jafari M, Soroushmehr S, Samavi S, Nallamothu B, et al. Segmentation of vessels in angiograms using convolutional neural networks. *Biomed Signal Processing Control*. (2018) 40:240–51. doi: 10.1016/j.bspc.2017.09.012
14. Jo K, Kweon J, Kim Y, Choi J. Segmentation of the main vessel of the left anterior descending artery using selective feature mapping in coronary angiography. *IEEE Access*. (2019) 7:919–30. doi: 10.1109/ACCESS.2018.2886009
15. Liu Y, Zhang X, Wan W, Liu S, Liu Y, Liu H, et al. Two new stenosis detection methods of coronary angiograms. *Int J Comput Assisted Radiol Surgery*. (2022) 17:521–30. doi: 10.1007/s11548-021-02551-6
16. Antczak K, Liberadzki Ł editors. *Stenosis detection with deep convolutional neural networks*. MATEC web of conferences. Les Ulis: EDP Sciences (2018).
17. Ovalle-Magallanes E, Avina-Cervantes J, Cruz-Aceves I, Ruiz-Pinales J. Hybrid classical–quantum convolutional neural network for stenosis detection in X-Ray coronary angiography. *Expert Syst Appl*. (2022) 189:116112. doi: 10.1016/j.eswa.2021.116112
18. Ovalle-Magallanes E, Avina-Cervantes J, Cruz-Aceves I, Ruiz-Pinales J. Transfer learning for stenosis detection in X-Ray coronary angiography. *Mathematics*. (2020) 8:1510. doi: 10.3390/math8091510
19. Galassi F, Alkhalil M, Lee R, Martindale P, Kharbada R, Channon K, et al. 3d reconstruction of coronary arteries from 2d angiographic projections using non uniform rational basis splines (NURBS) for accurate modelling of coronary stenoses. *PLoS One*. (2018) 13:23. doi: 10.1371/journal.pone.0190650
20. Garcia J, Movassaghi B, Casserly I, Klein A, Chen S, Messenger J, et al. Determination of optimal viewing regions for x-ray coronary angiography based on a quantitative analysis of 3d reconstructed models. *Int J Cardiovasc Imaging*. (2009) 25:455–62. doi: 10.1007/s10554-008-9402-5
21. Rodriguez-Granillo G, García-García H, Wentzel J, Valgimigli M, Tsuchida K, van der Giessen W, et al. Plaque composition and its relationship with acknowledged shear stress patterns in coronary arteries. *J Am Coll Cardiol*. (2006) 47:884–5. doi: 10.1016/j.jacc.2005.11.027
22. Markl M, Wegent F, Zech T, Bauer S, Strecker C, Schumacher M, et al. In Vivo wall shear stress distribution in the carotid artery: effect of bifurcation geometry, internal carotid artery stenosis, and recanalization therapy. *Circulation*. (2010) 3:647–55. doi: 10.1161/CIRCIMAGING.110.958504
23. Nasr-Esfahani E, Samaivi S, Karimi N, Soroushmehr SMR, Ward K, Jafari MH. *Vessel extraction in X-Ray angiograms using deep learning*. Orlando, FL: IEEE (2016). doi: 10.1109/EMBC.2016.7590784
24. Ovalle-Magallanes E, Alvarado-Carrillo D, Avina-Cervantes J, Cruz-Aceves I, Ruiz-Pinales J, Correa R. Deep Learning-Based Coronary Stenosis Detection In x-Ray Angiography Images: Overview And future Trends. In: Lim C, Vaidya A, Chen Y, Jain V, Jain L editors. *Artificial intelligence and machine learning for healthcare: vol 2: emerging methodologies and trends*. Cham: Springer International Publishing (2023). p. 197–223.

25. Vavere A, Simon G, George R, Rochitte C, Arai A, Miller J, et al. Diagnostic performance of combined noninvasive coronary angiography and myocardial perfusion imaging using 320 row detector computed tomography: design and implementation of the core320 multicenter, multinational diagnostic study. *J Cardiovasc Comput Tomograp.* (2011) 5:370–81. doi: 10.1016/j.jcct.2011.11.001
26. Rochitte C, George R, Chen M, Arbab-Zadeh A, Dewey M, Miller J, et al. Computed tomography angiography and perfusion to assess coronary artery stenosis causing perfusion defects by single photon emission computed tomography: the core320 study. *Eur Heart J.* (2013) 35:1120–30. doi: 10.1093/eurheartj/ehd488
27. Szegedy C, Vanhoucke V, Ioffe S, Shlens J, Wojna Z editors. *Rethinking the inception architecture for computer vision.* Las Vegas, NV: IEEE (2016).
28. Alderman E, Stadius M. The angiographic definitions of the bypass angioplasty revascularization investigation. *Coronary Artery Dis.* (1992) 3:1189–208.
29. Park S, Kang S, Ahn J, Shim E, Kim Y, Yun S, et al. Visual-functional mismatch between coronary angiography and fractional flow reserve. *JACC.* (2012) 5:1029–36. doi: 10.1016/j.jcin.2012.07.007
30. Johnson N, Kirkeeide R, Gould K. Coronary anatomy to predict physiology. *Circulation.* (2013) 6:817–32. doi: 10.1161/CIRCIMAGING.113.000373
31. Singh S, Ajayi N, Lazarus L, Satyapal K. Anatomic study of the morphology of the right and left coronary arteries. *Folia Morphol.* (2017) 76:668–74. doi: 10.5603/FM.a2017.0043
32. Wang J, Wei J, Yang Z, Wang S. Feature selection by maximizing independent classification information. *IEEE Trans Knowl Data Eng.* (2017) 29:828–41. doi: 10.1109/TKDE.2017.2650906
33. Zhou B, Khosla A, Lapedriza A, Oliva A, Torralba A editors. Learning deep features for discriminative localization. *arXiv.* (2016). [Preprint]. doi: 10.48550/arXiv.1512.04150
34. Lin T, Goyal P, Girshick R, He K, Dollár P editors. *Focal loss for dense object detection. proceedings of the IEEE international conference on computer vision.* Piscataway, NJ: IEEE (2017).
35. Lin T, Dollár P, Girshick R, He K, Hariharan B, Belongie S editors. *Feature pyramid networks for object detection. proceedings of the IEEE conference on computer vision and pattern recognition.* San Juan, PR: IEEE (2017).
36. Zreik M, Hamersvelt RW, Wolterink JM, Leiner T, Viergever MA, Išgum I. A recurrent cnn for automatic detection and classification of coronary artery plaque and stenosis in coronary ct angiography. *IEEE Trans Med Imaging.* (2019) 38:1588–98. doi: 10.1109/TMI.2018.2883807

# Frontiers in Cardiovascular Medicine

Innovations and improvements in cardiovascular treatment and practice

Focuses on research that challenges the status quo of cardiovascular care, or facilitates the translation of advances into new therapies and diagnostic tools.

## Discover the latest Research Topics

[See more →](#)

### Frontiers

Avenue du Tribunal-Fédéral 34  
1005 Lausanne, Switzerland  
[frontiersin.org](https://frontiersin.org)

### Contact us

+41 (0)21 510 17 00  
[frontiersin.org/about/contact](https://frontiersin.org/about/contact)



### Frontiers in Cardiovascular Medicine

